

https://dspace.org/

Hot deformation, corrosion and oxidation behaviour of TiNbTaVW and CrNbTaVW refractory high entropy alloys for high-temperature applications

Bamisaye, Olufemi Sylvester

2024

University of the Witwatersrand, Johannesburg

https://hdl.handle.net/10539/47564

Bamisaye, Olufemi Sylvester . (2024). Hot deformation, corrosion and oxidation behaviour of TiNbTaVW and CrNbTaVW refractory high entropy alloys for high-temperature applications [PhD thesis, University of the Witwatersrand, Johannesburg]. WIReDSpace. https://hdl.handle.net/10539/47564

Downloaded from a DSpace repository. https://dspace.org/



UNIVERSITY OF THE
WITWATERSRAND,
JOHANNESBURG

Hot deformation, corrosion and oxidation behaviour of TiNbTaVW and CrNbTaVW refractory high entropy alloys for high-temperature applications

Prepared by

Olufemi Sylvester Bamisaye

(2503285)

A thesis submitted to the School of Chemical and Metallurgical Engineering, Faculty of Engineering and the Built Environment, University of the Witwatersrand, Johannesburg, in fulfilment of the requirements for the degree of Doctor of Philosophy in Engineering

December, 2024

Declaration

- I am aware that plagiarism (the use of someone else's work without their permission and/or without acknowledging the original source) is wrong.
- I confirm that the work submitted for assessment for the above course is my own unaided work.
- I have followed the required conventions in referencing the thoughts and ideas of others.
- I understand that the University of the Witwatersrand may take disciplinary action against me if there is a belief that this is not my own unaided work or that I have failed to acknowledge the source of the ideas or words in my writing.

Student Name: Olufemi Sylvester Bamisaye

Student number: 2503285

Student signature: ……...

Abstract

The world's technological growth and development drive a persistent demand for new class of materials with excellent mechanical properties that surpass those of existing commercial materials used in high temperature structural applications. In search of this new class of material, refractory high entropy alloys (RHEAs), which comprise high-melting-point refractory elements are considered by researchers. In this study, two RHEAs (TiNbTaVW and CrNbTaVW) were developed and their structural, mechanical and performance properties were evaluated. The RHEAs were compared with commercial grade IN718 alloy. Thermo-Calc software with SSOL4 database was used to determine the phases present and the volume of the phases. Empirical calculations were also used to predict the phases and stability of the RHEAs. Thermo-Calc and empirical calculations accurately predicted the solid solution phases in the TiNbTaVW and CrNbTaVW. The RHEAs were produced by vacuum arc melting. The TiNbTaVW RHEA comprise of dendritic BCC solid solution structure, while the CrNbTaVW RHEA comprise dendritic structure with multiphases (BCC1, BCC2, and $Cr(VNb)_2$ C15-Laves). The TiNbTaVW and CrNbTaVW has higher hardness of 522±10 HV and 688±21 HV than the commercial IN718 alloy with 301±14 HV. The higher hardness of the RHEAs was attributed to the solid solution strengthening mechanism and second phase strengthening. The corrosion behaviour of TiNbTaVW and CrNbTaVW was compared with the commercial IN718 alloy in 3.5 wt% NaCl solution and 1M H_2SO_4 solution. The TiNbTaVW and CrNbTaVW had superior corrosion resistance as compared to commercial IN718 alloy in both 3.5 wt.% NaCl and 1M H_2SO_4 solutions. The corrosion rate of CrNbTaVW RHEA is lower than the TiNbTaVW RHEA and IN718 alloy in both 3.5 wt.% NaCl and 1M H_2SO_4 solutions. The oxidation behaviour of TiNbTaVW and CrNbTaVW were compared with the commercial IN718 alloy at 850°C and 1050°C for 15h. The IN718 has a superior oxidation resistance at 850°C and 1050°C than the TiNbTaVW and CrNbTaVW RHEAs. The hot deformation test was conducted only on the TiNbTaVW and IN718 because the CrNbTaVW disintegrated during loading at the jaws of the Gleeble machine. This disintegration could be attributed to stress concentrations that exist between the two BCC phases and the $Cr(VNb)_2$ Laves phase during loading. The TiNbTaVW and IN718 flow curves decreased with an increasing deformation temperature at a constant strain rate. Globular and elongated grains in the TiNbTaVW alloy at 950°C and 1000°C confirmed that dynamic globularisation and dynamic recovery are the softening mechanisms. At 1050°C, globular

grains indicated dynamic globularisation as the softening mechanism. In IN718, equiaxed and elongated grains at 950°C and 1050°C suggested both dynamic recrystallisation and dynamic recovery as the softening mechanisms. At 1000°C, the dominance of equiaxed grains signified dynamic recrystallisation as the only softening mechanism. The TiNbTaVW RHEA has higher temperature strengths of 910 MPa, 870 MPa, and 658 MPa, compared to the IN718 alloy, with 72 MPa, 87 MPa, and 61 MPa at 950°C/10^{-3} s^{-1}, 1000°C/10^{-3} s^{-1}, and 1050°C/10^{-3} s^{-1}, respectively. The higher temperature strength of the TiNbTaVW RHEA can be attributed to both solid solution strengthening and grain boundary strengthening. The TiNbTaVW and CrNbTaVW RHEAs have superior hardness, corrosion resistance and high temperature strength than the IN718 alloy. However, the IN718 alloy has better oxidation resistance than TiNbTaVW and CrNbTaVW. Improving the oxidation resistance of the RHEAs is important for establishing them as leading high-temperature materials. Achieving a balance between the high-temperature properties of RHEAs could develop their application in high-temperature environments, offering more material options for advanced engineering.

Keywords: Refractory high entropy alloy; Structural applications, Softening mechanism; High-temperature oxidation; Corrosion behaviour.

Dedication

This work is dedicated to researchers (living and dead) who has contributed knowledge to the advancement of high temperature alloys.

Acknowledgements

An old Yoruba adage says “Gbogbo nkan ti o ba ti ni ibeere ni o ma ni opin.” Which means “Everything that has a beginning must have an end.”

- I am highly grateful for my supervisors: Prof. Nthabiseng Maledi, Prof. Michael Oluwatosin Bodunrin and the late Prof. Josias Van Der Merwe for their immense support, guidance, patience, advice, financial assistance, and incisive criticism of my work throughout my doctoral journey. To be fair, I am really grateful and it was a privilege to have been mentored under your tutelage.
- I would like to thank Miss Zaynab Cader and Mr Collen Makola for all the assistance and countless hours on SEM. Special thanks also goes to Miss Letta Ntuli for her assistance on XRD.
- I deeply appreciate Mr Rodney Gurney and Mr Hopewell Gumede for their assistance with cutting, drilling and machining of my samples. Their technical assistance has been highly helpful. I also appreciate other technical staff: Mr Shadrach Moqabolane, Miss Matshidiso Tsotetsi, and Mr Donald Mahole
- I deeply appreciate Dr Desmond Klenam for constant mentorship and countless hours of discussion on high entropy alloys.
- I would like to thank Dr Maria Ntsoaki Mathabathe of Council for Scientific and Industrial Research and Mr Stevens Magogo at the University of Pretoria for their advice during oxidation cross-section analysis.
- I deeply appreciate Dr Tunde Awosusi for his encouragement and linking me up with my supervisors. I will not fail to mention my friends: Tunde Lawal, Kolade Ajayi, Nicola Rundora, Dr Smarte Aniekwe, Dr Oreva Eterigho-Ikelegbe, Zaynab Carder, Dr Fabunmi Sanmi, Dr Darlington Ashiegbu, Iyanu Williams, and Iyanu Akinyemi.
- I would like to thank my parents Mr Simeon Bamisaye and Mrs Janet Bamisaye for their support and prayers. I deeply appreciate the financial assistance and support from my brother James Bamisaye. Special thanks go to my other siblings, Tope, Bisi, Bukola, Bimpe, and Bola for their prayers and support. I say thank you.
- I would like to thank the management of Air Force Institute of Technology, Kaduna for granting me study leave to achieve my dreams abroad. I say thank you.

Contributions from this study

Journal Articles

- **Olufemi Sylvester Bamisaye**, Nthabiseng Maledi, Josias Van der Merwe, Desmond Edem Primus Klenam, Michael Oluwatosin Bodunrin, Akeem Damilola Akinwekomi, A comprehensive review on the deformation behaviour of refractory high entropy alloys at elevated temperatures, Manufacturing Review. 10, 12 (2023) 008.
- **Olufemi Sylvester Bamisaye**, Nthabiseng Maledi, Josias Van der Merwe, Michael Oluwatosin Bodunrin, Microstructure, hardness, oxidation, and corrosion behaviour of TiNbTaVW refractory high entropy alloy in 3.5 wt% NaCl and 1 M H_2SO_4. Journal of Alloys and Compounds. 983 (2024) 173803.
- **Olufemi Sylvester Bamisaye**, Nthabiseng Maledi, Josias Van der Merwe, Michael Oluwatosin Bodunrin, Microstructure, hardness, oxidation, and corrosion behaviour of $Cr(VNb)_2$ Laves containing CrNbTaVW refractory high entropy alloy in 3.5 wt% NaCl and 1 M H_2SO_4. International Journal of Refractory Metals and Hard Materials. 121 (2024) 106661.
- **Olufemi Sylvester Bamisaye**, Nthabiseng Maledi, Josias Van der Merwe, Michael Oluwatosin Bodunrin, Flow behaviour and microstructure of hot-worked TiNbTaVW refractory high-entropy alloy. Advanced Engineering Materials. 2400538 (2024) 1-11.

Conference Proceedings

- **Olufemi Sylvester Bamisaye**, Nthabiseng Maledi, Josias Van der Merwe, Desmond Edem Primus Klenam, Michael Oluwatosin Bodunrin, Dominant softening mechanisms in hot worked refractory high entropy alloys: An overview, ARUA Centre of Excellence Materials, Energy and Nanotechnology Mini Conference, Johannesburg, South Africa, Book of Abstracts, p. 14, 19th August 2022.

Journal articles and conference proceedings from this PhD work are detailed in Appendix M.

Table of Contents

Declaration ..... **ii**
Abstract ..... **iii**
Dedication ..... **v**
Acknowledgements ..... **vi**
Contributions from this study ..... **vii**
Table of Contents ..... **viii**
List of Figures ..... **xiii**
List of Tables ..... **xx**
List of Abbreviations ..... **xxii**
Chapter 1: Introduction **1**
1.1 Background 1
1.2 Problem statement and justification of the research 4
1.3 Research questions 6
1.4 Research hypothesis 6
1.5 Research aim and objectives 6
1.6 Thesis structure 7
Chapter 2: Literature review **9**
2.1 Introduction 9
2.2 High entropy alloy 9
2.2.1 Core effects of high entropy alloy 10
2.2.2 Empirical rules for phase prediction in high entropy alloy 14
2.3 CALPHAD thermodynamic modelling 18
2.4 Alloy production method 19
2.4.1 Vacuum arc melting process 19
2.4.2 Vacuum induction melting process 20
2.4.3 Powder metallurgy 21
2.5 Refractory high entropy alloy 22
2.6 Bibliometric analysis on global research of RHEAs 23
2.7 Research on microstructure and hardness properties of RHEA 24
2.8 Hot deformation of metallic materials at elevated temperatures 29
2.8.1 Dynamic recovery process 30
2.8.2 Dynamic recrystallisation process 32

2.9 Stress-strain flow behaviour of RHEA during hot deformation 41
2.10 Microstructural evolution during hot deformation of RHEA 48
2.11 Unsafe deformation behaviour in hot deformed RHEA 53
2.12 Compressive strength of RHEA during hot deformation 55
2.13 Corrosion overview 60
2.13.1. Corrosion behaviour of refractory high entropy alloys in chloride solution 62
2.13.2. Corrosion behaviour of refractory high entropy alloys in acidic media 67
2.14 Oxidation overview 69
2.14.1 Oxidation kinetics equation 72
2.14.2 Oxidation behaviour of refractory high entropy alloy 73
2.15 Summary 81
2.16 Design considerations for developing proposed refractory high entropy alloys 82
Chapter 3: Experimental procedure 84
3.1 Introduction 84
3.2 Materials 84
3.3 Alloy design 84
3.3.1 Empirical phase calculation 84
3.3.2 Thermo-Calc modelling 85
3.4 Powder compaction 85
3.5 Alloys production 85
3.6 Alloy sample cutting 85
3.7 Metallographic preparation 86
3.7.1 Mounting 86
3.7.2 Grinding and polishing 86
3.7.3 Etching 86
3.8 Alloys characterisation 86
3.8.1 Optical microscopy 86
3.8.2 Scanning electron microscopy 87
3.8.3 X-ray diffraction analysis 87
3.9 Hardness measurements 87
3.10 Corrosion tests 87
3.11 Oxidation test 88
3.12 Hot compression testing 88
Chapter 4: Bibliometric analysis on arc-melted RHEAs 90

4.1 Introduction 90
4.2 Bibliometric analysis of global research on arc-melted RHEAs 90
4.3 Statistical and bibliometric analysis 91
4.4 Trend of scientific publication in arc-melted RHEA from 2010 to 2024 92
4.5 Publication per source for arc-melted RHEA 93
4.6 Analysis of co-authorship of researchers 94
4.7 Analysis of institutional and international co-authorship 95
4.9 Co-occurrence network of author keywords 103
4.10 Summary 105
Chapter 5: Phase prediction, microstructural analysis, and hardness properties 107
5.1 Empirical approaches to predict phases in TiNbTaVW and CrNbTaVW 107
5.2 Thermo-Calc modelling of TiNbTaVW and CrNbTaVW 108
5.3 Phase analysis of TiNbTaVW, CrNbTaVW and IN718 110
5.4 Microstructural analysis 112
5.4.1 Microstructure and composition analysis of TiNbTaVW, CrNbTaVW and IN718 112
5.4.2 EDX compositional analysis of TiNbTaVW, CrNbTaVW and IN718 114
5.5 Hardness of TiNbTaVW, CrNbTaVW and IN718 115
5.6 Discussion 116
5.6.1 TiNbTaVW and CrNbTaVW phase prediction 116
5.6.2 Hardness properties of TiNbTaVW and CrNbTaVW 118
5.7 Summary 119
Chapter 6: Electrochemical corrosion behaviour in chloride and acidic solution 121
6.1. Electrochemical corrosion behaviour in chloride solution 121
6.1.1 Open circuit potential measurement of TiNbTaVW, CrNbTaVW and IN718 in chloride solution 121
6.1.2Potentiodynamic polarisation measurement of TiNbTaVW, CrNbTaVW and IN718 in chloride solution 122
6.1.3 Microstructural observation of TiNbTaVW, CrNbTaVW and IN718 in chloride solution 123
6.2 Electrochemical corrosion behaviour in acidic solution 128
6.2.1 Open circuit potential measurement of TiNbTaVW, CrNbTaVW and IN718 in acidic solution 128
6.2.2 Potentiodynamic polarisation measurement of TiNbTaVW, CrNbTaVW and IN718 in acidic solution 129
6.2.3 Microstructural observation of TiNbTaVW, CrNbTaVW and IN718 in acidic

solution 130
6.3 **Discussion** 135
6.3.1 Corrosion resistance of TiNbTaVW, CrNbTaVW, and IN718 in 3.5 wt% NaCl and 1M H_2SO_4 solution 135
6.4 Summary 140
Chapter 7: Cyclic oxidation behaviour **143**
7.1 Oxidation analysis of TiNbTaVW, CrNbTaVW and IN718 143
7.1.1 Cyclic oxidation behaviour of TiNbTaVW, CrNbTaVW and IN718 143
7.2 Phase analysis, surface and cross-section morphologies of oxidised TiNbTaVW, CrNbTaVW and IN718 145
7.2.1 Phase analysis of oxidised TiNbTaVW, CrNbTaVW and IN718 145
7.2.2 Surface morphologies of oxidised TiNbTaVW, CrNbTaVW, and IN718 147
7.2.3 Cross-section analysis of oxidised TiNbTaVW, CrNbTaVW and IN718 151
7.3. Discussion 154
7.4 Summary 162
Chapter 8: Hot deformation behaviour of TiNbTaVW and IN718 ..... **164**
8.1 Analysis of flow stress of hot deformed TiNbTaVW and IN718 164
8.2 Microstructural evolution of hot deformed TiNbTaVW and IN718 165
8.3 Macrostructure of hot deformed TiNbTaVW and IN718 169
8.4 High temperature strength of TiNbTaVW and IN718 169
8.5. Discussion 172
8.5.1 Serrations and sudden stress drop phenomenon 172
8.5.2 Occurrence of dynamic recovery and recrystallisation 175
8.6 Summary 177
Chapter 9: Conclusions and recommendations **179**
9.1 Conclusions 179
9.2 Suggestions for future research work 186
References **189**
Appendix A: EDX of microstructural observation of TiNbTaVW in chloride solution 221
Appendix B: EDX of microstructural observation of CrNbTaVW in chloride solution 222
Appendix C: EDX of microstructural observation of IN718 in chloride solution 223
Appendix D: EDX of microstructural observation of TiNbTaVW in acidic solution 224
Appendix E: EDX of microstructural observation of CrNbTaVW in acidic solution 225

Appendix F: EDX of microstructural observation of IN718 in acidic solution 226
Appendix G: EDX of surface morphology of oxidised TiNbTaVW.....227
Appendix H: EDX of surface morphology of oxidised CrNbTaVW 229
Appendix I: EDX of surface morphology of oxidised IN718 231
Appendix J: EDX of cross-sectional morphology of oxidised TiNbTaVW.....233
Appendix K: EDX of cross-sectional morphology of oxidised CrNbTaVW 235
Appendix L: EDX of cross-sectional morphology of oxidised IN718.....236
Appendix M: Publications and conference proceedings 238

List of Figures

Figure 2.1: The entropy of mixing as a function of the number of elements in equimolar alloys in the completely disordered state (Yeh et al., 2007) 11
Figure 2.2: The various classifications of alloys according to their entropy of mixing (Yeh et al., 2007) 11
Figure 2.3: XRD patterns of binary to 7 element equiatomic alloys (Yeh et al., 2007) 12
Figure 2.4: Schematic diagram of the potential energy change during the migration of a Ni atom (Tsai & Yeh, 2014) 13
Figure 2.5: Vickers hardness of the $Al_xCoCrCuFeNi$ HEA system with different aluminum contents (Tong et al., 2005). 14
Figure 2.6: A descriptive diagram of the arc melting method (Alshataif et al., 2020) 20
Figure 2.7: Schematic diagram of the vacuum induction melting process (Alshataif et al., 2020) 21
Figure 2.8: Schematic diagram of the preparation of spark plasma sintering (Han et al., 2020). 22
Figure 2.9: SEM images of microstructures (a) $Ti_2VNbMoZr_1$, (b) $Ti_2VNbMoZr_{1.5}$, (c) $Ti_2VNbMoZr_2$, and (d) $Ti_2VNbMoZr_3$ RHEAs (Li et al., 2022) 26
Figure 2.10: SEM images of microstructures (a) HfMoNbTaTiVWZr (Gao et al., 2015), (b) CrNbTiZr (Senkov et al., 2013), and (c) CrNbTiVZr RHEAs (Senkov et al., 2013) 27
Figure 2.11: The four different stages of flow stress during hot deformation (Lin & Chen, 2011) 29
Figure 2.12: Stress-strain curves for metallic materials exhibiting DRV and DRX (Eleti, 2019) 30
Figure 2.13: Optical microstructures of deformed 42CrMo steel at 1050°C with strain rates of (a) 0.01 s^{-1}; (b) 0.1 s^{-1}; (c) 1 s^{-1}; (d) 10 s^{-1}; (e) 50 s^{-1} (Lin et al., 2008). 32
Figure 2.14: Microstructures of hot deformed 42CrMo steel under strain rate of 0.1 s^{-1} and temperatures of (a) 850°C; (b) 950°C; (c) 1050°C; (d) 1150°C (Lin et al., 2008). 35
Figure 2.15: The EBSD inverse pole figure (IPF) map of deformed as-cast $TiAlVNb_2$ (a) 10^{-2} s^{-1}/1000°C (b) 10^{-3} s^{-1}/1100°C (Bai et al., 2021) 38
Figure 2.16: Schematic graph showing CDRX by local lattice rotation (Huang & Logé, 2016). (a) Grain boundary sliding, leading to the stress concentrations at the triple points; (b) Boundary bulges formed by local migration; (c) Part sliding, and part dislocation motion,

leading to mantle formation; (d) Shear of bulges in mantle, leading to asymmetric bulges and local lattice rotation.....40
Figure 2.17: Schematic graph showing the nucleation of DDRX grain (Huang & Logé, 2016). (a) Boundary corrugation accompanied by the evolution of sub-boundaries. (b) Partial grain boundary sliding/shearing, leading to the development of inhomogeneous local strains. (c) Bulging of parts of a serrated grain boundary accompanied with the evolution of dislocation sub-boundaries or twinning, leading to the formation of a new DDRX grain.....40
Figure 2.18: (a) Sharp stress drop in hot deformed HfNbTaTiZr RHEA at 1000°C/10^{-3} s^{-1} and strain of 0.06 (Eleti et al., 2019). (b) Interrupted test on hot deformed HfNbTaTiZr RHEA at 1000°C/10^{-3} s^{-1} and a strain of 0.06 (Eleti et al., 2019). (c-e) Sharp stress drop in $Ti_2ZrHfV_{0.5}Ta_{0.2}$ RHEA at different strain rates (10^{-1}-10^{-3}) and temperatures (900-1000°C) (Li et al., 2022). (f) Stress-strain curve of the strain aging experiment on the $Ti_2ZrHfV_{0.5}Ta_{0.2}$ RHEA at 900°C/10^{-1} s^{-1} and a strain of ~0.1 (Li et al., 2022) 42
Figure 2.19: Flow stress curves of the $TiAlVNb_2$ RHEA at 1000–1200°C and 0.1 s^{-1}–0.001 s^{-1} (Bai et al., 2021).....43
Figure 2.20: The flow stress curves of Ni_3Al-based superalloy deformed at 1050-1250°C with strain rate of 0.1 s^{-1} (Wu et al., 2017) 44
Figure 2.21: Stress–strain curves at 800°C, 900°C, 1000°C, 1100°C, 1200°C with different strain rates: (a) 0.1 s^{-1}, (b) 0.01 s^{-1}, (c) 0.001 s^{-1} (Guo et al., 2016).....45
Figure 2.22: Serrated flows in deformed CrMoNbV RHEA at wide range of temperatures (Feng et al., 2021) 46
Figure 2.23: SEM images of the microstructure with 50% sample height reduction (a) NbTaTi deformed at 1000°C; (b) NbTaZr deformed at 1000°C (Senkov et al., 2021).....48
Figure 2.24: Microstructure of the MoNbHfZrTi RHEA after deformation at 900°C with different strain rates: (a) 0.1 s^{-1} (b) 0.01 s^{-1}, (c) 0.001 s^{-1} (Guo et al., 2016).....51
Figure 2.25: The inverse pole figure map of $TiAlVNb_2$ RHEA at 10^{-2} s^{-1}/1200°C (a) and 10^{-3} s^{-1}/1100°C (b) (Bai et al., 2021) 52
Figure 2.26: EBSD maps of HfNbTaTiZr RHEA hot compressed to 50% reduction at various temperatures and strain rates. Deformed at (a, b, c) 1000°C, (d) 1200°C (Eleti et al., 2019). 53
Figure 2.27: Crack propagation in hot compressed RHEAs at 800°C (a-e) and 1600°C (f): (a) Broken carbide and crack in TiNbTaZrHf based composite (Li et al., 2022). (b) Microcracks observed inside the silicides containing $HfNbTiVSi_{0.5}$ (Zhang et al., 2016). (c) Microcracks observed inside the deformed $Nb_{40}Ti_{25}Al_{15}V_{10}Ta_5Hf_3W_2$ (Pang et al., 2022). (d) Severe

cracks at grain boundaries of $W_{0.4}MoNb_xTaTi$ (Wei et al., 2021). (e) Fracture feature of river-like appearance for $ZrTiHfNbMo_{2.0}$ (Chen et al., 2018). (f) Cracks propagation in WReTaMo (Wei et al., 2021) 54
Figure 2.28: Surface morphology of RHEAs after potentiodynamic polarisation tests in chloride solution. (a) corrosion products formation in MoTaNbVTi RHEA (Poulia et al., 2019). (b) pits formation within dendrite regions and boundaries of ReTaWNbMo RHEA (Yan & Song, 2020). (c) huge pits and cracks formation in TiZrTaNbSn RHEA (Li et al., 2021). (d) pits formation of Zr_5Al_3 phase within the intergranular part of AlNbTiZrSi RHEA (Bi et al., 2023). (e) pitting formation and dissolution of Zr_5Al_3 phase of $AlNbTiZrSi_{1.0}$ RHEA (Bi et al., 2023). (f) dissolution and pits formation of HCP phase of $AlTiVCrCu_{0.4}$ RHEA (Liu et al., 2023).....65
Figure 2.29: surface morphology of RHEA after potentiodynamic polarisation in acidic solution. (a) uncorroded surface of TaNbHfZrTi RHEA in 11.5 M HNO_3 (Jayaraj et al., 2017); (b) corroded surface (flaky morphology) of TaNbHfZrTi RHEA in 11.5 M HNO_3 + 0.05 M NaF (Jayaraj et al., 2017); (c) open pits on the surface of $TiCrVNb_{0.5}Al_{0.5}$ (Li et al., 2021); (d) pits and dissolution of V-rich Sigma phase in the MoNbFeCrV RHEA (Xiang et al., 2019). 68
Figure 2.30: SEM cross-sectional micrographs of the oxide scales formed on the RHEAs at high temperatures. (a) pores formation at oxide scale of $AlNbTiVZr_{0.25}$ RHEA at 800°C (Yurchenko et al., 2018); (b) oxide scales buckling of TaMoCrTiAlSn RHEA at 1100°C (Müller et al., 2018); (c-e) pores and cracks within the oxide scales of CrMoNbTaV RHEA at 900°C, 1000°C and 1100°C (Xiao et al., 2019).....76
Figure 3.1: The experimental procedure for alloy development.....84
Figure 3.2: Hot deformation testing of the alloys with Gleeble machine 89
Figure 4.1: Schematic flow chart for bibliometric analysis of arc-melted RHEAs. 91
Figure 4.2: Annual scientific outputs arc-melted RHEAs. 92
Figure 4.3: Co-authorship clustering map of authors based on number of publications. 95
Figure 4.4: Co-occurrence network map of author keywords. 103
Figure 5.1: Phase proportions of TiNbTaVW RHEA.....109
Figure 5.2: Phase proportions of CrNbTaVW RHEA.....109
Figure 5.3: XRD pattern of the phase present in TiNbTaVW RHEA. 110
Figure: 5.4: XRD pattern of the phases present in CrNbTaVW RHEA. 111
Figure 5.5: XRD pattern of the phases present in IN718.....111

Figure 5.6: Optical and SEM-BSE Images of TiNbTaVW, CrNbTaVW and IN718. (a-b) Dendritic microstructures of TiNbTaVW at dendrite (white) and interdendrite region (grey); (c-d) Dendritic microstructures of CrNbTaVW showing BCC1 (white), BCC2 (grey), and $Cr(VNb)_2$ C15-Laves (dark); (e-f) Microstructures of IN718 alloy showing γ and γ'' structures. 113
Figure 5.7: Hardness values of TiNbTaVW, CrNbTaVW and IN718 116
Figure 6.1: OCP curves of TiNbTaVW, CrNbTaVW and IN718 in 3.5 wt% NaCl solution. 122
Figure 6.2: Potentiodynamic polarisation curves of TiNbTaVW, CrNbTaVW and IN718 in 3.5 wt% NaCl solution. 123
Figure 6.3: SEM image of the TiNbTaVW RHEA surface after exposure in 3.5 wt% NaCl (a); Higher magnification SEM image of the TiNbTaVW RHEA surface showing pits and corrosion products (b); SEM image of the CrNbTaVW RHEA surface after exposure in 3.5 wt% NaCl (c); Higher magnification SEM image of the CrNbTaVW RHEA surface showing pits and corrosion products (d); SEM image of the IN718 showing pits, corroded surface and corrosion products after exposure in 3.5 wt% NaCl (e). 125
Figure 6.4: XRD of corrosion products formed on the TiNbTaVW RHEA surface 127
Figure 6.5: XRD of corrosion products formed on the CrNbTaVW RHEA surface 127
Figure 6.6: XRD of corrosion products formed on the IN718 alloy surface 128
Figure 6.7: OCP curves of TiNbTaVW, CrNbTaVW and IN718 alloy in 1M H_2SO_4 129
Figure 6.8: Potentiodynamic polarisation curves of TiNbTaVW, CrNbTaVW and IN718 in 1M H_2SO_4 130
Figure 6.9: SEM image of the TiNbTaVW RHEA surface after exposure in 1M H_2SO_4 showing pits and corrosion products (a); SEM image of the CrNbTaVW RHEA surface after exposure in 1M H_2SO_4 showing pits and corrosion products (b); SEM image of the IN718 alloy after exposure in 1M H_2SO_4 showing pits and corroded surface (c). 131
Figure 6.10: XRD of corrosion products formed on the TiNbTaVW RHEA surface 133
Figure 6.11: XRD of corrosion products formed on the CrNbTaVW RHEA surface 134
Figure 6.12: XRD of corrosion products formed on the IN718 alloy surface 134
Figure 6.13: Schematic diagrams of the TiNbTaVW RHEA corrosion process during the potentiodynamic polarisation tests in 3.5 wt% NaCl (a); 1 M H_2SO_4 (b) 138

Figure 6.14: Schematic diagram of the pits of BCC1 phase in CrNbTaVW RHEA in 3.5 wt% NaCl solution (a-b); Schematic diagram of the pits of BCC1 phase and dissolution of $Cr(VNb)_2$ Laves phase in CrNbTaVW RHEA in 1 Mol H_2SO_4 solution (c-d). 139
Figure 6.15: Schematic diagram of the uniform corrosion and pits in IN718 alloy in 3.5 wt% NaCl solution (a); Schematic diagram of the uniform corrosion and pits in IN718 alloy in 1 Mol H_2SO_4 solution (b).....140
Figure 7.1: Cyclic oxidation curve of TiNbTaVW, CrNbTaVW and IN718 at 850°C 144
Figure 7.2: Cyclic oxidation curve of TiNbTaVW, CrNbTaVW and IN718 at 1050°C 144
Figure 7.3: XRD pattern of identified oxides in TiNbTaVW at 850°C.....145
Figure 7.4: XRD pattern of identified oxides in CrNbTaVW at 850°C 145
Figure 7.5: XRD pattern of identified oxides in IN718 at 850°C.....146
Figure 7.6: XRD pattern of identified oxides in TiNbTaVW at 1050°C.....146
Figure 7.7: XRD pattern of identified oxides in CrNbTaVW at 1050°C 147
Figure 7.8: XRD pattern of identified oxides in IN718 at 1050°C.....147
Figure 7.9: Surface morphology of TiNbTaVW RHEA showing cracks, pores, and spalled oxides at 850°C after 15 hours (a); Higher magnification of surface morphology of TiNbTaVW RHEA showing granular and rod-shaped oxides at 850°C after 15 hours (b)...148
Figure 7.10: Surface morphology of CrNbTaVW RHEA showing cracks, voids, pores, and spalled oxides at 850°C after 15 hours (a); Higher magnification of surface morphology of CrNbTaVW RHEA showing granular and rod-shaped oxides at 850°C after 15 hours (b). 149
Figure 7.11: Surface morphology of IN718 alloy showing compact structure at 850°C after 15 hours (a); Higher magnification of surface morphology of IN718 alloy showing round-shaped, cloudy-shaped, rod-shaped and block-shaped oxides at 850°C after 15 hours (b)...149
Figure 7.12: Surface morphology of TiNbTaVW RHEA showing crack and spalled oxides at 1050°C after 15 hours (a); Higher magnification of surface morphology of TiNbTaVW RHEA showing granular and rod-shaped oxides at 1050°C after 15 hours (b).....150
Figure 7.13: Surface morphology of CrNbTaVW RHEA showing spalled surface layer at 1050°C after 15 hours (a); Higher magnification of surface morphology of CrNbTaVW RHEA showing granular and rod-shaped oxides at 1050°C after 15 hours (b).....151
Figure 7.14: Surface morphology of IN718 alloy showing compact and refined structure at 1050°C after 15 hours (a); Higher magnification of surface morphology of IN718 alloy showing globular and block-shaped oxides at 1050°C after 15 hours (b). 151

Figure 7.15: Cross-sectional morphologies of the TiNbTaVW RHEA showing cracks and oxide scales at 850°C and 1050°C after 15 hours (a-b). 152
Figure 7.16: Cross-sectional morphologies of the CrNbTaVW RHEA showing cracks, voids, and oxide scales at 850°C and 1050°C after 15 hours (a-b). 153
Figure 7.17: Cross-sectional morphologies of IN718 alloy showing oxide scales at 850°C and 1050°C after 15 hours (a-b). 154
Figure 7.18: Schematic diagram of the oxidation mechanism of TiNbTaVW RHEA at 850°C and 1050°C after 15 hours (a-b). 161
Figure 7.19: Schematic diagram of the oxidation mechanism of CrNbTaVW RHEA at 850°C and 1050°C after 15 hours (a-b). 161
Figure 7.20: Schematic diagram of the oxidation mechanism of IN718 alloy at 850°C and 1050°C after 15 hours (a-b). 162
Figure 8.1: True stress-strain curves at 950°C to 1050°C and a strain rate of 10^{-3} s^{-1} for (a) TiNbTaVW and (b) IN718. 165
Figure 8.2: Optical micrograph and SEM-BSE image of TiNbTaVW after deformation at 950°C/10^{-3} s^{-1} showing globular grains (black arrows), elongated grains (blue arrows), and voids (red arrows) (a-b). Optical micrograph and SEM-BSE image of IN718 after deformation at 950°C/10^{-3} s^{-1} showing equiaxed grains (black arrows) and elongated grains (blue arrows) (c-d). 166
Figure 8.3: Optical micrograph and SEM-BSE image of TiNbTaVW after deformation at 1000°C/10^{-3} s^{-1} showing globular grains (black arrows), elongated grains (blue arrows), and voids (red arrows) (a-b). Optical micrograph and SEM-BSE image of IN718 after deformation at 1000°C/10^{-3} s^{-1} showing equiaxed grains (blue arrows) and globular grains (black arrows) (c-d). 167
Figure 8.4: Optical micrograph and SEM-BSE image of TiNbTaVW after deformation at 1050°C/10^{-3} s^{-1} showing globular grains (black arrows), elongated grains (blue arrows), and voids (red arrows) (a-b). Optical micrograph and SEM-BSE image of IN718 after deformation at 1050°C/10^{-3} s^{-1} showing equiaxed (black arrows), elongated recrystallised grains (blue arrows), and voids (red arrows) (a-b). 168
Figure 8.5: Stereo images of the TiNbTaVW and IN718 surface after deformation at 950°C to 1050°C/10^{-3} s^{-1} 169
Figure 8.6: High-temperature strength of TiNbTaVW and IN718 compared to superalloys (Amiri et al., 2013; Bibhanshu et al., 2020; Chen et al., 2023; Tang et al., 2021) and other

RHEAs (Chen et al., 2016; Han et al., 2017; Pang et al., 2022; Wang et al., 2021) at 950°C to 1050°C 170
Figure 8.7: Strain versus time profile at 950°C/10^{-3} for (a) TiNbTaVW and (b) IN718. Strain versus time profile at 1000°C/10^{-3} for (c)TiNbTaVW and (d) IN718. Strain versus time profile at 1050°C/10^{-3} for (e) TiNbTaVW and (f) IN718. 174

List of Tables

Table 2.1: Solid solution parameters.....18
Table 2.2: Summary of microstructure and hardness properties of single and multi-phase RHEAs. 28
Table 2.3: Summary of flow stress behaviour of hot deformed refractory high entropy alloys. 47
Table 2.4: Summary of compressive strength of hot deformed RHEAs. 58
Table 2.5a: Summary of oxidation behaviour of refractory high entropy alloys.....79
Table 2.5b: Summary of oxidation behaviour of refractory high entropy alloys 80
Table 3.1: Elemental mass required to produce 500 g of the RHEAs for arc-melting. 85
Table 4.1: Bibliometric analysis of the top research journals from 2010 to 2024. 93
Table 4.2: Analysis of institutional co-authorship. 96
Table 4.3: Publication analysis per country. 98
Table 4.4: Top 25 most-influential arc-melted RHEA articles. 100
Table 4.5: The most-influential as-cast RHEA articles in the past five years (2019-2024) ..101
Table 5.1: Physical properties of elements in TiNbTaVW and CrNbTaVW RHEAs (rsc.org), (Xiang et al., 2020) 107
Table 5.2: Enthalpy of mixing for TiNbTaVW and CrNbTaVW binary subsystem… 107
Table 5.3: Calculated empirical phase parameters.....108
Table 5.4: Crystallographic data of phases present in the TiNbTaVW, CrNbTaVW, IN718. 112
Table 5.5: Composition distribution of the TiNbTaVW RHEA 114
Table 5.6: Composition distribution of the CrNbTaVW RHEA… 114
Table 5.7: Composition distribution of the IN718 alloy 115
Table 6.1: Electrochemical parameters for TiNbTaVW, CrNbTaVW and IN718 in 3.5 wt% NaCl. 123
Table 6.2**:** EDX compositions of the TiNbTaVW, CrNbTaVW and IN718 after exposure in 3.5 wt% NaCl. 126
Table 6.3: Electrochemical parameters for TiNbTaVW, CrNbTaVW and IN718 in 1M H_2SO_4 130
Table 6.4: EDX composition of the TiNbTaVW, CrNbTaVW and IN718 alloy after potentiodynamic polarisation test in 1M H_2SO_4 132
Table 9.1: Comparison of the formability of TiNbTaVW and superalloys… 183

Table 9.2: Comparison of the hardness of TiNbTaVW, CrNbTaVW, superalloys and high temperature properties of TiNbTaVW and superalloys..... 184
Table 9.3: Comparison of the corrosion and oxidation properties of TiNbTaVW, CrNbTaVW and superalloys.....185

List of Abbreviations

HEA	High Entropy Alloy
BCC	Body Centered Cubic
FCC	Face Centered Cubic
HCP	Hexagonally Close Packed
RHEA	Refractory High Entropy Alloy
MCA	Multicomponent Alloy
CALPHAD	Calculation of Phase Diagram
TMP	Thermo-mechanical Processing
WH	Work Hardening
DRV	Dynamic Recovery
DRX	Dynamic Recrystallisation
SFE	Stacking Fault Energy
CDRX	Continuous Dynamic Recrystallisation
DDRX	Discontinuous Dynamic Recrystallisation
GBS	Grain Boundary Sliding
VEC	Valence Electron Concentration
PM	Powder Metallurgy
SPS	Spark Plasma Sintering
SRX	Static Recrystallisation
GB	Grain Boundary
HAGB	High Angle Grain Boundary
LAGB	Low Angle Grain Boundary
OCP	Open Circuit Potential
XRD	X-ray Diffraction
SEM	Scanning Electron Microscopy
EDX	Energy Dispersive Spectroscopy
BSE	Back Scattered Electron

Chapter 1
Introduction

1.1 Background

The world's technological growth and development drives a persistent demand for new materials with excellent mechanical properties, to fulfil several high temperature structural applications. Currently, advanced materials such as titanium alloys and nickel-based superalloys (i.e. Inconel 718 and Haynes 230) are some of the main commercially used alloys. However, these materials are already reaching their design limits as working temperatures approach their melting points (Reed, 2006). Turbine inlet temperature in advanced turbine engines is now approaching temperatures beyond 1200°C and superalloys can only operate at temperatures below 1150°C (Butler et al., 2022; Ouyang, 2017). For example, wrought Inconel 718 superalloy, with a high temperature yield strength of 85 MPa at 1050°C (Bambach et al., 2018) cannot withstand temperatures in the hottest sections of advanced gas engines turbine. Therefore, promising materials with high temperature mechanical properties beyond 1200°C are required.

In 2004, Cantor et al. (2004) and Yeh et al. (2004) proposed a novel design idea of alloys known as high entropy alloy (HEA). These new alloys were seen as potential structural materials for higher temperature applications. HEAs are different from other known engineering alloys because they comprise at least five main elements or multi-principal elements at near equiatomic percentages (Cantor et al., 2004; Yeh et al., 2004). HEAs with as few as three or four elements have been reported, with a maximum element concentration of more than 35 atomic percent (Bodunrin et al., 2017; Chen & Sutrisna, 2021; Lee & Cava, 2019; Sathiyamoorthi et al., 2018; Uporov et al., 2022). In addition, many HEAs now contain intermetallic compounds and complex phases, both of which have a major effect on the microstructures and properties of the materials (Jahangiri et al., 2023; Müller et al., 2020; Nong et al., 2018; Waseem et al., 2018; Yurchenko et al., 2018).

The tendency to occupy the unknown middle areas of complex composition space may promote novel alloys with improved property combinations (Cantor et al., 2004). The unique combination of properties existing among HEAs alloy include high strength, high hardness, good ductility, fatigue resistance, radiation resistance, oxidation, corrosion and wear resistance (Bi et al., 2023; Butler & Chaput, 2019; Gorr et al., 2017; Ivanov et al., 2021; Ji et al., 2022;

Miracle et al., 2014; Peng et al., 2023; Tsau & Wang, 2018; Xiao et al., 2020; Xu et al., 2023; Yan et al., 2022; Zemanate et al., 2023). These properties are founded on the idea that the high configurational entropies of mixing would stabilise solid-solution phases (Murty et al., 2014). Furthermore, high-entropy effect, cocktail effect, sluggish diffusion effect, and lattice distortion effect give the alloys their unique properties (Miracle & Senkov, 2017; Murty et al., 2014; Pickering & Jones, 2016).

The refractory high entropy alloy (RHEA) which comprise high-melting-point refractory elements were introduced in 2010 as potential candidates for higher temperature structural materials due to their high hardness, oxidation resistance, wear resistance, corrosion resistance, and high temperature strength above 1100°C (Senkov et al., 2010). These characteristics are due to their increased melting temperature and solid solution strengthening of the materials (Miracle & Senkov, 2017; Raman et al., 2021).

Alloying enhancement using elements such as Hf, Ti, Mo, Zr, Nb, Cr, V, and Re has been recently reported to increase RHEAs high temperature strength and ductility (Han et al., 2017; Tong et al., 2020; Wei et al., 2021; Yao et al., 2021; Yi et al., 2021). Wan et al. (2021) developed the WReTaMo alloy by replacing Nb with Re to achieve a yield strength of 172 MPa and plastic strain of 25% at 1600°C. Feng et al. (2021) developed the CrMoNbV alloy by addition of Cr to achieve a yield strength of 1062 MPa at 1000°C. Huang et al. (2020) developed Ti_xZrVNb by adding Ti to achieve a yield strength of 236 MPa and plastic strain of 50% at 1000°C. To design promising RHEAs other than the ones that are already reported in literature, there must be a balance among high temperature stability, oxidation, and corrosion properties (Miracle & Senkov, 2017).

Corrosion is the degradation of materials that occurs as a result of electrochemical reactions between the material and the environment (Shaw & Kelly, 2006; Song, 2014). The common environment service conditions for corrosion-resistant materials include chloride, acid, and pressurised high-temperature water. In materials design, elemental addition might affect the corrosion performance by altering the structure of the phase, multiphase and element segregation, reducing the passivity and nobility of the phases, and influencing the dissolution kinetics (Shi et al., 2017).

The RHEAs with high corrosion resistance contain large amounts of passivation promoting elements such as Ti, Zr, Cr, Mo, W and Hf which facilitate the formation of stable barrier films

(Gao et al., 2024; Jayaraj et al., 2017; Kang et al., 2023; Qiu et al., 2017, 2018; Yao et al., 2023; Yao et al., 2021). According to Zhou et al. (2019), superior passivity in RHEA is mostly attributed to the single-phase solid solution formation comprising a large quantity of passivity-promoting elements (Hf, Nb, Ta, Ti, Cr, Al and Zr). Also, the entropy stabilised single solid solution phase that is formed in HEAs can also contribute to the prevention of pitting corrosion, which would preferably occur at the phase boundaries where there are large composition variations (Shi et al., 2017).

Oxidation resistance is a vital property for alloys that are exposed to high temperatures for an extended period of time. In many applications, components experience cyclic oxidation that involve periodic start-up and shutdown at high temperatures (Young et al., 2008). The oxide scale may fail due to various external loads that may lead to cracking and spalling of the oxide scale and ultimately to exposure of the bare-metal surface (Moon & Lee, 1993).

Oxide scale spallation generally emanates through cracks and decohesion of the oxide interface or by fractures on planes around the primary oxide (Chan, 1997). The adhesion of the oxide layer to the material substrate depends on the thickness of the scale, its growth rate, the stress state, the interfacial energy, and the elastic properties of the oxide (Lekakh et al., 2023). Cracks are generally due to the volumetric expansion mismatch among the different oxides formed (Sheikh et al., 2020). The oxide scale compactness is described by the Pilling Bedworth ratio (PBR), which can be defined as the ratio of the oxide volume to the volume of the alloy from which the oxide forms. If the PBR<1, oxide scale is discontinuous and porous, when PBR>2, there is an internal stress between oxides and matrix that is high which leads to the formation of pores and cracks around oxides (Cao et al., 2019; Mevrel, 1986). The best protection of the oxide scale occurs when PBR is between 1 and 1.5, when the oxide scale is the densest (Cao et al., 2019).

Thermo-mechanical processing at higher temperatures is an effective method of simulating the fabrication process of RHEAs after casting (Eleti, 2019). The high-temperature properties of RHEAs such as flow behaviour, microstructural evolution, and softening mechanisms are important for determining optimum thermo-mechanical processing parameters (Dong et al., 2020; Guo et al., 2016; Liu et al., 2021; Wang et al., 2023). Studies on fundamental softening mechanisms of RHEAs are still limited (Eleti et al., 2019, 2020; Wang et al., 2023). Hence the optimum working conditions for making components from the proposed alloys are still limited.

Further research on the high temperature deformation will help to determine the optimum working parameters for RHEAs when they are produced in large volumes.

This research work explored the corrosion, oxidation, and hot deformation behaviour of TiNbTaVW and CrNbTaVW RHEAs in comparison with commercial IN718 alloy. The RHEAs were produced using the vacuum arc melting technique. High temperature compression tests were carried out to assess the flow behaviour, microstructural evolution, and high temperature strength of the TiNbTaVW and CrNbTaVW RHEAs. Corrosion performance of the TiNbTaVW and CrNbVTaW RHEAs were evaluated in aqueous chloride and sulphuric acid solutions. The oxidation behaviour of the RHEAs was also evaluated at high temperatures.

1.2 Problem statement and justification of the research

Achieving a balance between high-temperature strength, corrosion resistance, and oxidation resistance is essential for considering RHEAs as a potential replacement for superalloys. Unlike conventional alloys, RHEAs exhibit higher softening temperatures (0.6–0.8 T_m) (Butler et al., 2021; Senkov & Woodward, 2011). However, certain RHEAs, such as $HfNbTiVSi_{0.5}$, $ZrTiHfNb0.5Ta_{0.5}$, $TiAl_{20}VNbMo$, and HfNbTaTiZrW, demonstrate low-temperature strengths of 240 MPa, 112 MPa, 180 MPa, and 295 MPa at temperatures ≥ 1000°C, but with high ductility ≥ 35% (Zhang et al., 2016; Feng et al., 2021; Xu et al., 2019; Wang et al., 2019). The addition of elements such as Mo, Nb, Ta, Ti, Cr, and W help balance ductility, yield strength, and thermal stability. Multi-phase high-temperature strengthening is achieved by introducing phases such as carbides (e.g., Mo_2C and TaC) (Wu et al., 2021; Wei et al., 2021), and interstitial elements such as oxygen (Chen et al., 2018). Despite extensive research on high-temperature properties of RHEAs, most studies focus on strength and ductility, neglecting fundamental softening mechanisms such as dynamic recovery and dynamic recrystallisation that are essential for processability and large-scale manufacturing. This limits the understanding of optimal working conditions for RHEAs. There is a need to evaluate the influence of high temperatures and strain rates on flow stress, microstructural changes, and compressive strength, and to compare fundamental softening mechanisms between RHEAs and conventional alloys.

Corrosion is a common failure mode for metals, costing around 3% of the world's gross domestic product (Zhou et al., 2019). RHEAs with high corrosion resistance contain passivity-promoting elements such as Ti, Cr, Nb, and W, which form stable barrier films (Jayaraj et al.,

2017; Qiu et al., 2018; Xiang et al., 2019; Patel 2021). However, corrosion studies have shown pits and corroded surfaces in single-phase RHEAs such as ReTaWNbMo (Yan et al., 2020) and $TiCrVNb_{0.5}Al_{0.5}$ (Li et al., 2021) in chloride and acidic solutions. For the dual-phase RHEAs, phase dissolution and pits were observed in MoNbFeCrV (Xiang et al., 2019) and AlNbTiZr (Bi et al., 2023) in acidic and chloride solution. The reasons for these observations are not fully elucidated in the literature. Furthermore, corrosion studies on dual-phase and multi-phase RHEA containing C15_Laves phase in chloride and acidic solution have not been reported so far. Understanding elemental segregation, interface defects, and composition differences in passive films of RHEAs is crucial for improving corrosion resistance in both chloride and acidic environments.

Oxide scales may fail due to external loads, leading to cracking, spalling, and exposure of the metal surface (Moon & Lee, 1993). Cyclic oxidation is more complex than isothermal oxidation due to spalling during cooling (Moon & Lee, 1993). Most RHEA oxidation studies have been conducted under isothermal conditions (Butler & Chaput, 2019; Liu et al., 2014; Senkov et al., 2012; Su et al., 2023), limiting the understanding of spallation behaviour and oxide scale compactness at high temperatures. Research on the effects of high temperatures on oxidation performance of RHEAs is necessary for their design and development for high-temperature environments.

This research involved producing RHEAs using Ti, Cr, Nb, V, Ta, and W via arc-melting, demonstrating properties like hardness, high-temperature strength, oxidation and corrosion resistance. The combination of these elements would induce lattice distortion and second-phase hardening, thereby enhancing hardness (Coury et al., 2018; Wu et al., 2021; Xu et al., 2023). Elements like Cr, Ti, and Ta form oxides of $CrTaO_4$, Cr_2O_3, TiO_2 and $TiTaO_4$ (Butler et al., 2017; Du et al., 2022; Lo et al., 2019; Xiao et al., 2019) that act as barriers against oxidation, while Ti, Cr, Nb, W, and Ta reduce phase dissolution rates and promote passivation, enhancing corrosion resistance (Nyby et al., 2021; Patel et al., 2021; Wang et al., 2022). V protects RHEAs from localised corrosion, such as pitting, in NaCl and H_2SO_4 solutions (Li et al., 2014; Kumar et al., 2018). The addition of high-melting-point elements ensures thermal stability and maintains high-temperature resistance, making them crucial in RHEA design (Wang et al., 2019; Zheng et al., 2022).

1.3 Research questions

a. What is the trend of research outputs based on RHEAs produced by vacuum arc melting technique?
b. What is the influence of compositions on the microstructure and hardness of the TiNbTaVW and CrNbTaVW RHEAs?
c. What are the effects of 3.5 wt% NaCl and 1 Mol H_2SO_4 solutions on the corrosion performance of TiNbTaVW and CrNbTaVW RHEAs compared to the IN718 alloy?
d. What are the effects of high temperatures and varying exposure times on the oxidation kinetics, surface oxide morphology, and cross-sectional morphology of TiNbTaVW and CrNbTaVW RHEAs compared to the IN718 alloy?
e. What are the effects of high temperatures and strain rate on the deformation behaviour of TiNbTaVW and CrNbTaVW RHEAs compared to the IN718 alloy? What are the dominant softening mechanisms during deformation of the TiNbTaVW and CrNbTaVW RHEAs compared to the IN718 alloy?

1.4 Research hypothesis

It is anticipated that higher hardness in TiNbTaVW will be achieved through solid solution strengthening, while CrNbTaVW will benefit from the Cr-induced Laves phase, known for increasing hardness. The addition of passivating elements in these RHEAs is expected to form protective oxide films, enhancing corrosion resistance and eliminating pits, pores, and phase dissolution. Stable oxides like $CrTaO_4$, Cr_2O_3, TiO_2, and $TiTaO_4$ are expected to act as barriers against oxygen influx, reducing oxidation kinetics at high temperatures. High melting point elements are foreseen to enhance thermal stability without weakening the RHEAs during high-temperature compression. Additionally, the softening mechanisms of dynamic recovery and recrystallisation observed in conventional alloys are expected in these RHEAs. Overall, TiNbTaVW and CrNbTaVW are proposed to exhibit excellent hardness, corrosion, oxidation, high-temperature strength, and hot workability compared to the commercial IN718 alloy.

1.5 Research aim and objectives

The aim of this research work was to produce and assess the behaviour/performance of RHEAs based on the TiNbTaVW and CrNbTaVW systems for high temperature applications, in comparison to the IN718 alloy. This was achieved by the following specific objectives:

a. Conducting a bibliometric mapping using Vosviewer software to identify research trends and key focus areas in arc-melted RHEAs;

b. Assessing the influence of composition on microstructure and hardness based on empirical calculation, Thermo-calc simulation and experimental techniques;

c. Evaluating the corrosion performance of TiNbTaVW and CrNbTaVW RHEAs in 3.5 wt% NaCl and 1 Mol H_2SO_4 compared to the IN718 alloy;

d. Determining the oxidation kinetics, surface oxide morphology, and cross-sectional morphology of TiNbTaVW and CrNbTaVW RHEAs at 850°C/1050°C for 15 hours, in comparison to the IN718 alloy;

e. Assessing the influence of high temperatures and strain rate on the flow behaviour, microstructural evolution, and compressive strength of the TiNbTaVW and CrNbTaVW RHEAs in comparison to the IN718 alloy. Determining the dominant softening mechanisms during high temperature deformation of the RHEAs compared to the IN718 alloy.

1.6 Thesis structure

There are nine chapters in this thesis. The chapters start with the brief introduction of the contents and ends with summary of the main findings. The nine chapters are listed as follows:

- Chapter one provides the background of the study, problem statement, questions, aims and objectives.
- Chapter two discussed a systematic review of the existing literature about the research area of study. High entropy alloy and its core effects, empirical and Thermo-Calc predictions, corrosion, oxidation, and hot deformation behaviour of metallic materials was reviewed. Important findings in the literature are identified and summarised.
- Chapter three details the information on the materials, equipment and experimental methods explored for performing the research work.
- Chapter four presents the results on the bibliometric analyses of global research on as-cast RHEAs.
- Chapter five presents the findings on the empirical approaches, thermo-calc, phase analysis, hardness, microstructure and compositional analysis of TiNbTaVW, CrNbTaVW, and IN718.

- Chapter six reports on the electrochemical corrosion behaviour of TiNbTaVW, CrNbTaVW, and IN718 in chloride and acidic media.
- Chapter seven presents the findings on oxidation kinetics, surface oxide morphology, and cross-section morphology of oxidised TiNbTaVW, CrNbTaVW, and IN718 at different time and temperatures.
- Chapter eight reports the findings on flow stress behaviour, microstructural evolution, and high temperature strength of hot deformed TiNbTaVW, CrNbTaVW, and IN718.
- Chapter nine summarises the overall findings and conclusions, with recommendations for future research work. The references cited in the thesis and supplementary information are presented at the end of the chapter.

Chapter 2
Literature review

2.1 Introduction

This chapter presents the review of findings in literature based on mechanical properties, oxidation, corrosion and high temperature properties of RHEAs. The empirical parameters and Thermo-Calc for phase prediction in high entropy alloys are also discussed. The importance of bibliometric mapping in determining gaps and latest trends in research are also discussed. The summary of the findings is highlighted.

2.2 High entropy alloy

Over a thousand years, the development of new functional materials, metals, and alloys has been the primary driving force behind the progression of human civilization. For instance, in the traditional method of alloy design, which consisted of combining a single principal elementwith a few minor alloying elements to improve the material's structural, chemical, and mechanical properties. The alloys were built with a solvent element as their foundation, with various solute atoms added to improve specific properties (Miracle, 2019; Mishra et al., 2021;Zhu et al., 2023). In the past, scientists based the design of conventional alloys on the edges of a phase diagram, despite the fact that these edges occupy only a small portion of the design space (Ye et al., 2016). However, with the advent of multicomponent alloys (MCA), attention has shifted to the central region of the phase diagram. This region contains an unexplored portion of several different classes of alloys, including HEAs, bulk metallic glasses, and intermetallics (Cantor et al., 2004; Yeh et al., 2004). Cantor et al. (2004) and Yeh et al. (2004)first reported HEA as a type of novel structure materials that demonstrated superior propertiesof conventional alloys.

The HEAs contain at least five primary elements at percentages between 5 – 35% and the variation in their atomic radii is less than 12% (Yeh et al., 2004). HEAs have a propensity to form a single-phase solid solution structure, such as FCC, BCC, or HCP (Guo et al., 2011; Murty et al., 2014; Tsai & Yeh, 2014). In recent years, HEAs has attracted a significant amount of attention because of their exceptional mechanical properties, such as strength, hardness, high temperature phase stability, improved wear, corrosion, and oxidation resistance (Chen et al., 2006; Li et al., 2013; Yeh et al., 2004). The HEAs design concept can be explained by referring to the Gibbs phase rule, which can be found in Equation 2.1. This rule states that the number

of phases (P) formed at the equilibrium condition and at constant pressure is stated as a function of mixing elements (C) (Hillert, 1993).

$$F+P = C+1 \quad (2.1)$$

The degree of freedom denoted by 'F' is made up of a number of variables that can be altered independently without affecting the phases that are already in equilibrium. The high entropy of mixing in the HEA system would prevent the formation of multiple phases and results in a simple solid solution (Cantor et al., 2004; Yeh et al., 2004). Based on this, a number of different principal elements were mixed to create a novel alloy that was later given the name HEA. The four core effects which explained the physical properties of HEA include: high entropy effect, lattice distortion effect, sluggish diffusion effect and cocktail effect (Murty et al., 2014; Yeh, 2006; Yeh et al., 2004). These core effects are described in detail in the following subsection.

2.2.1 Core effects of high entropy alloy

2.2.1.1 High entropy effect

At high temperatures, the high mixing entropy in alloy systems competes with the mixing enthalpy to lower the Gibbs free energy, which in turn promotes the formation of simple solid solutions. The high entropy effect led to an increase in the solubility of solid solutions, which in turn led to simpler microstructures. This effect also limited the formation of intermetallic compounds and elemental phases. As a result, single-phase solid solution HEA with a high entropy of mixing are more stable than alloys that are composed of similar constituent elements with a lower entropy of mixing (Guo et al., 2011; Otto et al., 2013). As shown in Figure 2.1, the entropy of mixing for solution phases increases from the small values for conventional alloys to large values for HEAs and non-equimolar compositions. HEAs have a large entropy of mixing in the solid solution state, whereas the intermetallic compounds have small entropy of mixing (Yeh et al., 2007). The resulting solid solution state tends to be more stable than the compound state especially at high temperatures. This is as a result of entropy effect in lowering the free energy of mixing (Otto et al., 2013; Gao et al., 2015).

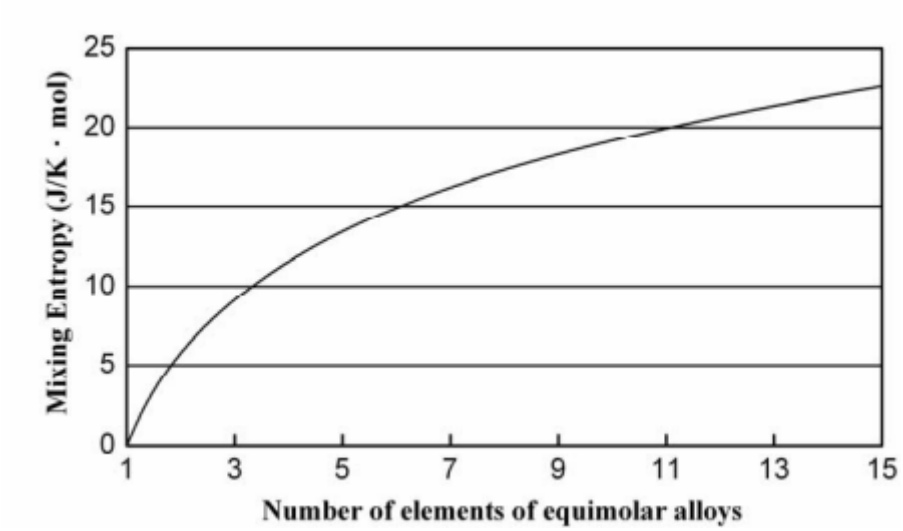

Figure 2.1: The entropy of mixing as a function of the number of elements in equimolar alloys in the completely disordered state (Yeh et al., 2007).

Figure 2.2 shows the entropy of mixing effect and the classification of HEA into three fields: low-entropy alloys, medium-entropy alloys and high-entropy alloys. According to Yeh et al. (2007), low-entropy alloys are conventional alloys, medium-entropy alloys are the alloys that comprise 2-4 major elements, and HEAs are the alloys that comprise at least five major elements in near or equi-atomic proportions. The high entropy effect, which promotes the occurrence of the disordered solution phase is primarily found in the HEA field and should beless prevalent in the medium-entropy alloys. In terms of the microstructure and properties that can be obtained from HEAs, the stabilisation of the solid solution phase is very significant.in terms of the microstructure and properties which can be obtained in these materials (Pickering et al., 2016; Otto et al., 2013).

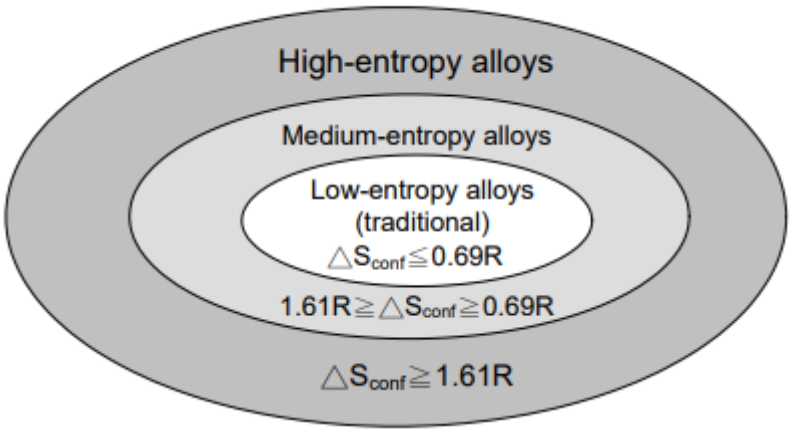

Figure 2.2: The various classifications of alloys according to their entropy of mixing (Yeh et al., 2007).

2.2.1.2 Lattice distortion effect

In conventional alloys, a lower lattice distortion is found because most of the solvent atoms have the same kind of atoms as their neighbours, unlike the HEAs whose solid solution is often a whole solute matrix. In HEAs, every atom is surrounded by different kinds of atom with different atomic sizes, hence resulting in higher lattice strain (Zhang et al., 2008). Individual crystal structure and bonding energy among constituent elements are also believed to cause higher lattice distortion (Yeh et al., 2007). There are incoherent bindings that can occur between an atom and its first neighbours, and this incoherency varies from site to site within the lattice, which results in a greater degree of lattice distortion. Yeh et al. (2007) conducted research on the effect of lattice distortion in as-cast Cu-Ni-Al-Co-Cr-Fe-Si alloy systems, and found that the number of CuNiAlCoCrFeSi constituent phases does not increase proportionallywith the number of elements, as shown in Figure 2.3. Furthermore, BCC and FCC are the major phases, while all peak intensities decrease as the number of elements increases.

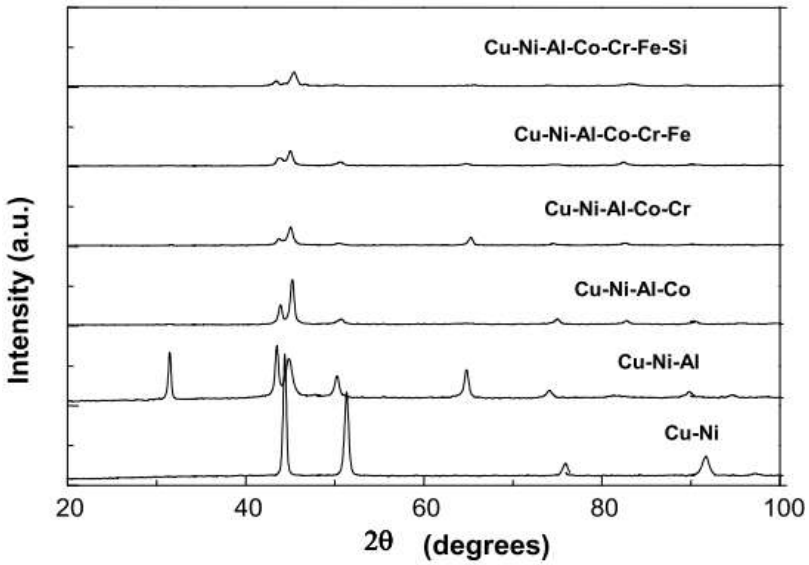

Figure 2.3: XRD patterns of binary to 7 element equiatomic alloys (Yeh et al., 2007).

2.2.1.3 Sluggish diffusion

The sluggish diffusion in HEAs refers to slower phase transformation kinetics and diffusion (Tsai & Yeh, 2014). This can be explained in two aspects: Firstly, the immediate neighbours of an atom before and after it jumps into a vacancy site are distinct from one another. When anatom jumps into a low-energy site, it becomes 'trapped,' and the chance that it will jump out of that site will be lower. However, if the site is a high-energy site, then the atom has a higher chance of moving back to its original site. Regardless of these situations, the diffusion process

is still slowed down in HEAs. For instance, Tsai et al. (2014) conducted a study on the effect of local energy fluctuation on the diffusion of CoCrFeMnNi alloys utilising the seven-bond model. As shown in Figure 2.4, the mean potential energy difference between lattice sites for the Ni atoms that diffuse in the CoCrFeMnNi alloys is 60.3 meV, which is a value that is approximately 50% higher than that of the FeCrNi alloys. Furthermore, the mean difference inpotential energy just after each migration for pure metals is equal to zero, whereas for HEA itis the largest.

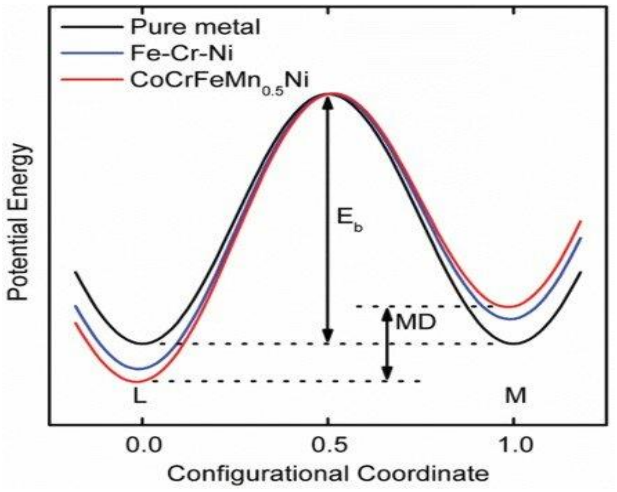

Figure 2.4: Schematic diagram of the potential energy change during the migration of a Ni atom (Tsai & Yeh, 2014).

The energy difference leads to a significantly longer occupation time at low-energy sites (1.73 times longer than that at high-energy sites). When compared to pure metal and FeCrNi, the diffusivity of CoCrFeMnNi HEA is the lowest. Secondly, the rate of diffusion of each elementin a HEA is different, particularly those with high melting points, which are less active than others. Therefore, these elements have lower success rates for jumping into vacancies when in competition with other elements (Tsai & Yeh, 2014). During the nucleation and growth of a new phase, the coordinated diffusion of several elements is important because it requires the redistribution of all elements to reach the desired composition. Grain growth also requires the collaboration of all elements to ensure the migration of grain boundaries is accomplished. If the elements move slowly, they will become the rate-limiting factor, which will cause the transformation to be slowed down (Hamdi et al., 2023).

2.2.1.4 Cocktail effect

The cocktail effect is based on the idea that the properties resulting from the combination of principal elements cannot be obtained from only a single principal element. For instance,

simple solid-solution structures of BCC and FCC was found in the as-cast $CuCoNiCrAl_xFe$ HEA as shown in Figure 2.5 (Tong et al., 2005). It was also discovered that the number of Al contents in the $CuCoNiCrAl_xFe$ HEA system had a significant impact on the phase transformations as well as the mechanical properties. An increase in the Al contents up to 0.5 demonstrated a simple FCC phase, whereas an increase in the amount of Al contents up to 0.8 produced a phase mixture consisting of both FCC and BCC. The $CuCoNiCrAl_xFe$ HEA system contained a single ordered BCC phase because of Al additions greater than 2.8. As shown in Figure 2.5, the hardness of the alloy increased from 133 to 655 HV when the Al contents increased to 3.0. The contribution of Al atoms to the hardness increase was related to a solution-hardening mechanism (Tong et al., 2005).

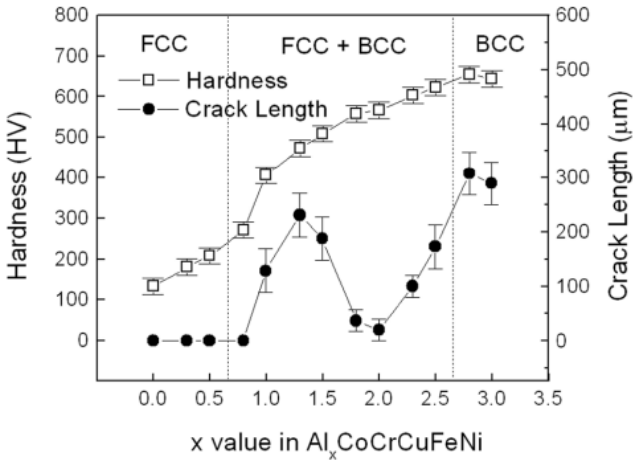

Figure 2.5: Vickers hardness of the $Al_xCoCrCuFeNi$ HEA system with different aluminum contents (Tong et al., 2005).

2.2.2 Empirical rules for phase prediction in high entropy alloy

The formation of a solid solution in binary alloys is governed by Hume-Rothery rules, which were developed in the 1950-1960s to specify the conditions for obtaining a high degree of solubility between two elements of a binary alloy. In order to stabilise a solid solution, all fourof the following factors need to be satisfied (Yang & Zhang, 2012; Zhang et al., 2008):

a. There must be at least a minimum difference between the electronegativities of the binary mixing elements.

b. The difference in atomic radius from one element to another must be less than 15%.

c. The chemical valence of the binary mixing elements must not differ by more than 1.

d. In order for a solid solution formation, all of the constituent elements' crystal structures have to be identical.

However, the Hume-Rothery rules do not explain why the different crystal structures of the individual elements form a single-phase solid solution of a particular crystal structure, such as FCC or BCC. For this reason, in the case of HEAs, additional factors are required for the purpose of explaining this effect. One example of such a factor is the entropy of mixing which involve the combined effect of four different forms of entropy: configurational, vibrational, magnetic dipole, and electric randomness entropy (Sheikh, 2016; Yeh et al., 2004). The Hume-Rothery rules have been extended by a number of researchers to apply to HEAs. These rules are currently being utilised in the process of predicting phase stability and simple solid solution phases in HEAs. These parameters include entropy of mixing (ΔS_{mix}), enthalpy of mixing (ΔH_{mix}), valence electron concentration (VEC), lattice distortion (δ), electronegativity difference ($\Delta\overline{X}$), and thermodynamic parameter (Ω) (Guo et al., 2011, Yang & Zhang et al., 2012; Troparevsky et al., 2015, Zhang et al., 2008). The configuration entropy of mixing has the major contribution in the alloy system at equilibrium condition. Equation 2.2 states the relationship of configuration entropy as a function of number of ways of mixing the elements (Brewer, 1974; Guo et al., 2011; Yang & Zhang, 2012).

$$\Delta S_{conf} = -K \ln N = -R \sum_{i=1}^{n} C_i \ln C_i \qquad (2.2)$$

Where, ΔS_{conf} is the configurational entropy (kJ/mol K), N is the number of elements, K is the Boltzmann constant, R is the gas constant (J/mol K), and C_i is the molar fraction of mixing elements.

The ΔS_{mix} of an alloy increase in accordance with the number of constituent elements (Guo et al., 2011). If an alloy at an equiatomic ratio contains five elements that make up its composition, the ΔS_{mix} of the alloy in an ideal case is 1.61 R (13.38 J/K mol). The entropy would therefore reach its maximum value at an equiatomic ratio expressed using Equation 2.3 (Yang & Zhang, 2012; Zhang et al., 2008).

$$\Delta S_{mix} = R \ln N \qquad (2.3)$$

In terms of thermodynamics, the goal of a system is to reach a stable or metastable equilibrium state in which its Gibbs free energy is as low as possible (Yang & Zhang, 2012; Zhang et al., 2008). At any temperature, the ΔH_{mix} and ΔS_{mix} are related to Gibbs free energy (Zhang et al., 2008). The Gibb's free energy expressed in Equation 2.4 plays a significant part in the

development of an alloy; where it must be negative for a stable phase formation in the alloy systems.

$$\Delta G_{mix} = \Delta H_{mix} - T\Delta S_{mix} \quad (2.4)$$

Where, ΔG_{mix} is the Gibbs free energy of mixing (kJ/mol), ΔH_{mix} is the configuration mixing enthalpy (kJ/mol), and T is the absolute temperature (K).

Other criteria for an increase in the rate of solid solution formation in HEAs is the presence of a negative ΔH_{mix} between the alloying elements (Troparevsky et al., 2015; Yang & Zhang, 2012; Zhang et al., 2008). The ΔH_{mix} expressed in Equation 2.5 determines the difference between the formation of amorphous phases and the formation of solid solutions.

$$\Delta H_{mix} = \sum_{i=1,\ i\neq j}^{n} 4\Delta H ij^{mix} C_i\, C_j \quad (2.5)$$

Where, C_i and C_j are the atomic percentages of the ith and j^{th} components and ΔHij^{mix} is the enthalpy of mixing between binary elements and predicted from Miedema model.

The Ω parameter in Equation 2.6 was proposed by Yang and Zhang (2012) in determining the possibility of solid solutions and ascertaining whether the ΔS_{mix} effect counteracts the ΔH_{mix} effects of the solid solution. If $T_m\Delta S_{mix}$ has more contribution than the ΔH_{mix} ($\Omega > 1$), HEAs form simple solid solution. However, if the value of ΔH_{mix} is higher (positive) ($\Omega < 1$) than $T_m\Delta S_{mix}$, the free energy will increase, leading to the formation of segregation and ordered compounds. Hence, the value of thermodynamic parameter is proposed to be ≥ 1.1 for the formation of solid solution (Yang & Zhang, 2012).

$$\Omega = \frac{T_{m\Delta S_{mix}}}{\Delta H_{mix}},\ T_m = \sum_{i=1}^{n} C_i\ (T_m)i \quad (2.6)$$

Where $(T_m)i$ is the melting temperature of the ith element.

During the elements mixing, there could be possibility of atomic distortion due to the large atomic size difference between the mixing elements and this leads to an increase in the lattice strain. These have a significant impact on the likelihood of solid solution formation (Guo et al., 2011; Yang & Zhang, 2012). In order to determine the effect of atomic size of mixing elements, atomic size mismatch parameter was proposed and expressed in Equation 2.7 (Yang & Zhang, 2012). The atomic size mismatch parameter ($\delta \leq 6.6$) was proposed to distinguish between solid

solution, amorphous, and intermetallic forming alloys (Guo et al., 2011).

$$\delta = \sqrt{\sum_{i=1}^{n} C_i(1 - r_i/\bar{r})^2}, \bar{r} = \sum_{i=1}^{n} C_i \times r_i \quad (2.7)$$

Where, $\bar{r} = \sum_{i=1}^{n} C_i \times r_i$ is the average atomic radius (pm) of mixing elements.

The VEC parameter is the total number of electrons that can fit in the valence band, including those in the 'd' shell (Mizutani, 2011). The crystal structure has a significant impact on the properties of HEAs. It is important to determine VEC parameter once the solid solution formation criteria are met using Equation 2.8 (Guo et al., 2011).

$$VEC = \sum_{i=1}^{n} C_i \ (VEC) \quad (2.8)$$

Where C_i is the atomic percentage of the ith component and $(VEC)i$ is the valence electron of the ith component. According to Guo et al. (2011), FCC and BCC crystal structures would be stable, if VEC $\geq$ 8 and VEC $\leq$ 6.87 respectively.

A small difference in Pauling electronegativity of the constituent elements should create a solid solution based on the Hume-Rothery rules expressed in Equation 2.9 (Mizutani, 2011; Murty et al., 2014).

$$\Delta\chi = \sqrt{\sum_{i=1}^{n} C_i(X_i - \bar{X})^2}, \bar{X} = \sum_{i=1}^{n} C_i \times X_i \quad (2.9)$$

Where, X is electronegativity of the ith components, $\bar{X}$ is the average electronegativity of the components.

All the above listed criteria help in the formation of a simple crystal structure with complete solid solution, thereby having a significant influence on the mechanical properties and the microstructure of multi-component HEAs.

Table 2.1 gives the summary of the solid solution and phase forming parameters range which must be satisfied during the alloy development.

Table 2.1: Solid solution parameters.

Solid solution parameters	Range of parameters	References
Entropy of mixing	$\Delta S_{mix} \geq 1.5R$	(Brewer, 1974; Guo et al., 2011; Yang & Zhang, 2012)
Valence electron	VEC < 6.87 = BCC VEC ≥ 8 = FCC 6.87 ≤ VEC < 8 = BCC + FCC	(Brewer, 1974; Guo et al., 2011)
Enthalpy of mixing	-11.6 KJ/mol ≤ ΔH_{mix} ≤ 3.2	(Troparevsky et al., 2015; Yang & Zhang, 2012; Zhang et al., 2008).
Atomic size mismatch	$\delta \leq 6.6\%$ = BCC $\delta \geq 6.6\%$ = FCC and Laves	(Troparevsky et al., 2015; Wu et al., 2018; Yang & Zhang, 2012; Zhang et al., 2008)
Thermodynamic parameter	$\Omega \geq 1.1$= solid solution phase while suppressing intermetallic formation and ordered phase.	(Troparevsky et al., 2015; Yang & Zhang, 2012)
Pauling electronegativity	$\bar{X}$ must be small to form a solid solution	(Mizutani, 2011; Murty et al., 2014)

2.3 CALPHAD thermodynamic modelling

The acronym CALPHAD was originally an abbreviation for "Calculation of Phase Diagrams,"but it has since been expanded to mean "Computer Coupling of Phase Diagrams and Thermochemistry" (Saunders & Miodownik, 1998). This is an alternative approach to predicting the stable phases in binary and multi-component alloy systems as a function of temperature and concentration using computer calculations. It makes use of binary and occasionally ternary phase diagrams for the purpose of predicting thermodynamic properties and phase equilibria for multi-component systems that are otherwise either not available or very difficult to produce experimentally (Chen et al., 2018; Yang & Zhang, 2012).

The CALPHAD method calculate the percentage of different phases that are present as well as the solidification pathways (Terms, 2014). This predicting phase diagrams technique was developed using several different software packages, including ThermoCalc, FactSage, JMatPro, and Pandat. ThermoCalc uses databases such as TCHEA1 and SSOL4, and has been utilised in determining the formation of various phases in HEAs. In order to obtain accurate thermodynamic descriptions of the BCC and FCC phases, the TCHEA1 database was developed specifically for HEAs by combining different experimental methods with first-principle calculations and CALPHAD modelling (Chen et al., 2018).

The newly developed 15-element framework consisted of Al, Co, Cr, Cu, Fe, Hf, Mn, Mo, Nb,Ni, Ta, Ti, V, W, and Zr, and is capable of being calculated in both the binary and ternary modules (Mao et al., 2017). In the HEA system, the TCHEA1 database have the ability to predict phase equilibrium as well as phase composition by using an extrapolation to a high order system (Chen et al., 2018; Mao et al., 2017). The SSOL4 database can be utilised in HEAs to predict and extrapolate higher-order multicomponent systems through the combination of several systems that have been thoroughly evaluated. The SSOL4 solutions database is a thermodynamic database that contains information on a variety of multi-component solution phases operating within a chemical framework consisting of 78 elements (Thermo-Calc Database, 2006).

The SSOL4 database was created for use in a variety of applications, including the study of alloy solution phases and significant intermetallic compound phases. It includes thermodynamic data that have been subjected to a critical evaluation for binary, ternary, and higher order systems. There is a total of 600 multicomponent solution phases and a large number of intermetallic compound phases included in SSOL4 (Thermo-Calc Database, 2006). The CALPHAD method has certain limitations like instances where the calculated data does not agree with experimentally determined data. This is because of the assumptions made in the model and experimental results not reaching equilibrium (Zhang et al., 2012). The calculated phase diagrams for the multi-component systems assume an equilibrium state, whereas the experimental data is produced from a non-equilibrium state. This could be because the alloys were produced in the form of an as-cast structure, or it could be because the homogenisation after casting was not sufficient to reach the equilibrium state due to the sluggish diffusion of the elements (Chen et al., 2018; Mao et al., 2017; Terms, 2014; Zhang et al., 2012).

2.4 Alloy production method

2.4.1 Vacuum arc melting process

Arc melting, which involves the liquid state melting of elements in either a high vacuum or an inert atmosphere, is one of the primary development methods for RHEAs. It is the most widely used processing technique for HEAs development because the process can reach high temperatures of about 3000°C, to melt metals that have high melting points. Figure 2.6 depicts a typical schematic of the arc melting method. This method involves placing alloy ingots or alloy powders inside a metallic crucible before melting with tungsten electric arc under an inert gas (argon atmosphere) (Alshataif et al., 2020). In order to ensure homogeneity of the alloy,

ingots of the alloy or powders are repeatedly solidified by the coolant that is situated beneath the metallic crucible. The arc melting process is useful for melting refractory elements with high melting temperatures because it can ensure a homogenous mixture of elements throughout the melting process.

Dendritic with inter-dendritic segregation observed in HEAs is as a result of the significant differences in melting temperature that exist between the elemental mixtures and the arc melting process (Chen et al., 2022). The rate at which the material solidified also contributes to the formation of additional defects such as pores and residual stresses. According to research conducted by Lilensten et al. (2014), increased solidification rates lead to grain refinement and a decrease in micro-segregation. Furthermore, it was discovered that the cold rolling post-processing and annealing of arc melted RHEAs was useful in producing a homogenous composition with good mechanical properties (Maiti & Steurer, 2014; Senkov et al., 2014; Senkov et al., 2014).

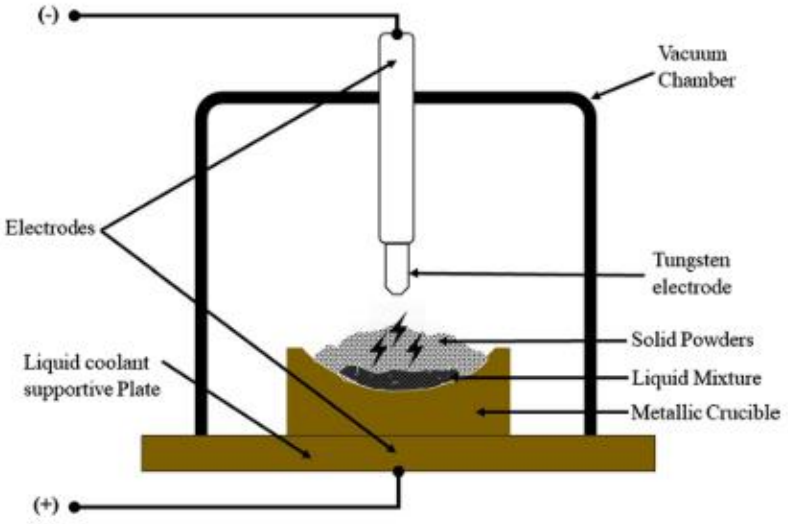

Figure 2.6: A descriptive diagram of the arc melting method (Alshataif et al., 2020).

2.4.2 Vacuum induction melting process

Vacuum induction melting is a process of heating electrical conducting materials through electromagnetic induction causing a magnetic field. This magnetic field diffuses the electrical current as it passes through the conducting materials, and as a result, it generates an eddy current that heat the materials. As shown in Figure 2.7, the ingot placed inside the crucible furnace blocks the input current. This causes a magnetic field to form, which rapidly melts the electrically conductive materials from the inside under high vacuum conditions. The ingot must

be cooled and remelted multiple times to produce homogenous HEA (Gromov et al., 2021; Yaoet al., 2016). In comparison to the additive manufacturing process, the vacuum induction melting process allows for greater precision in controlling the rate of heating and cooling, and also achieving homogeneity in the final product.

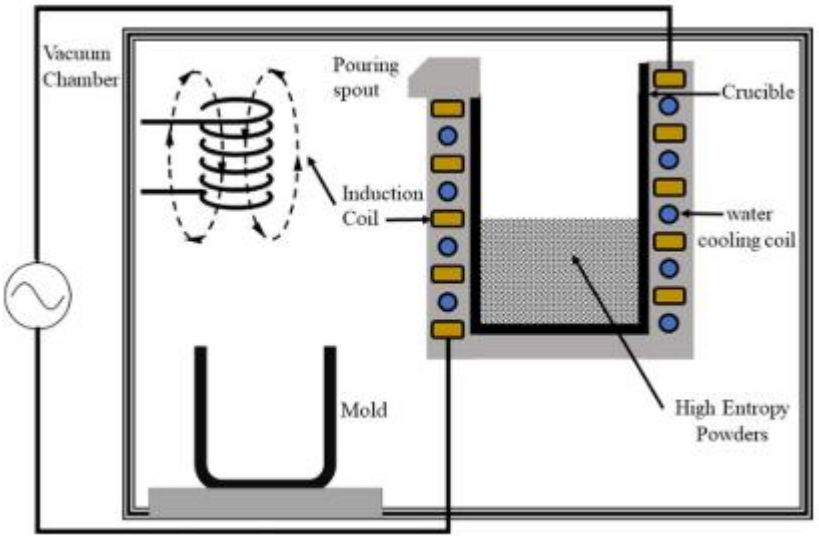

Figure 2.7: Schematic diagram of the vacuum induction melting process (Alshataif et al., 2020).

2.4.3 Powder metallurgy

Another method of processing that can be utilised to get rid of the segregation issues that occur in RHEAs during the solidification process is powder metallurgy (PM) process. The PM involves the use of elemental or mechanically alloyed powder mixtures, that are consolidationin vacuum using spark plasma sintering (SPS) (Han et al., 2020; Razumov et al., 2021; Shkodich et al., 2020). Depending on the desired sintering parameters, it is possible to create dense products using SPS that also contain nanostructures with little grain growth (Alshataif et al., 2020). The high rate of solidification that occurs during the PM process leads to the formation of microstructures that are fine-grained and homogenous in composition.

After processing, it is possible to maintain a homogeneous bulk single solid solution alloy with improved microstructural features and mechanical properties. As shown in Figure 2.8, the pressure ram is functioning as an electrode and is connected to a direct current source. After aDC current of 750–1500 A is passed through the powder mixture in a graphite die, the powder particles are simultaneously compressed with a uniaxial pressure of 25-150 MPa by a graphite punch (Han et al., 2020). Graphite paper is placed between the sample and the graphite die in order to prevent the powder mixture from reacting with the die. Consolidation of powders can

occur in a very short amount of time when a high current pulse, uniaxial pressure, and a vacuum or inert atmosphere are all present at the same time.

Currently, the development of RHEAs is accomplished through the implementation of additive manufacturing techniques such as laser-melt deposition, direct metal deposition, laser powderbed fusion, and laser engineered net shaping (Buranich, 2020; Dada et al., 2020; Dobbelstein et al., 2019; Li et al., 2019; Makhmutov et al., 2021; Melia et al., 2020; Sun et al., 2020; Wang et al., 2021). The starting powders for additive manufacturing of HEAs are developed primarily through gas atomisation, water atomisation, and mechanical alloying (Melia et al., 2020; Moorehead et al., 2020).

In the process of mechanical alloying, elemental powders are subjected to high-energy ball milling at room temperature for an extended period. This results in the diffusion of elements into each other to aid the production of homogenous alloy (Varalakshmi et al., 2008, 2010). The rapid rate of solidification in additively manufactured HEAs makes it difficult for segregation to take place on either a micro or macro scale. On the other hand, the release of a gas from either the substrate or the powder was found to be responsible for the formation of pores (Cattano, 2019; Dobbelstein et al., 2020; Sun et al., 2020).

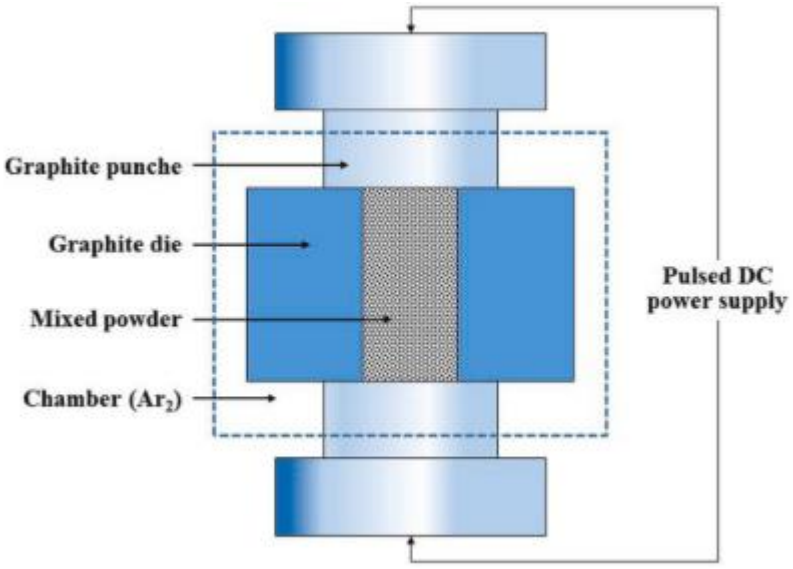

Figure 2.8: Schematic diagram of the preparation of spark plasma sintering (Han et al., 2020).

2.5 Refractory high entropy alloy

The high entropy alloying method was used to develop new refractory alloys, which contain a number of the principal alloying elements in concentrations that are close to equiatomic. The RHEAs were first developed by Senkov et al. (2020) for high temperature structural metals and

consists of refractory metals (W, Mo, Ta, Nb and Re) having melting points around 2000°C and higher. In addition, there is a broader definition of refractory metals that includes nine other elements, such as Ti, Zr, Hf, V, Cr, Ru, Os, Rh and Ir. The RHEAs are mostly based on group IV (Ti, Zr, and Hf), group V (V, Nb, and Ta), and group VI (Cr, Mo, and W) elements (Sheikh, 2016).

These metals and alloys are used in applications that are of the utmost importance and require high corrosion resistance as well as high temperature strength. The RHEA typically revolves around the elemental groupings of HfNbTaZr (Huang et al., 2021; Eleti et al., 2019; Zherebtsovet al., 2020; Senkov et al., 2014), CrMoNbTa (Senkov et al., 2014; Katz-Demyanetz et al., 2020), MoNbTaW (Zhang et al., 2016; Kanchi et al., 2022; Liu et al., 2021), and CrNbVZr (Yurchenko et al., 2018; Fang et al., 2019). Non-refractory components such as Al and Si help lower alloy density and increase mechanical, oxidation, and corrosion characteristics (Kuang et al., 2022; Li et al., 2020; Li et al., 2022; Qiao et al., 2021; Yan et al., 2022). Ceramic particulates such as TiC, TaC, Mo_2C, silicides, and nitrides are added to RHEAs to prevent high-temperature softening (Guo et al., 2016; Wei et al., 2019; Wei et al., 2021). Low-density RHEAs favour Cr, Nb, Ti, V, and Zr, whereas Mo, Nb, Ta, and W alloys may give the highest melting temperature (Miracle & Senkov, 2017).

2.6 Bibliometric analysis on global research of RHEAs

Scientific publications can be assessed adequately using scientometric method (Chang et al., 2015; Vieira & Gomes, 2009). Science mapping or bibliometric review is a quantitative study done to identify research development in a field over time, organisational and geographic distributions of research, and the emerging areas in that field (Akinwekomi & Akhtar, 2022; van Eck & Waltman, 2014). Furthermore, bibliometric mapping helps to understand historical and evolutionary changes in a research field, assists experts in enriching their knowledge of a certain field, and create a comprehensive visual reference platform for future researchers (Chang et al., 2015; Heersmink et al., 2011).

Text/data mining techniques involve the use of bibliographical data on a large scale to analyse and visualise different types of bibliometric networks based on the outputs of the academic literature in a particular scientific field (van Eck & Waltman, 2014). The bibliometric review is therefore deemed fit for research study using content analysis which gives room for drawing logical inferences from literature collected from a database.

Some of the research fields that have benefitted from bibliometric reviews include computational intelligence (van Eck & Waltman, 2007), emerging applications of three dimensional printing during COVID-19 (Ahmed et al., 2021), robotics and automation (Aghimien et al., 2020), library and information science (Chang et al., 2015), microbial fuel cell (Khudzari et al., 2018), blockchain technology in built environment (Akinradewo et al., 2022), and conversion technologies for carbon dioxide (Xing et al., 2020). HEAs have also benefitted from bibliometric mapping, such as bibliometric mapping of literature on high- entropy/multicomponent alloys (Akinwekomi & Akhtar, 2022) and bibliometric analysis of powder metallurgy-based high-entropy/multicomponent alloys (Akinwekomi et al., 2024). It is interesting to note that no such bibliometric mapping of literature review has been undertaken on arc melted RHEAs. This research conducted a bibliometric mapping of literature on arc melted RHEAs and the results of the analysis are presented in Chapter 4.

2.7 Research on microstructure and hardness properties of RHEA

In this section, the microstructure as well as the hardness properties of single-phase and multi-phase RHEAs are presented. During the casting process, the typical microstructure is dendritic that segregates into dendrites and an inter-dendritic region (Senkov et al., 2011; Li et al., 2022). Xiao et al. (2019) investigated the microstructure and hardness properties of as-cast CrMoNbTaV RHEA. A single BCC phase with dendritic structure that segregated in dendriteand interdendrite regions. The inter-dendritic region enriched in Cr and V elements have lowermelting points, whereas the dendrite region enriched in Mo and Ta elements, have relatively higher melting points. The element Nb, which has a moderate melting point, was distributed evenly between dendrites and inter-dendritic regions. The microhardness value of the inter-dendritic regions is about 950 HV, while the corresponding value for the dendrite regions is about 896 HV. The high hardness at the interdendrite region was linked to Cr content which have large atomic radius difference. In addition, the large difference of the atomic radius that exists between Cr and the other four elements caused a more significant lattice distortion effectin the alloy. This effect strengthened the alloy and improve its microhardness.

Senkov et al. (2011) produced as-cast $Nb_{25}Mo_{25}Ta_{25}W_{25}$ and $V_{20}Nb_{20}Mo_{20}Ta_{20}W_{20}$ RHEAs and found a dendritic single-phase BCC structure for both alloys. The $Nb_{25}Mo_{25}Ta_{25}W_{25}$ had an average grain size of 200 mm, while $V_{20}Nb_{20}Mo_{20}Ta_{20}W_{20}$ had an average grain size of 80 mm. The microhardness test results for both alloys showed that they have a high microhardness value of 455 HV and 553 HV, respectively. In another study, Poulia et al. (2016) investigated

the microstructure and hardness of the $Mo_{20}Ta_{20}W_{20}Nb_{20}V_{20}$ alloy at room temperature. A dendritic structure of single BCC phase with fine grains of about 20 μm in diameter are observed. The dendrite arms are enriched in heavier elements (W, Ta, and Mo), while the interdendritic regions contain elements with lower melting temperatures (V and Nb). The Vickers micro hardness of the RHEA is 773 HV. The exceptional hardness in this alloy is greater than any individual element, suggesting a solid-solution-like strengthening mechanism.

To further enhance the mechanical properties of NbMoTaW and VNbMoTaW RHEAs, Han etal. (2017) added Ti to the elemental system, which led to the formation of a single BCC phase structure. The EDS analysis showed that the dendrite regions of the RHEAs are rich in Ta andW but have a low concentration of Ti and V, whereas the inter-dendrite regions are rich in Ti,V, and Nb but have a low concentration of W. In addition, the Mo content in the inter-dendriteregions was a little bit higher than that in the dendrite regions. The reported hardness values for the RHEAs are 498.7 HV and 510.3 HV, respectively. The addition of Ti to the RHEAs resulted in a solid solution hardening that resulted in increased hardness. Furthermore, the segregation of ductile elements like Ti and Nb in the inter-dendrite regions enhances lattice strain, leading to a significant improvement in hardness.

Tong et al. (2021) conducted research on the microstructure and hardness properties of as-cast NbTaW, $(NbTaW)_{0.95}Mo_{0.05}$, $(NbTaW)_{0.85}Mo_{0.15}$, and $(NbTaW)_{0.75}Mo_{0.25}$ RHEAs and found a dendritic single-phase BCC structure in all the alloys. A severe element segregation due to an increase in Mo content was observed. The lower melting point elements of Nb and Mo have a higher concentration in the inter-dendrite region, the Ta and W elements with high melting point have a higher concentration in the dendritic region. The hardness value of 410.2 HV, 568.3 HV, 783.5 HV and 778.3 HV were reported for NbTaW, $(NbTaW)_{0.95}Mo_{0.05}$, $(NbTaW)_{0.85}Mo_{0.15}$, and $(NbTaW)_{0.75}Mo_{0.25}$ respectively, due to an increase Mo content that resulted in a solid solution hardening.

Li et al. (2022) reported two BCC phases with dendritic structure for $Ti_2VNbMoZr_1$ and $Ti_2VNbMoZr_{1.5}$ RHEAs (Figure 2.9a and Figure 2.9b), while an equiaxed dendritic microstructure with two BCC phases was observed for the $Ti_2VNbMoZr_2$ and $Ti_2VNbMoZr_3$ RHEAs (Figure 2.9c and Figure 2.9d). The hardness value of 415 HV, 423 HV, 434 HV and 406 HV were reported for $Ti_2VNbMoZr_1$, $Ti_2VNbMoZr_{1.5}$, $Ti_2VNbMoZr_2$ and $Ti_2VNbMoZr_3$ were due to solid solution strengthening.

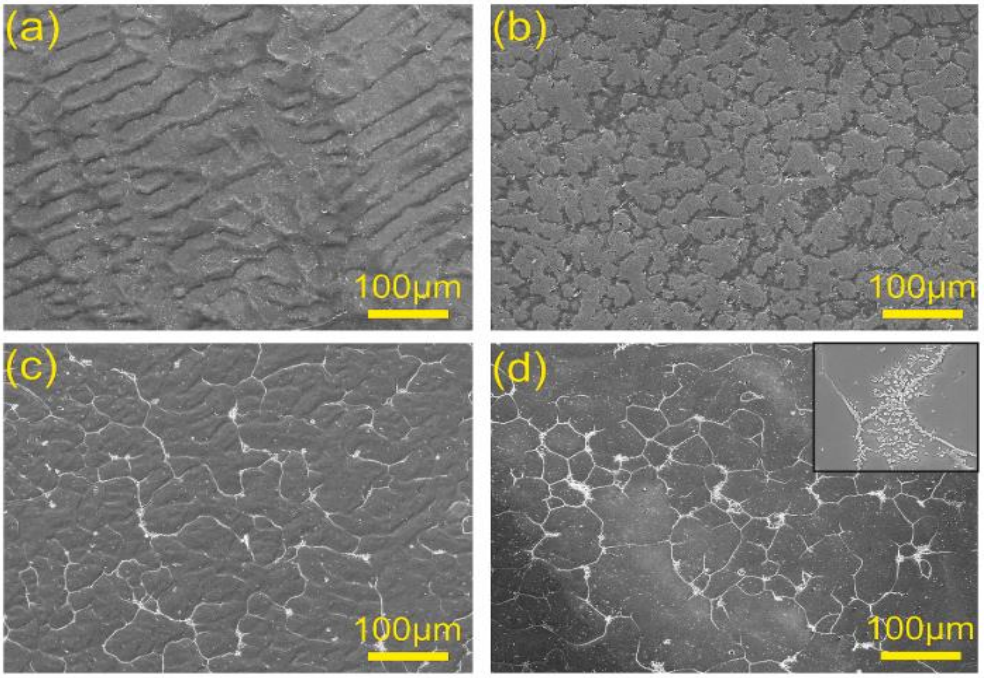

Figure 2.9: SEM images of microstructures (a) $Ti_2VNbMoZr_1$, (b) $Ti_2VNbMoZr_{1.5}$, (c) $Ti_2VNbMoZr_2$, and (d) $Ti_2VNbMoZr_3$ RHEAs (Li et al., 2022).

Gao et al. (2015) developed the as-cast HfMoNbTaTiVWZr RHEA and observed two BCC phases in addition to a C15 Laves phase (Figure 2.10a). The elemental distributions found inside the grains show that Ta, Mo, and Nb tend to segregate in the dendrite region, while Hf,Ti, V, and Zr tend to segregate in the inter-dendrite regions. The results of the Rockwell hardness tests showed HRC values of 54.6± 1.3.

Senkov et al. (2013) designed and investigated the microstructure and mechanical properties of CrNbTiZr and CrNbTiVZr RHEA. The microstructure of CrNbTiZr and CrNbTiVZr were comprised of BCC phase and an ordered Laves (C15) phase which can be distinguished by their bright and dark contrasts in the SEM backscatter conditions (Figure 2.10b). The bright regions of the CrNbTiZr microstructure have a higher concentration of Nb and Ti and a lowerconcentration of Cr. At the same time, the darker areas are rich with Cr; the concentration being twice the average concentration in the alloy (Figure 2.10c). There are three distinct colour regions present in the microstructure of CrNbTiVZr: bright, grey, and dark grey. The Vickers hardness of the CrNbTiZr and CrNbTiVZr alloy are measured to be 418 HV and 481.3 HV, respectively. The summary of microstructure and hardness properties of other single and multi-phase RHEAs is shown in Table 2.2.

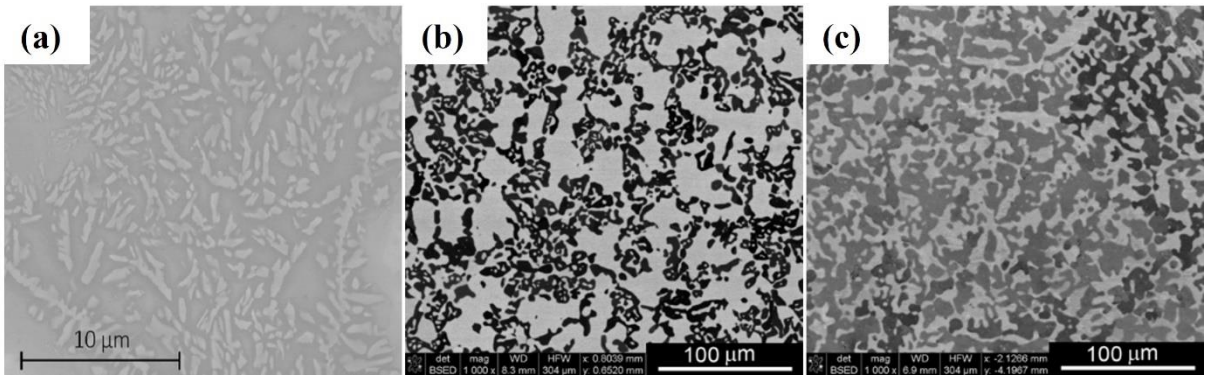

Figure 2.10: SEM images of microstructures (a) HfMoNbTaTiVWZr (Gao et al., 2015), (b) CrNbTiZr (Senkov etal., 2013), and (c) CrNbTiVZr RHEAs (Senkov et al., 2013).

Table 2.2: Summary of microstructure and hardness properties of single and multi-phase RHEAs.

Alloy composition	Manufacturing technique	Hardness (HV)	Microstructure	Findings	References
$AlTiVCrCu_{0.4}$	As-cast	871	BCC+HCP	It was found that the HCP phase contributed more to the hardness	(Liu et al., 2023)
$(AlNbTiVCr)_{98}Ni_2$	As-cast	741	BCC+C14 Laves+C15 Laves	The high hardness is attributed to solid solution strengthening by significant lattice distortion and second phase strengthening (C14 Laves+C15 Laves)	(Xu et al., 2023)
$AlNbTiVZr_{0.5}$	As-cast	665	B2+C14 Laves	The hardness increased due to structure refinement of the B2 phase	(Stepanov et al., 2018)
HfMoScTaZr	As-cast	959	BCC	The high hardness is attributed to solid-solution strengthening	(Nie et al., 2021)
MoNbFeCrV	As-cast	826	BCC+ C15 Laves	The high hardness is attributed to solid solution strengthening and Laves phase strengthening	(Xiang et al., 2019)
$Al_{1.5}NbTiMoV$	As-cast	556	BCC	Solid solution hardening and binding energy contributed to the hardness observed in the alloy	(Chen et al., 2014)
ZrNbMoHfV	As-cast	539	BCC1+BCC2 + Laves	The high hardness is attributed to solid solution strengthening and Laves phase strengthening	(Guo et al., 2014)
TaNbHfZrTi	As-cast	390	BCC	The high hardness is attributed to solid solution strengthening	(Senkov et al., 2011)
$WNbMoTaZr_1$	As-cast	557	BCC1+BCC2	The high hardness is attributed to solid solution strengthening and refined grain sizes	(Chen et al., 2022)
$TiMoNbZr_{0.5}$	As-cast	516	BCC	The high hardness is attributed to solid solution strengthening of the BCC phase	(Chen et al. 2021)
$Al_1TiZrNbHf$	As-cast	420	BCC1+BCC2	Solid-solution hardening and secondary BCC phase enhances the hardness of the alloy	(Bhardwaj et al., 2021)
$HfZrVTaMoWTi_2Nb_2$	As-cast	503	BCC1+BCC2 + C15 Laves	The C15 Laves contributed to the hardness	(Yao et al., 2021)
TiVCrNbTa	As-cast	586	BCC+ C15 Laves	The hardness is attributed to combination of solid solution strengthening of the BCC phase and C15 Laves phase	(Liu et al., 2023)

2.8 Hot deformation of metallic materials at elevated temperatures

Thermo-mechanical processing (TMP), such as hot deformation, results in microstructure refinement, often leading to improved strength in a material (Humphreys & Hatherly, 2004). TMP describes a combination of plastic deformation of metallic materials with heat treatments which is often carried out at a temperature above 0.4 T_m (Eleti et al., 2019). TMP has been applied to a wide variety of materials such as nickel super alloys, magnesium alloys, zirconium alloys, niobium alloys, tantalum alloys, titanium alloys, aluminium alloys, and high strength low alloy steels (Qu et al., 2011; Massih, 2013; Behera et al., 2014; Saxena et al., 2014; Aba-perea et al., 2016; Iturbe et al., 2017; Wang et al., 2019; Wu et al., 2021).

High temperature deformation and mechanical properties of materials is governed by controlling the microstructures during TMP (Amiri et al., 2013; Eleti et al., 2019; Jiang et al., 2018; Wang et al., 2013). During hot deformation process, a metal or alloy deforms under conditions of high temperature (greater than 0.6 T_m) and strain rates (Sakai & Jonas, 1984, 2001; Sellars & Tegart, 1972). Microstructural evolutions of metals or alloys are often caused by the respective hot deformation mechanisms, such as work hardening (WH), dynamic recovery (DRV) and dynamic recrystallisation (DRX) (Chen et al., 2014; Doherty et al., 1998; McQueen & Ryan, 2002; Sellars & Tegart, 1972). The understanding of metals and alloys flow behaviour and microstructure under hot deformation condition is of great importance for materials engineers during metal forming processes such as forging, hot rolling, and extrusion. Materials response to variables such as strain rates and temperatures is described in four different stages of the flow stress shown in Figure 2.11 (Lin & Chen, 2011).

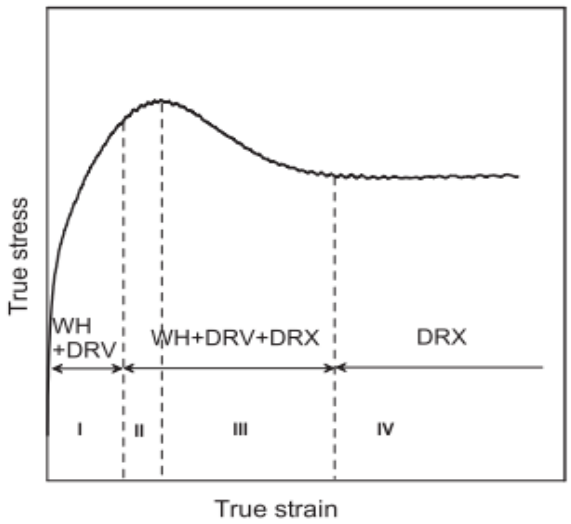

Figure 2.11: The four different stages of flow stress during hot deformation (Lin & Chen, 2011).

During stage I, which can be identified by a sharp increase in flow stress as a result of WH and DRV at lower strains (Figure 2.11), the material undergoes WH. At this stage, the WH rate is greater than the softening rate. The DRX process takes place during the transition stage, whichis referred to as Stage II. During this stage, there is a competition between the WH phenomenon and the softening phenomenon caused by DRV. In addition, the flow stress rises during stage II, but not as steeply during stage I. The sharp decrease in flow stress that can be observed during the softening stage (stage III) can be attributed to DRV and DRX, both of which initiate the softening of the material. The final stage of the flow stress that occurs during hot deformation is known as the steady-state stage. This is the stage in which the flow stress remains constant. This is caused by DRX or DRV when the material is in equilibrium with WH. The processes of DRV and DRX in metallic materials or alloys are discussed in Sections 2.8.1 and 2.8.2 respectively.

2.8.1 Dynamic recovery process

The DRV processes occurs as a result of the annihilation or rearrangement of dislocations during deformation (Sakai & Jonas, 2001). This process results in suppressed WH. The DRV is another type of softening mechanism that is activated when thermally activated dislocations climb and glide over one another. The stress strain curve shown in Figure 2.12 indicates that the DRV is generally known by steady-state flow stress, which specifies the build-up of dislocations when it reaches a dynamic equilibrium with the rate of annihilation of dislocations. According to Sakai & Jonas (2001), DRV flow stress exhibits simple shapes, and strain hardening takes place at low strains, followed by steady-state flow at high strains.

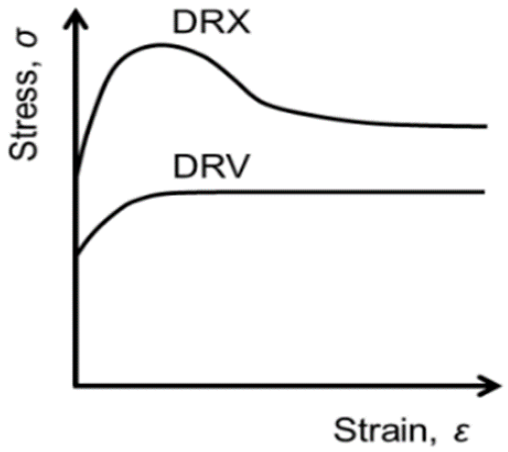

Figure 2.12: Stress-strain curves for metallic materials exhibiting DRV and DRX (Eleti, 2019).

In both BCC metals and alloys, which are known for their low stacking fault energies (SFE), and FCC metals and alloys, which are known for their high SFE, it is easy for DRV softeningto take place (Bai et al., 2021; Doherty et al., 1997). According to Sakai & Jonas (2001), the DRV process is slowed down in materials with low-to-medium SFE, such as copper and nickel, because dislocation climb, and cross-slip are impeded. The obstruction causes a delay in the annihilation and rearrangement of the dislocations, which results in the formation of subgrains. Under these conditions, DRV forms, and the flow curves typically display the distinctive shape showed in Figure 2.12. The DRV process is primarily controlled by the diffusion of rate-controlling atoms while the material is being deformed. In metallic materials and alloys having BCC crystals, the atoms diffusivity is initially higher than in those having FCC crystals becauseof the loose packing of the atoms in the BCC crystals. The cross-slip of screw dislocations is easy to occur in BCC and high SFE FCC materials (Doherty et al., 1997).

In addition, the possibility of dislocation climb assisted by the diffusion of vacancies during high-temperature deformation is another factor that contributes to the annihilation of dislocations or their rearrangement. In terms of microstructure, DRV does not show any significant changes in grain shape but rather exhibits well-developed sub-grain structures within the grain's interiors. When the strain rate is higher, it is possible for sub-grain structuresto be produced in the initial grains. This results in the production of more nuclei per unit volumeof the grains due to the increased amount of deformation energies stored in the material (Lin etal., 2008). When the strain rate is increased, this mechanism has the potential to produce grains of a finer size.

The effect of strain rate on the microstructures of 42CrMo steel at a strain of 60% and a temperature of 1050°C was investigated (Lin et al., 2008). As shown in Figure 2.13a and b, the lower the strain rate (0.01 s^{-1} and 0.1 s^{-1}), the bigger the grains, and the average grain sizes. However, at high strain rates of 1 s^{-1}, 10 s^{-1}, and 50 s^{-1} in Figure 2.13c-e, finer grain with average grain sizes of 45.52 μm, 30.53 μm and 20.77 μm were observed. The DRV rate increased with decreasing strain rate. At this stage, the energy stored during deformation is not enough for full recrystallisation, thus, the degree of recrystallisation is small. This can be seen in the grain sizes in Figure 2.13 a-b which are larger (133.93 μm and 78.58 μm) at lower strain rates (0.01 s^{-1} and 0.1 s^{-1}) than those under high strain rate.

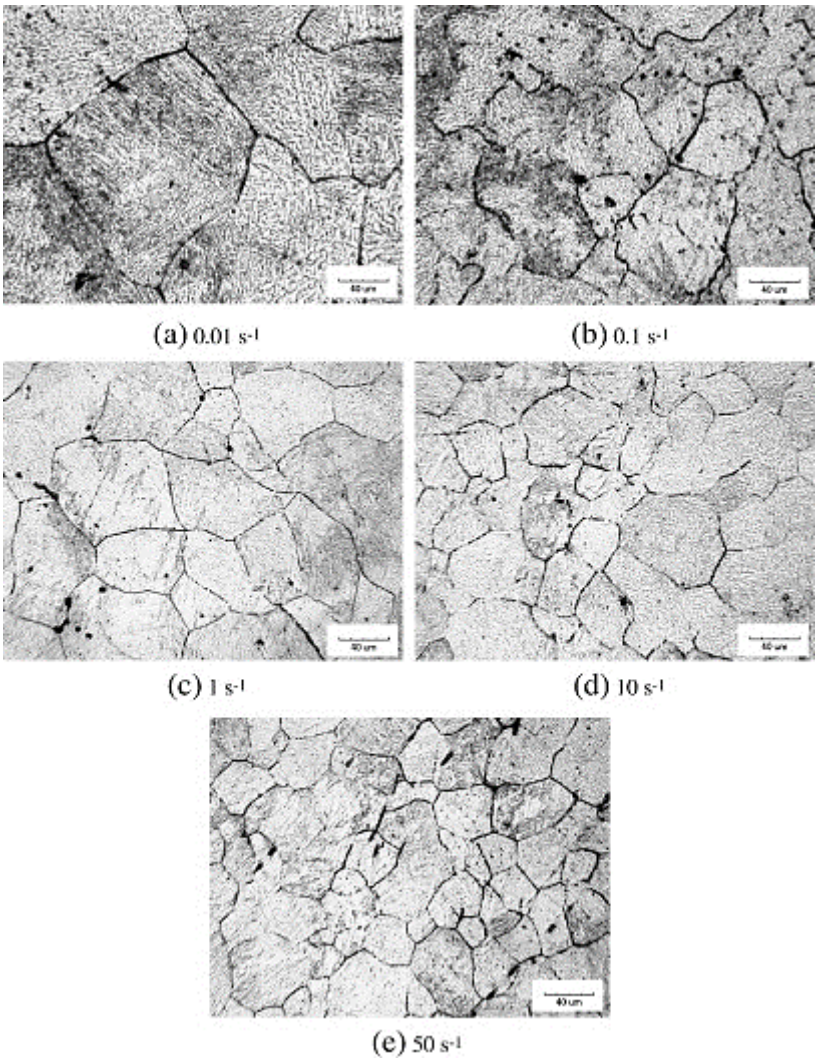

Figure 2.13: Optical microstructures of deformed 42CrMo steel at 1050°C with strain rates of (a) 0.01 s^{-1}; (b) 0.1 s^{-1}; (c) 1 s^{-1}; (d) 10 s^{-1}; (e) 50 s^{-1} (Lin et al., 2008).

According to Huang and Logé (2016), defects in the material, such as dislocations and interfaces, cause it to become thermodynamically unstable during the deformation process. When subjected to high temperatures, metallic materials tend to remove these defects using thermally activated methods in order to minimize the amount of free energy that is released by the system. Furthermore, DRV, which occurs as a result of the annihilation and rearrangementof dislocations, helps the microstructure to be partially restored to initial structure it had prior to the deformation. This is different from the process of DRX, which involves the migration ofhigh grain boundaries between deformed grains (Doherty et al., 1998). Therefore, DRV mostly brings relatively homogeneous microstructural changes.

2.8.2 Dynamic recrystallisation process

The recrystallisation process involves the nucleation and growth of a new grain, which leads to a significant change in the material's microstructure as well as its mechanical properties

(Doherty et al., 1998; McQueen & Imbert, 2004; Sakai & Jonas, 1984). In deformed materials, recrystallisation is defined as the creation of new strain-free grains with high angle grain boundaries (greater than 10 to 15° misorientation) (Doherty et al., 1998). Furthermore, it can be defined as a process that is thermally initiated and involves the formation of new strain-free grains at the deformed grain by completely consuming the material's original grains (Humphreys & Hatherly, 2004). There are two primary reasons why the recrystallisation process of plastically deformed metals and alloys is essential to the processing of metallic alloys. First, to restore the ductility of material that had been hardened by low temperature deformation ($0.5T_m$), and second, to control the grain structure of the final product. In the process of recrystallisation, the nucleation rate is controlled by the movement of the grain boundaries and the separation of the dislocations, both of which are determined by the diffusion of atoms (Humphreys & Hatherly, 2004).

For the HEAs, slow diffusion at high temperature could result in a restricted movement of dislocations, thereby delaying the process of recrystallisation (Tsai et al., 2009; Wu et al., 2014). During the recrystallisation process, microstructural changes take place. These changes control the metallurgical phenomena, which in turn leads to improvements in the material's mechanical properties. Until the process of complete recrystallisation is finished, the microstructure is separated into areas that are recrystallised and non-recrystallised. When the full process of recrystallisation is finished, the strength and hardness of the deformed material decrease, while a significant increase in ductility occurs. Nevertheless, the refined microstructure through the Hall-Petch effect in the recrystallised material improved the strength in comparison to the original material before the deformation process (Tsai et al., 2009; Wu et al., 2014).

The process of recrystallisation can typically involve either static or dynamic procedures (Sakai, 1995; Sakai & Jonas, 1984). The static recrystallisation (SRX) refers to a type of recrystallisation process that takes place after cold deformation or annealing (Huang & Logé, 2016; Sakai, 1995; Sakai & Jonas, 2001). In the process known as DRX, recrystallisation process occurs during straining if the temperature is greater than $0.5T_m$ (Sellars & Tegart, 1972). The process of DRX typically takes place at a homologous temperature of about 0.7-$0.8T_m$ and a strain rate of about 0.1 to 1 s^{-1} for materials that have a low stacking fault energy (Prasad & Rao, 2015). For materials that have a high stacking fault energy, the strain rates may be in the range of 0.0001 to 1 s^{-1} (Prasad & Rao, 2015). It refers to a process that takes place

during hot deformation and involves the formation of new grains (Humphreys & Hatherly, 2004). At the nucleation strain, during DRX, new grains begin to appear, and eventually fully replace the initial microstructure at high strains. The occurrence of DRX lowers the flow stress and increases the deformability of materials. In the stress-strain curve in Figure 2.12, DRX occurrence is established by a hump of the flow stress, due to the its softening effect. In addition, it can be specified by broad peaks and/or oscillations that occur just before the steady-state flow stress. During deformation at higher temperatures, DRX can bring about significant microstructural changes. As a result, the temperature at which the deformation occurs has a significant impact on the size, fraction and recrystallisation mechanism of grains (Lin et al., 2008; Doherty et al., 1998; Humphreys & Hatherly, 2004; Azarbarmas et al., 2016).

One of the effects of thermally initiated phenomena during the recrystallisation process is the observation of a large fraction of recrystallised grains when the temperature is increased (Azarbarmas et al., 2016). The recrystallised grains at high temperatures grew more easily and developed into a coarse grain because dislocation mobility is faster and diffusion rate increased at high temperatures. For example, the effect of temperature on the microstructures of 42CrMo steel was investigated by Lin et al. (2008) under the strain rate of 0.1 s^{-1} and temperatures of 850°C, 950°C, 1050°C, and 1150°C (Figure 2.14). At a lower temperature of 850°C, elongated grains with serrations developed in the grain boundaries, indicating the presence of DRX during the hot deformation process (Figure 2.14a). The "necklace" type of DRX can be identified by the small grains (22.97 μm) and are located along the grain boundaries of larger grains (Eleti et al., 2020; Lin et al., 2008; Sellars & Tegart, 1972). The “necklace” type grains showed that the DRX is not complete.

According to Humphreys & Hatherly (2004), DRX preferentially occurs along initial grain boundaries (GBs), often appearing to decorate initial grain boundaries. Thus, the resulting microstructures are referred to the necklace-like structure shown in Figure 2.14a. Also, in Figure 2.14a, the DRX begins at the boundaries of the old grains. This is followed by the nucleation of new grains at the boundaries of the growing grains at 950°C (Figure 2.14b). Equiaxed grain structures are visible at 1050°C (Figure 2.14c). An increase in the forming temperature results in a larger average grain size of 100.01 μm at 1150°C (Figure 2.14d). This clearly shows that at higher temperature, grain growth takes place during deformation with equiaxed grain structures. At this temperature, the material undergoing hot deformation will completely recrystallise.

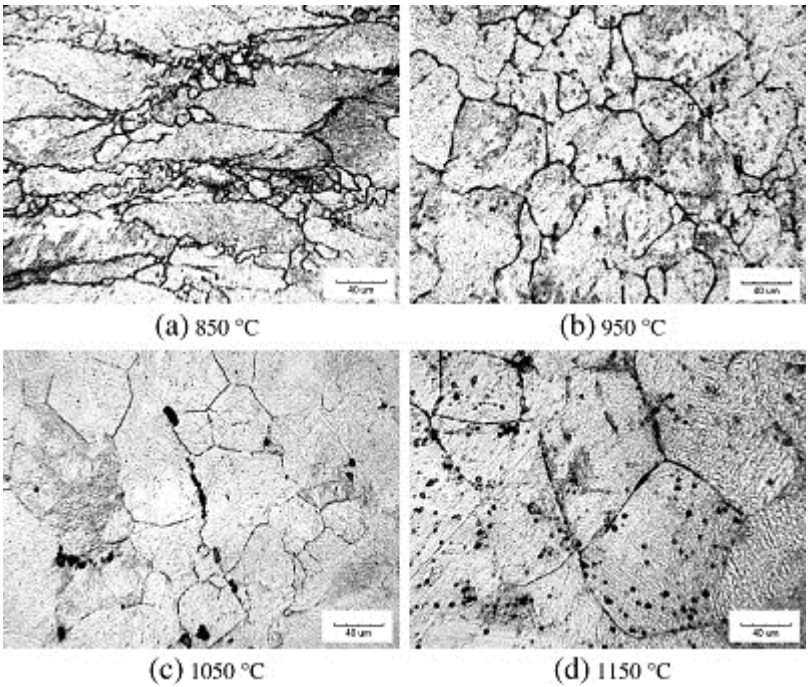

Figure 2.14: Microstructures of hot deformed 42CrMo steel under strain rate of 0.1 s^{-1} and temperatures of (a) 850°C; (b) 950°C; (c) 1050°C; (d) 1150°C (Lin et al., 2008).

Nucleation takes place preferentially where the strain and orientation gradients are high, implying it is an inhomogeneous phenomenon (Humphreys & Hatherly, 2004). At low-to-medium strains, such sites develop near grain boundaries and coarse particles. At medium to high strains, different kinds of dislocation sub-boundaries are formed, and the misorientationsof these sub-boundaries increase with strain. Shear bands are another common type of band that can form in materials that have low SFE. These various regions are all capable of functioning as preferential nucleation sites. DRX not only makes materials workable, but it also changes the microstructure of the materials (Poliak & Jonas, 2003). For example, as-cast RHEAs having an initial dendritic structure is transformed into an equiaxed microstructure after subsequent thermo-mechanical processing of the material (Dong et al., 2020; Eleti et al., 2020; Hu et al., 2020). At different strain rates, the temperature causes a significant increase inthe average grain diameter in structures that have undergone DRX. Likewise, grain size decreases at DRX temperatures as strain rates are increased (Humphreys & Hatherly, 2004; Poliak & Jonas, 2003; Prasad & Rao, 2015).

During DDRX, grain boundaries are preferred sites for nucleation, so a large initial grain size provides fewer nucleation sites, and recrystallisation kinetics is slower (Humphreys & Hatherly, 2004). At the same time, heterogeneities such as deformation and shear bands, which

are also sites for nucleation, are more readily formed in materials with large grain sizes. Except recrystallisation kinetics, the initial grain size also largely determines the shape of the stress-strain curve during DDRX, i.e., single peak or multi peaks (Humphreys & Hatherly, 2004). If the ratio of the recrystallised and initial grain size (D_S/D_0) is larger than 2 (grain coarsening), an oscillatory stress-strain curve with multi peaks is obtained (Sakai & Jonas, 1984). Lower ratio of $D_S/D_0<2$ (grain refining) leads to a smooth curve with a single peak. It should be mentioned that the D_S at steady state is not linked to the D_0, instead, it depends sensitively on temperature and strain rate which determines the steady state flow stress. This means the same D_S will be obtained if the samples of different D_0 are deformed at the same condition, either by grain coarsening or grain refinement (Huang & Logé, 2016).

2.8.2.1 Mechanism of dynamic recrystallisation

During the deformation process, an increase in deformation temperature encourages the formation of DRX grains and speeds up the migration rate of dynamically recrystallised GBs. (Dong et al., 2020). The high-deformation temperature can supply more thermal activation energy for the development of DRX grains, whereas the decreased strain rate offers sufficient time for dislocation motion, grain-boundary migration, and ultimately the grains grow and their strength is softened (Dong et al., 2020). According to Huang & Logé (2016), the mechanism of DRX can be broken down into two distinct types: continuous dynamic recrystallisation (CDRX) and discontinuous dynamic recrystallisation (DDRX). The CDRX can be identified by the transition of grain boundaries from low angles to high angles and the even distribution of recrystallised grains (Sakai & Jonas, 2001). There is a presence of nucleation and growth of new grains in the DDRX mechanism, and these new grains originate from GBs that have a higher dislocation density (Bai et al., 2021; Huang & Logé, 2016).

The DDRX exhibits nucleation by GB bulging, which is then followed by the growth of recrystallized grains (Guo et al., 2016; Eleti, 2019). However, GB bulging needs developing subgrains near the pre-existing GBs in order to provide the driving force required for local migration of the GB. It is possible for the same material to establish either DDRX or CDRX or both DDRX and CDRX during the hot deformation mechanism (Bai et al., 2021). In most cases, the progression of the DRX mechanism can be observed with a decrease in the temperature at which the deformation is taking place. The increased deformation temperature promoted DRX grains development during deformation, and the increased deformation

temperature can also accelerate the migration rate of dynamically-recrystallised GBs (Dong et al., 2020).

The high temperature of deformation has the potential to supply a greater amount of thermal activation energy for the formation of DRX grains. A decrease in strain rate provides enough time for dislocation motion, GB migration, and ultimately the growth of grains, which results in a weakening of the material's strength (Dong et al., 2020). Based on the industrial processing conditions, bulging of GBs, GB sliding, and sub-grain rotation are the mostly accepted mechanisms for identifying DRX mechanisms. These mechanisms are explained in Sections 2.8.2.2 and 2.8.2.3.

2.8.2.2 Bulging of grain boundaries and subgrain rotation

A recrystallisation mechanism known as bulging occurs in initial GBs (Humphreys & Hatherly, 2004; Poliak & Jonas, 2003; Sakai & Jonas, 1984). This mechanism is analogous to the strain-induced GB migration seen during SRX (Humphreys & Hatherly, 2004; Sakai & Jonas, 1984) According to Azarbarmas et al. (2016), the typical characteristics of DDRX with many dynamic recrystallised grains are serrations and bulging along the GBs. The grains that are located along the pre-existing GBs through bulging mechanism form a necklace structure as a result of the DDRX mechanism (Humphreys & Hatherly, 2004). In addition, the primary driving force behind the bulging mechanism is the difference in dislocation density that exists between the grains.

Dislocation triple junctions have the potential to act as nucleation sites during the process of new DRX grains being formed. Triple junctions have surplus energy beyond the energy of neighbouring GBs, and the dislocation density at or near triple junctions is significantly higher than at neighbouring GBs (Yu et al., 2022). For instance, in the hot compression of the $TiAlVNb_2$ RHEA some fine dynamic recrystallised grains with noticeable misorientation from the original grains can be found in Figure 2.15 (Bai et al., 2021). Figure 2.15a demonstrates how the serrated GBs of coarse grains bulge towards the adjacent grains as a result of the migration of high angle grain boundaries (HAGBs), which form some sub-grains.

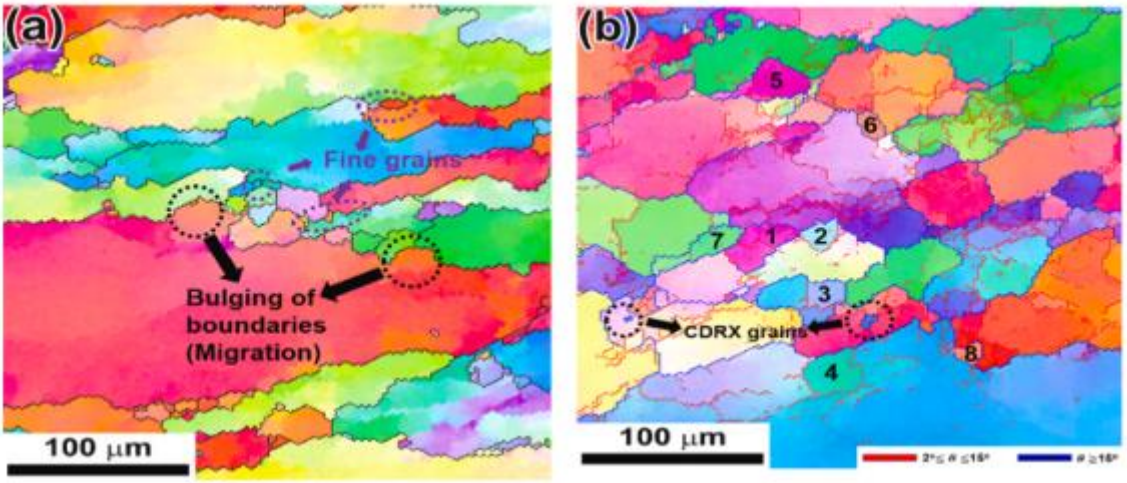

Figure 2.15: The EBSD inverse pole figure (IPF) map of deformed as-cast $TiAlVNb_2$ (a) 10^{-2} s^{-1}/1000°C (b) 10^{-3} s^{-1}/1100°C (Bai et al., 2021).

The sub-grains (labelled as 1-4) are surrounded by sub-boundaries (Figure 2.15b) forming dynamic recrystallised grains. According to Huang & Logé (2016), the beginning of DRX is heavily dependent on increased energy storage produced by the propagation and collision of dislocations close to the boundaries during the high-temperature deformation. In addition, the grain sizes of some newly formed fine grains, denoted as 5-8 in Figure 2.15b, are comparable to the grain sizes of the sub-grains, denoted as 1–4, that are surrounded by sub-boundaries. This indicates that some sub-grains may be on the point of transitioning from low angle grain boundaries (LAGBs) to high angle grain boundaries.

The DRV process, which occurs via LAGBs and is assisted by dislocation arrangements, would continue to increase their misorientation by the continued absorption of dislocation (Huang & Logé, 2016). Furthermore, since many of the grains surpass 10° or even 15°, which shows that the progressive sub-grain rotation happens and helps the transformation of LAGBs into HAGBs in deformed grains. This indicates that the CDRX process also occurred (Bai et al., 2021). These confirmed the possibility that both DDRX and CDRX could occur in the same material during the hot deformation mechanism.

2.8.2.3 Grain boundary sliding

The grain boundary sliding (GBS) is another mechanism for DRX that comprises the creation of new grains for the subsequent layer of the necklace microstructure (Eleti et al., 2020; Kaibyshev et al., 2002). The GBS occurs partially on serrated section and develops a local strain field along the grain boundaries. The GBS refers to a relative motion of grains that is caused by shear along the GB, with the potential to cause grains to rotate. As a result, grains

that have been deformed by GBS frequently maintain their equiaxed shape and shows inhibited grain growth. It could be concluded that the high temperature DRX grains size stability of alloys could be due to the possibility of GBS mechanism. Sometimes the deformed materials did not have a fully fine-grained structure, but rather a heterogeneous necklace microstructure composed of recrystallised coarse grains (core regions) and surrounding fine DRX grains (necklace regions) (Eleti et al., 2020).

Figure 2.16 shows the schematic graph of CDRX by local lattice rotation (Huang & Logé, 2016). In Figure 2.16a, GBS most often occurs at boundaries with favourable orientations. The movement of HAGBs, which is driven by the difference in stored energy between these boundaries, causes the formation of serrations shown in Figure 2.16b. Since GBS shown in Figure 2.16a can remove the small serrations developed, large serrations or bulges will first develop on non-sliding boundaries when the strains are high (Figure 2.16c). Once the bulges are established, GBS can still activate on the protruded regions, and the other parts of the boundary must accommodate the strain via plastic deformation. This leads to local lattice rotation and an asymmetric shape of the boundary, which ultimately results in the development of subgrains as shown in Figure 2.16d. Therefore, new grains start to emerge after the subgrain misorientation becomes sufficiently large.

For DDRX which is seen to occur through GB bulging/sliding (Figure 2.17). During plastic deformation, fluctuations in boundary shape are produced because of the incompatibilities between grains (Huang & Logé, 2016). In Figure 2.17a, the developed fluctuations prevent further GB sliding or shearing, dislocations then accumulate leading to high dislocation density gradients followed by subgrain formation near the original GBs. Local concentration of strainsis developed owing to the continuous deformation, and partial GBS, or shearing takes place, resulting in additional inhomogeneous strain (Figure 2.17b). Under low temperature or high strain rate deformation, strain induced subgrain boundary can then be formed. In contrast, twinning is favoured under high temperature or low strain rate deformation. According to Huang & Logé (2016), The DDRX nucleus will form by the bulging of a part of the serrated GBs assisted by the additional inhomogeneous strain.

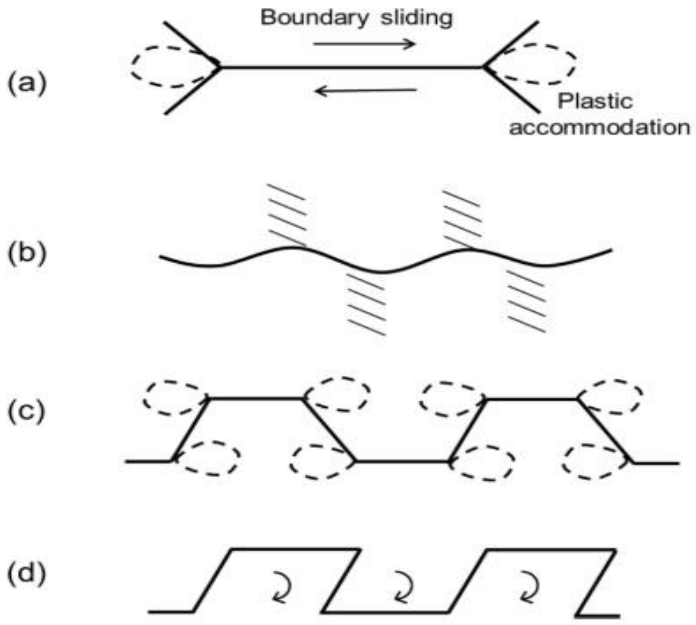

Figure 2.16: Schematic graph showing CDRX by local lattice rotation (Huang & Logé, 2016). (a) Grain boundary sliding, leading to the stress concentrations at the triple points; (b) Boundary bulges formed by local migration; (c) Part sliding, and part dislocation motion, leading to mantle formation; (d) Shear of bulges in mantle, leading to asymmetric bulges and local lattice rotation.

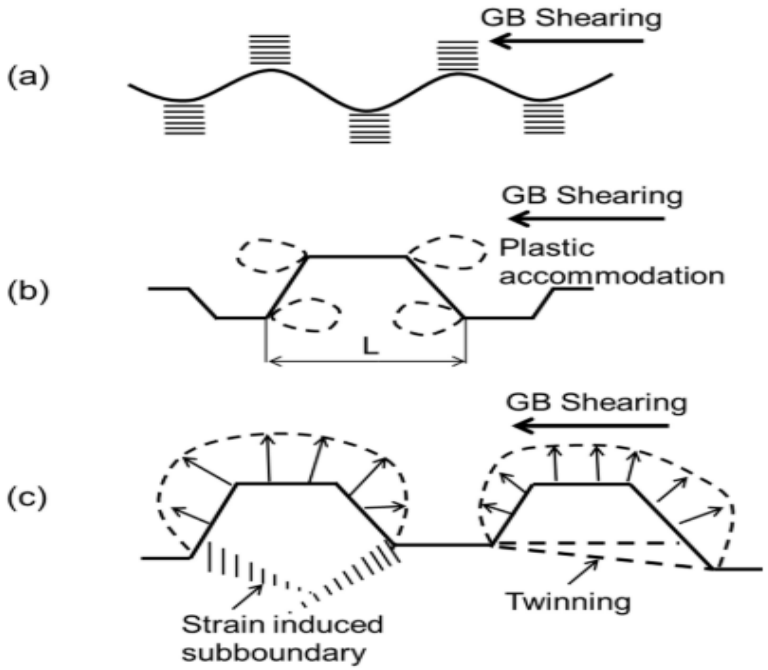

Figure 2.17: Schematic graph showing the nucleation of DDRX grain (Huang & Logé, 2016). (a) Boundary corrugation accompanied by the evolution of sub-boundaries. (b) Partial grain boundary sliding/shearing, leading to the development of inhomogeneous local strains. (c) Bulging of parts of a serrated grain boundary accompanied with the evolution of dislocation sub-boundaries or twinning, leading to the formation of a new DDRX grain.

2.9 Stress-strain flow behaviour of RHEA during hot deformation

At the initial stage of deformation, dislocation is produced and then accumulated intensely. At that point, work hardening surpasses the dynamic softening (Lin et al., 2008, Wu et al., 2016; Miura et al., 2009). According to Wu et al. (2016), the static precipitation of the strengthening phases will generate in the samples during preheating and stabilisation at the deformation temperature. Hence, the flow stress increases sharply at the early stage. Nevertheless, energy stored during deformation quickly accumulates with increase of strain and then offers enough driving force for the dislocation movement, and then the dynamic softening occurs to counteract the effect of work hardening (Wu et al., 2016). The flow stress behaviour of RHEA has been reported in some literatures (Guo et al., 2016; Liu et al., 2021; Senkov et al., 2012; Wan et al., 2021).

Senkov et al. (2011) studied the high temperature compression of $Nb_{25}Mo_{25}Ta_{25}W_{25}$ and $V_{20}Nb_{20}Mo_{20}Ta_{20}W_{20}$ RHEA at 600-1600°Cwith a strain rate of 0.001 s^{-1}. At 600°C and 800°C, $Nb_{25}Mo_{25}Ta_{25}W_{25}$ undergoes continuous strengthening, whereas at higher temperatures (1000°C, 1200°C, and 1400°C) it reaches a peak stress at an intermediate strain. The strain softening at these temperatures is an indicator of plastic instability and spallation of the surface material observed at higher strains. At 1600°C, almost steady state flow at a constant stress of ~590-600 MPa was observed and the yield stress for $Nb_{25}Mo_{25}Ta_{25}W_{25}$ steadily decreased as a function of temperature. For the $V_{20}Nb_{20}Mo_{20}Ta_{20}W_{20}$ RHEA deformed at temperatures of 1400°C and 1600°C, a rapid decline in yield stress and apparent softening was observed. The flow stress in most metals and alloys decreases with an increase in deformation temperature and the decrease in strain rate (Lin et al., 2008; Miura et al., 2009; Azarbarmas et al., 2016; Wu et al., 2016).

At higher temperatures, sharp drop in flow stress at early stages of deformation has been observed in some RHEAs (Figure 2.18). Eleti et al. (2019) noticed that the flow stress of HfNbTaTiZr RHEA at 1000°C/10^{-3} s^{-1} showed a distinctive sharp stress drop around yielding, followed by continuous flow softening. The sharp drops of the flow stress are clearly observedat early stages of hot deformation (Figure 2.18a). To reveal the mechanism of sharp stress drop, Eleti et al. (2019) performed an interrupted deformation test at 1000°C, with the temperature held for 600 s, and then deformed at a strain rate of 0.001 s^{-1} (Figure 2.18b). It was found that the unusual stress drop in the HfNbTaTiZr RHEA was due to either dislocation unlocking by solute atoms or the ending of short-range order by dislocation motion. Short-range order can

have a profound effect on the stacking-fault energy and dislocation motion, which have noticeable influence on the plastic deformation of HEAs (George et al., 2020).

Li et al. (2022) observed a sharp stress drop in $Ti_2ZrHfV_{0.5}Ta_{0.2}$ RHEA at 900–1100°C and a strain rate of 10^{-2}–10^{-1} s^{-1} (Figure 2.18c–e). To reveal the mechanism of sharp stress drop, an interrupted hot deformation and strain aging experiment at 900°C/0.1 s^{-1} with a strain of 0.1 and held for intervals of 0 s and 600 s (Figure 2.18f). The sharp stress drop was also attributedto the unlocking of dislocations pinned by the Cottrell atmosphere or short-range order. The unusual yield-drop phenomena in RHEAs are commonly observed in alloy compositions comprising TiZrHfVTa (Li et al., 2022), AlNbTaTiZr (Senkov et al., 2020), HfNbTaTiZr (Eletiet al., 2019), AlNbTiVZr (Yu et al., 2022), and MoNbHfZrTi (Guo et al., 2016).

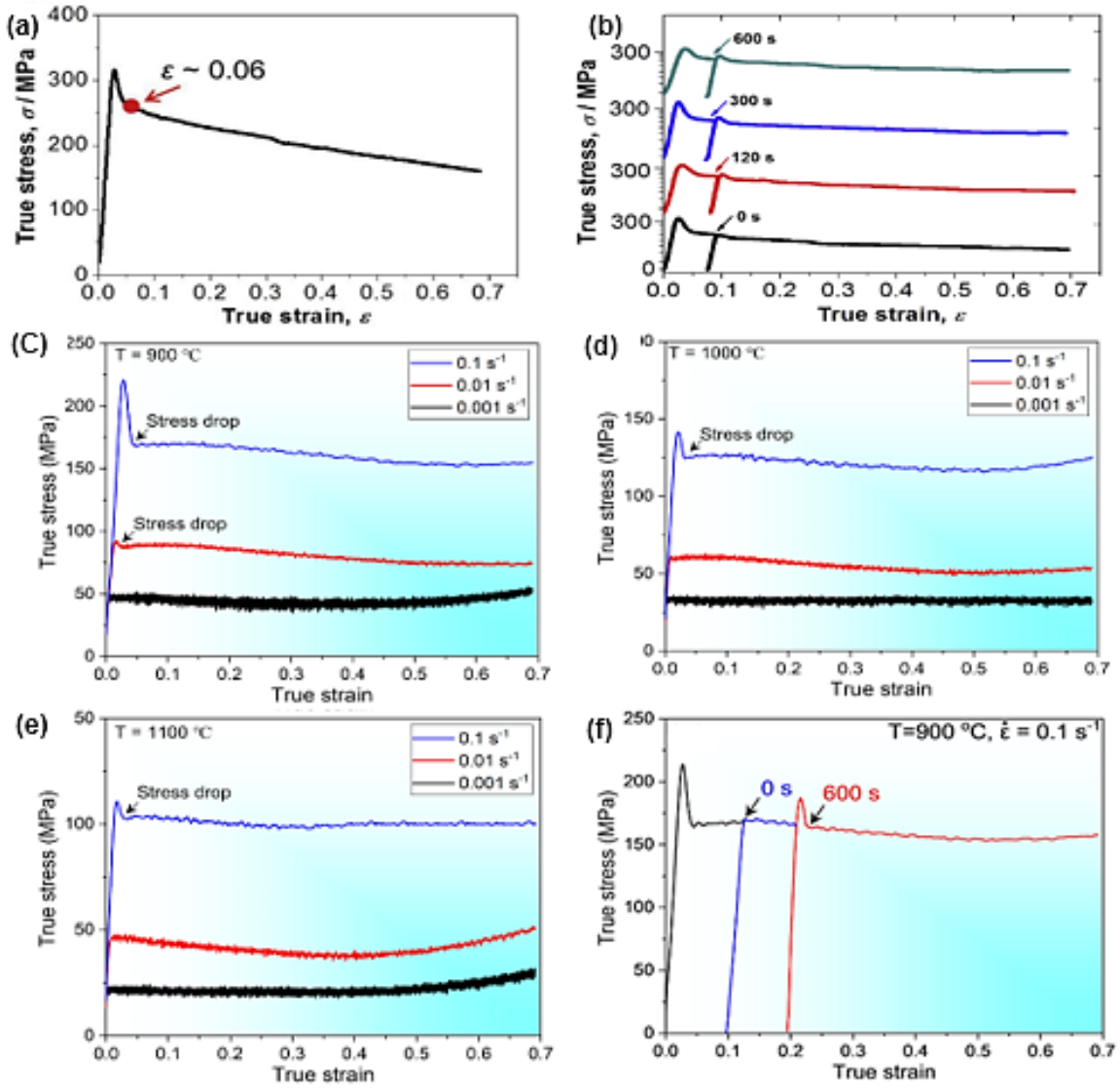

Figure 2.18: Sharp stress drop (a) and Interrupted test (b) in hot deformed HfNbTaTiZr RHEA at 1000°C/10^{-3} s^{-1} and strain of 0.06 (Eleti et al., 2019). (c-e) Sharp stress drop in $Ti_2ZrHfV_{0.5}Ta_{0.2}$ RHEA at different strain rates (10^{-1}-10^{-3}) andtemperatures (900-1000°C) (Li et al., 2022). (f) Stress-strain curve of the strain aging experiment on the$Ti_2ZrHfV_{0.5}Ta_{0.2}$ RHEA at 900°C/10^{-1} s^{-1} and a strain of ~0.1 (Li et al., 2022).

Bai et al. (2021) investigated the high temperature deformation of $TiAlVNb_2$ RHEA at strain rates from 1×10^{-3} s^{-1} - 1×10^{-1} s^{-1} and temperatures from 1000-1200°C. The flow stress of the $TiAlVNb_2$ at the initial stage of deformation shows an obvious work hardening phenomenon, as shown in Figure 2.19. This is followed by flow stress drops due to temperature increase or decrease in strain rate, which is generally linked to more thermal activation (Liang et al., 2014). The increased temperature results in the quicker movement of GB and dislocation, thereby showing softening and stress decreasing. In the event of strain rate decrease, deformation period will be delayed, and dislocation stacking degree will be reduced, leading to the decreasein flow stress.

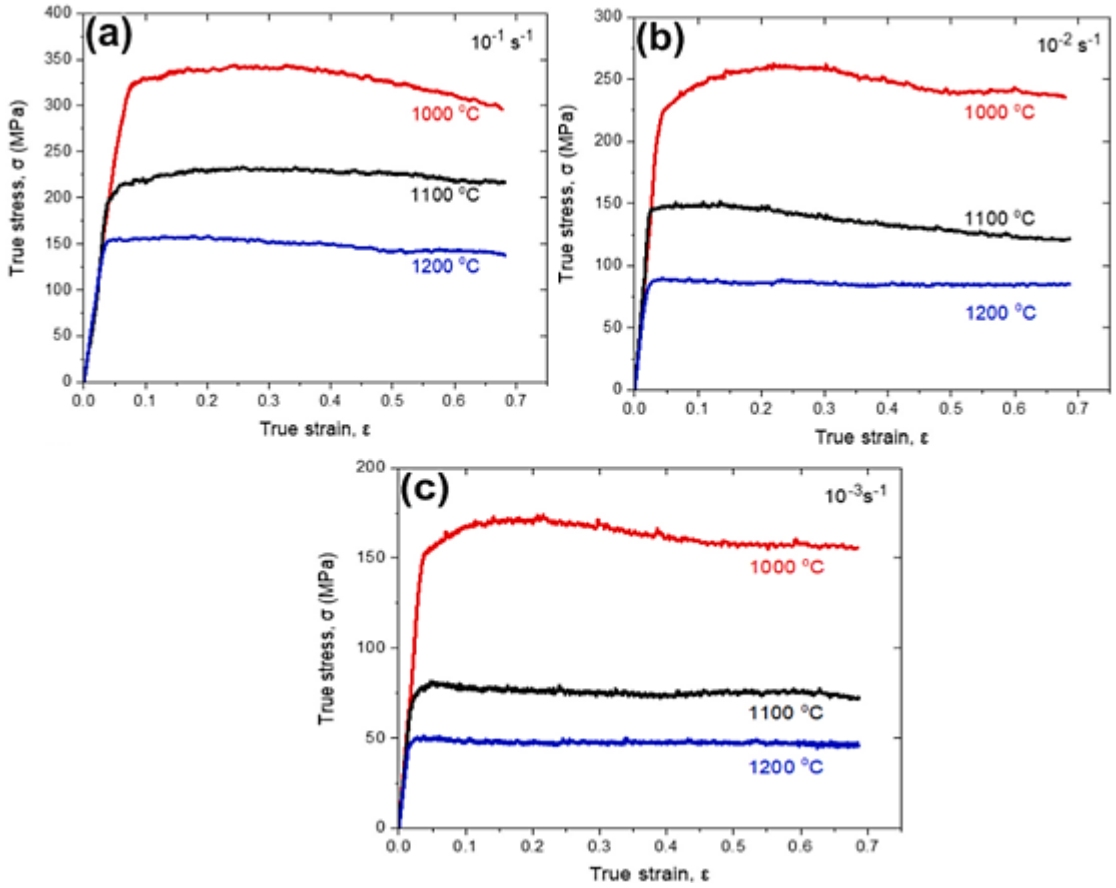

Figure 2.19: Flow stress curves of the $TiAlVNb_2$ RHEA at 1000–1200°C and 0.1 s^{-1}–0.001 s^{-1} (Bai et al., 2021).

Bai et al. (2021) also found that at strain rates of 10^{-1}–10^{-3} and temperatures of 1000-1100°C, the flow stresses in some curves exhibited decreasing trends after peak flow stress. The decreasing trend was attributed to DRX taking place in the $TiAlVNb_2$ RHEA. Likewise, the flow stress at 10^{-1} s^{-1}/1100°C, 10^{-3} s^{-1}/1100°C, 10^{-1} s^{-1}/1200°C, 10^{-2} s^{-1}/1200°C and 10^{-3} s^{-1}/1200°C remained stable after peak flow stress (Figure 2.19). After deformation, some flow

curves of some alloys could show fluctuation (Figure 2.20). For example, in Figure 2.20, Ni_3Al-based superalloy deformed at 1050-1250°C with strain rate of 0.1 s^{-1}. The fluctuations according to Wu et al. (2017) can be attributed to an alternation between the effect of work hardening and the dynamic softening which is caused by the fast-growing grains at high temperature and DRX.

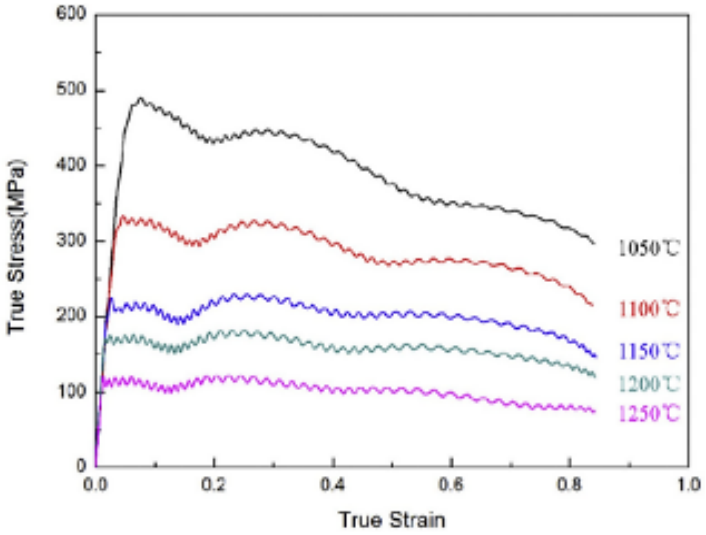

Figure 2.20: The flow stress curves of Ni_3Al-based superalloy deformed at 1050-1250°C with strain rate of 0.1 s^{-1} (Wu et al., 2017).

The hot deformation characteristics of MoNbHfZrTi RHEA were studied at the strain rate of 0.001–0.1 s^{-1} at the temperatures of 800–1200°C (Guo et al., 2016). The stress-strain curve reveals work hardening before the sample fractured at 800°C when the strain rate was 0.1 s^{-1} and 0.01 s^{-1} (Figure 2.21). A peak stress with increasing strain was identified at a strain rate of 0.1 s^{-1}, and then the stress decreased as the strain was further increased at 900°C (Figure 2.21a). Whereas at low strain rates (0.01 s^{-1} and 0.001 s^{-1}), peak stress with increasing strain was identified but then decreased and slowly reached a steady value as the strain increased. This flow curves characteristics belongs to DRX occurrence during hot deformation of alloys with low SFE (Guo et al., 2016). The stress decreased with the increasing strain since the effect of work hardening could be neutralised or partially neutralised by the occurrence of the DRV and DRX. In general, for the hot deformation mechanism of MoNbHfZrTi, both the DDRX and CDRX occurred concurrently. This is evident in Figure 2.21 where the serrated flow stress shows DDRX and the broad peak stress shows the CDRX (Guo et al., 2016).

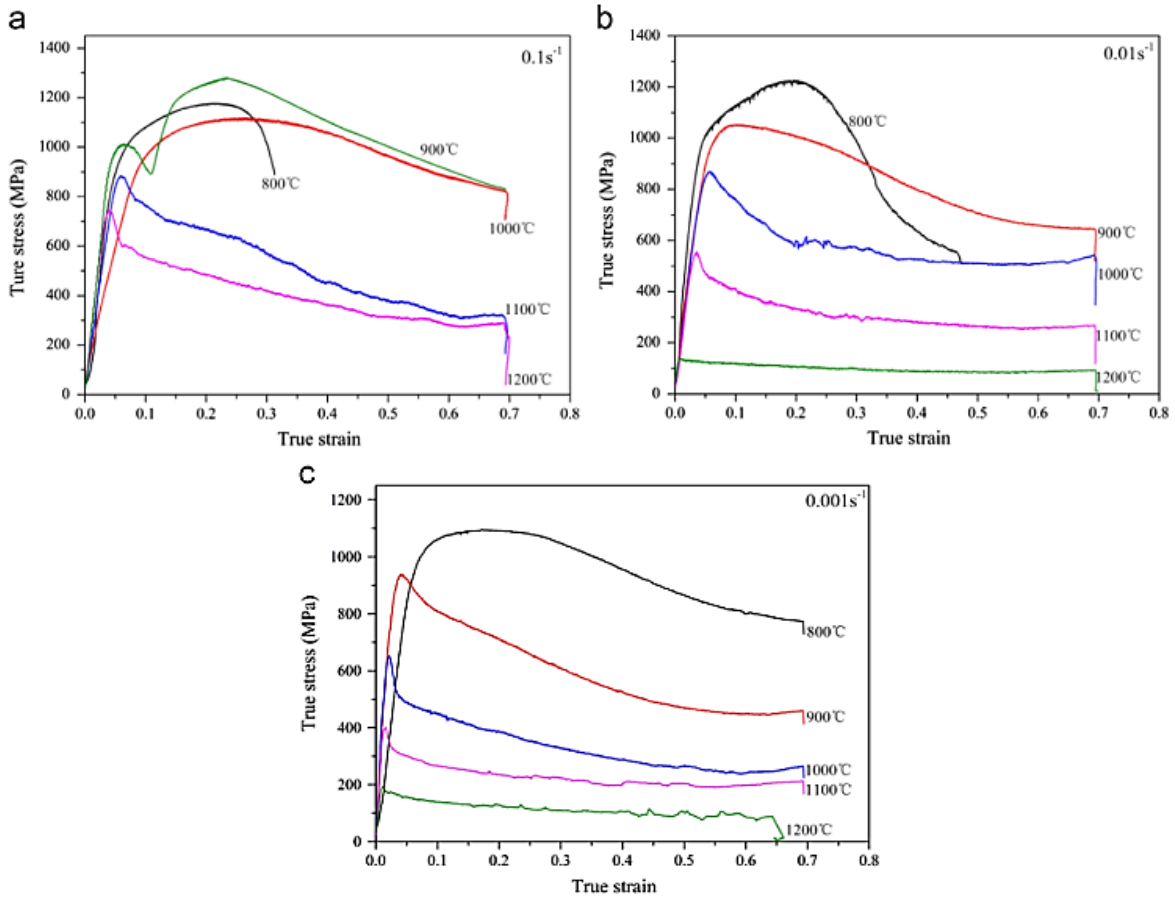

Figure 2.21: Stress–strain curves at 800°C, 900°C, 1000°C, 1100°C, 1200°C with different strain rates: (a) 0.1 s^{-1}, (b) 0.01 s^{-1}, (c) 0.001 s^{-1} (Guo et al., 2016).

Wei et al. (2021) observed work hardening after yielding in $W_{0.4}MoNb_xTaTi$ (x= 1.1, 1.3 and 1.5) RHEA hot deformed at strain rate of 10^{-3} s^{-1} and temperatures (800-1100°C). At 800°C and 1000 °C, a decrease in the yield stress was observed and attributed to the energy providedby the high temperature. The more the energy, the more the dislocations movement and grain boundaries, resulting in the drop of yield strength. After reaching the yield point, there was a pronounced steady-state flow stages signifying DRX on the stress-strain curves.

Feng et al. (2021) discovered serrated flows in deformed CrMoNbV RHEA when the temperature exceeded 500°C and a strain rate 2 x 10^{-4} s^{-1} (Figure 2.22). This could be linked to the interaction between dislocations and the local stress area caused by the coarse local atomic environment (Zhang et al., 2017). It was later seen at 1000°C that the serrated flows become less obvious compared to those at 500-900°C, indicating that a diffusion-mediated deformation mechanism took place.

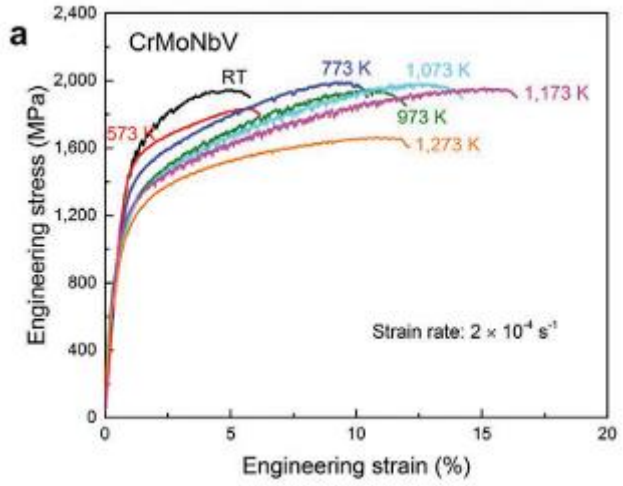

Figure 2.22: Serrated flows in deformed CrMoNbV RHEA at wide range of temperatures (Feng et al., 2021).

The $Al_{10}Nb_{15}Ta_5Ti_{30}Zr_{40}$ deformed at temperatures ranging from 250-1200°C and strain rate of 10^{-3} s^{-1} exhibited peak stress at 600°C at the start of deformation and then decreased continuously till end of deformation (Senkov et al., 2020). At 800°C, the yield stress decreased at a strain of 0.05. In addition, at temperature range of 250–500°C, the deformed alloy has almost the same stress values. At 600°C, a rapid stress drop occurred at the beginning of deformation, which followed by a continuous decrease in the flow stress. Senkov et al. (2020) described the deformation behaviour at temperatures ($T \geq 600$°C) as a softening feature with the occurrence of sharp stress drop almost immediately after yielding. The presence of a large peak stress followed by a sharp stress drop at the beginning of deformation can be a result of low mobility of dislocations present prior to deformation. The softening feature was likened to DRV and DRX. Summary of flow stress in hot deformed RHEAs is shown in Table 2.3 at different strain rate, strain and wide range of temperatures.

Table 2.3: Summary of flow stress behaviour of hot deformed refractory high entropy alloys.

Alloy composition	Strain rate (s^{-1})	strain	Temp. (℃)	Findings	references
$AlNb_2TiV$	10^{-3}	0.33	600, 800 and 1000	An increase in temperature leads to a decrease in yield stress, initially slowly at 600°C and 800°C, and then rapidly at 1000°C. Softening with steady flow was observed signifying DRV.	(Liu et al., 2021)
$ZrTiHfNb_{0.5}Ta_{0.5}$	10^{-3}	0.5	700, 800, and 900	The stress increased rapidly and then decreased to a stable value with an increase in deformation.	(Chen et al., 2018)
WReTaMo	10^{-3}	0.25	1600	At 1600°C, the alloy shows continuous strengthening without peak stress until the final testing points at strain of 25%.	(Wan et al., 2021)
$Nb_{40}Ti_{25}Al_{15}V_{10}Ta_5Hf_3W_2$	10^{-3}	0.69	800, 900 and 1000	Samples deformed at 800°C show strain hardening during deformation up to ~0.22 true strain, then stress decreases gradually with increasing strain. Samples deformed at 900°C and 1000°C show persistent softening after yielding which signifies DRV and DRX.	(Pang et al., 2022)
$Nb_{30}Mo_{30}Hf_{20}Co_{20}$	10^{-4}	0.6	600, 800, 1000	Steep and extended strain hardening stage was observed in the flow stress curves at 22°C and 600°C. Softening with steady-flow stages was observed at 1000°C, signifying DRV.	(Yurchenko et al., 2021)
$C_xHf_{0.25}NbTaW_{0.5}$	10^{-3}	-	1000, 1200, 1400	A continuous hardening before the yield was observed in all the specimens. As the temperature increased, the steady-state stress appeared at lower strain values.	(Wu et al., 2022)
TaNbHfZrTi	10^{-5} to 10^{-1}	-	750	Deformation strengthening occurred and the flow stress increased continuously with an increase in the plastic strain at high-strain rates.	(Senkov et al., 2012)
Ti_xZrVNb	10^{-3}	-	600 and 800	A serrated curve was observed at 800°C due to the alternating softening deformation and recrystallisation.	(Huang et al., 2020)
HfMoNbTaTi	10^{-2}	0.8	800, 1000 and 1200	A continuous drop in the flow stress started at the peak stress (strain = 0.027), followed by a steady-state flow stage from a strain of 0.8. The DRX behaviour was observed during compression at 1200°C.	(Yang et al., 2021)
$NbCrMo_{0.5}Ta_{0.5}TiZr$	10^{-3}	-	800, 1000 and 1200	At 1000°C, a DRX of the alloy occurs after a short stage of WH. At 1200°C, further decrease in the flow stress, followed by weak softening and a DRV.	(Senkov & Woodward, 2011)
HfMoNbTaTiZr	10^{-3}	0.3	800, 1000 and 1200	At 800°C, work hardening occurred. At 1000°C and 1200°C, DRX was observed in the flow curves.	(Tseng et al., 2019)

2.10 Microstructural evolution during hot deformation of RHEA

When metallic materials are subjected to hot deformation processes, their microstructures and properties can be enhanced, and the optimum parameters for processing the materials can be established. For example, good strength and ductility are often achieved during hot deformation processes due to grain refinement (Guo et al., 2016). It is for this reason that several researchers have used both experimental and computational techniques to provide further understanding of forming processing in many metallic systems (Jonas et al., 1969; Dong et al., 2020; Hu et al., 2020; Bai et al., 2021; Eleti et al., 2019).

Senkov et al. (2021) reported the microstructural evolution of deformed NbTaTi and NbTaZr RHEAs at 1000°C. Prior to the deformation, the microstructure of NbTaTi consisted of coarse, polygonal grains of ~0.4 mm in diameter, whereas NbTaZr consisted of finer equiaxed grains of ~40 μm in diameter. Furthermore, coarse, needle-like or plate-like, dark second-phase particles were present at NbTaZr grain boundaries, some of which propagated inside the grains. After deformation at 1000°C, NbTaTi microstructure showed a noticeable elongation of grains and formation of characteristic patterns in the directions inclined about 60–70° to the compression direction (Figure 2.23a). This signifies DRX of the grains. At 1000°C, NbTaZr microstructure which was initially equiaxed grains became elongated and many plate-like Zr-rich second phase particles located at GBs became oriented in the directions of plastic flow (Figure 2.23b). Also, the nano-lamellar structure, which was present inside grains in undeformed samples, coarsened and partially transformed to a mixture of globular-like particles.

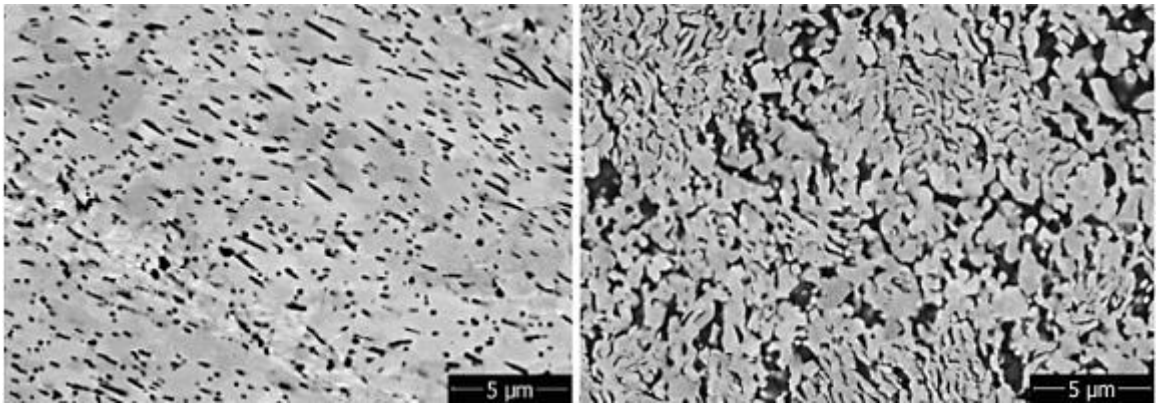

Figure 2.23: SEM images of the microstructure with 50% sample height reduction (a) NbTaTi deformed at 1000°C; (b) NbTaZr deformed at 1000°C (Senkov et al., 2021).

Guo et al. (2021) studied the evolution of compositional and microstructural heterogeneities in hot deformed $TaMo_{0.5}ZrTi_{1.5}Al_{0.1}Si_{0.2}$ RHEA at 1000°C. The microstructure after casting and annealing at 1300°C for 48 hours showed a dendritic microstructure. Silicides was also observed in the core region of interdendrite that later forms a butterfly-like eutectic morphology with the BCC_A2#2 phase. At 1000°C, DRX occurs within the inter-dendrite zone, resulting in the formation of sub-micron grains. The generation of such heterogeneous recrystallisation zones explains why flow stress decreases with strain after reaching the maximum in the compressive stress-strain curve. Furthermore, the amount of dynamic recrystallised grains around silicides was lower than that in silicide-free region which suggested that silicides probably suppress the DRX occurrence. Therefore, high temperature strength of $TaMo_{0.5}ZrTi_{1.5}Al_{0.1}Si_{0.2}$ RHEA was enhanced. A heterogeneous necklace microstructure also formed through DRX.

The microstructural evolution of an as-cast MoNbHfZrTi RHEA shows a dendritic structure before hot compression (Dong et al., 2020). After high temperature compression, there are many HAGBs in the DRX region, which indicated a gradual conversion from a LAGB to HAGBs. These observations confirm the occurrence of the DDRX. Also, a necklace-like structure was formed which composed of fine recrystallised grains along the initial grain boundaries suggesting DDRX. To be specific, at 1100°C and 0.5 s^{-1}, necklace-like structures with fine undistorted grains (1.8 μm) were observed along the original grain boundaries. At 1100°C and 0.1 s^{-1}, necklace-like structures was still observed with fine undistorted grains (2.2 μm) along the shear-deformation region, the fraction of the DRX grains is 0.42. The size and fraction of the DRX grains increase at 1100°C/0.01s^{-1} and 1250°C/0.01s^{-1}.

Juan et al. (2015) studied the mechanical properties and microstructure of hot compressed HfMoTaTiZr RHEA at 800-1200°C. HfMoTaTiZr RHEA showed (Ta, Mo)-rich dendrite and (Zr, Hf)-rich interdendrite after compression at 800°C. The dendrites and inter-dendrites are observed to elongate laterally at ~55°. In some regions, however, the dendritic structure is elongated in directions about 60°, which are related to the formation of shear bands. At 1100°C, almost all grains are elongated laterally and at 1200 °C, the grains are severely deformed and elongated laterally. The microstructures of NbTiVZr RHEA showed an equiaxed grains before hot compression (Jia et al., 2020). At 800°C, deformed microstructure of NbTiVZr comprised of pits that occur at the grain boundaries. Jia et al. (2020) also found that numerous grain

boundaries were surrounded by an increasing number of precipitates as temperature is increased.

The microstructure of MoNbHfZrTi in the as-cast condition shows dendritic structure (Guo et al., 2016). At 900°C, the initial microstructure of dendritic structure transformed to elongated equiaxed structure while part of the cast dendritic structure remained inside the equiaxed grainsat the higher strain rate of 0.1 s^{-1} (Figure 2.24). At a strain rate of 0.001 s^{-1}, fine particles or grains were formed along the GBs, which were determined to be DRX grains (Figure 2.24c). Guo et al. (2016) also mentioned that the decrease of the strain rate promoted the formation of DRX grains leading to the decrease of the stress. At 1100°C, the microstructure exhibited the same trend, such that at lower strain rate, DRX formation is favourable.

The lower strain rate and the higher deformation temperature can provide more time and energy for GB migration which can promote the development of the DRX process (Guo et al., 2016). The nucleation mechanism of DDRX and CDRX occurred simultaneously for the MoNbHfZrTi alloy during hot deformation. The DDRX is the primary mechanism and CDRXis the secondary mechanism. The effect of CDRX was weakened with the increase of deformation temperature and with the decrease of strain rate.

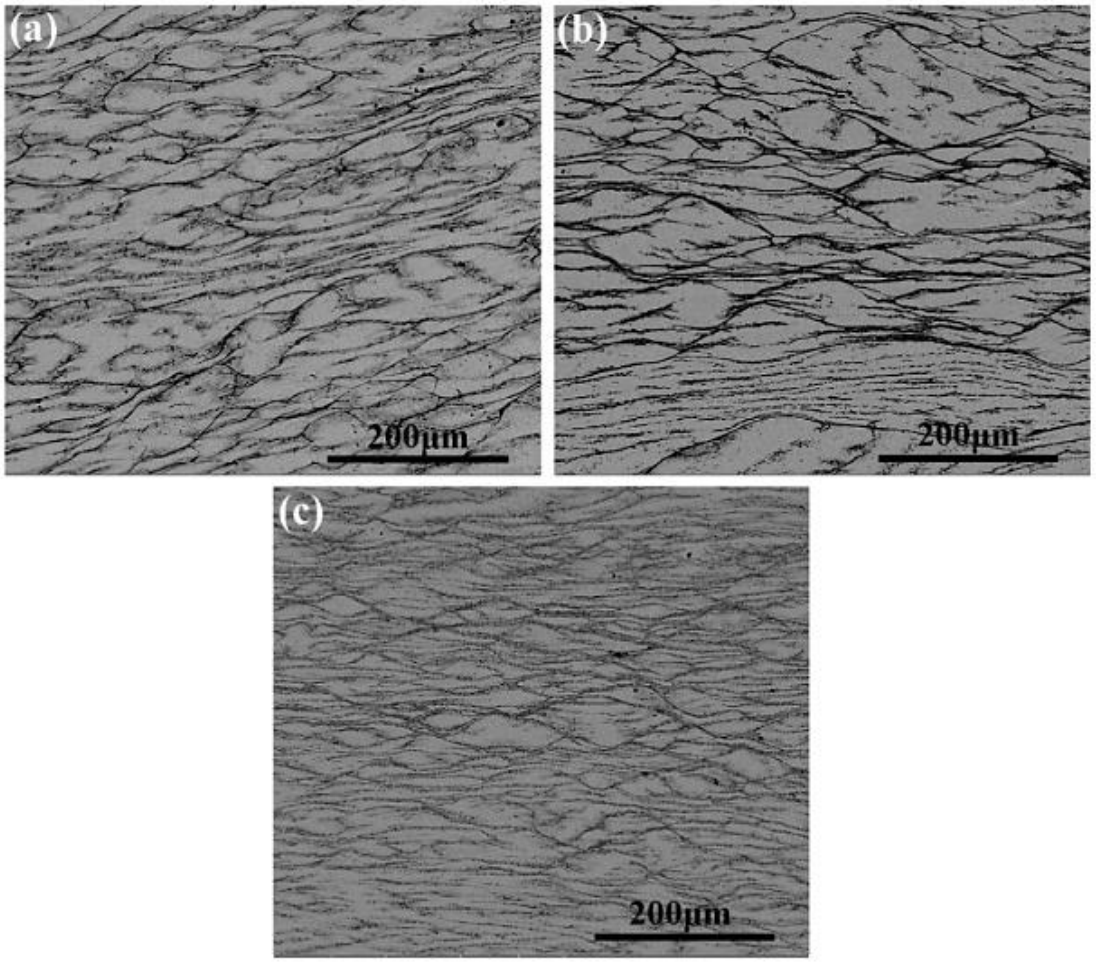

Figure 2.24: Microstructure of the MoNbHfZrTi RHEA after deformation at 900°C with different strain rates: (a) 0.1 s^{-1} (b) 0.01 s^{-1}, (c) 0.001 s^{-1} (Guo et al., 2016).

A coarse grain with a dendritic structure was found in the as-cast $TiAlVNb_2$ RHEA (Bai et al., 2021). After hot deformation, fine grains occurred along the original GBs in the samples that were deformed at lower temperatures or higher strain rates, such as at 10^{-1} s^{-1}/1000°C, 10^{-1} s^{-1}/1100°C, 10^{-2} s^{-1}/1000°C and 10^{-3} s^{-1}/1000°C (Figure 2.25). The fraction and grain size of the fine grains increased with increasing deformation temperature or the decreasing strain rate. Some of the fine grains have an equiaxed morphology; while the others were elongated due to on-going compression (Figure 2.25).

The $TiAlVNb_2$ RHEA is composed of relatively uniform coarse grains at the highest temperature (1200°C) and lowest strain rate (10^{-3} s^{-1}). Some fine dynamic recrystallised grains with clear misorientation from the initial grains can be found in grain boundaries and triple junctions of grains, as shown in Figure 2.25a. Serrated grain boundaries of coarse grains bulge towards the adjacent grains by migration of high angle grain boundaries, which form some sub-grains (labelled as 1–4) surrounded by sub-boundaries (Figure 2.25a). This was classified as a

DRX grain formation mechanism and is strongly dependent on increased energy storage caused by the propagation and pile-up of dislocations near the boundaries during the high-temperature compression. It was also discovered that the grain sizes of some newly-formed fine grains (labeled as 5–8) are comparable to these of the sub-grains (labeled as 1–4) surrounded by sub-boundaries. This suggests that the sub-grains may be on the point of forming DRX grains, as shown in Figure 2.25b.

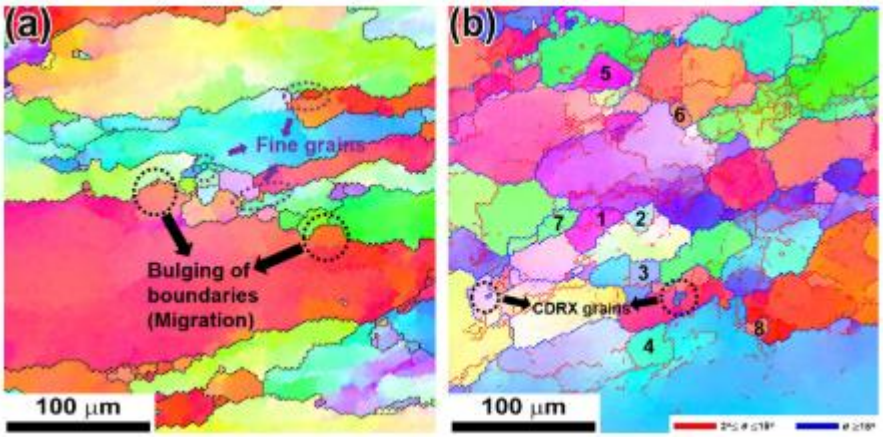

Figure 2.25: The inverse pole figure map of $TiAlVNb_2$ RHEA at 10^{-2} s^{-1}/1200°C (a) and 10^{-3} s^{-1}/1100°C (b) (Bai et al., 2021).

Eleti et al. (2019) found the microstructure in hot deformed HfNbTaTiZr RHEA to have a fine, equiaxed grains in the necklace structures. The equiaxed grains in the necklace structures are bounded by blue HAGBs, which are recrystallised grains (Figure 2.26). In connection to the continuous flow softening observed after the sharp stress-drop in HfNbTaTiZr RHEA, typical necklace microstructures composed of coarse, uncrystallised grains surrounded by fine DRXed grains were detected (Figure 2.26a-c). At 1200°C and strain rate of 10^{-3}, a more homogeneous microstructure comprised of coarse grains was observed and possibly corresponds to DRX grains after substantial grain growth (Figure 2.26d).

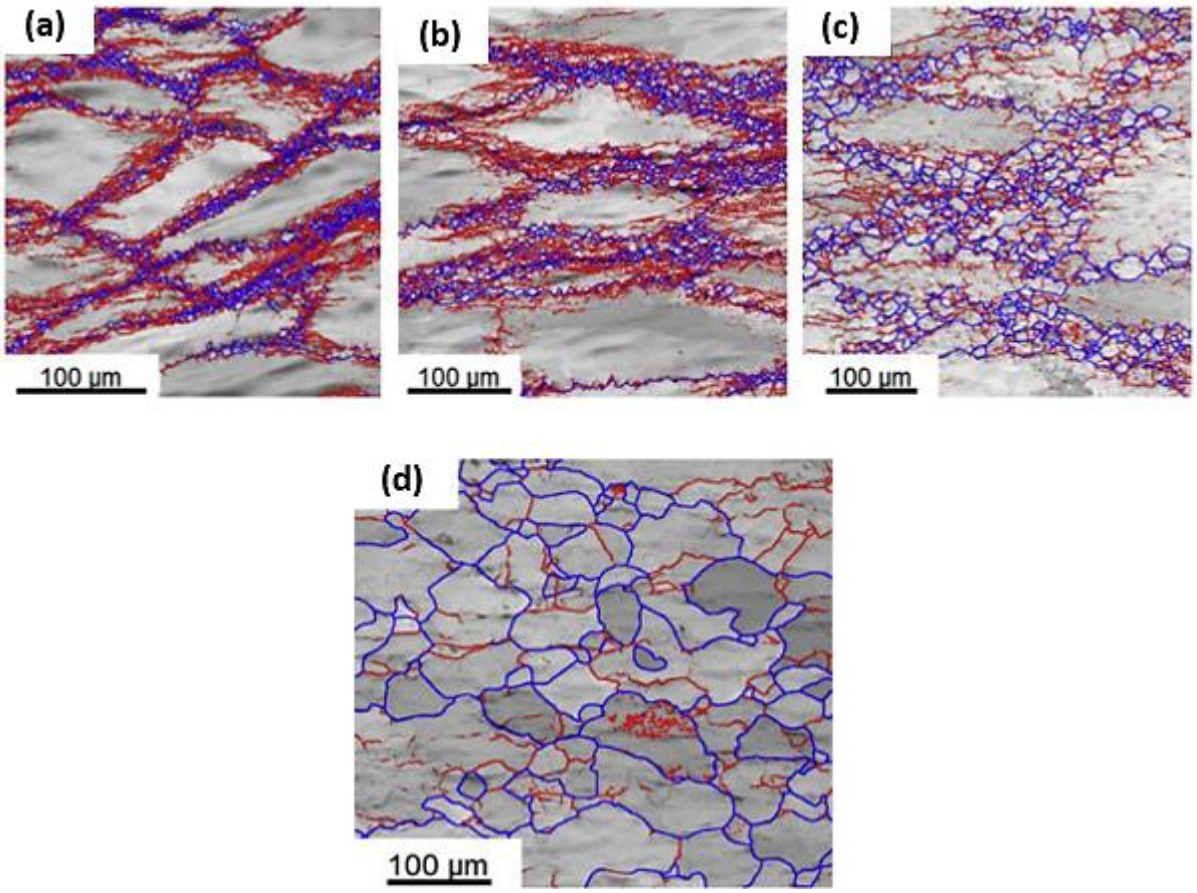

Figure 2.26: EBSD maps of HfNbTaTiZr RHEA hot compressed to 50% reduction at various temperatures and strain rates. Deformed at (a, b, c) 1000°C, (d) 1200°C (Eleti et al., 2019).

2.11 Unsafe deformation behaviour in hot deformed RHEA

During the deformation process, compressive stress concentration occurs, which causes a sharp increase in local energy. When the stress concentration reached a certain value, crack propagation began to appear, releasing energy. The VNbMoTaW RHEA exhibited much lower plastic strain, and its fracture started via crack propagation along a direction inclined at 10° relative to the loading axis, with significant involvement of grain boundaries during crack growth (Senkov & Woodward, 2011). In the deformed microstructures of $(VNbTiTa)_{100-x}Si_x$ (x=2.5, 5) RHEAs at 1000°C, silicide was discovered in eutectics which became broken after compression and the broken fragments were circulated within the original inter-dendrite areas (Xu et al., 2022). At 1200°C, silicide elongated and broke in $Si_{2.5}$ and Si_5 alloys. Similarly, Li et al. (2022) found that some of the carbides in the TiNbTaZrHf-based composites cracked along the loading direction at the side regions at 800°C (Figure 2.27a).

The appearance of micro-cracks at the sides of carbides confirmed their load-bearing effect during the high temperature deformation process. Furthermore, at 1000°C and 1200°C, a small amount of carbides cracked along the loading direction but dropped significantly, indicating that carbides continued to play a role in sharing and transferring applied stress from the matrix during the deformation process (Li et al., 2022).

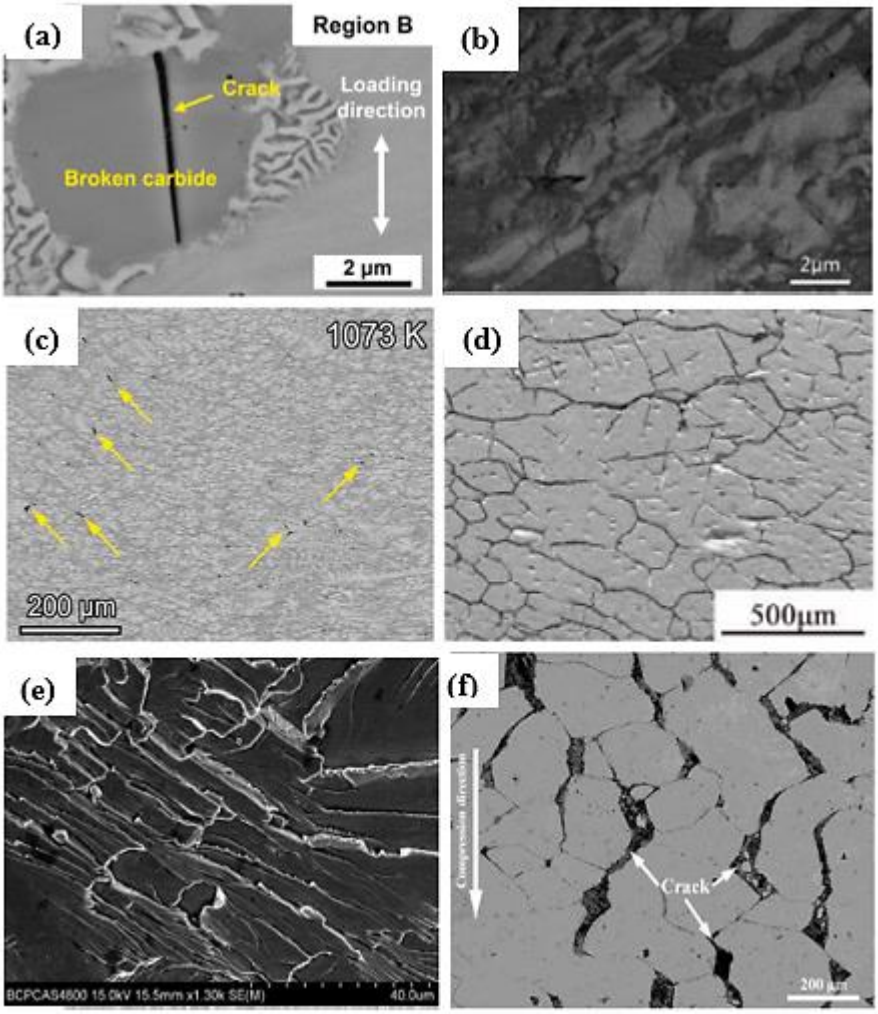

Figure 2.27: Crack propagation in hot compressed RHEAs at 800°C (a-e) and 1600°C (f): (a) Broken carbide and crack in TiNbTaZrHf based composite (Li et al., 2022). (b) Microcracks observed inside the silicides containing $HfNbTiVSi_{0.5}$ (Zhang et al., 2016). (c) Microcracks observed inside the deformed $Nb_{40}Ti_{25}Al_{15}V_{10}Ta_5Hf_3W_2$ (Pang et al., 2022). (d) Severe cracks at grain boundaries of $W_{0.4}MoNb_xTaTi$ (Wei et al., 2021). (e) Fracture feature of river-like appearance for $ZrTiHfNbMo_{2.0}$ (Chen et al., 2018). (f) Cracks propagation in WReTaMo (Wei et al., 2021).

As shown in Figure 2.27b, the silicide containing $HfNbTiVSi_{0.5}$ alloy deformed at 800°C and 1000°C showed severe deformation due to plastic flow and few microcracks were observed inside the silicides (Zhang et al., 2016). A few microcracks observed in the silicide containing $HfNbTiVSi_{0.5}$ correspond to high interfacial adhesion between the matrix and silicides.

Pang et al. (2022) observed some microcracks at 800℃ and 900℃ in $Nb_{40}Ti_{25}Al_{15}V_{10}Ta_5Hf_3W_2$ RHEA. The microcracks are intergranular originated from triple grain boundaries at 800℃ after compression (Figure 2.27c). Microcracks were also observed at 900℃ but decreased with increasing temperature until no microcracks could be seen at 1000℃. The pile up of massive dislocations at grain boundaries and its resultant stress concentration speeds up the formation and extension of microcracks, which are detrimental to deformation stability (Figure 2.27c).

The hot deformed $W_{0.4}MoNb_xTaTi$ RHEA at temperatures of 800℃, 1000℃ and 1100℃ exhibited cracks propagation (Wei et al., 2021). Most especially for $W_{0.4}MoNb_{1.3}TaTi$ in Figure 2.27d, which exhibited severe cracks at grain boundaries at 800℃. The cracks originated at the grain boundaries and later propagated along the grain boundaries. Meanwhile, few cracks extended into the grains. However, at an increased temperature of 1000-1100℃ with increased niobium concentration ($Nb_{1.5}$) the propagation of cracks was suppressed. As the testing temperature increases, the atomic activity and dislocation migration rate rise significantly. Therefore, the local stress concentration could be efficiently improved, which would prevent crack initiation and propagation.

When the molybdenum content of the $ZrTiHfNbMo_{2.0}$ RHEA was increased, poor plasticity and a river-like appearance for the fracture feature (Figure 2.27e) were observed at 800°C (Chen et al., 2018). Rhenium containing WReTaMo RHEA deformed at 1600℃ experienced GBS that contributed to the deformation as only intergranular cracks are observed (Wan et al.,2021). As shown in Figure 2.27f, cracks were observed in the WReTaMo RHEA that initiatedat the grain boundaries and then propagated along the grain boundaries (Wei et al., 2021).

2.12 Compressive strength of RHEA during hot deformation

A rapid decrease in the strength of RHEAs is known to generally occur due to the intensification of diffusion-related processes above $0.5–0.6T_m$ (Li et al., 2022, 2022; Li et al., 2022; Senkov et al., 2012). The high solid solution hardening effect and strong atomic bonding contribute to the good mechanical properties of RHEAs at elevated temperatures (Han et al., 2017). According to Senkov et al. (2021), the RHEAs have extremely high strength at $T \leq 800–1000$°C, single-phase RCCAs are generally stronger at $T \geq 1000–1200$°C than the multi-phase RHEAs. The rapid loss of strength of multi-phase RCCAs at 800–1000°C was attributed to dissolution of secondary phases at solvus temperatures. Senkov & Woodward (2011) deformed

$Nb_{20}Cr_{20}Mo_{10}Ta_{10}Ti_{20}Zr_{20}$ RHEA at 800-1200℃ and strain rate of 10^{-3} s^{-1}. At 800℃, the yield stress and compressive strength of the alloy is 983 MPa and 1100 MPa, respectively. When the temperature was raised to 1000℃ at same strain rate of 10^{-3} s^{-1}, the yield stress and compressive strength of the alloy decreased to 546 MPa and 650 MPa, respectively. Finally, at a temperatureof 1200℃, the yield stress was 170 MPa while the compressive strength of 190 MPa was reached shortly after yielding and followed by weak softening.

Senkov et al. (2011) studied the high temperature mechanical properties of NbMoTaW and VNbMoTaW RHEAs at 600-1600℃ and a fixed strain rate of 10^{-3} s^{-1}. The compressive stresses of the deformed NbMoTaW were: 561, 552, 548, 506, 421 and 405 MPa at temperatures: 600, 800, 1000, 1200, 1400 and 1600℃, respectively. For the VNbMoTaW RHEA, the compressive stresses were: 862, 846, 842, 735, 656, and 477 MPa at temperatures: 600, 800, 1000, 1200, 1400 and 1600℃, respectively. The strong resistance to high temperature softening of the alloys was likely due to slow diffusion of elements, which directly relates to high melting points of RHEAs (Senkov et al., 2011).

The high compressive strength of $ZrTiHfNbMo_x$ RHEAs (x=0.5, 1.0, 1.5) were studied at 800 and 900℃ (Chen et al., 2018). The compressive strength of $ZrTiHfNbMo_{0.5}$ alloy at 800℃ and 900℃ was 585 MPa and 288 MPa, respectively, with plasticity of 50%. When the molybdenum content of ZrTiHfNbMo increases to x=1.0, the compressive strength of the alloy increased significantly to 1099 MPa at 800℃ and 804 MPa at 900℃. Further increase of the molybdenum content to x=1.5 increases the compressive strength to 1155 MPa at 800℃ and 897 MPa at 900℃ with plasticity greater than 40% and 50%. The high temperature strength was attributed to controlling the molybdenum content addition.

Feng et al. (2021) added Cr to enhance the high temperature compressive properties of CrMoNbV RHEA at 1000℃. The compressive strength of CrMoNbV was 1062 MPa at 1000℃. Rhenium was also added to WReTaMo RHEA to enhance the high temperature compressive properties at 1600℃ (Wan, et al., 2021). A yield strength of 172 MPa and peak compressive strength of 244 MPa with plasticity greater than 25% was found and was attributed to the high melting temperature. Similarly, by substituting Re with Nb and Ti, Wan et al. (2021) studied the high temperature compression properties of WTaMoNbTi RHEA at 1600°C at a strain rate of 10^{-3} s^{-1}. The WTaMoNbTi RHEA showed a yield strength of 173 MPa and compressive strength of 218 MPa with plasticity above 25%. Wan et al. (2021) indicated that

the addition of Ti to the WTaMoNb was effective to improve the high temperature strength and plasticity. Furthermore, the addition of Ti increased the lattice constant, thereby intensify the effect of solid solution hardening.

The effect of Ti content on the high temperature mechanical properties of Ti_xZrVNb with varying elemental compositions revealed high strength (Huang et al., 2020). At 600°C, the TiZrVNb, $Ti_{1.5}ZrVNb$ and Ti_2ZrVNb RHEAs exhibited high strength of 923 MPa, 886 MPa, and 922 MPa with plasticity greater than 25%. However, the compressive strength decreased at 800°C to 233 MPa, 236 MPa, and 211 MPa for the TiZrVNb, $Ti_{1.5}ZrVNb$ and Ti_2ZrVNb RHEAs, respectively, due to high temperature softening.

Senkov et al. (2021) reported compressive strength of 268 MPa and 129 MPa for the NbTaTi RHEA at 800°C and 1200°C, while the NbTaZr alloy compressive strength decreases to 530 MPa (800°C) and 183 MPa (1200°C). Furthermore, Jia et al. (2020) reported the high temperature yield and compressive strength of NbTiVZr alloy to be 878 and 1167 MPa at 600°C. The compressive strength later decreases to 500 MPa when the temperature was increased to 800°C and finally dropped to 200 MPa at 1000°C. The Al containing Nb_2TiV RHEA at 10^{-3} s^{-1} exhibited a decrease in compressive strength (694 MPa and 612 MPa) at an increase in temperature of 600°C and 800°C (Liu et al., 2021).

Table 2.4 summarises the yield strength of other hot deformed RHEAs at different strain rates, strains, and temperatures. The addition of Mo has shown a good ability to softening resistance of RHEAs at higher temperatures than RHEAs without Mo. However, the excessive addition of Mo tends to decrease the high temperature compressive strength. W and Mo have strong strengthening effects, which induce phase boundaries that act as dislocation movements and therefore strengthen RHEA at high temperatures. The addition of Ti and Zr into RHEA simultaneously helps with high temperature strength, plasticity and density reduction. Excessive additions of Ti, Zr, and Hf weaken the high temperature yield strength due to their melting points and self-diffusion activation energies. Cr also enhances the high temperature strength of RHEA through the formation of second-phase particles and solid solution strengthening. Research progress has been made in creating a balance in the toughening and high temperature strength of RHEA by introducing carbides, silicides, and oxides, as shown in Table 2.4.

Table 2.4: Summary of compressive strength of hot deformed RHEAs.

Alloy composition	Strain	Strain rate (s^{-1})	Temperature (°C)	Compressive strength (MPa)	Plasticity (%)	References
HfMoNbTaTiZr	-	10^{-3}	800 1000 1200	1007 814 556	>20 30 30	(Tseng et al., 2019)
$Zr_{2.0}TiHfVNb_{2.0}$	0.69	10^{-3}	800 900 1200	647 476 165	50 50 50	(Chen et al., 2018)
HfNbTaTiZrW	-	10^{-3}	800 1000 1200	535 295 92	>35 >35 >35	(Wang et al., 2019)
HfNbTaTiZrMoW	-	10^{-3}	800 1000 1200	577 409 345	>35 >35 >35	(Wang et al., 2019)
$TiAl_{20}VNbMo$	-	10^{-3}	800 1000	624 180	>50 >50	(Xu et al., 2019)
NbMoCrTiAl	-	10^{-3}	800 1000 1200	860 594 105	0.135 >0.15 >0.24	(Chen et al., 2016)
$NbTaW_{0.5}(Mo_2C)_{20}$	-	10^{-3}	1200 1400	1026 697	22.3 >30	(Wu et al., 2022)
$C_{0.25}Hf_{0.25}NbTaW_{0.5}$	-	10^{-3}	1000 1200 1400	868 792 749	50 50 50	(Wu et al. 2021)
$Re_{0.5}MoNbW(TaC)_{0.5}$	0.48	10^{-3}	1000 1200	937 901	15.9 35	(Wei et al., 2019)

$Ti_2VNbMoZr_2$	-	10^{-3}	800	977	>50	(Li et al. 2022)
$Zr_1NbMoTaW$	-	10^{-3}	1000	555	25	(Li et al. 2021)
$(VNbTiTa)_{90}Si_{10}$	-	10^{-3}	1000 1200	646 133	>50 >50	(Xu et al. 2022)
TiNbTaZrHf	-	10^{-3}	800 1000 1200	1351 508 105	38.5 44 >50	(Li et al. 2022)
$ZrTiHfNb_{0.5}Ta_{0.5}O_{0.2}$	-	10^{-3}	800	966 537	>50 >50	(Chen et al. 2018)
$HfNbTiVSi_{0.5}$	0.69	10^{-3}	800 1000	875 240	50 50	(Zhang et al. 2016)
$ZrTiHfNb_{0.5}Ta_{0.5}$	0.69	10^{-3}	800 900	170 112	50 50	(Feng et al., 2021)
$ZrTiHfNb_{0.5}Mo_{0.5}$	0.69	10^{-3}	800 900	539 274	50 50	(Feng et al., 2021)
$W_{0.4}MoNb_{1.3}TaTi$	0.69	10^{-3}	800 1000 1100	1125 905 425	44.7 37.2 48.3	(Wei et al. 2021)
TiVNbMoTaW	-	10^{-3}	800 1000 1200	791 753 659	>10 >25 10	(Han et al. 2017)
$V_1NbMoTa$	-	10^{-3}	800 1000	933 811	>51 >51	(Wang et al. 2021)

2.13 Corrosion overview

Corrosion is the degradation of materials which occurs as a result of electrochemical reactions between the material and the environment. There are different forms of corrosion which include uniform corrosion, pitting corrosion, crevice corrosion, hydrogen induced cracking, stress corrosion cracking and microbial induced corrosion (Davis, 2000; Shaw & Kelly, 2006). Corrosion is more likely to occur along GBs, around defects and in areas where microstructures have large segregation of alloying elements (Li et al., 2021). Hence, the uniformity of the microstructure and chemical composition can inhibit the occurrence of localised corrosion in the alloys (Li et al., 2019).

Microstructure and composition are the two key factors to the corrosion performance of an alloy (Swanson, 2018; Li et al., 2019). Generally, some metals or alloys would show inherently low corrosion rates due to the formation of passive films. However, the localised pitting, which rapidly leads to the failure of metals, cannot be avoided once the passive film breaks down (Shiet al., 2017). Usually, the HEAs with high corrosion resistance contains large amounts of passivity-promoting elements such as Ti, Zr, Hf, Cr, Mo, and W, which facilitate the formation of stable barrier films (Qiu et al., 2017). The entropy-stabilised single solid solution phase in HEAs helps prevent pitting corrosion, which typically occurs at phase boundaries with significant compositional variations (Shi et al., 2017).

Passivity promoter elements such as Hf, Zr, and Ti can promote the formation and growth of a passive film, as a result of the relatively high heat of adsorption of oxygen (Tomashov, 1964). While, W, Nb and Ta acted as dissolution moderators or blockers, lowering the dissolution rate of the base metal. When these elements are incorporated in the passive film, they improve corrosion resistance (Liu et al., 2023; Nyby et al., 2021; Wang et al., 2022). During the corrosion process in the chloride-containing solution, the detrimental Cl^- anions would be adsorbed on the interface of the passive layer and the solution, and then penetrate through the oxide films. Successful native passive films can form protective layers over the surface, which act as barriers to the penetration of Cl^- anions if the elements for passivation are present in high enough concentrations (Presuel-Moreno et al., 2008). Therefore, the property of the passive film is highly dependent on the alloying elements (Presuel-Moreno et al., 2008). One of the major disadvantages of passive materials is their susceptibility to localised pitting corrosion (Swanson, 2018; Li et al., 2019).

Pitting is known to be associated with metallographic features such as second phases particles, inclusions, and defects (Williams et al., 2000; Frankel et al., 2017; Li et al., 2019). The resulting segregation caused by second phases particles, inclusions, and defects decreases an alloy's resistance to pitting corrosion, due to their greater susceptibility to pit initiation (Williams et al., 2000; Frankel et al., 2017; Li et al., 2019). Also, the chemical composition of an alloy determines the composition of passive film, which influences the initiation process of pitting corrosion (Williams et al., 2000; Frankel et al., 2017; Li et al., 2019). Element segregation has certain effect on alloys corrosion resistance in such a way that the uneven distribution of elements in the passive film can promote the formation of galvanic cells, therefore accelerating the electrochemical process and deteriorating the corrosion resistance (Li et al., 2021; Shi et al., 2017).

Accelerated assessment of corrosion performance can be made using electrochemical corrosion tests. When no external current or potential is applied to a metal immersed in an electrolyte, the system eventually reaches equilibrium and the net current measured is zero. The potential developed on the surface of the electrode when the metal is immersed into the electrolyte is called the open circuit potential (OCP). Potentiodynamic polarisation tests are extensively usedto identify critical corrosion parameters such as pitting potential, passivation range, corrosion current, and re-passivation potentials in an accelerated way. Corrosion rate is calculated in Equation 2.10 using ASTM G102-89 (ASTM Standard G102-89, 1999).

$$\text{Corrosion rate} = \frac{K \times icorr \times EW}{Density} \tag{2.10}$$

Where, K is 3.27×10^{-3} mm g/(μA·cm·year), i_{corr} is the corrosion current density, and EW is the equivalent weight. Equivalent weight is calculated from the expression in Equation 2.11

$$\text{Equivalent weight} = \left(\sum \frac{f_i \times n_i}{W_i}\right)^{-1} \tag{2.11}$$

Where, f_i is the mass fraction, w_i is the atomic weight, and n_i is the valence of the i_{th} element in the alloy.

2.13.1. Corrosion behaviour of refractory high entropy alloys in chloride solution

The corrosion resistance of HEAs in chloride solutions has been studied to better understand the resistance of HEAs compared to conventional corrosion resistant alloys of similar compositions. Passivation is a typical characteristic of HEAs, arising due to the common addition of passivating promoting elements such as Cr, Ti, Ni, Mo and Al. Each element may influence the alloy structure and passive film composition, giving rise to distinct electrochemical responses, depending on the alloying type and content (Nascimento et al., 2022).

The addition of V to $TiZr_{0.5}NbCr_{0.5}$ increases pitting corrosion resistance in NaCl solution (Kumar et al., 2018). It was also reported by Kumar et al. (2018) that RHEA without W is more prone to pitting corrosion in the 3.5 wt% NaCl solution than the alloy containing W. Swanson (2018) mentioned that HEAs that contain Cr compositions greater than 13 wt% can be associated with the enhanced corrosion resistant properties. In most aqueous solutions, Ti exhibits a low critical passivation potential and a wide passive region, which indicates its excellent corrosion resistance (Fu et al., 2021).

The corrosion behaviour of single BCC phase $Hf_{0.5}Nb_{0.5}Ta_{0.5}Ti_{1.5}Zr$ RHEA was investigated in the 3.5 wt% NaCl solution at 25°C (Zhou et al., 2019). Two passive regions were observed, with the first passive region from −0.1 V to 1.47 V displaying a stable passive current density, whereas the second passive region was noted from 1.9 V to –8.36 V displaying sporadic current fluctuations. The excellent corrosion resistance of the $Hf_{0.5}Nb_{0.5}Ta_{0.5}Ti_{1.5}Zr$ was attributed to the existence of metallic Ta and OH^- in the passive film. Furthermore, the alloying concept of HEAs is another factor that ensures that the high content of passivity-promoting elements is homogeneously distributed in the single-phase solid solution (Zhou et al., 2019).

The corrosion behaviour of single BCC phase $Mo_{15}Nb_{20}Ta_{10}Ti_{35}V_{20}$ RHEA was investigated in the 3.5 wt% NaCl solution (Gao et al., 2023). The polarisation behaviour showed secondary passivation characteristics, which included passivation, transition and secondary passivation. When entering the secondary passivation, the accumulation of corrosion products (TiO_2 and Ti_2O_3) blocked ion channels and inhibited further development of corrosion. The $Mo_{15}Nb_{20}Ta_{10}Ti_{35}V_{20}$ RHEA had excellent corrosion resistance with pitting potential reaching 2.285 V.

Similarly, Poulia et al. (2019) investigated the electrochemical polarisation behaviour of single-phase BCC MoTaNbVTi RHEA in 3.5 wt.% NaCl. The surface of the sample was not affected by the presence of the corrosive medium (Figure 2.28a). However, the formation of some oxidised layers of sodium chloride salts were observed in individual areas of the surface. This indicated that the alloy showed no signs of severe corrosion, while some residues of the corrosion solution simply covered its surface. The signs of corrosion did not penetrate the material as both the dendrite and the interdendrite areas have no traces of corrosion. Therefore, the observation of the sample does not reveal any selective galvanic interdendrite corrosion.

Another single BCC phase ReTaWNbMo RHEA was investigated in 3.5 wt% NaCl solution (Yan & Song, 2020). It was found that the polarisation curve showed a wide passive plateau region without the occurrence of pitting corrosion and transpassivation. Further clarification using SEM led to the discovery of pitting corrosion sites within dendrite regions and boundaryof dendrite and interdendrite regions (Figure 2.28b). This indicate that the intracrystalline corrosion mostly governs the corrosion process of the ReTaWNbMo RHEA. It was further observed that Mo and W content within boundary of dendrite and interdendrite regions is less than the dendrite region. Therefore, the corrosion sites prefer to appear within the dendrite regions.

Li et al. (2021) evaluated the corrosion resistance of the single BCC phase $TiCrVNb_{0.5}Al_{0.5}$ RHEA in 3.5 wt% NaCl solution. It was found that the passive zone of the RHEA is wide and straight, which indicated that the passive film performance of $TiCrVNb_{0.5}Al_{0.5}$ is good and stable. Corrosion kinetics parameters of $TiCrVNb_{0.5}Al_{0.5}$ showed a low corrosion current density (8.91×10^{-8} $A \cdot cm^{-2}$) and a wide passive zone (2.4 V), which means that when corrosion occurs, the HEA has a low corrosion rate. The excellent corrosion resistance in the chloride environment was attributed to the passive film formed by the high concentration of Cr^{3+}, Ti^{4+} and Al^{3+} and the single-phase BCC structure with uniform element distribution. The uniformity of the microstructure and chemical composition can inhibit the occurrence of localised corrosion in the alloy (Li et al., 2021).

The corrosion behaviour of TiZrNb, TiZrTa, and TiZrHf RHEAs was investigated in a 0.9 wt% NaCl solution (Wang et al., 2022). The TiZrNb and TiZrTa has dendritic structure with BCC, BCC1 and BCC2 phases. However, TiZrHf comprise α phase laths structure with single HCP phase. It was found that there was a rapid increase in the OCP in the first 3 h for the RHEAs, due to the formation and growth of the passive film on the surface. Afterwards, the OCP varied

slowly and then became relatively stable, suggesting that the protective passive film acted as a barrier against ion transport, reducing metal ion release. Among the alloys, TiZrNb contained the most positive potential at about -1.87 ± 5.50 mV, followed by TiZrTa (−49.40 ± 10.80 mV), and TiZrHf (−75.38 ± 8.60 mV). This implies that a better passive film occurred when there was more anodic OCP in this passivating system. Also, all the polarisation curves have a large passive region. The enhanced corrosion resistance was attributed to the improved passive film resistance as a result of alloying.

Similarly, Li et al. (2021) studied the effect of Sn and Mo on corrosion property of TiZrTaNb RHEAs in 3.5 wt% NaCl. The TiZrTaNbSn and TiZrTaNbMo comprises of dual phases (BCC1 and BCC2). The passivation current density (I_{pass}) of TiZrTaNbMo and TiZrTaNbSn alloys were 1.02×10^{-3} a·cm^{-2} and 5.2×10^{-2} a·cm^{-2}, respectively. This showed that TiZrTaNbMo entered the passivation stage and a protective passivation film was formed on the surface. The corrosion resistance increased with the decrease of I_{corr}, hence, TiZrTaNbMo showed the best corrosion resistance while TiZrTaNbSn showed the worst corrosion resistance. A small number of corrosion products were attached to the surface of TiZrTaNbMo, and no obvious corrosion was observed. However, the TiZrTaNbSn surface was severely corroded, many corrosion pits and cracks were also observed (Figure 2.28c). The severe corrosion in TiZrTaNbSn alloy was attributed to the interdendritic segregation of the Sn element.

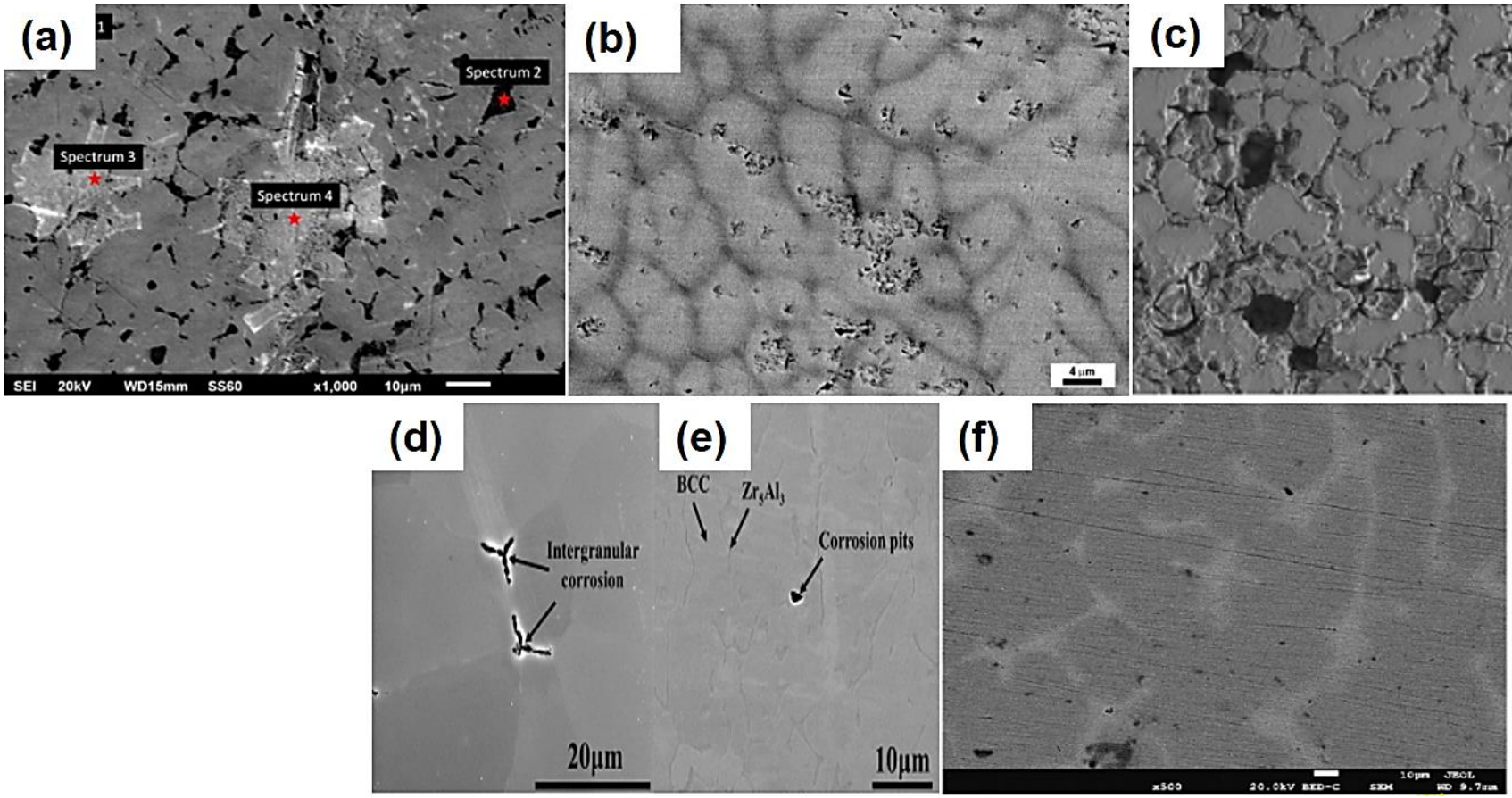

Figure 2.28: Surface morphology of RHEAs after potentiodynamic polarisation tests in chloride solution. (a) corrosion products formation in MoTaNbVTi RHEA (Poulia et al., 2019). (b) pits formation within dendrite regions and boundaries of ReTaWNbMo RHEA (Yan & Song, 2020). (c) huge pits and cracks formation in TiZrTaNbSn RHEA (Li et al., 2021). (d) pits formation of Zr_5Al_3 phase within the intergranular part of AlNbTiZrSi RHEA (Bi et al., 2023). (e) pitting formation and dissolution of Zr_5Al_3 phase of $AlNbTiZrSi_{1.0}$ RHEA (Bi et al., 2023). (f) dissolution and pits formation of HCP phase of $AlTiVCrCu_{0.4}$ RHEA (Liu et al., 2023).

The dual phase (BCC and Zr_5Al_3) containing AlNbTiZrSi and $AlNbTiZrSi_{1.0}$ corrosion performance were investigated in 3.5 wt% NaCl (Bi et al., 2023). The linear polarisation curves for the RHEAs exhibited active dissolution, activation-passive transition, passive, and transpassive regions. Corrosion of AlNbTiZrSi is mostly at the intergranular region of the Zr_5Al_3 phase, resulting in the formation of pits (Figure 2.28d). For the $AlNbTiZrSi_{1.0}$, Zr_5Al_3 phase undergoes preferential dissolution and evolves into pits at the phase boundary (Figure 2.28e). This means that the Zr_5Al_3 phase is more susceptible to corrosion in the $AlNbTiZrSi_{1.0}$ RHEA than the BCC phase.

The corrosion properties of dual phase (BCC + HCP) $AlTiVCrCu_{0.4}$ RHEA was investigated in chloride solution (Bi et al., 2023). Two short passivations zone and dissolution trend were observed. The surface morphology of the $AlTiVCrCu_{0.4}$ after linear polarisation consisted of deeper cracks at the grid line locations (Figure 2.28f). The EDS point analysis of its passivated film consisted mainly of Al, Ti, V and Cr elements, which correspond to the BCC phase composition. It was inferred that this zone is the BCC phase. The Al, Cu and Ti composition in the crack zone was almost zero, while Al, Cu and Ti are the main elements of the HCP phase, signifying that it is mainly the HCP phase that dissolves in the cracked zone.

Furthermore, the deposition of Cl and Na elements was detected in the dissolution zone, signifying that the Cl and Na ions first broke through the protective film of the HCP phase and entered the alloy matrix. This is further evidence that the grain boundaries and HCP phases begin to dissolve slowly, and when dissolution is complete, the alloy surface begins to stabilise again, as only the corrosion-resistant BCC phase remains. The XPS analysis showed that the BCC phase passive film consists of Al_2O_3, V_2O_5 and Cr_2O_3 that made it more protective than the HCP consisting of Al_2O_3 and CuO.

Xiang et al. (2019) studied the corrosion behaviour of MoNbFeCrV, MoNbFeCrTi and MoNbFeVTi RHEAs in chloride solution. The MoNbFeCrV and MoNbFeCrTi has dual phase comprising of BCC and Laves phase, while MoNbFeVTi comprise of dual phase comprising of BCC and B2 phase. It was found that all the alloys exhibited spontaneous passivation and pseudo-passive behaviour due to the lack of distinct active–passive transition characteristic. The MoNbFeCrV alloy has the most negative corrosion potential (-671 mV), which is about 200 mV lower than the MoNbFeCrTi and MoNbFeVTi alloys. However, the MoNbFeCrV alloy has the lowest corrosion current density (0.07 $\mu A/cm^2$), which is about one-fifth of the corrosion current density for the MoNbFeCrTi and MoNbFeVTi alloys.

It was also revealed that the alloys were under passivation even when the potential was about 1.0 V above the OCP. The breakdown potential was not observed for the MoNbFeCrV,

MoNbFeCrTi and MoNbFeVTi RHEAs, signifying that they exhibit excellent corrosion resistance in the chloride solution. No pits were formed on the three RHEAs surfaces. The MoNbFeCrV and MoNbFeCrTi RHEAs phases (BCC and Laves) could still be distinguished after the potentiodynamic polarisation test. Furthermore, MoNbFeVTi alloy phases (BCC and B2) were also observed after the potentiodynamic polarisation test.

2.13.2. Corrosion behaviour of refractory high entropy alloys in acidic media

Jayaraj et al. (2017) studied the corrosion behaviour of a single BCC phase TaNbHfZrTi RHEA in 11.5 M HNO_3 and 11.5 M HNO_3 + 0.05 M NaF at room temperature. The corrosion rate in 11.5 M HNO_3 was negligible when compared to exposure in 11.5 M HNO_3 + 0.05 M NaF (0.27 mm/yr). The TaNbHfZrTi RHEA in 11.5 M HNO_3 solution showed uncorroded surface, indicating a high corrosion resistance of the alloy (Figure 2.29a). However, a corroded surface (flaky morphology) was observed when the alloy was exposed in 11.5 M HNO_3 + 0.05 M NaF solution, as shown in Figure 2.29b. This confirms the unstable nature of the pseudo-passive film behaviour formed in 11.5 M HNO_3 + 0.05 M NaF.

Li et al. (2021) evaluated the corrosion resistance of a single BCC phase $TiCrVNb_{0.5}Al_{0.5}$ RHEA in 1 M HCl solution. It was found that a passive zone and secondary passive zone were observed for RHEA. The current density of the RHEA increased when the potential was at 0.9 V and then became stable. This indicate that the passive film on the surface of the alloy has a strong repair ability, which improves the corrosion resistance of the RHEA. Corrosion kinetics parameters of $TiCrVNb_{0.5}Al_{0.5}$ showed the breakdown potential and corrosion current density to be 1.91 V and $3.12 \times 10^{-7} A \cdot cm^{-2}$, respectively, signifying that $TiCrVNb_{0.5}Al_{0.5}$ has excellent pitting resistance and good corrosion resistance in 1 M HCl solution. Nevertheless, the corrosion surface of $TiCrVNb_{0.5}Al_{0.5}$ were covered with wide and open pits that proved that pitting corrosion actually occurred (Figure 2.29c). The passive film layer comprises of mainly Cr_2O_3 and Al_2O_3. The Cr_2O_3 and Al_2O_3 passive layer is not enough to prevent pitting corrosion when exposed in 1 M HCl solution because the oxide on the surface of passive film is converted into soluble chloride when the applied potential increased. This is due to oxygen replacement by chloride rich ions on the electrode surface, resulting in a decrease in corrosion resistance.

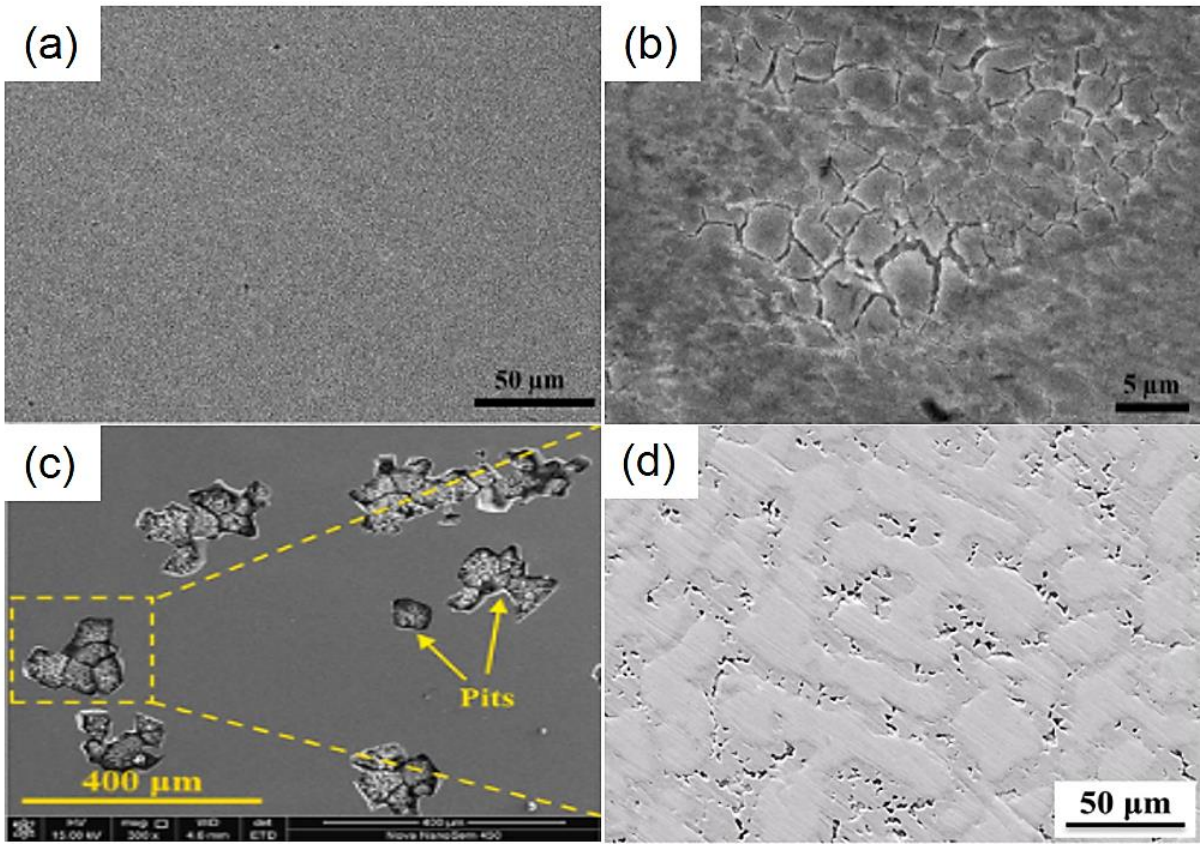

Figure 2.29: surface morphology of RHEA after potentiodynamic polarisation in acidic solution. (a) uncorroded surface of TaNbHfZrTi RHEA in 11.5 M HNO_3 (Jayaraj et al., 2017); (b) corroded surface (flaky morphology) of TaNbHfZrTi RHEA in 11.5 M HNO_3 + 0.05 M NaF (Jayaraj et al., 2017); (c) open pits on the surface of $TiCrVNb_{0.5}Al_{0.5}$ (Li et al., 2021); (d) pits and dissolution of V-rich Sigma phase in the MoNbFeCrV RHEA (Xiang et al., 2019).

Xiang et al. (2019) studied the corrosion behaviour of MoNbFeCrV, MoNbFeCrTi, and MoNbFeVTi RHEAs in 0.5 M H_2SO_4 solution. The MoNbFeCrV and MoNbFeCrTi has dual phase comprising of BCC and Laves phase, while MoNbFeVTi comprise of dual phase comprising of BCC and B2 phase. It was found that the RHEAs showed spontaneous passivation and pseudo-passive behaviour. The E_{corr} values are -275 mV, -258 mV and -285 mV for the MoNbFeCrV, MoNbFeCrTi, and MoNbFeVTi RHEAs, respectively. The lowest corrosion current density among the RHEAs was reported for MoNbFeVTi (0.70 µA/cm^2), followed by MoNbFeCrV (0.91 µA/cm^2) and the MoNbFeCrTi (1.35 µA/cm^2). It was found that the passive films are broken for the MoNbFeCrV RHEA when the potential was too high versus open circuit potential. Also, it was observed that V-rich Sigma phase in the MoNbFeCrV RHEA specially dissolved and pits were also formed, as shown in Figure 2.29d. The surface morphologies of the MoNbFeCrTi and MoNbFeVTi RHEAs remain unaffected after the potentiodynamic polarisation test.

Li et al. (2014) investigated the corrosion behaviour of $TiZr_{0.5}NbCr_{0.5}$, $TiZr_{0.5}NbCr_{0.5}V$ and $TiZr_{0.5}NbCr_{0.5}Mo$ RHEAs containing dual phase (BCC and Cr_2Zr Laves) in 0.5 M H_2SO_4. The

corrosion current density for the $TiZr_{0.5}NbCr_{0.5}$, $TiZr_{0.5}NbCr_{0.5}V$ and $TiZr_{0.5}NbCr_{0.5}Mo$ RHEAs are 0.452, 0.0204, and 0.0526 $\mu A/cm^2$, respectively. It was found that the addition of V and Mo elements to the RHEAs made the corrosion potential to shift positively and the corrosion current density to decrease. This indicates that $TiZr_{0.5}NbCr_{0.5}V$ and $TiZr_{0.5}NbCr_{0.5}Mo$ have better corrosion resistance than that of $TiZr_{0.5}NbCr_{0.5}$ in the H_2SO_4 solution. The corrosion rates of the $TiZr_{0.5}NbCr_{0.5}$, $TiZr_{0.5}NbCr_{0.5}V$ and $TiZr_{0.5}NbCr_{0.5}Mo$ RHEAs are 3.55×10^{-3} mm/yr, 1.44×10^{-4} mm/yr and 3.69×10^{-4} mm/yr. This means that $TiZr_{0.5}NbCr_{0.5}V$ and $TiZr_{0.5}NbCr_{0.5}Mo$ RHEAs have lower corrosion rate than $TiZr_{0.5}NbCr_{0.5}$ alloy in H_2SO_4 solution, due to addition of Mo and V which can form protective passivation films on the surface of the RHEA alloys.

2.14 Oxidation overview

Oxidation resistance is essential for components that perform at high temperatures (Senkov et al., 2012). When RHEAs are exposed under oxidative atmosphere, several phenomena, such as formation of protective oxide layers, surface volatilisation, and internal oxidation could take place in one alloy system (Lo et al., 2018). Therefore, a clear understanding of the oxidation kinetics is of utmost importance when alloys are newly designed.

Two very important terminologies during oxidation of alloys are selective oxidation and internal oxidation (Khanna, 2016). Internal oxidation is a process when an oxide is formed within the matrix of the base alloy, just below the external oxide (Khanna, 2016; Xing et al., 2022). This possibility occurs when the concentration of alloying element is very less and takes more time to diffuse to oxide/gas interface. Under such condition, the oxygen diffuses faster from environment through oxide and reaches oxide metal interface, further diffuses into metal and forms oxide wherever it meets the low concentration diffusing metal ion, resulting in precipitation of the oxide within the substrate matrix (Birks et al., 2006; Chan, 1997; Khanna, 2016).

In the selective oxidation, the concentration of the oxide forming element reaches beyond a critical concentration then diffuses faster towards the metal/gas interface and immediately forms a selective oxide scale of that element which protects it from further oxidation. One of the very important criteria to select material for high temperature oxidation resistance is the stability of the oxide layer formed. Usually, the oxidation tests are carried out at a fixed temperature and weight gain is measured as a function of time from which kinetics are predicted.

At high temperatures, it is very common to see that oxidation resistance of the refractory metals are extremely poor, which is attributed to their high chemical activity with respect to oxygen (Senkov et al., 2012). The poor oxidation resistance is a serious potential barrier to the long-term application of RHEAs at high temperatures. There are two extreme cases that can be expected in the oxidation of metallic alloys (Senkov et al., 2012). Firstly, the oxide fails to form a continuous passive layer due to either oxide evaporation or crack formation induced byvolume mismatch between the oxide and the alloy. This eventually leads to easy oxidation of the alloy underneath the oxide layer. Secondly, a stable and dense surface oxide layer forms and retards oxygen diffusion through the layer, so that further oxidation is prevented. Hence, the compactness of oxides plays an important role in oxidation of alloys.

The oxidation resistance of conventional alloys can be improved by incorporating the elements that form a stable and thick oxide layer on the surface of a material at higher temperatures; for example, Al, Si, and Cr (Müller et al., 2018; Telu et al., 2013; Yan et al., 2022). The high-temperature oxidation resistance of Cr-containing alloys, alloys oxide film without Cr experienced much higher oxidation rates and scale spallation than the Cr-containing alloys (Holcomb et al., 2015).

The addition of Al or Cr can lead to the formation of a continuous Al_2O_3 or Cr_2O_3 film that obstructs the direct diffusion of oxygen into the matrix (Müller et al., 2018, 2019). Also, Hf can enhance the bonding of oxide scale and matrix, while elements such as V, Mo and W usually lead to fast oxidation because of the high solubility of oxygen and easy evaporation of oxide (Butler et al., 2017).

Adding too much composition of V element will have an adverse effect on the high temperature oxidation resistance of the RHEA (Xiao et al., 2019). This is because oxides including VO, VO_2, and V_2O_5 all have a low melting point and easy to volatilise at high temperature (Lo et al., 2018). As the oxidation temperature increase, V oxides comes out from the alloy oxide scale, and destroys the formation of the dense oxide layer. A significant decrease in mass change indicating good oxidation performance usually comes along with an enhancement of the oxidation protectiveness, is clearly recognised if Cr and Al were added to RHEA (Gorr et al., 2021).

For example, TaMoCrTiAl alloy has highest oxidation resistance after 20 h at 1000°C because the alloy contains Cr, Al, and Ta with the seemingly best oxidation performance (Gorr et al.,

2021). Most RHEA form complex oxides such as $CrNbO_4$ and $CrTaO_4$ which possess rather moderate protective properties (Butler et al., 2017; Butler & Chaput, 2019; Lo et al., 2019).

The oxide $CrTaO_4$ possesses a number of unique properties that are highly important for the development of refractory metal based high temperature structural materials (Müller et al., 2020): (i) the oxide $CrTaO_4$ forms in a wide temperature range from 500°C to 1500°C exhibiting low growth rates, (ii) $CrTaO_4$ possess high adhesive properties (iii) since the oxide $CrTaO_4$ is prone to dissolve other metallic components, a harmful competition between oxides can be avoided, (iv) the protectiveness of refractory metal based alloys can be realized if alloys contain required concentrations of Cr and Ta. In addition to complex oxides, simple oxides such as TiO_2, Al_2O_3, and V_2O_5 were also formed on the oxide scale of RHEA (Butler & Chaput, 2019; Müller et al., 2019; Senkov et al., 2012).

The vast majority of RHEAs oxidise to form thick oxide scales, while some seem to form thin oxide scales that provide significant protectiveness resulting in low values of the mass gain. At lower temperatures of 700-900°C, RHEAs without elements that form a stable and thick oxide layer tends to undergo pesting (Gorr et al., 2021). Pesting phenomenon involves the fast disintegration of the metallic substrate due to intergranular oxidation, which can occur at already moderate temperatures of 600-800°C (Maruyama & Yanagihara, 1997). According to Gorr et al. (2021), features such as phase composition, impurities, and macroscopic defects such as cracks and porosity also affect the formation and growth of oxide scales. Although $CrTaO_4$, which possesses the rutile-type crystal structure, has not been known as a protective oxide in the past, it obviously possesses a potential to protect RHEA as a relatively low mass gain was measured even at 1500°C (Lo et al., 2019).

Jayaraj et al. (2018) listed the four reasons for the non-protective oxide to include;

a. formation of a smaller oxide volume than the volume of the alloy.
b. low vapor pressure and evaporation of the formed oxide products.
c. in-stability of the oxide layer because of high oxygen solubility and high oxygen transport rates in the matrix.
d. continuous spallation.

The oxide binding energy and electronegativity of elements are very important for the high temperature oxidation of HEAs because it is related to the order of oxide formation (Wei et al., 2021). If the oxidation resistance of the oxides formed is relatively poor, it will accelerate the

reaction of oxygen with other alloy elements, thus worsening the oxidation resistance of HEAs (Wei et al., 2021).

2.14.1 Oxidation kinetics equation

Kinetic behaviour basically means the variation of oxidation rate with time and this variation can be logarithmic, parabolic or linear, giving rise to three important kinetic laws: logarithmic, parabolic, and linear kinetics, respectively (Khanna, 2016; Lo et al., 2020; Müller et al., 2018; Senkov et al., 2012). The most important law which is usually followed by important high temperature metals and alloys is parabolic law (Khanna, 2016). This law predicts that the rateof oxide layer formation is inversely related to time, which means that as the time increases, the rate of scale formation is continuously decreased. The linear oxidation usually leads to poor oxidation resistance due to the weak protection of oxide scales, while the exponential oxidation results in high resistance in oxidation due to multiple factors such as protective oxide scales and low solubility of oxygen (Birks et al., 2006; Khanna, 2016; Senkov et al., 2012).

A linear curve between the mass gain per unit surface area and time is normally associated with the fact that the alloy does not form a protective oxide film and results in continuous oxidation at a constant rate. The parabolic oxidation curves result from ions or electrons penetrating the oxide film, making this the rate controlling process. As the oxide layer thickens, the oxidation rate continuously decreases (Khanna, 2016). Lastly, a logarithmic rate law assumes that there is a transfer of electrons through the oxide film. Oxidation process is either the movement of ions inwards into the metal or ions moving outwards to the surface exposed to the oxidising atmosphere (Khanna et al., 2016; Birks et al., 2006).

Oxidation kinetics are very crucial in understanding the oxidation behaviour of any material that can be explained by the power law (Anne et al., 2021; Birks et al., 2006; Khanna, 2016).

$$\Delta m = k_i t^n \qquad (2.12)$$

Where Δm is mass gain per initial surface area after the oxidation, k_i is the oxidation rate constant, and t is exposure time, n is the power-law exponent that defines the type of oxidation kinetics such as linear, parabolic, exponential and cubic growth rates. For example, oxidation kinetics follows linear growth when n = 1, and parabolic kinetics when n = 0.5 (Anne et al., 2021; Birks et al., 2006; Khanna, 2016).

The experimental oxidation kinetics are determined by choosing the satisfactory values of coefficient of determination (R^2) in mass gain per initial surface area (mg/cm^2) vs. exposure time. Other oxidation kinetics laws are as follows;

The linear kinetics are explained with the Equation 2.13 (Anne et al., 2021; Birks et al., 2006; Khanna, 2016).

$$\Delta m = k_l t \quad (2.13)$$

The parabolic kinetics are explained with the Equation 2.14 (Anne et al., 2021; Birks et al., 2006; Khanna, 2016).

$$\Delta m^2 = k_p t + c_0 \quad (2.14)$$

The cubic kinetics are explained with the Equation 2.15 (Anne et al., 2021; Birks et al., 2006; Khanna, 2016).

$$\Delta m^3 = k_c t + c_0 \quad (2.15)$$

The exponential kinetics are explained with the Equation 2.16 (Anne et al., 2021; Birks et al., 2006; Khanna, 2016)

$$\Delta m = k_e \exp^{(nt)} \quad (2.16)$$

Where, k_l, k_p, k_c, k_e are oxidation rate constants of linear, parabolic, cubic, and exponential kinetics, respectively.

2.14.2 Oxidation behaviour of refractory high entropy alloy

In the process of the high-temperature oxidation of metal, a complete and dense oxide film is formed that can have a protective effect on the metal. Generally, the higher the oxidation temperature, the faster the oxidation rate of the alloy (Kai et al., 2016, 2020). Elemental alloying plays a major effect in reducing the oxidation rate of alloys. The role of Cr in the oxidation process of HEA include; grain size decrease in alloy which reduce coarsening and reducing the contact between oxygen to improve oxidation resistance and formation of dense Cr_2O_3 (Senkov et al., 2012; Wang et al., 2020; Xiao et al., 2019). Hf and Zr play an inseparable role in accelerating oxidation because Zr and Hf have high oxygen affinity and a large atomic radius, which leads to the weakening of interatomic bonds and an increase in intermetallic diffusion coefficient at high temperatures (Sheikh et al., 2018). Therefore, it is easier for oxides to form and cause the material to peel off. For the Ta element on high-temperature oxidation of RHEAs, $CrTaO_4$ is the main reason for its high oxidation resistance (Lo et al., 2019; Müller

et al., 2020). During the growth of $CrTaO_4$-based oxides, a large number of elements are dissolved, which potentially inhibits these elements from reacting with oxygen and improves the oxidation resistance (Lo et al., 2019; Müller et al., 2019).

The isothermal oxidation behaviour of $Al_xTiZrNbHfTa$ (x=0, 0.3, 0.5, 0.75, and 1.0) RHEAs were investigated at 700-1300°C for 1-100 hours (Chang et al., 2018). It was found that the $Al_0TiZrNbHfTa$ sample exhibited partial pesting especially from 700°C to 900°C. Aluminium additions of 5 at.% inhibited pesting at 700°C to 900°C. Further Al additions lead to the improvement of the oxidation resistance, but gradually reduced with increasing Al content. However, at 1300°C, $Al_xTiZrNbHfTa$ alloys exhibited poor oxidation resistance. The mass gain of $Al_0TiZrNbHfTa$ exhibited at 700°C did not follow near-parabolic growth rate. All the alloy samples showed sub-parabolic behaviour at 900°C, while at 1100°C, all of the alloys exhibited sub-parabolic/near cubic behaviour indicating an accelerated oxidation process. A near linear behaviour was observed at 1300°C until mass gain essentially stops from approximately 10 hours onward in all alloys. The poor oxidation behaviour of $Al_0TiZrNbHfTa$ was attributed to mixed oxides formed in the oxidation layer and their low-density structure (Chang et al., 2018).

Yurchenko et al. (2018) investigated the oxidation behaviour of the $AlNbTiVZr_{0.25}$ RHEA at 800°C and 900°C. The specific mass gains after oxidation at 800°C and 900°C were 107.5 mg/cm^2 and 225.5 mg/cm^2 for 100 hours and 50 hours, respectively. At 800°C, the oxidation affected all the grains homogeneously and oxide whiskers with the average transversal size of ~500 nm was found at the surface. At 800°C, the main reason for severe oxidation were the pores, which served as places for accelerated ingress of oxygen toward the bare metal (Figure 2.30a). It also appeared as a result of the evaporation of V-rich oxides formation of complex unprotective $TiNb_2O_7$, $AlNbO_4$, and Nb_2Zr6O_{17} oxides from the very beginning of oxidation. The same oxidation mechanisms were observed at 900°C that led to the disintegration of the RHEA sample after 50 hours.

Similarly, Müller et al. (2018) studied the effect of microalloying with Si and Al on oxidation resistance of TaMoCrTiAlSn RHEA at 900°C-1100°C for 48 hours. The oxidation curves between 900°C-1000°C obeyed the parabolic rate law after a short period of transient oxidation indicating that the growth of the oxide scale proceeds through solid-state diffusion. At 1100°C, TaMoCrTiAlSi exhibited increasing oxidation rates after 30 hours of exposure. It was found that a mixture of Cr, Ti and Ta-rich oxides was detected below the alumina scale. XRD result indicated the formation of TiO_2, Cr_2O_3, Al_2O_3, and $CrTaO_4$ in the oxide scale after 48 hours of

air exposure at 1000°C. After 48 hours of exposure to air at 1100°C, the oxide scales are locally more buckled, as shown in Figure 2.30b (Müller et al., 2018).

The oxide scale thickness increase with increasing temperatures of 900°C (1.3-1.9 μm), 1000°C (3.7-5.6 μm) and 1100°C (9.2-16.3 μm) after 48 hours of exposure. Müller et al. (2018) also found a pronounced zone of internal corrosion underneath the oxide scales of TaMoCrTiAlSi at 900°C, 1000°C, and 1100°C (Figure 2.30b). Furthermore, oxidised phase boundaries between the Mo and Ta-rich BCC solid-solution matrix and the Laves phase were observed, particularly in the vicinity of the large Laves phase particles. Oxide scales formed on top of Laves phase particles after 48 hours of oxidation at 1000°C further yield the formation of Ta-rich oxides beneath a thin outermost layer of chromia. The oxide scale formed on top of the Laves phase was much thinner and more protective than that formed on top of the matrix phase (Müller et al., 2018).

The oxidation performance of NbZrTiCrAl RHEA was investigated at 800-1200°C for 50 hours (Zhang et al., 2019). A slow mass gain of the RHEA occurred during the whole oxidation process at 800°C, and the oxide scale formed on the surface after 50 hours oxidation was still dense and complete. For the oxidation at 1000°C, the mass gain of the RHEA increased slowlyin the initial 25 hours but increased a bit fast after. When being oxidised at an elevated temperature of 1200°C, an increase mass gain of the RHEA was observed. It was found that $CrNbO_4$ was the predominant oxide in all the oxidation products of the RHEA, and some amount of ZrO_2, TiO_2, $ZrNb_2O_7$ and Al_2O_3 were also present. The outer oxide layer of the RHEA after oxidation at 1200°C for 5 hours possess a distinct layered structure with textured porosity. This was ineffective in preventing oxygen diffusion, and the weak bonding strength between sub-layer interfaces led to cracks. Furthermore, with the increase of oxidation time, the thick oxidised layer shows a large amount of growth stress and thermal stress for the growth of oxides. This caused the formed oxidised layer to crack easily in the subsequent oxidation process. Furthermore, a large number of oxygen diffusion channels were generated that facilitated oxygen to diffuse faster into the interior (Zhang et al., 2019).

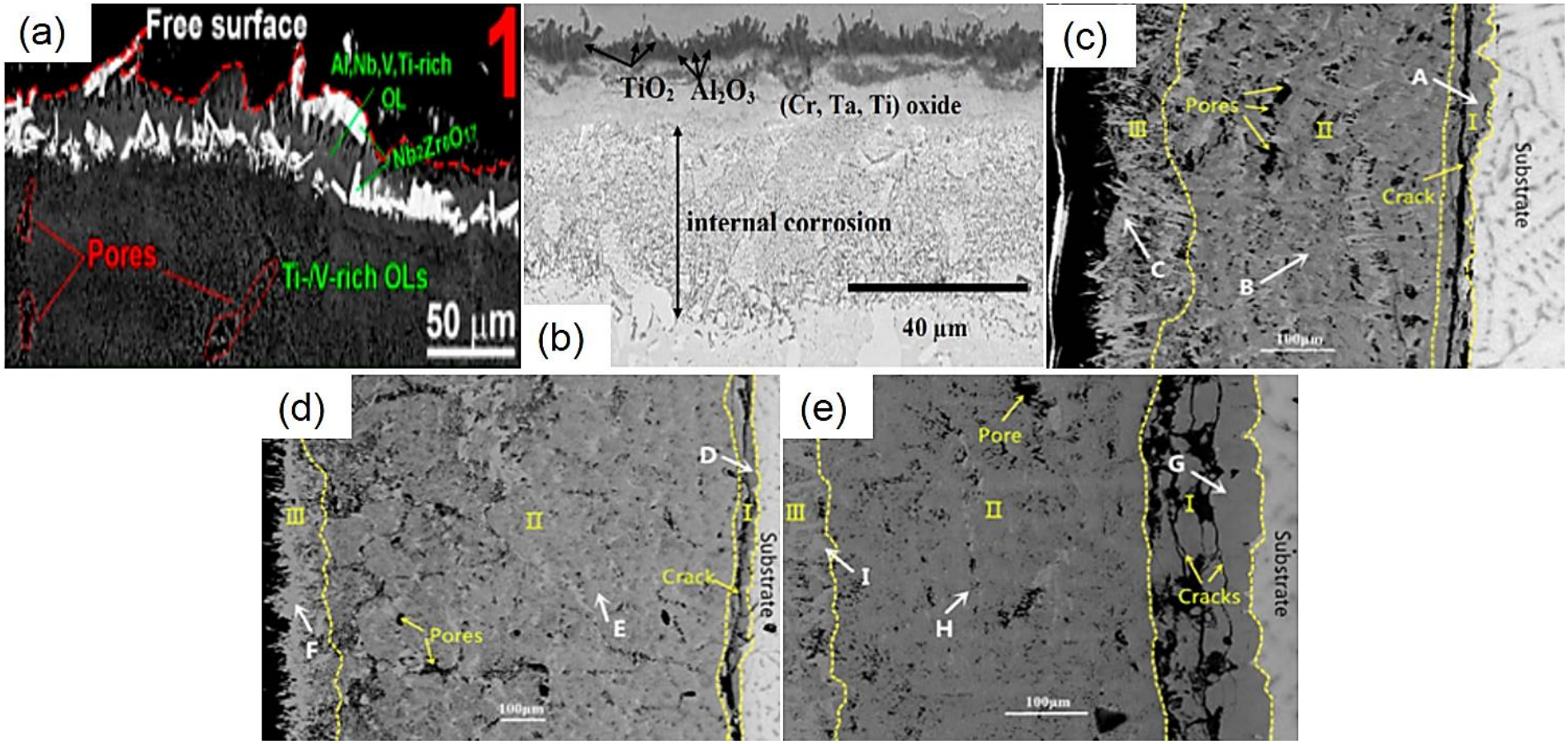

Figure 2.30: SEM cross-sectional micrographs of the oxide scales formed on the RHEAs at high temperatures. (a) pores formation at oxide scale of $AlNbTiVZr_{0.25}$ RHEA at 800°C (Yurchenko et al., 2018); (b) oxide scales buckling of TaMoCrTiAlSn RHEA at 1100°C (Müller et al., 2018); (c-e) pores and cracks within the oxide scales of CrMoNbTaV RHEA at 900°C, 1000°C and 1100°C (Xiao et al., 2019).

The isothermal oxidation behaviour of $NbCrMo_{0.5}Ta_{0.5}TiZr$ RHEA was studied at 1000°C for 100 hours in air (Senkov et al., 2012). It was found that the weight of the oxidised sample was 1397.1 mg during first 10 h at 1000°C. After 100 hours at 1000°C, the weight of the oxidised sample increased to 1620.7 mg and the thickness of the oxide scale was ~ 1.75 mm. It was also observed that during cooling after the high-temperature exposure, the oxide layer separated from the sample surface. The oxide layer separation from the surface was attributed to different coefficients of thermal expansion of the oxide and the alloy. The oxide layer formed on the $NbCrMo_{0.5}Ta_{0.5}TiZr$ alloy surface consisted of several oxides: Cr_2O_3, $CrNbO_4$, Nb_2O_5, $CrTaO_4$, $MoTiTa_8O_{25}$, Cr_2TiO_5, $Cr_2Ti_5O_{13}$, $Nb_3Cr_2O_{10}$, $Ta_{12}MoO_{33}$, $Nb_2Zr_8O_{21}$, Ta_4O_5 and Ti_2ZrO_6.

Xiao et al. (2019) investigated the isothermal oxidation behaviour of CrMoNbTaV RHEA at 900-1100°C in air for 5-25 hours. Xiao et al. (2019) found that CrMoNbTaV alloy obey pseudo-parabolic rate law at 900°C and 1000°C. This indicated that the growth of the oxide scale proceeds through solid state diffusion. At 5 hours and 1100°C, the mass change was foundto increase, followed by continuous reduction. The morphologies of the oxides formed at 900°C, 1000°C and 1100°C showed long rod-shaped oxidation products, but oxides at 1100°C was somewhat larger than those of 900°C and 1000°C. The type of oxidation products formed on the alloy at 900°C and 1000°C consisted of combination of simple and complex oxides: Nb_2O_5, NbO_2, $CrTaO_4$, $CrNbO_4$, Ta_9VO_{25}, Nb_9VO_{25} and TaO. While at 1100°C, $CrTaO_4$ and $CrNbO_4$ disappeared from the surface due to the detachment of oxide scale from the matrix when the oxidation temperature was increased.

The thicknesses of oxide scales of the CrMoNbTaV at 900°C, 1000°C and 1100°C were 530 μm, 1132 μm, and 600 μm at 900°C, 1000°C and 1100°C, respectively. The oxide scales formed on the CrMoNbTaV surface were classified into three regions (Figure 2.30 c,d,e). In region one, a thin oxide (mixture of Cr, Mo, Nb, Ta, and V) was formed and attached to the substrate region. A distinct crack was also observed in the region I at 900°C and 1000°C, while more cracks are formed in it as the oxidation temperature increased to 1100°C (Figure 2.30c-e). A thick and porous oxide (mixture of Cr, Nb, Ta, and V) was found in region two and comprise largest thickness of gray and white regions. In region three, a relatively thin outer region was observed consisting a mixture of Nb, Ta, and V oxides.

Butler et al. (2017) examined the high temperature oxidation behaviours of NbTiZrV and NbTiZrCr RHEAs at 1000°C for 100 hours. It was discovered at 8 hours of oxidation that the NbTiZrV alloy was completely oxidised. At this stage, four oxides comprising $TiNb_2O_7$, TiO_2,

$Nb_2Zr_6O_{17}$, and V_2O_5 were detected from the NbTiZrV alloy surface. This oxide mixture did not aid in oxidation resistance, the oxidation proceeded primarily via internal oxidation. The NbTiZrCr alloy displayed much lower mass gains after 100 hours of oxidation exposure. This was primarily attributed to the formation of a complete external oxidation layer. It was found that in short oxidation tests, the preference for internal oxidation led to the sequential oxidation of the most stable oxide formers such as Ti to form TiO_2 and Zr to form ZrO_2. These oxides then reacted with other oxides in NbTiZrV alloy to form internal scales consisting of a mixture of complex and simple oxides: TiO_2, $TiNb_2O_7$, and $Nb_2Zr_6O_{17}$.

Ouyang et al. (2022) investigated the oxidation behaviour of the $Ti_{38}V_{15}Nb_{23}Hf_{24}$ RHEA at high temperatures of 800-1300°C for 1 hour. At 800°C and 900°C, the oxide scales formed on the surface of the alloy matrix are homogeneous and dense, a characteristic of external oxidation behaviour. In contrast, the morphologies of the oxide scales at 1000-1300°C comprised of white precipitated particles as well as pores and the porosity of the oxide scales increased with the elevated temperatures. Above 1000°C, the slopes of the mass gain curves are also gradually increased which demonstrated that 1000°C is the critical temperature for occurrence of the transition from external oxidation to internal oxidation of the RHEA. At 900°C for 1hour, mixed oxides of $Ti_2Nb_{10}O_{29}$ and $Hf_6Nb_2O_{17}$ were observed in the topside of the oxide layer, which gradually turned to dense composite oxides of $(TiVNbHf)_{100-x}O_x$ with FCC structure. In addition, slight $V_2Ti_7O_{17}$ like oxides coexisted in the composite oxides. The top-surface of the oxide scale of 1000°C consisted of $TiNb_2O_7$ and Nb_2O_5, while below the top-surface, $V_3Ti_6O_{17}$ and HfO_2 was gradually enhanced with an increased oxide layer. The summary of reported literatures on oxidation behaviour of RHEAs at different temperatures, oxidation time, mass gain, and other conditions are listed in Table 2.5a and b.

Table 2.5a: Summary of oxidation behaviour of refractory high entropy alloys.

Alloy composition	Duration (hrs)	Temperature (°C)	Oxidation test	Key findings	References
TaMoCrTiAl	12	500, 1000, 1300, 1400 and 1500	Isothermal	$CrTaO_4$ formed from 500°C to 1500°C exhibiting low growth rates. The $CrTaO_4$ possessed high adhesive properties.	(Gorr et al., 2020)
$Al_xCr_yMo_zNbTiZr$	20	1000	Isothermal	The oxidation at 1000°C for 1 hour led to a 0.5-13.38 mg/cm^2 gain in the mass. At 1000°C for 20 hours, the RHEA showed a mass gain of 20 mg/cm^2 after prolonged oxidation.	(Waseem et al., 2018)
$Ti_2ZrHf_{0.5}VNb_{0.5}Al_x$	1-50	800	isothermal	The Al addition reduces oxidation mass gain of the $Ti_2ZrHf_{0.5}VNb_{0.5}Al_x$ RHEAs to 112.1 mg·cm^{-2} after 50 hours oxidation. It was discovered that twisting and cracking of Al_2O_3 oxide layer and the formation of evaporable oxide V_2O_5 that accelerate the oxidation process.	(Qiao et al., 2021)
AlNbTiZr	50	600, 800 and 1000	isothermal	The mass gain behaviour of AlNbTiZr was nearly parabolic indicating the formation of protective oxide layers at 600, 800 and 1000°C for 3 hours. The long-term oxidation for 50 hours at 600, 800 and 1000°C confirmed that the oxide layers were protective, intact, and spallation did not occur.	(Jayaraj et al., 2018)
$Al_xCrTiMo$	1, 4 and 7	1000		The oxidation kinetics exhibited moderate mass gain in Al-containing RHEAs with content 0.5 to 1 during the process of oxidation. The reduction of mass increase rate occurred twice during the oxidation process of $Al_{0.25}CrTiMo$. The oxidation layers consisted of TiO_2, Al_2O_3 and Cr_2O_3 from exterior to interior of alloy.	(Zhang et al., 2021)
$TiNbTa_{0.5}Zr$	5, 10, 15, 20 and 40	1000	isothermal	$TiNbTa_{0.5}Zr$ exhibited exponential oxidation behaviour. The oxidation products at 1000°C for 10 hours are TiO_2, Nb_2O_5, Ti_3O_5, and ZrO_2. The oxide scale is thick and the zone affected by oxidation is about 300 µm in thickness.	(Cao et al., 2019)

Table 2.6b: Summary of oxidation behaviour of refractory high entropy alloys.

Alloy composition	Duration (h)	Temperature (°C)	Oxidation test	Key findings	references
$TiNbTa_{0.5}ZrAl$	5, 10, 15, 20 and 40	1000	isothermal	$TiNbTa_{0.5}ZrAl$ exhibited exponential oxidation behaviour. The main oxides in the oxide scale are TiO_2, Nb_2O_5, Ti_3O_5 and ZrO_2, and Al_2O_3. The oxide scale becomes thinner (150 µm in thickness) with aluminium addition. The formed Al_2O_3 oxide scale is dense and well adhered with the $TiNbTa_{0.5}ZrAl$ substrate leading to high oxidation resistance of the refractory.	(Cao et al., 2019)
$TiNbTa_{0.5}ZrAlMo_{0.5}$	5, 10, 15, 20 and 40	1000	isothermal	$TiNbTa_{0.5}Zr$ exhibited linear oxidation behaviour. The oxidation products at 1000°C for 10 hours are TiO_2, Nb_2O_5, Ti_3O_5 and ZrO_2, Al_2O_3 and MoO_3. The oxide scale becomes weak with Mo addition and separated from the substrate. Perpendicular and parallel cracks are found on the surface which lead to a pathway for oxygen to diffuse into the substrate. This eventually led to a fast oxidation of the $TiNbTa_{0.5}ZrAlMo_{0.5}$ RHEA.	(Cao et al., 2019)
$Al_{0.5}Cr_{0.25}Nb_{0.5}Ta_{0.5}Ti_{1.5}$	100	800 and 1,100	isothermal	Alloying of Al and Zr enhanced the oxidation resistance of $Al_{0.5}Cr_{0.25}Nb_{0.5}Ta_{0.5}Ti_{1.5}$ with Al having the more significant effect, whereas Zr plays a positive role in relieving the cracking trend in multilayered oxide scales. At 1100°C, protective oxide scales of Al_2O_3 did not form thereby leading to performance failure.	(Sheikh et al., 2020)
$Al_{20}Nb_{30}Ta_{10}Ti_{30}Zr_{10}$	1000	0.5, 4 and 100	isothermal	After 100 hours of oxidation, the oxide product includes $NbAlO_4$, ZrO_2, $Ti_7Al_2O_{15}$, $Ta_2Nb_4O_{15}$, TiO_2, ZrO_2, TiO_2, ZrO_2, and Ta_2Al and Al-rich oxide. It was found that the slowest growing layer was the outer composite oxide, consisting of $NbAlO_4$, ZrO_2, $Ti_7Al_2O_{15}$, and $Ta_2Nb_4O_{15}$. This provided an inherent resistance to the inward flux of oxygen, thus slowing the overall oxidation rate.	(Butler & Chaput, 2019)

2.15 Summary

- Combination of empirical phase prediction and CALPHAD can assist the phase prediction and design of HEAs.
- During as-cast process of RHEAs, the typical microstructure is dendritic. This microstructure consists of dendrite and an inter-dendrite region. Apart from single-phase, addition of elements such as Cr, Ti and Zr can inhibit dual or multi-phase in RHEAs.
- The high hardness of RHEAs can be attributed to a solid-solution-like strengthening mechanism by significant lattice distortion and second phase strenghtening.
- Microstructural evolutions of metals or alloys are often caused by the respective hot deformation mechanisms, such as WH, DRV and DRX.
- The typical characteristics of DDRX are serrations and bulging along the grain boundaries. The grains that are located along the pre-existing grain boundaries through bulging mechanism form a necklace structure as a result of the DDRX mechanism.
- CDRX mechanism involves the transformation of LAGBs into HAGBs in deformed grains.
- All the probable mechanisms influencing deformation in metallic alloys, such as WH, DRX, and DRV, have also been observed in RHEAs. The DDRX and CDRX occurred concurrently in some of the hot deformed RHEAs.
- Sharp drops in flow stress occur in RHEA, which may be attributed to the unlocking of dislocations pinned by the Cottrell atmosphere or short-range order.
- The resistance to high temperature softening of RHEAs can be attributed to slow diffusion of elements, high thermal stability, and second phase strengthening mechanism.
- The addition of Cr, Al, W, V, Nb, Mo, Ta, Zr, Ti, and Hf contributed to the high temperature strength and plasticity of RHEAs.
- RHEAs can be passivated, in some instances showing secondary passivation characteristics.
- Segregation of elemental composition of RHEAs can lead to pitting corrosion sites despite having excellent corrosion resistance. Single-phase BCC structure with uniform microstructure and chemical composition can inhibit the occurrence of localised corrosion.

- The accumulation of corrosion products such as Cr_2O_3, V_2O_5, TiO_2 and Ti_2O_3 form a good passive film that blocked ion channels and inhibit the further development of corrosion in RHEAs.
- Dual phase and multi-phase in RHEAs can lead to intergranular corrosion, with one of the phases been dissolved or corroded with pits in both chloride and acidic solutions.
- The passive layer sometimes might not be enough to prevent pitting corrosion when exposed in both chloride and acidic solutions. The oxygen can be replaced by chloride and sulphate ions on the electrode surface in both chloride and acidic solutions, leading to a decrease in corrosion resistance.
- Reasons for the non-protective oxide are formation of a smaller oxide volume than the volume of the alloy, low vapor pressure and evaporation of the formed oxide products, instability of the oxide layer, and continuous spallation.
- Pesting can occur in RHEAs at temperatures range from 700 to 900°C.
- The oxide scale thickness of RHEAs increases with increasing temperatures. The thick oxidised layer concentrates a large amount of growth stress and thermal stress for oxides growth. This caused the formed oxidised layer to be easily cracked in the subsequent oxidation process, and then a large number of oxygen diffusion channels were generated that facilitated oxygen to diffuse faster into the interior.
- A pronounced zone of internal corrosion underneath the oxide scales can also be observed during oxidation of RHEAs.

2.16 Design considerations for developing proposed refractory high entropy alloys

The TiNbVTaW and CrNbTaVW was selected since individual elements Ti, Cr, Nb, V, Ta, and W demonstrate excellent properties such as high temperature strength, hardness, oxidation and corrosion properties. The atomic radius difference of Ti and Cr with other elements such as Nb, V, Ta, and W can form lattice distortion effect that can lead to higher hardness. The large increase in strength due to small atomic radius elements suggests a solid solution- like hardening mechanism (Cui et al., 2023; Han et al., 2017; Roy et al., 2021; Zheng et al., 2022). Second phase hardening such as the addition of Cr and Zr have been reported to induce a Laves phase for increased hardness (Coury et al., 2018; Wu et al., 2021; Xu et al., 2023).

The HEAs with high corrosion resistance contains large amounts of passivity-promoting elements such as Ti, Cr, and W which facilitate the formation of stable barrier films (Zhang et

al., 2022; Jayaraj et al., 2017; Qiu et al., 2018; Xiang et al., 2019). Ti exhibits a low critical passivation potential and a wide passive region, which indicates it's on resistance (Fu et al., 2021). V has been reported to protect RHEAs from localised corrosion, such as pitting, in NaCl and H_2SO_4 solutions (Li et al., 2014). The addition of Nb, W, and Ta has been reported to reduce the rate of dissolution of materials (Nyby et al., 2021; Z. Wang et al., 2022). Kumar et al. (2018) reported that RHEAs without W are more susceptible to pitting corrosion in a 3.5 wt% NaCl solution. The alloys containing W, Ti, and Nb have strong passivation potentials, which enable oxide films to form in HEAs with compact packing structures, and chloride ions cannot simply penetrate (Patel et al., 2021).

The elemental addition of Ti and Ta can form stable oxides of TiO_2 and $TiTaO_4$ that can prevent the influx of oxygen to the outer interface and reduce the oxidation kinetics (Schellert et al., 2023). The high diffusion of Cr can enable the synthesis of $CrTaO_4$, Cr_2O_3, and $CrNbO_4$ that would form a barrier for both inward diffusion of oxygen and outward diffusion. These will provide protection against oxidation at high temperatures (Butler et al., 2017; Du et al., 2022; Lo et al., 2019; Xiao et al., 2019). It was suggested by Senkov et al. (2018) that elements such as Cr and Ti be added to improve ductility, yield strength and thermal stability. Cr and Ti were also added because of their low densities (7.1 and 4.2 g/cm^{-3}) and their high melting points (1907, 1670, and 1855 °C). According to Tong et al. (2020) elements having high melting points are important in refractory high entropy alloy design because of their thermal stability and ability to not weaken the alloys high temperature resistance. According to Tseng et al. (2019), Nb and Ta is for higher ductility at high temperatures. The addition of W and Ta can greatly balance the mechanical properties of RHEAs at higher temperatures (Wang et al., 2019;Zheng et al., 2022).

Chapter 3

Experimental procedure

3.1 Introduction

This chapter details the information on the materials, equipment and experimental methods explored in this study. A comprehensive description on the alloys design (empirical phase calculation and Thermo-Calc modelling), alloys production, characterisation techniques, oxidation testing, corrosion testing as well as hot compression testing are presented.

3.2 Materials

The starting powders comprising niobium (99.9% purity), vanadium (99.9% purity), tantalum (99.95% purity), titanium (99.7% purity), chromium (99.9%) and tungsten (99.9%) supplied by Weartech (pty) Limited, South Africa were used to produce the RHEAs. A commercial IN718 superalloy was also obtained for comparison purposes.

3.3 Alloy design

The design consideration steps followed when developing the RHEAs is shown in Figure 3.1. The range of TiNbTaVW and CrNbTaVW RHEAs developed were obtained through empirical calculation and Thermo-Calc modelling.

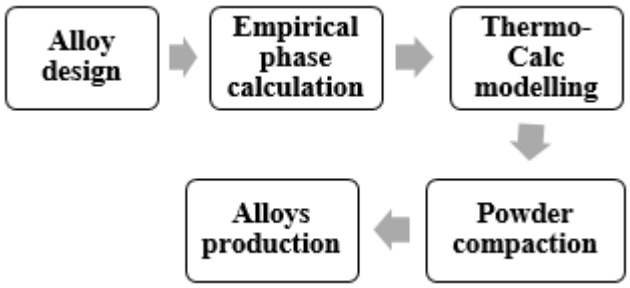

Figure 3.1: The experimental procedure for alloy development.

3.3.1 Empirical phase calculation

The targeted solid solution phases of the designed alloys were obtained based on thermodynamic data calculations: entropy of mixing (ΔS_{mix}), enthalpy of mixing (ΔH_{mix}), valence electron concentration (VEC), lattice distortion (δ), electronegativity difference ($\Delta\overline{X}$), and thermodynamic parameters (Ω). The obtained calculated values were varied with solid solution range of parameters listed in Table 2.1. These values were also compared with Thermo-calc modelling results to validate the solid solution phases of the alloys.

3.3.2 Thermo-Calc modelling

Thermo-Calc modelling was performed to predict equilibrium phases in the RHEAs, and determine the total phases in atomic percentage, transformation temperatures and other critical temperatures under equilibrium conditions. The elemental compositions of TiNbTaVW and CrNbTaVW RHEAs were entered into Thermo-Calc software using the solid solution (SSOL4) thermodynamic database to obtain the desired information.

3.4 Powder compaction

The Nb, V, Ta, Cr, Ti, and W powders were weighed in proportion using a Boeco digital weighing balance with 0.0001 g accuracy. The actual elemental mass needed to produce 500 gof the RHEAs for arc-melting is given in Table 3.1. The powders were then mixed and cold compacted under a load of 300 kN using Amster compressive strength testing machine. The description of the melting process is described in Section 3.5 under alloy production.

Table 3.1: Elemental mass required to produce 500 g of the RHEAs for arc-melting.

Alloy no.	Nb	V	Ta	Cr	Ti	W
TiNbTaVW	83.5	45.5	162.5	-	43.0	165.5
CrNbTaVW	83.0	45.0	161.5	46.5	-	164.0

3.5 Alloys production

Alloy compacts were melted in a water-cooled copper hearth arc-melting furnace under ultra-high purity argon gas to produce 35 mm x 35 mm square arc-melted alloy. The arc melting furnace can reach temperatures exceeding 3500°C. The melting chamber was evacuated to 5 $x10^{-3}$ Pa and refilled with pure argon gas three times at a pressure of 5 x 10^3 Pa to extract oxygen. Chemical homogeneity was achieved by flipping and remelting the as-cast samples three times.

3.6 Alloy sample cutting

The TiNbTaVW, CrNbTaVW, and IN718 samples were cut into sections for preparation of different tests such as microstructural, hardness, hot compression, oxidation and corrosion using a Gold San CNC wire cutting EDM machine operating at 20 V. Water was used as the coolant throughout the cutting of the samples to prevent the samples from overheating.

3.7 Metallographic preparation

The sectioned samples underwent standard procedures sample preparation for microstructural analysis which included mounting, grinding, polishing and etching.

3.7.1 Mounting

The cut samples were hot mounted in phenolic resin (Struers Polyfast) using a Bainmount twinH auto hot mounting press. The hot mounting process was done at a temperature of 160°C and a pressure of 150 bar for a period of 10 minutes, with water as the coolant.

3.7.2 Grinding and polishing

Mounted samples were ground on the Struers Tegramin-20 grinding machine using Struers MD-Piano 2000 and Struers MD-Piano 4000 resin-bonded diamond grinding discs. The Struers Tegramin-20 automatic grinding machine was set to a grinding speed of 150 rpm for 5 minutes under a force of 50 N and water was used as lubricant. After the grinding operation, the samples were cleaned of grinding particles using water between each stage. Thereafter, ground samples were polished using Akasel polishing cloth with 3.0 μm two-in-one polycrystalline diamond suspension for 10 minutes under a force of 10 N and wheel speed of 100 rpm.

3.7.3 Etching

The polished TiNbTaVW and CrNbTaVW RHEA samples were etched by swabbing with standard Kroll's reagent (92 vol.% distilled water, 6 vol.% nitric acid and 2 vol.% hydrofluoric acid) for 30 seconds. The obtained commercial IN718 alloy was etched in marble reagent (CuSO4:10 g; HCl:50 mL; distilled water:50 mL) for 30 seconds. Etched samples were rinsed with water for a minute and dried with compressed air.

3.8 Alloys characterisation

The microstructural features of the alloys were analysed using optical, stereomicroscopy and scanning electron microscopy (SEM). Compositions were determined using energy dispersive spectroscopy (EDX) on the SEM, while the identification of phases was done using X-ray diffraction (XRD).

3.8.1 Optical microscopy

The Olympus SC50 optical microscopy was used to study the microstructures of the as-cast and hot deformed samples. The digital camera of the microscope was connected to Olympus stream essentials to view, capture, record and store the micrographs of samples in digital form.

In order to obtain optimum resolution of the microstructures, contrast was enhanced by adjusting the dark field illumination, polarised light and the phase contrast of the microscopicsystem.

3.8.2 Scanning electron microscopy

The microstructural analysis of the TiNbTaVW RHEA, CrNbTaVW RHEA and IN718 alloy were examined using a high-resolution Carl Zeiss Sigma Field Emission Gun Scanning Electron microscope (FEG-SEM) equipped with BSE, SEI and EDX detectors and ZEISS Smart SEM Software for data analysis. The electron high tension equipment was adjusted to 20 kV (EHT). The OXFORD INSTRUMENT x-act PentalFET Precision energy dispersive X- ray (EDX) detector was employed for elemental composition analysis and data was examined using Oxford INCA software. Image J software (open-source software for image analysis, National Institutes of Health) was used to calculate the sizes of grain, pores, voids, and cracks.

3.8.3 X-ray diffraction analysis

X-ray diffraction technique was utilised in order to identify the phases present in the TiNbTaVW RHEA, CrNbTaVW RHEA and IN718 alloy samples and determine their crystal structures. The phase identification of oxides scale constituents and corrosion products were also investigated by XRD. The XRD patterns of the alloy samples was examined using a Bruker D2 phaser diffractometer with Co-Kα radiation source [λ = 1.78899 Å] with a 0.02° step size. All the XRD scans were performed at voltage setting of 30 kV and a current of 25 mA within the range of 2θ = 20−110° at a temperature of 25°C. The obtained XRD patterns were then analysed using PANalytical Xpert Highscore software.

3.9 Hardness measurements

The Vickers hardness test was conducted on the polished cross-sectional area of the alloys using a FutureTech Vickers hardness tester equipped with a diamond indenter. The measurements were taken under a load of 300 gf and a dwell time of 15 seconds according to ASTM standard E92-17 (ASTM E 92-17, 2017). Ten readings were taken at different positionson each sample to obtain a Vickers hardness average.

3.10 Corrosion tests

Sectioned TiNbTaVW RHEA, CrNbTaVW RHEA and IN718 alloy samples were hot-mounted in clear resin at a temperature of 180°C and a pressure of 150 bar, ground, and polished to a

mirror-like finish. After polishing, the samples were rinsed in water and air-dried. The samples with a surface area of 0.283 cm^2 were subjected to the corrosive solutions. The corrosion test was performed using a three-electrode electrochemical cell connected to a Gamry® potentiostat. The alloy samples were used as the working electrode, while a platinum wire and Ag/AgCl saturated with 3M KCl were used as the counter and reference electrodes, respectively. The OCP test in the 3.5 wt% NaCl and 1 M H_2SO_4 solutions was conducted for 3600 seconds after immersion in the solutions to reach a stable value. Afterward, potentiodynamic polarisation tests were performed at a scan rate of 0.167 mV/s in the potential range of −0.5 to 2.5 V at room temperature. The corrosion current density (I_{corr}), corrosion potential (E_{corr}), and corrosion rate were determined using the polarisation technique according to ASTM standard G102-89 (ASTM International, 2020).

3.11 Oxidation test

The TiNbTaVW RHEA, CrNbTaVW RHEA, and IN718 oxidation test samples were sectioned using a Gold San CNC wire cutting EDM machine to nominal dimensions of 6.0 × 6.0 × 7.0 mm^3. The surfaces of the samples were ground using P1200 SiC paper, cleaned in ultrasonic acetone, and dried in air. Cyclic oxidation tests were carried out in a muffle furnace under a static air at 850°C and 1050°C for 15 hours at a heating rate of 10°C/min. The samples were placed in an alumina crucible and then moved to the muffle furnace once the specified temperatures were reached. Each cycle consists of 2 hours of heating at the specified temperatures in the furnace, followed by 20 minutes of air cooling at room temperature. The mass changes of the alloy samples before and after oxidation were measured using a Boeco digital weighing balance (accuracy= 0.0001g) to characterise the oxidation kinetics. The surface and cross-sectional morphology of the oxidised samples were examined using SEM, and the identification of the oxides was determined using XRD.

3.12 Hot compression testing

The TiNbTaVW RHEA, CrNbTaVW RHEA, and IN718 alloy were subjected to hot compression testing using a Gleeble 3500 thermo-mechanical simulator. Rectangular samples for hot-compression tests were machined using Gold San CNC wire cutting EDM machine to 6 x 6 x 9 mm^3. A type R (platinum-rhodium) thermocouple was welded to the mid span of the rectangular test samples using a spot welder for precise temperature control and measurement. Afterwards, the samples were then placed on the Hydrawedge autoloader. Graphite foil and

nickel paste were placed between the Iso-T tungsten carbide anvils and the specimen to reduce the effect of friction during deformation. Prior to the compression test, the deformation chamber was evacuated until 2.0 x 10^0 Pa and later, filled with inert Ar gas to prevent oxidation. For each test, the samples were heated from room temperature to a set deformation temperature of 950°C, 1000°C, and 1050°C at a heating rate of 5°C s^{-1}, and held at this temperature for 180 s to ensure homogenisation before compression (Figure 3.2). The samples were deformed at a strain rate of 10^{-3} s^{-1} and total strain of 0.1 followed by air cooling to retain the microstructure. The hot deformation mechanism of the alloys was assessed and analysed using flow stress and microstructural evolution of the deformed samples. The stress-strain data obtained from the hot compression tests were plotted to analyse the shape of the stress-strain curves. The microstructural analysis of the deformed samples obtained from hot compression testing was examined using optical microscopy and SEM.

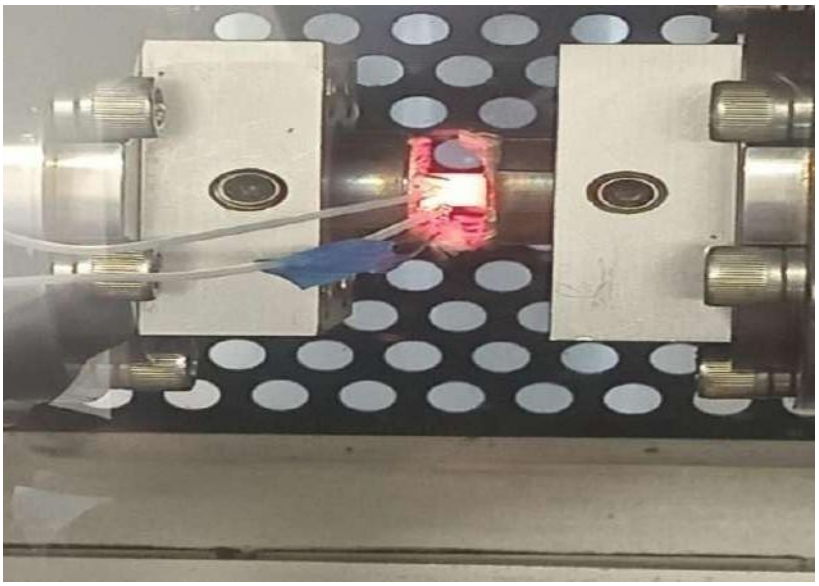

Figure 3.2: Hot deformation testing of the alloys with Gleeble machine.

Chapter 4

4.1 Introduction

This chapter presents the first research objectives which discusses the trend of research outputs based on arc-melted refractory high entropy alloys.

4.2 Bibliometric analysis of global research on arc-melted RHEAs

Bibliometric analysis utilises outputs of the academic literature in a particular scientific field study to create networks of citations relationship between authors, journals, countries, co-authorship analysis of authors, or co-occurrence of keywords (van Eck & Waltman, 2014). Published literature was assessed to determine the global research on vacuum arc-melted refractory high entropy alloys. In the selection phase for the databases for the bibliometric analyses, Scopus and Web of Science were considered due to their popularity and efficiency (Khudzari et al., 2018). After a preliminary search in both databases, the Scopus database was chosen because it has more published articles related to the topic and most of the articles on the Web of Science are also indexed on Scopus. The schematic flow chart in Figure 4.1 shows the steps used to complete the bibliometric analysis in this work.

The searches were done using keywords such as "refractory high entropy alloy", "refractory complex concentrated alloy", "refractory high entropy alloy" and “arc melting”, "refractory complex concentrated alloy" and “arc melting”, "refractory high entropy alloy" and “as- cast”, "refractory complex concentrated alloys" and “as-cast” from 2010 to 2024. The keywords were examined in the title, abstracts and then integrated to prevent double counting. After integration, 895 articles were extracted from the database. Further text cleaning was employed to eliminate some articles not related to arc-melted RHEAs to bring the final number of articles to 674. The articles or documents that were eliminated contained incomplete bibliographic data, keywords relating to sintering, computational study, magnetron sputtering, additive manufacturing, and review journals etc.

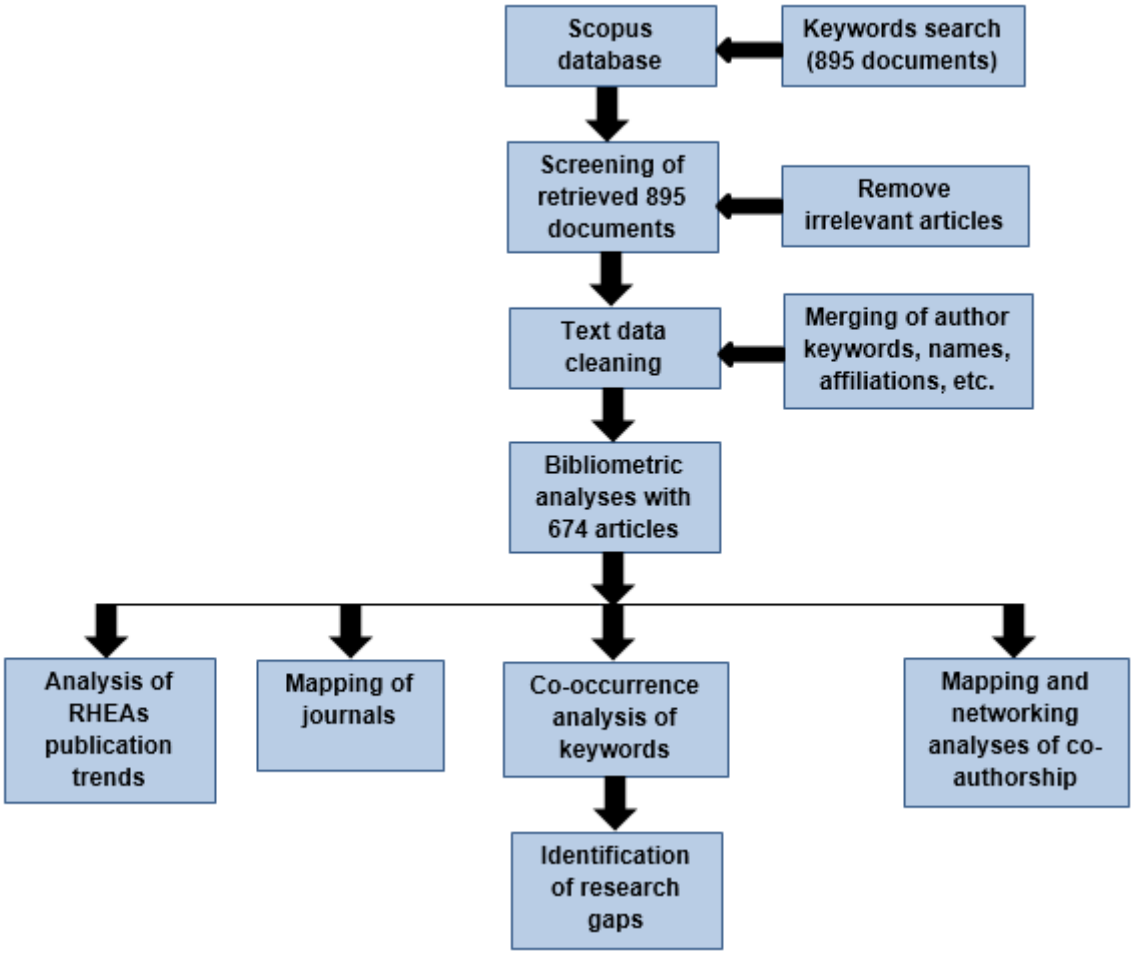

Figure 4.1: Schematic flow chart for bibliometric analysis of arc-melted RHEAs.

4.3 Statistical and bibliometric analysis

After text cleaning of the articles, they were statistically analysed to investigate the trend of publication growth over the years. Also, bibliometric analyses comprising co-occurrence of article keywords, co-citation between articles, co-citation between scientific journals, and co-authorship between countries, were undertaken. This is important in identifying the main research interests and directions, citation patterns, influential journals for scientific works, and scientific collaboration between institutions and countries. Free, open-source science mapping software known as VOSviewer 1.6.16 by van Eck and Waltman was utilised for these analyses (van Eck & Waltman, 2007). The software is a distance-based map wherein the relationship between items is reflected by the length of the distance between them. Invariably, a shorter distance between two items indicates a strong relationship between them. Thus, it is easier to identify clusters of related items (van Eck & Waltman, 2007). Furthermore, each item of analysis (journal, author, country, etc.) is represented by a node (circle or rectangle). The larger it is, the more influential/important the item. The importance of an item may be assessed based on, for

instance, the number of documents, citations, average citations, etc. Items of the same colour belong to the same cluster and thus indicate their co-citation of RHEA research (Akinwekomi & Akhtar, 2022; van Eck & Waltman, 2010, 2014).

4.4 Trend of scientific publication in arc-melted RHEA from 2010 to 2024

Trend analysis is an important scientific tool that enables researchers to predict and plan research directions (Chang et al., 2015). The annual scientific outputs on the arc-melted RHEAs are shown in Figure 4.2. According to the Scopus database, the first article on arc-melted RHEAs was published in 2010. Only one article was published in that year. In 2011, the number of research articles increased to 3, and later dropped to one article per year in 2013. Afterwards, in 2014 and 2015, The publications increased to 16 articles, but decreased to 9 articles in 2017. This decline may be attributed to the adoption of alternative methods for synthesising RHEAs, such as magnetron sputtering, sintering, and additive manufacturing. Also, the high cost of RHEAs, which contain expensive alloying elements, might have discouraged researchers from exploring them in detail. However, an increasing trend in publications is observed from 2018 to 2023. As of August 2024, the number of articles increased to 302. It is expected that this increase will continue as researchers design more advanced RHEAs and more applications areas are explored.

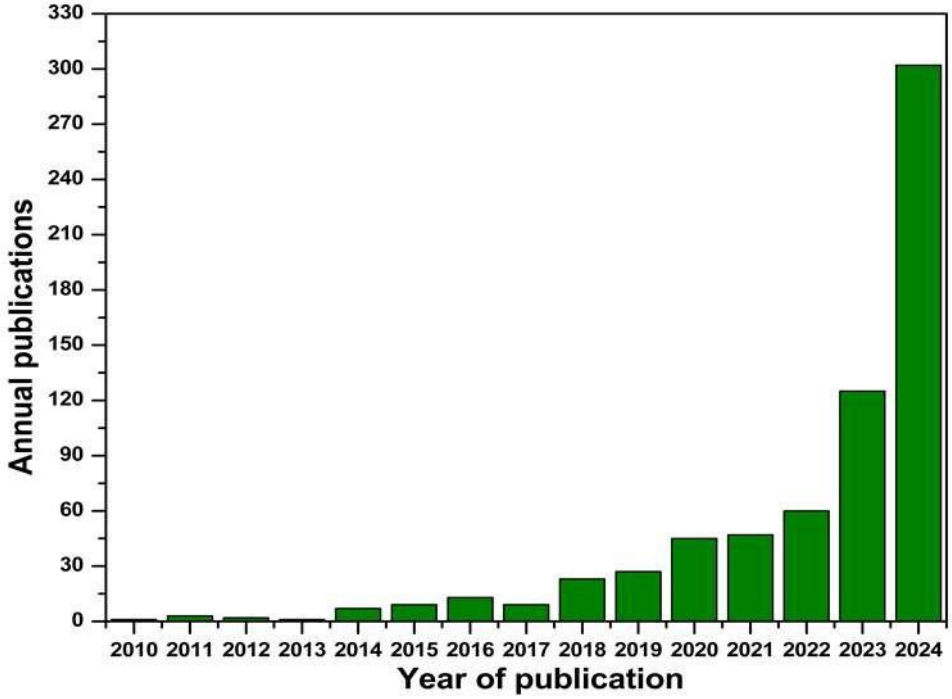

Figure 4.2: Annual scientific outputs arc-melted RHEAs.

4.5 Publication per source for arc-melted RHEA

To identify publishers with the most publications on arc-melted RHEAs and their respective citations, the minimum number of articles in a journal and minimum number of citations of a journal were set to 5 and 20, respectively. These criteria were selected to facilitate the analysis of 375 scientific sources. Only 11 publishers and 155 documents met this requirement and are shown in Table 4.1.

Table 4.1: Bibliometric analysis of the top research journals from 2010 to 2024.

S/N	Journal	Number of articles	Citations
1	Journal of Alloys and Compounds	39	3354
2	Materials Science and Engineering A	20	2374
3	Intermetallics	16	6707
4	Materials Letters	15	1441
5	Acta Materialia	14	2392
6	International Journal of Refractory Metals and Hard Materials	14	791
7	Scripta Materialia	9	834
8	Journal of Materials Science and Technology	9	340
9	Materials and Design	7	581
10	Corrosion Science	7	355
11	Entropy	5	569

The analysis revealed that the Journal of Alloys and Compounds ranked first with 39 publications and 3354 citations (Table 4.1). This was followed by Materials Science and Engineering A, which had 20 publications and 2374 citations. The next journals in the list were Intermetallics, Materials Letters, Acta Materialia, International Journal of Refractory Metals and Hard Materials, and Scripta Materialia. Together, these five journals accounted for 68 articles and 12165 citations. Notably, Intermetallics with fewer publications (16), had more citations (6707) than the top two journals (Journal of Alloys and Compounds and Materials Science and Engineering A). This high citation count in Intermetallics is partly due to pioneering research articles on RHEAs published in the journal.

Furthermore, Acta Materialia, with fewer publications (14) had more citations (2392) than Materials letters (1441). Scripta Materialia with 9 publications had more citations (834) than

the International Journal of Refractory Metals and Hard Materials, which had 14 publications and 791 citations. This strongly suggests that the quality of research published in these journalsis high. Journal reputation has been shown to enhance article citations (Liskiewicz et al., 2021; Tahamtan et al., 2016). Other factors contributing to high citation counts in top research journals may include the novelty of the research, prominence of the author, the reputation of the publishing journal, and the journal's publication model (open access or subscription-based) (Akinwekomi & Akhtar, 2022; Liskiewicz et al., 2021; Tahamtan et al., 2016).

4.6 Analysis of co-authorship of researchers

Scientific collaboration among researchers is important for enabling knowledge exchange, technology transfer, and gaining access to expensive and specialized research facilities. It also serves as an important metric for university rankings (Khudzari et al., 2018). Using VOSviewer, a co-authorship cluster density map of authors was generated based on the criteria "minimum number of documents per author = 5" and "minimum number of citations per author= 10". Forty-seven connected researchers met these criteria and are displayed in the co- authorship cluster density map in Figure 4.3. Researchers are grouped into eight clusters: Cluster 1 (red; 9 researchers), cluster 2 (green; 8 researchers), cluster 3 (blue; 8 researchers), cluster 4 (yellow; 7 researchers), cluster 5 (purple; 4 researchers), cluster 6 (cyan; 4 researchers), cluster 7 (orange; 4 researchers), and cluster 8 (brown; 3 researchers). Researchers in each cluster represents a collaborating group. The brightness of a node associated with a researcher implies a stronger, collaborative network (Akinwekomi & Akhtar, 2022).

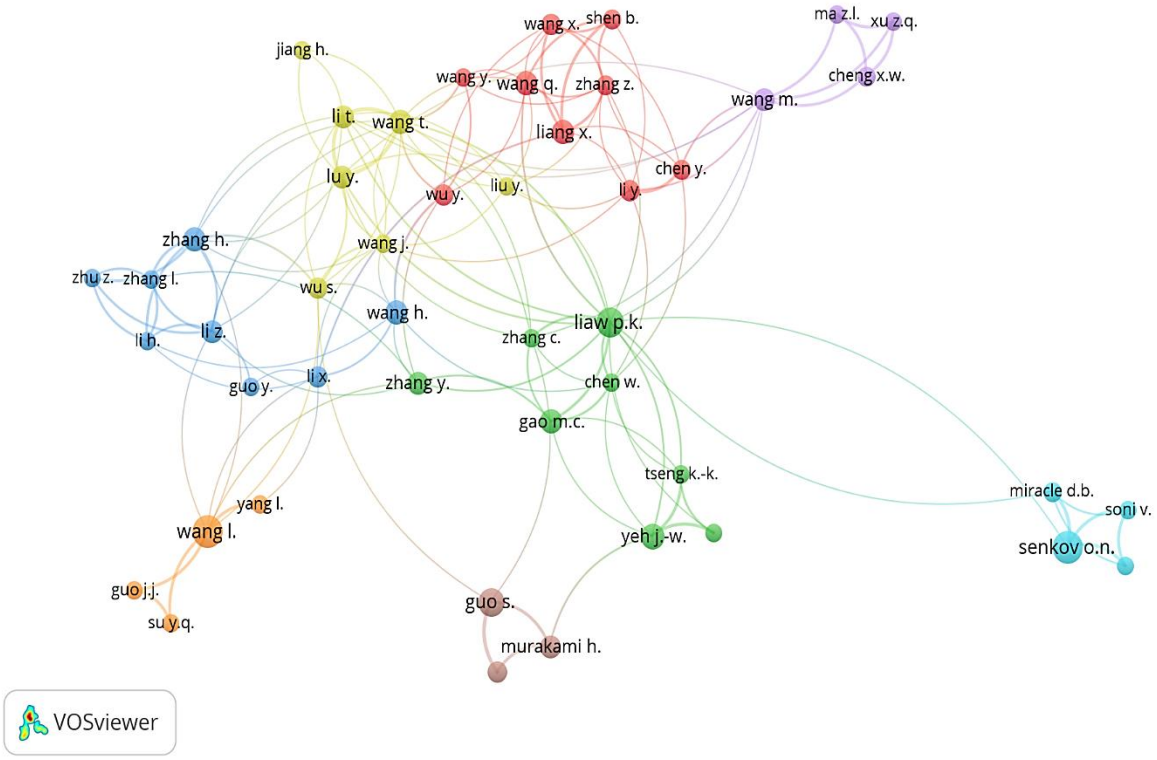

Figure 4.3: Co-authorship clustering map of authors based on number of publications.

The most influential researchers in each cluster are as follows: Cluster 1 (red; Liang X; 9 articles), cluster 2 (green; Liaw P.K.; 13 articles), cluster 3 (blue; Zhang H., 9; Wang H., 9 articles), cluster 4 (yellow; Wang T.; 9 articles), cluster 5 (purple; Wang M.; 8 articles), cluster6 (cyan; Senkov O. N.; 17 articles), cluster 7 (orange; Wang I.; 16 articles), and cluster 8 (brown; Guo S.; 13 articles). Overall, the most prominent authors across all clusters are Senkov O.N and Wang I. There are several factors that may affect the diversity of research collaboration. Some of these are availability of a large number of foreign postgraduatestudents/visiting scholars and big research funds (Khudzari et al., 2018).

4.7 Analysis of institutional and international co-authorship

The criteria for generating the analysis of institutional co-authorship involves setting “minimum number of documents of an institution” and “minimum number of citations of an institution” to 5 and 10, respectively. Of the 703 institutions, 22 meet the thresholds and are indicated in Table 4.2.

Table 4.2: Analysis of institutional co-authorship.

S/N	Institution	Country	Number of published articles	Citations	Total link strength
1	Key Laboratory of Solidification Control and Digital Preparation Technology (Liaoning Province), School of Materials Science and Engineering, Dalian University of Technology, Dalian, 116024, China	China	15	485	9
2	School of Materials Science and Engineering, Beijing Institute of Technology, Beijing, 100081, China	China	15	598	4
3	National Key Laboratory of Science and Technology on Materials Under Shock and Impact, Beijing, 100081, China	China	9	462	9
4	Defence Innovation Institute, Academy of Military Science, Beijing, 100071, China	China	9	108	5
5	National Key Laboratory for Precision Hot Processing of Metals, School of Materials Science and Engineering, Harbin Institute of Technology, Harbin, 150001, China	China	8	557	2
6	Institut Für Werkstofftechnik, Universität Siegen, Paul-Bonatz-Str. 9-11, Siegen, 57068, Germany	Germany	7	663	5
7	Department of Materials Science and Engineering, National Tsing Hua University, Hsinchu, 30013, Taiwan	Taiwan	6	1132	1
8	Department of Materials Science and Engineering, The University of Tennessee, Knoxville, Tn 37996, United States	United States	6	660	3
9	Department of Nanoscience and Nanoengineering, Waseda University, 3-4-1 Okubo Shinjuku, Tokyo, 169-8555, Japan	Japan	6	278	5
10	Department of Materials Science and Engineering, University of North Texas, Denton, TX 76203, United States	United States	6	237	1
11	Laboratory of Bulk Nanostructured Materials, Belgorod National Research University, Belgorod, 308015, Russian Federation	Russian Federation	6	120	2
12	School of Materials Science and Engineering, University of Science and Technology of China, Hefei, 230026, China	China	6	106	4
13	Belgorod National Research University, Belgorod, 308015, Russian Federation	Russian Federation	6	23	1
14	Air Force Research Laboratory, Materials and Manufacturing Directorate, Wright-Patterson Air Force Base, OH 45433, United States	United States	5	7277	4
15	UES, INC., Dayton, OH 45432, United States	United States	5	5556	4

16	Advanced Materials and Manufacturing Processes Institute, University of North Texas, Denton, TX 76207, United States	United States	5	527	5
17	Department of Materials Science and Engineering, University of North Texas, Denton, TX 76207, United States	United States	5	527	5
18	Industrial and Materials Science, Chalmers University of Technology, Göteborg, 41296, Sweden	Sweden	5	277	5
19	Institut Für Angewandte Materialien, Karlsruher Institut Für Technologie (Kit), Karlsruhe, Germany	Germany	5	253	5
20	State Key Laboratory of Solidification Processing, Northwestern Polytechnical University, Xi'an, 710072, China	China	5	115	2
21	School of Materials Science and Engineering, Jiangsu Key Laboratory for Advanced Metallic Materials, Southeast University, Nanjing, 211189, China	China	5	83	5
22	School of Mechanical Engineering, Hefei University of Technology, Hefei, 230009, China	China	5	35	3

The highest number of publications (15) were published by the Dalian University of Technology, China and Beijing Institute of Technology, China. Despite these institutions having the highest institutional co-authorship, their total citation counts are lower than those of the National Tsing Hua University, Taiwan; the Air Force Research Laboratory, United States; and UES, INC., Dayton, United States. According to van Eck & Waltman (2020), the total link strength indicates the strength of co-authorship of an item (e.g., institutions) with others, suggesting that some institutions have higher collaboration levels with other institutions. Also, in Table 4.2, 9 out of the 22 institutions listed are situated in China based on the total number of research articles. To advance knowledge in this field, it is imperative to encourage and establish inter-institutional collaboration. Beyond inter-institutional collaboration, international collaborations are also vital for enhancing knowledge sharing and technology transfer. To generate the publication analysis per country in Table 4.3, the "minimum number of documents of a country" is set to 5 while the "minimum number of citations of a country" is set to 10.

Table 4.3: Publication analysis per country.

S/N	Country	Number of articles	Citations
1	China	216	6284
2	United States	70	13101
3	Germany	34	1701
4	Japan	23	1516
5	Russia	21	897
6	Taiwan	17	1718
7	Sweden	14	948
8	France	14	871
9	South Korea	14	643
10	India	11	174
11	United Kingdom	8	507
11	Ukraine	7	754
12	Greece	7	281
13	Austria	5	45

Table 4.3 presents the publication analysis by country, with 39 countries contributing to the papers, while 13 countries meet the threshold. Some countries overlap on the same article due to collaborations between authors from different countries. According to Table 4.3, China has the highest number of publications (216) and citation counts (6284). This is followed by the United States (70 publications and 13101 citations), Germany (34 publications and 1701 citations), Japan (23 publications and 1516 citations), and Russia (21 publications and 897

citations). Interestingly, the United States, with 70 publications, has more citations than China, which has 216 publications. Additionally, Taiwan, with 17 publications, has more citations than Germany, Japan, and Russia.

4.8 Citations analysis of most influential articles on arc-melted RHEA

To analyse the citation impact of the most influential articles on arc-melted RHEAs (2010-2024), a threshold of 100 citations per document was set, resulting in 27 articles meeting this criterion. Table 4.4 shows that the most cited article is Senkov et al. (2011) with 2696 citations, followed by Senkov et al. (2010) with 2388 citations. This is expected, as pioneering research articles typically accumulate the most citations as subsequent studies frequently reference them. Completing the top five most influential works are two articles by Senkov O.N. with a combined total of 2321 citations and an article by Juan C.C. with 510 citations. The top two most cited journals, both published in intermetallics, have a combined total of 5084 citations.

Additionally, 6 articles published in the Journal of Alloys and Compounds have a combined total of 3277 citations, which is less than the combined citations of the top two articles published in Intermetallics. More details about the most-cited articles and publication outlets can be found in Table 4.4. To identify the most influential articles from the last five years, a minimum citation threshold of 100 was set, resulting in 13 articles meeting this criterion.

Table 4.5 shows that the most cited article is El-Atwani (2019) with 466 citations. Acta Materialia features three journals on the list with a combined total of 447 citations, while Science Advances and Scripta Materialia each have two journals on the list with a combined total of 615 citations.

Table 4.4: Top 25 most-influential arc-melted RHEA articles.

S/N	First author and year	Article title	Journal	Citations
1	Senkov O.N. (2011)	Mechanical properties of $Nb_{25}Mo_{25}Ta_{25}W_{25}$ and $V_{20}Nb_{20}Mo_{20}Ta_{20}W_{20}$ refractory high entropy alloys	Intermetallics	2696
2	Senkov O.N. (2010)	Refractory high-entropy alloys	Intermetallics	2388
3	Senkov O.N. (2011)	Microstructure and room temperature properties of a high-entropy TaNbHfZrTi alloy	Journal of Alloys and Compounds	1562
4	Senkov O.N. (2014)	Effect of aluminum on the microstructure and properties of two refractory high-entropy alloys	Acta Materialia	759
5	Juan C.C. (2015)	Enhanced mechanical properties of HfMoTaTiZr and HfMoNbTaTiZr refractory high-entropy alloys	Intermetallics	510
6	Zou Y. (2014)	Size-dependent plasticity in a $Nb_{25}Mo_{25}Ta_{25}W_{25}$ refractory high-entropy alloy	Acta Materialia	489
7	Stepanov N.D. (2015)	Structure and mechanical properties of a light-weight AlNbTiV high entropy alloy	Materials Letters	469
8	El-Atwani O. (2019)	Outstanding radiation resistance of tungsten-based high-entropy alloys	Science Advances	466
9	Senkov O.N. (2011)	Microstructure and properties of a refractory $NbCrMo_{0.5}Ta_{0.5}TiZr$ alloy	Materials Science and Engineering A	450
10	Senkov O.N. (2014)	Microstructure and properties of Aluminum-Containing Refractory High-Entropy Alloys	JOM	448
11	Senkov O.N. (2015)	Microstructure and properties of a refractory high-entropy alloy after cold working	Journal of Alloys and Compounds	393
12	Yao H.W. (2017)	Mechanical properties of refractory high-entropy alloys: Experiments and modeling	Journal of Alloys and Compounds	387
13	Han Z. D. (2017)	Effect of Ti additions on mechanical properties of NbMoTaW and VNbMoTaW refractory high entropy alloys	Intermetallics	363
14	Liu C.M. (2014)	Microstructure and oxidation behaviour of new refractory high entropy alloys	Journal of Alloys and Compounds	360
15	Sheikh S. (2016)	Alloy design for intrinsically ductile refractory high-entropy alloys	Journal of Applied Physics	356
16	Gorr B. (2015)	Phase equilibria, microstructure, and high temperature oxidation resistance of novel refractory high-entropy alloys	Journal of Alloys and Compounds	350
17	Guo N.N. (2015)	Microstructure and mechanical properties of refractory MoNbHfZrTi high-entropy alloy	Materials and Design	330
18	Yang X. (2012)	Microstructure and compressive properties of $NbTiVTaAl_x$ high entropy alloys	Procedia Engineering	325
19	Maiti S. (2016)	Structural-disorder and its effect on mechanical properties in single-phase TaNbHfZr high-entropy alloy	Acta Materialia	293
20	Senkov O.N. (2012)	Oxidation behaviour of a refractory $NbCrMo_{0.5}Ta_{0.5}TiZr$ alloy	Journal of Materials Science	287

21	Senkov O.N. (2016)	Development of a refractory high entropy superalloy	Entropy	284
22	Yurchenko N.Y. (2017)	Structure and mechanical properties of B2 ordered refractory $AlNbTiVZr_x$ (x = 0–1.5) high-entropy alloys	Materials Science and Engineering A	274
23	Fazakas E. (2014)	Experimental and theoretical study of $Ti_{20}Zr_{20}Hf_{20}Nb_{20}X_{20}$ (X = V or Cr) refractory high-entropy alloys	International Journal of Refractory Metals and Hard Materials	262
24	Han Z.D. (2017)	Microstructures and mechanical properties of TixNbMoTaW refractory high-entropy alloys	Materials Science and Engineering A	259
25	Couzinié J.P. (2015)	On the room temperature deformation mechanisms of a TiZrHfNbTa refractory high-entropy alloy	Materials Science and Engineering A	246
26	Chen H. (2016)	Microstructure and mechanical properties at elevated temperatures of a new Al-containing refractory high-entropy alloy Nb-Mo-Cr-Ti-Al	Journal of Alloys and Compounds	225
27	Senkov O.N. (2016)	Solution strengthening of ductile refractory $HfMo_xNbTaTiZr$ high-entropy alloys	Materials Letters	194

Table 4.5: The most-influential as-cast RHEA articles in the past five years (2019-2024).

S/N	**First author and year**	**Article title**	**Journal**	**Citations**
1	El-Atwani O. (2019)	Outstanding radiation resistance of tungsten-based high-entropy alloys	Science Advances	466
2	Wei S. (2020)	Natural-mixing guided design of refractory high-entropy alloys with as-cast tensile ductility	Nature Materials	272
3	Wang M. (2021)	A novel bulk eutectic high-entropy alloy with outstanding as-cast specific yield strengths at elevated temperatures	Scripta Materialia	249
4	Chen S.Y. (2019)	Phase transformations of HfNbTaTiZr high-entropy alloy at intermediate temperatures	Scripta Materialia	189
5	Lee C. (2020)	Lattice-distortion-enhanced yield strength in a refractory high-entropy alloy	Advanced Materials	177
6	Müller F. (2019)	On the oxidation mechanism of refractory high entropy alloys	Corrosion Science	177
7	Soni V. (2020)	Phase inversion in a two-phase, BCC+B2, refractory high entropy alloy	Acta Materialia	173
8	Motallebzadeh A. (2019)	Microstructural, mechanical and electrochemical characterisation of TiZrTaHfNb and $Ti_{1.5}ZrTa_{0.5}Hf0.5Nb_{0.5}$ refractory high-entropy alloys for biomedical applications	Intermetallics	159
9	Chen S. (2019)	Grain growth and Hall-Petch relationship in a refractory HfNbTaZrTi high-entropy alloy	Journal of Alloys and Compounds	154

10	Lee C. (2020)	Temperature dependence of elastic and plastic deformation behaviour of a refractory high-entropy alloy	Science Advances	149
11	Eleti R.R. (2019)	Unique deformation behaviour and microstructure evolution in high temperature processing of HfNbTaTiZr refractory high entropy alloy	Acta Materialia	147
12	Zhou Q. (2019)	Corrosion behaviour of $Hf_{0.5}Nb_{0.5}Ta_{0.5}Ti_{1.5}Zr$ refractory high-entropy in aqueous chloride solutions	Electrochemistry Communications	134
13	Wang M. (2023)	Lightweight, ultrastrong and high thermal-stable eutectic high-entropy alloys for elevated-temperature applications	Acta Materialia	127

4.9 Co-occurrence network of author keywords

A co-occurrence network is useful for identifying key research areas and potential future directions (Hussein & Zayed, 2021). A co-occurrence network map of author keywords was generated with the minimum occurrence set to 3, resulting in 98 out of 708 keywords meeting this threshold. Each circular node in Figure 4.4 represents a keyword, with the node size proportional to the number of articles in which the keyword appears.

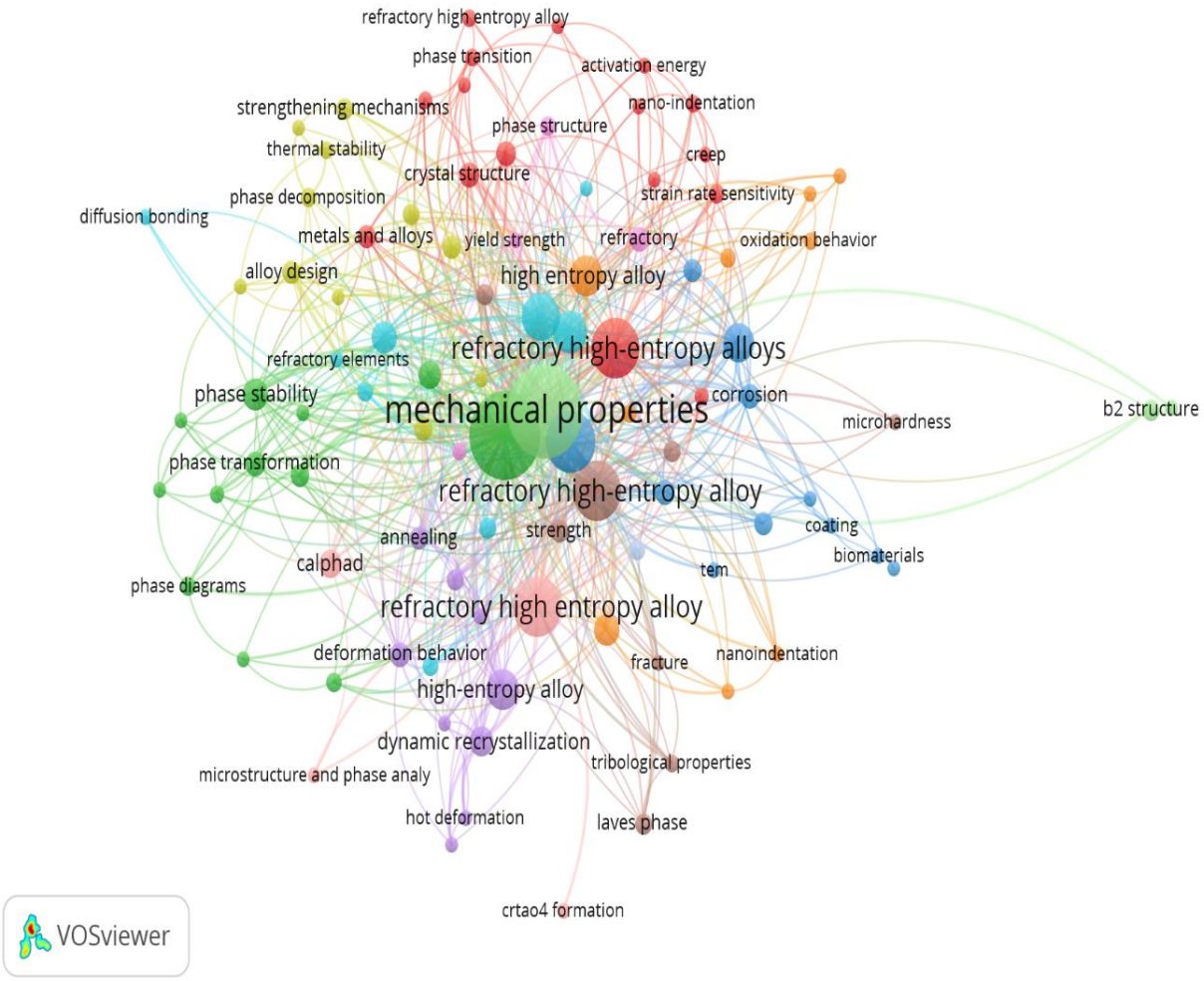

Figure 4.4: Co-occurrence network map of author keywords.

The distance between any two keywords indicates their relatedness, with shorter distances suggesting closer relationships (Heersmink et al., 2011). Keywords in the same colour belong

to the same cluster, indicating that they tend to co-occur more frequently with each other than with keywords in other clusters (Heersmink et al., 2011). The 98 keywords are grouped into twelve clusters. The largest cluster, shown in red, contains 16 keywords, with "refractory high entropy alloys" being the most frequently occurring keyword (44 occurrences and 74 links with other keywords). Other keywords in this cluster include "solid solution strengthening," "metals and alloys," "segregation," "specific strength," "grain growth," and "phase transition." Cluster 2, shown in green, includes 12 keywords, with "mechanical properties" as the most prominent (106 occurrences and 246 links). Other keywords in this cluster include "deformation and fracture," "precipitation strengthening," "ductility," "phase transformation," "high temperature," "specific yield strength," and "microstructure." Some keywords in Cluster 1 and Cluster 2 are correlated with each other but have different frequencies of occurrence. Cluster 3, shown in blue, includes 11 keywords such as "coatings," "wear," "oxidation resistance," "high entropy alloys," "oxidation," and "corrosion." Cluster 4, in dark yellow, also contains 11 keywords, including "low density," "hardness," "high temperature strength," "strengthening mechanism," "microstructures," and "thermal stability."

Cluster 5, shown in purple, includes 9 keywords, with "high entropy alloy" being the most frequently occurring. Other keywords in this cluster include "annealing," "dynamic recrystallisation," "hot deformation," "microstructure evolution," and "phase decomposition." Cluster 6, in cyan, includes 6 keywords such as "wear resistance," "elevated temperature," and "diffusion bonding." Cluster 7, shown in light orange, also includes 6 keywords, including "eutectic structure," "fracture toughness," "nanoindentation," and "oxidation behavior." Cluster 8, in dark brown, includes 8 keywords such as "fracture," "Laves phase," "plasticity," "strength," and "tribological properties." Cluster 9, in light purple, includes 4 keywords: "lattice distortion," "phase structure," "refractory," and "yield strength." Cluster 10, shown in dark red, includes 4 keywords: "$CrTaO_4$ formation," "CALPHAD," "microstructure and phase analysis," and "refractory high entropy alloy." Cluster 11, in light green, includes 3 keywords: "B2 structure," "mechanical properties," and "refractory high entropy alloy." The final cluster, shown in blue, includes 2 keywords: "deformation mechanism" and "lightweight."

Most studies on arc-melted RHEAs have focused on investigating mechanical properties, which explains the relatively high occurrence in the literature. However, other areas such as

deformation and fracture (3 occurrences), biomaterials (3 occurrences), hot deformation and deformation mechanism (3 occurrences), creep (3 occurrences), coatings (3 occurrences), corrosion (3 occurrences), and oxidation (16 occurrences) have also been investigated. The low number of occurrences for creep, coatings, fracture, biomaterials, corrosion, and hot deformation suggests that these areas could be future research directions. This is further evidenced by the text cleaning stage, where only a few articles were found reporting on the hot deformation behaviour and corrosion resistance of refractory high entropy alloys.

Departing from traditional applications (e.g., refractory materials, hard materials), some functional applications of arc-melted RHEAs, such as "hydrogen storage," "radiation," "thermal expansion," and "thermoelectric properties," have also appeared in the literature. However, these keywords did not appear in the network map because the co-occurrence network map of author keywords was set at a minimum occurrence threshold of 3. When the minimum occurrence threshold is set to 1, these functional application keywords appear in the network map. More research may be needed in these directions to fully harness the potential of RHEAs for these applications. It was also found that machine learning and computational approaches have been adopted to predict stable phases and their relative amounts, reduce costs, and minimise alloy development time. For example, CALPHAD has 10 occurrences and 21 links with other keywords, indicating its continued use in predicting phases before casting RHEAs. To fully exploit the potential of this computational approach, more research efforts may be needed in this area.

4.10 Summary

- The Scopus database were used to extract 895 articles related to arc-melted RHEAs. Further text cleaning eliminated articles not relating to arc-melted RHEAs to bring the final number of articles to 674.
- The first article on arc-melted RHEAs was published in 2010, and by 2024, the number of articles was 302.
- The Journal of Alloys and Compounds ranked first among publishers with the most publications on arc-melted RHEAs with 39 publications and 3,354 citations.

- The highest number of publications for institutional co-authorship were from Dalian University of Technology, China, and Beijing Institute of Technology, China.
- A publication analysis by country found that China had the highest number of publications (216).
- The following application areas such as creep, hydrogen storage, radiation, coating, thermal expansion, thermoelectric properties, fracture, biomaterials, corrosion, and hot deformation are less investigated.

Chapter 5

This chapter presents the experimental results addressing the second and third research objectives. The calculated empirical parameters and Thermo-Calc modelling for predicting phases in TiNbTaVW and CrNbTaVW RHEAs are discussed. A summary of the experimental findings on the microstructure and hardness of the refractory high entropy alloys are discussed.

5.1 Empirical approaches to predict phases in TiNbTaVW and CrNbTaVW

The physical properties of elements in the RHEAs and enthalpy of mixing for the selected alloy's binary subsystem are shown in Table 5.1 and Table 5.2. In Table 5.1, Ta and Ti have the largest atomic radius and the least electronegativitiy, while V has the smallest atomic radius in the TiNbTaVW RHEA. In the CrNbTaVW RHEA, Ta has the largest atomic radius and lowest electronegativity, while Cr has the smallest atomic radius. During the elements mixing, there could be the possibility of atomic distortion due to the large atomic size difference between the mixing elements, which leads to an increase in lattice strain. The large atomic size difference between so many components would considerably impact the formation of solid solutions in multi-component alloy (Guo et al., 2011; Yang & Zhang, 2012). Table 5.3 shows the results of the empirical parameters for predicting the phases and stability of TiNbTaVW and CrNbTaVW.

Table 5.1: Physical properties of elements in TiNbTaVW and CrNbTaVW RHEAs (rsc.org), (Xiang et al., 2020).

Elements	Ti	Cr	Nb	Ta	V	W
Atomic radius ($\dot{A}$)	1.46	1.27	1.43	1.46	1.32	1.39
Density (Kg/m^3)	4.50	7.19	8.57	16.4	6.00	19.3
Melting temperature (°C)	1670	1907	2477	3017	1910	3414
Valence electron	4	6	5	5	5	6
Electronegativity (χ)	1.54	1.66	1.60	1.50	1.63	2.36
Hardness (HV)	99	108	134	89	64	349

Table 5.2: Enthalpy of mixing for TiNbTaVW and CrNbTaVW binary subsystem.

TiNbTaVW										
i - j	TiNb	TiTa	TiV	TiW	NbTa	NbV	NbW	TaV	TaW	VW
$\Delta H_{ij\ mix}$	2	1	-2	-6	0	-1	-8	-1	-7	-1

CrNbTaVW										
i - j	CrNb	CrTa	CrV	CrW	NbTa	NbV	NbW	TaV	TaW	VW
$\Delta H_{ij\ mix}$	-7	-7	-2	1	0	-1	-8	-1	-7	-1

Table 5.3: Calculated empirical phase parameters.

Elements	ΔH_{mix} (KJ/mol)	ΔS_{mix} (kJ/mol K)	δ (%)	VEC	Ω	Δχ	$\Lambda = \Delta S_{mix}/\delta^2$
TiNbTaVW	-3.68	13.38	3.73	5.00	9.10	0.32	0.96
CrNbTaVW	-5.03	13.38	5.09	5.40	6.77	0.31	0.52

The enthalpy of mixing for TiNbTaVW shows that the TiTa (1), NbTa (0), NbV (-1), TaV (-1), and VW (-1) binary systems have good mutual solubility (Table 5.2). The enthalpy of mixing for CrNbTaVW shows that CrW (1), NbTa (0), NbV (-1), TaV (-1), and VW (-1) binary systems also have good mutual solubility (Table 5.2). When the value of ΔH_{mix} is close to zero, the different elements can randomly distribute in the alloy, and the solid-solution phases can stably occur in the solid phase (Yang & Zhang, 2012). Therefore, the formation of solid-solution phase is promoted in the TiNbTaVW and CrNbTaVW RHEAs. Also, based on the result in Table 5.3, solid solution formation is promoted in TiNbTaVW and CrNbTaVW RHEAs.

5.2 Thermo-Calc modelling of TiNbTaVW and CrNbTaVW

Thermo-calc using SGTE solution database version 4 (SSOL4) was used in determining different phases formation in TiNbTaVW and CrNbTaVW RHEAs, as illustrated in Figure 5.1 and Figure 5.2. The calculated equilibrium phase proportions of the TiNbTaVW RHEA are shown in Figure 5.1. The calculated equilibrium phase proportions of the TiNbTaVW RHEA shows a primary (BCC_A2 phase) formed at 2228°C and HCP_A3 phase formed at 499°C. The volume fractions of the obtained phases are given at 400°C (BCC_A2 = 89%; HCP_A3 = 11%) and 490°C (BCC_A2 = 98%; HCP_A3 = 2%).

The calculated equilibrium phase proportions of the CrNbTaVW RHEA are shown in Figure 5.2. It was observed that solidification starts at the liquidus temperature of 1850°C and solidification was completed at 2196°C with primary disordered BCC_A2 solid solution. Afterward, at a temperature below 1100°C, BCC_A2#3 and Laves (C15) phases was formed. The volume fractions of the obtained phases are given at 600°C (BCC_A2= 56%; BCC_A3= 29%; Laves_C15= 15%), 950°C (BCC_A2= 59%; BCC_A3= 40%; Laves_C15= 1%), and

1000°C (BCC_A2= 59%; BCC_A3= 41%).

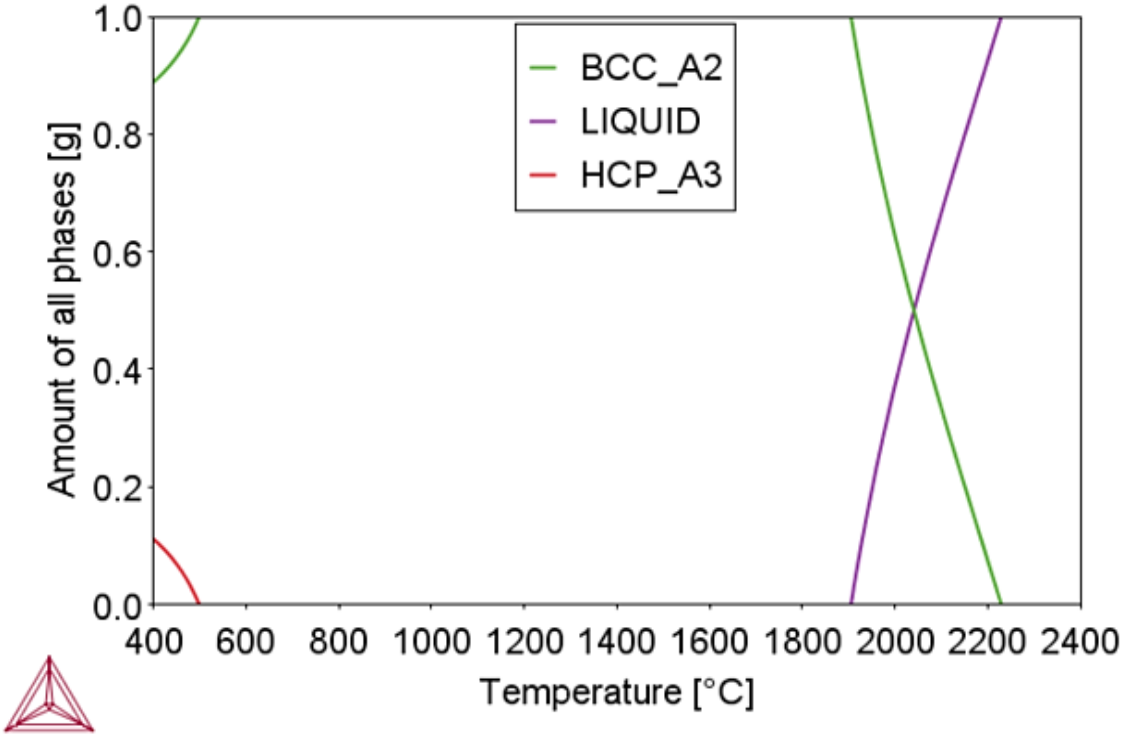

Figure 5.1: Phase proportions of TiNbTaVW RHEA.

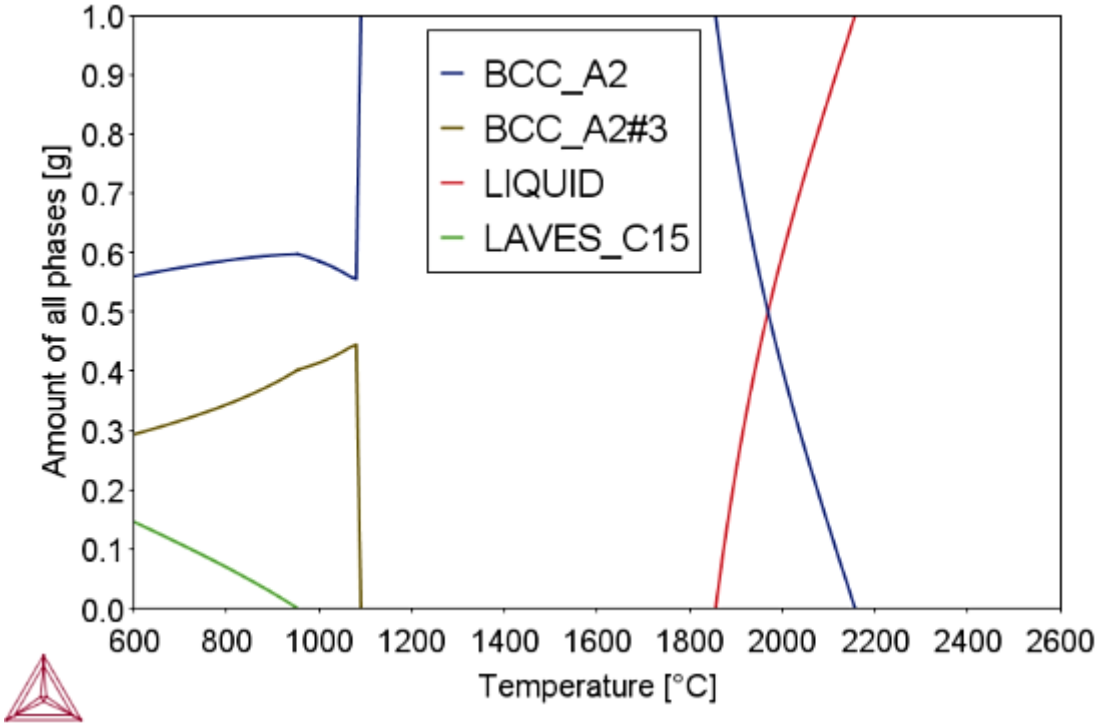

Figure 5.2: Phase proportions of CrNbTaVW RHEA.

5.3 Phase analysis of TiNbTaVW, CrNbTaVW and IN718

The phases present in the TiNbTaVW, CrNbTaVW, and IN718 were identified by XRD analysis and presented in Figures 5.3-5.5. The XRD analysis result of TiNbTaVW shows the peaks are indexed as BCC solid solution phase. The BCC solid solution phase was observed at a wide range of 2θ values between 46° and 103° (Figure 5.3). Also, a small peak at ~41° was not accounted for because it could not be identified. The XRD analysis result of the CrNbTaVW RHEA in Figure 5.4 shows the peaks are indexed as two BCC solid solution phases and $Cr(VNb)_2$ C15-Laves phase. The BCC1 solid solution phase was observed at a wide range of 2θ values between 46° and 104°. The BCC2 solid solution phase was observed between 49° and 104°. The $Cr(VNb)_2$ C15-Laves phase was observed at a wide range of 2θ values between 25° and 49°. The XRD spectra of IN718 in Figure 5.5 show that there are two major phases (γ and γ'') present. The γ phase was observed at a wide range of 2θ values between 52° and 91°, while γ'' phase was observed at a wide range of 2θ values between 52° and 113°. The γ and γ'' phases have been reported in some literature on wrought Inconel 718 (El-Bagoury et al., 2019; Huang et al., 2019; Luo et al., 2019; Popovich et al., 2017). The crystallographic data of the detected phases present in the TiNbTaVW, CrNbTaVW, and IN718 are shown in Table 5.4.

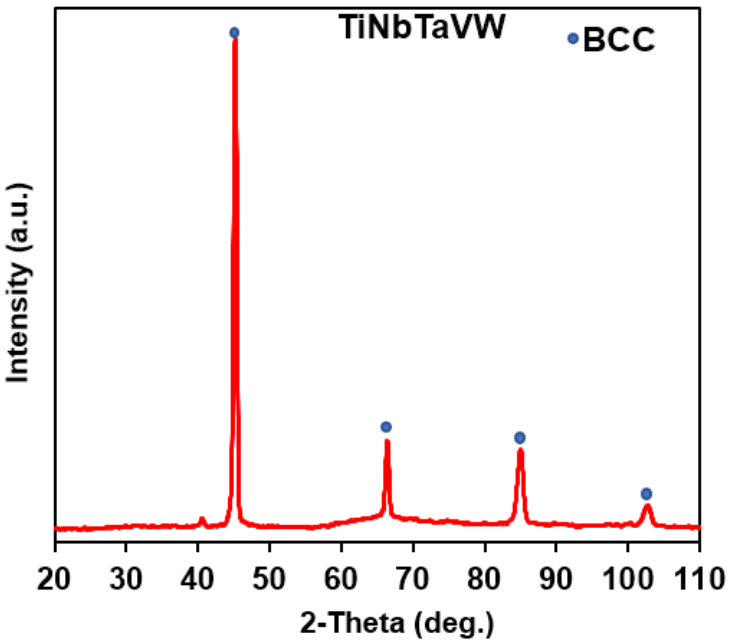

Figure 5.3: XRD pattern of the phase present in TiNbTaVW RHEA.

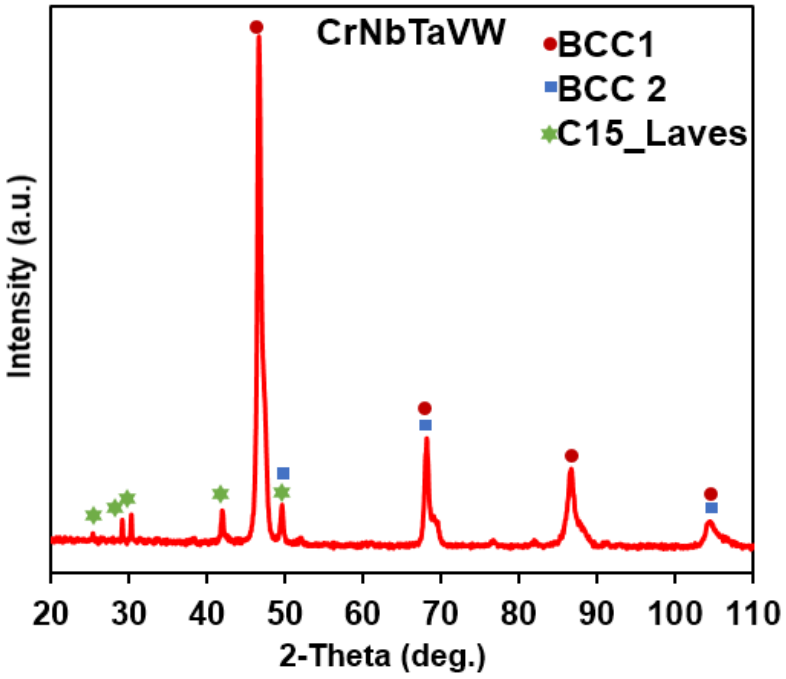

Figure: 5.4: XRD pattern of the phases present in CrNbTaVW RHEA.

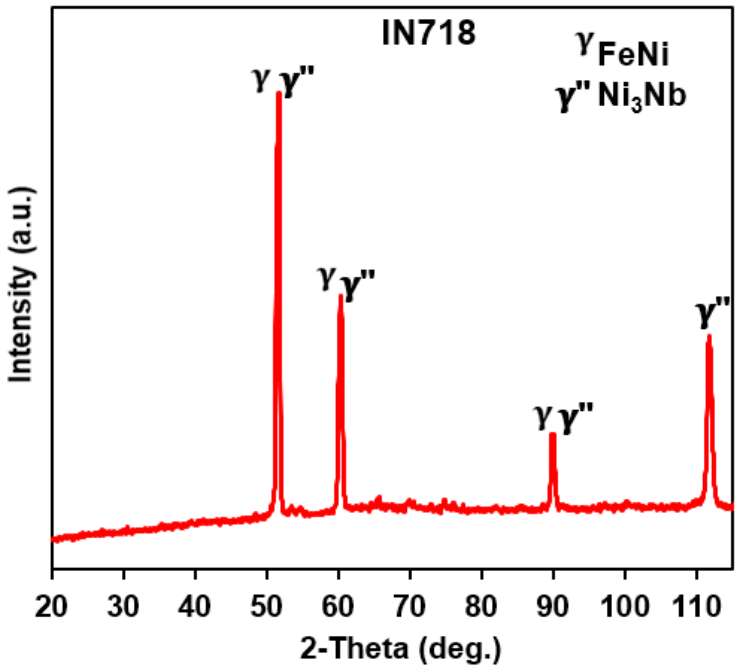

Figure 5.5: XRD pattern of the phases present in IN718.

Table 5.4: Crystallographic data of phases present in the TiNbTaVW, CrNbTaVW, and IN718.

Alloy	Phase	Space group (no.)	*a* (Å)	*b*(Å)	*c* (Å)	Cell vol. (10^6 pm^3)	Reference
CrNbTaVW	BCC1	Im-3m (229)	3.1840	3.1840	3.1840	32.28	96-900-6494
	BCC2	Im-3m (229)	3.1759	3.1759	3.1759	33.64	96-901-1599
	$Cr(VNb)_2$	Fd-3m (227)	7.0790	7.0790	7.0790	354.74	96-153-3579
TiNbTaVW	BCC	Im-3m (229)	3.2350	3.2350	3.2350	33.86	96-152-3322
IN718	γ	Fm-3m (225)	3.5920	3.5920	3.5920	46.35	96-152-4921
	γ''	I4/mmm (139)	3.6150	3.6150	7.4100	97.10	96-153-1756

5.4 Microstructural analysis

5.4.1 Microstructure and composition analysis of TiNbTaVW, CrNbTaVW and IN718

The optical and SEM images of TiNbTaVW, CrNbTaVW, and IN718 are shown in Figure 5.6. The TiNbTaVW RHEA showed a dendritic microstructure that segregates into grey dendrite and dark inter-dendrite regions, as shown in Figures 5.6a and 5.6b.

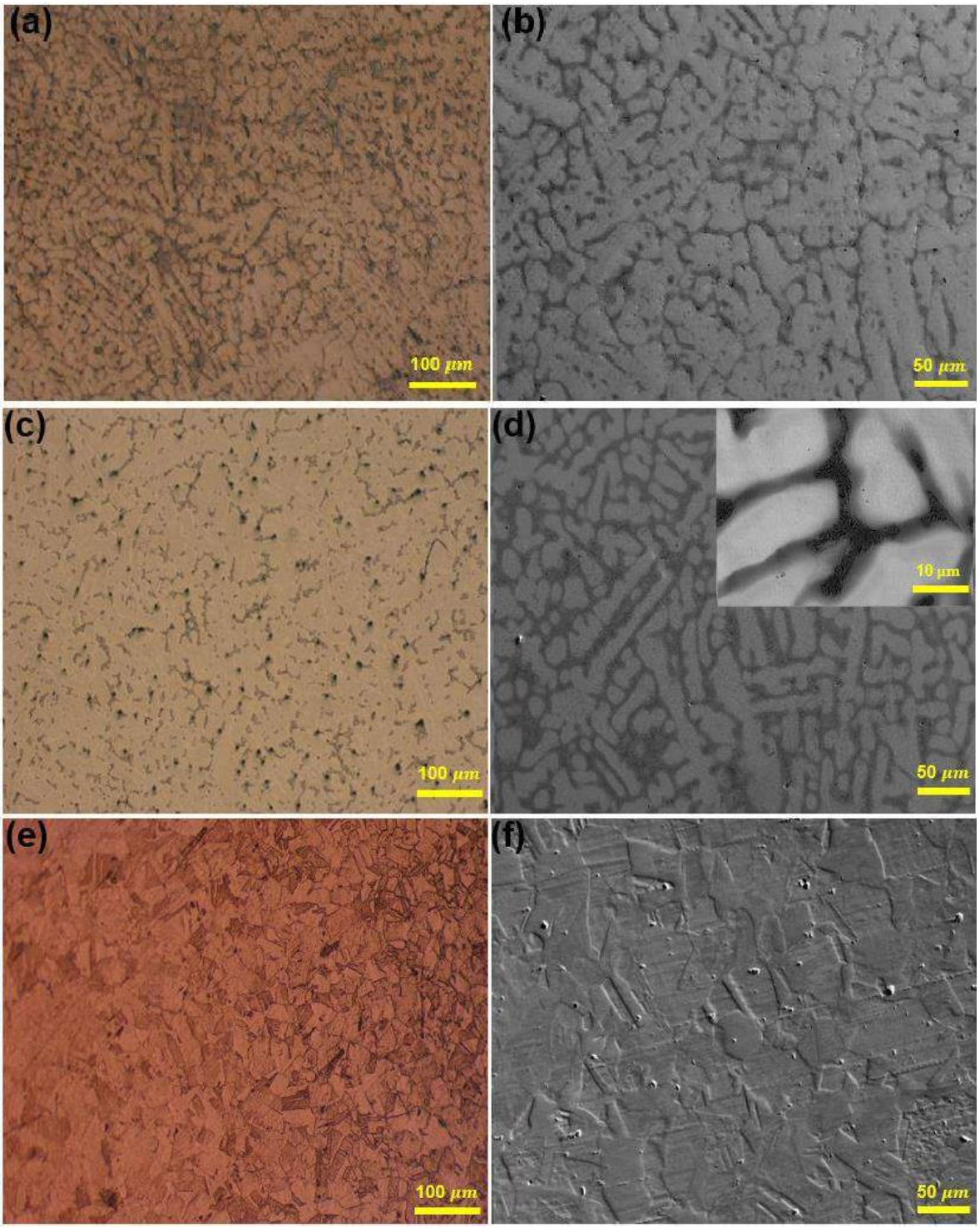

Figure 5.6: Optical and SEM-BSE images of TiNbTaVW, CrNbTaVW and IN718. (a-b) Dendritic microstructures of TiNbTaVW at dendrite (white) and interdendrite region (grey); (c-d) Dendritic microstructures of CrNbTaVW showing BCC1 (white), BCC2 (grey), and $Cr(VNb)_2$ C15-Laves (dark); (e-f) Microstructures of IN718 alloy showing γ and γ'' structures.

The optical and SEM images of CrNbTaVW in Figures 5.6c and 5.6d showed that the alloy exhibited a dendritic microstructure that segregated into a white phase (BCC1), grey phase (BCC2), and dark phase ($Cr(VNb)_2$). BCC and Laves phases have been reported in some Cr-containing as-cast RHEAs, for example, CrNbTiZr RHEA (Senkov et al., 2013) and CrHfNbTaTi RHEA (Yi et al., 2021). According to Butler et al. (2021), Laves particles precipitated inside grains during cooling in the solid state due to decreasing Cr solubility in the BCC phase. During the nucleation and growth of a new phase, the coordinated diffusion of several elements is important because it requires the redistribution of all elements to reach the desired composition (Tsai & Yeh, 2014). The optical and SEM images of IN718 showed that the microstructure comprises fine-distributed γ grains and γ'' precipitated grains (Figure 5.6e and Figure 5.6f). The γ''phase is the primary strengthening phase in most precipitation-hardenable nickel-based superalloys (Ganji & Rajyalakshmi, 2020).

5.4.2 EDX compositional analysis of TiNbTaVW, CrNbTaVW and IN718

The average compositions of the TiNbTaVW, CrNbTaVW, and IN718 is presented in Tables 5.5-5.7. The average compositions were obtained by EDX analysis on different locations on the alloys and were compared against the targeted nominal compositions. As seen in the EDX analysis result in Table 5.5 and Table 5.6, the targeted compositions of the TiNbTaVW and CrNbTaVW RHEAs are near-equiatomic ratios.

Table 5.5: Composition distribution of the TiNbTaVW RHEA.

Region	Ti	Nb	Ta	V	W
Actual	19±0.4	20±0.2	21±0.2	20±0.3	20±0.2
Dendrite (grey)	14±0.8	19±0.5	24±0.5	15±1.1	28±1.9
Interdendrite (dark)	32±1.5	19±0.3	12±0.8	29±0.6	8±1.0

Table 5.6: Composition distribution of the CrNbTaVW RHEA.

Region	Cr	Nb	Ta	V	W
Actual	16±0.5	22±0.2	21±0.2	22±0.2	19±0.9
BCC1	8±0.4	19±0.4	26±0.6	17±1.1	30±1.4
BCC2	32±1.2	20±0.4	13±0.5	30±0.8	5±0.6
$Cr(VNb)_2$ Laves	34±2.1	19±0.9	11±0.3	33±1.5	3±0.5

Table 5.7: Composition distribution of the IN718 alloy.

	Ti	Nb	Fe	Ni	Mn	S	C	Co	Al	Si	P	Cu
IN718	0.12±0.02	0.22±0.02	57.95±0.10	36.56±0.40	0.5±0.10	0.06±0.10	3.63±0.10	0.14±0.04	0.12±0.02	0.37±0.02	0.1±0.01	0.23±0.01

During the casting process, elements with a higher melting point tend to segregate in the dendrite regions, while elements with a lower melting point tend to segregate in the inter-dendrite regions (Chen et al., 2022; Senkov et al., 2010; Tseng et al., 2019). This is evidenced in the EDX analysis result in Tables 5.5 and 5.6. In the TiNbTaVW, Ta and W are more prominent in the dendrite regions, while the lower melting point elements comprising V and Ti segregated more in the inter-dendrite region. For the CrNbTaVW, it was found that the higher melting point elements of W and Ta segregated in the BCC1, while the lower melting point elements of V and Cr segregated more in the BCC2 and $Cr(VNb)_2$ Laves phase. However, Nb was distributed evenly in both the dendrite and inter-dendrite regions of TiNbTaVW and CrNbTaVW RHEAs. This highlights the influence of melting points on segregation that is typical in cast alloys. The chemical composition of the obtained IN718 alloy is presented in Table 5.7. It can be seen that the IN718 alloy in this study has a higher composition of Fe than Ni.

5.5 Hardness of TiNbTaVW, CrNbTaVW and IN718

The hardness of TiNbTaVW, CrNbTaVW and IN718 after ten indentations is shown in Figure 5.7. The TiNbTaVW RHEA and CrNbTaVW RHEA has higher hardness than that of the commercial IN718 alloy. In general, the CrNbTaVW RHEA with hardness value of 688±21 HV has more hardness than TiNbTaVW RHEA (522 ± 10 HV) and IN718 (301±14 HV). The TiNbTaVW and CrNbTaVW RHEAs has higher hardness than some reported as-cast RHEAs: $TiMoNbZr_{0.5}$ (516 HV) (Chen et al., 2021), $Hf_{0.25}NbTaW_{0.5}$ RHEA (514 HV) (Wu et al., 2021), $Al_{0.75}NbTiMoV$ (517 HV) (Chen et al., 2014), and $Nb_{25}Mo_{25}Ta_{25}W_{25}$ (458 HV) (Senkov et al., 2011). The increase in hardness of RHEAs have been attributed to solid solution strengthening, grain refinement, and second phase hardening (Cheng et al., 2017; Coury et al., 2019; Kang et al., 2021).

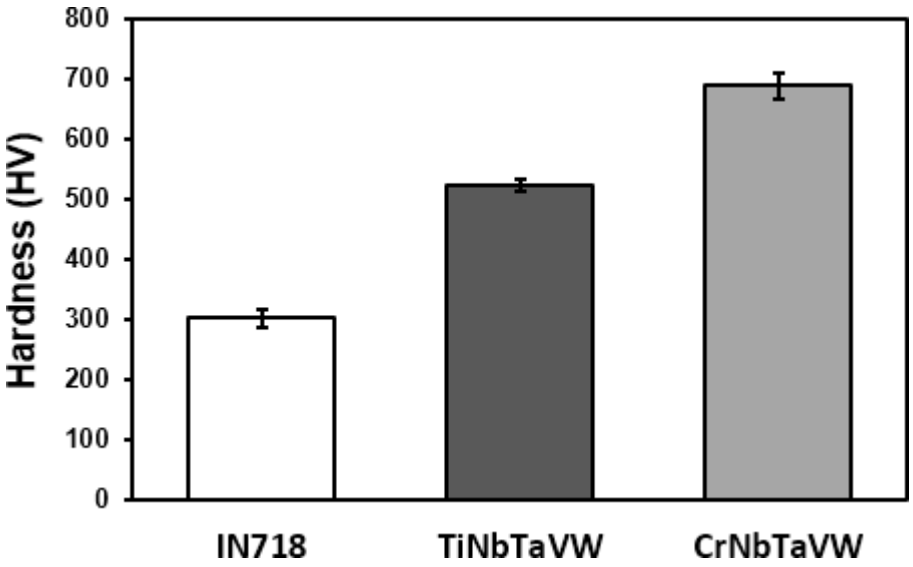

Figure 5.7: Hardness values of TiNbTaVW, CrNbTaVW and IN718.

5.6 Discussion

5.6.1 TiNbTaVW and CrNbTaVW phase prediction

The binary enthalpy values have a significant role in assessing how an element will interact with the other constitutents' elements in the RHEA. It is seen that NbW (-8), TaW (-7) and TiW (-6) have a significant negative enthalpy of mixing, the tendency of intermetallic compounds for TiNbTaVW. However, intermetallic phase was not observed in the thermo-calc simulation, XRD, the SEM micrograph of this alloy (Figure 5.1, Figure 5.3, and Figure 5.6b). Only an HCP phase was observed in the thermo-calc simulation and not by SEM and XRD in the TiNbTaVW RHEA, which could show that the observed microstructure is non-equilibrium and signifies a high-temperature one, which was quenched during cooling (Butler et al., 2021). According to Umut Tukac et al. (2022), as-cast samples are subjected to rapid cooling, sluggish diffusion mechanism does not allow microstructure to show any solid-state phase transformation at very low temperatures. Therefore, instead of the TiNbTaVW RHEA forming other BCC and HCP phases, the high-temperature phase becomes supersaturated and remains as a single BCC phase at room temperature (Umut Tukac et al., 2022).

In the CrNbTaVW, CrNb (-7), CrTa (-7), NbW (-8), TaW (-7), CrV (-2) have a significant negative enthalpy of mixing, indicating the formation of intermetallic compound. As seen from the thermo-calc simulation, XRD, micrograph (Figures 5.2, 5.5, and 5.6d), a Laves phase was formed which is in agreement with the binary enthalpy of CrV (-2), since it has a higher

negative enthalpy among the binary enthalpies. Laves phases are the largest group of intermetallic compounds (Fang et al., 2022). The main factors affecting the Laves phase structure are the atomic size factor and the electron concentration factor (Fang et al., 2022). The Laves phase formed due to the difference in atomic size and electronegativity between Cr and the other four elements making up the CrNbTaVW RHEA.

The binary enthalpies alone cannot predict the phases and crystal structure. Therefore, using the three criteria (Ω, δ, Λ) by (Guo et al., 2011; Yang & Zhang, 2012; Yurchenko et al., 2017) in Table 5.3, the calculated empirical parameters were used to predict the phases and crystal structure. The first criterion states that the disordered solid solution phase forms when $\Omega > 1.1$ and $\delta < 6.6\%$ (Yang & Zhang, 2012). The TiNbTaVW RHEA has $\Omega = 9.1$, which is greater than 1.1, while δ (3.73%) is less than 6.6%. The intermetallic phase was suppressed by the combination of Ω and δ. Hence, only the disordered solid solution BCC phase forms. The CrNbTaVW RHEA has $\Omega = 6.77$ which is greater than 1.1, while the δ (5.09%) is less than 6.6%. This means that the disordered solid solution BCC phase will form. Although Ω is greater than 1.1, it cannot differentiate between single and multi-phase solid solutions. To fill in the void, Λ parameter by Singh & Subramaniam (2014) can predict the formation of single and multi-phase solid solutions in multi-component alloys. If $\Lambda > 0.96$, a single-phase disordered solid solution forms, whereas $0.24<\Lambda<0.96$ gives multi-phase structures. The TiNbTaVW RHEA has a greater geometrical parameter of 0.96, which indicates a single-phase solid solution structure, while CrNbTaVW RHEA has a lesser geometrical parameter of 0.52, which indicates multi-phase structure.

The second criterion states that FCC and BCC crystal structures will be stable, if VEC ≥ 8 and VEC ≤ 6.87, respectively (Guo et al., 2011). In such a way that VEC < 6.87 = BCC, VEC ≥ 8 = FCC, and $6.87 \leq$ VEC < 8 = BCC + FCC. The TiNbTaVW and CrNbTaVW has a VEC of 5 and 5.4, which is less than 6.87. A stable BCC crystal structure is favoured to occur. The third criterion states that Laves phase forms when $\Delta\chi > 7\%$ and $\delta > 5\%$ in HEAs (Yurchenko et al., 2017). In TiNbTaVW RHEA, $\Delta\chi = 0.32$ and is lower than 7%. Also, δ for TiNbTaVW is 3.73%, which is lower than 5%. This shows that the Laves phase is not expected to occur in TiNbTaVW RHEA. XRD results also confirmed a single BCC solid solution phase (Figure 5.3). SEM images also confirmed a BCC phase without an HCP phase (Figure 5.6d).

Hence, the empirical calculations, thermo-calc, XRD, and SEM accurately predicted the single BCC solid solution phase in the TiNbTaVW RHEA.

In CrNbTaVW RHEA, $\Delta\chi$= 0.31 and is lower than 7%. However, the atomic size mismatch parameter for CrNbTaVW is 5.09, which is higher than 5%. Hence, the Laves phase is expected to occur in CrNbTaVW RHEA. The first two criteria successfully predicted the multi-phase BCC solid solutions phase, whereas in criterion three, only the lattice distortion parameter predicted the Laves phase. This provides a reasonable agreement with the experimental results as evidenced in thermo-calc simulation, XRD and SEM (Figure 5.2, Figure 5.4 and Figure 5.6d). It confirmed two BCC phases and a Lave phase. The phase separation agrees with Λ parameter which predicted the formation of multi-phase solid solutions in CrNbTaVW RHEA. The observed micro-segregation of CrNbTaVW phases shows a non-equilibrium solidification. According to Senkov et al. (2010), element segregation increases with an expansion of the liquidus and solidus temperature range. It is generally linked with an increase in the difference in the melting temperature (T_m) of the constituent elements, and an increase in the solidification rate. The addition of the lowest melting point element Cr and V expands the liquidus-solidus temperature range resulting in increased micro-segregation. As seen in Table 5.1, Cr and V possess similar atomic sizes and Pauling electronegativity, and Nb has similar Pauling electronegativity but a larger atomic size. Hence, from an electronic structure point of view, Nb can occupy V and Cr sites in C15 phase in CrNbTaVW RHEA. The thermo-calc simulation and empirical model agrees with SEM and XRD results to predict the phases in the CrNbTaVW RHEA.

5.6.2 Hardness properties of TiNbTaVW and CrNbTaVW

After ten indentations, the hardness value of TiNbTaVW, CrNbTaVW, and IN718 is 522±10 HV, 688±21 HV, and 301±14 HV, respectively. The RHEAs have higher hardness than IN718 alloy, but overall, the CrNbTaVW RHEA has higher hardness. Grain size and solid solution strengthening effect are two possible influences that resulted in the higher hardness of RHEAs (Zhang et al., 2012; Senkov et al., 2010; Wang et al., 2021). Fine grain strengthening lies in the effect of the grain boundary on dislocation slip, which serves as a pinning point impending further dislocation propagation (Zhang et al., 2019). At a given grain size, the hardness differences are a measure of the hardening effects of different

solutes. Grain refinement by the elemental addition of V can contribute to finer grain size that has a significant influence on hardness (Senkov et al., 2010). For example, grain size refinement was achieved in WNbMoTaV RHEA and V_1NbMoTa RHEA which contributed to enhanced hardness (Senkov et al., 2010; Wang et al., 2021).

In the CrNbTaVW RHEA, grain growth can be restricted by $Cr(VNb)_2$ Laves phase precipitation in the microstructure, which therefore reduces grain size, and improve hardness. The increased Cr composition to form the $Cr(VNb)_2$ Laves phase in CrNbTaVW RHEA thus led to solid solution strengthening, which further enhanced the hardness. The presence of the Cr promoting Laves phase have been reported to increase the hardness properties of RHEAs (Coury et al., 2018; Senkov et al., 2013). In the TiNbTaVW RHEA, distribution of Ti and Ta with a high atomic radius of 1.46 Å and V and W with a smaller atomic radius of 1.32 Å and 1.39 Å likely introduces lattice strains in both the dendrite and interdendrite regions. These lattice strains favour hardness. This is in agreement with TiNbMoTaW and TiVNbMoTaW RHEAs (Han et al., 2017), where the addition of Ti resulted in segregation of Ti and Nb at the inter-dendrite regions that favoured accommodation of the increased strain, which improved the hardness. The solid solution strengthening caused by large lattice misfit is an important component of solid solution/hardening mechanism in HEAs (Roy et al., 2021; Zheng et al., 2022). Cui et al. (2023) showed that large lattice misfit among phases contributed mainly to the excellent strengthening effect and mechanical properties of $Ti_{41}V_{27}Hf_{15}Nb_{15}O_2$ RHEA.

5.7 Summary

- The empirical methods used for the prediction of phase formation indicated the formation of disordered BCC solid solution phase in the TiNbTaVW RHEA and two BCC solid solution phases with a Laves phase in the CrNbTaVW RHEA. Therefore, the empirical methods are in agreement with the experimental observations in this study.
- Using the CALPHAD approach, one BCC disordered phase and a disordered HCP phase are stable at ~499°C, while only BCC disordered phase is stable above 500°C for the TiNbTaVW RHEA. When compared with SEM and XRD results,

HCP phase was not found which suggest that the kinetics are slow at lower temperatures. This provides a reasonable agreement with the experiment results in such a way that the primary BCC disordered phase was obtained.

- Using the CALPHAD approach, two BCC disordered phase and a Lave phase are stable at ~600°C, while only two BCC disordered phase is stable above 1000°C for the CrNbTaVW RHEA. This is in agreement with the experimental result with multi-phase formation.
- The TiNbTaVW RHEA exhibited single BCC phase and a dendritic microstructure, while CrNbTaVW RHEA exhibited a dendritic microstructure, which comprise multi-phases (BCC1, BCC2, and $Cr(VNb)_2$ Laves).
- The CrNbTaVW RHEA had a higher hardness of 688±21 HV than the TiNbTaVW (522±10 HV), and IN718 (301±14 HV). The higher hardness of CrNbTaVW RHEA was attributed to the solid solution strengthening and $Cr(VNb)_2$ Laves strengthening.

Chapter 6

This chapter addresses the fourth research objective. The results obtained from the electrochemical corrosion behaviour of the TiNbTaVW, CrNbTaVW, and IN718 in 3.5 wt.% NaCl and 1M H_2SO_4 and are presented in Sections 6.1 and 6.2. Discussion of the results is presented in Section 6.3.

6.1. Electrochemical corrosion behaviour in chloride solution

6.1.1 Open circuit potential measurement of TiNbTaVW, CrNbTaVW and IN718 in chloride solution

The OCP of TiNbTaVW, CrNbTaVW and IN718 in 3.5 wt% NaCl are presented in Figure 6.1. The stability of the oxide film formed on the surface of the alloys was evaluated by OCP for 3600 seconds. TiNbTaVW RHEA exhibited an initial potential of -0.20 V before a rapid decrease in the first 600 seconds and a slight increase at 650 seconds. Afterward, the OCP continued to decrease until it became stable at -0.217 V with increasing exposure time. The OCP curve of CrNbTaVW RHEA is stable throughout immersion, which indicates a stable passive film. The OCP for the IN718 alloy showed an initial potential of -0.186 V at the first 22 seconds before a rapid decrease till 3600 seconds at -0.24 V. Steady potential was achieved for TiNbTaVW, CrNbTaVW and IN718 after the oxide film was formed on the alloy surface. A great number of fluctuations was observed in the OCP curve of the IN718 alloy that indicated dissolution and re-passivation of the oxide film formed on the alloy's surface (Parkhutik, 2006; Zhou et al., 2019). It can also be attributed to the instability caused by the chloride ions in the solution. These results suggest that TiNbTaVW and CrNbTaVW oxide films is more stable than the IN718 in 3.5 wt% NaCl solution. Stable OCP has been attributed to the building of dense and protective oxide films on the alloy's surface (Murmey et al., 2023; Zheng et al., 2012).

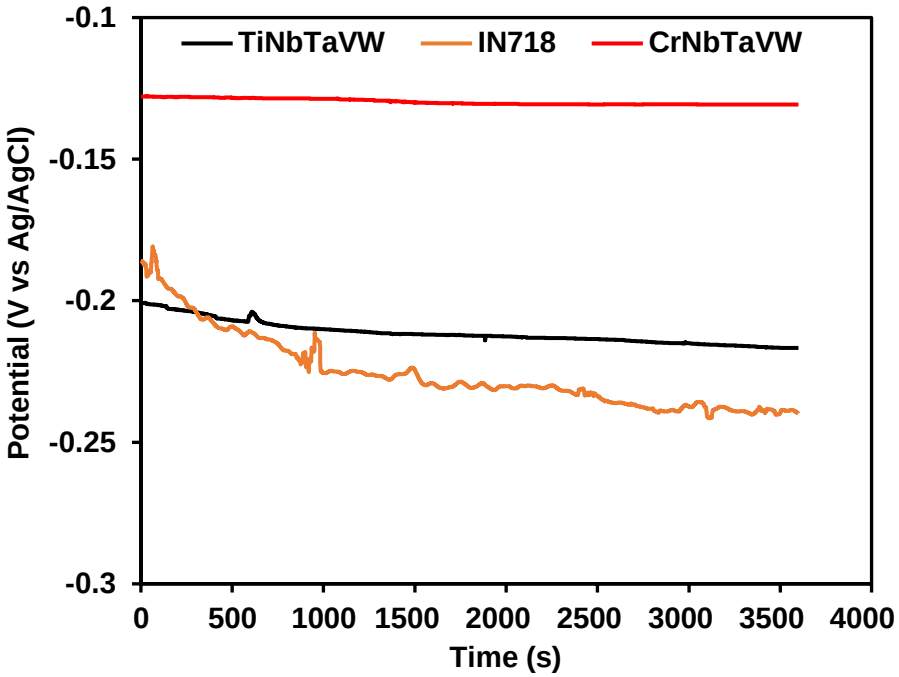

Figure 6.1: OCP curves of TiNbTaVW, CrNbTaVW and IN718 in 3.5 wt% NaCl solution.

6.1.2 Potentiodynamic polarisation measurement of TiNbTaVW, CrNbTaVW and IN718 in chloride solution

The potentiodynamic polarisation curves of TiNbTaVW, CrNbTaVW and IN718 in 3.5 wt.% NaCl after the OCP test are presented in Figure 6.2. It was observed that the anodic curves of TiNbTaVW and CrNbTaVW RHEAs exhibited a wide passivation region up to the final potential of 2.5 V, which indicates that the passive films are stable and good. The anodic curve of the IN718 alloy exhibited pseudo-passive behaviour up to 1.63 V and later passivated till the final potential. The passive zone is usually correlated to the stability of the passive film; a wide passive zone means a fairly stable passive film on the HEA's surface (Li et al., 2020). The areas with the blue arrow in the TiNbTaVW, CrNbTaVW, and IN718 anodic curves indicated that active corrosion took place when exposed to a chloride environment. The Cl^- ions attacked the protective layers, and the layers break, but the oxide layer starts rebuilding, as evidenced by the pseudo-passive and passive behaviours.

Also, transient currents were observed in regions indicated by green arrows on the passive region of TiNbTaVW and CrNbTaVW, which indicate instability of the passive film in response to chloride ion attack. The electrochemical corrosion parameters such as E_{corr}, I_{corr}, and corrosion rates obtained from the potentiodynamic polarisation curves in chloride solution

are presented in Table 6.1. All the alloys have high negative E_{corr} values of -0.139 V, -0.189 V and -0.295 V, indicating high susceptibility to corrosion. The CrNbTaVW has a lower I_{corr} value of 0.00265 μA/cm^2 than the TiNbTaVW and IN718 with 0.055 μA/cm^2 and 5.299 μA/cm^2. Based on the electrochemical parameters in Table 6.1, it is evident that the corrosion rate was lower in the CrNbTaVW than in the TiNbTaVW and IN718.

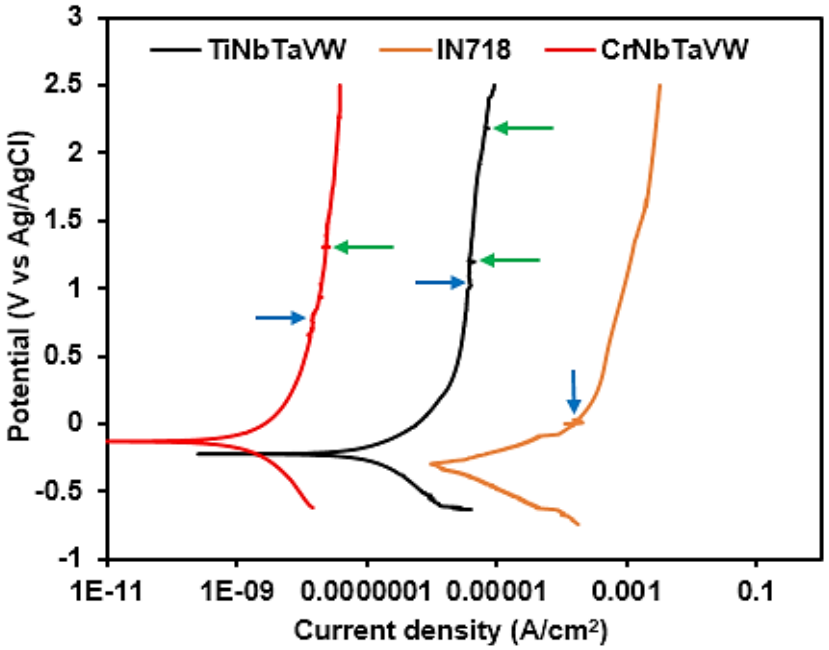

Figure 6.2: Potentiodynamic polarisation curves of TiNbTaVW, CrNbTaVW and IN718 in 3.5 wt% NaCl solution.

Table 6.1: Electrochemical parameters for TiNbTaVW, CrNbTaVW and IN718 in 3.5 wt% NaCl.

Alloy	E_{corr} (V)	I_{corr} (µA/cm^2)	Corrosion rate (mm/yr)
TiNbTaVW	-0.189±0.021	0.055±0.003	0.0003±0.0002
CrNbTaVW	-0.139±0.011	0.00265±0.001	0.000097±0.0008
IN718	-0.295±0.010	5.299±2.060	0.054±0.020

6.1.3 Microstructural observation of TiNbTaVW, CrNbTaVW and IN718 in chloride solution

The corrosion resistance of metals and alloys is correlated with the properties of their passive films (Zhang et al., 2021). The SEM images of the TiNbTaVW, CrNbTaVW, and IN718 after potentiodynamic polarisation in 3.5 wt% NaCl are presented in Figure 6.3. No obvious

corrosion regions were found on the TiNbTaVW RHEA's surface (Figure 6.3a); localised corrosion (pits; red arrows) with an average size of 5.65±2.1 μm initiated mainly on the dendrite region (Figure 6.3b). In CrNbTaVW RHEA, no obvious corrosion regions were found on the surface but pits (indicated by red arrows) with an average size of 2.43±0.4 μm (Figures 6.3c and 6.3d). However, the IN718 alloy's surface was highly corroded, and pits (indicated by red circle and red arrows) of an average size of 14.86±2.2 μm were also visible (Figure 6.3e). Corrosion products (indicated by green arrows) were also observed on the surface of the alloys (Figures 6.3a-e). The EDX compositions of TiNbTaVW, CrNbTaVW, and IN718 after potentiodynamic polarisation in chloride solution show the presence of oxygen, suggesting oxide formation on the surface (Table 6.2 and Appendix A-C). The deposition of Cl was also detected in TiNbTaVW, signifying that Cl^- might have broken through the film of the alloys. This is evidenced in the few pits found in the TiNbTaVW RHEA. It was found that W, Ta, and Nb has low compositions in both the dendrite and interdendrite region compared to compositions of Ti and V.

The observed elemental segregation and composition differences can induce the pits observed in TiNbTaVW RHEA. The elemental segregation, interface defects, and composition differences in the passive film accelerate the electrochemical process and deteriorate the corrosion resistance (Hashim et al., 2015; Li et al., 2014; Nyby et al., 2021). The deposition of Cl element in the compositions signified the presence of Cl^- which broke through the oxide layer of the IN718 alloy and led to the corroded surface and pits (Table 6.2). Also, Cl^- broke through the passive layer of CrNbTaVW RHEA and led to a few smaller pits. The CrNbTaVW RHEA did not show dissolution of elemental composition in BCC1, BCC2 and $Cr(VNb)_2$ Laves phases, as shown in Table 6.2. The addition of V protects RHEAs from localised corrosion, such as pitting in NaCl and H_2SO_4 solutions (Kumar et al., 2018). Despite substantial amount of V and almost evenly distributed Nb compositions in all the three phases, few pits were still observed at the RHEA surface. It was found that low W and Ta compositions were observed at BCC1 and $Cr(VNb)_2$ phases, which suggest that elemental segregation might have play a role in the formed pits.

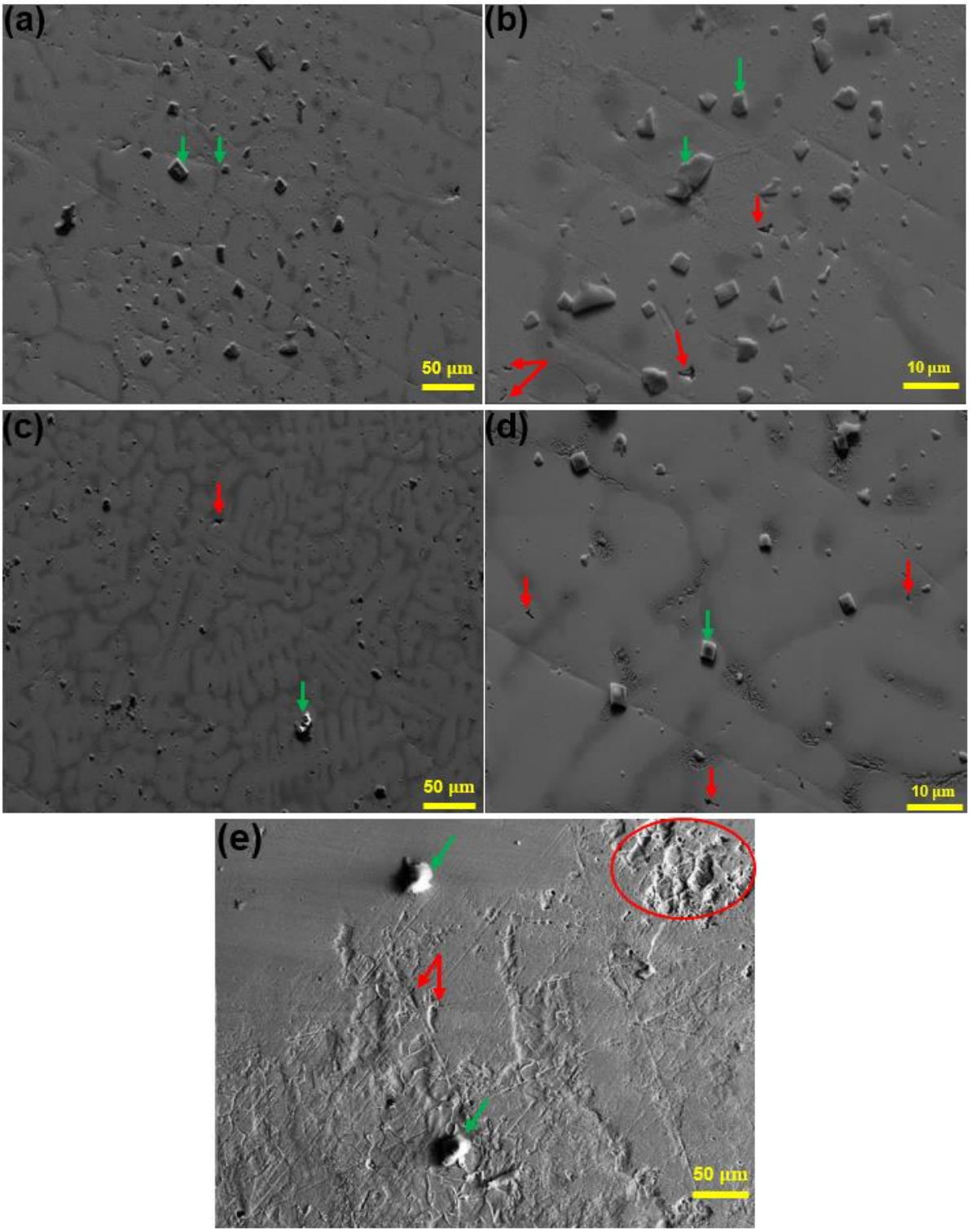

Figure 6.3: SEM image of the TiNbTaVW RHEA surface after exposure in 3.5 wt% NaCl (a); Higher magnification SEM image of the TiNbTaVW RHEA surface showing pits and corrosion products (b); SEM image of the CrNbTaVW RHEA surface after exposure in 3.5 wt% NaCl (c); Higher magnification SEM image of the CrNbTaVW RHEA surface showing pits and corrosion products (d); SEM image of the IN718 showing pits, corroded surface and corrosion products after exposure in 3.5 wt% NaCl (e).

Table 6.2**:** EDX compositions of the TiNbTaVW, CrNbTaVW and IN718 after exposure in 3.5 wt% NaCl.

IN718									
Al	Si	P	Ti	Mn	Fe	Ni	O	Na	Cl
0.15±0.01	0.42±0.20	0.07±0.01	0.06±0.02	0.23±0.01	41.23±15.60	23±5.70	28±8.50	5.5±2.70	1.34±0.70
TiNbTaVW									
Regions	Ti	Nb	Ta	V	W	O	Na	Cl	
Dendrite	15±1.5	10±2.0	9±2.5	16±1.0	10±1.0	32±3.5	5±2.0	3±1.0	
Interdendrite	16±2.1	12±2.0	11±1.5	17±3.2	8±1.2	34±6.5	-	2±3.0	
CrNbTaVW									
Regions	Ti	Nb	Ta	V	W	O	Na	Cl	
Dendrite (BCC1)	15±0.6	14±1.4	10±1.4	17±1.1	7±1.2	24±5.2	6±1.0	7±2.0	
Interdendrite (BCC2)	11±1.1	13±0.7	15±0.2	15±0.9	12±0.9	27±2.0	4±0.1	3±0.8	
$Cr(VNb)_2$	16±1.0	12±2.2	9±3.6	17±1.7	4±4.6	35±3.4	5±1.6	4±0.9	

XRD analysis of the TiNbTaVW, CrNbTaVW, and IN718 after potentiodynamic polarisation in 3.5 wt% NaCl are presented in Figures 6.4-6.6. All the initial phases are still present, suggesting that no preferential phase dissolution occurred in the TiNbTaVW and CrNbTaVW RHEA when exposed to chloride solution (Figures 6.4 and 6.5). The corrosion products formed on the surface of the TiNbTaVW RHEA were identified as TiO_2 and VO (Figure 6.4). The corrosion product formed on the CrNbTaVW RHEA is identified to be VO_2 (Figure 6.5). The XRD pattern of the IN718 alloy showed a reduction of peaks between 60° and 110° that differs from initial phase peaks (Figure 6.6). It was also observed that no new peaks were formed, which shows that limited oxides were deposited on the IN718 alloy surface. Therefore, no protection was offered and this led to a corroded surface and pits when exposed to 3.5 wt% NaCl solution.

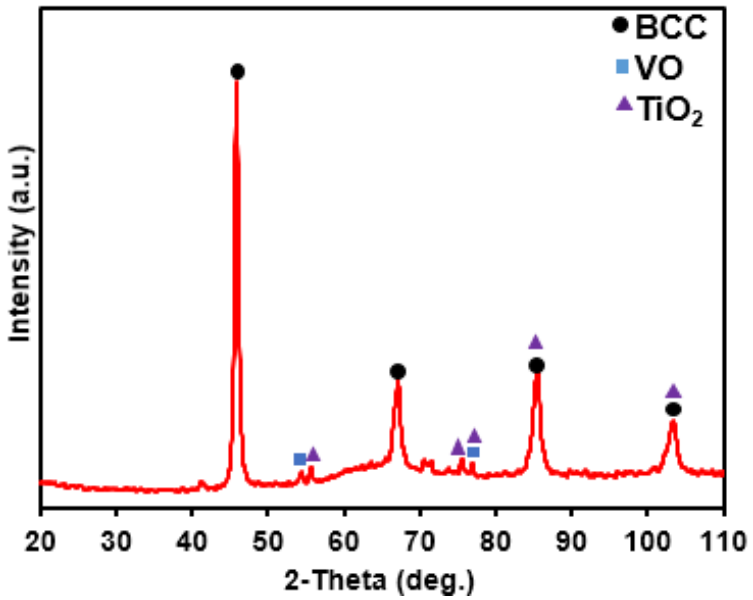

Figure 6.4: XRD of corrosion products formed on the TiNbTaVW RHEA surface.

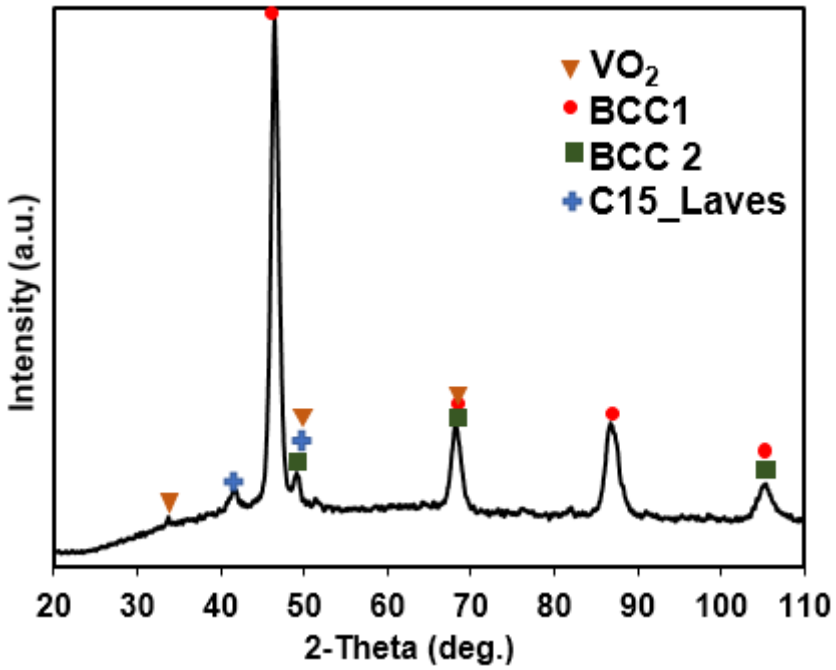

Figure 6.5: XRD of corrosion products formed on the CrNbTaVW RHEA surface.

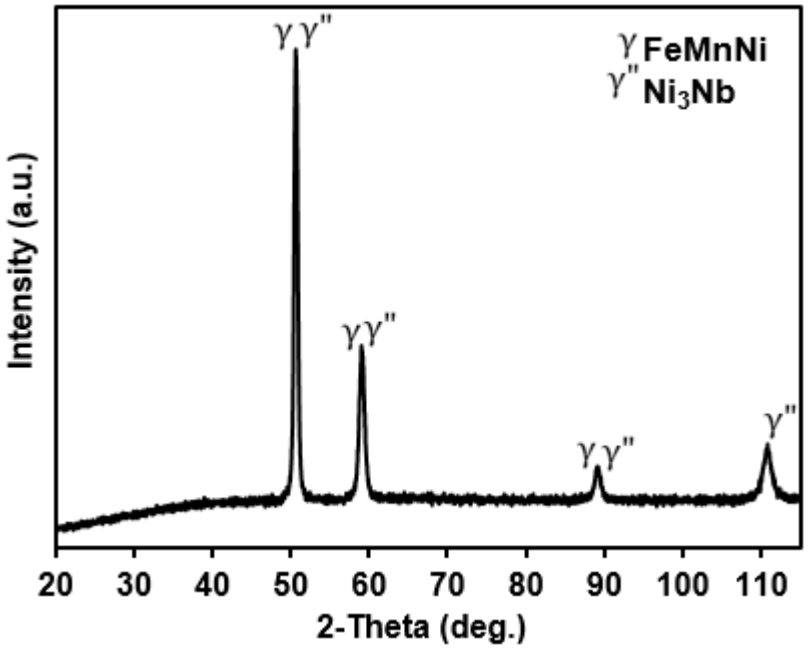

Figure 6.6: XRD of corrosion products formed on the IN718 alloy surface.

6.2 Electrochemical corrosion behaviour in acidic solution

6.2.1 Open circuit potential measurement of TiNbTaVW, CrNbTaVW and IN718 in acidic solution

The OCP of TiNbTaVW, CrNbTaVW, and IN718 in 1M H_2SO_4 are presented in Figure 6.7. The OCP curve of TiNbTaVW RHEA showed an initial noble value (-0.11 V) in the first 5 seconds due to the formation and growth of the passive film on the surface, but the OCP later dropped drastically till 3600 seconds. The OCP curve of CrNbTaVW RHEA showed an initial increase in OCP but later dropped in potential to 2586 seconds. Afterward, stability was achieved in the OCP for 3600 seconds at -0.17 V. In the IN718 alloy, the OCP curve is noticeably unstable. Fluctuations were seen in TiNbTaVW, CrNbTaVW and IN718, indicating the breaking and rebuilding of the oxide film on the alloy's surface. The TiNbTaVW and CrNbTaVW has a higher potential for noble values than the IN718 alloy, which is an indication that a well protective passive film was formed.

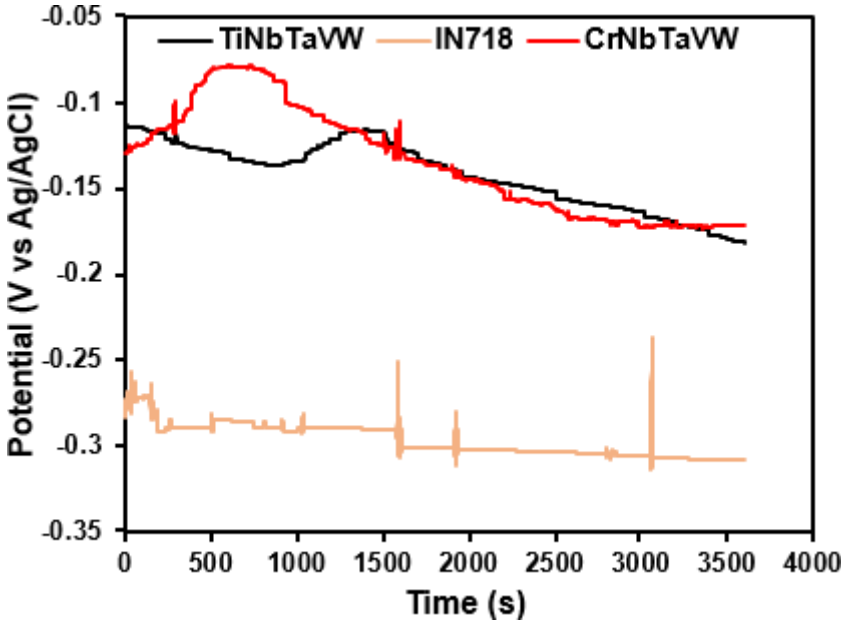

Figure 6.7: OCP curves of TiNbTaVW, CrNbTaVW and IN718 alloy in 1M H_2SO_4.

6.2.2 Potentiodynamic polarisation measurement of TiNbTaVW, CrNbTaVW and IN718 in acidic solution

The potentiodynamic polarisation curves of TiNbTaVW, CrNbTaVW and IN718 in 1M H_2SO_4 is shown in Figure 6.8. The TiNbTaVW RHEA potentiodynamic polarisation curve exhibited passive behaviour up to the final potential of 2.5 V. A breakage in the anodic curve was observed from 1.06 V to 1.13 V (indicated by blue arrow), which signifies that active corrosion took place when exposed to an acidic environment. Active dissolution and pits (indicated by blue circle) were observed in the anodic curve of CrNbTaVW RHEA at 0.18 V to 0.46 V and later passivated to a final potential of 2.5 V. The IN718 alloy potentiodynamic polarisation curve exhibited active corrosion/dissolution (indicated by blue arrow), passivation, and transpassivation. The sulphate ions attack the protective layer of the IN718 alloy and the layer breaks, but the oxide layer starts rebuilding, as evidenced by the passivation region. The electrochemical corrosion parameters such as E_{corr}, I_{corr}, and corrosion rates obtained from the polarisation curve in 1M H_2SO_4 are presented in Table 6.3. The TiNbTaVW and CrNbTaVW RHEAs have high negative E_{corr} values of -0.172 V and -0.147 V than the IN718 (-0.377 V), which indicate higher susceptibility to corrosion. The CrNbTaVW RHEA has a lower I_{corr} value of 0.0039 $\mu A/cm^2$ than the TiNbTaVW (0.175 $\mu A/cm^2$) and IN718 (104.59 $\mu A/cm^2$). Based on the electrochemical parameters in

Table 6.3, it is evident that the corrosion rate is lower in the CrNbTaVW and TiNbTaVW than the IN718 in 1M H_2SO_4. This shows that an oxide protective layer was formed on the CrNbTaVW and TiNbTaVW surface.

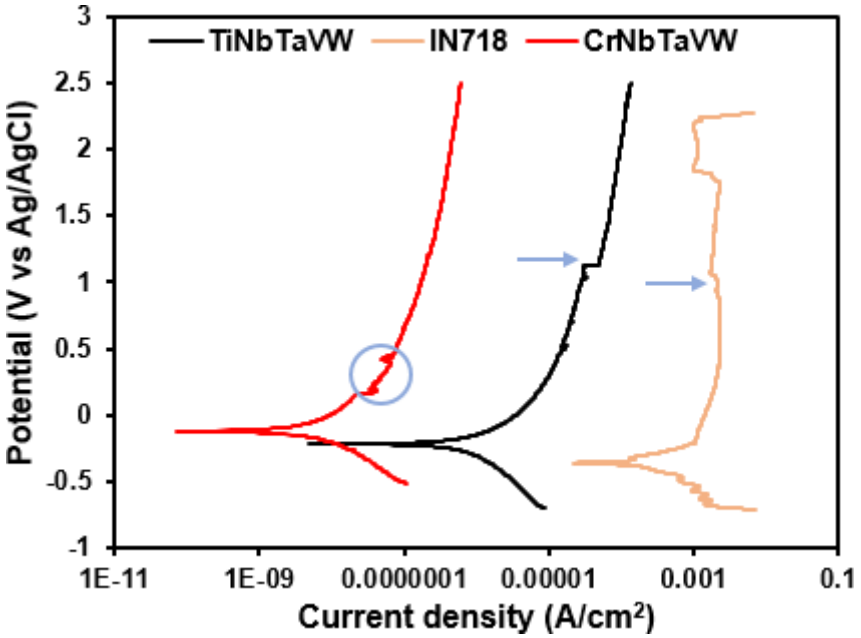

Figure 6.8: Potentiodynamic polarisation curves of TiNbTaVW, CrNbTaVW and IN718 in 1M H_2SO_4.

Table 6.3: Electrochemical parameters for TiNbTaVW, CrNbTaVW and IN718 in 1M H_2SO_4.

Alloy	Ecorr (V)	I_{corr} (µA/cm^2)	Corrosion rate (mm/yr)
TiNbTaVW	-0.172±0.02	0.175±0.09	0.0009±0.0005
CrNbTaVW	-0.147±0.02	0.0039±0.01	0.00013±0.0001
IN718	-0.377±0.01	104.59±4.01	1.12±0.0010

6.2.3 Microstructural observation of TiNbTaVW, CrNbTaVW and IN718 in acidic solution

The SEM images of the TiNbTaVW, CrNbTaVW, and IN718 after potentiodynamic polarisation in 1M H_2SO_4 are presented in Figure 6.9. Deposits of corrosion products (indicated by green arrows) were seen on different regions of the TiNbTaVW and CrNbTaVW RHEA surface (Figures 6.9a and 6.9b). Pits (indicated by red arrows) of an average size of 4.1±0.9 µm and 2.46±0.23 µm were found mostly at the interdendrite (dark region) of the

TiNbTaVW RHEA surface and at BCC1 (white region) of the CrNbTaVW RHEA surface (Figures 6.9a and 6.9b). The IN718 alloy surface was corroded with pits (indicated by red arrows) of average size of 6.27±0.68 μm (Figure 6.9c). The observed pits imply that the sulphate ions broke through the passive layer of the alloys.

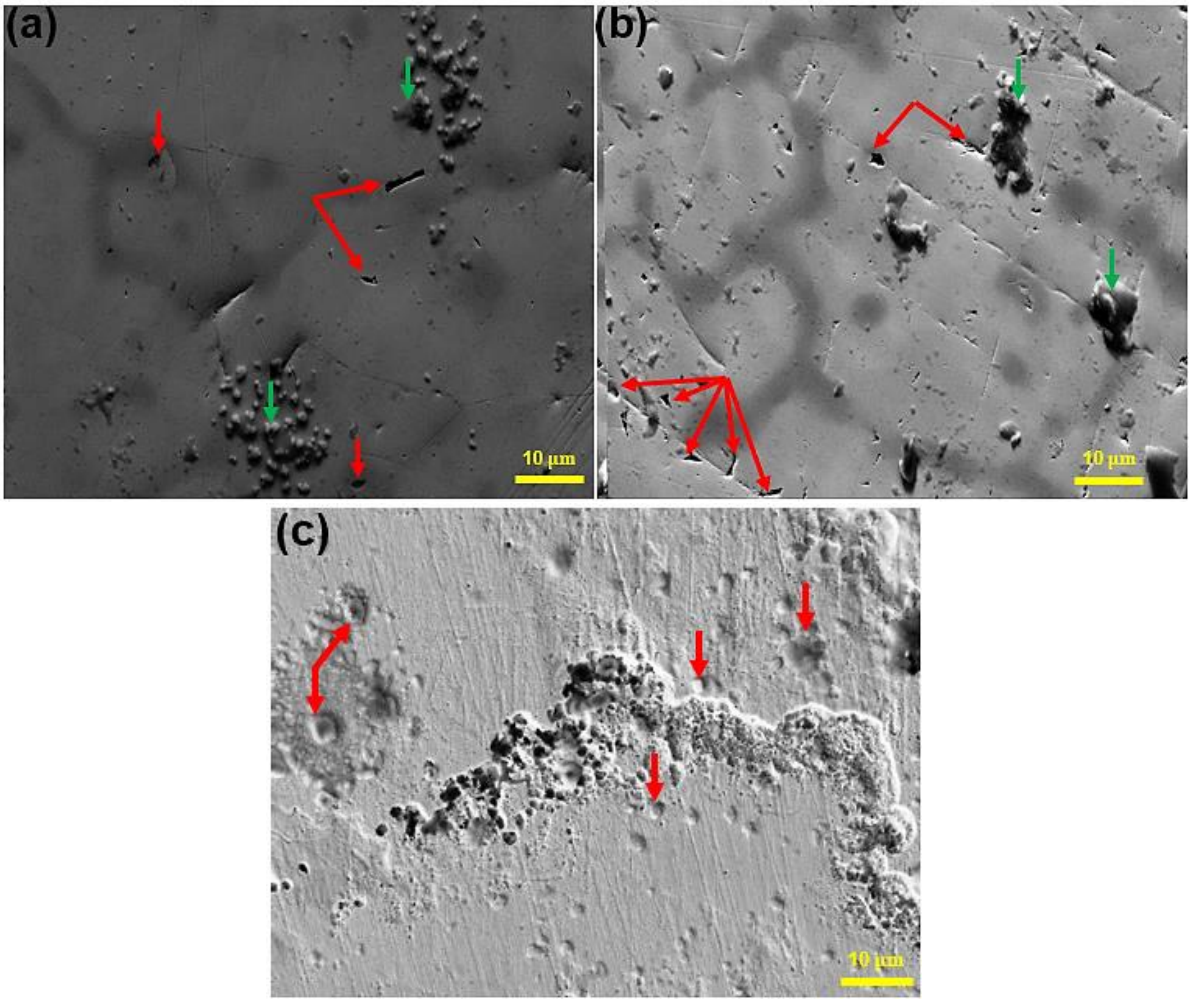

Figure 6.9: SEM image of the TiNbTaVW RHEA surface after exposure in 1M H_2SO_4 showing pits and corrosion products (a); SEM image of the CrNbTaVW RHEA surface after exposure in 1M H_2SO_4 showing pits and corrosion products (b); SEM image of the IN718 alloy after exposure in 1M H_2SO_4 showing pits and corroded surface (c).

The EDX compositions of the TiNbTaVW, CrNbTaVW and IN718 after potentiodynamic polarisation in 1M H_2SO_4 are presented in Table 6.4 and Appendix D-F. The EDX compositions of IN718 after the test show the elemental compositions were still intact after exposure to acidic solution. Elemental segregation and composition differences of Ti in the dendrite region with segregation and composition differences of Ta and W in the interdendrite

region could enable pits in the TiNbTaVW. In the CrNbTaVW RHEA, BCC1 which was segregated in the dendrite region still retained a substantial amount of Nb, Ta, V, W, but lower Cr compositions. BCC2 in the interdendrite region still retained a substantial amount of Cr, Nb, and V but lower W and Ta compositions. The $Cr(VNb)_2$ C15-Laves dissolved after corrosion exposure in 1M H_2SO_4 (Figure 6.10). This might be correlated with the OCP in Figure 6.7, where there was a rapid increase in the potential and oscillations due to the dissolution and rebuilding of the oxide film on the alloy surface. Elemental segregation of Cr in the dendrite region and segregation of Ta and W in interdendrite region might play a role in the pits and phase dissolution that was observed. Selective dissolution of Cr_2Nb Laves was observed in CrMoNbWV RHEA in the 0.5 M H_2SO_4 (Razumov et al., 2021). The formation and dissolution behavior of the oxide film in an acidic solution was also observed for Cr containing $AlCoCrFeNi_{2.1}$ HEA (Wei & Qin, 2022). Also, selective dissolution of the V-rich Sigma phase was also reported in a MoNbFeCrV RHEA after the polarisation test in 0.5 M H_2SO_4 (Xiang et al., 2019).

Table 6.4: EDX composition of the TiNbTaVW, CrNbTaVW and IN718 after potentiodynamic polarisation test in 1M H_2SO_4.

TiNbTaVW						
Regions	Ti	Nb	Ta	V	W	O
Dendrite	12±0.9	15±0.6	15±0.6	14±0.5	16±0.9	28±2.8
Interdendrite	20±1.2	16±0.9	12±0.9	19±1.1	9±1.2	24±4.2
CrNbTaVW						
Regions	Cr	Nb	Ta	V	W	O
Dendrite (BCC1)	10±1.2	18±0.7	21±1.0	17±0.9	20±1.9	14±1.2
Interdendrite (BCC2)	18±3.5	17±1.8	12±0.3	23±3.3	6±1.2	24±7.2
IN718						
Si	P	S	Mn	Fe	Ni	O
0.42±0.09	0.15±0.08	3.06±0.01	0.26±0.10	46.16±8.40	25.04±3.10	24.91±9.90

The XRD patterns of TiNbTaVW, CrNbTaVW, and IN718 after potentiodynamic polarisation in 1M H_2SO_4 is shown in Figures 6.10-6.12. The TiNbTaVW RHEA only contains WO_3 and BCC solid solution phases (Figure 6.10). Although good corrosion resistance was observed

for the RHEA, the passive layer containing WO_3 could not prevent the occurrence of pits. The corrosion product formed on the CrNbTaVW RHEA only contains VO_2 (Figure 6.11). BCC1 and BCC2 phases are still present, while the peaks of $Cr(VNb)_2$ C15-Laves phase are no longer present. This further indicate that active dissolution of $Cr(VNb)_2$ C15-Laves phase actually occurred when exposed to acidic solution. The formed VO_2 is not sufficient to protect the CrNbTaVW RHEA from pits and the dissolution of $Cr(VNb)_2$ C15-Laves phase. Similar to the chloride solution, no new peaks were observed for the IN718 alloy in acidic solution, but peaks were reduced between 90° and 110° (Figure 6.12). These show that low or minimal corrosion products were deposited on the IN718 alloy's surface after potentiodynamic polarisation. The lack of a protective film explains the corroded surface and pits observed in the IN718 alloy when exposed to the acidic solution.

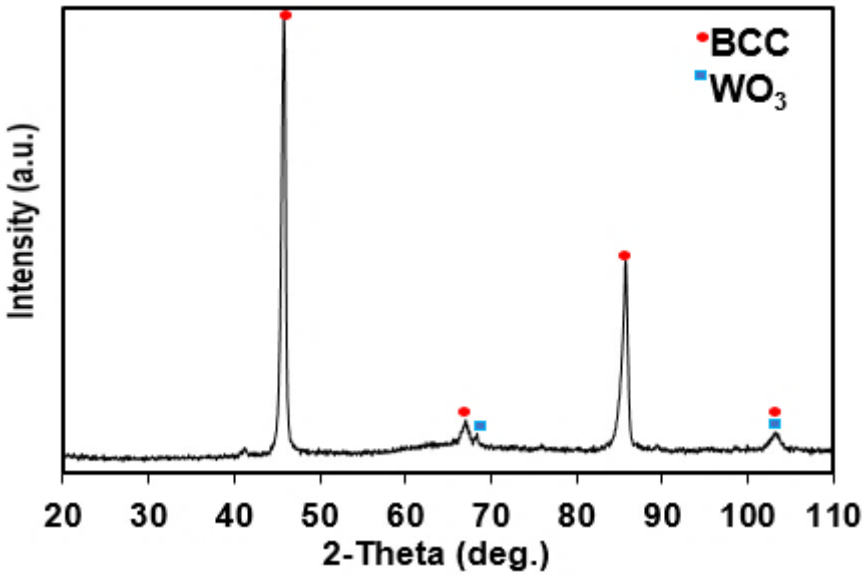

Figure 6.10: XRD of corrosion products formed on the TiNbTaVW RHEA surface.

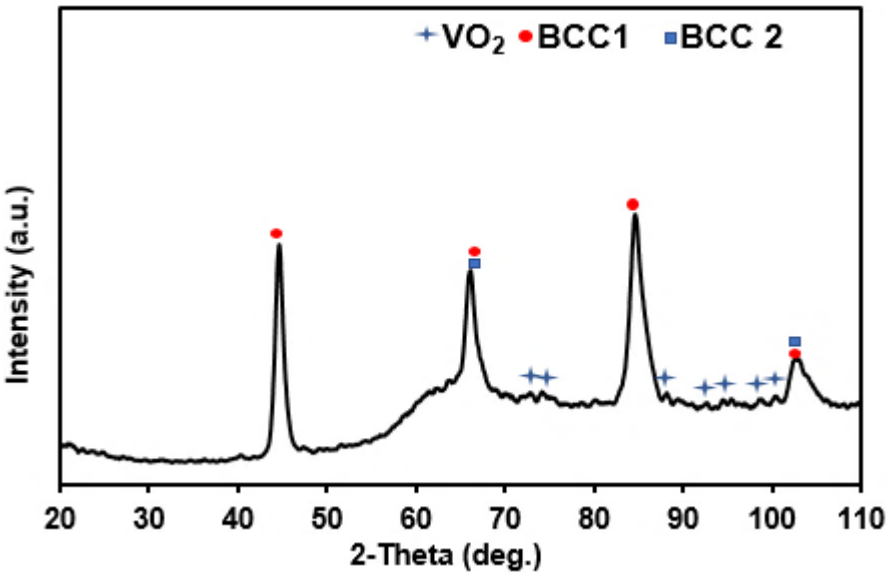

Figure 6.11: XRD of corrosion products formed on the CrNbTaVW RHEA surface.

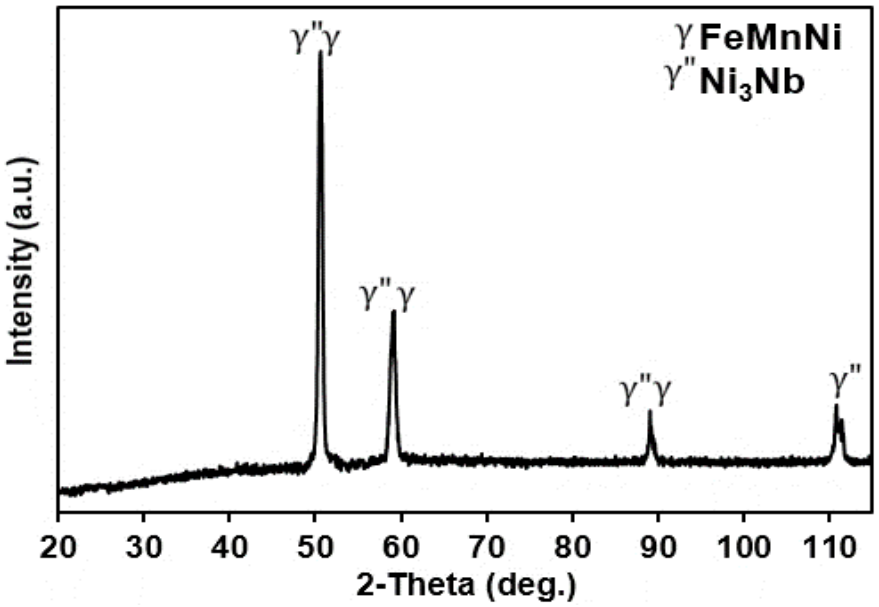

Figure 6.12: XRD of corrosion products formed on the IN718 alloy surface.

6.3 Discussion

6.3.1 Corrosion resistance of TiNbTaVW, CrNbTaVW, and IN718 in 3.5 wt% NaCl and 1M H_2SO_4 solution

Passivation is a characteristic of HEAs, arising due to the addition of passivating promoting elements such as Cr and Ti. The passivating promoting element may influence the alloy structure and passive film composition, giving rise to different electrochemical responses depending on the alloying type and content (Nascimento et al., 2022). The passivity of the oxide film formed on the surface of the TiNbTaVW and CrNbTaVW in 3.5 wt% NaCl and 1M H_2SO_4 solutions was evaluated by the OCP measurement. TiNbTaVW and CrNbTaVW has a nobler value in both 3.5 wt% NaCl and 1M H_2SO_4 than IN718. The increase in nobler value for the OCP has been attributed to the growth of the oxide layer on the alloy (Atapour et al., 2010). However, the TiNbTaVW and CrNbTaVW showed different behaviours in 3.5 wt% NaCl and 1M H_2SO_4 solutions. The OCP remained stable throughout immersion in 3.5 wt% NaCl for TiNbTaVW and CrNbTaVW, while a rapid increase and decrease in the OCP indicating dissolution of the protective film was seen in 1M H_2SO_4. The dissolution of the protective film on the TiNbTaVW and CrNbTaVW can be attributed to the complexity of SO_4^{2-} ions in the solution. The variations in the OCP showed that the TiNbTaVW and CrNbTaVW is sensitive to sulphate containing solution. Fluctuations in OCP were observed for IN718 alloy in both 3.5 wt% NaCl and 1M H_2SO_4 solutions but less for TiNbTaVW and CrNbTaVW. Dissolution of the oxide film occurs in both solutions for the IN718 alloy, indicating that the observed fluctuations in OCP are the result of rebuilding the oxide layer on the alloy surface. Based on the OCP results, it can be concluded that the TiNbTaVW and CrNbTaVW RHEA surface film is more stable than the IN718 alloy in 3.5 wt% NaCl and 1M H_2SO_4 solution.

The good corrosion resistance of titanium-containing alloys in many chloride and sulphide solutions has been attributed to the stable and adherent passive film that forms spontaneously on the metal surface (Atapour et al., 2010; Neto & Rainforth, 2020; Pandey et al., 2020). These oxides have two layers comprising the inner layer (TiO) and outer layer (TiO_2) passive films of the exposed samples (Ciszak et al., 2016; Neto & Rainforth, 2020; Pandey et al., 2020; Pouilleau et al., 1997). TiO_2 and VO were found on the surface of the TiNbTaVW RHEA after

potentiodynamic polarisation in chloride containing solution. Ti exhibits a low passivation potential and is easily passivated, forming TiO_2 which further improves corrosion resistance (Fu et al., 2021; Zhou et al., 2022). In the acidic solution, WO_3 only formed on the TiNbTaVW surface. WO_3 is a selective cation oxide that can act as an effective pitting inhibitor that restricts the binding of anions such as Cl^- and Br^{-1} (Kumar et al., 2018; Pourbaix, 1974).

For the CrNbTaVW only VO_2 was formed on the surface of the CrNbTaVW RHEA in both chloride and acidic solutions. It was established that Cr containing element produce excellent corrosion resistance, which is attributed to the thin protective passive film consisting of Cr oxides (Luo et al., 2018). Thick and stable passivation films often show a strong ability to hinder ion migration and participate in the reaction, resulting in good protection against corrosion (Sun et al., 2023). During the corrosion process in the chloride-containing solution the detrimental Cl^- anions would be adsorbed on the interface of the passive layer and the solution, and then penetrate through the oxide films causing pitting corrosion (Shi et al., 2017). The uniform distribution of passivation elements, such as Cr, Ti, Al, Zr, Ta, Nb, and Hf could form a homogeneous protective oxide film and decrease the likelihood of pit formation (Zhou et al., 2019).

The microstructure and composition are the two main factors in the corrosion performance of an alloy (Li et al., 2019). Alloy heterogeneities such as inclusions, impurities, and second phases have been reported to be detrimental to the continuity of the overlying passive film of alloys because the oxides formed at these sites or along their periphery are often not protective (Williams et al., 2000; Frankel et al., 2017; Li et al., 2019). Thus, the oxide in these areas often acts as the weak spot for breakdown. The preferential corrosion sites in HEAs are phase boundaries, defects, elemental segregation, and multiphase microstructure (Li et al., 2021; Yao et al., 2023). Hence, the microstructure uniformity and chemical composition can prevent the occurrence of localised corrosion in the alloy. The SEM images of TiNbTaVW RHEA in chloride and acidic solution comprise pits, while CrNbTaVW RHEA in chloride solution showed few pits, while in acidic solution, more pits and selective dissolution of $Cr(VNb)_2$ Laves took place.

In RHEAs with less or no W particles, chloride ions gather at the pitted regions, and the adsorption of chloride ions weakens the neigbouring passive film of the pits and worsens pit formation (Zhou et al., 2021). HEAs that contain Cr compositions greater than 13 wt% can be associated with enhanced corrosion resistant properties (Swanson, 2018). Despite the high chromium compositions in the CrNbTaVW RHEA, pits were still found when exposed to NaCl solution. In the H_2SO_4 solution, low Cr composition (10 wt%) was observed in the BCC1, which may have caused the few pits observed in the BCC1 region and none in the BCC2 region (Figure 10). Regardless of the effects of the aggressive corrosive solutions, the resistance to passive film breakdown is determined by the properties of the passive film including its continuity, formation ability, and film stability (Li et al., 2019). Only VO_2 was formed on the surface of the CrNbTaVW RHEA in both chloride and acidic solutions. The VO_2 layer was able to prevent phase dissolution and surface corrosion in chloride solution, but not enough protection against localised corrosion (pitting). Despite the presence of TiO_2, VO, and WO_3 on the TiNbTaVW RHEA's surface, few pits were found in both chloride and acidic solutions. The next paragraphs provide insight into why the pit eventually formed.

The main corrosion mechanism for TiNbTaVW RHEA in chloride and acidic solutions is localised corrosion due to the segregation of the elemental compositions in both the dendrite and interdendrite regions, as shown in Figure 6.13. The pits mainly appear at the dendrite region when exposed to chloride solution, which is related to the breakdown of the passive film on the alloy's surface (Figure 6.13a). Since pitting is related to the metal surface passive film, pits observed in single-phase alloys exposed to chloride solution can be attributed to the destruction of the alloy's surface passive film by Cl^- ions (Liu et al., 2023). Uniform microstructures and non-segregation of elemental compositions can inhibit the inhomogeneity of electrochemical performance among phases and grain boundaries (Xing et al., 2022). In a chloride solution, segregation of elemental compositions was observed, in which there's a higher Ti and V content in both the dendrite and interdendrite regions than the NbTaW content in both regions (Figure 6.13a).

The elemental composition segregation might have resulted in different electrochemical responses in the dendrite and interdendrite regions to cause a protective layer breakdown, as illustrated in Figure 6.13a. The breakdown of the layer allowed the ingress of Cl^- ions, which

replace the O element especially at the weak spots of passive film and pits were formed. In the acidic solution, TiV-rich compositions were found in the interdendrite region and near evenly distributed TiNbTaVW compositions in the dendrite region. At this rate, the TiV-rich interdendrite region became the anode, while the near evenly distributed TiNbTaVW dendrite region became the cathode. The coupling effect of the elemental segregations resulted in the protective layer breakdown, and ingress of sulphate ions was allowed at the passive film weak spots. These eventually led to pit formed at the interdendrite region (Figure 6.13b). This phenomenon has been reported in HEAs such as MoTaNbVW (Ananiadis et al., 2021) and TiVCrNb (Yao et al., 2023). The fact that there are just a few pits on the surface of TiNbTaVW RHEA in both the chloride and acidic solutions is evidence of limited localised corrosion.

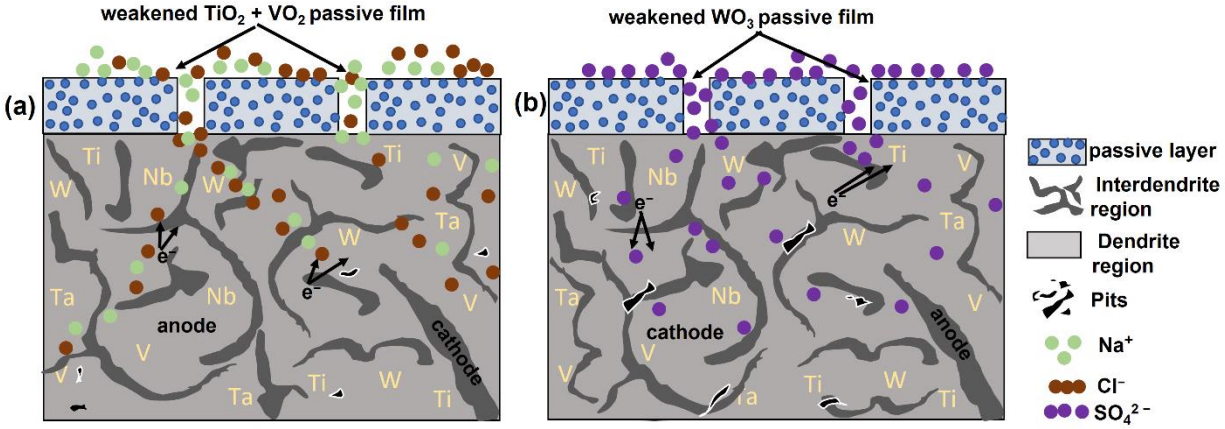

Figure 6.13: Schematic diagrams of the TiNbTaVW RHEA corrosion process during the potentiodynamic polarisation tests in 3.5 wt% NaCl (a); 1 M H_2SO_4 (b).

Figure 6.14 illustrates the corrosion mechanism of the CrNbTaVW RHEA when exposed to 3.5 wt% NaCl and 1 Mol H_2SO_4 solutions. At the beginning of corrosion in NaCl environment (Figure 6.14a), Cl^- is adsorbed on the passive film, which makes some metal cations in the passive film dissolve into the solution. In the CrNbTaVW RHEA multiphases of BCC1, BCC2, and $Cr(VNb)_2$ Laves, Cl^- will be preferentially adsorbed in these phases and detrimental to the passive film continuity. It was observed that pitting occurred mostly in BCC1 and regions between the BCC1 and BCC2 phases (Figure 6.14b). The pits can be initiated by the elemental segregation of the elements that comprises the two phases. If there is a significant potential difference between the two phases, galvanic coupling can result in localised corrosion (pits) (Liu et al., 2023; Wang et al., 2022). The passive film properties made BCC1 phase the anode and BCC2 phase the cathode, the passive film eventually

weakened resulting in the pitting of BCC1 phase under the combined effect of galvanic coupling and Cl^- (Figure 6.14b). In an acidic solution, fluctuations were observed in passive film indicating dissolution of the protective film (Figure 6.1).

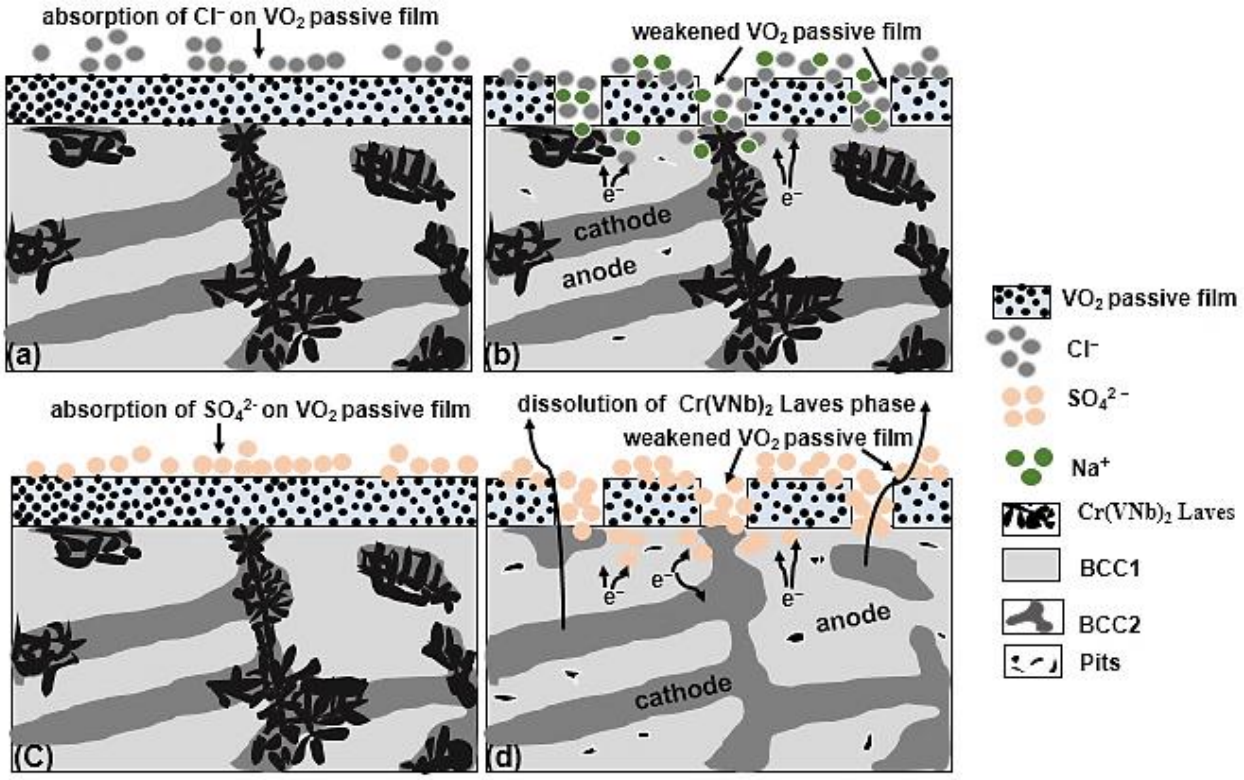

Figure 6.14: Schematic diagram of the pits of BCC1 phase in CrNbTaVW RHEA in 3.5 wt% NaCl solution (a-b); Schematic diagram of the pits of BCC1 phase and dissolution of $Cr(VNb)_2$ Laves phase in CrNbTaVW RHEA in 1 Mol H_2SO_4 solution (c-d).

The dissolution of the protective film on the alloy can be attributed to the complexity of the SO_4^{2-} ions in the solution (Figure 6.7). As the CrNbTaVW RHEA is immersed in the 1M H_2SO_4 (Figure 6.14c), the anode and cathode areas are electrically connected and constitute the corrosion cell, leading to the existence of electric potential. Pits initiate mainly on the BCC1 phase and the boundaries of the BCC1 and BCC2 phases (Figure 6.14d). The observed pit in the BCC1 phase could be attributed to combined effect of SO_4^{2-} ions and galvanic coupling of the BCC1 phase (anode) and BCC2 phase (cathode) (Figure 6.14d). The $Cr(VNb)_2$ Laves phase was formed on top of the BCC2 phase and boundaries between the two phases are often weak zones and preferential to initiate corrosion. The potential difference between dual phases brings about a strong driving force for phase dissolution (Wang et al., 2022; Peng et al., 2023). As a result of coupling effects between the $Cr(VNb)_2$ Laves phase (anode) and

BCC2 phase (cathode), the $Cr(VNb)_2$ Laves was eventually dissolved (Figure 6.14d). Despite the pits observed in the BCC1 phase and the dissolution of $Cr(VNb)_2$ Laves, the CrNbTaVW RHEA still has a high corrosion resistance in both the chloride and acidic solutions.

Figure 6.15 illustrates the corrosion mechanism of IN718 alloy when exposed to 3.5 wt% NaCl and 1 Mol H_2SO_4 solutions. At the beginning of corrosion in the NaCl environment (Figure 6.15a), Cl^- ions are adsorbed on the passive film, leading to the dissolution metal cations into the solution. The Cl^- ions attack and penetrated the passive film of the IN718 alloy, resulting in a corroded surface and pits formation (Figure 6.3e and Figure 6.15a). This was confirmed by fluctuations in the OCP curve (Figure 6.1) and active corrosion observed in the potentiodynamic polarisation curve (Figure 6.2). In the acidic solution, the presence of pits and a corroded surface indicated that SO_4^{2-} ions penetrated the passive film of the IN718 alloy (Figure 6.9c and Figure 6.15b). This is evidenced by the unstable OCP curve (Figure 6.7) and active corrosion/dissolution observed in the potentiodynamic polarisation curve (Figure 6.8). The absence of a stable and adherent passive film led to corroded surface and pit formation when IN718 was exposed to 3.5 wt% NaCl and 1 Mol H_2SO_4 solutions.

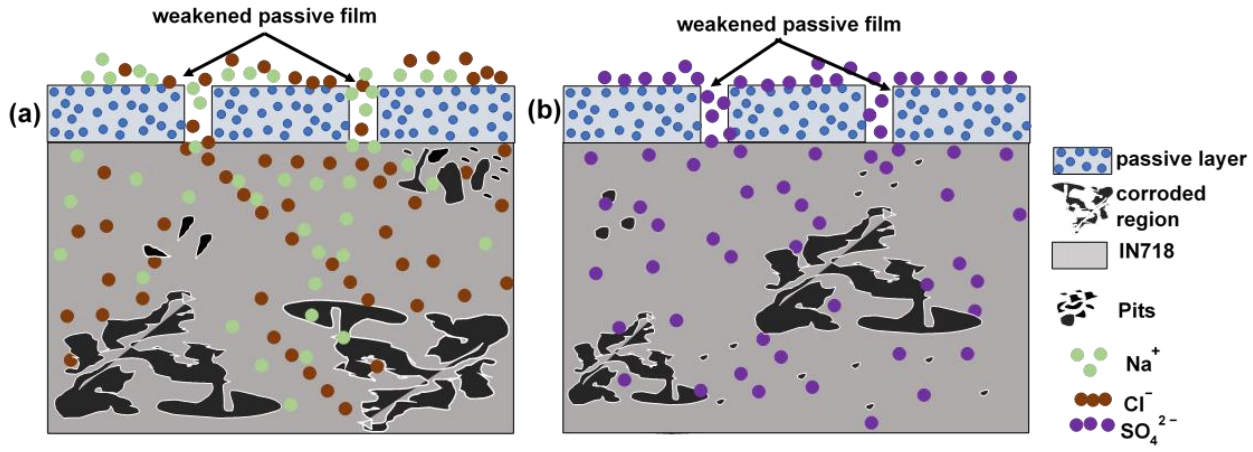

Figure 6.15: Schematic diagram of the uniform corrosion and pits in IN718 alloy in 3.5 wt% NaCl solution (a); Schematic diagram of the uniform corrosion and pits in IN718 alloy in 1 Mol H_2SO_4 solution (b).

6.4 Summary

- In chloride solution, TiNbTaVW and CrNbTaVW RHEA oxide film is more stable than the IN718 alloy. A great number of fluctuations was observed in the OCP curve

of the IN718 alloy that was attributed to the instability caused by the chloride ions in the solution and dissolution and re-passivation of the oxide film. In acidic solution, fluctuations were seen in TiNbTaVW, CrNbTaVW and IN718, suggesting the breaking and rebuilding of the oxide film on the surface.

- Potentiodynamic polarisation curves of TiNbTaVW, CrNbTaVW and IN718 showed that active corrosion took place when exposed to chloride environment. Transient currents were observed in TiNbTaVW and CrNbTaVW RHEA that indicated instability of the passive film in response to chloride ion attack. In acidic solution, active corrosion also took place as observed from the potentiodynamic polarisation curves.
- Few pits were observed on the TiNbTaVW and CrNbTaVW surface after potentiodynamic polarisation in 3.5 wt% NaCl and 1M H_2SO_4 solutions. In 3.5 wt% NaCl, interdendrite region of the TiNbTaVW and BCC1 region in the CrNbTaVW was more susceptible to pitting corrosion. In 1M H_2SO_4 solution, interdendrite region of the TiNbTaVW and BCC1 in the CrNbTaVW was more susceptible to pitting corrosion, while the $Cr(VNb)_2$ Laves phase was more susceptible to selective dissolution in the CrNbTaVW.
- In 3.5 wt% NaCl, the corrosion products formed on the TiNbTaVW RHEA surface were TiO_2 and VO, while only VO_2. was formed on the CrNbTaVW RHEA surface. While limited oxides were deposited on the IN718 alloy surface. In 1M H_2SO_4, the corrosion products formed on the TiNbTaVW and CrNbTaVW surface were WO_3 and VO_2. Also, limited oxides were deposited on the IN718 alloy surface. In conclusion, the deposited corrosion products on the RHEAs could not prevent pit occurrence in 3.5 wt% NaCl and 1M H_2SO_4 solutions.
- In 3.5 wt% NaCl solution, the TiNbTaVW and CrNbTaVW had a lower corrosion rate of 0.0003±0.0002 mm/yr and 0.000097±0.0008 mm/yr than the IN718 alloy (0.0539±0.02 mm/yr). In 1M H_2SO_4 solution, TiNbTaVW and CrNbTaVW had a lower corrosion rate of 0.0009±0.0005 mm/yr and 0.00013±0.00012 mm/yr than the IN718 alloy (1.12±0.001 mm/yr). In conclusion, the corrosion rate of CrNbTaVW RHEA was lower than the TiNbTaVW RHEA and IN718 alloy in both 3.5 wt% NaCl and 1M H_2SO_4 solutions.

- The main corrosion mechanism of the TiNbTaVW RHEA in chloride and acidic solutions is localised corrosion due to segregation of elemental compositions that resulted in different electrochemical potentials that eventually breakdown the protective layer and allow ingress of chloride and sulphate ions.
- The main corrosion mechanism of the CrNbTaVW RHEA in chloride and acidic solutions is localised corrosion due to segregation of elemental compositions and multi-phases that resulted in different electrochemical potentials that eventually breakdown the protective layer and allow ingress of chloride and sulphate ions.
- The main corrosion mechanism of the IN718 alloy in chloride and acidic solutions is active corrosion and localised corrosion due to absence of a stable and adherent passive film.

Chapter 7

This chapter addresses the fifth research objective. The results obtained from cyclic oxidation behaviour of TiNbTaVW, CrNbTaVW, and IN718 at 850°C and 1050°C for 15 hours are presented in Sections 7.1 to 7.4. The oxidation mechanisms of the TiNbTaVW, CrNbTaVW, and IN718 are also presented. Discussion of the results is presented in Section 7.5.

7.1 Oxidation analysis of TiNbTaVW, CrNbTaVW and IN718

7.1.1 Cyclic oxidation behaviour of TiNbTaVW, CrNbTaVW and IN718

The cyclic oxidation curves of TiNbTaVW, CrNbTaVW and IN718 at 850°C and 1050°C are shown in Figures 7.1-7.2. At 850°C, the TiNbTaVW RHEA exhibited mass gain at the initial stages of oxidation before mass loss and then became stationary with increasing oxidation time, as shown in Figure 7.1. The CrNbTaVW RHEA also exhibited a mass gain at the initial stages. The fast mass gain at the initial stages is attributed to the alloys reaction with oxygen that facilitated the oxide scale (Zhang et al., 2021). After 3 hours of oxidation at 850°C, the CrNbTaVW RHEA exhibited rapid mass loss which can be attributed to oxide layer spallation. At 9-15 hours, the mass curve is stationary because the oxide scale gets thicker, thereby protecting the surface of the CrNbTaVW RHEA from direct contact with oxygen. The oxidation rate of the TiNbTaVW RHEA slowed down at some point with increasing time, indicating that when the oxide scale gets thicker, the oxygen diffusion processes become slower. Hence, a decrease in mass loss for the TiNbTaVW and CrNbTaVW at 850°C (Figure 7.1). The IN718 alloy exhibited an almost stationary trend throughout the oxidation test at 850°C after 15 hours.

Figure 7.2 shows cyclic oxidation curves of the TiNbTaVW, CrNbTaVW and IN718 at 1050°C. An initial mass gain was observed for TiNbTaVW RHEA after 3 hours, followed by a continuous mass loss with increasing oxidation time. After 9-15 hours, a continuous mass loss was observed for the CrNbTaVW RHEA. The IN718 alloy exhibited an almost stationary trend throughout the oxidation test. The IN718 alloy had a lower mass gain of 4.41 mg/cm^2 and 10.84 mg/cm^2 at 850°C and 1050°C, respectively, whereas the TiNbTaVW RHEA exhibited mass losses of −23.58 mg/cm^2 and −45.92 mg/cm^2 at 850°C and 1050°C. The CrNbTaVW RHEA exhibited mass losses of −25.17 mg/cm^2 and −35.91 mg/cm^2 at 850°C

and 1050°C. The IN718 alloy had a better oxidation resistance than the TiNbTaVW and CrNbTaVW over the entire 15 hours of oxidation.

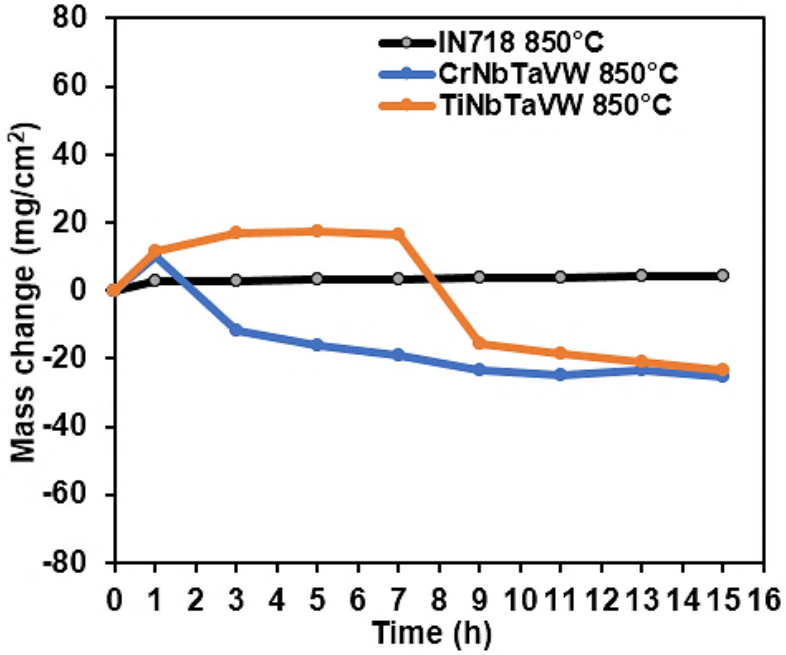

Figure 7.1: Cyclic oxidation curve of TiNbTaVW, CrNbTaVW and IN718 at 850°C.

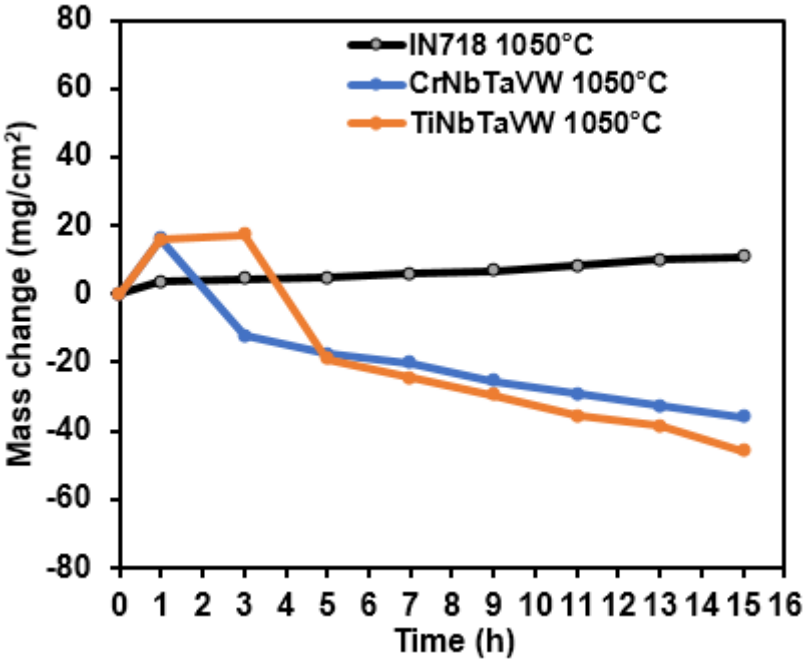

Figure 7.2: Cyclic oxidation curve of TiNbTaVW, CrNbTaVW and IN718 at 1050°C.

7.2 Phase analysis, surface and cross-section morphologies of oxidised TiNbTaVW, CrNbTaVW and IN718

7.2.1 Phase analysis of oxidised TiNbTaVW, CrNbTaVW and IN718

The XRD patterns of the oxidised TiNbTaVW, CrNbTaVW and IN718 samples at 850°C are shown in Figures 7.3-7.5. The identified oxides of TiNbTaVW RHEA at 850°C were VO_2, V_2O_3, Ta_2O_5, TiO_2, WO_3, Ta_2O_5, $TiVO_4$, $TiTaO_4$, and $Nb_2O_5WO_3$, as shown in Figure 7.3. The identified oxides of CrNbTaVW RHEA at 850°C were VO_2, V_2O_3, WO_3, Cr_2O_3, $CrVO_3$, Cr_2WO_6, and $Nb_2O_5WO_3$, as shown in Figure 7.4. The identified oxides of IN718 at 850°C were MnO, MnO_2, Al_2O_3, Fe_3O_4, SiO_2, TiO_2, Fe_2O_3, and Ni_2Ti_4O, as shown in Figure 7.5.

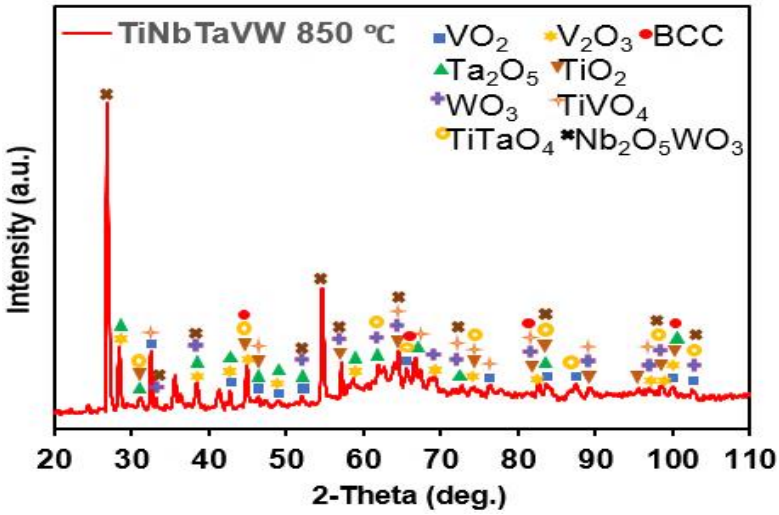

Figure 7.3: XRD pattern of identified oxides in TiNbTaVW at 850°C.

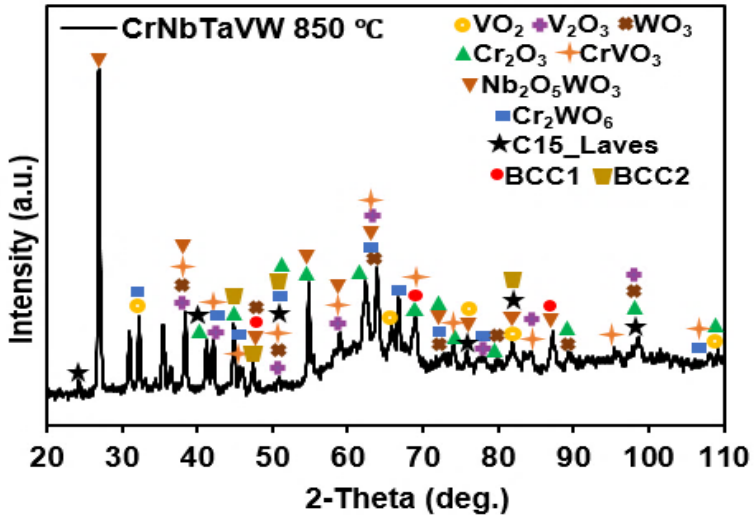

Figure 7.4: XRD pattern of identified oxides in CrNbTaVW at 850°C.

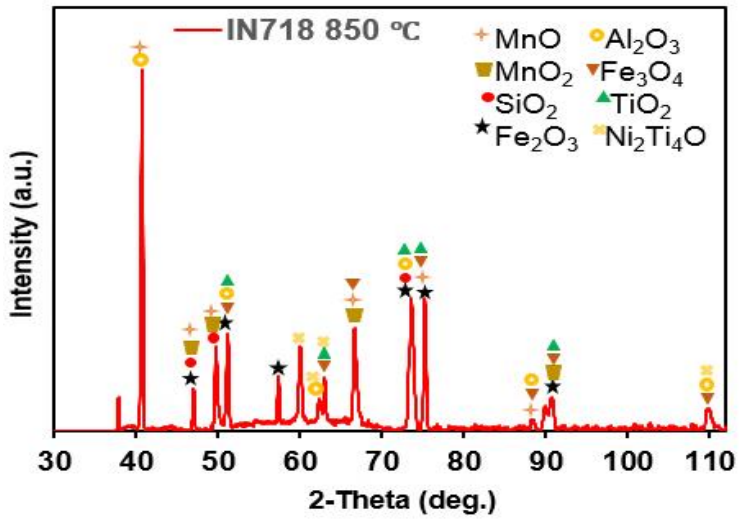

Figure 7.5: XRD pattern of identified oxides in IN718 at 850°C.

The XRD patterns of the oxidised TiNbTaVW, CrNbTaVW and IN718 samples at 1050°C are shown in Figures 7.6-7.8. The oxides of TiNbTaVW RHEA at 1050°C were oxides of Ti_2O_3, TiO_2, VO_2, V_2O_5, WO_3, $TiNbO_4$, and $Ta_8W_8O_{44}$, as shown in Figure 7.6. At 1050°C, identified oxides of CrNbTaVW were VO_2, V_2O_3, WO_3, Cr_2O_3, Cr_2WO_6, $CrVO_3$, $Nb_2O_5WO_3$, and $CrTaO_4$, as shown in Figure 7.7. The identified oxides of IN718 alloy at 1050°C were MnO, MnO_2, Fe_3O_4, Mn_2O_3, $NiMn_2O_4$, and Fe_2MnO_4 (Figure 7.8).

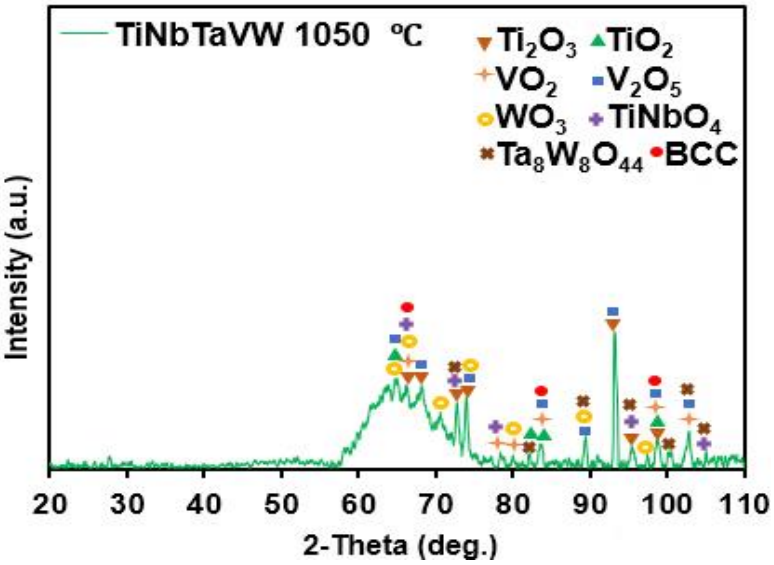

Figure 7.6: XRD pattern of identified oxides in TiNbTaVW at 1050°C.

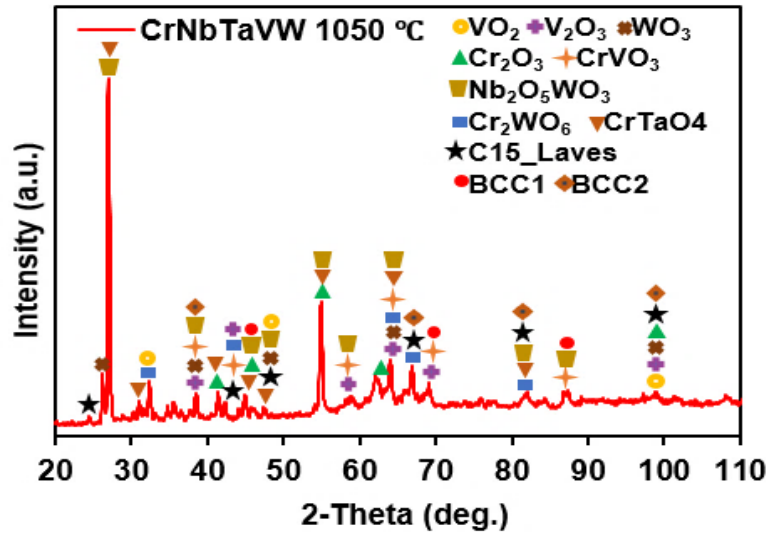

Figure 7.7: XRD pattern of identified oxides in CrNbTaVW at 1050°C.

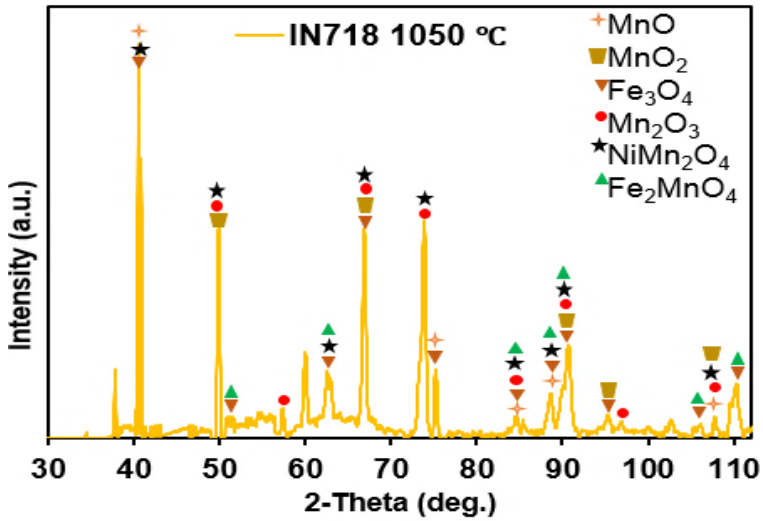

Figure 7.8: XRD pattern of identified oxides in IN718 at 1050°C.

7.2.2 Surface morphologies of oxidised TiNbTaVW, CrNbTaVW, and IN718

The SEM images of the surface morphologies of TiNbTaVW, CrNbTaVW and IN718 at 850°C and 1050°C after 15 hours are shown in Figures 7.9-7.13. A compact surface oxide layer containing spalled W-rich oxide particles (indicated by green arrows), cracks (blue arrows; 14.7±0.97 μm), and pores (red arrows; 4.9±0.39 μm) was observed for the TiNbTaVW RHEA at 850°C (Figure 7.9a and Appendix G). Viewing the surface scale layer under higher magnification reveals granular-shaped and rod-shaped oxides with sizes of 0.98±0.07 μm and 1.61±0.19 μm dispersed all over the surface (Figure 7.9b and Appendix G). The EDS compositions showed that the granular-shaped oxides are Ti-rich, while rod-

shaped oxides are mostly NbTaWV-rich (Appendix G). Some of the rod-shaped and granular-shaped oxides were attached to one another like a chain of networks.

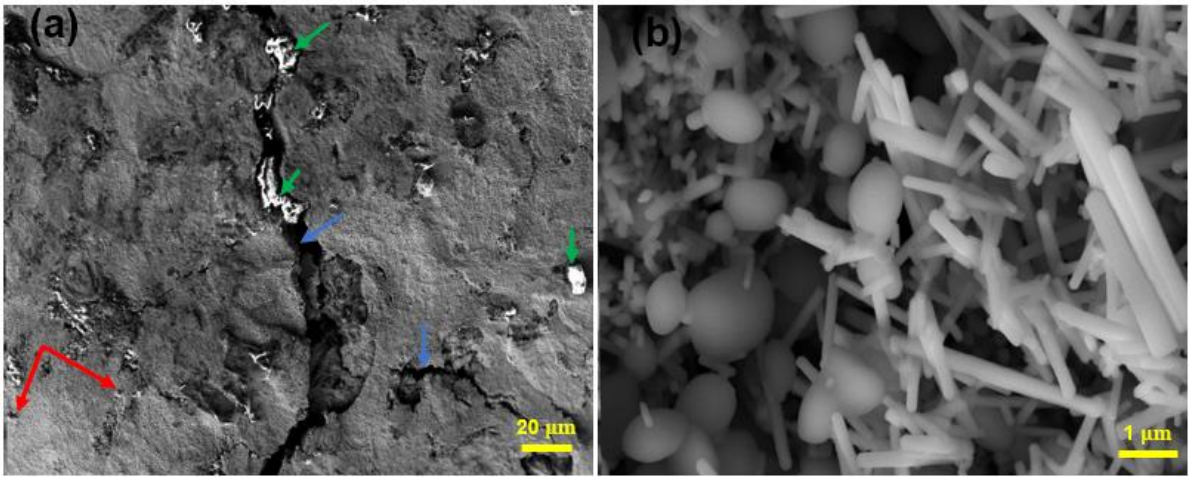

Figure 7.9: Surface morphology of TiNbTaVW RHEA showing cracks, pores, and spalled oxides at 850°C after 15 hours (a); Higher magnification of surface morphology of TiNbTaVW RHEA showing granular and rod-shaped oxides at 850°C after 15 hours (b).

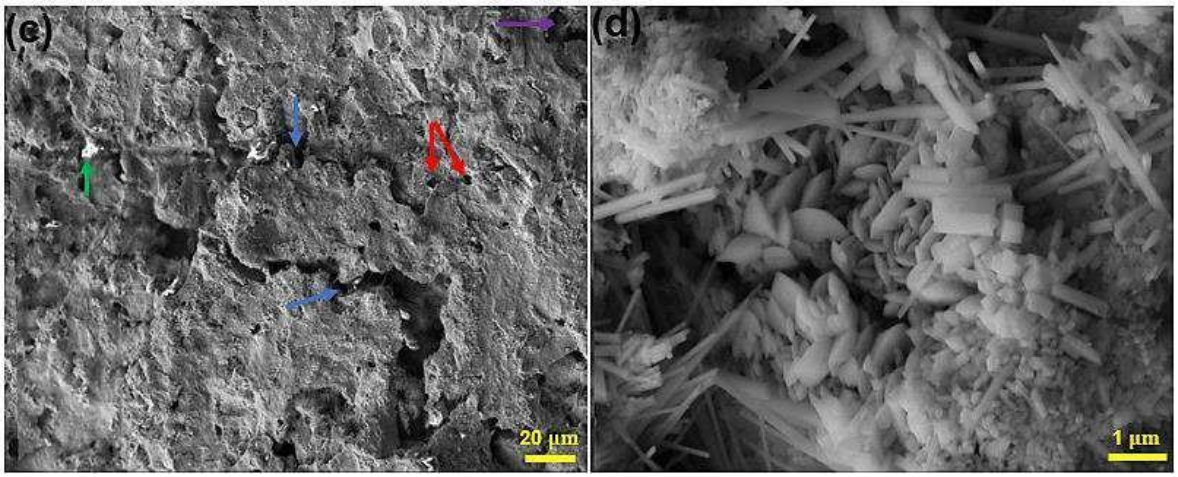

Figure 7.10: Surface morphology of CrNbTaVW RHEA showing cracks, voids, pores, and spalled oxides at 850°C after 15 hours (a); Higher magnification of surface morphology of CrNbTaVW RHEA showing granular and rod-shaped oxides at 850°C after 15 hours (b).

The SEM images of the surface scale layer of CrNbTaVW RHEA at 850°C after 15 hours are shown in Figure 7.10. At 850°C, the surface scale layer was spalled with cracks (blue arrows; 15.5±2.14 µm), pores (red arrows; 6.1±0.39 µm), and voids (purple arrow; 12.7±0.39 µm) (Figure 7.10a). Cr-rich spalled oxides (indicated by green arrow) were also found on the surface (Appendix H). Viewing the surface scale layer under higher magnification at 850°C also reveals granular-shaped (0.68±0.04 µm) and rod-shaped (1.24±0.11 µm) oxides that were dispersed all over the surface (Figure 7.10b). The EDS compositions showed that the granular-

shaped oxides are rich in Cr, while rod-shaped oxides are NbTaW-rich (Appendix H).

The SEM images of the surface scale layer of the IN718 alloy at 850°C after 15 hours are shown in Figure 7.11. The IN718 alloy surface scale layer consisted of a compact structure with no cracks, pores, or voids (Figure 7.11a). According to Jayaraj et al. (2018), the formation of a crack-free stable surface oxide layer, which protects the alloy from direct contact with oxygen and diffusion through the oxide layer, becomes the rate-controlling process for the oxidation reaction. Viewing the top surface oxides of the IN718 alloy at higher magnification revealed block-shaped (0.45±0.04 μm), rod-shaped (0.39±0.03 μm), round-shaped (white colour; 0.53±0.05 μm) and cloudy-shaped oxides (dark colour; 0.50±0.04 μm), as shown in Figure 7.11b. The block-shaped oxides are Fe-rich, rod-shaped oxides are FeMnNi-rich, round-shaped oxides (white) are TiFeSi-rich, and cloudy-shaped oxides (dark) are AlSi-rich (Appendix I).

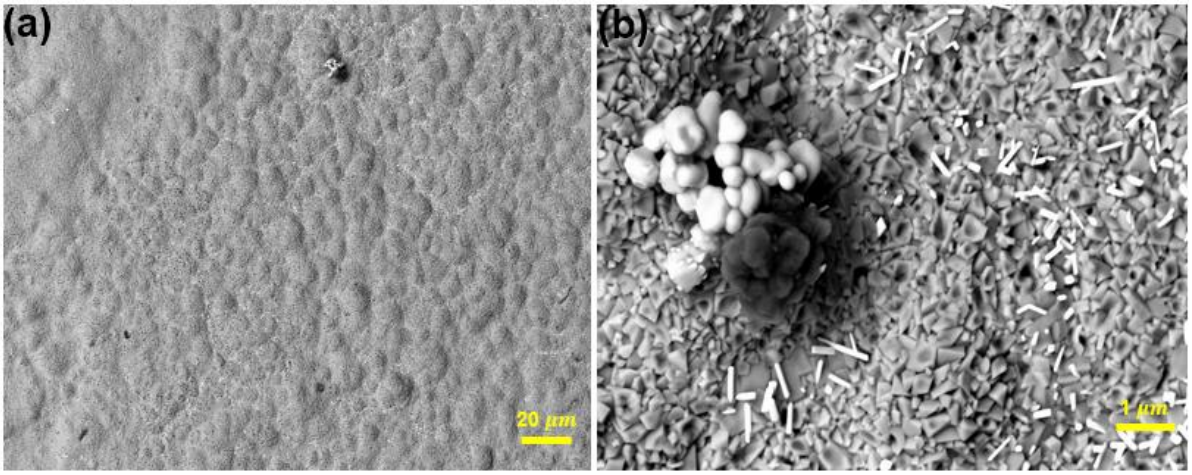

Figure 7.11: Surface morphology of IN718 alloy showing compact structure at 850°C after 15 hours (a); Higher magnification of surface morphology of IN718 alloy showing round-shaped, cloudy-shaped, rod-shaped and block-shaped oxides at 850°C after 15 hours (b).

The SEM images of the surface scale layer at 1050°C after 15 hours are shown in Figure 7.12. The surface scale layer of the TiNbTaVW is compact with a crack (blue arrow; 6.1±0.34 μm) and spalled Ti-rich oxides (indicated by green arrows), as shown in Figure 12a. Viewing the surface scale layer at higher magnification revealed granular-shaped and rod-shaped oxides with sizes of 1.47±0.13 μm and 1.83±0.23 μm that were dispersed all over the surface (Figure 12b). It was observed that the size of the granular-shaped and rod-shaped oxides was

somewhat larger than those observed at 850°C. The granular-shaped oxides are Ti-rich, while rod shaped oxides are mostly NbTaWTi-rich (Appendix G).

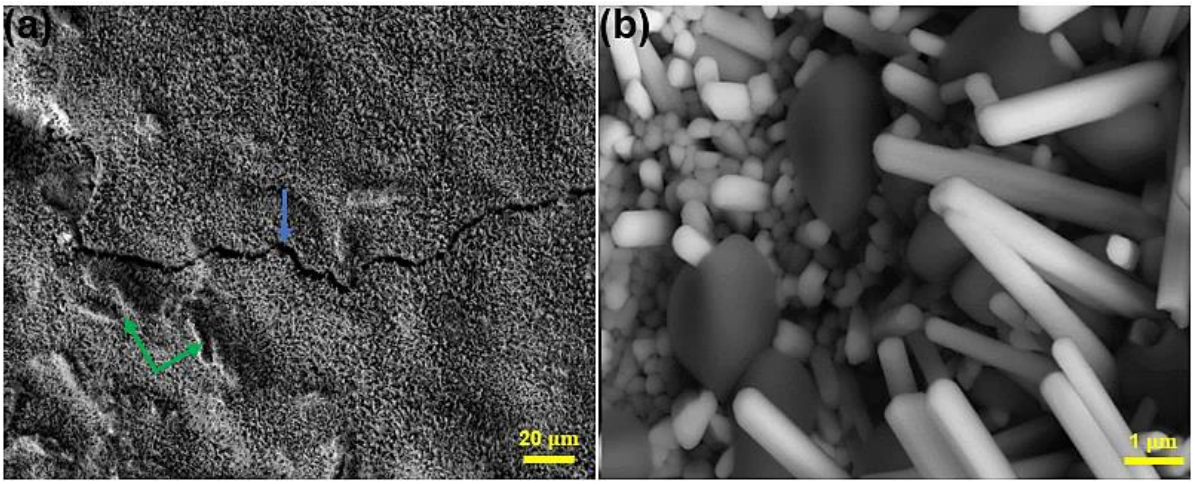

Figure 7.12: Surface morphology of TiNbTaVW RHEA showing crack and spalled oxides at 1050°C after 15 hours (a); Higher magnification of surface morphology of TiNbTaVW RHEA showing granular and rod-shaped oxides at 1050°C after 15 hours (b).

Figure 7.13a shows that the surface morphology of CrNbTaVW RHEA at 1050°C were spalled. Viewing the surface oxides at higher magnification also revealed granular-shaped (0.66±0.03 µm) and rod-shaped (2.73±0.21 µm) oxides that were dispersed all over the alloy surface (Figure 7.13b). However, the size of the rod-shaped oxides was somewhat larger than that observed at 850°C. Therefore, high temperatures have a major impact on the growth and nucleation of oxides (Figure 7.12b and Figure 7.13b). The EDS compositions at 1050°C showed that the granular-shaped oxides are rich in Cr, while rod-shaped oxides are rich in NbTaW (Appendix H). The IN718 surface scale layer comprises a more refined structure that is free of cracks, pores, or voids at 1050°C, as shown in Figure 7.14a. In Figure 7.14b, the surface oxide layer exhibited globular (0.35±0.02 µm) and block-shaped oxide (1.11±0.12 µm) structures that were mostly enriched in Fe (Appendix I).

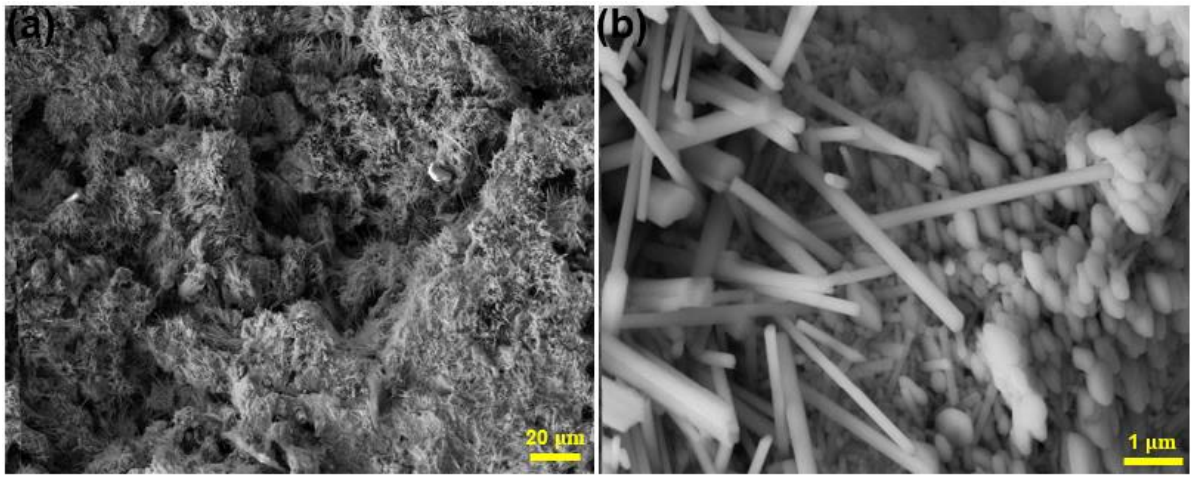

Figure 7.13: Surface morphology of CrNbTaVW RHEA showing spalled surface layer at 1050°C after 15 hours (a); Higher magnification of surface morphology of CrNbTaVW RHEA showing granular and rod-shaped oxides at 1050°C after 15 hours (b).

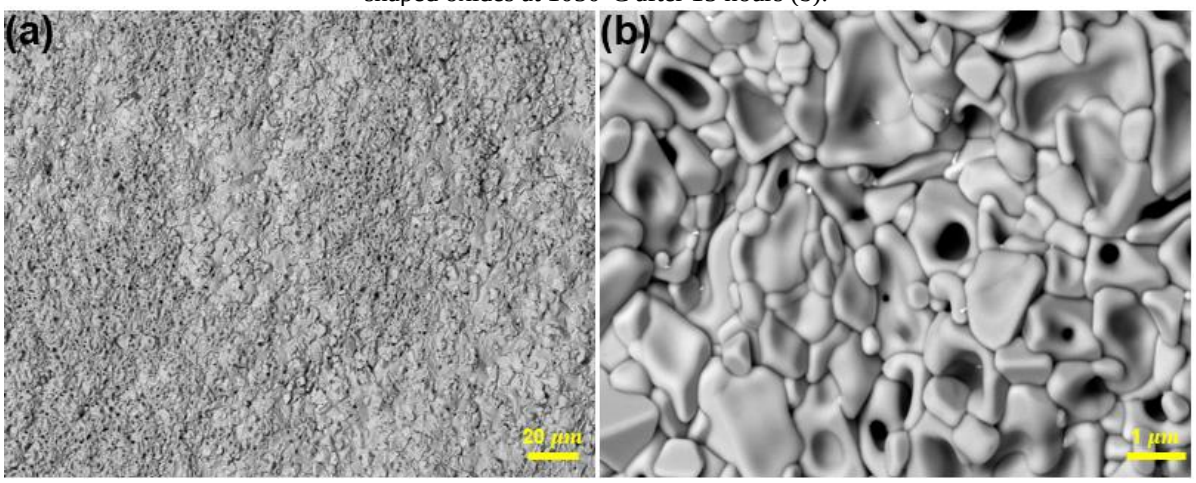

Figure 7.14: Surface morphology of IN718 alloy showing compact and refined structure at 1050°C after 15 hours (a); Higher magnification of surface morphology of IN718 alloy showing globular and block-shaped oxides at 1050°C after 15 hours (b).

7.2.3 Cross-section analysis of oxidised TiNbTaVW, CrNbTaVW and IN718

The SEM images of the cross-section morphologies of the oxidised TiNbTaVW, CrNbTaVW and IN718 at 850°C and 1050°C after 15 hours are shown in Figures 7.15-7.17. The cross-section of the oxidised TiNbTaVW after 15 hours at 850°C is shown in Figure 7.15. A 368±1.1 µm thick oxidised layer with a dark contrast and an internal oxidation region was observed for the TiNbTaVW RHEA at 850°C (Figure 7.15a). The thick oxide layer contained cracks with a thickness of 22±1.1 µm spread throughout the oxide layer. The EDS compositions at 850°C showed mostly NbTaWV-rich oxides for the thick oxide layer and VTiNb-rich oxides for the internal oxidation zone (Appendix J). A 375±3.7 µm thick oxidised

layer with a dark contrast and an internal oxidation region was also observed for the TiNbTaVW RHEA at 1050°C, as shown in Figure 7.15b. Cracks of 15.7±1.1 µm was also observed in the thick oxide layer, as shown in Figure 7.15b. The EDS compositions of the thick oxide layer at 1050°C contained mainly VNbWTa-rich oxides and TiVNbW-rich oxides for the internal oxidation zone (Appendix J). It was observed that as the oxidation temperature increased from 850°C to 1050°C, the thickness of the oxide layer increased from 368 µm to 375 µm. The cracks formed at 850°C and 1050°C limited the formation of a reliable diffusion barrier because cracks allow the ingress of oxygen to the metallic substrate, therefore increasing the oxidation rate of the metallic substrate.

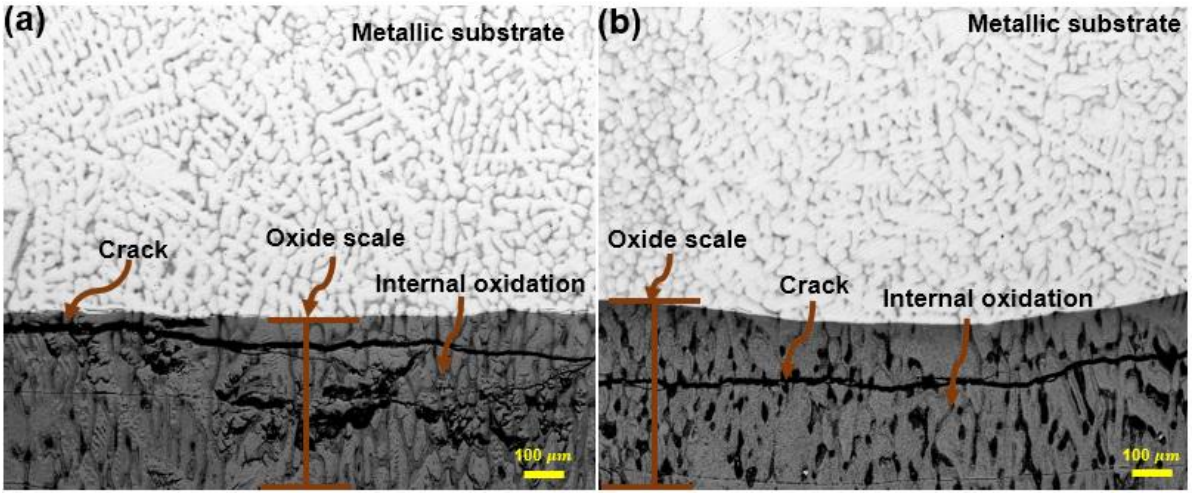

Figure 7.15: Cross-sectional morphologies of the TiNbTaVW RHEA showing cracks and oxide scales at 850°C and 1050°C after 15 hours (a-b).

SEM images of the cross-section morphologies of CrNbTaVW RHEA after oxidation at 850°C and 1050°C for 15 hours are shown in Figure 7.16. At 850°C, a 260±7.8 µm thick oxidised layer with a grey contrast and a 29±5.5 µm thick internal oxidation zone was observed (Figure 7.16a). The thick oxide layer contained tiny cracks that were connected to voids that are 31±1.7 µm thick. It is believed that the cracks grew to form the observed voids. The EDS compositions at 850°C/15 hours showed mostly WNbTa-rich oxides for both the thick oxide layer and internal oxidation zone (Appendix K). At 1050°C, a 603±9.1 µm thick oxidized layer with a grey contrast was observed (Figure 7.16b). Cracks and voids of 8.5±0.81 µm and 35±2.71 µm was also observed in the thick oxide layer (Figure 7.16b). The EDS compositions of the thick oxide layer at 1050°C/15 h showed majorly WNbTaCr-rich oxides (Appendix K). As the oxidation temperature increased from 850°C to 1050°C, the thickness

of the oxide layer increased from 260 μm to 603 μm. Oxide layer tends to serve as a reliable diffusion barrier that effectively isolates the substrate from oxygen and therefore the oxidation rate of the metallic substrate is decreased (Gorr et al., 2017). The oxide layers are porous with voids and cracks at 850°C and 1050°C that limit the formation of a reliable diffusion barrier. The voids and cracks allow the ingress of oxygen into the metallic substrate and therefore the oxidation rate of the metallic substrate is increased.

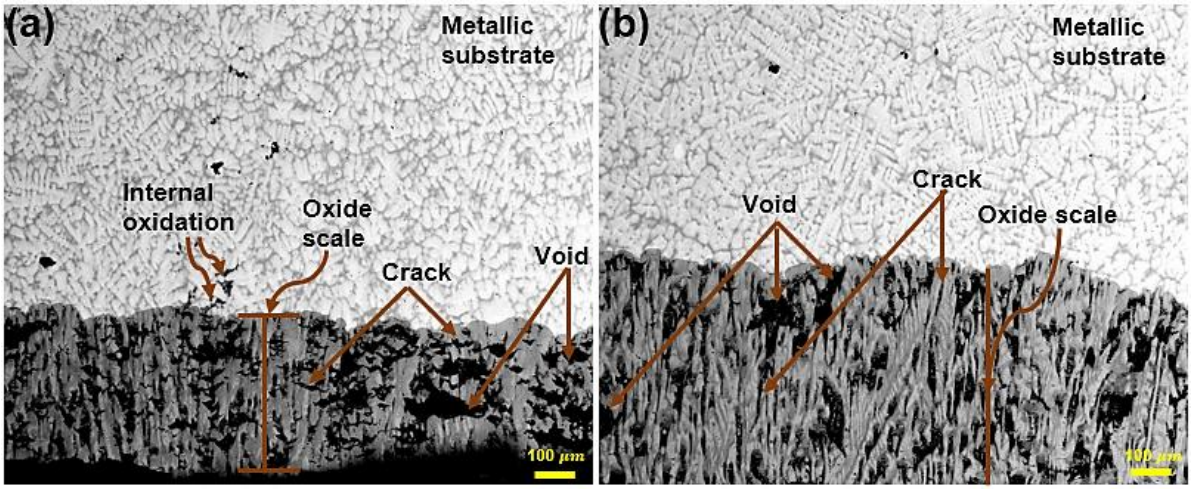

Figure 7.16: Cross-sectional morphologies of the CrNbTaVW RHEA showing cracks, voids, and oxide scales at 850°C and 1050°C after 15 hours (a-b).

SEM images of the cross-section morphologies of the IN718 alloy after oxidation at 850°C and 1050°C for 15 hours are shown in Figure 7.17. The IN718 alloy displayed two layers at 850°C and 1050°C, which were defined as the outer oxide layer and internal oxide layer, as shown in Figures 7.17a and 7.17b. At 850°C after 15 hours, a 38.6±1.1 μm thick outer oxide layer and 46.1±1.4 μm thick internal oxide layer was observed in Figure 7.17a. The EDS compositions of the outer oxide layer at 850°C after 15 hours was mostly FeNi-rich oxide phase, while the internal oxide layer consisted of mostly FeNi-rich oxides (Appendix L). The outer oxide layer had a thickness of 15.34±0.6 μm, while the internal oxide layer had a thickness of 66.8±3.3 μm at 1050°C, as shown in Figure 7.17b. EDS compositions of the outer oxide layer and internal oxide layer at 1050°C after 15 hours comprised mostly FeNi-rich oxide (Appendix L). It was observed that the internal oxide layer had more thickness than the outer oxide layer at 850°C and 1050°C. The IN718 alloy exhibited a lower oxidation rate at both temperatures because the outer and internal oxide layers served as effective diffusion

barriers.

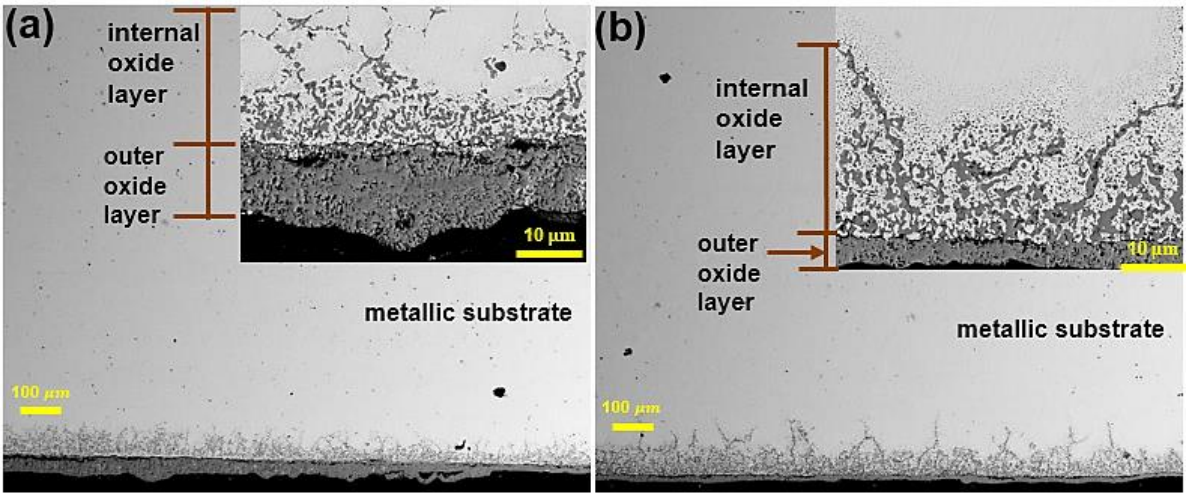

Figure 7.17: Cross-sectional morphologies of IN718 alloy showing oxide scales at 850°C and 1050°C after 15hours (a-b).

7.3. Discussion

At 850°C and 1050°C, mass loss was observed in the curve of TiNbTaVW and CrNbTaVW which is attributed to oxide layer spallation. This occurs when the oxide is unable to form a continuous passive layer and retard further oxidation of the substrate alloy (Senkov et al., 2012). It can also be attributed to the accumulation of cracks, pores, and voids that led to the ingress of oxygen. For the IN718 alloy, stationary trend was observed in the curves that indicates a crack and pore free stable surface oxide film forms, which protects the alloy from direct contact with oxygen. The oxidation behaviour of IN718 at 850°C and 1050°C after 15 hours was superior to that of TiNbTaVW and CrNbTaVW because the surface oxides form a continuous passive layer, and therefore, a controlled diffusion mechanism was observed. This occurs when the surface oxide volume is equal to or greater than the volume of the alloy involved in the reaction, and the oxide is well attached to the matrix (Senkov et al., 2012). During the initial stages of oxidation at both temperatures, oxygen was dissolved in TiNbTaVW and CrNbTaVW, leading to the formation of simple oxides such as TiO_2, Cr_2O_3, VO_2, V_2O_3, Ta_2O_5, WO_3, Ti_2O_3, and V_2O_5.

The standard Gibbs free energy (oG_f: kJ mol^{-1}) of simple oxides observed in the TiNbTaVW RHEA have been reported (Su et al., 2023; Hunter et al., 2019; Yan et al., 2022; Zhang et al., 2023; Zheng et al., 2013). At 850°C, the stability and formation of favourable oxides followed

the order: TiO_2 (-743) > V_2O_3 (-639) > Ta_2O_5 (-624) > VO_2 (-521) >WO_3 (-384). At 1050°C, the order was: Ti_2O_3 (-771) > TiO_2 (-710) > VO_2 (-467) > V_2O_5 (-408) > WO_3 (-346). At 850°C and 1050°C, WO3 had the largest negative Gibbs free energy, making it the least stable simple oxide formed on the surface of the TiNbTaVW RHEA after 15 hours.

For the CrNbTaVW RHEA, stability and formation of the simple oxides at 850°C using the Gibbs free energy (^oG_f: kJ mol^{-1}) values followed the following order: V_2O_3 (-639) > Cr_2O_3 (-555) > VO_2 (-521) > WO_3 (-384) (Su et al., 2023; Hunter et al., 2019). At 1050°C, the stability and the formation of favorable oxides followed the order: V_2O_3 (-602) > Cr_2O_3 (-527) > VO_2 (-467) > WO_3 (-346) (Su et al., 2023; Hunter et al., 2019). The WO_3 had the largest ^oG values, making it the least stable simple oxide formed on the surface of the CrNbTaVW RHEA at 850°C and 1050°C.

As oxidation proceeds, the simple oxides continuously reacted and combined into complex oxides with increasing temperature and oxidation time. The possible reactions involved in the formation of the complex oxides at 850°C and 1050°C for TiNbTaVW and CrNbTaVW are represented in Equations (6.1)–(6.10).

$$8WO_3(s) + 4Ta_2O_5(s) = Ta_8W_8O_{44}(s) \quad (6.1)$$

$$TiO_2(s) + VO_2(s) = TiVO_4(s) \quad (6.2)$$

$$TiO_2(s) + NbO_2(s) = TiNbO_4(s) \quad (6.3)$$

$$TiO_2(s) + TaO_2(s) = TiTaO_4(s) \quad (6.4)$$

$$2TaO_2(s) + VO_2(s) = Ta_2VO_6(s) \quad (6.5)$$

$$CrO\ (s) + VO_2\ (s) = CrVO_3(s) \quad (6.6)$$

$$Cr_2O_3\ (s) + WO_3(s) = Cr_2WO_6(s) \quad (6.7)$$

$$Nb_2O_5\ (s) + WO_3(s) = Nb_2O_5.WO_3(s) \quad (6.8)$$

$$1/2Cr_2O_3\ (s) + 1/2Ta_2O_5\ (s) = CrTaO_4(s) \quad (6.9)$$

$$1/2Cr_2O_3\ (s) + 1/2Nb_2O_5\ (s) = CrNbO_4(s) \quad (6.10)$$

The formation of $TiTaO_4$ can prevent the influx of Ti to the outer interface and reduce the oxidation kinetics (Schellert et al., 2023). It was observed that $TiTaO_4$ formed in the TiNbTaVW RHEA at 850°C and possibly serving as a barrier for outward Ti diffusion. The high diffusion coefficient of Cr facilitated its rapid incorporation into Cr-containing RHEA

oxide layer (Zhang et al., 2018), enabling the synthesis of VO_2, Ta_2O_5, and Nb_2O_5 into $CrVO_3$, $CrTaO_4$, and Nb_2O_5. Also, Cr_2O_3 reacted with the less stable WO_3 to synthesise Cr_2WO_6 through a solid–state reaction. Oxide scales of Nb and Ta have a strong bond to the base metals that get weakened at higher temperatures and could form non-protective oxides (Nb_2O_5 and Ta_2O_5) (Müller et al., 2019). Ta_2O_5 was observed on the surface of the TiNbTaVW RHEA at 850°C, suggesting it may have contributed to the cracks, pores, and voids that allowed rapid oxygen ingress and increased the oxidation rate.

WO_3 is easy to sublimate due to its lower sublimation temperature and can react with Ta_2O_5 and Nb_2O_5 to form complex oxides ($Ta_8W_9O_{47}$ and $Nb_8W_9O_{47}$) (Yan et al., 2022). The formed $Ta_8W_9O_{47}$ oxide during the oxidation of WTaNbTiAl was ineffective in protecting the alloy substrate (Yan et al., 2022). However, $Ta_8W_8O_{44}$, rather than $Ta_8W_9O_{47}$, was found in the TiNbTaVW RHEA. The protectivity of $Ta_8W_8O_{44}$ oxide cannot yet be ascertained. Similarly, WO_3 reacts with Nb_2O_5 to form $Nb_2O_5.WO_3$. The effectiveness of $CrVO_3$ and $Nb_2O_5.WO_3$ in providing oxidation resistance for the CrNbTaVW RHEA remains unclear.

Oxides such as VO_2 and V_2O_5 are volatile at high temperatures and can initiate pores and spallation (Lo et al., 2018; Xiao et al., 2019; Yurchenko et al., 2018). VO_2 and V_2O_5 oxides were found in the $AlNbTiVZr_{0.25}$ RHEA, causing pores, cracks, and spallation, which serve as preferential sites for the rapid ingress of oxygen toward the exposed metal, thereby causing severe oxidation (Xiao et al., 2019; Yurchenko et al., 2018). VO_2 and V_2O_5 were also observed at 850°C and 1050°C after 15 hours in TiNbTaVW and CrNbTaVW, which could hinder the formation of protective oxides and facilitate the nucleation of pores and cracks. An oxide layer with $CrTaO_4$ had been reported to effectively retard oxygen diffusion and provide protection against oxidation at high temperatures (Du et al., 2022; Liu et al., 2010; Lo et al., 2019; Xiao et al., 2019).

At 1200°C, a protective $CrTaO_4$ oxide layer acted as a barrier to cation outward diffusion and reduced oxygen inward diffusion in the TaMoCrTiAl RHEA (Schellert et al., 2023). Similarly, a $CrTaO_4$ oxide layer was observed in the W containing MoTaTiCr RHEAs that retarded oxygen diffusion and provided protection against oxidation at 1000°C (Moghaddam et al., 2022). Oxides of Cr_2WO_6 and Cr_2O_3 formed a protective thin layer on the W-Cr-Pd alloys (Kafri et al., 2018). In the W-Cr alloys by Hou et al. (2019), oxide scale of Cr_2WO_6 is

poor and does not offer protection against oxidation. However, the Cr_2O_3 scale was sufficient to offer a better protective scale for the W-Cr alloys. At a particular stage during the oxidation of CrNbTaVW RHEA at 1050°C after 15 hours, oxides such as $CrTaO_4$, $CrNbO_4$, and Cr_2O_3 would have formed a barrier for both inward diffusion of oxygen and outward diffusion. These would have prevented more pores, cracks, and total degradation of the CrNbTaVW RHEA. The oxygen ions diffusion is hindered to some extent by the Cr_2O_3 which slowed down the oxidation rate of the oxidised CrNbTaVW RHEA.

The oxide layer's adhesion to the metallic substrate is determined by the thickness of the scale and its growth rate, the stress state, the interfacial energy, and the elastic properties of the oxide (Jahangiri et al., 2023). In a typical cyclic oxidation process, the oxide scale thickens through diffusional growth, and as the sample cools, the oxide spalls, reducing the oxide thickness to bare metal (Barrett, 1988). As the sample is returned to the furnace for further oxidation, oxide scale growth resumes, but the growth rate corresponds to the reduced scale thickness. According to Jeong et al. (2018), the metal substrate contracts faster than the oxide layer as the oxidised sample cools down, causing compressive stresses and the formation of shear cracks within the oxide layer. The oxygen enrichment on an alloy's surface is strongly related to oxide cracking because oxygen dissolution increases lattice constants, leading to the volumetric expansion of the oxides (Sheikh et al., 2018). The volumetric expansion mismatch causes stresses within the oxides, which increase as the oxides grow and are later released by cracking and spallation of the oxides from the base alloy. Two internal stresses in the oxide scale cause spalling: growth stress, which develops during the oxidation process, and thermal stress, which arises from temperature changes (Latu-Romain et al., 2018; Zheng et al., 2011).

At 850°C and 1050°C after 15 hours, cracks, pores, and oxide layer spallation appeared in the TiNbTaVW and CrNbTaVW RHEAs, which can be attributed to both the growth stress during oxidation and the thermal stress during cooling to room temperature of oxidised samples. The growth stress is formed mainly by the volume difference between the oxide and the metal forming the oxide and can be expressed by the Pilling-Bedworth ratio (PBR) in Equation (6.11) (Mevrel, 1986).

$$\text{PBR} = \frac{\text{volume per metal ion in oxide}}{\text{volume per metal atom in metal}} \quad (6.11)$$

The oxide scale is discontinuous and porous if PBR<1 (Cao et al., 2019). For PBR>2, the internal stress between oxides and matrix is high, which easily leads to the formation of pores, cracks and oxide layer spallation around oxides (Cao et al., 2019; Moghaddam et al., 2022). The formed pores and cracks will merge and cause a separation between the oxide scale and the metallic substrate. Using Equation (6.11), the PBR for TiO_2, VO_2, V_2O_3, Ta_2O_5, WO_3, Ti_2O_3, and V_2O_5 was 1.77, 2.17, 1.84, 2.48, 3.39, 1.50, and 3.24. The internal stress between VO_2, Ta_2O_5, WO_3, V_2O_5 and the TiNbTaVW substrate was high, leading to the formation of pores, cracks, and spallation of the oxide layer.

For the CrNbTaVW, the PBR for VO_2, V_2O_3, WO_3, and Cr_2O_3 was 2.17, 1.84, 3.39, and 2.02. The internal stress between VO_2, WO_3, and Cr_2O_3 and CrNbTaVW substrate was high, leading to the formation of pores, cracks and spallation at 850°C and 1050°C. The growth strain (ε) induces a change in volume that is expressed in Equation (6.12) (Panicaud et al., 2006).

$$\varepsilon = \sqrt[3]{\text{PBR}} - 1 \quad (6.12)$$

The ε value was calculated by substituting the PBR values for VO_2, Ta_2O_5, WO_3, Cr_2O_3 and V_2O_5 in Equation (6.12). If PBR> 1, a compressive stress develops in the oxides scale, while a tensile stress develops in the scale when PBR< 1. Since the PBR for the observed oxides in TiNbTaVW and CrNbTaVW is greater than 1, it is assumed that a compressive stress was produced on the oxide scales. The calculated ε values for VO_2, Ta_2O_5, WO_3, and V_2O_5 in TiNbTaVW were 0.296, 0.353, 0.503, and 0.481. The calculated ε values for VO_2, WO_3, and Cr_2O_3 in CrNbTaVW were 0.296, 0.503, and 0.264.

The growth stress (σ_G) can be calculated based on growth strain in Equation (6.13) (Zheng et al., 2011).

$$\sigma_G = \varepsilon E_{oxides} \quad (6.13)$$

Where E_{oxides} is the Young's modulus of VO_2 (140 GPa) (Song & White, 2016), Ta_2O_5 (217 GPa) (Weyant et al., 2005), WO_3 (300 GPa) (Zhu et al., 2008), Cr_2O_3 (260 GPa) (Zheng et al., 2011), and V_2O_5 (286 GPa) (Jachmann & Hucho, 2005) oxides. By substituting E_{oxides} and ε values into Equation (6.13), the σ_G for TiNbTaVW was calculated to be 41.4 GPa, 76.6

GPa, 150.8 GPa, and 105.7 GPa for VO_2, Ta_2O_5, WO_3, and V_2O_5, respectively. The σ_G in VO_2 was less than that of Ta_2O_5, WO_3, and V_2O_5. Since the σ_G of VO_2 was lower, only decohesion was initiated on the oxide scale, but cracks, pores, and spalling were initiated by Ta_2O_5, WO_3, and V_2O_5.

The σ_G for CrNbTaVW was calculated to be 41.4 GPa, 150.8 GPa, and 68.7 GPa for VO_2, WO_3, and Cr_2O_3. The σ_G in VO_2 and Cr_2O_3 is less than that of WO_3. It can be assumed that decohesion was only initiated on the oxide scale by VO_2 and Cr_2O_3, while cracks, pores, and spalling was initiated by WO_3. As mentioned earlier, thermal stress (σ_T) occurs during cooling to room temperature and is formed due to different thermal expansions between the oxide scales and the TiNbTaVW and CrNbTaVW. The σ_T is expressed in Equation (6.14) (Zheng et al., 2011).

$$\sigma_T = E_{oxides} (\alpha_{alloy} - \alpha_{oxides}) \Delta T \quad (6.14)$$

Where α_{alloy} and α_{oxides} are the thermal expansion coefficients of TiNbTaVW and CrNbTaVW and the oxides, respectively. ΔT is the difference between the oxidation temperature and room temperature during cooling.

The $\alpha_{TiNbTaVW}$ was calculated to be 10.781×10^{-6} K^{-1} using the rule of mixture. While α_{oxides} for VO_2, Ta_2O_5, WO_3, and V_2O_5 were 2.1×10^{-6} K^{-1} (Song & White, 2016), 3.0×10^{-6} K^{-1} (Weyant et al., 2005), 8.9×10^{-6} K^{-1} (Besozzi et al., 2019), and 7.0×10^{-6} K^{-1} (Jachmann & Hucho, 2005). The σ_T is assumed to be generated mainly by VO_2, Ta_2O_5, WO_3, V_2O_5 at 850 °C and by VO_2, WO_3, and V_2O_5 at 1050 °C. The σ_T generated by VO_2, Ta_2O_5, WO_3, V_2O_5 at 850 °C was estimated to be 1.003 GPa, 1.393 GPa, 0.466 GPa, and 0.686 GPa. At 1050 °C, σ_T generated by VO_2, WO_3, and V_2O_5 was 1.246 GPa, 0.578 GPa, and 0.853 GPa. From the results, σ_T is lower than σ_G, and the thermal expansion coefficient of the alloy was larger than that of the oxides. Hence, the σ_T in the scale should be compressive, which is the same as growth stress (Zheng et al., 2011).

The $\alpha_{CrNbTaVW}$ was calculated to be 10.698×10^{-6} K^{-1} using the rule of mixture. While α_{oxides} for VO_2, WO_3, and Cr_2O_3 was 2.1×10^{-6} K^{-1} (Song & White, 2016), 8.9×10^{-6} K^{-1} (Besozzi et al., 2019), and 9.6×10^{-6} K^{-1} (Zheng et al., 2011). The σ_T is assumed to be generated mainly by VO_2, WO_3, and Cr_2O_3 at 850 °C and 1050 °C. The σ_T generated by VO_2, WO_3, and

Cr_2O_3 at 850 °C was estimated to be 0.993 GPa, 0.445 GPa, and 0.199 GPa. At 1050 °C, σ_T generated by VO_2, WO_3, and Cr_2O_3 was 1.234 GPa, 0.553 GPa, and 0.248 GPa. From the results, it can be observed that σ_T is lower than σ_G and the thermal expansion coefficient of the alloy is larger than that of the oxides. Hence, the σ_T in the scale should be compressive, which is the same as growth stress. The failure of protective oxide scales could be due to the mismatch in volume expansion between VO_2, WO_3, and Cr_2O_3 oxides, and the CrNbTaVW substrates, which led to the build-up of thermal stress and growth stress.

The summary of the oxidation mechanisms of TiNbTaVW, CrNbTaVW, and IN718 at 850°C and 1050°C for 15 hours is given in Figures 7.18-7.20. During the initial stage of oxidation at 850°C and 1050°C, oxygen diffused inside the dendrite and the interdendrite regions of the TiNbTaVW. In the CrNbTaVW, oxygen diffused internally through the BCC1, BCC2 and $Cr(VNb)_2$ Laves. The oxygen reacted with elements that comprise the TiNbTaVW and CrNbTaVW and forms simple and complex oxides on the surface and cross-sectional morphologies. Some of the formed oxide scales might not be protective due to the mismatch in volume expansion between the oxides and RHEA's substrates. The mismatch will eventually generate two internal stresses (growth stress and thermal stress).

During cooling, spallation, pores, and cracks emerge due to thermal stress caused by the different thermal expansion coefficients of the oxides and RHEA's metallic substrates (Figure 7.18a and Figure 7.18b; Figure 7.19a and Figure 7.19b). Growth stress due to the micro-inhomogeneity of the oxide species is formed, which was eventually released via pores and cracks (Figure 7.18a and Figure 7.18b; Figure 7.19a and Figure 7.19b). The observed pores and cracks served as fast migration channels for oxygen into the TiNbTaVW and CrNbTaVW substrates and eventually increased the oxidation rate. Therefore, the major factors influencing the pores, cracks, voids and spallation observed in the TiNbTaVW and CrNbTaVW at 850°C and 1050°C after 15 hours is growth stress and thermal stress.

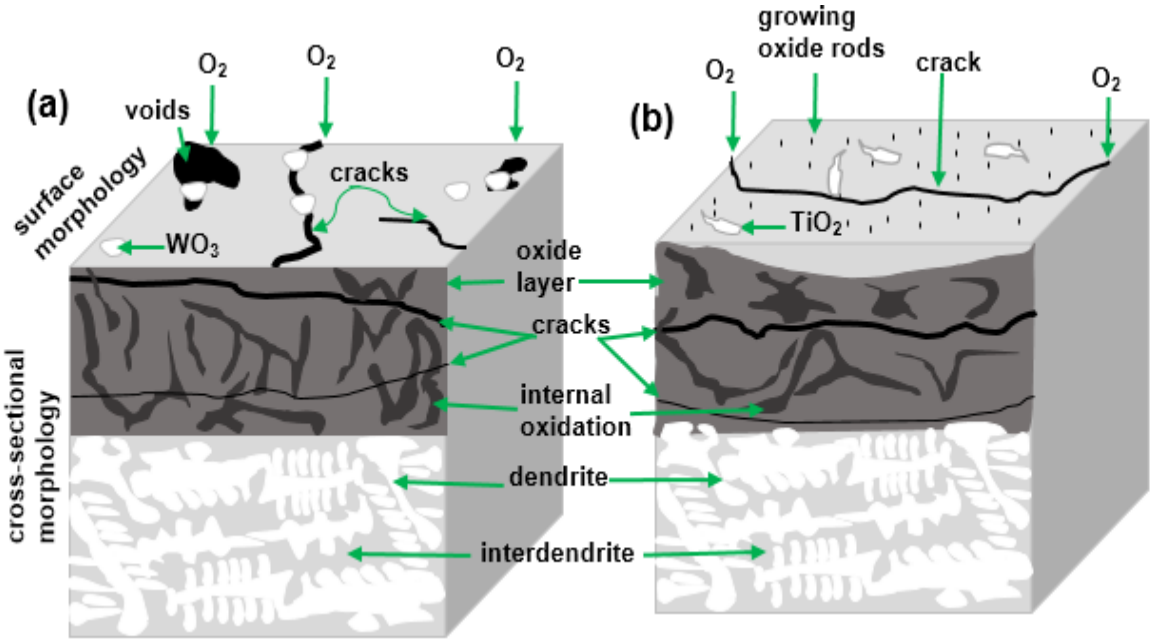

Figure 7.18: Schematic diagram of the oxidation mechanism of TiNbTaVW RHEA at 850°C and 1050°C after 15 hours (a-b).

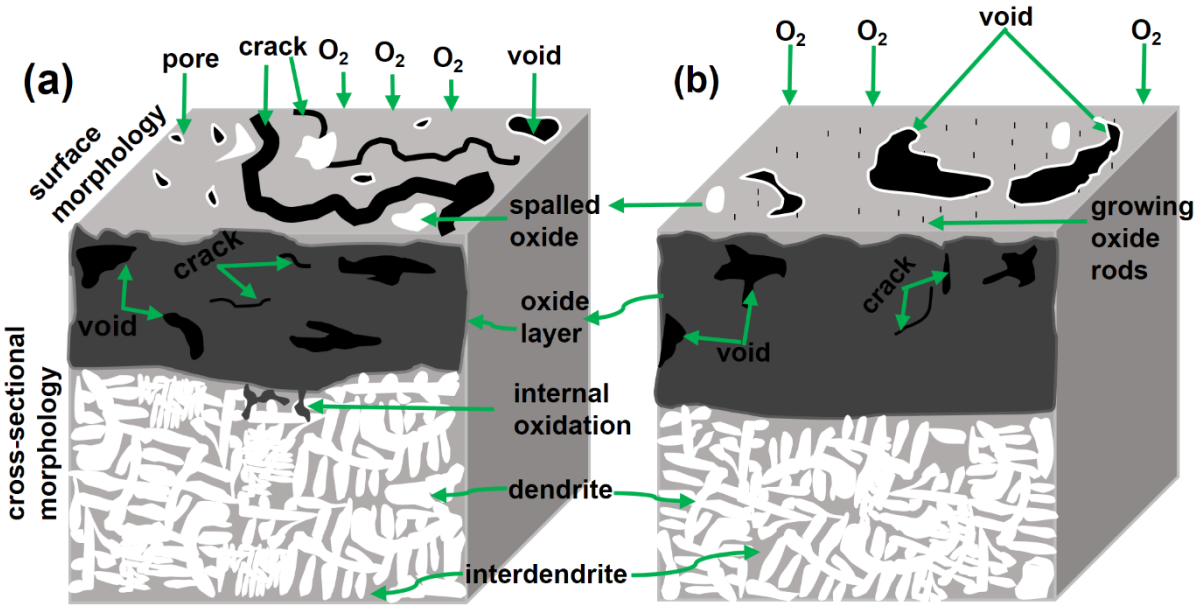

Figure 7.19: Schematic diagram of the oxidation mechanism of CrNbTaVW RHEA at 850°C and 1050°C after 15 hours (a-b).

Oxygen diffuses into the IN718 alloy at 850°C (Figure 7.20a) and 1050°C (Figure 7.20b), leading to the growth of protective oxides such as Al_2O_3, Fe_3O_4, and TiO_2. Al_2O_3 layer acts as a diffusion barrier against oxygen ingress into the alloy, thereby improving the alloy's performance against high-temperature oxidation (Abbaszadeh et al., 2020). TiO_2 is a thermodynamically stable oxide that forms an adherent layer, providing good oxidation

resistance and resulting in lower mass gains (Jain et al., 2019; Yan et al., 2022; Wang et al., 2023). Fe_3O_4 contributes to high oxidation resistance by inhibiting the migration of iron cations within the oxide scale. By hindering Fe migration, the concentration of iron cations in the scale is reduced, which slows the oxidation rate of the alloy (Liu et al., 2019). Furthermore, Fe_3O_4 inhibits oxygen diffusion, thereby protecting the matrix and further lowering the oxidation rate (Ji et al., 2022). The Al_2O_3, Fe_3O_4, and TiO_2 inhibit the formation of pores, cracks, and spallation that could serve as rapid migration channels for oxygen on the surface and cross-sectional layers of IN718, thereby reducing the oxidation rate (Figure 7.20).

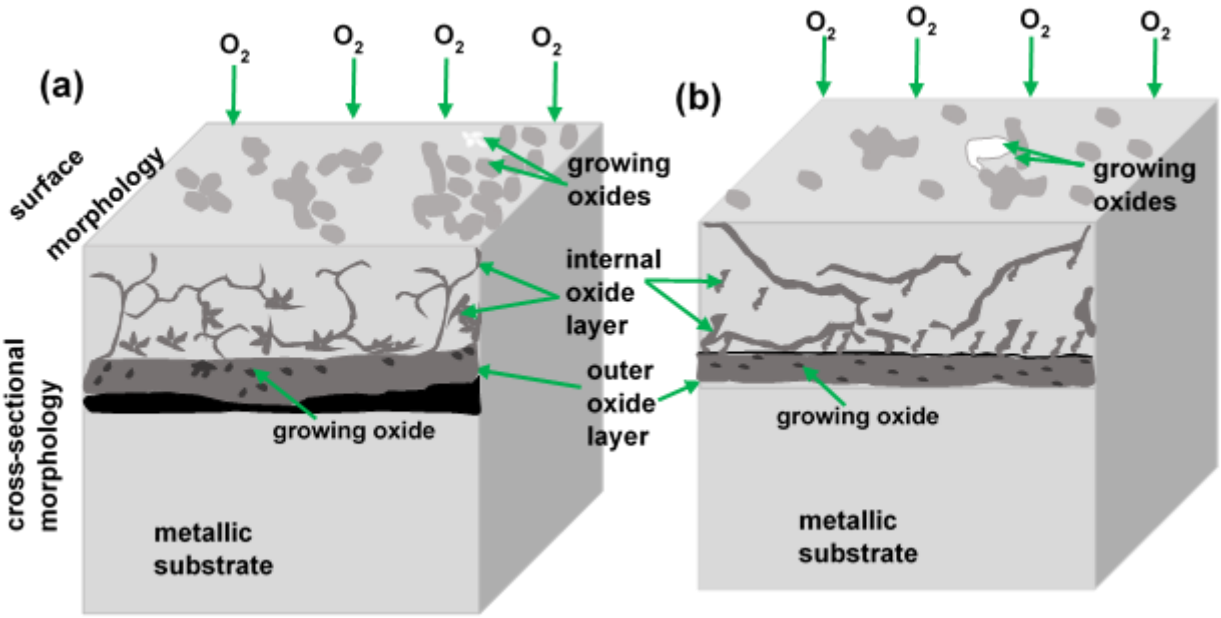

Figure 7.20: Schematic diagram of the oxidation mechanism of IN718 alloy at 850°C and 1050°C after 15 hours (a-b).

7.4 Summary

- The IN718 alloy had a lower mass gain of 4.41 mg/cm^2 and 10.84 mg/cm^2 at 850°C and 1050°C after 15 hours. The TiNbTaVW RHEA exhibited a mass loss of -23.58 mg/cm^2 and -45.92 mg/cm^2 at 850°C and 1050°C after 15 hours. The CrNbTaVW RHEA exhibited a mass loss of -25.17 mg/cm^2 and -35.91 mg/cm^2 at 850°C and 1050°C after 15 hours. Therefore, the IN718 alloy has better oxidation resistance than the TiNbTaVW and CrNbTaVW.
- It was found that the surface scale layer of TiNbTaVW and CrNbTaVW at 850°C and

1050°C after 15 hours comprise granular-shaped and rod-shaped oxides. The size of rod-shaped oxides becomes larger as temperature increased to 1050 °C. The surface scale layer of IN718 at 850°C after 15 hours comprise block-shaped, rod-shaped, round-shaped, and cloudy-shaped oxides. While at 1050°C after 15 hours, globular and block-shaped oxides were observed.

- The cross-sectional morphology result showed that a 368±1.1 μm thick oxidised and internal oxidation region were observed for the TiNbTaVW RHEA at 850°C. A 260±7.8 μm thick oxidised layer and a 29±5.5 μm thick internal oxidation zone was observed for the CrNbTaVW RHEA. A 375±3.7 μm thick oxidised layer and an internal oxidation region were also observed for the TiNbTaVW RHEA at 1050°C. At 1050°C, a 603±9.1 μm thick oxidised layer was observed for the CrNbTaVW RHEA.
- The IN718 alloy displayed two layers at 850°C, which were defined as the outer oxide layer (38.6±1.1 μm) and internal oxide layer (46.1±1.4 μm). At 1050°C, outer oxide layer had a thickness of 15.34±0.6 μm, while the internal oxide layer had a thickness of 66.8±3.3 μm.
- The oxidation mechanisms of the TiNbTaVW and CrNbTaVW at 850°C and 1050°C showed that the growth stress during oxidation and the thermal stress during cooling to room temperature of oxidised samples contributed to pores, voids, cracks, and oxide layer spallation. The oxidation mechanism of IN718 at 850°C and 1050°C showed that protective oxides such as Al_2O_3, Fe_3O_4, and TiO_2 inhibit the formation of pores and cracks that could act as migration channels for oxygen on the surface and cross-sectional layers, thereby reducing the oxidation rate.

Chapter 8

This chapter presents the experimental results addressing the sixth research objective. The influence of high temperatures and strain rate on the flow behaviour of TiNbTaVW RHEA and IN718 alloy was discussed, while the CrNbTaVW was not reported due to disintegration during loading and deformation. The influence of high temperatures and strain rate on the microstructural evolution of the TiNbTaVW RHEA and IN718 alloy were discussed. The compressive strength is also discussed. Lastly, the findings of the experimental results were summarised.

8.1 Analysis of flow stress of hot deformed TiNbTaVW and IN718

The stress-strain curves of the TiNbTaVW and IN718 obtained at 950°C to 1050°C and a strain rate of 10^{-3} s^{-1} are shown in Figure 8.1. The flow stress of both TiNbTaVW and IN718 is sensitive to deformation temperature, with high temperatures reducing the flow stress. High temperatures accelerate the movement of grain boundaries and dislocations, leading to softening and decreased stress (Bai et al., 2021). At 950°C, a steady-state flow stress followed by a reduction in flow stress was observed in the TiNbTaVW (Figure 8.1a). At 1000°C, a broad peak stress followed by a reduction in flow stress was observed. While at 1050°C, continuous flow softening was observed in the TiNbTaVW.

A broad peak stress has been attributed to DRX (Huang & Logé, 2016; Luton & Sellars, 1969), while continuous flow softening can suggest dynamic globularisation, flow localisation or wedge cracking (Prasad & Seshacharyulu, 1998; Seshacharyulu et al., 2002). Continuous flow softening occurs when the rate of softening surpasses the work hardening rate (Quan et al., 2013; Sakai et al., 2014). Similarly, at 950°C and 1050°C, the flow curve of the IN718 alloy exhibits a steady-state flow stress, as shown in Figure 8.1b. While at 1000°C, a steady-state stress followed by a reduction in flow stress was observed. A steady-state flow stress suggests either DRV or DRX (McQueen & Imbert, 2004; McQueen & Ryan, 2002).

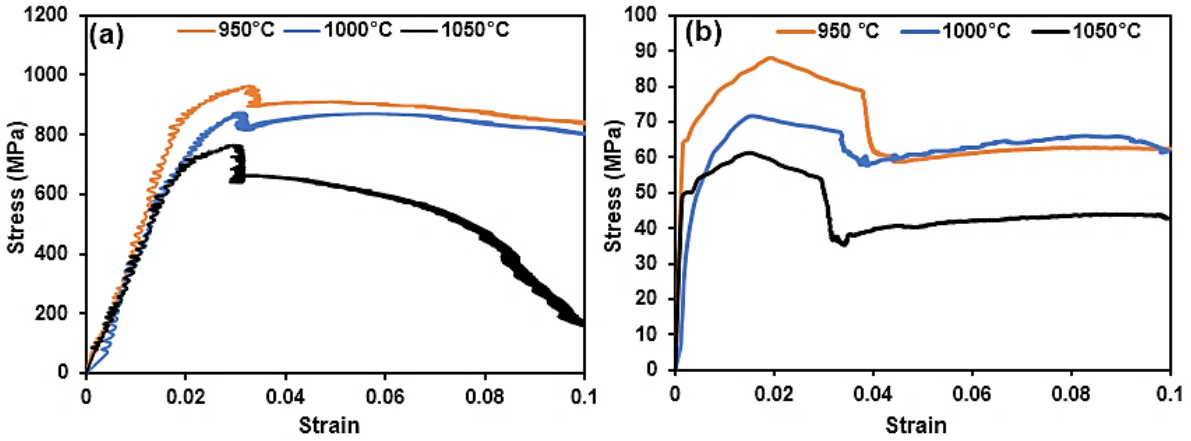

Figure 8.1: True stress-strain curves at 950°C to 1050°C and a strain rate of 10^{-3} s^{-1} for (a) TiNbTaVW and (b) IN718.

At 950°C to 1050°C, the flow stress of TiNbTaVW and IN718 at the elastic deformation stage exhibit a behaviour characterised by a sudden increase in the flow stress followed by a drop. Similar phenomena have been reported in other alloys such as Ti-6Al-4V (Bodunrin et al., 2020), HfNbTaTiZr (Eleti et al., 2019), $Ti_2ZrTa_{0.75}$ (Wang et al., 2023), $AlNbTi_3VZr_{1.5}$ (Yu et al., 2022), and $Ti_2ZrHfV_{0.5}Ta_{0.2}$ (Li et al., 2022). This phenomenon may occur due to dislocation unlocking by solute atoms or the ending of short-range order (Li et al., 2022). Additionally, it could result from a change in strain rate at low strain during the hot deformation experiment (Bodunrin et al., 2020). Serrations were detected in the elastic region of the TiNbTaVW flow curve at 950°C to 1050°C. It was also detected at the plastic region of the TiNbTaVW and IN718 flow curves at 1050°C and 1000°C. Serrations occur due to the repeated pinning and depinning of solute atoms on dislocations (Brechtl et al., 2020; Rodriguez, 1984; Sharghi-Moshtaghin & Asgari, 2008; Zhang et al., 2017).

8.2 Microstructural evolution of hot deformed TiNbTaVW and IN718

The optical and SEM-BSE images of TiNbTaVW and IN718 after deformation at 950°C, 1000°C, and 1050°C at a strain rate of 10^{-3} s^{-1} are presented in Figure 8.2-Figure 8.4. The deformed TiNbTaVW RHEA did not exhibit localised deformation features such as adiabatic shear bands but only voids (red arrow) at 950°C (Figure 8.2a and Figure 8.2b). The microstructure of TiNbTaVW at 950°C comprises globular (black arrows) and elongated grains (blue arrows), as shown in Figures 8.2a and 8.2b. Grain sizes of 44.45±5.0 µm were observed at 950°C. At higher temperatures and lower strain rates, more time and energy can

aid grain boundary migration and eventually promoting DRX. Elongated grains were also observed in some regions of the microstructure, suggesting DRV. At 950°C, no cracks or adiabatic shear bands appear in the microstructure of IN718 (Figures 8.2c and 8.2d). Equiaxed (black arrows) and elongated grains (blue arrows) are present in the microstructure at 950°C, with grain sizes of 40.3±6.9 µm. Equiaxed grains (black arrows) are commonly seen in metals and alloys dynamically recrystallised during hot compression (Eleti et al., 2019).

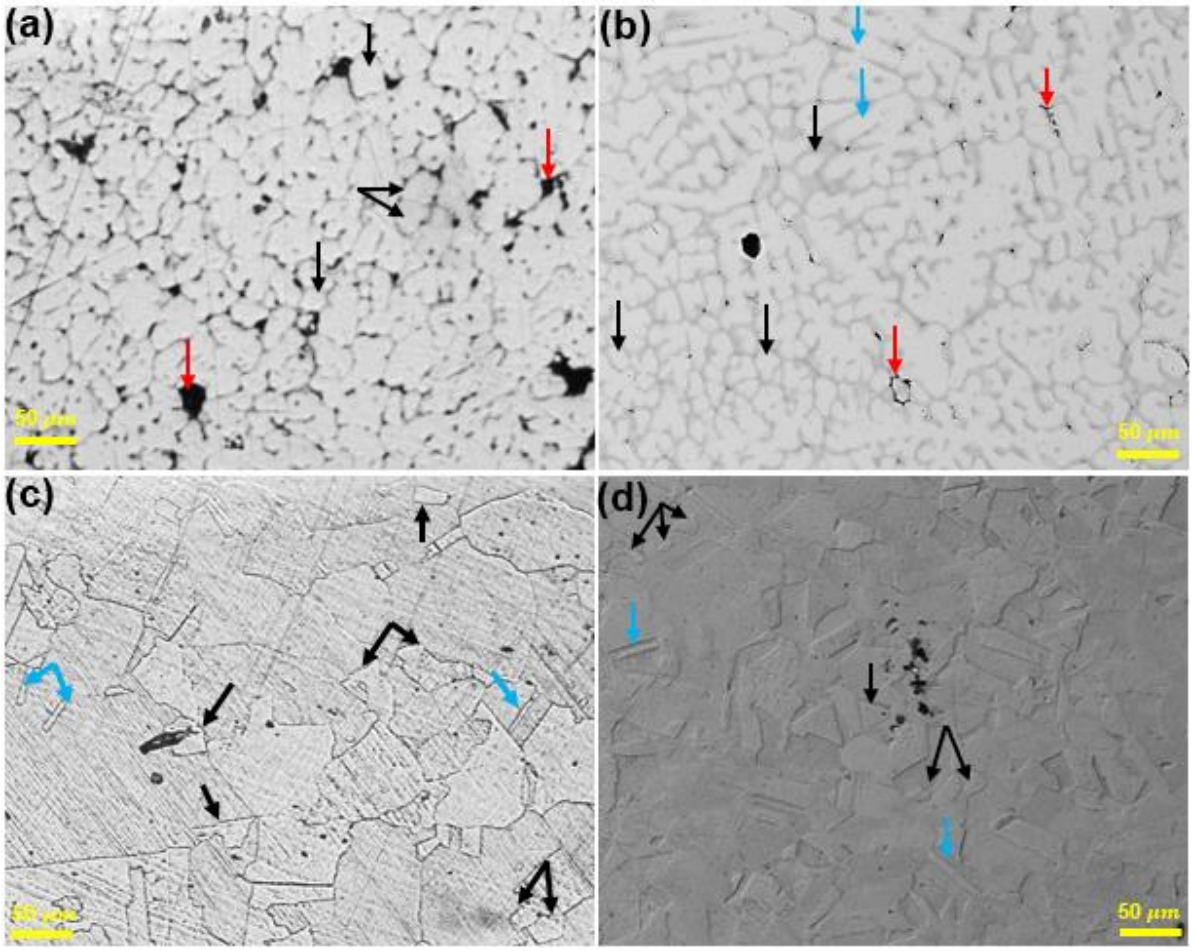

Figure 8.2: Optical micrograph and SEM-BSE image of TiNbTaVW after deformation at 950°C/10^{-3} s^{-1} showing globular grains (black arrows), elongated grains (blue arrows), and voids (red arrows) (a-b). Optical micrograph and SEM-BSE image of IN718 after deformation at 950°C/10-3 s-1 showing equiaxed grains (black arrows) and elongated grains (blue arrows) (c-d).

At 1000°C, the TiNbTaVW RHEA comprises globular (black arrows) and elongated grains (blue arrows), as shown in Figure 8.3a and Figure 8.3b. Some of the elongated grains are rotated in certain regions of the microstructure. The elongated grains suggest DRV. Finer grains (35.01±4.1 µm) were observed compared to grains at 950°C (44.45±5.0 µm). Voids

(red arrows) are still found in some regions of the microstructure. The globular grains also indicate that DRX occurred when the TiNbTaVW RHEA was deformed at 1000°C. For the IN718 at 1000°C, equiaxed (blue arrows) and globular (black arrows) grains were observed. A refined grain size of 38.31±7.5 µm was observed compared to 40.3±6.9 µm at 950°C, as shown in Figures 8.3c and 8.3d. No visible cracks or voids are detected in the microstructure of IN718 at 1000°C.

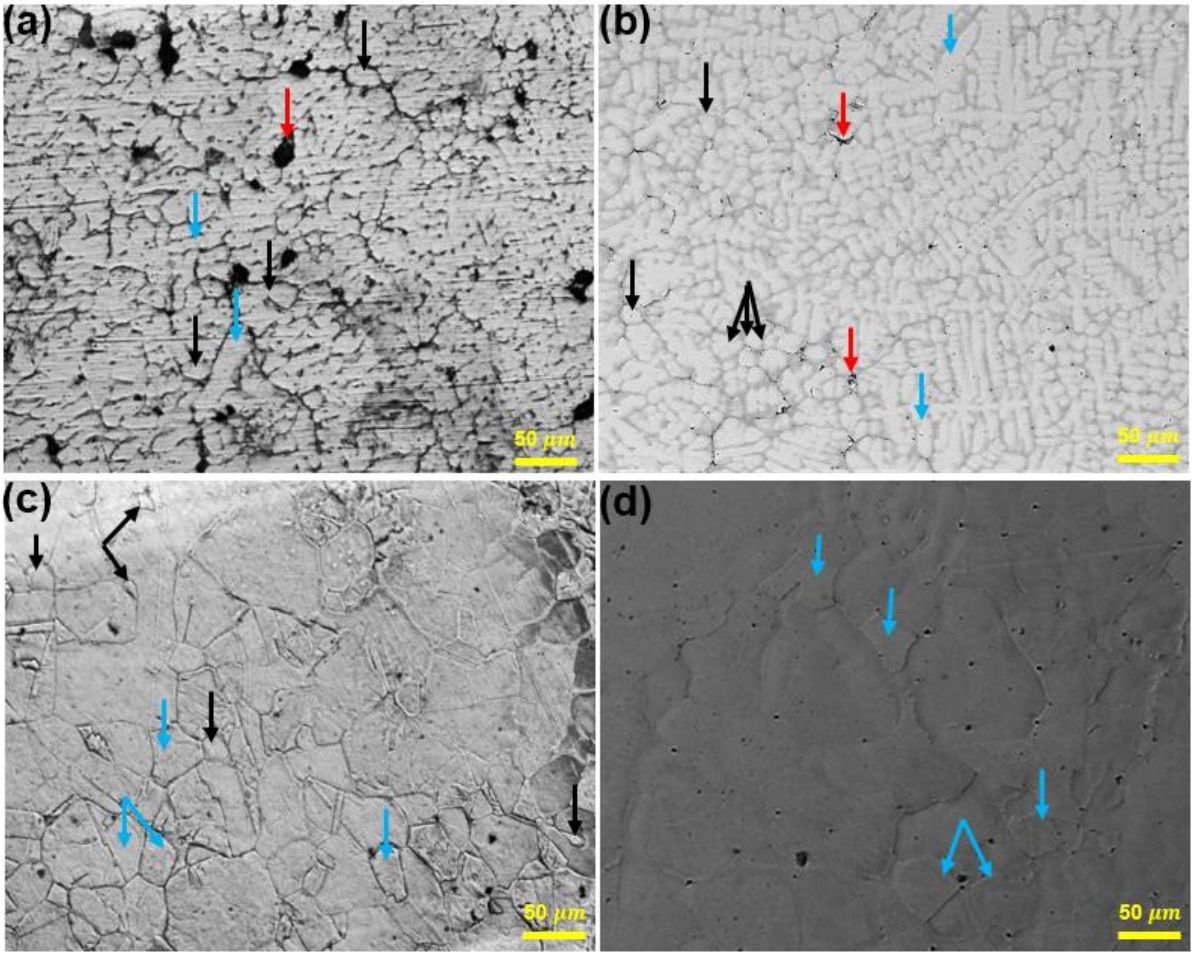

Figure 8.3: Optical micrograph and SEM-BSE image of TiNbTaVW after deformation at 1000°C/10^{-3} s^{-1} showing globular grains (black arrows), elongated grains (blue arrows), and voids (red arrows) (a-b). Optical micrograph and SEM-BSE image of IN718 after deformation at 1000°C/10^{-3} s^{-1} showing equiaxed grains (blue arrows) and globular grains (black arrows) (c-d).

As the temperature was increased to 1050°C, the TiNbTaVW RHEA exhibited mostly globular (black arrows) microstructures, as shown in Figure 8.4a and Figure 8.4b. A few elongated grains (blue arrows) were observed at 1050°C, indicating that most elongated grains at 1000°C had fragmented into smaller globular grains. The presence of more globular grains

indicates that the process of dynamic globularisation was almost complete as the deformation temperature was increased to 1050°C. This further signifies that the softening mechanism at 1050°C is DRX.

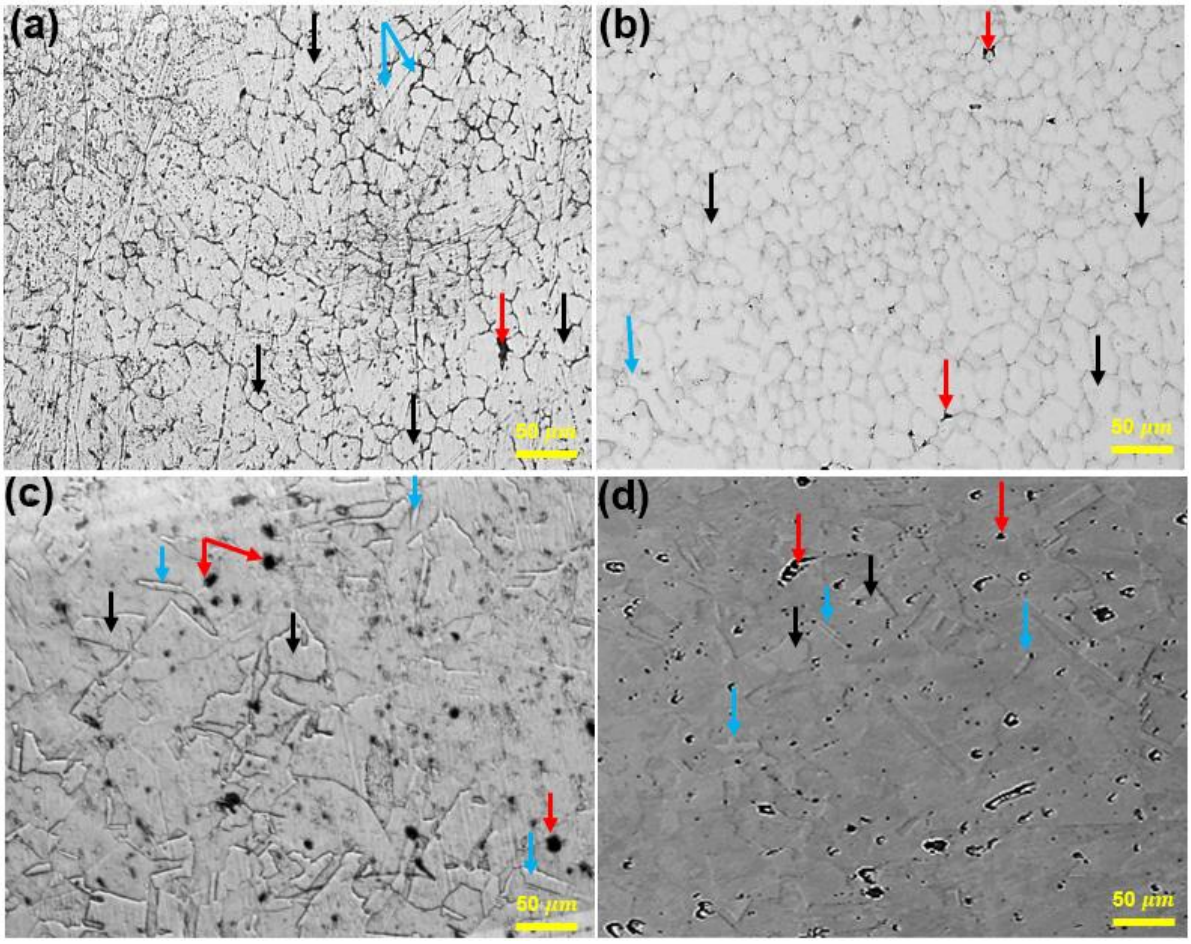

Figure 8.4: Optical micrograph and SEM-BSE image of TiNbTaVW after deformation at 1050°C/10^{-3} s^{-1} showing globular grains (black arrows), elongated grains (blue arrows), and voids (red arrows) (a-b). Optical micrograph and SEM-BSE image of IN718 after deformation at 1050°C/10^{-3} s^{-1} showing equiaxed (black arrows), elongated recrystallised grains (blue arrows), and voids (red arrows) (a-b).

The grain size (31.43±3.9 μm) of the TiNbTaVW RHEA at 1050°C is more refined compared to the grain sizes observed at 950°C and 1000°C. Voids were still observed at 1050°C, as shown in Figures 8.4a and 8.4b. Few elongated (blue arrows) and several equiaxed (black arrows) grains were found in many regions of IN718 (Figures 8.4c and Figures 8.4d). This signifies that the DRV and DRX softening mechanisms occur in IN718 at 1050°C. The grain size of IN718 at 1050°C is 34.84±3.9 μm, which is more refined than the grains observed at 950°C and 1000°C. Micro and huge voids (red arrows) appear in many regions of IN718 at 1050°C. Some of the voids were found within elongated recrystallised and equiaxed grains.

8.3 Macrostructure of hot deformed TiNbTaVW and IN718

Stereo images of the hot deformed TiNbTaVW and IN718 at 950-1050°C/$10^{-3}s^{-1}$ are presented in Figure 8.5. Cracks appeared on the TiNbTaVW RHEA's surface at 950°C to 1050°C, as shown in Figures 8.5a-c. During the hot compression process, stress concentration occurs, leading to an increase in local energy. Once the stress concentration attains a certain threshold, energy is released in the form of cracks. According to Abubaker et al. (2022), resultant stress concentration intensifies the creation and spread of microcracks unfavorable to deformation stability. At 950°C to 1050°C, surface spallation can be observed in the hot deformed IN718 alloy (Figure 8.5d-f).

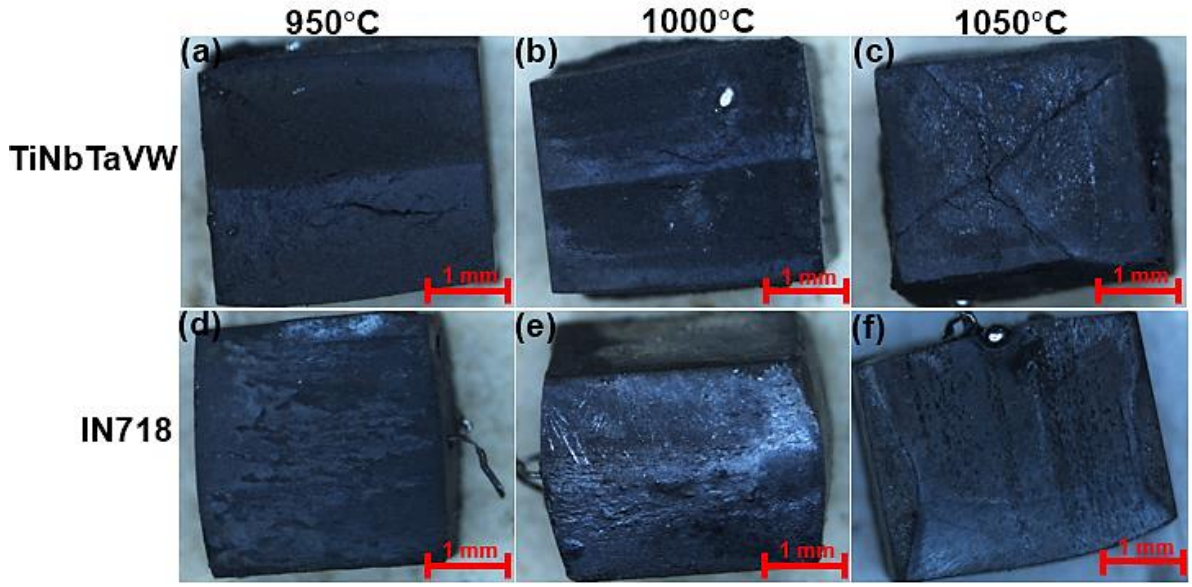

Figure 8.5: Stereo images of the TiNbTaVW and IN718 surface after deformation at 950°Cto 1050°C/10^{-3} s^{-1}.

8.4 High temperature strength of TiNbTaVW and IN718

The high-temperature compression strength of the TiNbTaVW RHEA and the IN718 alloy, compared to other RHEAs and alloys used for high-temperature applications, is depicted in Figure 8.6. The TiNbTaVW RHEA exhibits higher temperature strengths of 910 MPa, 870 MPa, and 658 MPa compared to the IN718 alloy, which has 72 MPa, 87 MPa, and 61 MPa at 950°C/10^{-3} s^{-1}, 1000°C/10^{-3} s^{-1}, and 1050°C/10^{-3} s^{-1}, respectively. The high-

temperature strength of TiNbTaVW RHEA at 950°C to 1050°C surpasses that of the compared RHEAs and superalloys, as shown in Figure 8.6. However, at 1000°C and 1050°C, the high-temperature strength of TiNbTaVW decreases significantly. According to Yurchenko et al. (2023), the loss of strength in RHEAs can be induced by the activation of diffusion-controlled processes.

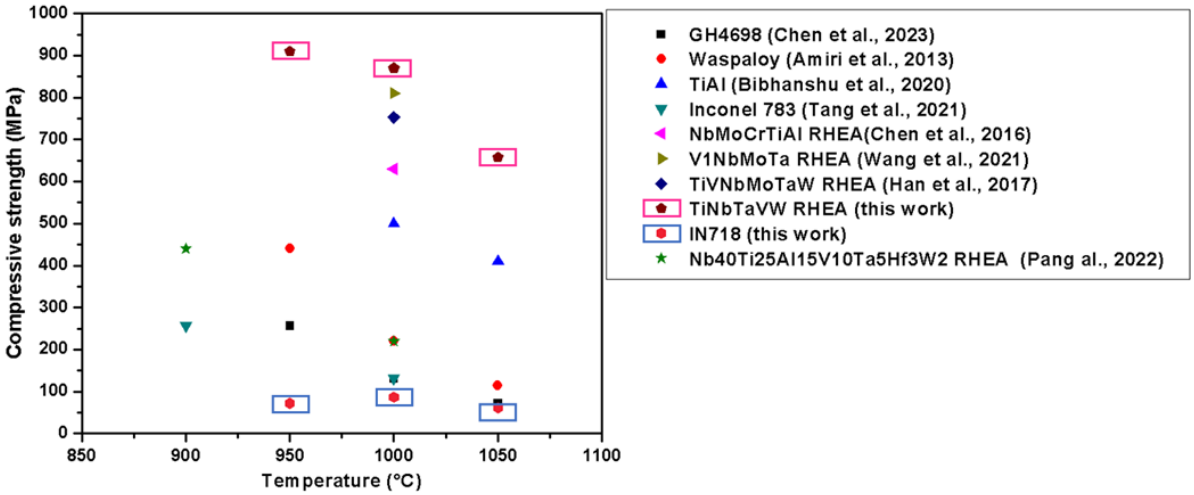

Figure 8.6: High-temperature strength of TiNbTaVW and IN718 compared to superalloys (Amiri et al., 2013; Bibhanshu et al., 2020; Chen et al., 2023; Tang et al., 2021) and other RHEAs (Chen et al., 2016; Han et al., 2017; Pang et al., 2022; Wang et al., 2021) at 950°C to 1050°C.

According to Senkov et al. (2021), the decreasing strength of RHEAs at higher temperatures can be attributed to diffusion-controlled processes that start to dominate as the solid solution diminishes. Compared with conventional alloys, RHEAs exhibit a higher softening temperature (0.6 to 0.8 T_m) (Butler et al., 2021; Senkov & Woodward, 2011). The high-temperature strength of the TiNbTaVW can be attributed to the addition of high melting elements such as Nb, Ta, and W. The addition of Ta, Nb, and Mo can greatly balance the mechanical properties of RHEAs at higher temperatures (Wang et al., 2019; Zheng et al., 2022). Solid solution strengthening effectively functions in RHEAs at temperatures below 1186°C (Senkov et al., 2021). Furthermore, the higher temperature strength of the TiNbTaVW RHEA can also be linked to the considerably larger atomic radii of Ti (1.46 Å), Ta (1.46 Å), and Nb (1.43 Å) compared to the atomic radii of V (1.32 Å) and W (1.39 Å). This difference in atomic radii causes lattice distortion, which enhances strengthening via solid solution. High entropy alloys have excellent high-temperature strength due to the solid solution

strengthening effect induced by severe lattice distortion and the thermodynamically favourable high-entropy effect (Zheng et al., 2022).

The strengthening mechanisms of alloys mainly comprise grain boundary strengthening (Hall-Petch), solid solution strengthening, and second-phase particle strengthening (Kalali et al., 2021; Nie et al., 2021; Raman et al., 2021). In this study, the TiNbTaVW RHEA has a single-phase BCC structure, so second-phase particle strengthening (precipitation strengthening and interstitial strengthening) does not exist in the solid solution. Therefore, grain boundary strengthening and solid solution strengthening are expected to be the main strengthening mechanisms. The solid solution strength can be determined as: (Nie et al., 2021; Zheng et al., 2022).

$$\sigma_{cs} = \sigma_{mix} + \Delta\sigma_{ss} \quad (8.1)$$

where σ_{cs} is the compressive strength of the TiNbTaVW RHEA at 950°C to 1050°C (910 MPa, 870 MPa, and 658 MPa), σ_{mix} is the individual elemental compressive strength at 950°C to 1050°C estimated using the rules of mixture, and $\Delta\sigma_{ss}$ is the solid solution strength. The individual elemental high-temperature values at 950°C to 1050°C for Ti (55 MPa, 44 MPa, and 37 MPa) (Su et al., 2020), Nb (107 MPa, 97 MPa, and 87 MPa) (Behera et al., 2024), and Ta (150 MPa, 124 MPa, and 92 MPa) (Zarghani et al., 2023) are considered. Furthermore, the elemental high-temperature values are 155 MPa, 79 MPa, and 52 MPa for V (Behera et al., 2024) and 407 MPa, 381 MPa, and 324 MPa for W (Lin et al., 2015). Using Equation (8.1), the $\Delta\sigma_{ss}$ is 735 MPa, 726 MPa, and 538 MPa at 950°C, 1000°C, and 1050°C, respectively.

In addition to solid solution strengthening, the effect of grain size was also considered. Grain boundary strengthening is recognised for its efficiency in grain refining, increasing the strength of polycrystalline metals and alloys (Huang et al., 2023). The grain boundary contribution to the strength of the TiNbTaVW RHEA satisfies the temperature dependence of the Hall-Petch relationship as defined in Equation (8.2) (Sun et al., 2019):

$$\sigma_{cs}(T) = 120 + 659d^{-0.5} + 597\exp(-T/120) - 0.39Td^{-0.5} \quad (8.2)$$

where d is the grain size of 44.45 μm, 35.01 μm, and 31.43 μm at temperatures of 950°C (1223K), 1000°C (1273K), and 1050°C (1323K). By substituting the d and T values into

Equation (8.2), the grain boundary contribution to the compressive strength of TiNbTaVW RHEA is 147 MPa, 147 MPa, and 145 MPa, respectively. It is evident that both solid solution strengthening and grain boundary strengthening contribute to the high-temperature strength of the TiNbTaVW RHEA.

8.5. Discussion

8.5.1 Serrations and sudden stress drop phenomenon

Several softening mechanisms, such as DRV, DRX, dynamic globularisation, superplasticity, and flow localisation can occur during hot deformation. Among these mechanisms, DRV, DRX, dynamic globularisation, and superplasticity are considered safe, while flow localisation, wedge cracking, and adiabatic shear banding are unsafe (Mosoma et al., 2023; Prasad & Seshacharyulu, 1998). During the initial stages of deformation, flow stress increases as dislocations interact and multiply. As dislocation density rises, the driving force for recovery also increases (Humphreys & Hatherly, 2004). Subsequently, due to the effect of DRX, dislocation density significantly decreases, leading to a gradual drop in flow stress. At 950°C, the TiNbTaVW RHEA flow curve exhibits a steady-state flow stress followed by a drop in flow stress, indicating the occurrence of DRV and DRX (Figure 8.1a). At 1000°C, a broad peak stress followed by a drop in flow stress indicates DRX. At 1050°C, continuous flow softening was observed, indicating dynamic globularisation as the main softening mechanism (Prasad & Seshacharyulu, 1998; Seshacharyulu et al., 2002). For the IN718 alloy, steady-state stress was more evident at 950°C and 1050°C, indicating the occurrence of DRV or DRX, while a drop in flow stress at 1000°C indicates DRX (Figure 8.1b).

A series of initial peak rises and sudden stress drops were observed in TiNbTaVW and IN718 at 950°C to 1050°C, which differ from the stress drop phenomenon typically attributed to DRX (Huang & Logé, 2016). Eleti et al. (2019) conducted an interrupted hot deformation experiment to elucidate further the reason behind the initial peak rise and sudden stress drop. They found a distinctive drop in the flow stress of the HfNbTaTiZr RHEA around yielding at a strain of ~0.1, followed by continuous flow softening at 1000 to 1200°C/10^{-2} to 10^{-4} s^{-1}. An interrupted test conducted at 1000°C, held for 600 s, and then deformed at a strain rate of 0.001 s^{-1} revealed no clearly observed DRX grains corresponding to the large stress drop. The authors attributed this unusual stress drop to either dislocation unlocking by solute atoms or

the ending of short-range ordered structures. Li et al. (2022) also found a stress drop at a strain of ~0.05 when $Ti_2ZrHfV_{0.5}Ta_{0.2}$ was deformed at 900°C to 1100°C/10^{-1} to 10^{-2} s^{-1}. An interrupted deformation test was carried out at 900°C/10^{-1} s^{-1}, held for 0 s and 600 s intervals, and then deformed at a strain rate of 0.1 s^{-1}. The drop in the flow stress of $Ti_2ZrHfV_{0.5}Ta_{0.2}$ was attributed to dislocation unlocking pinned by a Cottrell atmosphere or short-range order.

However, in the TiNbTaVW, the pinning of dislocations by solute atoms or interstitial solute atoms (N and C) is unlikely to occur because it is an equiatomic alloy. The rapid increase in flow stress and subsequent stress drops in TiNbTaVW and IN718 in this study are not caused by dislocation pinning but rather by a change in strain rate at a strain of 0.03 to 0.035, as depicted in Figure 8.7. The high strain rates (0.06 s^{-1}) at the beginning of deformation, compared to 0.001 s^{-1}, contributed to a rapid increase in flow stress and stress drops observed on the flow curves of the TiNbTaVW RHEA. For IN718, the high strain rates (0.1 s^{-1}) at the beginning of deformation compared to 0.001 s^{-1} led to the rapid increase in flow stress and stress drops observed on the flow curves. Although the overall strain rate remained unaffected, the misleading initial peak rise and stress drops in the flow stress were not a consequence of the microstructural response to the imposed parameters but were due to variations in the hydraulic motion regulating the compression jaws of the Gleeble simulator.

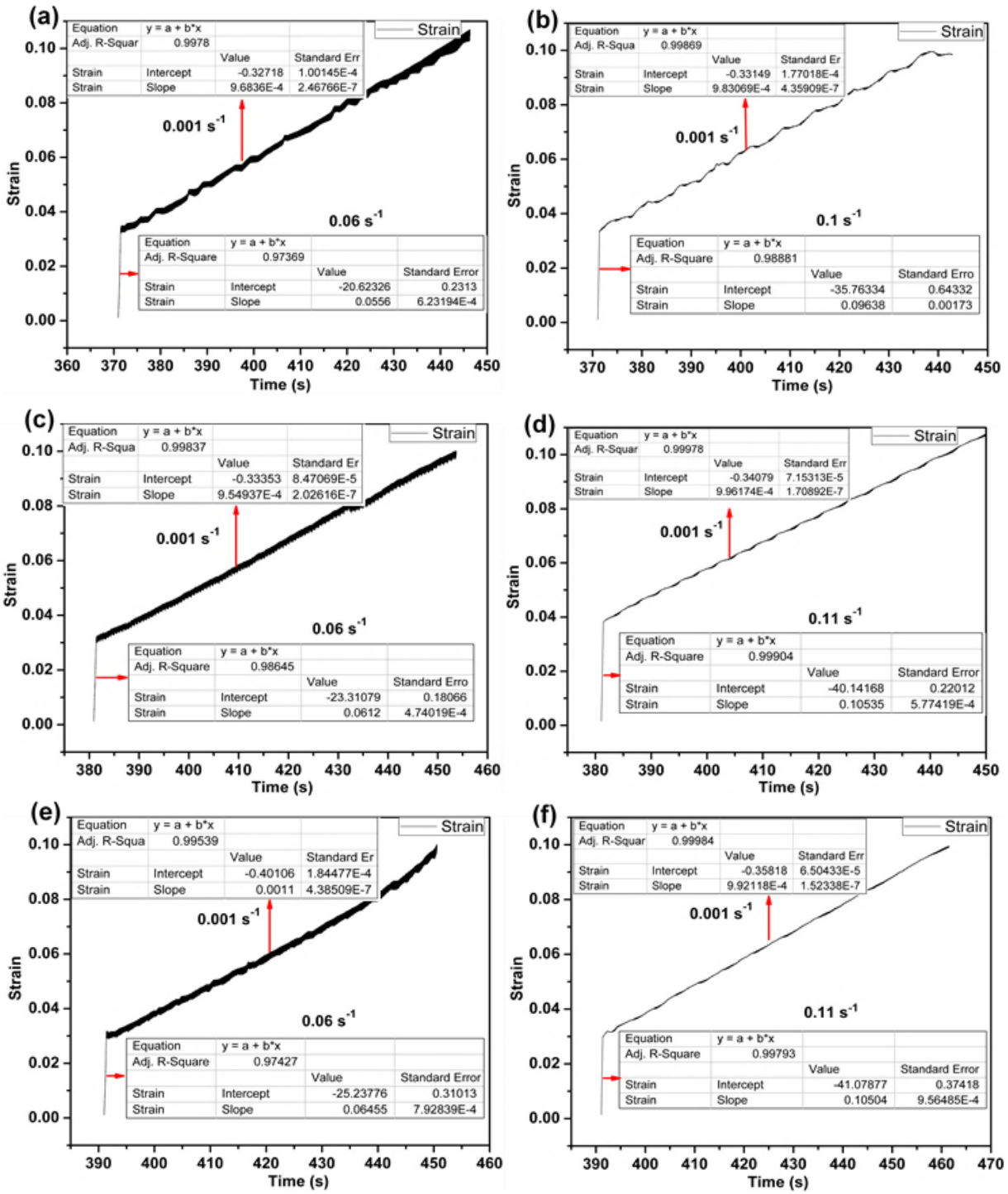

Figure 8.7: Strain versus time profile at 950°C/10^{-3} for (a) TiNbTaVW and (b) IN718. Strain versus time profile at 1000°C/10^{-3} for (c)TiNbTaVW and (d) IN718. Strain versus time profile at 1050°C/10^{-3} for (e) TiNbTaVW and (f) IN718.

Serrations, characterised by jerky stress-strain curves in solid materials, arise from dislocation motion (Zhang et al., 2017). It has been observed in flow curves of hot deformed RHEAs such as $Ti_2ZrHfV_{0.5}Ta_{0.2}$ (Li et al., 2022), $Al_xNb_{40}Ti_{40}V_{20}$-x (Yurchenko et al., 2023), and NbZrTiTa (Wang et al., 2023). In the TiNbTaVW RHEA, serrations were seen in both the elastic and plastic regions. At the elastic deformation stage, serrations were observed in the initial peak flow curve of the TiNbTaVW RHEA at 950°C to 1050°C before the sudden stress drop. Serrated flow stress curves are classified into Type A, Type B, and Type C (Zhang et al., 2017). The observed serrations in the flow curve of the TiNbTaVW RHEA at the elastic region are similar to Type B (Wang et al., 2023; Zhang et al., 2017). Type-B serrations often emerge at the beginning of serrated flow stress, yielding higher temperatures and lower strain rates (Zhang et al., 2017). Type-B serrations emerge at multiple points along the flow curves, propagate briefly, and then disappear. The elastic region serrations in some RHEAs, like MoNbVTiHf (Meng et al., 2022), MoNbTaW (Antonaglia et al., 2014), and HfNbTaTiZr (Hsu et al., 2023) also disappear before the stress drop and are often attributed to machine noise as dislocations at this stage are immobile. Since the serrations occurred at the elastic region in the TiNbTaVW RHEA and dislocation will be immobile at this stage, it can be said that the serrations are a result of machine noise. However, serrations observed in the plastic region of the flow curves of TiNbTaVW at 1050 °C and IN718 at 1000°C can be attributed to dislocation motion. Dislocation motion is essential to describe plasticity in crystalline materials as their mobility controls the material's ability to accommodate strain and modify its microstructure (Galindo-Nava et al., 2012).

8.5.2 Occurrence of dynamic recovery and recrystallisation

Grain growth is primarily driven by atomic diffusion and lower strain rates coupled with higher temperatures (Guo et al., 2016; Wang et al., 2023; Wang et al., 2023). This provides sufficient time and energy for atomic diffusion, facilitating grain boundary movement and eventual grain growth. Globular and elongated grains were observed in the TiNbTaVW alloy at 950°C, signifying both DRV and dynamic globularisation as the softening mechanisms. This corroborates with the flow curve at 950°C having steady-state flow stress followed by a drop in flow stress. Similarly, at 1000°C, globular and elongated grains were observed in the TiNbTaVW alloy. However, the flow curve only shows the characteristics of DRX and as

confirmed by the globular grains. The occurrence of elongated grains also signifies DRV. Therefore, the softening mechanisms of TiNbTaVW at 1000°C are still considered DRV and dynamic globularisation. The occurrence of both globular and elongated grains has also been observed in the $TiAlVNb_2$ RHEA (Bai et al., 2021).

At 1050°C, dynamic globularisation is the softening mechanism, as corroborated by the continuous flow softening in the flow curve. Dynamic globularisation has been previously reported as a form of DRX (Bodunrin et al., 2019; Li et al., 2021; Ouyang et al., 2020; Seshacharyulu et al., 2002; Wu et al., 2011). This mechanism occurs at low strain rates and high deformation temperatures (Bodunrin et al., 2020). Equiaxed and elongated grains were observed in IN718 at 950°C and 1050°C, as corroborated by steady-state stress, suggesting either DRV or DRX (McQueen & Imbert, 2004; McQueen & Ryan, 2002). Due to the occurrence of equiaxed and elongated grains, the softening mechanisms for IN718 at 950°C and 1050°C are both DRX and DRV. However, at 1000°C, mostly equiaxed grains were observed, as corroborated by oscillations and a reduction in the flow curve, signifying DRX. Therefore, DRX is the softening mechanism for IN718 at 1000°C. The refinement of grains in TiNbTaVW and IN718 is attributed to the characteristics of repeated nucleation and limited growth during DRX. This DRX occurrence promotes grain refinement and reduces deformation resistance in alloys, enhancing their workability and mechanical properties (Guo et al., 2016).

Voids were detected near recrystallised grains during the deformation of TiNbTaVW at 950°C to 1050°C, as shown in Figures 8.2-8.5. The presence of voids, cracks, and cavities at grain boundaries results from stress concentration, which is more prone to occur at grain boundaries and triple-junction points (Sajjadi et al., 2016; Wei et al., 2021). Under stress loading conditions, cracks propagate along HAGBs, resulting in brittle fracture of the alloy in the intergranular region (Huang et al., 2024). The higher presence of voids at 950°C and 1000°C compared to 1050°C may be due to limited dislocation mobility and diffusion (Abubaker et al., 2022; Sajjadi et al., 2016), which fail to relieve stress concentrations. According to Zhao et al. (2019), cracks, voids, and pores can be eliminated with increasing deformation temperature and decreasing strain rate. As the temperature was increased to 1050°C in TiNbTaVW, the number of voids decreased.

However, minipores and large voids were observed in IN718 at 1050°C (Figures 8.5c and 8.5d), possibly due to stress concentration and inadequate diffusion rates at grain boundaries (Sajjadi et al., 2016). Refined grains can impede crack and pore propagation during deformation by increasing the energy barrier required to create new surfaces (Abubaker et al., 2022; Xiao et al., 2022). The TiNbTaVW RHEA at 1050°C comprises refined globular grains, which could reduce void propagation, as shown in Figures 8.5a and 8.5b.

Second phases and intermetallics can cause cracks and fracture in RHEAs. For instance, Xu et al. (2022) observed a premature failure and macrocracks that are distributed in the M_3Si phase during compression of $VNbTiTaSi_x$ RHEA. Cao et al. (2021) found intergranular cracks in the $TiNbTa_{0.5}ZrAl_{0.5}$ RHEA that spread by connecting the HCP precipitates. The HCP phase cause stress concentration during loading and eventually lead to a rapid crack propagation. In this study, CrNbTaVW RHEA has multiphases (BCC1, BCC2 and $Cr(VNb)_2$ Laves). Laves phases extreme brittleness and poor fracture toughness are limitations that arise because of their high resistance to dislocations motion (Rabadia et al., 2018). The formation of Cr_2Nb Laves phase in $Al_1CrNbVMo$ RHEA makes it difficult to be hot compressed (Kang et al., 2021). Furthermore, the TiVZrMo RHEA developed by Zhuo et al. (2023) comprise of three phases (BCC1, BCC2 and (MoV)Zr Laves). The (MoV)Zr Laves combined with phase boundaries, acted as potential initiation sites for cracks in the TiVZrMo RHEA. The existence of the two BCC phases among the (MoV)Zr Laves phase caused a mismatch in deformation between these phases, which obstructed crack propagation and caused the formation of fracture regions. Therefore, it could be said that the stress concentrations between the two BCC phases and the $Cr(VNb)_2$ Laves might have contributed to the disintegration of the CrNbTaVW RHEA during loading.

8.6 Summary

- The TiNbTaVW and IN718 flow curves decreased with an increasing deformation temperature at a constant strain rate.
- The presence of both globular and elongated grains in the TiNbTaVW alloy at 950°C and 1000°C confirmed that dynamic globularisation and DRV are the softening mechanisms. At 1050°C, mainly globular grains were observed, indicating dynamic globularisation as the softening mechanism. In IN718, equiaxed and elongated grains at 950°C and 1050°C

suggested both DRX and DRV as the softening mechanisms. At 1000°C, the dominance of equiaxed grains signified DRX as the only softening mechanism.

- Voids were found in the microstructure of the TiNbTaVW RHEA at 950°C to 1050°C, whereas minipores and voids were only detected at 1050°C for the IN718.
- The TiNbTaVW RHEA has higher temperature strengths of 910 MPa, 870 MPa, and 658 MPa, compared to the IN718 alloy, with 72 MPa, 87 MPa, and 61 MPa at 950°C/10^{-3} s^{-1}, 1000°C/10^{-3} s^{-1}, and 1050°C/10^{-3} s^{-1}, respectively. The higher temperature strength of the TiNbTaVW RHEA can be attributed to both solid solution strengthening and grain boundary strengthening.

Chapter 9

9.1 Conclusions

In this research, two RHEAs (TiNbTaVW and CrNbTaVW) were developed as a potential replacement to the commercial IN718 nickel-based alloy for structural applications. The target structural applications include high temperature materials industries, hydrogen storage, nuclear industries, chemical industries, and coating industries. Based on the achieved objectives, the following conclusions were made from the research:

1. **Conducting a bibliometric mapping using Vosviewer software to identify research trends and key focus areas in as-cast RHEAs**

a) The Scopus database were used to extract 674 articles relating to as-cast RHEAs. The first article on the arc-melted RHEAs was published in 2010 and in 2024, the number of articles was 302.
b) The highest number of publications for institutional co-authorship were published by the Dalian University of Technology, China and Beijing Institute of Technology, China. The publication analysis per country found China to have the highest number of publications on the arc-melted RHEAs.
c) Some functional applications of as-cast RHEA such as “hydrogen storage”, “radiation”, “fracture’, “thermal expansion”, “thermoelectric properties”, “biomaterials”, “corrosion”, and hot deformation have been less investigated.

2. **Assessing the influence of composition on microstructure and hardness based on empirical calculation, thermo-calc simulation and experimental techniques**

a) The empirical methods used for the prediction of phase formation indicated the formation of a single BCC solid solution phase in the TiNbTaVW RHEA and two BCC solid solution phases with a Laves phase in the CrNbTaVW RHEA.
b) Using the CALPHAD approach, one BCC disordered phase and a disordered HCP phase are stable at ~499°C, while only BCC disordered phase is stable above 500°C for the TiNbTaVW RHEA. When compared with SEM and XRD results,

HCP phase was not found which suggest that the kinetics are slow at lower temperatures. Two BCC disordered phase and a Lave phase are stable at ~600°C for the CrNbTaVW RHEA.

c) The empirical calculations and CALPHAD approach are consistent with the phases observed in the TiNbTaVW and CrNbTaVW RHEAs, as confirmed by experimental observations.

d) The TiNbTaVW RHEA exhibited single BCC phase and a dendritic microstructure, while CrNbTaVW RHEA exhibited two BCC phases (BCC1 and BCC2) and $Cr(VNb)_2$ C15_Laves phase.

e) The CrNbTaVW RHEA had a higher hardness of 688±21 HV than the TiNbTaVW (522±10 HV), and IN718 (301±14 HV). The higher hardness of CrNbTaVW RHEA was attributed to the solid solution strengthening and $Cr(VNb)_2$ Laves strengthening.

3. Evaluating the corrosion performance of TiNbTaVW and CrNbTaVW RHEAs in 3.5 wt% NaCl and 1 Mol H_2SO_4 compared to the IN718 alloy

a) The TiNbTaVW and CrNbTaVW had lower corrosion rate of 0.0003±0.0002 mm/yr and 0.000097±0.0008 mm/yr than the IN718 alloy (0.054±0.02 mm/yr) in 3.5wt% NaCl solution. Similar observations were made in 1M H_2SO_4 solution, where TiNbTaVW and CrNbTaVW had lower corrosion rate of 0.0009±0.0005 mm/yr and 0.00013±0.00012 mm/yr than the IN718 alloy (1.12±0.001 mm/yr). The lower corrosion rate exhibited by the TiNbTaVW and CrNbTaVW RHEAs is attributed to the quality of the passive films.

b) Few pits were observed on the surface of TiNbTaVW and CrNbTaVW RHEAs after potentiodynamic polarisation in 3.5 wt% NaCl and 1M H_2SO_4 solutions. IN718 alloy was highly corroded, with large pits forming on the surface of the alloy.

c) The interdendrite region of the TiNbTaVW and BCC1 region in the CrNbTaVW was more susceptible to pitting corrosion in 3.5 wt% NaCl and 1M H_2SO_4 solution, while the $Cr(VNb)_2$ Laves phase was more susceptible to selective dissolution in the CrNbTaVW.

d) The main corrosion mechanism of the TiNbTaVW and CrNbTaVW RHEAs in chloride and acidic solutions is localised corrosion due to segregation of elemental compositions that resulted in different electrochemical potentials that eventually broke down the protective layer and allowed an ingress of chloride and sulphate ions.
e) The main corrosion mechanism of the IN718 alloy in chloride and acidic solutions is active corrosion and localised corrosion due to the absence of a stable passive film.

4. Determining the oxidation kinetics, surface oxide morphology, and cross-sectional morphology of TiNbTaVW and CrNbTaVW RHEAs at 850°C/1050°C for 15 hours, in comparison to the IN718 alloy

a) The IN718 alloy had a mass gain of 4.41 mg/cm^2 and 10.84 mg/cm^2 at 850°C and 1050°C, respectively after 15 hours. The TiNbTaVW RHEA exhibited a mass loss of -23.58 mg/cm^2 and -45.92 mg/cm^2 at 850°C and 1050°C after 15 hours. The CrNbTaVW RHEA exhibited a mass loss of -25.17 mg/cm^2 and -35.91 mg/cm^2 at 850°C and 1050°C after 15 hours. Therefore, the IN718 alloy has better oxidation resistance than the TiNbTaVW and CrNbTaVW.
b) The surface scale layer of TiNbTaVW and CrNbTaVW at 850°C and 1050°C after 15 hours comprise granular-shaped and rod-shaped oxides. The surface scale layer of IN718 at 850°C after 15 hours comprise block-shaped, rod-shaped, round-shaped, and cloudy-shaped oxides. While at 1050°C after 15 hours, globular and block-shaped oxides were observed.
c) The cross-sectional morphology showed a thick oxidised and internal oxidation region for the TiNbTaVW RHEA at 850°C and 1050°C. The cross-sectional morphology of CrNbTaVW RHEA was comprised of a thick oxidised and internal oxidation region at 850°C. While only thick oxidised layer was observed for the CrNbTaVW RHEA. The IN718 alloy displayed a thin outer oxide layer and internal oxide layer with no pores or cracks that protects the ingress of oxygen to the metallic substrate and eventually lowers the oxidation rate of IN718 alloy.
d) The oxidation mechanisms of the TiNbTaVW and CrNbTaVW at 850°C and 1050°C showed that the growth stress during oxidation and the thermal stress during cooling

to room temperature of oxidised samples contributed to pores, voids, cracks, and oxide layer spallation. The oxidation mechanism of IN718 showed that the Al_2O_3, Fe_3O_4, and TiO_2 inhibited the formation of pores and cracks that could act as migration channels for oxygen on the surface and cross-sectional layers, thereby reducing the oxidation rate.

5. **Assessing the influence of high temperatures and strain rate on the flow behaviour, microstructural evolution, and compressive strength of the TiNbTaVW and CrNbTaVW RHEAs in comparison to the IN718 alloy. Determining the dominant softening mechanisms during high temperature deformation of the RHEAs compared to the IN718 alloy**

    a) The TiNbTaVW and IN718 flow curves decreased with an increasing deformation temperature at a constant strain rate.
    b) At 1050°C, mainly globular grains were observed, indicating dynamic globularisation as the softening mechanism. In IN718, equiaxed and elongated grains at 950°C and 1050°C suggested both DRX and DRV as the softening mechanisms. At 1000°C, the dominance of equiaxed grains signified DRX as the only softening mechanism.
    c) The TiNbTaVW RHEA has higher temperature strengths of 910 MPa, 870 MPa, and 658 MPa, compared to the IN718 alloy, with 72 MPa, 87 MPa, and 61 MPa at 950°C/10^{-3} s^{-1}, 1000°C/10^{-3} s^{-1}, and 1050°C/10^{-3} s^{-1}, respectively.

The comparison of the hardness, corrosion and oxidation properties, high temperature properties, and formability of RHEAs in this study as compared with conventional alloys is given in Tables 9.1-9.3. The RHEAs have superior hardness, corrosion and high temperature strength than the superalloys. However, the superalloys have superior oxidation resistance than TiNbTaVW and CrNbTaVW and formability than TiNbTaVW. Suggestions for future research work and on how to improve the RHEAs properties are given in Section 9.2.

Table 9.1: Comparison of the formability of TiNbTaVW RHEA and superalloys.

Alloy composition	Strain rate (s^{-1})	Temperature (°C)	Plasticity (%)	References
TiNbTaVW	10^{-3}	950 1000 1050	10 10 10	(This work)
IN600	10^{-3}	950 1000 1050	>60 >60 >60	(Gajalappa et al., 2021)
FGH96	10^{-3}	1000 1050	>80 >80	(Wei et al., 2012)
IN625	10^{-3}	950 1000 1050	>50 >50 >50	(Medeiros et al., 1999)
TiAl	10^{-3}	950 1050	>50 >50	(Gupta et al., 2012)
$Ni_{15}Cr_4W_3Mo_2Al_3Ti$	10^{-3}	1000 1050	70 70	(Mingjie et al., 2010)
Nimonic 80A	10^{-3}	950 1000	70 70	(Mirzaee et al., 2022)
GH4945	10^{-3}	1000 1050	70 70	(Shi et al., 2017)
Hastelloy C-276	10^{-3}	1000 1050	>90 >90	(Zhang et al., 2015)

Table 9.2: Comparison of the hardness of TiNbTaVW, CrNbTaVW, superalloys and high temperature properties of TiNbTaVW and superalloys.

Alloys	TiNbTaVW (this work)	CrNbTaVW (this work)	IN718 (this work)	IN625 (Tümer et al., 2021)	IN825 (Rajkumar et al. 2022)	Hastelloy C-276 (Atapek et al., 2023)	IN825 (Chigilipalli et al., 2022)	IN617 (Avinash et al. 2023)	TiAl (Brotzu et al., 2018)	Haynes 282 (Polkowska et al., 2020)
Hardness (HV)	522	688	301	283	258	231	165	282	335	247
High temperature properties										
Alloys	TiNbTaVW (this work)	IN718 (this work)	IN600 (Gajalappa et al., 2021)	GH690 (Wei et al., 2012)	IN625 (Medeiros et al., 1999)	TiAl (Gupta et al., 2012)	$Ni_{15}Cr_4W_3Mo_2Al_3Ti$ (Mingjie et al., 2010)	Nimonic 80A (Mirzaee et al., 2022)	GH4945 (Shi et al., 2017)	Hastelloy C-276 (Zhang et al., 2015)
950℃	910 MPa	72 MPa	109 MPa	-	154 MPa	120 MPa	-	227 MPa	-	-
1000℃	870 MPa	87 MPa	78 MPa	113 MPa	103 MPa	-	79 MPa	112 MPa	118 MPa	187 MPa
1050℃	658 MPa	61 MPa	65 MPa	87 MPa	72 MPa	63 MPa	43 MPa	-	88 MPa	141 MPa

Table 9.3: Comparison of the corrosion and oxidation properties of TiNbTaVW, CrNbTaVW and superalloys.

Corrosion properties										
Alloys	TiNbTaVW (this work)	CrNbTaVW (this work)	IN718 (this work)	IN625 (Tümer et al., 2021)	IN825 (Rajkumar et al., 2022; Delgado-Alvarado et al., 2007)	Hastelloy C-276 (Atapek et al., 2023)	IN690 (Gaona-Tiburcio et al., 2014)	IN800 (Gaona-Tiburcio et al., 2014)	IN617 (Gaona-Tiburcio et al., 2014)	TiAl (Delgado-Alvarado et al., 2007)
Nacl (mm/yr)	0.0003	0.00009	0.054	0.007	0.066	0.0193	-	-	0.0259	0.018
Acidic (mm/yr)	0.0009	0.00013	1.12	-	0.506		32.855	38.756	-	-
Oxidation properties										
Alloys	TiNbTaVW (this work)	CrNbTaVW (this work)	IN718 (this work)	Haynes 282 (Tung et al., 2024)	TiAl (Terner et al., 2015)	$Ni_{48}Cr_{28}W_5$ (Liu et al., 2015)	Ni–Cr–Al (Sun et al., 2021)	Nimonic95 (Li et al., 2021)	GH738 (Wang et al., 2021)	IN617 (Saber et al., 2017)
850°C (mg/cm^2)	−23.58	-25.17	4.41	0.225	0.184	-	0.251	0.133	0.111	0.1744
1050°C (mg/cm^2)	−45.92	-35.91	10.84	-	-	1.1	0.923	0.934	10.44	0.575

9.2 Suggestions for future research work

1. **Corrosion performance**
   a) Pitting and selective dissolution were evident in TiNbTaVW and CrNbTaVW RHEAs. Future studies may consider adding aluminium to the TiNbTaVW RHEA to prevent pitting. Beyond elemental segregation, another preferential corrosion site in RHEAs is their multiphase microstructures. Further research could focus on optimising the CrNbTaVW RHEA composition to eliminate the multiphase structure and generate a single-phase RHEA, which could reduce pitting and phase dissolution. Further research could investigate the effect of other C14 and C15 Laves phases on the corrosion behaviour of RHEAs in chloride and acidic solutions.
   b) The application of machine learning and high-throughput screening methods is important for accelerating the development of RHEAs. Machine learning and high-throughput screening methods can be applied to predict the relative corrosion resistance for a wide range of TiNbTaVW and CrNbTaVW compositions, offering an efficient way to design corrosion-resistant RHEAs.
   c) In-depth studies of corrosion mechanisms should also be conducted on other developed RHEAs, with the focus on the effects of empirical parameters, such as severe lattice distortion on the corrosion behaviour. The density functional theory and molecular dynamics simulations can be used to reveal the influence of different elements in TiNbTaVW and CrNbTaVW RHEAs on passive film formation.

2. **Oxidation performance**
   a) The mismatch in volume expansion of the high PBR WO_3 observed in the TiNbTaVW and CrNbTaVW at 850°C and 1050°C contributed to pores, voids, cracks, and oxide layer spallation. The addition of Al is one method to enhance oxidation resistance of RHEAs. Future research could explore replacing W with Al to improve the oxidation resistance of the TiNbTaVW and CrNbTaVW RHEAs. The Al_2O_3 oxide has a low PBR of 1.29, which can hinder the formation of pores, voids, cracks, and oxide layer spallation in TiNbTaVW and CrNbTaVW RHEAs. The Al could also induce Nb and Ta to form $AlNbO_4$ and $AlTaO_4$ instead of Nb_2O_5 and Ta_2O_5 oxides, that will prevent volatile oxidation and hinder the oxygen ions diffusion and metal cations, thereby

reducing the oxidation rate. However, Al concentration should be carefully controlled to prevent inducing other brittle Laves or Sigma phases that will deteriorate mechanical properties.

b) Accelerating the development of oxidation-resistant RHEAs through machine learning could inspire new experimental and theoretical designs for high-temperature oxidation-resistant RHEAs.

c) Further research could utilise the preferential interactivity parameter (PIP) to map and predict the distribution of different elements within TiNbTaVW and CrNbTaVW RHEAs in an oxidising environment. A mechanistic understanding of these parameters could pave the way for designing robust alloys with superior bulk and surface properties.

3. High temperature performance

a) While high-temperature strength was achieved at 950°C-1050°C for the TiNbTaVW RHEA, it only deformed by 10%. Future research should focus on improving the formability of the TiNbTaVW RHEA. The CrNbTaVW RHEA was not suitable for hot deformation due to its extreme brittleness. The extreme brittleness of Laves phase is a limitation due to its high resistance to dislocation motion. Future research could optimise the CrNbTaVW RHEA composition to eliminate the multiphases and generate a single-phase alloy, which could reduce resistance to dislocation motion and improve deformability.

b) Future research should also explore combining machine learning with density functional theory and thermodynamic databases to develop advanced plasticity models for simulating the hot deformation behaviour of RHEAs at various scales. These models can help predict microstructural changes and mechanical responses under different processing conditions. Machine learning techniques could also predict the behaviour of RHEAs during hot deformation based on processing parameters and alloy composition, potentially accelerating the design and optimisation of new RHEAs with excellent formability.

c) The flow stress of hot-deformed IN718 at 1000°C is higher than at 950°C, which could be attributed to strain rate sensitivity. Further studies at the atomistic level of deformation are needed to fully understand this phenomenon.
d) Future research could assess the residual stress profiles and anisotropy from hot deformation to understand how these factors influence the long-term performance and reliability of RHEAs in service. Long-term studies on the creep and fatigue behaviour of hot-deformed RHEAs are necessary to ensure their durability and reliability in high-stress, high-temperature environments.
e) A high level of characterisation using transmission electron microscopy, electron backscatter diffraction, and atomic force microscopy should be considered in future studies to investigate the microstructural evolution of hot deformed TiNbTaVW RHEA.

References

Aba-perea, P. E., Pirling, T., Withers, P. J., Kelleher, J., Kabra, S., & Preuss, M. (2016). Determination of the high temperature elastic properties and diffraction elastic constants of Ni-base superalloys. *Materials and Design*, *89*, 856–863.

Abbaszadeh, S., Pakseresht, A., Omidvar, H., & Shafiei, A. (2020). Investigation of the high-temperature oxidation behaviour of the $Al_{0.5}CoCrFeNi$ high entropy alloy. *Surfaces and Interfaces*, *21*, 100724.

Abubaker, M., Wang, T., Feng, C., Sun, H., Wang, B., Hamza, M., Afifi, M. A., & Liao, W. (2022). A superb mechanical behaviour of newly developed lightweight and ductile $Al_{0.5}Ti_2Nb1Zr_1W_x$ refractory high entropy alloy via nano-precipitates and dislocations induced-deformation. *Materials & Design*, *222*, 111034.

Polkowska, A., Lech, S., & Polkowski, W. (2020). The effect of cold rolling degree on microstructure, crystallographic texture and mechanical properties of Haynes 282 wrought nickel superalloy. *Materials Science and Engineering A*, 787, 139478.

Aghimien, D. O., Aigbavboa, C. O., Oke, A. E., & Thwala, W. D. (2020). Mapping out research focus for robotics and automation research in construction-related studies: A bibliometric approach. *Journal of Engineering, Design and Technology*, *18*(5), 1063–1079.

Ahmed, A., Azam, A., Mahmood, M., Bhutta, A., Ahmad, F., Aslam, R., & Tahir, Z. (2021). Discovering the technology evolution pathways for 3D printing (3DP) using bibliometric investigation and emerging applications of 3DP during COVID-19. *Cleaner Environmental Systems*, *3*, 100042.

Akinradewo, O., Aigbavboa, C., Oke, A., & Edwards, D. (2022). A roadmap for present focus and future trends of blockchain technology in the built environment. *African Journal of Science, Technology, Innovation and Development*, *15*(2), 153–165.

Akinwekomi, A. D., & Akhtar, F. (2022). Bibliometric mapping of literature on high-entropy/multicomponent alloys and systematic review of emerging applications. *Entropy*, *24*(3), 329.

Akinwekomi, A. D., Bamisaye, O. S., & Bodunrin, M. O. (2024). Powder metallurgy processing of high entropy alloys: Bibliometric analysis and systematic review. *Reviews on Advanced Materials Science*, *63*, 0188.

Alshataif, Y. A., Sivasankaran, S., Al-Mufadi, F. A., Alaboodi, A. S., & Ammar, H. R. (2020). Manufacturing methods, microstructural and mechanical properties evolutions of high-entropy alloys: A review. In *Metals and Materials International* (Vol. 26, Issue 8). The Korean Institute of Metals and Materials.

Amiri, A., Bruschi, S., Sadeghi, M. H., & Bariani, P. (2013). Investigation on hot deformation behaviour of Waspaloy. *Materials Science and Engineering: A*, *562*, 77–82.

Ananiadis, E., Argyris, K. T., Matikas, T. E., Sfikas, A. K., & Karantzalis, A. E. (2021). Microstructure and corrosion performance of aluminium matrix composites reinforced with refractory high-entropy alloy particulates. *Applied Sciences*, *11*(3), 1300.

Anne, B. R., Shaik, S., Tanaka, M., & Basu, A. (2021). A crucial review on recent updates of oxidation behaviour in high entropy alloys. *SN Applied Sciences*, *3*(3), 366.

Antonaglia, P. J., Xie, X., Tang, Z., Tsai, C. W., Qiao, J. W., Zhang, Y., Laktionova, M. O., Tabachnikova, E. D., Yeh, J. W., Senkov, O. N., Gao, M. C., Uhl, J. T., Liaw, P. K., & Dahmen, K. A. (2014). Temperature Effects on Deformation and Serration Behavior of High-Entropy Alloys (HEAs). *JOM*, *66*, 2002.

ASTM International. (2020). ASTM G59-97(2020). Standard test method for conducting potentiodynamic polarisation resistance measurements. *ASTM International*, *97*(Reapproved 2020).

ASTM Standard G102-89. (1999). Standard practice for calculation of corrosion rates and related information from electrochemical measurements.

ASTM Standard E92-17. (2017). Standard test methods for Vickers hardness and Knoop hardness of metallic materials.

Atapek, S. H., Tumer, M., Çelikkol, E., Kısasöz, A., & Kerimak, M. Z. (2023). Microstructural, mechanical and corrosion behavior of UNS S31803/Hastelloy C-276 dissimilar metal welds. CIRP *Journal of Manufacturing Science and Technology*, *40*, 129–141.

Atapour, M., Pilchak, A., Frankel, G. S., Williams, J. C., Fathi, M. H., & Shamanian, M. (2010). Corrosion behaviour of Ti-6Al-4V with different thermomechanical treatments and microstructures. *Corrosion*, *66*(6), 065004–9.

Avinash, B., Subramanian, K. M., & Rajkumar, V. (2023). Mechanical properties and corrosion behavior of Inconel 617 superalloy fabricated by wire arc additive manufacturing. *Journal of Materials Engineering and Performance*, *32*, 6270–6280.

Azarbarmas, M., Aghaie-Khafri, M., Cabrera, J. M., & Calvo, J. (2016). Dynamic recrystallisation mechanisms and twining evolution during hot deformation of Inconel 718. *Materials Science and Engineering A*, *678*, 137–152.

Bachani, S. K., Wang, C. J., Lou, B. S., Chang, L. C., & Lee, J. W. (2020). Microstructural characterisation, mechanical property and corrosion behaviour of VNbMoTaWAl refractory high entropy alloy coatings: Effect of Al content. *Surface and Coatings Technology*, *403*, 126351.

Bai, Z. C., Ding, X. F., Hu, Q., Yang, M., Fan, Z. T., & Liu, X. W. (2021). The unique deformation behaviour and microstructure evolution in high-temperature processing of a low-density $TiAlVNb_2$ refractory high-entropy alloy. *Journal of Alloys and Compounds*, *885*, 160962.

Bambach, M., Sizova, I., Silze, F., & Schnick, M. (2018). Hot workability and microstructure evolution of the nickel-based superalloy Inconel 718 produced by laser metal deposition. *Journal of Alloys and Compounds*, *740*, 278–287.

Barrett, C. A. (1988). Effect of 0.1 at.% zirconium on the cyclic oxidation resistance of NiAI. In *Oxidation of Metals* (Vol. 30, Issue 5), 1–30.

Behera, A. N., Kapoor, R., Sarkar, A., & Chakravartty, J. K. (2014). Hot deformation behaviour of niobium in temperature range 700-1500°C. *Materials Science and Technology*, *30*(6), 637–644.

Besozzi, E., Dellasega, D., Russo, V., Conti, C., Passoni, M., & Beghi, M. G. (2019). Thermomechanical properties of amorphous metallic tungsten-oxygen and tungsten-oxide coatings. *Materials and Design*, *165*, 107565.

Bhardwaj, V., Zhou, Q., Zhang, F., Han, W., Du, Y., Hua, K., & Wang, H. (2021). Effect of Al addition on the microstructure, mechanical and wear properties of TiZrNbHf refractory high entropy alloys. *Tribology International*, *160*, 107031.

Bi, D., Chang, Y., Luo, H., Pan, Z., Zhao, Q., Cheng, H., Wang, X., Qiao, C., Ni, Z., Liu, A., & Li, X. (2023). Corrosion behaviour and passive film characteristics of $AlNbTiZrSi_x$ high-entropy alloys in simulated seawater environment. *Corrosion Science*, *224*, 111530.

Birks, N., Heiler, G. H., & Pettit, F. (2006). *Introduction to the high temperature oxidation of metals* (2nd ed.). Cambridge University Press, 1-352.

Bodunrin, M. O., Chown, L. H., van der Merwe, J. W., & Alaneme, K. K. (2020). On the substitution of vanadium with iron in Ti–6Al–4V: Thermo-Calc simulation and processing map considerations for design of low-cost alloys. *Materials Science & Engineering A*, *791*, 139622.

Bodunrin, M. O., Chown, L. H., van der Merwe, J. W., & Alaneme, K. K. (2020). Hot working behaviour of experimental Ti-4.5Al-1V-3Fe alloy with initial lamellar microstructure. *International Journal of Advanced Manufacturing Technology*, *106*(5–6), 1901–1916.

Bodunrin, M. O., Obadele, B. A., Chown, L. H., & Olubambi, P. A. (2017). Corrosion behaviour of Al-Fe-Ti-V medium entropy alloy. *IOP Conference Series: Materials Science and Engineering*, *272*, 012028.

Brechtl, J., Chen, S., Lee, C., Shi, Y., Feng, R., Xie, X., Hamblin, D., Coleman, A. M., Straka, B., Shortt, H., Spurling, R. J., & Liaw, P. K. (2020). A review of the serrated-flow phenomenon and its role in the deformation behaviour of high-entropy alloys. *Metals*, *10*(8), 1101.

Brewer, L. (1974). Prediction of transition metal phase diagrams. *Journal of Nuclear Materials*, *51*, 2–11.

Brotzu, A., Felli, F., Marra, F., Pilone, D., & Pulci, G. (2018). Mechanical properties of a TiAl-based alloy at room and high temperatures. *Materials Science and Technology*, *34*(15), 1847–1853.

Buranich, V. (2020). Predicting the properties of the refractory high-entropy alloys for additive manufacturing-based fabrication and mechatronic applications. *Nanomaterials: Applications & Properties*, 9–13.

Butler, T. M., & Chaput, K. J. (2019). Native oxidation resistance of $Al_{20}Nb_{30}Ta_{10}Ti_{30}Zr_{10}$ refractory complex concentrated alloy (RCCA). *Journal of Alloys and Compounds*, *787*, 606–617.

Butler, T. M., Chaput, K. J., Dietrich, J. R., & Senkov, O. N. (2017). High temperature oxidation behaviours of equimolar NbTiZrV and NbTiZrCr refractory complex concentrated alloys (RCCAs). *Journal of Alloys and Compounds*, *729*, 1004–1019.

Butler, T. M., Senkov, O. N., Daboiku, T. I., Velez, M. A., Schroader, H. E., Ware, L. G., Titus, S., & Titus, M. S. (2022). Oxidation behaviours of CrNb, CrNbTi, and CrNbTaTi concentrated refractory alloys. *Intermetallics*, *140*, 107374.

Butler, T. M., Senkov, O. N., Velez, M. A., & Daboiku, T. I. (2021). Microstructures and mechanical properties of CrNb, CrNbTi, and CrNbTaTi concentrated refractory alloys. *Intermetallics*, *138*, 107323.

Cantor, B., Chang, I. T. H., Knight, P., & Vincent, A. J. B. (2004). Microstructural development in equiatomic multicomponent alloys. *Materials Science Engineering A*, *375–377*, 213–218.

Cao, Y., Liu, Y., Liu, B., Zhang, W. Dong, W, Wen, J., & Du, M. (2019). Effects of Al and Mo on high temperature oxidation behaviour of refractory high entropy alloys. *Transactions of Nonferrous Metals Society of China (English Edition)*, *29*(7), 1476–1483.

Cao, Y., Zhang, W., Liu, B., Liu, Y., Du, M., & Fu, A. (2021). Phase decomposition behaviour and its effects on mechanical properties of $TiNbTa_{0.5}ZrAl_{0.5}$ refractory high entropy alloy. *Journal of Materials Science and Technology*, *66*, 10–20.

Cattano, G. (2019). *Feasibility studies on Laser Powder Bed Fusion of powders mixtures based on Aluminium Alloys or High Entropy Alloys* [Doctoral Dissertation]. Politecnico di Torino, Italy.

Chan, K. S. (1997). A mechanics-based approach to cyclic oxidation. *Metallurgical and Materials Transactions*, *28*, 1–12.

Chang, C., Titus, M. S., & Yeh, J. (2018). Oxidation behaviour between 700 and 1300°C of refractory TiZrNbHfTa high-entropy alloys containing aluminum. *Advanced Engineering Materials*, *1700948*, 411–422.

Chang, Y. W., Huang, M. H., & Lin, C. W. (2015). Evolution of research subjects in library and information science based on keyword, bibliographical coupling, and co-citation analyses. *Scientometrics*, *105*(3), 2071–2087.

Chen, G. X., Yi, J., Xixi L., Xiubing H., Yongle, C., Zhihai L., Tong, Y. (2021). Effects of Zr content on the microstructure and performance of $TiMoNbZr_x$ high-entropy alloys. *Metals*, *11(8)*, 1315.

Chen, H., Kauffmann, A., Gorr, B., Schliephake, D., Seemüller, C., Wagner, J. N., Christ, H. J., & Heilmaier, M. (2016). Microstructure and mechanical properties at elevated temperatures of a new Al-containing refractory high-entropy alloy Nb-Mo-Cr-Ti-Al. *Journal of Alloys and Compounds*, *661*, 206–215.

Chen, H., Mao, H., & Chen, Q. (2018). Database development and CALPHAD calculations for high entropy alloys: Challenges, strategies, and tips. *Materials Chemistry and Physics*, *210*, 279–290.

Chen, M., Lin, S., Yeh, J., & Chen, S. (2006). Effect of vanadium addition on the microstructure, hardness, and wear resistance of $Al_{0.5}CoCrCuFeNi$ high-entropy alloy. *Metallurgical and Materials Transactions A*, *37A*, 1363–1369.

Chen, C. L. and Sutrisna (2021). Study of NiFeCoCr medium entropy alloy as a binder phase on W–Mo heavy tungsten alloy by secondary ball milling. *Intermetallics*, *138*, 107320.

Chen, S. H., Zhang, J. S., Guan, S., Li, T., Liu, J. Q., Wu, F. F., & Wu, Y. C. (2022). Microstructure and mechanical properties of $WNbMoTaZr_x$ (x = 0.1, 0.3, 0.5, 1.0) refractory high entropy alloys. *Materials Science & Engineering A*, *835*, 142701.

Chen, S. Y., Yang, X., Dahmen, K. A., Liaw, P. K., & Zhang, Y. (2014). Microstructures and crackling noise of $Al_xNbTiMoV$ high entropy alloys. *Entropy*, *16*(2), 870–884.

Chen, X. M., Lin, Y. C., Wen, D. X., Zhang, J. L., & He, M. (2014). Dynamic recrystallisation behaviour of a typical nickel-based superalloy during hot deformation. *Materials and Design*, *57*, 568–577.

Chen, Y., Li, Y., Cheng, X., Wu, C., Cheng, B., & Xu, Z. (2018). The microstructure and mechanical properties of refractory high-entropy alloys with high plasticity. *Materials*, *11*(2), 208.

Chen, Y., Li, Y., Cheng, X., Xu, Z., Wu, C., Cheng, B., & Wang, M. (2018). Interstitial strengthening of refractory $ZrTiHfNb_{0.5}Ta0.5O_x$ (X= 0.05, 0.1, 0.2) high-entropy alloys. *Materials Letters*, *228*, 145–147.

Chen, Y. W., Li, Y. K., Cheng, X. W., Wu, C., & Cheng, B. (2018). High-temperature mechanical properties and microstructure of $ZrTiHfNbMo_x$ (x=0.5, 1.0, 1.5) refractory high entropy alloys. *IOP Conference Series: Materials Science and Engineering*, *359*, 012033.

Cheng, C. Y., Yang, Y. C., Zhong, Y. Z., Chen, Y. Y., Hsu, T., & Yeh, J. W. (2017). Physical metallurgy of concentrated solid solutions from low-entropy to high-entropy alloys. *Current Opinion in Solid State and Materials Science*, *21*(6), 299–311.

Chigilipalli, B. K., & Veeramani, A. (2024). Investigation of microstructural properties and mechanical behavior of wire arc additively manufactured Incoloy 825. *Journal of Materials Engineering and Performance*, *33*, 2837–2852.

Ciszak, C., Popa, I., Brossard, J. M., Monceau, D., & Chevalier, S. (2016). NaCl induced corrosion of Ti-6Al-4V alloy at high temperature. *Corrosion Science*, *110*, 91–104.

Coury, F. G., Butler, T., Chaput, K., Saville, A., Copley, J., Foltz, J., Mason, P., Clarke, K., Kaufman, M., & Clarke, A. (2018). Phase equilibria, mechanical properties and design of quaternary refractory high entropy alloys. *Materials and Design*, *155*, 244–256.

Coury, F. G., Kaufman, M., & Clarke, A. J. (2019). Solid-solution strengthening in refractory high entropy alloys. *Acta Materialia*, *175*, 66–81.

Cui, D., Zhang, Y., Liu, L., Li, Y., Wang, L., Wang, Z., Li, J., Wang, J., & He, F. (2023). Oxygen-assisted spinodal structure achieves 1.5 GPa yield strength in a ductile refractory high-entropy alloy. *Journal of Materials Science and Technology*, *157*, 11–20.

Dada, M., Popoola, P., Mathe, N., Pityana, S., Adeosun, S., Aramide, O., & Lengopeng, T. (2020). Process optimization of high entropy alloys by laser additive manufacturing. *Engineering Reports*, *2*(10), 1–17.

Davis, J. R. (2000). Corrosion: understanding the basics. In *Choice Reviews Online* (Vol. 37, Issue 11), ASM International.

Delgado-Alvarado, C., & Sundaram, P. A. (2020). A study of the corrosion behavior of gamma titanium aluminide in 3.5 wt% NaCl solution and seawater. *Corrosion Science*, *49*(9), 3732–3741.

Dobbelstein, H., George, E. P., Gurevich, E. L., Kostka, A., Ostendorf, A., & Laplanche, G. (2020). Laser metal deposition of refractory high-entropy alloys for high-throughput synthesis and structure-property characterisation. *International Journal of Extreme Manufacturing*, *3*, 1–23.

Dobbelstein, H., Gurevich, E. L., George, E. P., Ostendorf, A., & Laplanche, G. (2019). Laser metal deposition of compositionally graded TiZrNbTa refractory high-entropy alloys using elemental powder blends. *Additive Manufacturing*, *25*, 252–262.

Doherty, R. D., Hughes, D. A., Humphreys, F. J., Jonas, J. J., Juul Jensen, D., Kassner, M. E., King, W. E., McNelley, T. R., McQueen, H. J., & Rollett, A. D. (1997). Current issues in Recrystallisation: A review. *Materials Science & Engineering A*, *238*, 219–274.

Dong, F., Yuan, Y., Li, W., Zhang, Y., Liaw, P. K., Yuan, X., & Huang, H. (2020). Hot deformation behaviour and processing maps of an equiatomic MoNbHfZrTi refractory high entropy alloy. *Intermetallics*, *126*, 106921.

Du, Y., Ding, D., Lai, L., Xiao, S., Guo, N., Song, B., & Guo, S. (2022). Effect of Y on the high-temperature oxidation behaviour of CrMoTaTi refractory high entropy alloy. *International Journal of Refractory Metals and Hard Materials*, *103*, 105755.

Eleti, R. R. (2019). *Deformation Mechanisms and Microstructure Evolution in HfNbTaTiZr High Entropy Alloy during Thermo-mechanical Processing at Elevated Temperatures* [PhD Thesis]. Kyoto University, Japan.

Eleti, R. R., Bhattacharjee, T., Shibata, A., & Tsuji, N. (2019). Unique deformation behaviour and microstructure evolution in high temperature processing of HfNbTaTiZr refractory high entropy alloy. *Acta Materialia*, *171*, 132–145.

Eleti, R. R., Chokshi, A. H., Shibata, A., & Tsuji, N. (2020). Unique high-temperature deformation dominated by grain boundary sliding in heterogeneous necklace structure formed by dynamic recrystallisation in HfNbTaTiZr BCC refractory high entropy alloy. *Acta Materialia*, *183*, 64–77.

Fang, L., Wang, J., Li, X., Tao, X., Ouyang, Y., & Du, Y. (2022). Effect of Cr content on microstructure characteristics and mechanical properties of $ZrNbTaHf_{0.2}Cr_x$ refractory high entropy alloy. *Journal of Alloys and Compounds*, *924*, 166593.

Feng, R., Feng, B., Gao, M. C., Zhang, C., Neuefeind, J. C., Poplawsky, J. D., Ren, Y., An, K., Widom, M., & Liaw, P. K. (2021). Superior high-temperature strength in a supersaturated refractory high-entropy alloy. *Advanced Materials*, *33*, 1–9.

Frankel, G. S., Li, T., & Scully, J. R. (2017). Perspective—localised corrosion: Passive film breakdown vs pit growth stability. *Journal of The Electrochemical Society*, *164*(4), C180–C181.

Fu, Y., Li, J., Luo, H., Du, C., & Li, X. (2021). Recent advances on environmental corrosion behaviour and mechanism of high-entropy alloys. *Journal of Materials Science and Technology*, *80*, 217–233.

Gajalappa, Y., Krishnaiah, A., Kumar, B., Eswaranna, K. K. S., & Goyal, P. (2021). Flow behaviour kinetics of Inconel 600 superalloy under hot deformation using Gleeble 3800. *Materials Today: Proceedings*, *45*(6), 5320–5322.

Galindo-Nava, E. I., & Rivera-Dıaz-del-Castillo, P. E. J. (2012). Modelling plastic deformation in BCC metals: Dynamic recovery and cell formation effects. *Materials Science & Engineering A*, *558*, 641–648.

Gaona-Tiburcio, C., Aguilar, L. M. R., Robledo, P. Z., López, F. E., Cabral Miramontes, J. A., Nieves-Mendoza, D., Castillo-González, E., & Almeraya-Calderón, F. (2021).

Electrochemical noise analysis of nickel-based superalloys in acid solutions. *Materials Today: Proceedings, 45*(6), 5320–5322.

Ganji, D. K., & Rajyalakshmi, G. (2020). Influence of alloying compositions on the properties of nickel-based superalloys: A review. *Lecture Notes in Mechanical Engineering*, 537–555.

Gao, M. C., Carney, C. S., Doğan, N., Jablonksi, P. D., Hawk, J. A., & Alman, D. E. (2015). Design of refractory high-entropy alloys. *Jom, 67*(11), 2653–2669.

Gao, Y., Chong, K., Liu, C., Cao, Y., Wu, D., & Zou, Y. (2024). Electrochemical corrosion and high temperature hot corrosion behaviour of NbTaTiV and CrNbTaTiV high entropy alloy. *Journal of Materials Research and Technology*, *28*, 216–234.

Gao, Y., Chong, K., Qiao, L., Li, Y., Liu, C., Guo, F., Wu, D., & Zou, Y. (2023). Synthesis and corrosion behaviour of $Mo_{15}Nb_{20}Ta_{10}Ti_{35}V_{20}$ refractory high entropy alloy. *Materials & Design, 228*, 111820.

Garg, M., Grewal, H. S., Sharma, R. K., Gwalani, B., & Arora, H. S. (2022). High oxidation resistance of AlCoCrFeNi high entropy alloy through severe shear deformation processing. *Journal of Alloys and Compounds*, *917*, 165385.

George, E. P., Curtin, W. A., & Tasan, C. C. (2020). High entropy alloys: A focused review of mechanical properties and deformation mechanisms. *Acta Materialia*, *188*, 435–474.

Gorr, B., Müller, F., Azim, M., Christ, H. J., Müller, T., Chen, H., Kauffmann, A., & Heilmaier, M. (2017). High-temperature oxidation behaviour of refractory high-entropy alloys: Effect of alloy composition. *Oxidation of Metals*, *88*(3–4), 339–349.

Gorr, B., Müller, F., Schellert, S., Christ, H. J., Chen, H., Kauffmann, A., & Heilmaier, M. (2020). A new strategy to intrinsically protect refractory metal-based alloys at ultra-high temperatures. *Corrosion Science*, *166*, 108475.

Gorr, B., Schellert, S., Müller, F., Christ, H., Kauffmann, A., & Heilmaier, M. (2021). Current status of research on the oxidation behaviour of refractory high entropy alloys. *Advanced Engineering Materials*, *23*, 1–14.

Gromov, V. E., Konovalov, S. V, Ivanov, Y. F., & Osintsev, K. A. (2021). *Advanced Structured Materials Structure and Properties of High-Entropy Alloys*. (Vol. 107, 2nd Ed.), Springer Nature Switzerland.

Guo, N. N., Luo, L. S., Su, Y. Q., & Guo, J. J. (2014). Microstructure and mechanical properties of ZrNbMoHfV high entropy alloy. *Materials Research Innovations*, *18*, S4766–S4769.

Guo, N. N., Wang, L., Luo, L. S., Li, X. Z., Chen, R. R., Su, Y. Q., Guo, J. J., & Fu, H. Z. (2016). Hot deformation characteristics and dynamic recrystallisation of the MoNbHfZrTi refractory high-entropy alloy. *Materials Science and Engineering A*, *651*, 698–707.

Guo, N. N., Wang, L., Luo, L. S., Li, X. Z., Chen, R. R., Su, Y. Q., Guo, J. J., & Fu, H. Z. (2016). Microstructure and mechanical properties of refractory high entropy ($Mo_{0.5}NbHf_{0.5}ZrTi$)BCC/M_5Si_3 in-situ compound. *Journal of Alloys and Compounds*, *660*, 197–203.

Guo, S., Ng, C., Lu, J., & Liu, C. T. (2011). Effect of valence electron concentration on stability of FCC or BCC phase in high entropy alloys. *Journal of Applied Physics*, *109*, 103505.

Guo, Y., He, J., Lu, W., Jia, L., & Li, Z. (2021). The evolution of compositional and microstructural heterogeneities in a $TaMo_{0.5}ZrTi_{1.5}Al_{0.1}Si_{0.2}$ high entropy alloy. *Materials Characterisation*, *172*, 110836.

Gupta, R. K, Pant, B., Kumar, V., Agarwala, V., & Sinha, P. P. (2013). Deformation behaviour of γ+α2 Ti aluminide processed through reaction synthesis. *Materials Science and Engineering A*, *559*, 49–67.

Han, J., Su, B., Lu, J., Meng, J., Zhang, A., & Wu, Y. (2020). Preparation of MoNbTaW refractory high entropy alloy powders by pressureless spark plasma sintering: Crystal structure and phase evolution. *Intermetallics*, *123*, 106832.

Han, Z. D., Chen, N., Zhao, S. F., Fan, L. W., Yang, G. N., Shao, Y., & Yao, K. F. (2017). Effect of Ti additions on mechanical properties of NbMoTaW and VNbMoTaW refractory high entropy alloys. *Intermetallics*, *84*, 153–157.

Hamdi, H., Abedi, H. R., & Zhang, Y. (2023). A review study on thermal stability of high entropy alloys: Normal/abnormal resistance of grain growth. *Journal of Alloys and Compounds*, *960*, 170826.

Hashim, A. A., Hammood, A. S., & Hammadi, N. J. (2015). Evaluation of high-temperature oxidation behaviour of Inconel 600 and Hastelloy C-22. *Arabian Journal for Science and Engineering*, *40*(9), 2739–2746.

Heersmink, R., van den Hoven, J., van Eck, N. J., & van Berg, J. D. (2011). Bibliometric mapping of computer and information ethics. *Ethics and Information Technology*, *13*(3), 241–249.

Hillert, M. (1993). Gibbs' phase rule applied to phase diagrams and transformations. *Journal of Phase Equilibria*, *14*(4), 418–424.

Holcomb, G. R., Tylczak, J., & Carney, C. (2015). Oxidation of CoCrFeMnNi high entropy alloys. *JOM*, *67*(10), 2326–2339.

Hou, Q. Q., Huang, K., Luo, L. M., Tan, X. Y., Zan, X., Xu, Q., Zhu, X. Y., & Wu, Y. C. (2019). Microstructure and its high temperature oxidation behaviour of W-Cr alloys prepared by spark plasma sintering. *Materialia*, *6*, 100332.

Tung, H. M., Chen, T. L., Lan, K. C., Liu, P. W., & Li, Y. C. (2024). The incipient oxidation behaviours of Haynes 282 at high temperatures. *Materials Chemistry and Physics*, 316, 129109.

Hsu, W. C., Shen, T. E., Liang, Y. C., Yeh, J. W., & Tsai, C. W. (2019). In situ analysis of the Portevin-Le Chatelier effect from low to high-entropy alloy in equal HfNbTaTiZr system. *Acta Materialia*, *253*, 118981.

Hu, M. I., Song, W. D., Duan, D. B., & Wu, Y. (2020). Dynamic behaviour and microstructure characterisation of TaNbHfZrTi high-entropy alloy at a wide range of strain rates and temperatures. *International Journal of Mechanical Sciences*, *182*, 1–12.

Huang, K., & Logé, R. E. (2016). A review of dynamic recrystallisation phenomena in metallic materials. *Materials and Design*, *111*, 548–574.

Huang, W., Yin, S., Wang, X., Guo, R., Wu, Y., & Qiao, J. (2019). Grain growth and Hall–Petch relationship in $Ti_{37}V_{15}Nb_{22}Hf_{23}W_3$ refractory high-entropy alloys. *Journal of Materials Research*, *38*, 1719–1729.

Huang, W., Yang, J., Yang, H., Jing, G., Wang, Z., & Zeng, X. (2019). Heat treatment of Inconel 718 produced by selective laser melting: Microstructure and mechanical properties. *Materials Science & Engineering A*, *750*, 98–107.

Huang, T., Wu, S., Jiang, H., Lu, Y., Wang, T., & Li, T. (2020). Effect of Ti content on microstructure and properties of Ti_xZrVNb refractory high-entropy alloys. *International Journal of Minerals, Metallurgy and Materials*, *27*(10), 1318–1331.

Humphreys, F. J., & Hatherly, M. (2004). Hot deformation and dynamic restoration. In M. B. T. R. and R. A. P. F. J. Humphreys (Ed.), *Recrystallisation and Related Annealing Phenomena* (2nd Ed., pp. 415–451). Elsevier.

Hussein, M., & Zayed, T. (2021). Crane operations and planning in modular integrated construction: Mixed review of literature. *Automation in Construction*, *122*, 103466.

Iturbe, A., Giraud, E., Hormaetxe, E., Garay, A., Ostolaza, K., Arrazola, P. J., Iturbe, A., Giraud, E., Hormaetxe, E., Garay, A., & Germain, G. (2017). Mechanical characterisation and modelling of Inconel 718 material behaviour for machining process assessment. *Materials Science and Engineering A*, *682*, 441–453.

Ivanov, I. A., Ryskulov, A., Kurakhmedov, A., Kozlovskiy, A., Shlimas, D., Zdorovets, M. V., Uglov, V. V., Zlotski, S. V., & Ke, J. (2021). Radiation swelling and hardness of high-entropy alloys based on the TiTaNbV system irradiated with krypton ions. *Journal of Materials Science: Materials in Electronics*, *32*(23), 27260–27267.

Jachmann, F., & Hucho, C. (2005). High elastic modulus in b-axis-oriented single crystal V_2O_5. *Solid State Communications*, *135*(7), 440–443.

Jahangiri, H., Mohagheghi, S., Asghari Alamdari, A., Gürcan Bayrak, K., Ayas, E., Ünal, U., & Motallebzadeh, A. (2023). High temperature oxidation behaviour of the AlCrFeMnTi light-weight high-entropy alloy. *ACS Applied Engineering Materials*, *1*(7), 1766–1774.

Jayaraj, J., Thinaharan, C., Ningshen, S., Mallika, C., & Kamachi Mudali, U. (2017). Corrosion behaviour and surface film characterisation of TaNbHfZrTi high entropy alloy in aggressive nitric acid medium. *Intermetallics*, *89*, 123–132.

Jayaraj, J., Thirathipviwat, P., Han, J., & Gebert, A. (2018). Microstructure, mechanical and thermal oxidation behaviour of AlNbTiZr high entropy alloy. *Intermetallics*, *100*, 9–19.

Jeong, H., Kim, S. H., Choi, W. S., & Choi, P. P. (2018). Spallation resistance of oxide scales on Alloy 617 enhanced by boron addition. *Corrosion Science*, *140*, 196–204.

Ji, F., Wang, Z., & Wu, L. (2022). High temperature oxidation and hot corrosion behaviours of $Fe_{65.7}Ni_{11.7}Ti_1Mo_{6.6}Co_{15}$ high entropy alloy. *Materials Today Communications*, *32*, 104063

Jia, Y., Zhang, L., Li, P., Ma, X., Xu, L., Wu, S., & Jia, Y. (2020). Microstructure and mechanical properties of Nb–Ti–V– Zr refractory medium-entropy alloys. *Frontiers in Materials*, *7*, 00172.

Jiang, H., Tian, S., Guo, W., Zhang, G., & Zeng, S. (2018). A hot deformation behaviour and deformation mechanism of two TiAl-Mo alloys during hot compression. *Materials Science & Engineering A*, *719*, 104–111.

Jonas, J. J., Sellars, C. M., & Tegart, W. J. (1969). Strength and structure under hot-working conditions. *Metallurgical Reviews*, *14*(1), 1–24.

Juan, C. C., Tsai, M. H., Tsai, C. W., Lin, C. M., Wang, W. R., Yang, C. C., Chen, S. K., Lin, S. J., & Yeh, J. W. (2015). Enhanced mechanical properties of HfMoTaTiZr and HfMoNbTaTiZr refractory high-entropy alloys. *Intermetallics*, *62*, 76–83.

Kafri, A., Makonovitsky, A., & Shneck, R. Z. (2018). On the mechanism of oxidation resistance of W-Cr-Pd alloys. *Defect and Diffusion Forum*, *383*, 133–141.

Kai, W., Cheng, F. P., Lin, Y. R., Chuang, C. W., Huang, R. T., Chen, D., Kai, J. J., Liu, C. T., & Wang, C. J. (2020). The oxidation behaviour of $Ni_2FeCoCrAl_x$ high-entropy alloys in dry air. *Journal of Alloys and Compounds*, *836*, 1–12.

Kai, W., Li, C. C., Cheng, F. P., Chu, K. P., Huang, R. T., Tsay, L. W., & Kai, J. J. (2016). The oxidation behaviour of an equimolar FeCoNiCrMn high-entropy alloy at 950°C in various oxygen-containing atmospheres. *Corrosion Science*, *108*, 209–214.

Kaibyshev, R., Goloborodko, A., Musin, F., Nikulin, I., & Sakai, T. (2002). The role of grain boundary sliding in microstructural evolution during superplastic deformation of a 7055 Aluminum alloy. *Materials Transactions*, *43*(10), 2408–2414.

Kalali, D. G., Antharam, S., Hasan, M., Karthik, P. S., Phani, P. S., Rao, K. B. S., & Rajulapati, K. (2020). On the origins of ultra-high hardness and strain gradient plasticity in

multi-phase nanocrystalline MoNbTaTiW based refractory high-entropy alloy. *Materials Science and Engineering A, 812*, 141098.

Kanchi, A., Rajulapati, K. V., Rao, B. S., Sivaprahasam, D., & Gundakaram, R. C. (2022). Influence of thermomechanical processing on microstructure and mechanical properties of MoNbTaW refractory high-entropy alloy. *Journal of Materials Engineering and Performance*, *31*(10), 7964–7972.

Kang, B., Kong, T., Ryu, H. J., & Hong, S. H. (2021). Superior mechanical properties and strengthening mechanisms of lightweight $Al_xCrNbVMo$ refractory high-entropy alloys (x = 0, 0.5, 1.0) fabricated by the powder metallurgy process. *Journal of Materials Science and Technology*, *69*, 32–41.

Kang, J., Liu, H., Du, H., Shi, J., Wang, L., Yang, L., & Dai, H. (2023). Microstructure, mechanical properties, electrical resistivity, and corrosion behaviour of $(AlCr)_x(HfMoNbZr)1\text{-}x$ films. *Applied Surface Science*, *629*, 157368.

Katz-Demyanetz, A., Gorbachev, I. I., Eshed, E., Popov, V. V., Popov, V. V., & Bamberger, M. (2020). High entropy $Al_{0.5}CrMoNbTa_{0.5}$ alloy: Additive manufacturing vs. casting vs. CALPHAD approval calculations. *Materials Characterization*, *167*, 110505.

Keshavarz, S., Zandrahimi, M., & Ebrahimifar, H. (2018). Isothermal and cyclic oxidation behaviour of AISI 430 ferritic stainless steel coated with titanium. *Journal of Advanced Materials and Processing*, *6*(2), 12–23.

Khanna, A. S. (2016). Fundamentals of high temperature oxidation/corrosion. *High Temperature Corrosion*, 1–31.

Khudzari, J., Kurian, J., Tartakovsky, B., & Raghavan, G. S. V. (2018). Bibliometric analysis of global research trends on microbial fuel cells using Scopus database. *Biochemical Engineering Journal*, *136*, 51–60.

Kuang, J., Zhang, P., Wang, Q., Hu, Z., Liang, X., & Shen, B. (2022). Formation and oxidation behaviour of refractory high-entropy silicide $(NbMoTaW)Si_2$ coating. *Corrosion Science*, *198*, 110134.

Kumar, D., Maulik, O., Sharma, V. K., Prasad, Y. V. S. S., & Kumar, V. (2018). Understanding the effect of tungsten on corrosion behaviour of $AlCuCrFeMnW_x$ high-entropy alloys in 3.5 wt% NaCl solution. *Journal of Materials Engineering and Performance*, *27*(9), 4481–4488.

Latu-Romain, L., Parsa, Y., Mathieu, S., Vilasi, M., & Wouters, Y. (2018). Chromia scale thermally grown on pure chromium under controlled $p(O_2)$ Atmosphere: I. spallation investigation using photoelectrochemical techniques at a mesoscale. *Oxidation of Metals*, *90*(3–4), 255–266.

Lee, Y. S. and Cava, R. J. (2019). Superconductivity in high and medium entropy alloys based on MoReRu. *Physica C: Superconductivity and its Applications*, *566*, 1353520.

Lee, C., Kim, G., Chou, Y. C., Musicó, B. L., Gao, M. C., An, K., Song, G., Chou, Y. C., Keppens, V., Chen, W., & Liaw, P. K. (2020). Temperature dependence of elastic and plastic deformation behaviour of a refractory high-entropy alloy. *Science Advances*, *6*(37), 1–12.

Lekakh, S. N., Neroslavsky, O., Li, M., Godlewski, L., & Zhu, W. (2023). Effect of spallation on oxidation kinetics of heat-resistant Cr–Ni austenitic steels on air and combustion atmosphere. *High Temperature Corrosion of Materials*, *99*(1–2), 79–99.

Li, B. Y., Peng, K., Hu, A. P., Zhou, L. P., Zhu, J. J., & Li, D. Y. (2013). Structure and properties of $FeCoNiCrCu_{0.5}Al_x$ high-entropy alloy. *Transactions of Nonferrous Metals Society of China (English Edition)*, *23*(3), 735–741.

Li, D., Chen, J., Etim, I. P., Liu, Y., Wu, C., Wang, J., & Su, X. (2013). High temperature oxidation behavior of Ni-based superalloy Nimonic95 and the effect of pre-oxidation treatment. *Vacuum*, *194*, 110582.

Li, J., Yang, X., Zhu, R., & Zhang, Y. (2014). Corrosion and serration behaviours of $TiZr_{0.5}NbCr_{0.5}V_xMo_y$ high entropy alloys in aqueous environments. *Metals*, *4*(4), 597–608.

Li, M., Chen, Q., Cui, X., Peng, X., & Huang, G. (2021). Evaluation of corrosion resistance of the single-phase light refractory high entropy alloy $TiCrVNb_{0.5}Al_{0.5}$ in chloride environment. *Journal of Alloys and Compounds*, *857*, 158278.

Li, Q., Ma, T., Jin, Y., Wang, X., Dong, D., & Zhu, D. (2021). Effect of Sn and Mo on microstructure and electrochemical property of TiZrTaNb high entropy alloys. *Crystals*, *11*(12), 1527.

Li, Q., Zhang, H., Li, D., Wang, X., Chen, Z., & Huang, S. (2019). Manufacture of WNbMoTa high performance high-entropy alloy by laser additive manufacturing. *Jixie Gongcheng Xuebao/Journal of Mechanical Engineering*, *55*(15), 10–16.

Li, T., Lu, Y., Li, Z., Wang, T., & Li, T. (2022). Hot deformation behaviour and microstructure evolution of non-equimolar $Ti_2ZrHfV_{0.5}Ta_{0.2}$ refractory high-entropy alloy. *Intermetallics*, *146*, 107586.

Li, T., Miao, J., Lu, Y., Wang, T., & Li, T. (2022). Effect of Zr on the as-cast microstructure and mechanical properties of lightweight $Ti_2VNbMoZr_x$ refractory high-entropy alloys. *International Journal of Refractory Metals and Hard Materials*, *103*, 105762.

Li, T., Swanson, O. J., Frankel, G. S., Gerard, A. Y., Lu, P., Saal, J. E., & Scully, J. R. (2019). Localised corrosion behaviour of a single-phase non-equimolar high entropy alloy. *Electrochimica Acta*, *306*, 71–84.

Li, T. T., Jiao, W., Miao, J., Lu, Y., Guo, E., Wang, T., Li, T. T., & Liaw, P. K. (2021). A novel ZrNbMoTaW refractory high-entropy alloy with in-situ forming heterogeneous structure. *Materials Science and Engineering A*, *827*, 142061.

Li, X., Fu, A., Cao, Y., Xu, S., & Gao, S. (2022). High-temperature mechanical properties and deformation behaviour of carbides reinforced TiNbTaZrHf composite. *Journal of Alloys and Compounds*, *894*, 1–10.

Li, Z., Wang, L., Wang, B., Li, Z., Li, Z., Zhang, Y., Luo, L., Chen, R., Su, Y., & Guo, J. (2022). Oxidation behaviour of Ti-Nb-Mo-Al-Si_x refractory high entropy alloy at 1000°C. *Corrosion Science*, *206*, 110504.

Liang, H., Guo, H., Nan, Y., Qin, C., Peng, X., & Zhang, J. (2014). The construction of constitutive model and identification of dynamic softening mechanism of high-temperature deformation of Ti–5Al–5Mo–5V–1Cr–1Fe alloy. *Materials Science and Engineering: A*, *615*, 42–50.

Lilensten, L., Couzinié, J. P., Perrière, L., Bourgon, J., Emery, N., & Guillot, I. (2014). New structure in refractory high-entropy alloys. *Materials Letters*, *132*, 123–125.

Lin, Y. C., Chen, M. S., & Zhong, J. (2008). Constitutive modeling for elevated temperature flow behaviour of 42CrMo steel. *Computational Materials Science*, *42*(3), 470–477.

Lin, Y. C., Chen, M.S., & Zhong, J. (2008). Microstructural evolution in 42CrMo steel during compression at elevated temperatures. *Materials Letters*, *62*(14), 2132–2135.

Lin, Y. C., & Chen, X. M. (2011). A critical review of experimental results and constitutive descriptions for metals and alloys in hot working. *Materials and Design*, *32*(4), 1733–1759.

Liskiewicz, T., Liskiewicz, G., & Paczesny, J. (2021). Factors affecting the citations of papers in tribology journals. *Scientometrics*, *126*(4), 3321–3336.

Liu, C., Gao, Y., Chong, K., Guo, F., Wu, D., & Zou, Y. (2023). Effect of Nb content on the microstructure and corrosion resistance of $FeCoCrNiNb_x$ high-entropy alloys in chloride ion environment. *Journal of Alloys and Compounds*, *935*, 168013.

Liu, C. M., Wang, H. M., Zhang, S. Q., Tang, H. B., & Zhang, A. L. (2014). Microstructure and oxidation behaviour of new refractory high entropy alloys. *Journal of Alloys and Compounds*, *583*, 162–169.

Liu, C. T., Ma, J., & Sun, X. F. (2010). Oxidation behaviour of a single-crystal Ni-base superalloy between 900 and 1000°C in air. *Journal of Alloys and Compounds*, *491*(1–2), 522–526.

Liu, J., Chen, Y., & Zhang, J. (2019). Oxidation behaviour of Ni–Mo–Si alloy coatings fabricated on carbon steel by laser cladding. *Surface and Coatings Technology*, *375*, 903–910.

Liu, K., Li, X., Wang, J., Zhang, Y., Guo, X., Wu, S., & Yu, H. (2023). Investigation of mechanical and corrosion properties of light and high hardness cast $AlTiVCrCu_{0.4}$ high entropy alloy. *Materials Characterisation*, *200*, 112878.

Liu, Q., Wang, G., Liu, Y., Sui, X., Chen, Y., & Luo, S. (2021). Hot deformation behaviours of an ultrafine-grained MoNbTaTiV refractory high-entropy alloy fabricated by powder metallurgy. *Materials Science and Engineering A*, *809*, 1–10.

Liu, X. W., Bai, Z. C., Ding, X. F., Yao, J. Q., Wang, L., Su, Y. Q., Fan, Z. T., & Guo, J. J. (2021). A novel light-weight refractory high-entropy alloy with high specific strength and intrinsic deformability. *Materials Letters*, *287*, 1–4.

Lo, K. C., Chang, Y. J., Murakami, H., Yeh, J. W., & Yeh, A. C. (2019). An oxidation resistant refractory high entropy alloy protected by $CrTaO_4$-based oxide. *Scientific Reports*, *9*(1), 3–4.

Lo, K. C., Murakami, H., Yeh, J. W., & Yeh, A. C. (2020). Oxidation behaviour of a novel refractory high entropy alloy at elevated temperatures. *Intermetallics*, *119*, 1–6.

Lo, K. C., Yeh, A. C., & Murakami, H. (2018). Microstructural investigation of oxidised complex refractory high entropy alloys. *Materials Transactions*, *59*(4), 556–562.

Luo, H., Li, Z., Mingers, A. M., & Raabe, D. (2018). Corrosion behaviour of an equiatomic CoCrFeMnNi high-entropy alloy compared with 304 stainless steels in sulfuric acid solution. *Corrosion Science*, *134*, 131–139.

Luo, S., Huang, W., Yang, H., Yang, J., Wang, Z., & Zeng, X. (2019). Microstructural evolution and corrosion behaviors of Inconel 718 alloy produced by selective laser melting following different heat treatments. *Additive Manufacturing*, *30*, 100875.

Luton, M. J., & Sellars, C. M. (1969). Dynamic recrystallisation in nickel and nickel-iron alloys during high temperature deformation. *Acta Metallurgica*, *17*, 1033–1042.

Maiti, S., & Steurer, W. (2014). Structure and properties of refractory high-entropy alloys. *TMS Annual Meeting*, 1093–1097.

Makhmutov, T., Razumov, N., Kim, A., Ozerskoy, N., Mazeeva, A., & Popovich, A. (2021). Synthesis of $CoCrFeNiMnW_{0.25}$ high-entropy alloy powders by mechanical alloying and plasma spheroidisation processes for additive manufacturing. *Metals and Materials International*, *27*(1), 50–54.

Mao, H., Chen, H. L., & Chen, Q. (2017). TCHEA1: A thermodynamic database not limited for "high entropy" alloys. *Journal of Phase Equilibria and Diffusion*, *38*(4), 353–368.

Maruyama, T., & Yanagihara, K. (1997). High temperature oxidation and pesting of $Mo(Si,Al)_2$. *Materials Science and Engineering A*, *239–240*(1–2), 828–841.

Massih, A. R. (2013). High-temperature creep and superplasticity in zirconium alloys. *Journal of Nuclear Science and Technology*, *50*(1), 21–34.

McQueen, H. J., & Imbert, C. A. C. (2004). Dynamic recrystallisation: Plasticity enhancing structural development. *Journal of Alloys and Compounds*, *378*(1–2), 35–43.

McQueen, H. J., & Ryan, N. D. (2002). Constitutive analysis in hot working. *Materials Science and Engineering A*, *322*(1–2), 43–63.

Medeiros, S. C., Frazier, W. G., & Prasad, Y. V. R. K. (1999). Hot deformation mechanisms in a powder metallurgy nickel base superalloy IN625. *Metallurgical and Materials Transactions* A, *31*, 2000–2317.

Meng, G., Gao, R., Fenghua, L., & Yu, J. (2022). MoNbV, MoNbVTi and MoNbVTiHf multicomponent refractory alloys—Compositional modulated mechanical properties investigating. *Materials Today Communications*, *33*, 104320.

Melia, M. A., Whetten, S. R., Puckett, R., Jones, M., Heiden, M. J., Argibay, N., & Kustas, A. B. (2020). High-throughput additive manufacturing and characterisation of refractory high entropy alloys. *Applied Materials Today*, *19*, 100560.

Mevrel, R. (1986). Cyclic oxidation of high-temperature alloys. *Materials Science and Technology*, *3*(7), 531–535.

Mingjie, Z., Fuguo, L., Shuyun, W., & Chenyi, L. (2010). Characterization of hot deformation behavior of a P/M nickel-base superalloy using processing map and activation energy. *Materials Science and Engineering A*, *527*(24–25), 6771–6779.

Miracle, D. B. (2019). High entropy alloys as a bold step forward in alloy development. *Nature Communications*, *10*, 1805.

Miracle, D. B., Miller, J. D., Senkov, O. N., Woodward, C., Uchic, M. D., & Tiley, J. (2014). Exploration and development of high entropy alloys for structural applications. *Entropy*, *16*, 494–525.

Miracle, D. B., & Senkov, O. N. (2017). A critical review of high entropy alloys and related concepts. *Acta Materialia*, *122*, 448–511.

Mirzaee, M., Khodabandeh, A. R., & Ebrahimi, G. (2022). Influence of strain rate on the interactions between precipitation and recrystallization during hot deformation of ni-based superalloy Nimonic 80A. *Journal of Materials Engineering and Performance*, *31*, 1803–1817.

Mishra, R. S., Haridas, R. S., & Agrawal, P. (2021). High entropy alloys – tunability of deformation mechanisms through integration of compositional and microstructural domains. *Materials Science and Engineering A*, *812*, 141085.

Miura, S., Murasato, Y., Sekito, Y., Tsutsumi, Y., Ohkubo, K., Kimura, Y., Mishima, Y., & Mohri, T. (2009). Effect of microstructure on the high-temperature deformation behaviour of Nb-Si alloys. *Materials Science and Engineering A*, *510–511*(C), 317–321.

Mizutani, U. (2011). *Hume-Rothery Rules for Structurally Complex Alloy Phases* (1st ed.). CRC Press.

Moghaddam, A. O., Sudarikov, M., Shaburova, N., Zherebtsov, D., Zhivulin, V., Ashurali Solizoda, I., Starikov, A., Veselkov, S., Samoilova, O., & Trofimov, E. (2022). High temperature oxidation resistance of W-containing high entropy alloys. *Journal of Alloys and Compounds, 897,* 162733.

Moon, C.O., & Lee, S.B. (1993). Analysis on failures of protective-oxide layers and cyclic oxidation. *Oxidation of Metals*, *39*(2), 1–13.

Moorehead, M., Bertsch, K., Niezgoda, M., Parkin, C., Elbakhshwan, M., Sridharan, K., Zhang, C., Thoma, D., & Couet, A. (2020). High-throughput synthesis of Mo-Nb-Ta-W high-entropy alloys via additive manufacturing. *Materials and Design*, *187,* 108358.

Mosoma, D., Klenam, D., Maunganidze, T., & Bodunrin, M. (2023). Hot working behaviour of low-cost Ti-3.4Fe bio-implant alloy. *The International Journal of Advanced Manufacturing Technology*, *126,* 2025–2036.

Motallebzadeh, A., Peighambardoust, N. S., Sheikh, S., Murakami, H., Guo, S., & Canadinc, D. (2019). Microstructural, mechanical and electrochemical characterisation of TiZrTaHfNb and $Ti_{1.5}ZrTa_{0.5}Hf_{0.5}Nb_{0.5}$ refractory high-entropy alloys for biomedical applications. *Intermetallics*, *113,* 106572.

Müller, F., Gorr, B., Christ, H. J., Chen, H., Kauffmann, A., & Heilmaier, M. (2018). Effect of microalloying with silicon on high temperature oxidation resistance of novel refractory high-entropy alloy Ta-Mo-Cr-Ti-Al. *Materials at High Temperatures*, *35*(1–3), 168–176.

Müller, F., Gorr, B., Christ, H. J., Chen, H., Kauffmann, A., & Heilmaier, M. (2020). Effect of Y additions on the oxidation behaviour of novel refractory high-entropy alloy NbMoCrTiAl at 1000°C in air. *Oxidation of Metals*, *94*(1–2), 147–163.

Müller, F., Gorr, B., Christ, H. J., Müller, J., Butz, B., Chen, H., Kauffmann, A., & Heilmaier, M. (2019). On the oxidation mechanism of refractory high entropy alloys. *Corrosion Science*, *159,* 1–11.

Murmey, P., Nichul, U., Chikode, M., & Hiwarkar, V. (2023). Effect of post-processing on corrosion behaviour of LPBF built Inconel 718 alloy. *JOM*, *75*(1), 32–44.

Murty, B. S., Yeh, J. W., & Ranganathan, S. (2014). *High-Entropy Alloys* (1st ed.). Butterworth-Heinemann.

Nascimento, C. B., Donatus, U., Ríos, C. T., De Oliveira, M. C. L., & Antunes, R. A. (2022). A review on corrosion of high entropy alloys: Exploring the interplay between corrosion properties, alloy composition, passive film stability and materials selection. *Materials Research*, *25,* 0442.

Neto, M. Q., & Rainforth, W. M. (2020). Effect of potential and microstructure on the tribocorrosion behaviour of beta and near beta Ti alloys I. *Biotribology*, *2,* 100141.

Nie, X. W., Cai, M. D., & Cai, S. (2021). Microstructure and mechanical properties of a novel refractory high entropy alloy HfMoScTaZr. *International Journal of Refractory Metals and Hard Materials*, *98*, 1–9.

Nong, Z. S., Lei, Y. N., & Zhu, J. C. (2018). Wear and oxidation resistances of AlCrFeNiTi-based high entropy alloys. *Intermetallics*, *101*, 144–151.

Nyby, C., Guo, X., Saal, J. E., Chien, S. C., Gerard, A. Y., Ke, H., Li, T., Lu, P., Oberdorfer, C., Sahu, S., Li, S., Taylor, C. D., Windl, W., Scully, J. R., & Frankel, G. S. (2021). Electrochemical metrics for corrosion resistant alloys. *Scientific Data*, *8*(1), 58.

Otto, F., Yang, Y., Bei, H., & George, E. P. (2013). Relative effects of enthalpy and entropy on the phase stability of equiatomic high-entropy alloys. *Acta Materialia*, *61*(7), 2628–2638.

Ouyang, D., Chen, Z. J., Yu, H. B., Chan, K. C., & Liu, L. (2022). Oxidation behaviour of the $Ti_{38}V_{15}Nb_{23}Hf_{24}$ refractory high-entropy alloy at elevated temperatures. *Corrosion Science*, *198*, 110513.

Ouyang, G. (2017). High temperature structure materials beyond nickel base superalloy. *Journal of Materials Science and Nanomaterials*, *1*(2), 8–9.

Pandey, A., Awasthi, A., & Saxena, K. K. (2020). Metallic implants with properties and latest production techniques: a review. *Advances in Materials and Processing Technologies*, *6*(2), 167–202.

Pang, J., Zhang, H. H., Zhang, L., Zhu, Z., Fu, H., Li, H., Wang, A., Li, Z., & Zhang, H. H. (2022). A ductile $Nb_{40}Ti_{25}Al_{15}V_{10}Ta_5Hf_3W_2$ refractory high entropy alloy with high specific strength for high-temperature applications. *Materials Science and Engineering A*, *831*, 1–9.

Panicaud, B., Grosseau-Poussard, J. L., & Dinhut, J. F. (2006). On the growth strain origin and stress evolution prediction during oxidation of metals. *Applied Surface Science*, *252*(16), 5700–5713.

Parkhutik, V. P. (2006). Oscillations of open-circuit potential during immersion plating of silicon in $CuSO_4$/HF solutions. *Russian Journal of Electrochemistry*, *42*(5), 512–522.

Patel, K., Sadeghilaridjani, M., Pole, M., & Mukherjee, S. (2021). Hot corrosion behaviour of refractory high entropy alloys in molten chloride salt for concentrating solar power systems. *Solar Energy Materials and Solar Cells*, *230*, *111222*.

Peng, Z., Li, B., Luo, Z., Chen, X., Tang, Y., Yang, G., & Gong, P. (2023). A lightweight $AlCrTiV_{0.5}Cu_x$ high-entropy alloy with excellent corrosion resistance. *Materials*, *16*(7), 2922.

Pickering, E. J., & Jones, N. G. (2016). Founding principles and future prospects high-entropy alloys: A critical assessment of their founding principles and future prospects. *International Materials Reviews*, *61*(3), 1–21.

Poliak, E. I., & Jonas, J. J. (2003). Initiation of dynamic recrystallisation in constant strain rate hot deformation. *ISIJ International*, *43*(5), 684–691.

Popovich, V. A., Borisov, E. V., Popovich, A. A, Sufiiarov, V. S., Masaylob, D. V., & Alzin, L. (2017). Impact of heat treatment on mechanical behaviour of Inconel 718 processed with tailored microstructure by selective laser melting. *Materials & Design*, *131*, 12–22.

Pouilleau, J., Devilliers, D., Garrido, F., Durand-Vidal, S., & Mahé, E. (1997). Structure and composition of passive titanium oxide films. *Materials Science and Engineering B*, *47*(3), 235–245.

Poulia, A., Georgatis, E., Lekatou, A., & Karantzalis, A. E. (2016). Microstructure and wear behaviour of a refractory high entropy alloy. *International Journal of Refractory Metals and Hard Materials*, *57*, 50–63.

Poulia, A., Mathiou, C., & Karantzalis, A. (2019). Electrochemical study of MoTaNbVTi high entropy alloy in aqueous environments. *Annales de Chimie: Science Des Materiaux*, *43*(4), 199–205.

Pourbaix, M. (1974). Applications of electrochemistry in corrosion science and in practice. *Corrosion Science*, *14*(1), 25–82.

Prasad, Y. V. R. K., & Seshacharyulu, T. (1998). Modelling of hot deformation for microstructural control. *International Materials Reviews*, *43*(6), 243–258.

Presuel-Moreno, F., Jakab, M. A., Tailleart, N., Goldman, M., & Scully, J. R. (2008). Corrosion-resistant metallic coatings. *Materials Today*, *11*(10), 14–23.

Qiao, D., Liang, H., Wu, S., He, J., Cao, Z., Lu, Y., & Li, T. (2021). The mechanical and oxidation properties of novel B2-ordered $Ti_2ZrHf_{0.5}VNb_{0.5}Al_x$ refractory high-entropy alloys. *Materials Characterisation*, *178*, 111287.

Qiu, Y., Thomas, S., Gibson, M. A., Fraser, H. L., & Birbilis, N. (2017). Corrosion of high entropy alloys. *Npj Materials Degradation*, 1–17.

Qiu, Y., Thomas, S., Gibson, M. A., Fraser, H. L., Pohl, K., & Birbilis, N. (2018). Microstructure and corrosion properties of the low-density single-phase compositionally complex alloy AlTiVCr. *Corrosion Science*, *133*, 386–396.

Qu, J., Long, B., Nan, D., Hui, W., Qing, W., Zeng, W., & Zhang, J. (2011). Hot deformation behaviour of nickel-based superalloy GH4720Li. *Journal of Iron and Steel Research International*, *18*(10), 59–65.

Quan, G. Z., Wang, Y., Liu, Y. Y., & Zhou, J. (2013). Effect of temperatures and strain rates on the average size of grains refined by dynamic recrystallisation for as-extruded 42CrMo steel. *Materials Research*, *16*(5), 1092–1105.

Rabadia, C. D., Liu, Y. J., Jawed, S. F., Wang, L., Li, Y. H., Zhang, X. H., Sercombe, T. B., Sun, H., & Zhang, L. C. (2018). Improved deformation behaviour in Ti-Zr-Fe-Mn alloys comprising the C14 type Laves and β phases. *Materials and Design*, *160*, 1059–1070.

Rajkumar, V., Vishnukumar, M., & Sowrirajan, A. (2022). Microstructure, mechanical properties and corrosion behaviour of Incoloy 825 manufactured using wire arc additive manufacturing. *Vacuum*, *203*, 111324.

Raman, L., Anupam, A., Karthick, G., Berndt, C. C., Siao, A., Ang, M., Murty, S. V. S. N., Fabijanic, D., Murty, B. S., & Sankar, R. (2021). A strengthening mechanism in CrMoNbTiW refractory high entropy alloy. *Materials Science & Engineering A*, *819*, 1–10.

Razumov, N., Makhmutov, T., Kim, A., Shemyakinsky, B., Shakhmatov, A., Popovich, V., & Popovich, A. (2021). Refractory CrMoNbWV high-entropy alloy manufactured by mechanical alloying and spark plasma sintering: Evolution of microstructure and properties. *Materials*, *14*(3), 621.

Rajkumar, V., Vishnukumar, M., Sowrirajan, M., & Kannan, A. R. (2021). Microstructure, mechanical properties and corrosion behaviour of Incoloy 825 manufactured using wire arc additive manufacturing. *Vacuum*, *203*, 111324.

Reed, R. C. (2006). *The superalloys fundamentals and applications* (1st ed.). Cambridge University Press.

Rodriguez, P. (1984). Serrated plastic flow. *Bulletin Materials Science*, *6*(4), 653–663.

Roy, A., Sreeramagiri, P., Babuska, T., Krick, B., Ray, P. K., & Balasubramanian, G. (2021). Lattice distortion as an estimator of solid solution strengthening in high-entropy alloys. *Materials Characterisation*, *172*, 110877.

Saber, D., Islam, S. E., & Abdel-Karim, R. (2017). High temperature cyclic oxidation of Ni based superalloys at different temperatures in air. Journal of Alloys and Compounds, *719*, 133–141.

Sajjadi, S. A., Chaichi, A., Ezatpour, H. R., Maghsoudlou, A., & Kalaie, M. A. (2016). Hot deformation processing map and microstructural evaluation of the Ni-based superalloy IN-738LC. *Journal of Materials Engineering and Performance*, *25*(4), 1269–1275.

Sakai, T. (1995). Materials Processing Technology. *Journal of Materials Processing Technology*, *53*, 349–361.

Sakai, T., Belyakov, A., Kaibyshev, R., Miura, H., & Jonas, J. J. (2014). Dynamic and post-dynamic recrystallisation under hot, cold and severe plastic deformation conditions. *Progress in Materials Science*, *60*(1), 130–207.

Sakai, T., & Jonas, J. (1984). Dynamic recrystallisation: Mechanical and microstructural considerations. *Acta Metallurgica*, *32*(2), 189–209.

Sakai, T., & Jonas, J. J. (2001). Plastic deformation: Role of recovery and recrystallisation. *Encyclopedia of Materials: Science and Technology*, 7079–7084.

Samal, S., Rahul, M. R., Kottada, R. S., & Phanikumar, G. (2016). Hot deformation behaviour and processing map of Co-Cu-Fe-Ni-Ti eutectic high entropy alloy. *Materials Science and Engineering A*, *664*, 227–235.

Sathiyamoorthi, P., Bae, J. W., Asghari-Rad, P., Park, J. M., Kim, J. G., & Kim, H. S. (2018). Effect of annealing on microstructure and tensile behaviour of CoCrNi medium entropy alloy processed by high-pressure torsion. *Entropy*, *20(11)*, 1–11.

Saunders, N., & Miodownik, A. P. (1998). *CALPHAD (Calculation of Phase Diagrams): A Comprehensive Guide* (Vol. 1).

Saxena, K. K., Yadav, S. D., Sonkar, S., Pancholi, V., Chaudhari, G. P., Srivastava, D., Dey, G. K., Jha, S. K., & Saibaba, N. (2014). Effect of temperature and strain rate on deformation behaviour of zirconium alloy: Zr-2.5Nb. *Procedia Materials Science*, *6*, 278–283.

Schellert, S., Weber, M., Christ, H. J., Wiktor, C., Butz, B., Galetz, M. C., Laube, S., Kauffmann, A., Heilmaier, M., & Gorr, B. (2023). Formation of rutile (Cr,Ta,Ti)O_2 oxides during oxidation of refractory high entropy alloys in Ta-Mo-Cr-Ti-Al system. *Corrosion Science*, *211*, 110885.

Sellars, C. M., & Tegart, W. J. M. (1972). Hot workability. *International Metallurgical Reviews*, *17*(1), 1–24.

Senkov, O. N., Couzinie, J. P., Rao, S. I., Soni, V., & Banerjee, R. (2020). Temperature dependent deformation behaviour and strengthening mechanisms in a low density refractory high entropy alloy $Al_{10}Nb_{15}Ta_5Ti_{30}Zr_{40}$. *Materialia*, *9*, 100627.

Senkov, O. N., Gild, J., & Butler, T. M. (2021). Microstructure, mechanical properties and oxidation behaviour of NbTaTi and NbTaZr refractory alloys. *Journal of Alloys and Compounds*, *862*, 158003.

Senkov, O. N., Isheim, D., Seidman, D. N., & Pilchak, A. L. (2016). Development of a refractory high entropy superalloy. *Entropy*, *18*(3), 102.

Senkov, O. N., Miracle, D. B., Chaput, K. J., & Couzinie, J. P. (2018). Development and exploration of refractory high entropy alloys - A review. *Journal of Materials Research*, *33*(19), 3092–3128.

Senkov, O. N., Scott, J. M., Senkova, S. V, Meisenkothen, F., Miracle, D. B., & Woodward, C. F. (2012). Microstructure and elevated temperature properties of a refractory TaNbHfZrTi alloy. *Journal of Materials Science*, *47*, 4062–4074.

Senkov, O. N., Scott, J. M., Senkova, S. V, Miracle, D. B., & Woodward, C. F. (2011). Microstructure and room temperature properties of a high-entropy TaNbHfZrTi alloy. *Journal of Alloys and Compounds*, *509*(20), 6043–6048.

Senkov, O. N., & Semiatin, S. L. (2015). Microstructure and properties of a refractory high-entropy alloy after cold working. *Journal of Alloys and Compounds*, *649*, 1110–1123.

Senkov, O. N., Senkova, S. V., Dimiduk, D. M., Woodward, C., & Miracle, D. B. (2012). Oxidation behaviour of a refractory $NbCrMo_{0.5}Ta_{0.5}TiZr$ alloy. *Journal of Materials Science*, *47*(18), 6522–6534.

Senkov, O. N., Senkova, S. V, Miracle, D. B., & Woodward, C. (2013). Mechanical properties of low-density, refractory multi-principal element alloys of the Cr-Nb-Ti-V-Zr system. *Materials Science & Engineering A*, *565*, 51–62.

Senkov, O. N., Senkova, S. V., & Woodward, C. (2014). Effect of aluminum on the microstructure and properties of two refractory high-entropy alloys. *Acta Materialia*, *68*, 214–228.

Senkov, O. N., Senkova, S. V, Woodward, C., & Miracle, D. B. (2013). Low-density, refractory multi-principal element alloys of the Cr–Nb–Ti–V–Zr system: Microstructure and phase analysis. *Acta Materialia*, *61*(5), 1545–1557.

Senkov, O. N., Wilks, G. B., Miracle, D. B., Chuang, C. P., & Liaw, P. K. (2010). Refractory high-entropy alloys. *Intermetallics*, *18*(9), 1758–1765.

Senkov, O. N., Wilks, G. B., Scott, J. M., & Miracle, D. B. (2011). Mechanical properties of $Nb_{25}Mo_{25}Ta_{25}W_{25}$ and $V_{20}Nb_{20}Mo_{20}Ta_{20}W_{20}$ refractory high entropy alloys. *Intermetallics*, *19*(5), 698–706.

Senkov, O. N., & Woodward, C. F. (2011). Microstructure and properties of a refractory $NbCrMo_{0.5}Ta_{0.5}TiZr$ alloy. *Materials Science and Engineering A*, *529*(1), 311–320.

Senkov, O. N., Woodward, C., & Miracle, D. B. (2014). Microstructure and properties of aluminum-containing refractory high-entropy alloys. *JOM*, *66*(10), 2030–2042.

Seshacharyulu, T., Medeiros, S. C., Frazier, W. G., & Prasad, Y. V. R. K. (2002). Microstructural mechanisms during hot working of commercial grade Ti-6Al-4V with lamellar starting structure. *Materials Science and Engineering*, *A325*, 112–125.

Sharghi-Moshtaghin, R., & Asgari, S. (2008). The characteristics of serrated flow in superalloy IN738LC. *Materials Science and Engineering A*, *486*(1–2), 376–380.

Shaw, B. A., & Kelly, R. G. (2006). What is corrosion? *Electrochemical Society Interface*, *15*(1), 24–26.

Sheikh, S. (2016). Alloy Design and Optimization of Mechanical Properties of High-Entropy Alloys. *PhD Thesis. Chalmers Tekniska Hogskola (Sweden)*.

Sheikh, S., Bijaksana, M. K., Motallebzadeh, A., Shafeie, S., Lozinko, A., Gan, L., Tsao, T. K., Klement, U., Canadinc, D., Murakami, H., & Guo, S. (2018). Accelerated oxidation in ductile refractory high-entropy alloys. *Intermetallics*, *97*, 58–66.

Sheikh, S., Gan, L., Ikeda, A., Murakami, H., & Guo, S. (2020). Alloying effect on the oxidation behaviour of a ductile $Al_{0.5}Cr_{0.25}Nb_{0.5}Ta_{0.5}Ti_{1.5}$ refractory high-entropy alloy. *Materials Today Advances*, *7*, 1–12.

Sheikh, S., Shafeie, S., Hu, Q., Ahlström, J., Persson, C., Veselý, J., Zýka, J., Klement, U., & Guo, S. (2016). Alloy design for intrinsically ductile refractory high-entropy alloys. *Journal of Applied Physics*, *120*(16), 1–5.

Shi, Z. X., Yan, X. F., Duan, C. H., Song, J. G., Zhao, M. H., & Wang, J. (2017). Hot deformation behavior of GH4945 superalloy using constitutive equation and processing map. *Journal of Iron and Steel Research, International*, *24*(6), 625–633.

Shi, Y., Yang, B., & Liaw, P. K. (2017). Corrosion-resistant high-entropy alloys: A review. *Metals*, *7*(43), 1–18.

Shi, Y., Yang, B., Xie, X., Brechtl, J., Dahmen, K. A., & Liaw, P. K. (2017). Corrosion of $Al_xCoCrFeNi$ high-entropy alloys: Al-content and potential scan-rate dependent pitting behaviour. *Corrosion Science*, *119*, 33–45.

Shkodich, N., Sedegov, A., Kuskov, K., Busurin, S., Scheck, Y., Vadchenko, S., & Moskovskikh, D. (2020). Refractory high-entropy HfTaTiNbZr-based alloys by combined use of ball milling and spark plasma sintering: Effect of milling intensity. *Metals*, *10*(9), 1–15.

Singh, A. K., & Subramaniam, A. (2014). On the formation of disordered solid solutions in multi-component alloys. *Journal of Alloys and Compounds*, *587*, 113–119.

Song, F., & White, B. E. (2014). *Growth of ultra-thin vanadium dioxide thin films using magnetron sputtering*. *PhD Thesis. University of New York*.

Song, G. L. (2014). The grand challenges in electrochemical corrosion research. *Frontiers in Materials*, *1*, 1–2.

Stepanov, N. D., Yurchenko, N. Y., Gridneva, A. O., Zherebtsov, S. V., Ivanisenko, Y. V., & Salishchev, G. A. (2018). Structure and hardness of B2 ordered refractory $AlNbTiVZr_{0.5}$ high entropy alloy after high-pressure torsion. *Materials Science and Engineering A*, *716*, 308–315.

Stepanov, N. D., Yurchenko, N. Y., Skibin, D. V, Tikhonovsky, M. A., & Salishchev, G. A. (2015). Structure and mechanical properties of the $AlCr_xNbTiV$ (x= 0, 0.5, 1, 1.5) high entropy alloys. *Journal of Alloys and Compounds*, *652*, 266–280.

Su, R., Zhang, H., Ouyang, G., Liu, L., Johnson, D. D., & Perepezko, J. H. (2023). Oxidation mechanism in a refractory multiple-principal-element alloy at high temperature. *Acta Materialia*, *246*, 118719.

Sun, B., Xia, M., Zhang, Z. Bin, Liang, X. B., & Shen, B. L. (2020). Property tuning and additive manufacturing of refractory high-entropy alloys. *Cailiao Gongcheng/Journal of Materials Engineering*, *48*(10), 1–16.

Sun, B., Zhang, T., Shi, J. Wang, B., & Zhang, X. (2020). Microstructural evolution during exposure in air and oxidation behavior of a nickel-based superalloy. *Vacuum*, *183*, 109801.

Sun, P., Wang, D., Song, W., Tang, C., Yang, J., Xu, Z., Hu, Q., & Zeng, X. (2023). Influence of W content on microstructure and corrosion behaviour of laser cladded Inconel 718 coating. *Surface and Coatings Technology*, *452*, 129079.

Swanson, O. (2018). Corrosion of High-Entropy Alloys in Chloride Solutions. *Master's Dissertation*. Graduate School of The Ohio State University.

Tahamtan, I., Askar, A. S., & Ahamdzadeh, K. (2016). Factors affecting number of citations: a comprehensive review of the literature. *Scientometrics*, *107*, 1195–1225.

Telu, S., Mitra, R., & Pabi, S. K. (2013). High temperature oxidation behaviour of W-Cr-Nb alloys in the temperature range of 800-1200°C. *International Journal of Refractory Metals and Hard Materials*, *38*, 47–59.

Terms, C. (2014). *Alloy Phase Diagram Database ™ Introduction to Phase Diagrams*. 1–24.

Terner, M., Biamino, S., & Baudana, G. (2015). Initial oxidation behavior in Air of TiAl-2Nb and TiAl-8Nb alloys produced by electron beam melting. *Journal of Material Engineering and Performance*, *24*, 3982–3988.

Thermo-Calc Database, G. (2006). *Thermo-Calc Database Guide*.

Tomashov, N. D. (1964). Passivity and corrosion resistance of metal systems. *Corrosion Science*, *4*(1–4), 315–334.

Tong, C., Chen, M., Chen, S., Yeh, J., Shun, T., Lin, S., & Chang, S. (2005). Mechanical performance of the $Al_xCoCrCuFeNi$ high-entropy alloy system with multiprincipal elements. *Metallurgical and Materials Transactions A*, *36*, 1263–1271.

Tong, Y., Bai, L., Liang, X., Chen, Y., Zhang, Z., Liu, J., Li, Y., & Hu, Y. (2020). Influence of alloying elements on mechanical and electronic properties of $NbMoTaW_X$ (X= Cr , Zr , V , Hf and Re) refractory high entropy alloys. *Intermetallics*, *126*, 1–9.

Tong, Y., Bai, L., Liang, X., Hua, M., Liu, J., Li, Y., Zhang, J., & Hu, Y. (2021). Mechanical performance of $(NbTaW)_1{-}xMo_x$ (x = 0, 0.05, 0.15, 0.25) refractory high entropy alloys: Perspective from experiments and first principles calculations. *Journal of Alloys and Compounds*, *873*, 1–11.

Troparevsky, M. C., Morris, J. R., Wang, Y., Lupini, A. R., & Malcolm, G. (2015). Beyond atomic sizes and Hume-Rothery rules: Understanding and predicting high-entropy alloys. JOM, *67*(10), 2350–2363.

Tsai, C. W., Chen, Y. L., Tsai, M. H., Yeh, J. W., Shun, T. T., & Chen, S. K. (2009). Deformation and annealing behaviours of high-entropy alloy $Al_{0.5}CoCrCuFeNi$. *Journal of Alloys and Compounds*, *486*(1–2), 427–435.

Tsai, M. H., & Yeh, J. W. (2014). High-entropy alloys: A critical review. *Materials Research Letters*, *2*(3), 107–123.

Tsau, C. H., & Wang, W. L. (2018). Microstructures, hardness and corrosion behaviours of $FeCoNiNb_{0.5}Mo_{0.5}$ and FeCoNiNb high-entropy alloys. *Materials*, *11*(16), 1–12.

Tseng, K. K., Juan, C. C., Tso, S., Chen, H. C., Tsai, C. W., & Yeh, J. W. (2019). Effects of Mo, Nb, Ta, Ti, and Zr on mechanical properties of equiatomic Hf-Mo-Nb-Ta-Ti-Zr alloys. *Entropy*, *21*(1), 15.

Tümer, M., Mert, T., & Karahan, T. (2021). Investigation of microstructure, mechanical, and corrosion behavior of nickel-based alloy 625/duplex stainless steel UNS S32205 dissimilar weldments using ERNiCrMo-3 filler metal. *Weld World*, *65*, 171–182.

Umut Tukac, O., Ozalp, A., & Aydogan, E. (2022). Development and thermal stability of $Cr_{10}Mo_{25}Ta_{25}Ti_{15}V_{25}$ refractory high entropy alloys. *Journal of Alloys and Compounds*, *930*, 167386.

Uporov, S., Sterkhov, E. and Balyakin, I. (2022). Magnetocaloric effect in ScGdHo medium-entropy alloy, *Journal of Superconductivity and Novel Magnetism*, *35*, 1539–1545.

van Eck, N. J., & Waltman, L. (2007). Bibliometric mapping of the computational intelligence field. *International Journal of Uncertainty, Fuzziness and Knowlege-Based Systems*, *15*(5), 625–645.

van Eck, N. J., & Waltman, L. (2010). Software survey: VOSviewer, a computer program for bibliometric mapping. *Scientometrics*, *84*(2), 523–538.

van Eck, N. J., & Waltman, L. (2014a). Visualizing bibliometric networks. In Y. Ding, R. Rousseau, & D. Wolfram (Eds.), *Measuring Scholarly Impact* (pp. 285–320). Springer, Cham.

van Eck, N. J., & Waltman, L. (2020). VOSviewer Manual version 1.6.16. In *Univeristeit Leiden* (Issue November, pp. 1–52).

Varalakshmi, S., Appa Rao, G., Kamaraj, M., & Murty, B. S. (2010). Hot consolidation and mechanical properties of nanocrystalline equiatomic AlFeTiCrZnCu high entropy alloy after mechanical alloying. *Journal of Materials Science*, *45*(19), 5158–5163.

Varalakshmi, S., Kamaraj, M., & Murty, B. S. (2008). Synthesis and characterisation of nanocrystalline AlFeTiCrZnCu high entropy solid solution by mechanical alloying. *Journal of Alloys and Compounds*, *460*(1–2), 253–257.

Vieira, E. S., & Gomes, J. A. N. F. (2009). A comparison of Scopus and Web of Science for a typical university. *Scientometrics*, *81*(2), 587–600.

Wan, Y., Mo, J., Wang, X., Zhang, Z., Shen, B., & Liang, X. (2021). Mechanical properties and phase stability of WTaMoNbTi refractory high-entropy alloy at elevated temperatures. *Acta Metallurgica Sinica (English Letters)*, *34*(11), 1585–1590.

Wan, Y., Wang, Q., Mo, J., Zhang, Z., Wang, X., Liang, X., & Shen, B. (2021). WReTaMo refractory high-entropy alloy with high strength at 1600°C. *Advanced Engineering Materials*, *24*, 1–8.

Wang, B., Shan, X., Zhao, H., Bai, S., Wang, B., Tian, Y., & Tang, Y. (2023). High-temperature deformation behaviour and microstructural evolution of NbZrTiTa refractory high entropy alloy. *Journal of Alloys and Compounds*, *936*, 168059.

Wang, B., Wang, Q., Lu, N., Liang, X., & Shen, B. (2022). Enhanced high-temperature strength of HfNbTaTiZrV refractory high-entropy alloy via Al_2O_3 reinforcement. *Journal of Materials Science and Technology*, *123*, 191–200.

Wang, B., Zhao, H., Shan, X., Tang, Y., Wang, B., & Tian, Y. (2023). Hot deformation behaviour and dynamic recrystallisation mechanism of $Ti_2ZrTa_{0.75}$ refractory complex concentrated alloy. *Materials Characterisation*, *203*, 113061.

Wang, J., Xue, H., & Wang, Y. (2021). Oxidation behavior of Ni-based superalloy GH738 in static air between 800 and 1000°C. *Rare Metals*, *40*, 616–625.

Wang, L., Wang, X., Zhu, X., Xu, X., Cui, J., Liao, B., Wang, X., & Wu, X. (2019). Role of vanadium addition on hot deformation behaviour of aluminum alloy 5083. *Metals*, *9*(7), 766.

Wang, M., Ma, Z. L., Xu, Z. Q., & Cheng, X. W. (2021). Designing V_xNbMoTa refractory high-entropy alloys with improved properties for high-temperature applications. *Scripta Materialia*, *191*, 131–136.

Wang, M., Ma, Z., Xu, Z., & Cheng, X. (2019). Microstructures and mechanical properties of HfNbTaTiZrW and HfNbTaTiZrMoW refractory high-entropy alloys. *Journal of Alloys and Compounds*, *803*, 778–785.

Wang, P., Wang, Y., Cui, F., Yang, X., Pan, A., & Wu, W. (2022). Microstructural evolution, mechanical properties and corrosion resistance of $CoCrFeNiW_{0.5}$ high entropy alloys with various annealing heat treatment. *Journal of Alloys and Compounds*, *918*, 165602.

Wang, Y., Jin, J., Zhang, M., Wang, X., Gong, P., Zhang, J., & Liu, J. (2021). Effect of the grain size on the corrosion behaviour of CoCrFeMnNi HEAs in a 0.5 M H_2SO_4 solution. *Journal of Alloys and Compounds*, *858*, 157712.

Wang, Y. L., Zhao, L., Wan, D., Guan, S., & Chan, K. C. (2021). Additive manufacturing of TiB_2-containing CoCrFeMnNi high-entropy alloy matrix composites with high density and enhanced mechanical properties. *Materials Science and Engineering A*, *825*, 141871.

Wang, Y., Zhang, M., Jin, J., Gong, P., & Wang, X. (2020). Oxidation behaviour of CoCrFeMnNi high entropy alloy after plastic deformation. *Corrosion Science*, *163*, 108285.

Wang, Z., Yan, Y., Wu, Y., Huang, X., Zhang, Y., Su, Y., & Qiao, L. (2022). Corrosion and tribocorrosion behaviour of equiatomic refractory medium entropy TiZr(Hf, Ta, Nb) alloys in chloride solutions. *Corrosion Science*, *199*(30), 110166.

Wang, Z., Yang, Y., Li, B., Zhang, Y., & Zhang, Z. (2013). Effect of hot-deformation on microstructure and mechanical properties of AZ80 magnesium alloy. *Materials Science & Engineering A*, *582*, 36–40.

Waseem, O. A., Auyeskhan, U., Lee, H. M., & Ryu, H. J. (2018). A combinatorial approach for the synthesis and analysis of $Al_xCr_yMo_zNbTiZr$ high-entropy alloys: Oxidation behaviour. *Journal of Materials Research*, *33*(19), 3226–3234.

Hunter, B. M. (2019). *Oxidation behaviour of refractory complex concentrated alloys: Computational and experimental studies.* PhD Thesis. University of Alabama.

Wei, L., & Qin, W. (2022). Corrosion mechanism of eutectic high-entropy alloy induced by micro-galvanic corrosion in sulfuric acid solution. *Corrosion Science*, *206*, 110525.

Wei, Q., Shen, Q., Zhang, J., Zhang, Y., Luo, G., & Zhang, L. (2019). Microstructure evolution, mechanical properties and strengthening mechanism of refractory high-entropy alloy matrix composites with addition of TaC. *Journal of Alloys and Compounds*, *777*, 1168–1175.

Wei, S., Kim, S. J., Kang, J., Zhang, Y., Zhang, Y., Furuhara, T., Park, E. S., & Tasan, C. C. (2020). Natural-mixing guided design of refractory high-entropy alloys with as-cast tensile ductility. *Nature Materials*, *19*(11), 1175–1181.

Wei, W., Wang, T., Wang, C., Wu, M., Nie, Y., & Peng, J. (2021). Ductile $W_{0.4}MoNb_xTaTi$ refractory high-entropy alloys with excellent elevated temperature strength. *Materials Letters*, *295*, 129753.

Wei, Y., Fu, Y., Pan, Z. M., Ma, Y. C., Cheng, H. X., Zhao, Q. C., Luo, H., & Li, X. G. (2021). Influencing factors and mechanism of high-temperature oxidation of high-entropy alloys: A review. *International Journal of Minerals, Metallurgy and Materials, 28*(6), 915–930.

Weyant, C. M., Faber, K. T., Almer, J. D., & Guiheen, J. V. (2005). Residual stress and microstructural evolution in tantalum oxide coatings on silicon nitride. *Journal of the American Ceramic Society*, *88*(8), 2169–2176.

Williams, D. E., Yang, Y., Webb, E. G., & Alkire, R. C. (2000). Explanation for initiation of pitting corrosion of stainless steels at sulfide inclusions. *Journal of Electrochemical Society, 147*(5), 1763–1766.

Wu, B., Li, J., Liu, L., Chen, X., Tan, J., Song, J., Rashad, M., & Pan, F. (2021). Effect of Zener–Hollomon parameter on high-temperature deformation behaviours of Mg–6Zn–1.5Y–0.5Ce–0.4Zr Alloy. *Acta Metallurgica Sinica (English Letters), 34*(5), 606–616.

Wu, C. S., Tsai, P. H., Kuo, C. M., & Tsai, C. W. (2018). Effect of atomic size difference on the microstructure and mechanical properties of high-entropy alloys. *Entropy, 20*(12), e20120967.

Wu, H., Wen, S. P., Huang, H., Gao, K. Y., Wu, X. L., Wang, W., & Nie, Z. R. (2016). Hot deformation behaviour and processing map of a new type Al-Zn-Mg-Er-Zr alloy. *Journal of Alloys and Compounds*, *685*, 869–880.

Wu, S., Qiao, D., Zhang, H., Miao, J., Zhao, H., Wang, J., Lu, Y., Wang, T., & Li, T. (2021). Microstructure and mechanical properties of $C_xHf_{0.25}NbTaW_{0.5}$ refractory high-entropy alloys at room and high temperatures. *Journal of Materials Science and Technology*, *97*, 229–238.

Wu, Y., Liu, Y., Li, C., Xia, X., Huang, Y., Li, H., & Wang, H. (2017). Deformation behaviour and processing maps of Ni_3Al-based superalloy during isothermal hot compression. *Journal of Alloys and Compounds*, *712*, 687–695.

Wu, Z., Bei, H., Otto, F., Pharr, G. M., & George, E. P. (2014). Recovery, recrystallisation, grain growth and phase stability of a family of FCC-structured multi-component equiatomic solid solution alloys. *Intermetallics*, *46*, 131–140.

Xiang, C., Fu, H. M., Zhang, Z. M., Han, E. H., Zhang, H. F., Wang, J. Q., & Hu, G. D. (2020). Effect of Cr content on microstructure and properties of $Mo_{0.5}VNbTiCr_x$ high-entropy alloys. *Journal of Alloys and Compounds*, *818*, 153352.

Xiang, C., Ming, Z., Hua, Z., Fu, M., Hou, E., Jian, H., Wang, Q., & Feng, H. (2019). Microstructure, mechanical properties, and corrosion behaviour of MoNbFeCrV, MoNbFeCrTi, and MoNbFeVTi high-entropy alloys. *Acta Metallurgica Sinica (English Letters)*, *32*(9), 1053–1064.

Xiao, B., Jia, W., Tang, H., Wang, J., & Zhou, L. (2022). Microstructure and mechanical properties of WMoTaNbTi refractory high-entropy alloys fabricated by selective electron beam melting. *Journal of Materials Science and Technology*, *108*, 54–63.

Xiao, J. K., Tan, H., Chen, J., Martini, A., & Zhang, C. (2020). Effect of carbon content on microstructure, hardness and wear resistance of $CoCrFeMnNiC_x$ high-entropy alloys. *Journal of Alloys and Compounds*, *847*, 156533.

Xiao, Y., Kuang, W., Xu, Y., Wu, L., Gong, W., Qian, J., Zhang, Q., & He, Y. (2019). Microstructure and oxidation behaviour of the CrMoNbTaV high-entropy alloy. *Journal of Materials Research*, *34*(2), 301–308.

Xing, L., Gu, C., Lv, Z., & Bao, Y. (2022). High-temperature internal oxidation behaviour of surface cracks in low alloy steel bloom. *Corrosion Science*, *197*, 110076.

Xing, X. W, Hu, J. Kang, L., & Li, W. (2022). Effect of Mo on microstructure, mechanical and corrosion properties of $FeCrNiMnMo_x$ high-entropy alloys. *China Foundry*, *19*(6), 464–472.

Xing, Y., Ma, Z., Su, W., Wang, Q., Wang, X., & Zhang, H. (2020). Analysis of research status of CO_2 conversion technology based on bibliometrics. *Catalysts*, *10*(370), 1–18.

Xu, F., Gao, X., Cui, H., Song, Q., & Chen, R. (2023). Lightweight and high hardness (AlNbTiVCr)100-$_x$Ni$_x$ high entropy alloys reinforced by Laves phase. *Vacuum*, *213*, 112115.

Xu, W., Zhang, L. W., Gu, S. D., & Zhang, J. L. (2012). Hot compressive deformation behaviour and microstructure evolution of HIPed FGH96 superalloy. *Transactions of Nonferrous Metals Society of China*, *22*(1), 66–71.

Xu, Z. Q., Ma, Z. L., Tan, Y., Wang, M., Zhao, Y., & Cheng, X. W. (2022). Effects of Si additions on microstructures and mechanical properties of VNbTiTaSix refractory high-entropy alloys. *Journal of Alloys and Compounds*, *900*, 163517.

Xu, Z. Q., Ma, Z. L., Wang, M., Chen, Y. W., Tan, Y. D., & Cheng, X. W. (2019). Design of novel low-density refractory high entropy alloys for high-temperature applications. *Materials Science and Engineering A*, *755*, 318–322.

Yan, D., & Song, K. (2020). Microstructures, mechanical properties, and corrosion behaviours of refractory high-entropy alloys. *Journal of Materials Engineering and Performance*, *29*, 399–409.

Yan, Y., McGarrity, K. A., Delia, D. J., Fekety, C., & Wang, K. (2022). The oxidation-resistance mechanism of WTaNbTiAl refractory high entropy alloy. *Corrosion Science*, *204*, 110377.

Yang, C., Bian, H., Aoyagi, K., Hayasaka, Y., Yamanaka, K., & Chiba, A. (2021). Synergetic strengthening in HfMoNbTaTi refractory high-entropy alloy via disordered nanoscale phase and semicoherent refractory particle. *Materials & Design*, *212*, 1–17.

Yang, X., Zeng, Z., Wang, X., Li, X., Guo, C., Xiao, X., & Yang, B. (2023). High-temperature oxidation behaviours of 321 steel with Y or Nb micro-alloying. *Crystals*, *13*(5), 781.

Yang, X., & Zhang, Y. (2012). Prediction of high-entropy stabilised solid-solution in multi-component alloys. *Materials Chemistry and Physics*, *132*, 233–238.

Yao, H., Miao, J., Liu, Y., Guo, E., Huang, H., Lu, Y., Wang, T., & Li, T. (2021). Effect of Ti and Nb contents on microstructure and mechanical properties of HfZrVTaMoWTi$_x$Nb$_y$ refractory high-entropy alloys. *Advanced Engineering Materials*, *23*, 1–7.

Yao, H. W., Qiao, J. W., Gao, M. C., Hawk, J. A., Ma, S. G., Zhou, H. F., & Zhang, Y. (2016). NbTaV-(Ti,W) refractory high-entropy alloys: experiments and modeling. *Materials Science & Engineering A*, *674*, 203–211.

Yao, H. W., Qiao, J. W., Hawk, J. A., Zhou, H. F., Chen, M. W., & Gao, M. C. (2017). Mechanical properties of refractory high-entropy alloys: Experiments and modeling. *Journal of Alloys and Compounds*, *696*, 1139–1150.

Yao, J. Y., Serrano, L. B., Santos, S. F., & Cardoso, K. R. (2023). Microstructure and corrosion behaviour of the Ti-V-Cr-Nb high-entropy alloys in 3.5 wt% NaCl solution. *Corrosion Science*, *218*, 111149.

Yao, Y., Jin, Y., Gao, W., Liang, X., Chen, J., & Zhu, S. (2021). Corrosion behaviour of $AlFeCrCoNiZr_x$ high-entropy alloys in 0.5 M sulfuric acid solution. *Metals*, *11*(9), 1471.

Ye, Y. F., Wang, Q., Lu, J., Liu, C. T., & Yang, Y. (2016). High-entropy alloy: Challenges and prospects. *Materials Today*, *19*(6), 349–362.

Yeh, J. W. (2006). Recent progress in high-entropy alloys. *Annales de Chimie: Science Des Materiaux*, *31*(6), 633–648.

Yeh, J. W., Chen, S. K., Lin, S. J., Gan, J. Y., Chin, T. S., Shun, T. T., Tsau, C. H., & Chang, S. Y. (2004). Nanostructured high-entropy alloys with multiple principal elements: Novel alloy design concepts and outcomes. *Advanced Engineering Materials*, *6*(5), 299–303.

Yeh, J. W., Chen, Y. L., Lin, S. J., & Chen, S. K. (2007). High-entropy alloys – A new era of exploitation. *Materials Science Forum*, *560*, 1–9.

Yi, J., Tang, S., Zhang, C., Xu, M., Yang, L. I. N., Wang, L. U., & Zeng, L. (2021). Microstructure and mechanical properties of a new refractory equiatomic CrHfNbTaTi high-entropy alloy. *JOM*, *73*(3), 934–940.

Young, D. J. (2008). *High Temperature Oxidation and Corrosion of Metals* (1st ed.). Elsevier.

Yu, Z., Xie, B., Zhu, Z., Xu, B., & Sun, M. (2022). High-temperature deformation behaviour and processing maps of a novel $AlNbTi_3VZr_{1.5}$ refractory high entropy alloy. *Journal of Alloys and Compounds*, *912*(5), 165220.

Yurchenko, N., Panina, E., Shaysultanov, D., Zherebtsov, S., & Stepanov, N. (2021). Refractory high entropy alloy with ductile intermetallic B2 matrix/hard BCC particles and exceptional strain hardening capacity. *Materialia*, *20*, 101225.

Yurchenko, N., Panina, E., Tojibaev, A., Novikov, V., Salishchev, G., Zherebtsov, S., & Stepanov, N. (2023). Effect of B2 ordering on the tensile mechanical properties of refractory $Al_xNb_{40}Ti_{40}V_{20-x}$ medium-entropy alloys. *Journal of Alloys and Compounds*, *937*, 168465.

Yurchenko, N., Panina, E., Zherebtsov, S., Salishchev, G., & Stepanov, N. (2018). Oxidation behaviour of refractory $AlNbTiVZr_{0.25}$ high-entropy alloy. *Materials*, *11*(12), 2526.

Yurchenko, N., Stepanov, N., & Salishchev, G. (2017). Laves-phase formation criterion for high-entropy alloys. *Materials Science and Technology*, *33*(1), 1153277.

Prasad, Y.V.R.K., & Rao, K.P. (2015). Hot Working Guide—A Compendium of Processing Maps, Second Edition. *ASM International*.

Zarghani, F., Ebrahimi, G. R., Taheri, J., & Ezatpour, H. R. (2023). Hot compressive deformation behavior of Ti-8Al-1Mo-1V titanium alloy at elevated temperatures: Focus on flow behavior, constitutive modeling, and processing maps. *Materials Today Communications*, 37, 107235.

Zemanate, A. M., Jorge Júnior, A. M., Andreani, G. F. D. L., Roche, V., & Cardoso, K. R. (2023). Corrosion behaviour of $AlCoCrFeNi_x$ high entropy alloys. *Electrochimica Acta*, *441*.

Zhang, B. Y., Zhou, Y. J., Lin, J. P., Chen, G. L., & Liaw, P. K. (2008). Solid-solution phase formation rules for multi-component alloys. *Advanced Engineering Materials*, *10*(6), 534–538.

Zhang, C, Zhang, L., Shen, W., Mengfei, L., & Gu, S. (2015). Characterisation of hot deformation behaviour of Hastelloy C-276 using constitutive equation and processing map. *Journal of Materials Engineering and Performance*, *24*(1), 149–157.

Zhang, H., Liu, P., Hou, J., Qiao, J., & Wu, Y. (2019). Prediction of strength and ductility in partially recrystallized $CoCrFeNiTi_{0.2}$ high-entropy alloy. *Entropy*, *21*(4), 1–11.

Zhang, L., Qi, L., Deng, S., Oguntuase, O., Deng, T., Wang, H., & Ojo, O. A. (2021). Analyses of Anodically Formed Passive Film and Corrosion Behaviour of Wire-arc Additive Manufactured ATI 718Plus® Superalloy. *Additive Manufacturing*, *48*, 102443.

Zhang, P., Li, Y., Chen, Z., Zhang, J., & Shen, B. (2019). Oxidation response of a vacuum arc melted NbZrTiCrAl refractory high entropy alloy at 800–1200°C. *Vacuum*, *162*, 20–27.

Zhang, R., Meng, J., Han, J., & Tulugan, K. (2021). Oxidation resistance properties of refractory high-entropy alloys with varied $Al_xCrTiMo$ content. *Journal of Materials Science*, *56*(4), 1–11.

Zhang, W., Hua, B., Yang, J., Chi, B., Pu, J., & Jian, L. (2018). Performance evaluation of a new Fe-Cr-Mn alloy in the reducing atmosphere of solid oxide fuel cells. *Journal of Alloys and Compounds*, *769*, 866–872.

Zhang, X., Cui, X., Jin, G., Dong, Y., Wang, Z., & Qi, Y. (2023). Microstructure evolution and performance enhancement of NbTaTiV-(Cr, Zr, W) single-phase refractory high-entropy alloy coatings: Role of additional elements. *Journal of Alloys and Compounds*, *951*, 169918.

Zhang, Y., Liu, J. P., Chen, S. Y., Xie, X., Liaw, P. K., Dahmen, K. A., Qiao, J. W., & Wang, Y. L. (2017). Serration and noise behaviours in materials. *Progress in Materials Science*, *90*, 358–460.

Zhang, Y., Liu, Y., Li, Y., Chen, X., & Zhang, H. (2016). Microstructure and mechanical properties of a refractory $HfNbTiVSi_{0.5}$ high-entropy alloy composite. *Materials Letters*, *174*, 82–85.

Zhang, Y., Yang, X., & Liaw, P. K. (2012). Alloy design and properties optimization of high-entropy alloys. *JOM*, *64*(7), 1–9.

Zhao, Q., Yang, F., Torrens, R., & Bolzoni, L. (2019). Comparison of the cracking behaviour of powder metallurgy and ingot metallurgy Ti-5Al-5Mo-5V-3Cr alloys during hot deformation. *Materials*, *12*(3), 457.

Zheng, L., Zhang, M. C., Chellali, R., Bouchikhaoui, H., & Dong, J. X. (2013). Oxidation property of powder metallurgy EP741NP Ni based superalloy at elevated temperatures. *Materials Technology*, *28*(3), 122–128.

Zheng, L., Zhang, M., Chellali, R., & Dong, J. (2011). Investigations on the growing, cracking and spalling of oxides scales of powder metallurgy Rene95 nickel-based superalloy. *Applied Surface Science*, *257*(23), 9762–9767.

Zheng, W., Lü, S., Wu, S., Chen, X., & Guo, W. (2022). Development of $MoNbVTa_x$ refractory high entropy alloy with high strength at elevated temperature. *Materials Science and Engineering A*, *850*, 1–9.

Zheng, Z. J., Gao, Y., Gui, Y., & Zhu, M. (2012). Corrosion behaviour of nanocrystalline 304 stainless steel prepared by equal channel angular pressing. *Corrosion Science*, *54*(1), 60–67.

Zhou, Q., Sheikh, S., Ou, P., Chen, D., Hu, Q., & Guo, S. (2019). Corrosion behaviour of $Hf_{0.5}Nb_{0.5}Ta_{0.5}Ti_{1.5}Zr$ refractory high-entropy in aqueous chloride solutions. *Electrochemistry Communications*, *98*, 63–68.

Zhou, Z., Li, H., Liu, Y., Niu, T., & Li, H. (2022). Effect of Ti on the corrosion behaviour of $(FeCrCoNi)100-xTi_x$ alloy. *Corrosion Science*, *209*, 110807.

Zhou, Z., Wang, L., Zhao, X., Wu, J., Zhang, F., & Pi, J. (2021). Effects of W addition on the Corrosion behaviours of FeCoNiCrMn high entropy alloy composites in the 3.5 wt% NaCl solution. *Surfaces and Interfaces*, *23*, 100956.

Zhu, C., Xu, L., Liu, M., Guo, M., & Wei, S. (2023). A review on improving mechanical properties of high entropy alloy: interstitial atom doping. *Journal of Materials Research and Technology*, *24*, 7832–7851.

Zhu, Y., Zhang, Y., Cheong, F. C., Sow, C. H., & Lim, C. T. (2008). Annealing effects on the elastic modulus of tungsten oxide nanowires. *Journal of Materials Research*, *23*(8), 2149–2156.

Zhuo, L., Sun, J., Chen, B., Zhan, M., & Jiang, C. (2023). Microstructure and mechanical performances of novel multi-phase refractory high entropy alloys in Ti-Zr-V-Mo fabricated by vacuum arc melting. *Vacuum*, *217*, 112544.

Zong, Y., Hashimoto, N., & Oka, H. (2022). Study on irradiation effects of refractory BCC high-entropy alloy. *Nuclear Materials and Energy*, *31*, 101158.

Appendix A: EDX of microstructural observation of TiNbTaVW in chloride solution

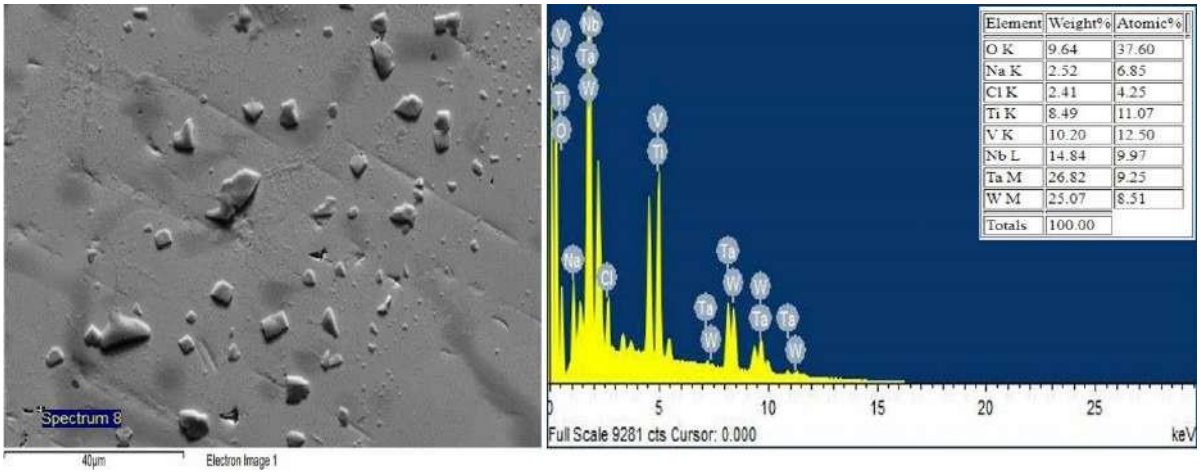

Element	Weight%	Atomic%
O K	9.64	37.60
Na K	2.52	6.85
Cl K	2.41	4.25
Ti K	8.49	11.07
V K	10.20	12.50
Nb L	14.84	9.97
Ta M	26.82	9.25
W M	25.07	8.51
Totals	100.00	

Figure A1: EDX point of dendrite compositions obtained from the TiNbTaVW RHEA after potentiodynamic polarisation in 3.5 wt.% NaCl.

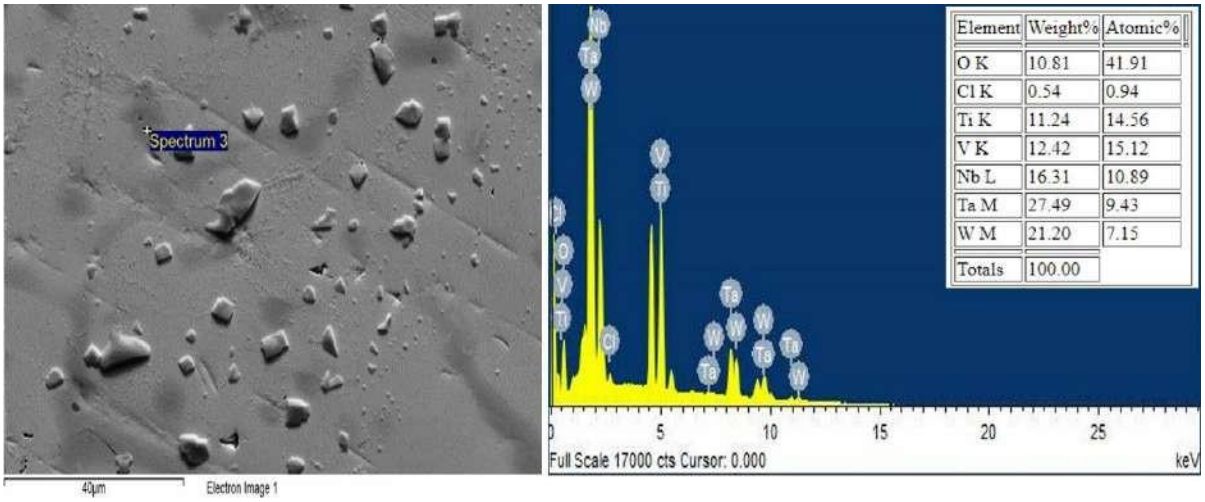

Element	Weight%	Atomic%
O K	10.81	41.91
Cl K	0.54	0.94
Ti K	11.24	14.56
V K	12.42	15.12
Nb L	16.31	10.89
Ta M	27.49	9.43
W M	21.20	7.15
Totals	100.00	

Figure A2: EDX point of interdendrite compositions obtained from the TiNbTaVW RHEA after potentiodynamic polarisation in 3.5 wt.% NaCl.

Appendix B: EDX of microstructural observation of CrNbTaVW in chloride solution

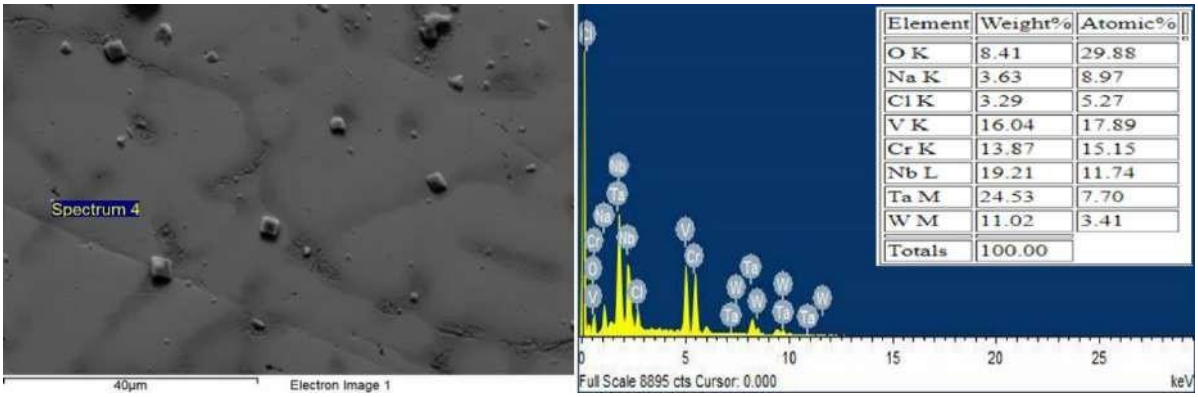

Figure B1: EDX point of BCC1 compositions obtained from the CrNbTaVW RHEA after potentiodynamic polarisation in 3.5 wt% NaCl.

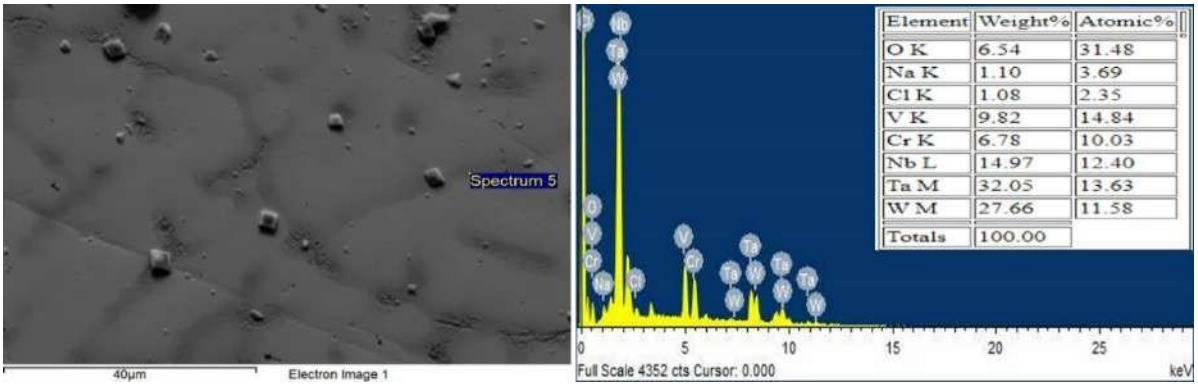

Figure B2: EDX point of BCC2 compositions obtained from the CrNbTaVW RHEA after potentiodynamic polarisation in 3.5 wt% NaCl.

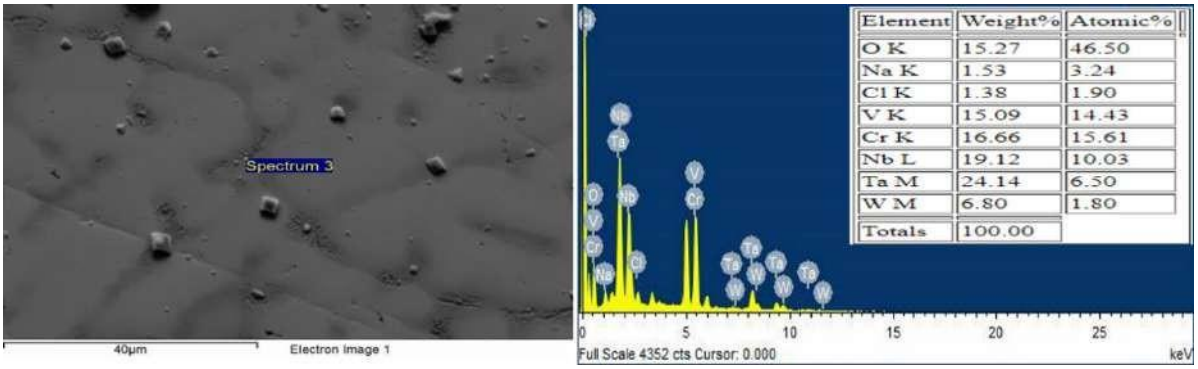

Figure B3: EDX point of $Cr(VNb)_2$ compositions obtained from the CrNbTaVW RHEA after potentiodynamic polarisation in 3.5 wt% NaCl.

Appendix C: EDX of microstructural observation of IN718 in chloride solution

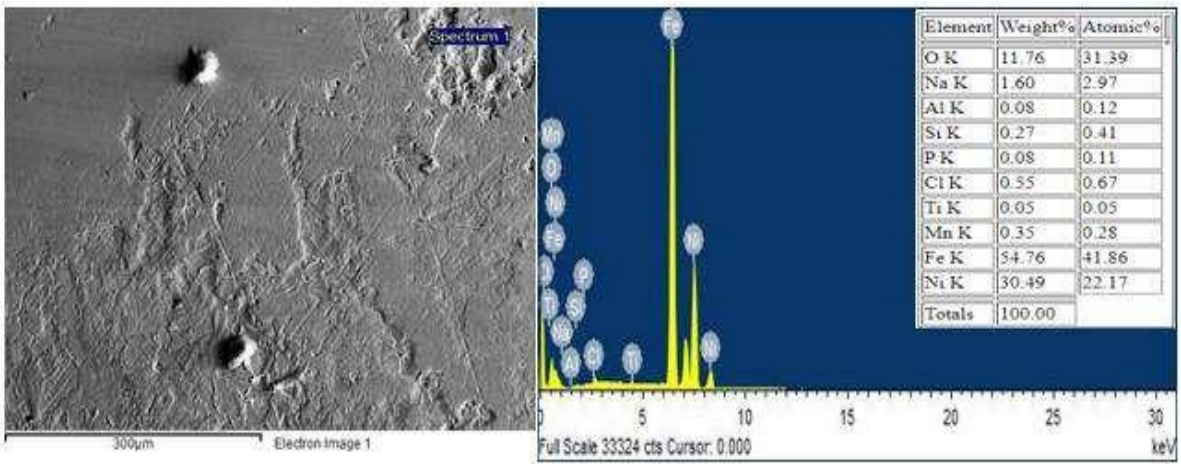

Figure C1. EDX point of compositions obtained from the IN718 alloy after potentiodynamic polarization in 3.5 wt% NaCl.

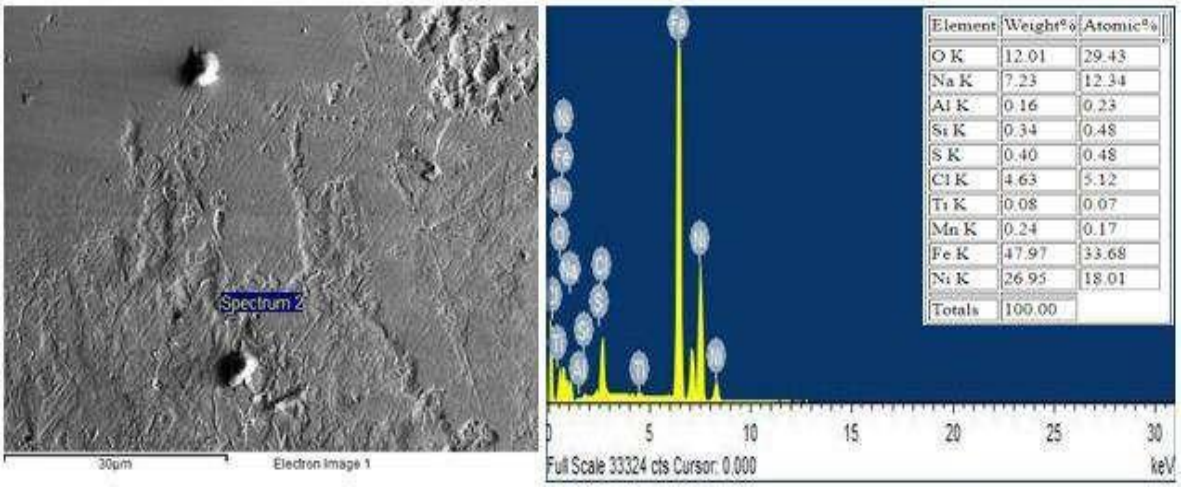

Figure C2. EDX point of compositions obtained from the IN718 alloy after potentiodynamic polarisation in 3.5 wt% NaCl.

Appendix D: EDX of microstructural observation of TiNbTaVW in acidic solution

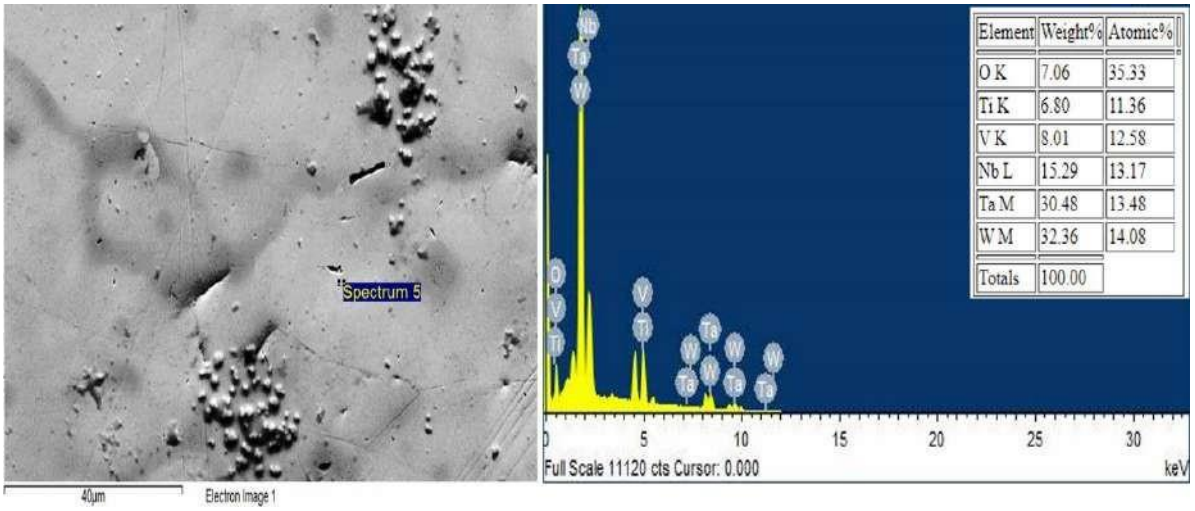

Element	Weight%	Atomic%
O K	7.06	35.33
Ti K	6.80	11.36
V K	8.01	12.58
Nb L	15.29	13.17
Ta M	30.48	13.48
W M	32.36	14.08
Totals	100.00	

Figure D1: EDX point of dendrite compositions obtained from the TiNbTaVW RHEA after potentiodynamic polarization in 1 Mol H_2SO_4.

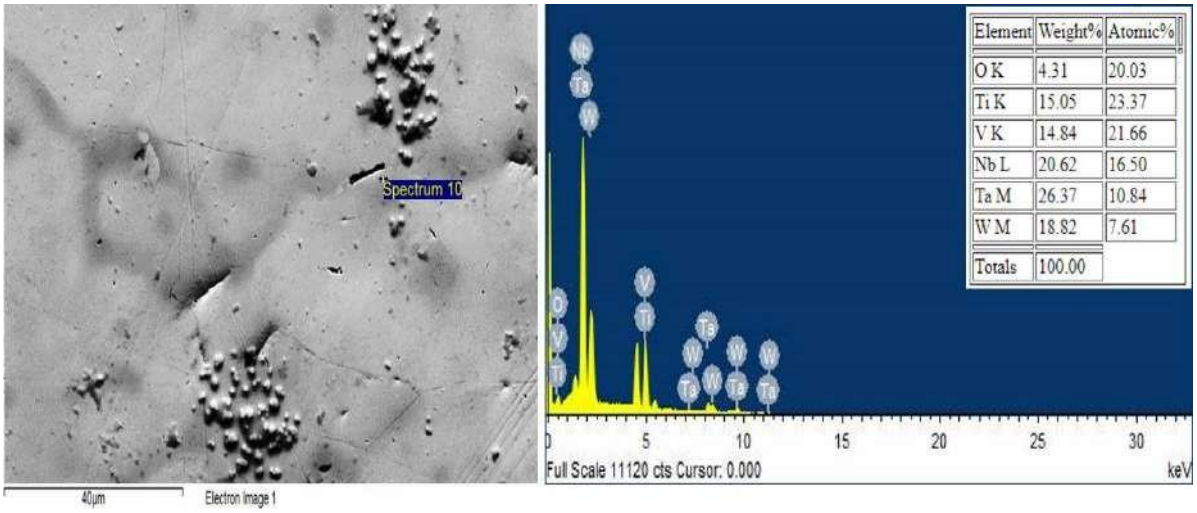

Element	Weight%	Atomic%
O K	4.31	20.03
Ti K	15.05	23.37
V K	14.84	21.66
Nb L	20.62	16.50
Ta M	26.37	10.84
W M	18.82	7.61
Totals	100.00	

Figure D2: EDX point of dendrite compositions obtained from the TiNbTaVW RHEA after potentiodynamic polarisation in 1 Mol H_2SO_4.

Appendix E: EDX of microstructural observation of CrNbTaVW in acidic solution

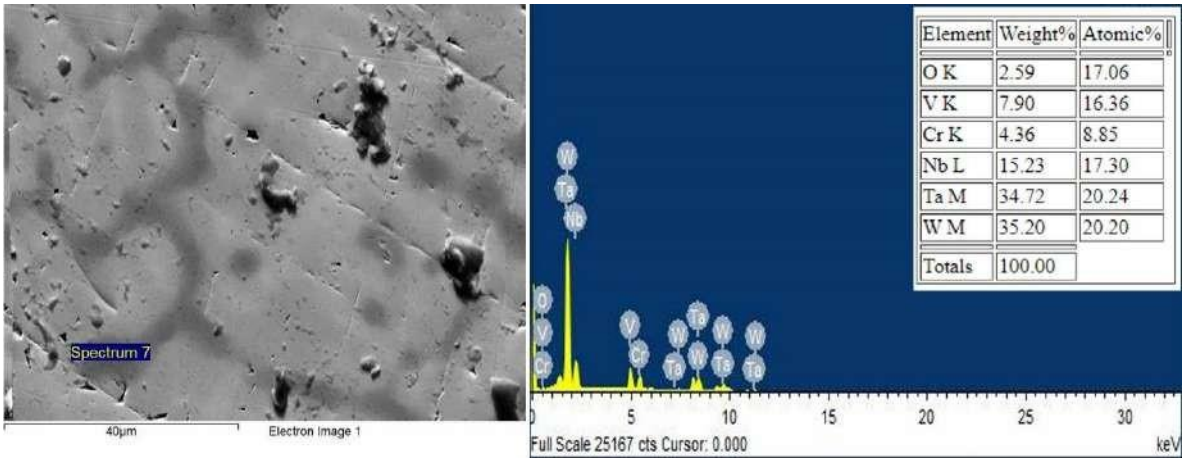

Element	Weight%	Atomic%
O K	2.59	17.06
V K	7.90	16.36
Cr K	4.36	8.85
Nb L	15.23	17.30
Ta M	34.72	20.24
W M	35.20	20.20
Totals	100.00	

Figure E1: EDX point of BCC1 compositions obtained from the CrNbTaVW RHEA after potentiodynamic polarisation in 1 Mol H_2SO_4.

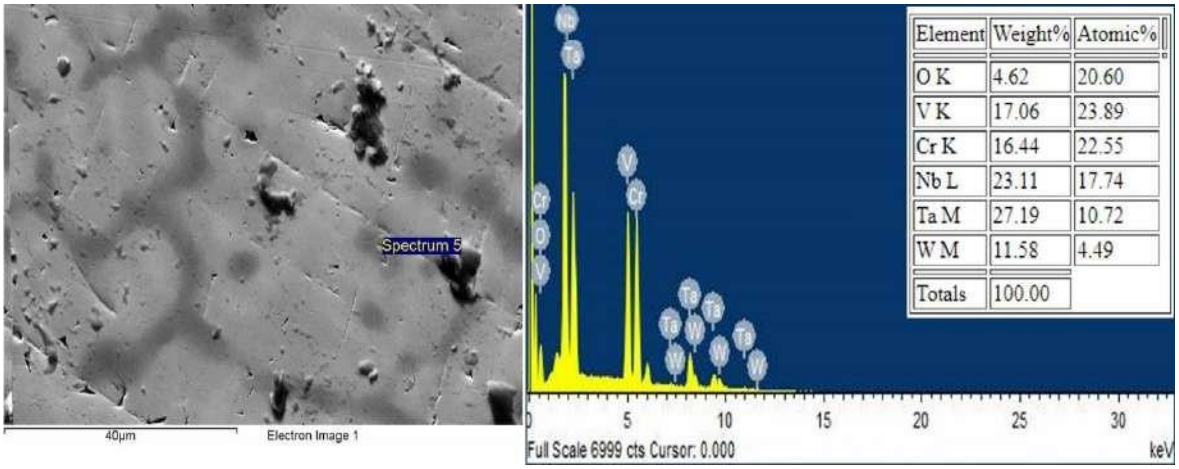

Element	Weight%	Atomic%
O K	4.62	20.60
V K	17.06	23.89
Cr K	16.44	22.55
Nb L	23.11	17.74
Ta M	27.19	10.72
W M	11.58	4.49
Totals	100.00	

Figure E2: EDX point of BCC2 compositions obtained from the CrNbTaVW RHEA after potentiodynamic polarisation in 1 Mol H_2SO_4.

Appendix F: EDX of microstructural observation of IN718 in acidic solution

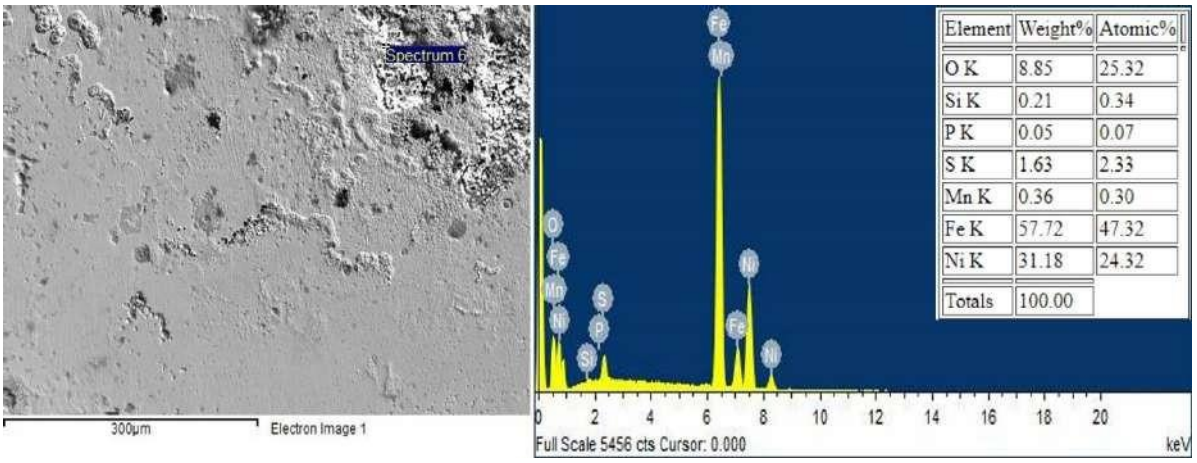

Element	Weight%	Atomic%
O K	8.85	25.32
Si K	0.21	0.34
P K	0.05	0.07
S K	1.63	2.33
Mn K	0.36	0.30
Fe K	57.72	47.32
Ni K	31.18	24.32
Totals	100.00	

Figure F1: EDX point of compositions obtained from the IN718 alloy after potentiodynamic polarisation in 1 Mol H_2SO_4.

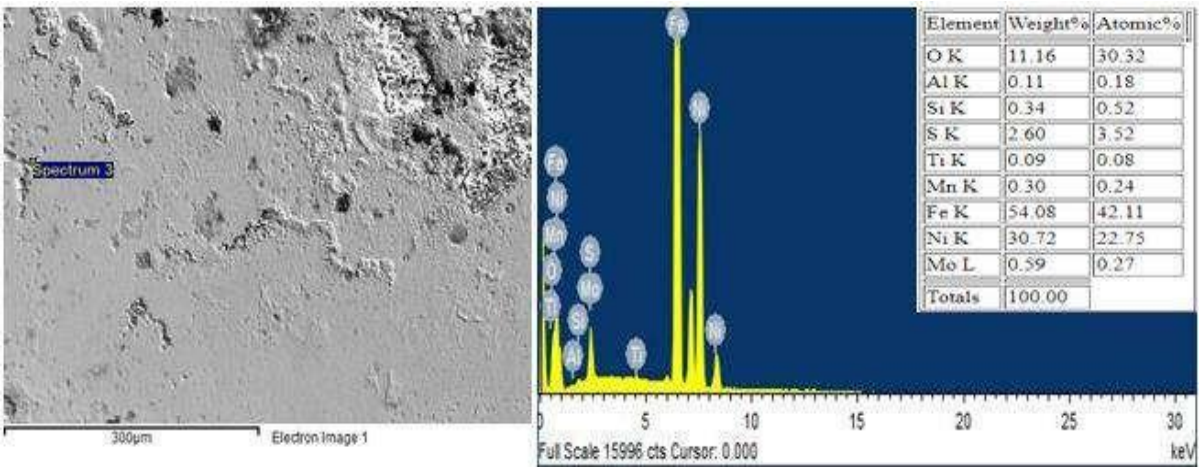

Element	Weight%	Atomic%
O K	11.16	30.32
Al K	0.11	0.18
Si K	0.34	0.52
S K	2.60	3.52
Ti K	0.09	0.08
Mn K	0.30	0.24
Fe K	54.08	42.11
Ni K	30.72	22.75
Mo L	0.59	0.27
Totals	100.00	

Figure F2: EDX point of compositions obtained from the IN718 alloy after potentiodynamic polarisation in 1 Mol H_2SO_4.

Appendix G: EDX of surface morphology of oxidised TiNbTaVW at 850°C and 1050°C

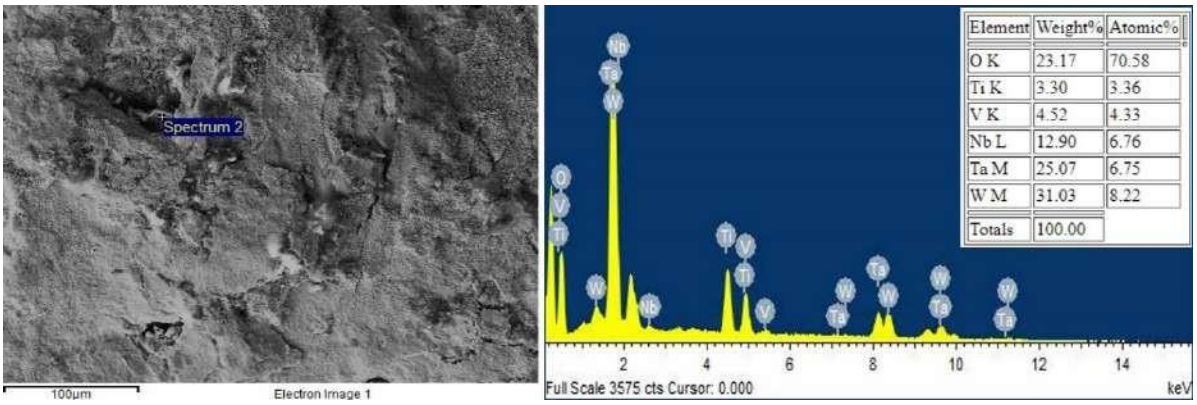

Figure G1: EDX point of spalled oxides at the surface morphology of the TiNbTaVW RHEA after oxidation at 850°C after 15 hours.

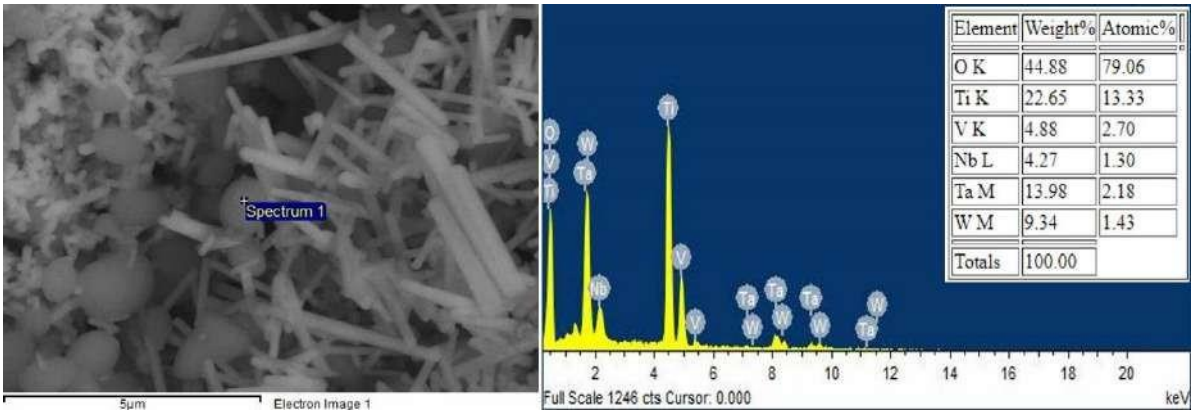

Figure G2: EDX point of granular-shaped oxides of the TiNbTaVW RHEA surface morphology after oxidation at 850°C after 15 hours.

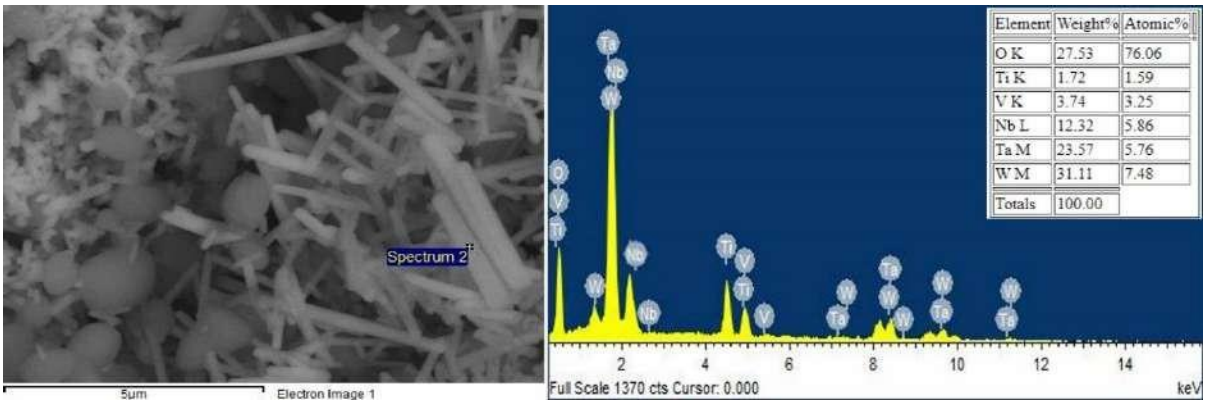

Figure G3: EDX point of rod-shaped oxides of the TiNbTaVW RHEA surface morphology after oxidation at 850°C after 15 hours.

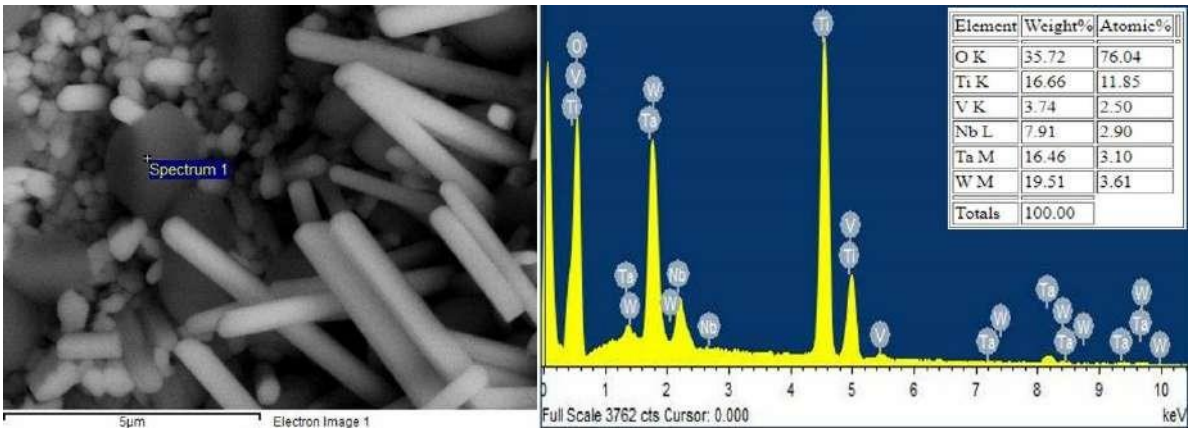

Figure G4: EDX point of granular-shaped oxides of the TiNbTaVW RHEA surface morphology after oxidation at 1050 °C after 15 hours.

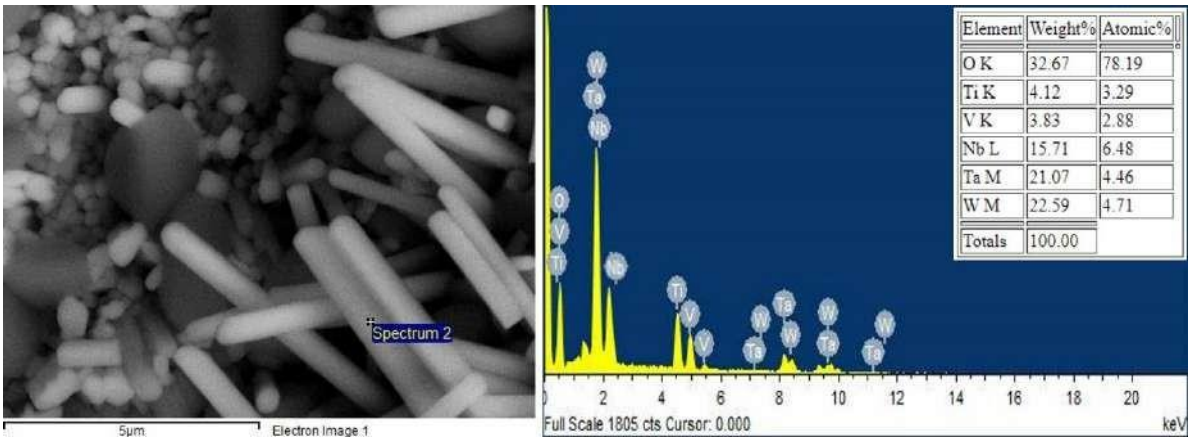

Figure G5: EDX point of rod-shaped oxides of the TiNbTaVW RHEA surface morphology after oxidation at 1050°C after 15 hours.

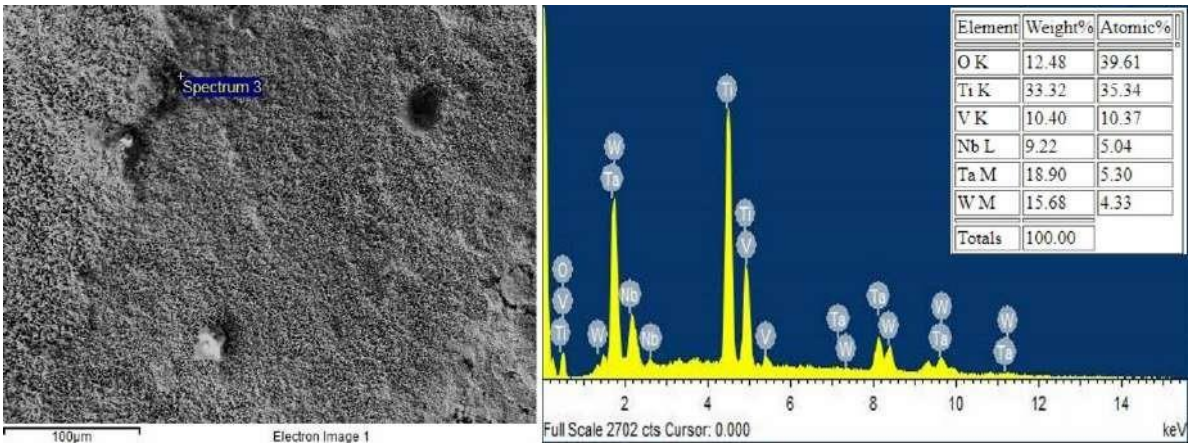

Figure G6: EDX point of spalled oxides at the surface morphology of the TiNbTaVW RHEA after oxidation at 1050°C after 15 hours.

Appendix H: EDX of surface morphology of oxidised CrNbTaVW at 850°C and 1050°C

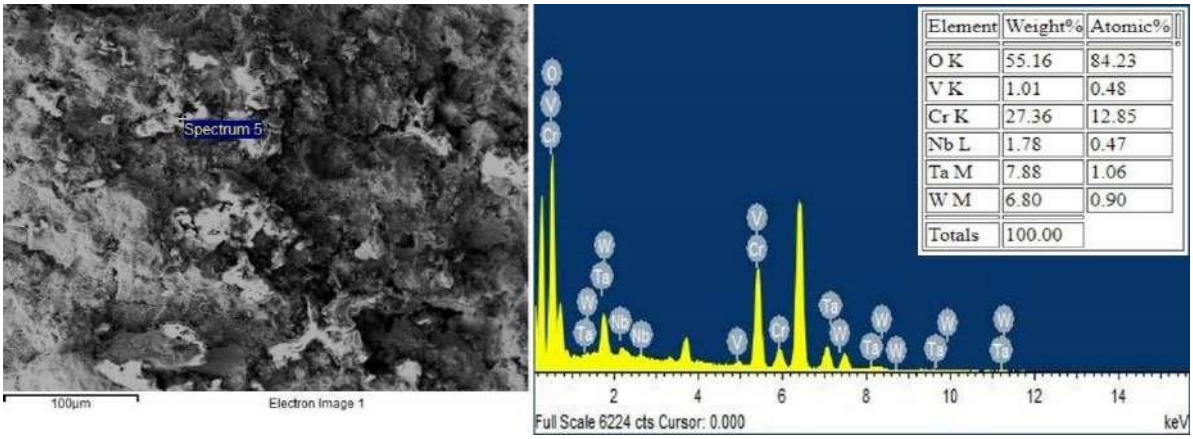

Figure H1: EDX point of spalled oxides at the surface morphology of the CrNbTaVW RHEA after oxidation at 850°C after 15 hours.

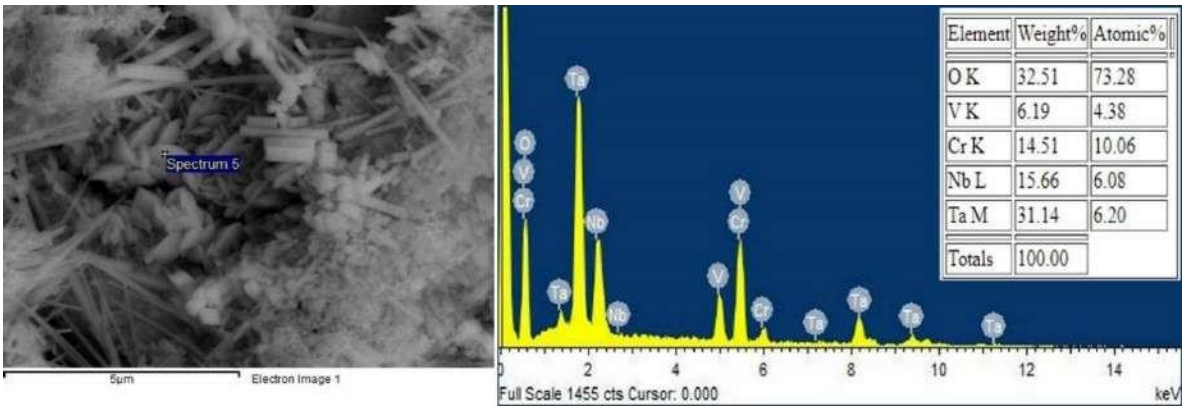

Figure H2: EDX point of granular-shaped oxides of the CrNbTaVW RHEA surface morphology after oxidation at 850°C after 15 hours.

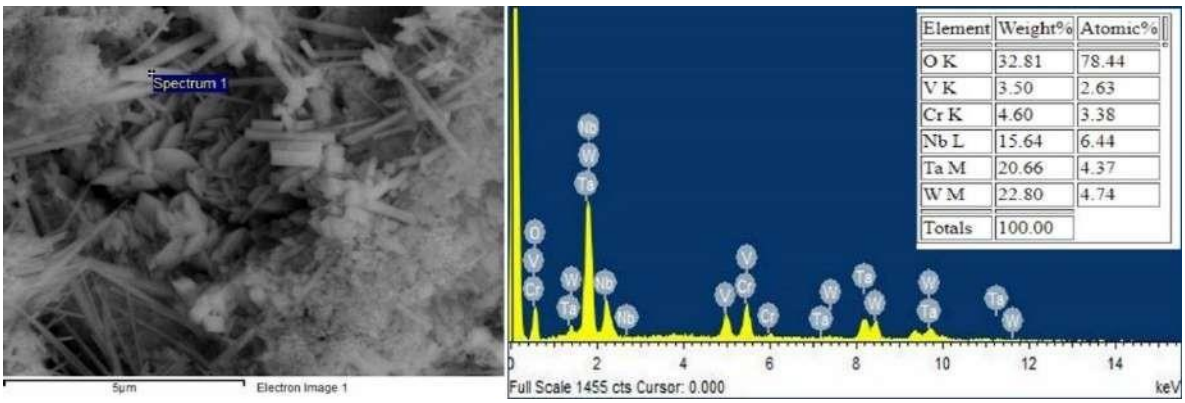

Figure H3: EDX point of rod-shaped oxides of the CrNbTaVW RHEA surface morphology after oxidation at 850°C after 15 hours.

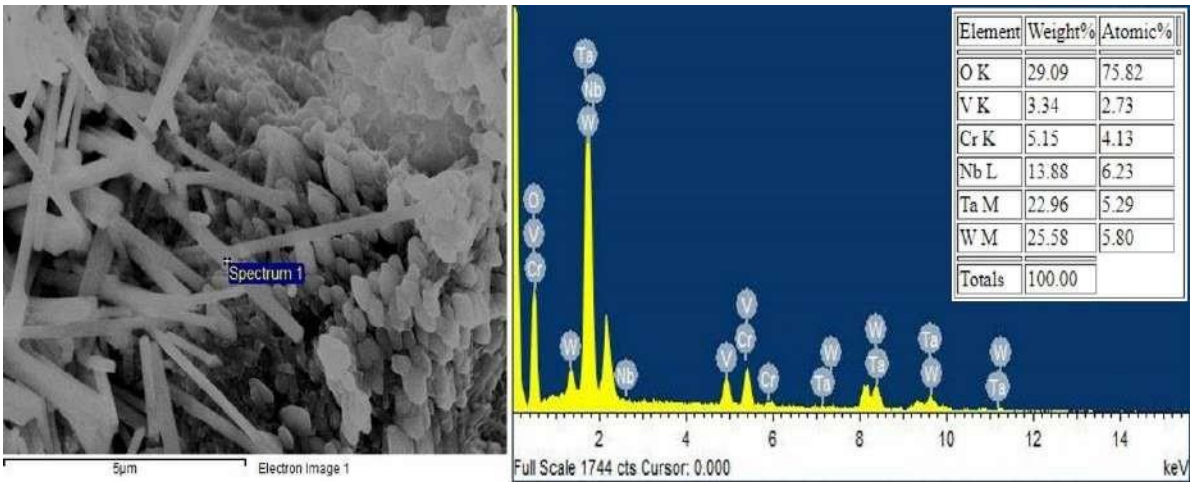

Figure H4: EDX point of rod-shaped oxides of the CrNbTaVW RHEA surface morphology after oxidation at 1050°C after 15 hours.

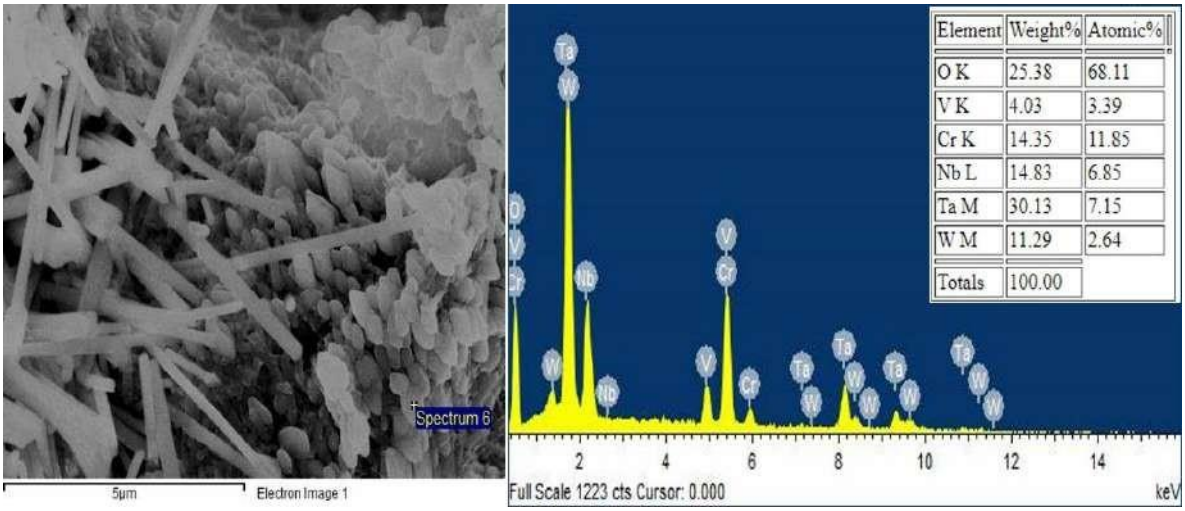

Figure H5: EDX point of granular-shaped oxides of the CrNbTaVW RHEA surface morphology after oxidation at 1050°C after 15 hours.

Appendix I: EDX of surface morphology of oxidised IN718 at 850°C and 1050°C

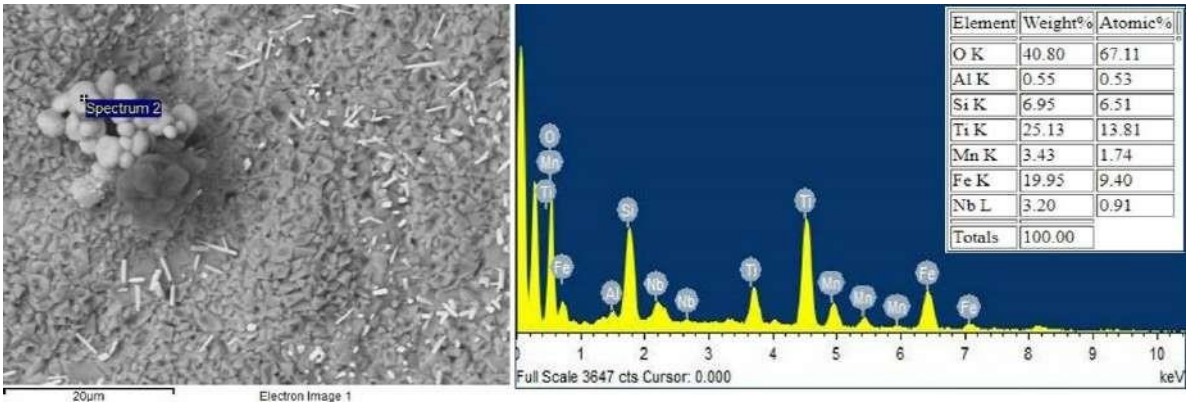

Figure I1: EDX point of round-shaped oxides of the IN718 alloy surface morphology after oxidation at 850°C after 15 hours.

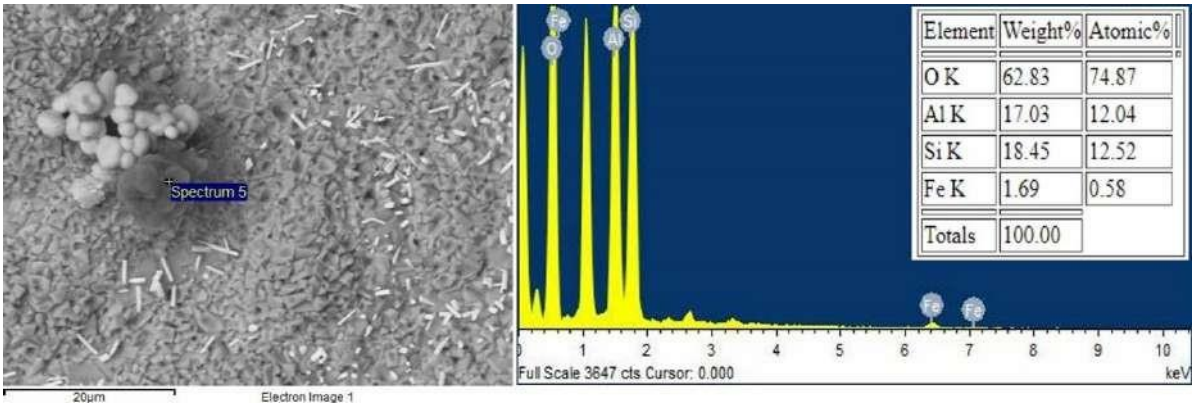

Figure I2: EDX point of cloudy-shaped oxides of the IN718 alloy surface morphology after oxidation at 850°C after 15 hours.

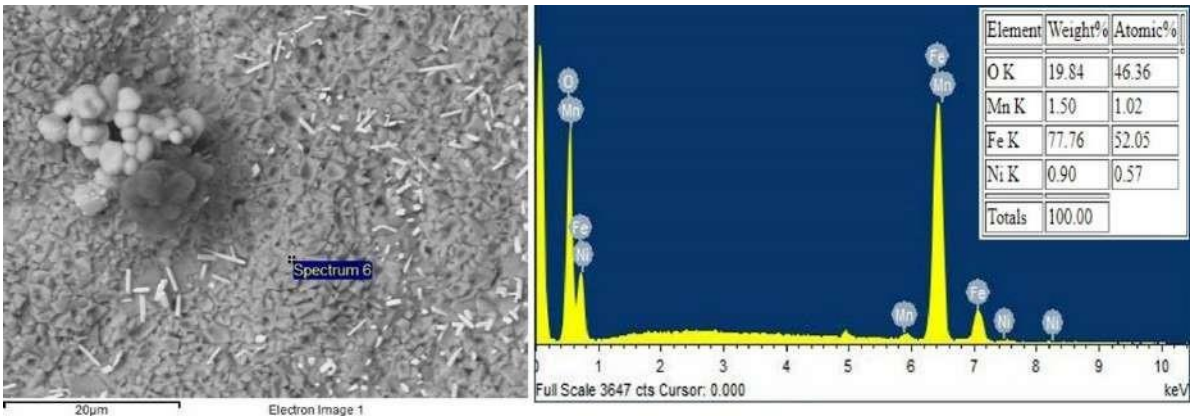

Figure I3: EDX point of block-shaped oxides of the IN718 alloy surface morphology after oxidation at 850°C after 15 hours.

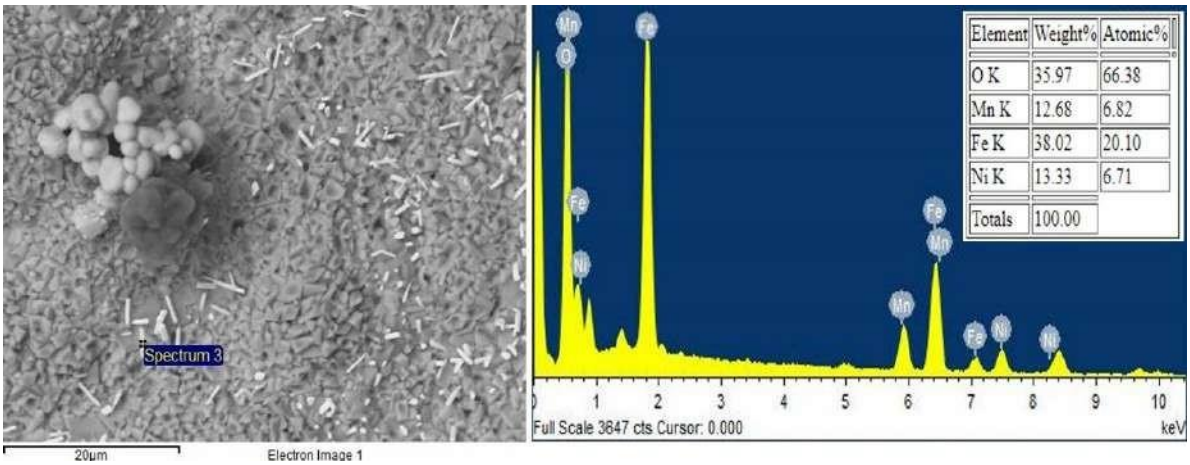

Figure I4: EDX point of rod-shaped oxides of the IN718 alloy surface morphology after oxidation at 850°C after 15 hours.

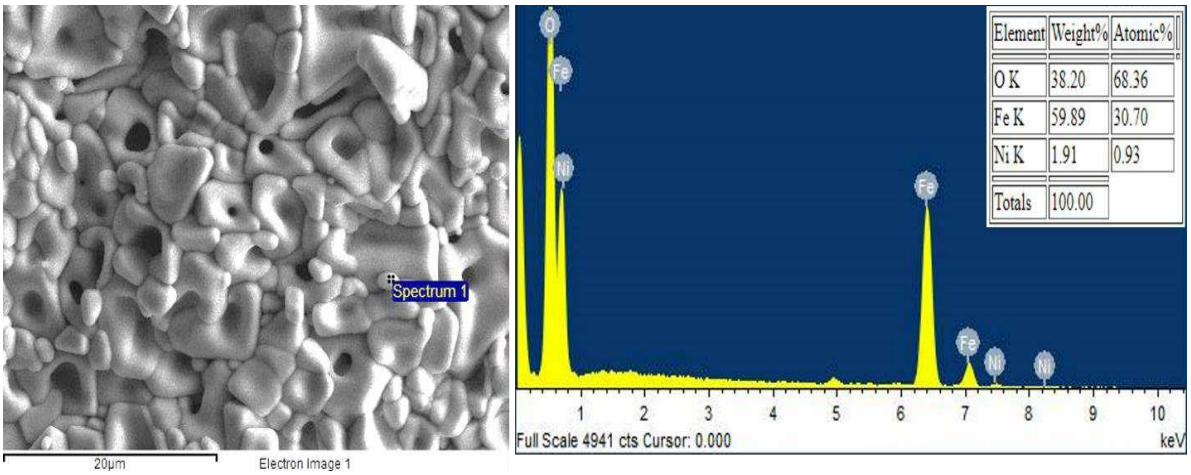

Figure I5: EDX point of globular-shaped oxides of the IN718 alloy surface morphology after oxidation at 850°C after 15 hours.

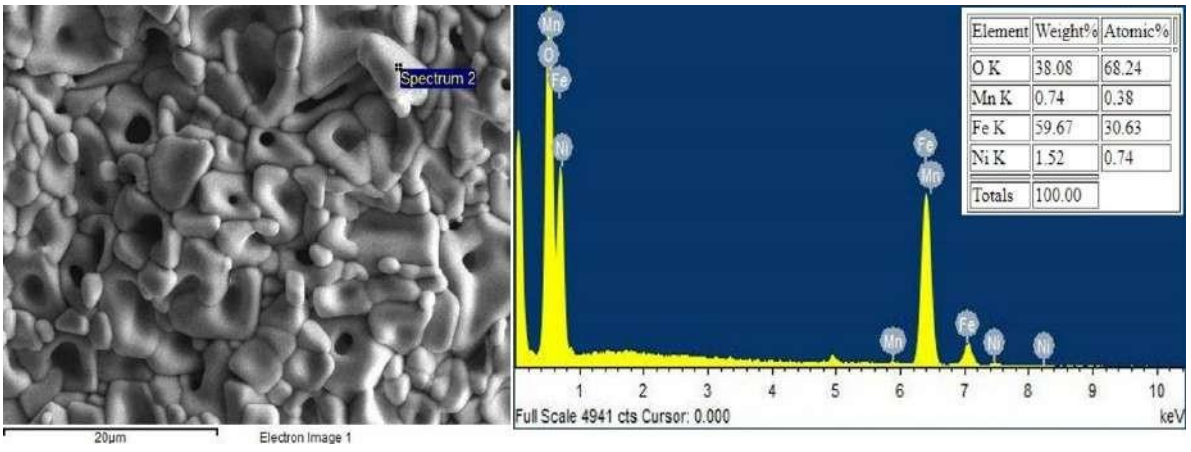

Figure I6: EDX point of block-shaped oxides of the IN718 alloy surface morphology after oxidation at 1050°C after 15 hours.

Appendix J: EDX of cross-sectional morphology of oxidised TiNbTaVW at 850°C and 1050°C

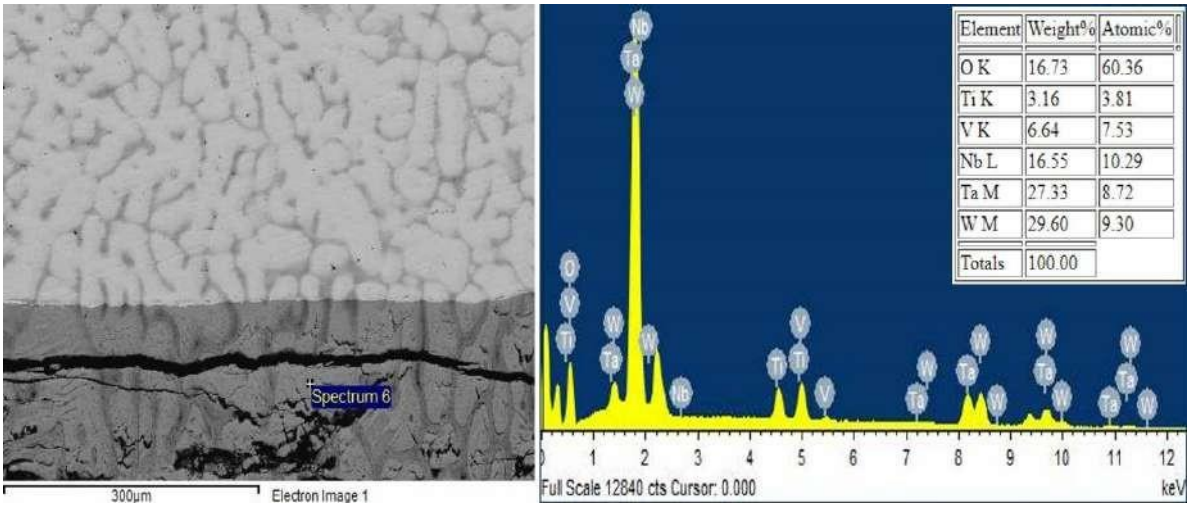

Figure J1: EDX point of TiNbTaVW RHEA oxide scale after oxidation at 850°C after 15 hours.

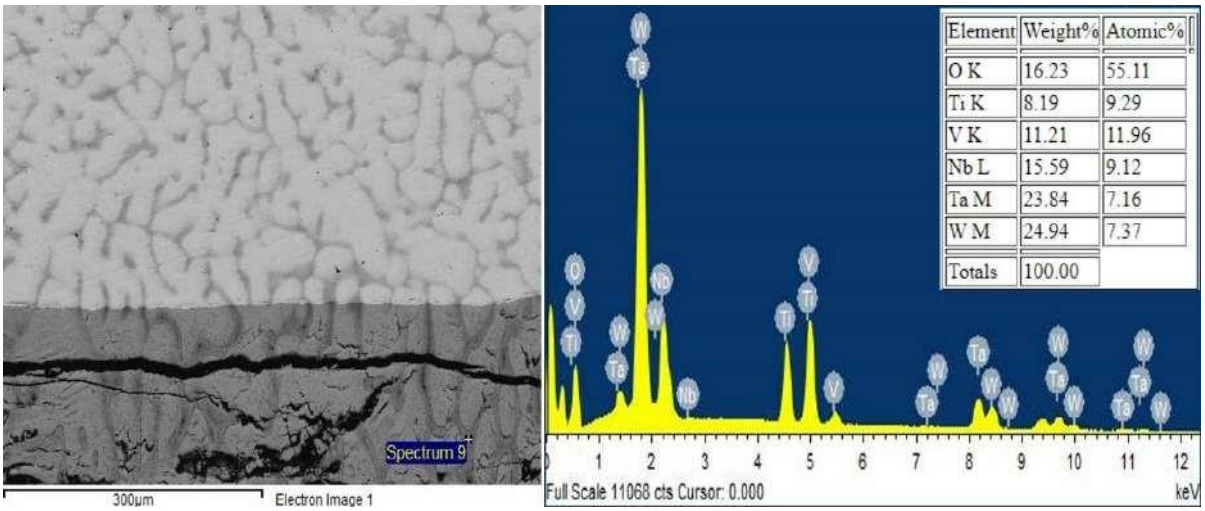

Figure J2: EDX point of TiNbTaVW RHEA internal oxidation layer after oxidation at 850°C after 15 hours.

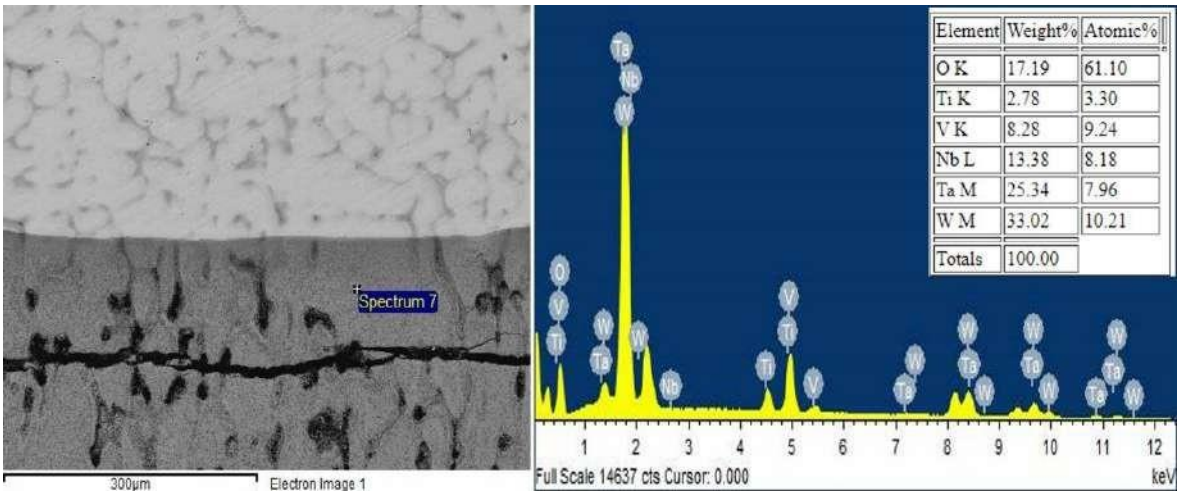

Figure J3: EDX point of TiNbTaVW RHEA oxide scale after oxidation at 1050°C after 15 hours.

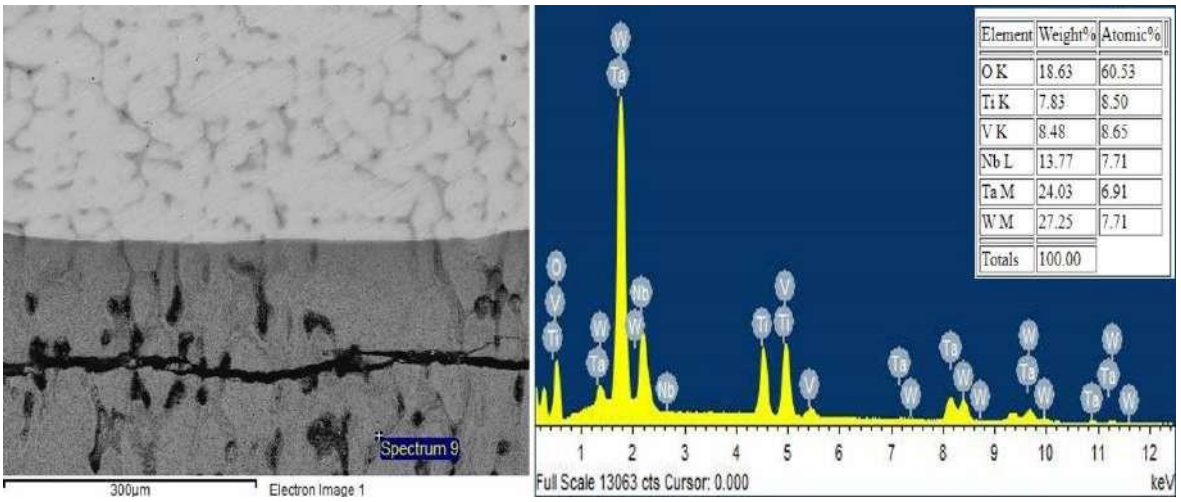

Figure J4: EDX point of TiNbTaVW RHEA internal oxidation layer after oxidation at 1050°C after 15 hours.

Appendix K: EDX of cross-sectional morphology of oxidised CrNbTaVW at 850°C and 1050°C

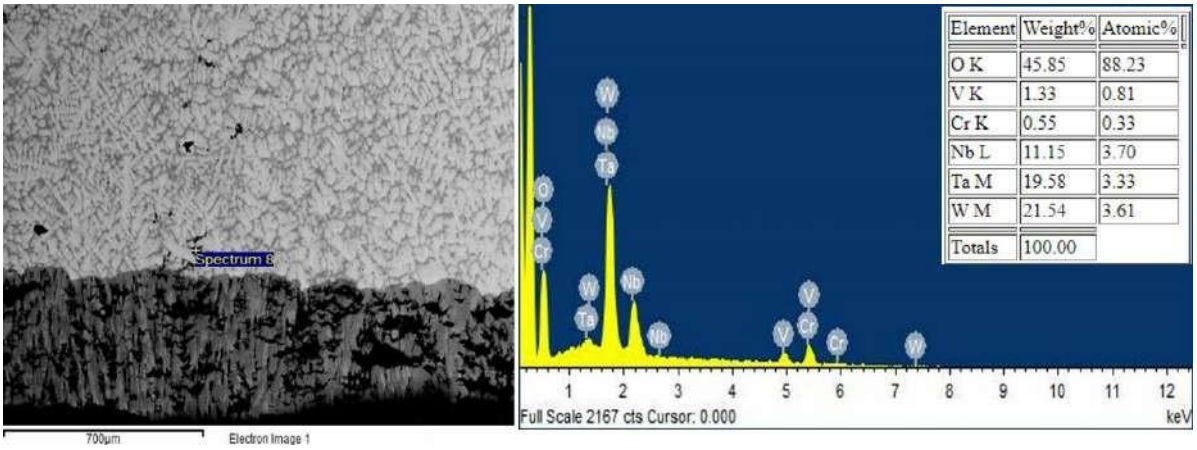

Figure K1: EDX point of internal oxidation area of the oxidised CrNbTaVW RHEA at 850°C after 15 hours.

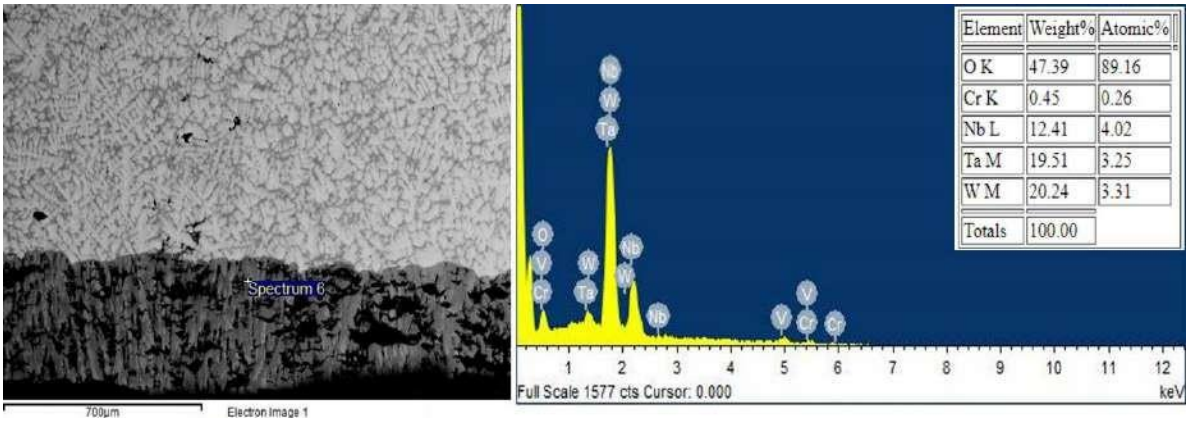

Figure K2: EDX point of oxide scale of the CrNbTaVW RHEA after oxidation at 850°C after 15 hours.

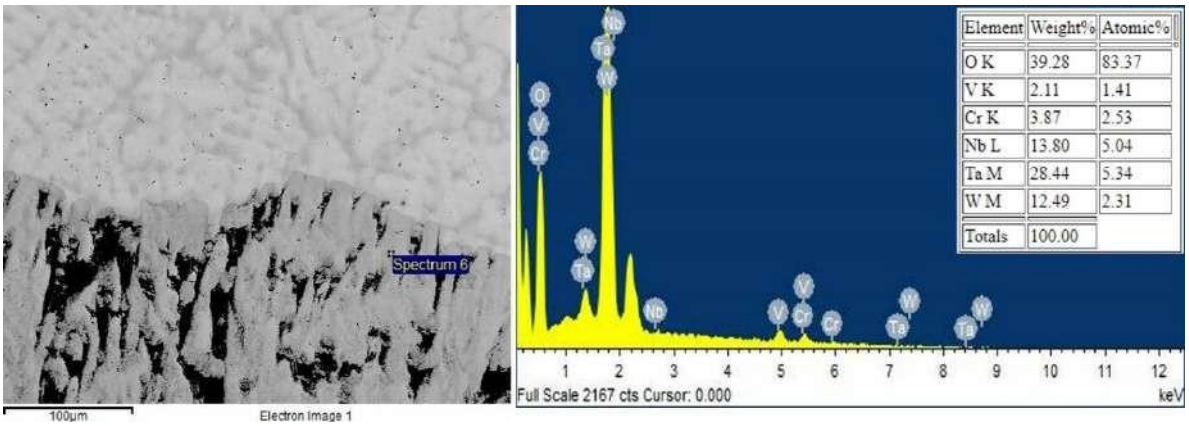

Figure K3: EDX point of oxide scale of the oxidised CrNbTaVW RHEA at 1050 °C after 15 hours.

Appendix L: EDX of cross-sectional morphology of oxidised IN718 at 850°C and 1050°C

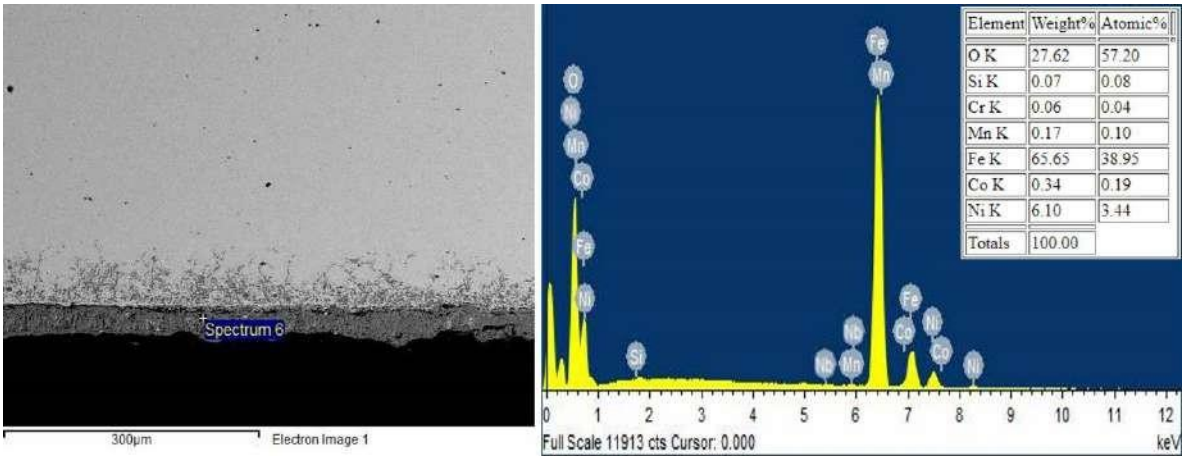

Figure L1: EDX point of oxide scale of the oxidised IN718 alloy at 850°C after 15 hours.

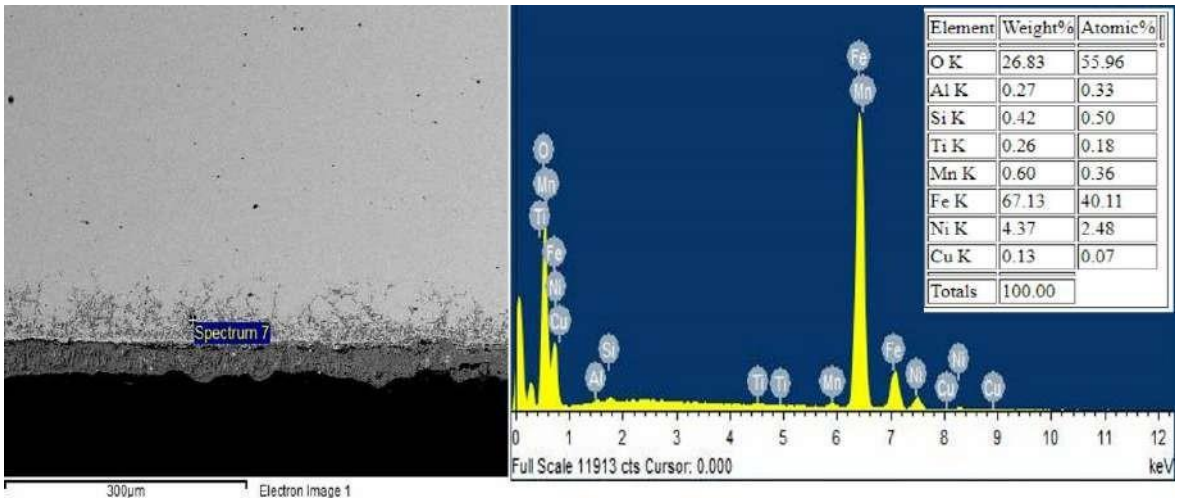

Figure L2: EDX point of internal oxidation layer of the oxidised IN718 alloy at 850°C after 15 hours.

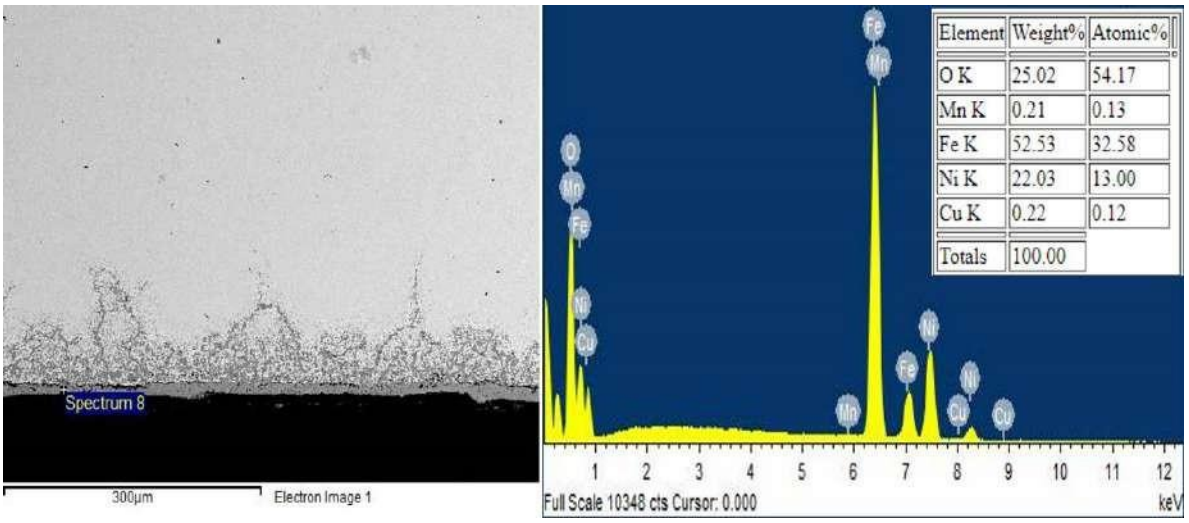

Figure L3: EDX point of oxide scale of the oxidised IN718 alloy at 1050°C after 15 hours.

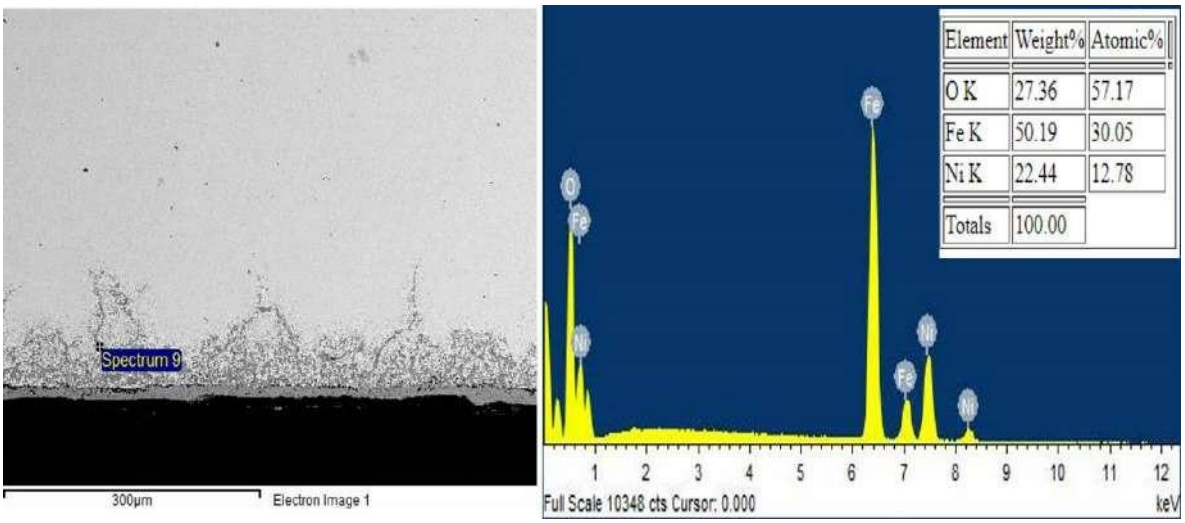

Figure L4: EDX point of internal oxidation layer of the oxidised IN718 alloy at 1050°C after 15 hours.

Appendix M: Publications and conference proceedings

A1: Journal articles

A2: Conference proceedings

Manufacturing Rev. 10, 12 (2023)
© O.S. Bamisaye et al., Published by EDP Sciences 2023
https://doi.org/10.1051/mfreview/2023008

Manufacturing Review
Available online at:
https://mfr.edp-open.org

Review

A comprehensive review on the deformation behavior of refractory high entropy alloys at elevated temperatures

Olufemi Sylvester Bamisaye[1,4,*], Nthabiseng Maledi[1,2], Josias Van der Merwe[1,2], Desmond Edem Primus Klenam[1,3], Michael Oluwatosin Bodunrin[1,2], and Akeem Damilola Akinwekomi[5]

[1] School of Chemical and Metallurgical Engineering, Faculty of Engineering and the Built Environment, University of the Witwatersrand, Johannesburg, South Africa
[2] DSI-NRF Centre of Excellence in Strong Materials, University of the Witwatersrand, Johannesburg, South Africa
[3] Academic Development Unit, Faculty of Engineering and the Built Environment, University of the Witwatersrand, Johannesburg, South Africa
[4] Mechanical Engineering Department, Faculty of Air Engineering, Air Force Institute of Technology, Kaduna, Nigeria
[5] Department of Metallurgical and Materials Engineering, Federal University of Technology Akure, Nigeria

Received: 1 December 2022 / Accepted: 19 April 2023

Abstract. Thermo-mechanical processing of refractory high entropy alloys (RHEAs) at high temperatures is very important. It is an effective method of modifying the microstructure, properties, and shaping into final components after casting. Using the Scopus database, 57 articles relating to the hot deformation of refractory high entropy alloys were extracted from 2011 to 2022. Despite the limited number of articles on hot deformation of RHEAs, it is important to find out if the dominant softening mechanisms reported in other metallic alloys are evident. This is the main impetus for this study since the hot deformation behavior has not been comprehensively studied. All the probable mechanisms influencing deformation in metallic alloys, such as work hardening, dynamic recrystallization, and dynamic recovery, have also been observed in RHEAs. The bulging phenomenon, serrated grain boundaries, and necklace-like structures reported in metallic alloys have also been detected in hot deformed RHEAs. Unsafe deformation behavior such as cracks that have been reported in metallic alloys, have also been observed in RHEAs. This review has provided a comprehensive study on the hot working processes of RHEAs and highlighted critical gaps for future research direction with some suggested limitations.

Keywords: Softening mechanism / refractory high entropy alloy / hot deformation / flow stress / microstructural evolution

1 Introduction

The world's technological growth and development drive a persistent demand for new materials having excellent mechanical properties to fulfil high temperature structural applications. In 2004, two different research groups showed that new alloy systems with simple microstructures could be synthesized from multi-principal elements in equimolar or near-equimolar ratios [1–4]. These new alloy systems have come to be known as high entropy alloys (HEA) [1] or multi-component alloys (MCA) [4,5] or compositionally complex alloys [6]. They are different from other known engineering alloys because they comprise at least five main elements or multi-principal elements at equiatomic percentages [1,7]. Some researchers have questioned the original definition of HEA as alloys comprising at least five elements with equiatomic percentages. These researchers reported that some HEAs can be developed with three or four elements, and the maximum element concentration may be more than 35%. These sets of alloys such as CoCrNi [8]; NiFeCoCr [9]; MoReRuRh [10]; ScGdHo [11] and AlFeTiV [12] have been called medium entropy alloys. In addition, many HEAs may contain intermetallic compounds and complex phases, which have major effects on the microstructures and properties of the materials. HEAs possess combination of properties such as high strength, high hardness, good ductility, outstanding wear resistance, good oxidation and corrosion resistance [13–15].

Refractory high entropy alloys (RHEAs) which have high-melting-point refractory elements, were introduced in 2010 as potential candidates for high temperature functional materials due to their high hardness, wear resistance, and high temperature strength above 1100 °C

* e-mail: bamisayesylvester1988@gmail.com

This is an Open Access article distributed under the terms of the Creative Commons Attribution License (https://creativecommons.org/licenses/by/4.0), which permits unrestricted use, distribution, and reproduction in any medium, provided the original work is properly cited.

when compared with Inconel 718 and Haynes 230 [16,17]. These characteristics are the result of increased melting temperature and solid solution strengthening [13,18]. The main potential applications of refractory high entropy alloys include tribology and thin film [19,20], hydrogen storage [21–24], nuclear materials [25–27], surface and coatings technology [28–30], and hard particles for wear resistance [31]. To optimise the behaviour of RHEAs at high temperatures for structural and functional applications, knowledge of the flow behaviour, microstructural evolution, and deformation mechanisms is important for determining their optimum thermo-mechanical processing parameters. According to Eleti [32], thermo-mechanical processing (TMP) at high temperatures is an effective method of modifying the microstructure and properties of RHEAs after casting. It is also used for shaping alloys into final components. TMP such as hot deformation, results in microstructural improvement, which often promotes strength and ductility of the material [33]. TMP describes the processes that combine plastic deformation of metallic materials with heat treatments. These processes are typically carried out at temperatures higher than 0.4 of the melting temperature (T_m) [34]. During hot deformation, a metal or alloy deforms under conditions of high temperature (greater than $0.6T_m$) and different strain rates of 10^{-1} to 10^{-3} s^{-1} [35,36].

The plastic deformation at such high temperatures frequently results in simultaneous changes in microstructures [34]. Deformation mechanisms of work hardening (WH), dynamic recovery (DRV), and dynamic recrystallization (DRX) are examples of mechanisms that can cause microstructural changes in metals and alloys [37,38]. Comprehensive understanding of the flow behaviour of metals and alloys and their microstructures under hot deformation conditions is crucial during metal forming processes such as forging, hot rolling, and extrusion. Currently, studies on refractory high entropy alloys have at least 700 scientific papers based on the Scopus database. Among those papers are the high temperature deformation behaviour of RHEAs [32,39–41]. Recently, some reviews on hot deformation behavior of high entropy alloys were published [42–46]. However, review papers regarding the hot deformation behaviour of RHEAs are still limited and not comprehensive. For example, Savaedi et al. [42] focused on the deformation mechanism of HEAs at high temperatures, but only one RHEA was found, highlighting microstructural evolution. In George et al. [47] high temperature compressive behaviour of HEAs, high temperature compressive behaviour was reported for only one RHEA.

This review paper will highlight some important findings on the hot deformation behaviour of RHEAs. Emphasis on flow stress, flow softening mechanisms, and microstructural evolution in deformed RHEAs. This review is structured as follows: Section 2 discusses the method for selecting the publications related to the scope of this study. It also describes the trend of scientific publication and citation analysis of hot deformed RHEAs. The flow stress behaviour of RHEA during hot deformation is presented in Section 3. The section also examines the occurrence of discontinuous dynamic recrystallization and continuous dynamic recrystallization, sharp stress drop, and steady-state flow processes in hot deformed RHEAs. Microstructural evolution in hot deformed refractory high entropy alloys is reported in Section 4. Dislocation motion mechanisms in hot deformed RHEAs are reported in Section 5. Section 6 depicts unsafe deformation behavior in hot deformed RHEAs. Section 7 illustrates constitutive modelling and processing maps in hot deformed RHEA. Section 8 contains discussion on the yield strength and compressive strength of reported RHEA during hot deformation. This review closes with a summary of this work (Sect. 9) and future research directions (Sect. 10).

2 Method for selecting publications considered in this review

Published literature was assessed to determine the dominant mechanisms influencing the hot deformation of RHEAs. In the selection phase for the databases for the review, Scopus and Web of Science were considered due to their popularity and efficiency [48]. After a preliminary search in both databases, Scopus was chosen. It has more published articles related to the topic and most articles on Web of Science are also indexed in Scopus. All the journal articles, conferences and monographs were searched and retrieved from the Scopus database using the following keywords: “hot deformation*” AND “refractory high entropy alloy*” OR “high temperature*” AND “refractory high entropy alloy*” OR “hot compression*” AND “refractory high entropy alloy*” OR “high temperature compression*” AND “refractory high entropy alloy*” OR “high temperature compression*” AND “refractory multi-component alloy*” OR “high temperature mechanical properties*” AND “refractory high entropy alloy*”. These keywords were utilised in searching the title, abstract and keyword field which produced 115 papers, but only 57 papers were related to the scope of this study. These 57 documents, comprising of mostly journal articles, were used for the review of the deformation behavior of RHEA.

2.1 Trend of scientific publication on hot deformation of RHEAs from 2011 to 2022

The annual scientific outputs on the hot deformation of RHEAs are shown in Figure 1. According to Scopus, the first article on the hot deformation of RHEAs was published in 2011. There were 2 articles published in that year. However, no publications were found in 2013 relating to hot deformation. This can be attributed to the area of focus within this period, which is mainly on alloy composition search, modelling and simulation of RHEAs. Also, RHEA contains expensive alloying elements that might make it difficult for researchers to explore in much detail considering the cost of making sufficient alloys for hot deformation testing. The publications gradually increased to five from 2014 to 2016 and later dropped to zero in 2017. In 2017, most publications on RHEA are centered on elemental alloying to improve mechanical properties, RHEA coating, oxidation studies of RHEA. Thereafter, in 2018, publications gradually increased to 5

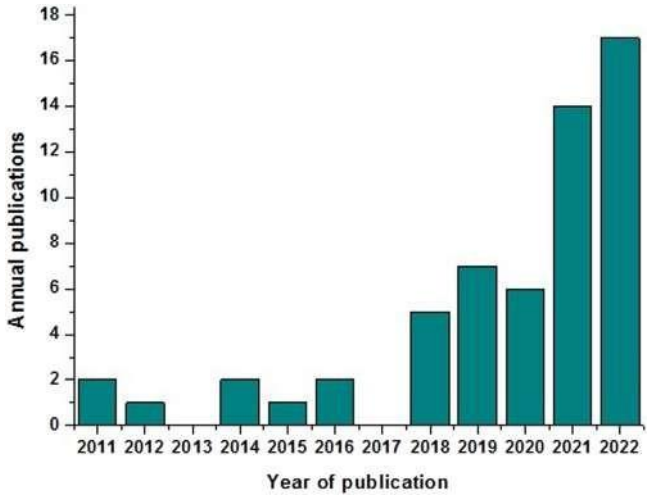

Fig. 1. Annual scientific outputs on hot deformation of RHEAs.

Table 1. Analysis of the top research journals.

Journal and where it was published	Number of articles	Citations
J Alloys Compd	6	108
Int J Refract Met Hard Mater.	3	13
Mater Lett	5	114
J Mater Sci Technol	2	17
Mater Sci Eng A	7	220
Mater Des	2	22
Scr Mater	1	13
Mater Charact	1	9
Intermetallics	4	1652
J Mater Sci	1	440
Int J Mech Sci	1	17
Acta Mater	3	108
Entropy	1	39
Materials	1	22
JOM	1	226

before increasing significantly to 49 from 2018 to 2022. The slight drop in 2020 might be due to the COVID-19 pandemic leading to lockdown and many restrictions which reduced research activities all over the world. In 2022, 17 articles have been published. It is projected that this increase will continue as researchers develop more RHEAs and conduct thermo-mechanical processing.

To determine the publishers with the most publications and citations, consideration was given to publications with at least five citations. Consequently, 39 articles meet these criteria and are shown in Table 1. In Table 1, Mater Sci Eng A had 7 publications with 220 citations to rank first. This is followed by the J Alloys Compd with 6 publications and 108 citations. The next are Mater Lett, Intermetallics, Acta Mater and the Int J Refract Met Hard Mater. Put together, these four journals have a combined total of 15 articles and 1887 citations on the deformation of RHEAs. Table 2 shows the publication analysis per country, with 11 countries contributing to the study on hot deformation of RHEA. Some countries overlap on the same article because the authors collaborated from different countries. From Table 2, China has the highest number of publications (34) and citation counts (616). This is followed by the United States (8 publications and 2313 citations), Japan (4 publications and 108 citations), and the Russian Federation (4 publications and 15 citations). Table 3 shows the citation analysis of the 10 most influential articles on the hot deformation of RHEA. The minimum number of citations for a document is selected to be 50, with 10 of the 50 articles meeting this criterion. The most influential article in terms of citation count is Senkov et al. [49] with 1347 citations. This is not strange because pioneering research articles usually have the highest citation counts as newer articles continue to refer to them.

Next are Senkov et al. [50] with 440 citations and Juan et al. [51] with 262 citations. Completing the top five most influential are two articles by Senkov et al. [52–53] with 255 and 226 citations. The top five most cited articles were published in 2011, 2012, and between 2014 and 2016. More details from Table 3 showed that four of the top five articles that made the top five were from Oleg Senkov, with a combined citation of 2268. Studies on the hot deformation of RHEA in the last decade need to be reviewed so that critical gaps can be identified, and this may draw the attention of more researchers into the field. Despite the limited number of articles on the hot deformation of RHEAs, it is interesting to find out if the dominant deformation mechanisms reported in other metallic alloys are evident in deformed RHEAs. This is the main impetus for reviewing these articles. The next section of the review paper will cover the occurrence of DRV and DRX in the flow curves of hot deformed RHEAs.

Table 2. Publication analysis per country.

Country	Number of articles	Citations
China	34	616
United States	8	2313
Russian Federation	4	15
Japan	4	108
India	3	37
Germany	3	11
Taiwan	2	299
Ukraine	1	12
Australia	1	2
Iran	1	7
South Korea	1	3

Table 3. Top 10 most influential studies on hot deformation of RHEAs.

First author and Year	Article title (doi)	Journal	Citations
Senkov et al. [49]	10.1016/j.intermet.2011.01.004	Intermetallics	1347
Senkov et al. [50]	10.1007/s10853-012-6260-2	J Mater Sci	440
Juan et al. [51]	10.1016/j.intermet.2015.03.013	Intermetallics	262
Senkov et al. [52]	10.1016/j.msea.2011.09.033	Mater Sci Eng A	255
Senkov et al. [53]	10.1007/s11837-014-1066-0	JOM	226
Guo et al. [54]	10.1016/j.msea.2015.10.113	Mater Sci Eng A	66
Eleti et al. [32]	10.1016/j.actamat.2019.04.018	Acta Mater	54
Zhang et al. [55]	10.1016/j.matlet.2016.03.092	Mater Lett	54
Guo et al. [56]	10.1016/j.jallcom.2018.10.230	J Alloys Compd	51
Xu et al. [57]	10.1016/j.msea.2019.03.054	Mater Sci Eng A	50

3 Flow stress behavior of RHEA during hot deformation

Dynamic recovery and dynamic recrystallization are desirable softening mechanisms during the deformation of metallic alloys. The DRV is one of the processes caused by the rearrangement of dislocations during deformation, which results in decreased strain hardening [34]. The DRV flow stresses have simple shapes, and there is strain hardening occurring at low strains followed by steady-state flow at high strains. In the case of DRX, it occurs during straining if the temperature is above $0.5T_m$ [33]. When DRX occurs, the flow stress is reduced and the materials' ability to deform is increased. DRX occurrence is established by a hump in the flow stress due to the softening effect of DRX [58]. It can also be specified by broad peaks and/or oscillations prior to the steady-state flow stress. The mechanisms can be classified into two types: continuous dynamic recrystallization CDRX and discontinuous dynamic recrystallization DDRX [57]. CDRX is characterised by a broad peak stress in the stress–strain curve, while DDRX has a single peak or multiple peaks in the stress–strain curve. The flow stress curves signifying softening mechanisms of Dynamic recovery and dynamic recrystallization have been observed in metallic alloys. For example, in the nickel-based superalloy (GH4169), there was a drop in flow stress related to the dynamic recrystallization softening mechanism at 980-1040 °C and strain rates (0.01-0.001 s^{-1}) [59]. For the *fi*21S alloy, the flow stress stays steady once it has reached its peak signifying dynamic recovery [60]. At 1100 °C and strain rates of 10^{-3} s^{-1}, the flow curves of IN718 alloy revealed a dynamic recrystallization mechanism. When the strain rates decrease to 10^{-3} s^{-1}, the dynamic recrystallization occur during the hot deformation of TB8 titanium alloy [61]. The flow stress of hot deformed C276 superalloy increases sharply with strain until a peak flow stress because of WH at the start of deformation, and then the flow stress reduces gradually with the strain because of dynamic recrystallization.

The flow stress behaviour of refractory high entropy alloys, especially the yield-drop like phenomena has been reported in some literatures [50,54,62,63]. In 2011, Senkov et al. [49] studied the high temperature compression of $Nb_{25}Mo_{25}Ta_{25}W_{25}$ and $V_{20}Nb_{20}Mo_{20}Ta_{20}W_{20}$ RHEAs at 600-1600 °C with a strain rate of 0.001 s^{-1}. At 600 and 800 °C, $Nb_{25}Mo_{25}Ta_{25}W_{25}$ RHEA undergoes continuous strengthening, whereas at higher temperatures (1000-1400 °C) it reachesa highstressatanintermediate strain [49]. According to Senkov et al. [49], the strain softening at these temperatures is an indicator of plastic uncertainty and spallation of the surface material observed at larger strains. At 1600 °C, nearly steady state flow at a fixed stress of ~590-600 MPa was observed, and so the yield stress for $Nb_{25}Mo_{25}Ta_{25}W_{25}$ RHEA steadily decreased as a function of temperature. For the $V_{20}Nb_{20}Mo_{20}Ta_{20}W_{20}$ RHEA deformed at temperatures (1400 and 1600 °C), a fast decline in yield stress and obvious softening was observed. The flow stress in most metals and alloys decreases with the increase in deformation temperature and the decrease in strain rate [64-67]. Also, when there is a reduction in the strain rate or an increase in the deformation temperature, the critical strain for dynamic recrystallization is decreased. Eleti et al. [32] observed a distinct sharp stress drop around yielding, followed by continuous flow softening, while deforming a HfNbTaTiZr RHEA at 1000-1200 °C, strain of 0.69, and strain rate of 10^{-2} to 10^{-4} s^{-1}. The sudden drops of the flow stress are visibly detected at initial stages of hot deformation (Fig. 2a). To reveal the mechanism of sharp stress drop, Eleti et al. [32] performed an interrupted deformation test at 1000 °C, held for 600 s, and then deformed at a strain rate of 0.001 s^{-1} (Fig. 2b). The unusualstress drop in the HfNbTaTiZr RHEA is due to either dislocation unlocking by solute atoms or the ending of short-range order by dislocation motion. Short-range order can have a profound effect on the stacking-fault energy and dislocation motion, which have noticeable influence on the plastic deformation of HEAs [68]. Similarly, in 2022, Li et al. [69] observed a sharp stress drop in $Ti_2ZrHfV_{0.5}Ta_{0.2}$ RHEA at 900-1100 °C and a strain rate of 10^{-2} to 10^{-1} s^{-1} (Figs. 2c–e). To reveal the mechanism of sharp stress drop, Li et al. [69] performed an interrupted hot deformation and strain aging experiment (Fig. 2f) at 900 °C/0.1 s^{-1} with a strain of 0.1 and held for intervals, 0 s and 600 s. The sharp stress drop was also attributed to the unlocking of dislocations pinned by the Cottrell atmosphere or short-range order. The unusual yield-drop phenomena in RHEAs are commonly observed in alloy compositions

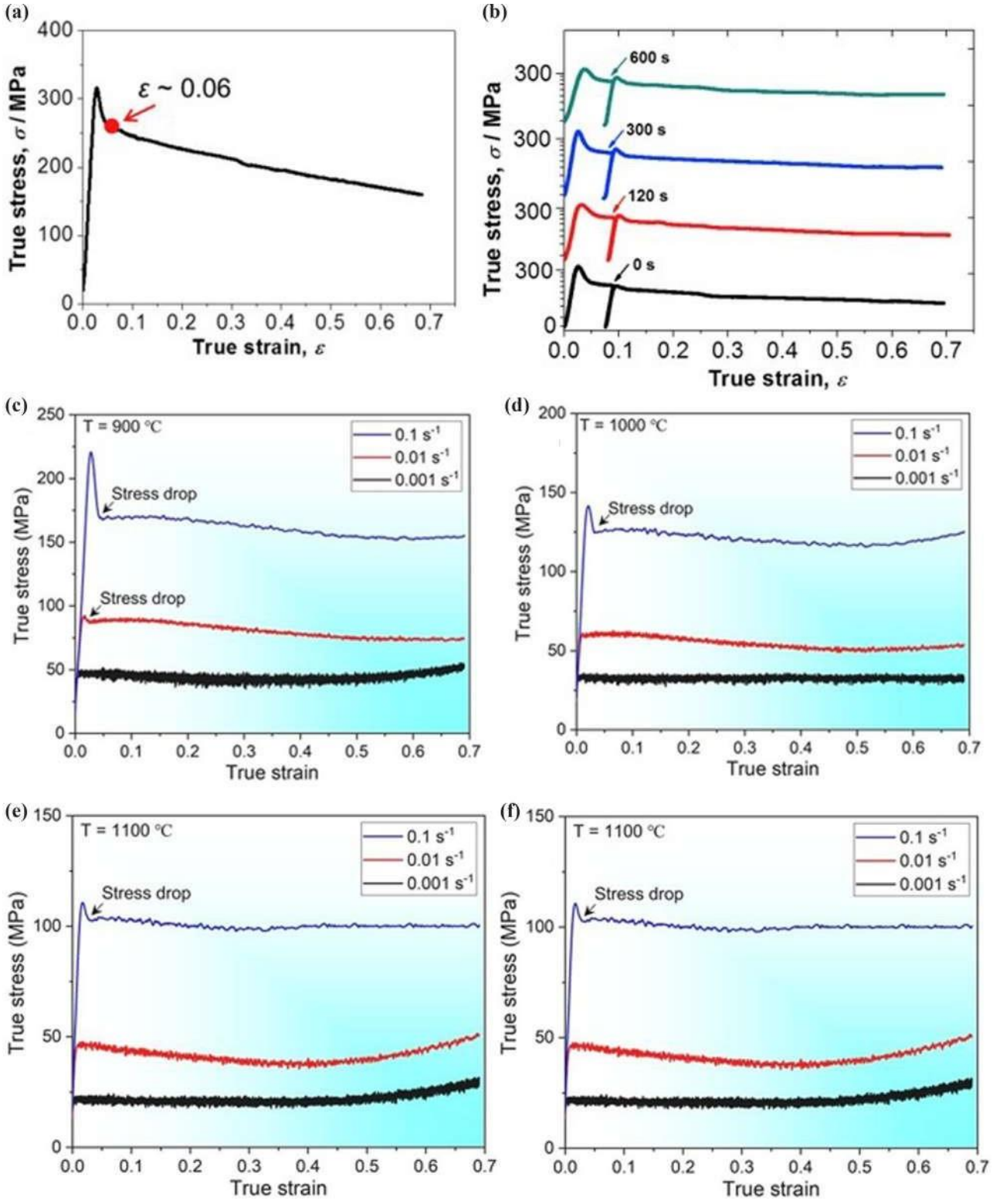

Fig. 2. (a) Sharp stress drop in hot deformed HfNbTaTiZr RHEA at 1000 °C/10^{-3} s^{-1} and strain of 0.06 [32]. (b) Interrupted test on hot deformed HfNbTaTiZr RHEA at 1000 °C/10^{-3} s^{-1} and a strain of 0.06 and then restarted after holding for 0 s, 120 s, 300 s, or 600 s [32]. (c–e) Stress–strain curves of $Ti_2ZrHfV_{0.5}Ta_{0.2}$ RHEA at different strain rates (10^{-1} to 10^{-3}) and temperatures (900–1000 °C) [69]. (f) Stress–strain curve of the strain aging experiment on the $Ti_2ZrHfV_{0.5}Ta_{0.2}$ RHEA at °C/10^{-1} s^{-1} through to the strain of ~0.1 for three times, with intervals between the first and third hot deformation of 0 s and 600 s [69].

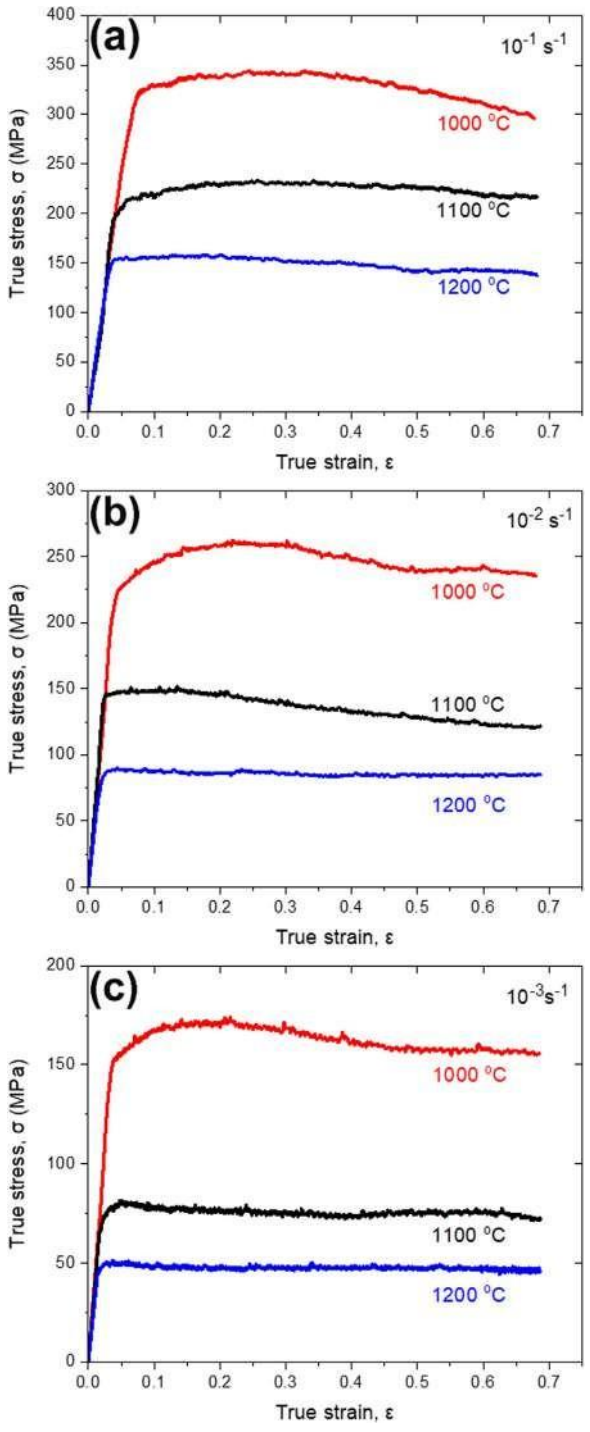

Fig. 3. Flow stress curves of the $TiAlVNb_2$ RHEA at different deformation temperatures of 1000-1200 °C and strain rates of 10^{-1} to 10^{-3} °C [72].

comprising TiZrHfVTa [69], AlNbTaTiZr [70], HfNbTaTiZr [30], AlNbTiVZr [71], TaNbHfZrTi [48], and MoNbHfZrTi [54].

Bai et al. [72] investigated the high temperature study of a $TiAlVNb_2$ RHEA at strain rates from 10^{-3} to 10^{-1} s^{-1} and temperatures from 1000 to 1200 °C. The flow stress of the $TiAlVNb_2$ RHEA at the start of deformation show an obvious work hardening phenomenon (Fig. 3). This is followed by flow stress drops due to temperature increase or decrease in strain rate, which is commonly linked to more thermal activation [73]. The increased temperature leads to the quicker movement of grain boundary and dislocation, thereby showing softening and stress decreasing. In the event of a decrease in strain rate, the deformation time will be delayed, and the dislocation stacking degree will be reduced, resulting in a flow stress decrease. Bai et al. [72] also found that at strain rates (0.1, 0.01 and 0.001) and temperatures (1000-1100 °C), the flow stresses in some curves display decreasing trends after peak flow stress. The decreasing trend can be attributed to DRX taking place in the $TiAlVNb_2$ RHEA. Similarly, the flow stress of deformed $TiAlVNb_2$ RHEA remains stable after peak flow stress at 0.1 s^{-1}/1100 °C, 0.001 s^{-1}/1100 °C, 0.1 s^{-1}/1200 °C, 0.01 s^{-1}/1200 °C, and 0.001 s^{-1}/1200 °C (Fig. 3). After deformation, some flow curves of some alloys could show fluctuations (Fig. 3). For example, in Figure 4, Ni_3Al-based superalloy hot compressed at 1050-1250 °C with a strain rate of 0.1 s^{-1}. The fluctuations, according to Wu et al. [74], can be attributed to an alternation between the effect of WH and the dynamic softening, which is caused by the fast-growing grains at high temperatures and DRX.

The hot deformation characteristics of MoNbHfZrTi RHEA were studied by Guo et al. [54] at a strain rate of 10^{-3}-10^{-1} s^{-1} and temperatures of 800-1200 °C. The stress-strain curve revealed WH before the sample fractured at 800 °C when the strain rate is 10^{-1} s^{-1} and 10^{-3} s^{-1} (Fig. 5). A peak stress with increasing strain was identified at a strain rate of 10^{-1} s^{-1}, and then the stress decreased as the strain was further increased at 900 °C (Fig. 5a). Whereas at low strain rates (0.01 s^{-1} and 0.001 s^{-1}), peak stress was identified with increasing strain but then decreased and slowly reached a stable value as the strain increased. Flow curve characteristics, as identified by Guo and co-workers, belong to dynamic recrystallization occurrence during hot compression of alloys with low SFE [75]. The stress decreases with the increasing strain since the effect of WH can be neutralised or partly neutralised by the formation of the dynamic softening mechanism such as DRV and DRX. In general, for the hot deformation mechanism of MoNbHfZrTi RHEA, both the DDRX and CDRX occur concurrently. This is evident in Figure 5 where the serrated flow stress shows DDRX and the broad peak stress shows the CDRX.

In 2021, Wei et al. [76] observed work hardening after yielding in $W_{0.4}MoNb_xTaTi$ (x = 1.1, 1.3, and 1.5) RHEA hot deformed at strain rates of 0.001 s^{-1} and temperatures of 800, 1000, and 1100 °C. At 800 and 1000 °C, a decrease in the yield stress was seen and related to the energy provided by the high temperature. After reaching the yield point, Wei et al. [76] indicated a distinct steady-state flow stages which were seen on the true stress-strain curves. During hot deformation of mechanical alloyed and spark plasma sintered MoNbTaTiV RHEA, Liu et al. [77] observed that flow stresses at temperatures (1100 and 1200 °C) exhibit similar trends. Also, the flow stresses are slowly reduced after attaining the maximum compressive stress when the

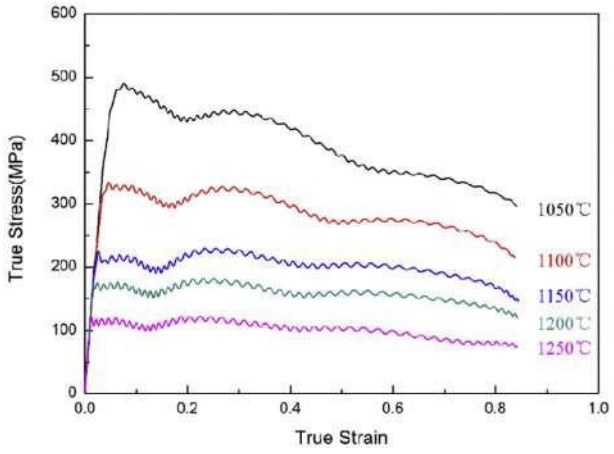

Fig. 4. The flow stress-strain curves in hot deformed Ni_3Al-based superalloy at 1050-1250 °C with strain rate of 0.1 s^{-1} [74].

strain rates are reduced to 5×10^{-2} s^{-1} and 5×10^{-3} s^{-1}. An obvious peak stress and stress reduction process were observed at 1300 °C and strain rates of 5×10^{-1} s^{-1} and 5×10^{-2} s^{-1}, followed by a steady state flow stress. Liu et al. [77] further noticed that the flow stresses instantly reached steady state at strain rates of 5×10^{-3} s^{-1} and 5×10^{-4} s^{-1}, which is comparable to the flow stress evolution at 1100 °C and 5×10^{-4} s^{-1} deformation conditions and 1200 °C and 5×10^{-4} s^{-1} deformation conditions. This clearly shows that smaller stresses are obtained during higher deformation temperatures and lower strain rates. This is further evident in the spark plasma sintered MoNbTaTiV RHEA at a strain rate of 5×10^{-2} s^{-1} and with temperature reduction (1200-1300 °C), the yield stress is rapidly reduced, and the flow stress quickly reaches a steady state. Typical DDRX flow stresses were formed at strain rates of 0.5 s^{-1} and temperatures (1200-1300 °C). Feng et al. [78] discovered serrated flows in deformed CrMoNbV RHEA alloy when the temperature exceeded 500 °C and the strain rate was 0.0002 s^{-1} (Fig. 6). This was attributed to the contact between dislocations and the local stress area due to the rugged local atomic environment [79]. The serrated flows became less obvious at 1000 °C compared to 500-900 °C, signifying a diffusion-mediated softening mechanism could become important.

The as-cast $Al_{10}Nb_{15}Ta_5Ti_{30}Zr_{40}$ alloy deformed at temperatures ranging from 250 to 1200 °C and a strain rate of 10^{-3} s^{-1} exhibited peak stress at 600 °C at the start of deformation and then continuously decreases until the end of deformation [70]. At 800 °C, the yield stress dropped considerably at a strain of 0.05 and later displayed a very minor decrease in the flow stress with increasing strain. The reduction in the flow stress indicated DRX. In addition, at a temperature range of 250-500 °C, the deformed alloy has almost the same stress values. At 600 °C, a fast stress drop occurred at the start of deformation, which was followed by a constant decrease in the flow stress. Senkov et al. [70] described the deformation behaviour at temperatures ($T \geq$ 600 °C) as a softening feature with the occurrence of a sharp stress drop almost immediately after yielding. The softening feature was likened to dislocation recovery and DRX. Furthermore, the sharp stress drop is followed by a slow flow stress decrease or the formation of a steady-state flow process. The occurrence of a large peak stress followed by a sharp stress drop at the start of deformation can be a result of the short mobility of dislocations present before deformation.

In summary, all the probable mechanisms influencing deformation in metallic alloys, such as WH, DRX, and DRV, have also been observed in refractory high entropy alloys. The sharp drops in the flow stress experienced in some reported RHEAs were attributed to the unlocking of dislocations pinned by the Cottrell atmosphere or short-range order. The DDRX and the CDRX occurred concurrently in some of the hot deformed RHEAs. This is evident in the flow curves of the RHEAs by the serrated and broad peak flow stress. A summary of the flow stress in other hot deformed RHEAs is shown in Table 4 at different strain rates, strains and temperatures. The next section covers the microstructural features observed in hot worked RHEAs.

4 Microstructural evolution during hot deformation of RHEA

In metallic alloys such as GH4169, Nb-1Zr-0.1C and IN718, bulging and serration formation, necklace-like structure, and LAGB movement to HAGB have been attributed to dynamic recrystallization, continuous and discontinuous dynamic recrystallization [59,64,88]. These microstructural features have also been seen in hot worked RHEAs. Senkov et al. [89] reported the microstructural evolution of hot deformed NbTaTi and NbTaZr RHEAs. Prior to the deformation, the microstructure of the NbTaTi RHEA comprised of coarse, polygonal grains of ~0.4 mm in diameter, whereas the NbTaZr RHEA comprised of finer equiaxed grains of ~40 mm in diameter. Furthermore, coarse, needle-like or plate-like, dark second-phase particles were observed at NbTaZr RHEA grain boundaries, some of which spread inside the grains. After deformation at 1000 °C, the NbTaTi RHEA microstructure showed elongation of grains and the creation of distinctive patterns in the directions inclined about 60-70° to the compression direction. This signifies dynamic recrystallization of the grains. The microstructure of the NbTaZr RHEA after deformation at 1000 °C showed elongated equiaxed grains (DRX) and many plate-like Zr-rich second phase particles situated at grain boundaries. Jia et al. [90] study on the NbTiVZr refractory medium entropy alloy showed an equiaxed grain microstructure before hot compression. At 800 °C, the grain boundaries are many and are bounded by an increasing number of precipitates as the temperature is increased. For the inner grain, a relatively loose microstructure can also be observed.

In the silicide containing $HfNbTiVSi_{0.5}$ RHEA by Zhang et al. [55], deformation bands from the longitudinal sections at 800 °C and 1000 °C were observed. This demonstrated that the matrix softened due to the strong thermal activation effect. The silicides are severely deformed by the plastic flow effect and become more

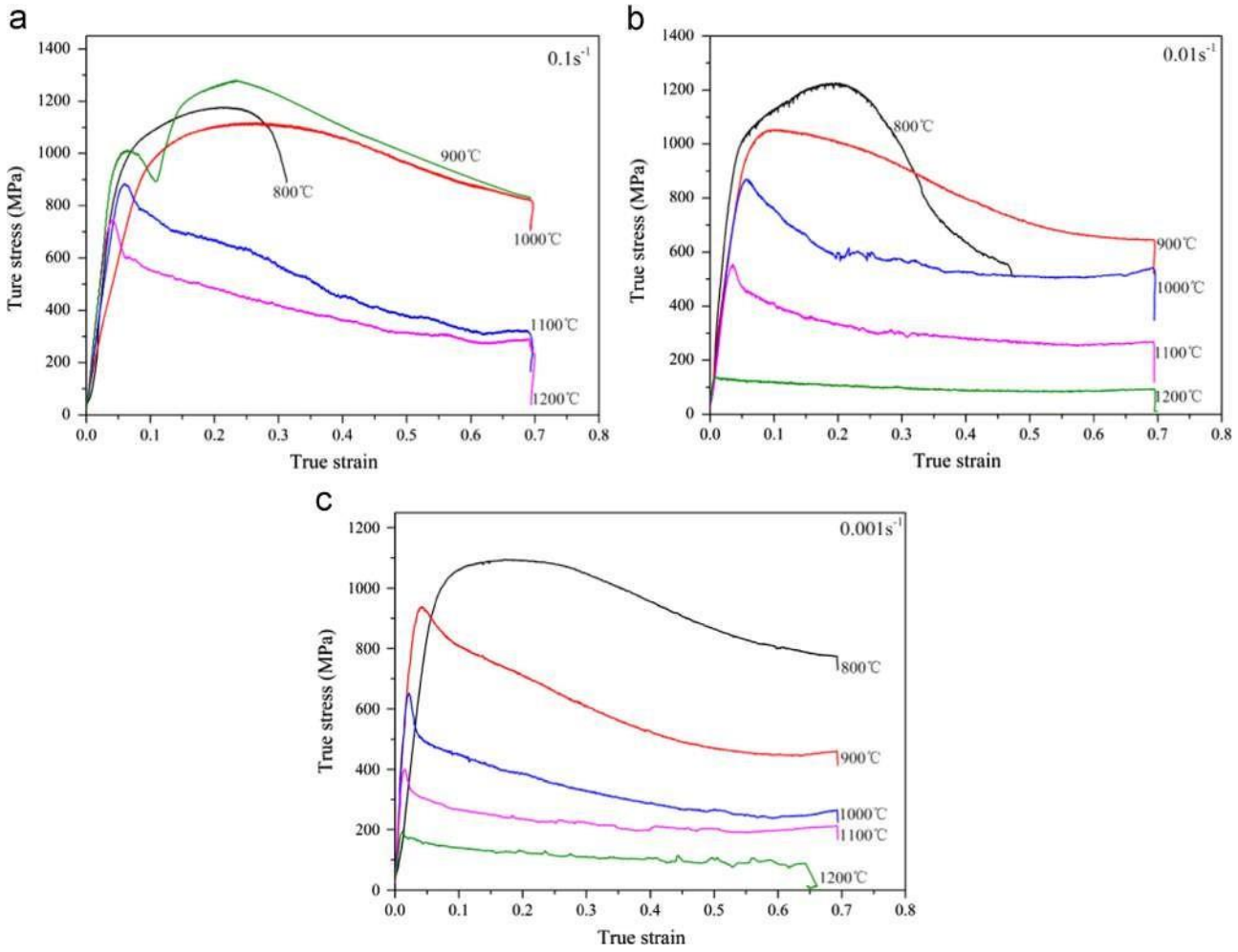

Fig. 5. Flow stress curves of MoNbHfZrTi RHEA at 800 °C, 900 °C, 1000 °C, 1100 °C, 1200 °C with different strain rates: (a) 10^{-1} s^{-1}, (b) 10^{-2} s^{-1}, (c) 10^{-3} s^{-1} [54].

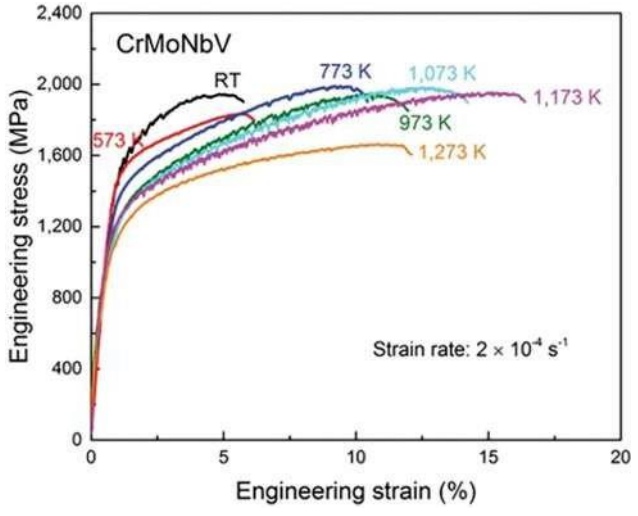

Fig. 6. Serrated flows in deformed CrMoNbV RHEA alloy at wide range of temperatures [78].

refined and homogeneous than in the as-cast conditions. Guo et al. [91] discovered a dendritic (BCC_A2#1) and inter-dendritic (BCC_A2#2) microstructure in a $TaMo_{0.5}ZrTi_{1.5}Al_{0.1}Si_{0.2}$ RHEA after casting and 48 hours of annealing at 1300 °C. Also, an HP16 silicide in the main region of the interdendrite later forms a butterfly-like eutectic morphology with the BCC_A2#2 phase. At 1000 °C, DRX start within the inter-dendritic region, leading in the creation of sub-micron grains. A heterogeneous necklace microstructure also formed through dynamic recrystallization (DRX) in the $TaMo_{0.5}ZrTi_{1.5}Al_{0.1}Si_{0.2}$ RHEA. Also, a necklace-like structure was formed in MoNbHfZrTi RHEA, which composed fine recrystallized grains along the initial grain boundaries, suggesting active DDRX [40]. To be specific, at 1100 °C and 0.5 s^{-1}, necklace-like structures with fine undistorted grains (1.8 mm) were observed along the original grain boundaries. Necklace-like structures were also observed with fine undistorted grains (2.2 mm) along the shear-deformation region at 1100 °C and 0.1 s^{-1}. These observations confirm the presence of DDRX.

Table 4. Summary of flow stress behaviour of hot deformed refractory high entropy alloys.

Alloy composition	Strain rate (s^{-1})	Strain	Temp. (°C)	Findings	References
$AlNb_2TiV$	10^{-3}	0.33	600, 800 and 1000	An increase in temperature leads to a decrease in yield stress, initially slowly at 600 and 800 °C, and then rapidly at 1000 °C. Softening with steady flow was observed indicating the occurrence of dynamic recovery.	[80]
$AlNbTi3VZr_{1.5}$	10^{-3} to 1	–	1100,1150, 1200,1250	All the flow stress softens, signifying the occurrence of DRX.	[71]
$ZrTiHfNb_{0.5}Ta_{0.5}$	10^{-3}	0.5	700, 800 and 900	The stress increased rapidly and then decreased to a stable value with an increase in deformation.	[81]
WReTaMo	10^{-3}	0.25	1600	At 1600 °C, the WReTaMo alloy shows continuous strengthening without peak stress until the final testing point at strain of 25%.	[82]
$Nb_{40}Ti_{25}Al_{15}V_{10}Ta_5Hf_3W_2$	10^{-3}	0.69	800, 900 and 1000	Samples deformed at 800 °C show strain hardening. Samples deformed at 900 °C and 1000 °C show persistent softening after yielding which signifies dynamic recovery and dynamic recrystallization.	[41]
$Nb_{30}Mo_{30}Hf_{20}Co_{20}$	10^{-4}	0.6	600, 800 and 1000	Steep and delayed strain hardening stage was observed in the flow stress curves at 22 °C and 600 °C. Softening with steady-flow stages was observed at 1000 °C, signifying dynamic recovery.	[83]
$C_xHf_{0.25}NbTaW_{0.5}$	1^{-3}	–	1000, 1200 and 1400	A continuous hardening after the yield was observed in all the specimens. As the temperature increased, the steady-state stress appeared at lower strain values.	[84]
TaNbHfZrTi	10^{-5} to 10^{-1}	–	750	Deformation strengthening occurred and the flow stress increased continuously with an increase in the plastic strain at high-strain rates	[50]
Ti_xZrVNb	10^{-3}	–	600 and 800	At 800°C, the strengths of the alloys significantly decreased. Furthermore, a serrated curve was also observed at 800 °C due to the alternating softening deformation and recrystallization	[85]
HfMoNbTaTi	10^{-2}	0.8	800, 1000 and 1200	A continuous drop in the flow stress started at the peak stress (strain = 0.027), proceeded by a steady-state flow stage from a strain of 0.8. Dynamic recrystallization behaviour was observed during compression at 1200 °C.	[86]

Table 4. (continued).

Alloy composition	Strain rate (s^{-1})	Strain	Temp. (°C)	Findings	References
$NbCrMo_{0.5}Ta_{0.5}TiZr$	10^{-3}	–	800, 1000 and 1200	At 1000 °C, dynamic recrystallization of the alloy occurs after a short stage of strain hardening. At 1200 °C, further decrease in the flow stress, followed by weak softening and a steady state flow (dynamic recovery).	[52]
HfMoNbTaTiZr	10^{-3}	–	800, 1000 and 1200	At 800 °C, work hardening occurred. At 1000 °C and 1200 °C, dynamic recrystallization occurred.	[87]

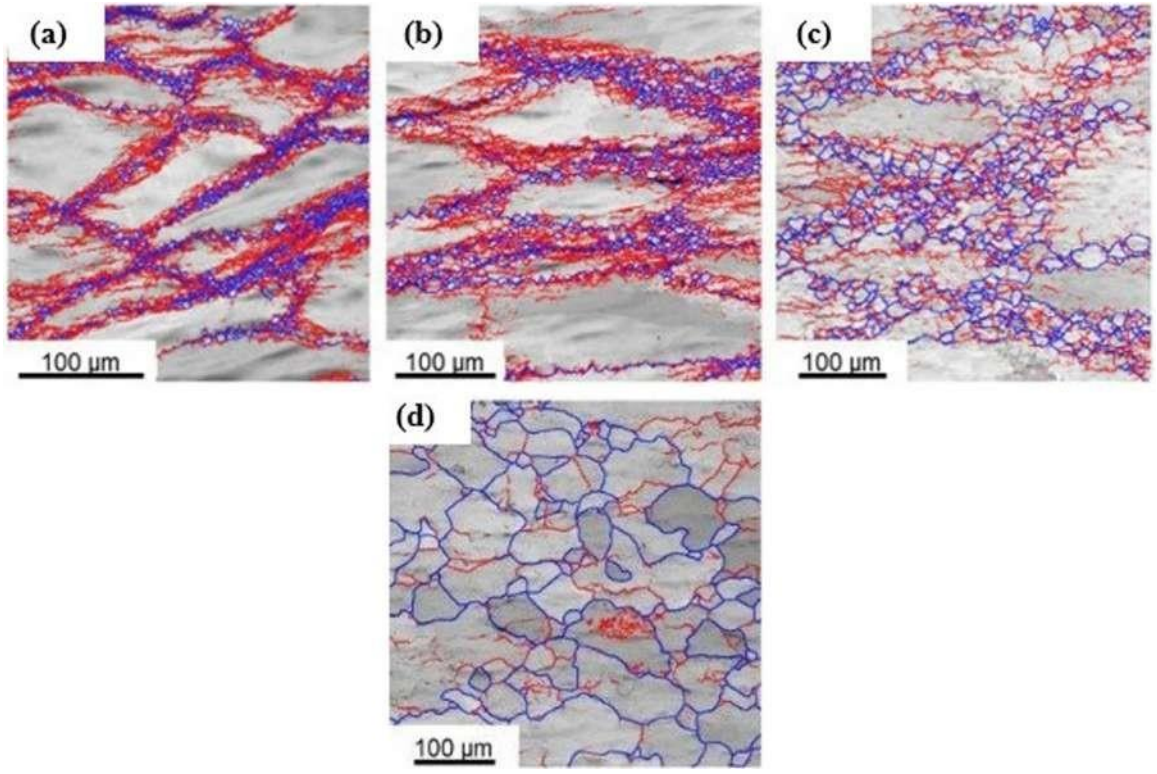

Fig. 7. EBSD maps of HfNbTaTiZr RHEA hot compressed to e = 0.69 at various temperatures and strain rates. Deformed at (a, b, c) 1000 °C, (d) 1200 °C [32].

Eleti et al. [32] studied the microstructure evolution in hot deformed HfNbTaTiZr RHEA and discovered fine, equiaxed grains in the necklace structures. The equiaxed grains in the necklace structures are bounded by blue HAGBs, which are recrystallized grains (Fig. 7). In connection to the continuous flow softening observed after the sharp stress-drop in HfNbTaTiZr RHEA, typical necklace microstructures composed of coarse, uncrystallized grains surrounded by fine dynamically recrystallized grains were detected (Figs. 7a, b, c). At 1200 °C and strain rate of 10^{-3}, a more homogeneous microstructure comprised of coarse grains in the specimen was observed and possibly corresponds to dynamic recrystallization (DRX) grains after substantial grain growth (Fig. 7d).

A low-density $TiAlVNb_2$ RHEA showed a coarse grain with a dendrite structure in the as-cast condition [72]. Fine grains occur along the original grain boundaries in the samples deformed at lower temperatures or higher strain rates, such as at 0.1 s^{-1}/1000 °C, 0.1 s^{-1}/1100 °C, 0.01 s^{-1}/1000 °C and 0.001 s^{-1}/1000 °C. The fraction and grain size of the fine grains increase with the increasing deformation temperature or decreasing strain rate. Part of the fine

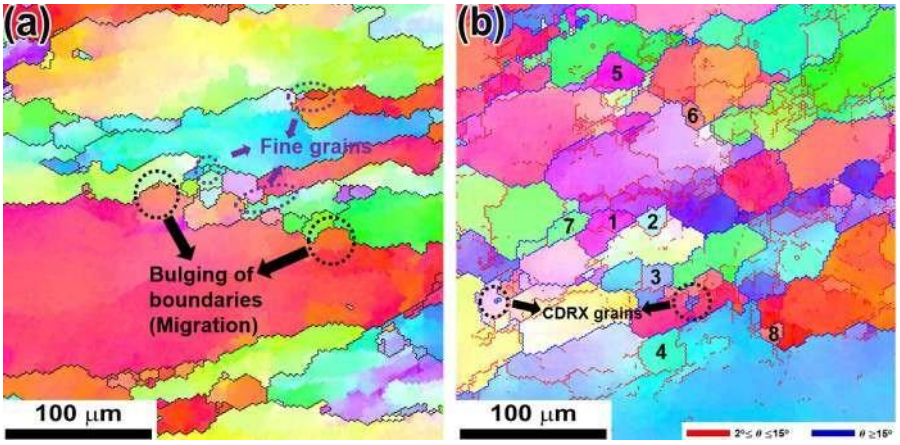

Fig. 8. The inverse pole figure map of $TiAlVNb_2$ RHEA at 10^{-2} s^{-1}/1200 °C (a) and 10^{-3} s^{-1}/1100 °C (b) [72].

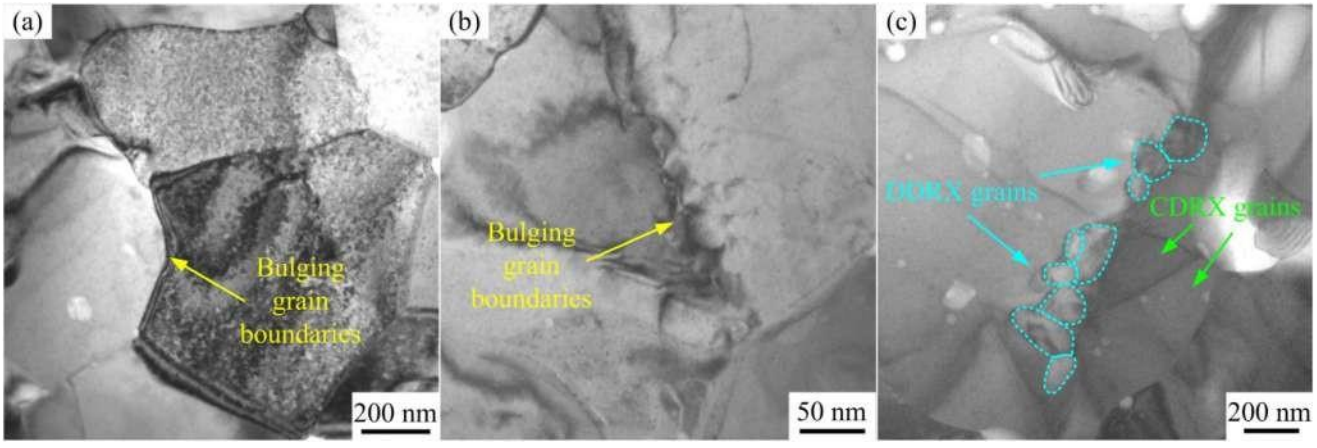

Fig. 9. Transmission electron microscopy images of the hot compressed MoNbTaTiV RHEA showing (a) and (b) bulging grain boundaries and (c) discontinuous dynamic crystallized grains and continuous dynamic crystallized grains [63].

grains are equiaxed, while the others appear elongated due to on-going compression. The $TiAlVNb_2$ RHEA is composed of relatively uniform coarse grains at the highest temperature (1200 °C) and lowest strain rate (0.001 s^{-1}). Some fine dynamic recrystallized grains with clear misorientation from the initial grains can be found in grain boundaries and triple junctions of grains (Fig. 8a). Serrated grain boundaries of coarse grains bulge towards the adjacent grains by migration of high angle grain boundaries, which form some sub-grains (labelled as 1-4) surrounded by sub-boundaries (Fig. 8b). This is classified as a DRX grain formation mechanism and is strongly dependent on increased energy storage caused by the propagation and pile-up of dislocations near to the boundaries during the high-temperature compression [33,66].

In the hot deformation processing of a MoNbTaTiV RHEA fabricated by powder metallurgy, the microstructural characteristics revealed nearly-equiaxed grains, apart from some deformation microstructures seen at 1100 °C and 0.05 s^{-1} [63]. With increasing deformation temperature and decreasing strain rate, the number of these ultrafine dynamically recrystallized grains gradually decreases. As shown from TEM images in Figure 9, the grain boundaries of the ultrafine grains act as a nucleation point for the deformed MoNbTaTiV RHEA. Furthermore, smaller bulging shapes were observed to be present (Figs. 9a and b). As a result, several ultrafine discontinuous dynamic recrystallized grains are produced, as shown in Fig. 9c. The grain boundaries bulging, which is caused by the nucleation of new grains and subsequent grain expansion, distinguishes discontinuous dynamic crystallized grains from other types of crystallized grains [75]. The bulging phenomenon was also observed in some studies on the hot deformation of arc-melted RHEA [54,72,92].

In summary, the bulging phenomenon, serrated grain boundaries, and necklace-like structures reported in metallic alloys have also been detected in hot deformed RHEAs. The necklace-like structures have been typically observed in FCC metals and alloys with medium or low stacking-fault energies but not often in BCC metals and alloys. The following elemental compositions:

TiZrHfNbTa, TiZrHfNbMo, TaNbHfZrTi, TiZrHfVTa, HfNbTaTiZr, MoNbHfZrTi, TaMoZrTiAlSi, and AlNbTiVZr RHEAs commonly have the necklace-like structures. The next section discusses the dislocation motion mechanisms observed in hot deformed RHEAs.

5 Dislocation motion mechanisms in hot deformed refractory high entropy alloy

Dynamic recrystallization and dynamic recovery are governed by dislocation geometry and movement during deformation. Inthe plastic deformationofmetallicmaterials, the important mechanism that governs mechanical properties is dislocation slip [93]. The dislocation multiplication rate rises with the increase in strain rate at the same deformation temperature and only happens inmetallicalloys with positive strain rate sensitivity [94]. According to Liu et al. [95], the softening mechanism in coarse grain alloys is dominated by dislocation movement, while that for ultrafine-grained alloys is mostly boundary gliding and rotation. Due to the lattice distortion effect in high entropy alloys, dislocations are likely to possess a rare dislocation core structure and the Peierls potential is fluctuated, which has a significant effect on mechanical properties [93]. Although there is still a lack of availability of widespread research on dislocation motion mechanisms in high temperature compressed refractory high entropy alloys. This section briefly discusses the types of dislocation motion mechanism in high temperature compressed RHEA.

A study of HfNbTaTiZr RHEA single crystals by Yasuda et al. [96] showed screw dislocations (1/2<111>) which control the deformation behaviour and it is similar to conventional BCC metals. The dislocation slip traces are a little wavy and are inclined to cross-slip and less sensitive to deformation temperature. Eleti et al. [32] observed plastic deformation by dislocation slip in a RHEA deformed at a strain of 0.69, similar to conventional BCC metals and alloys. In another study by Hu et al. [97] on the dynamic behaviour of TaNbHfZrTi RHEA at higher temperatures, it was found that the dominant softening mechanism is linked to the thermally activated screw dislocation at quasi-static conditions and the phonon drag controlled screw dislocation motion at high strain rates and high temperatures. Li et al. [98] studied ZrNbMoTaW RHEA with in-situ forming heterogeneous structure at 1000 °C. It was found that screw dislocation cross slip was the dominant plastic deformation mechanism. Pang et al. [41] studied the high temperature strength of the $Nb_{40}Ti_{25}Al_{15}V_{10}Ta_5Hf_3W_2$ RHEA deformed after 50% compression at 800 °C. A massive dislocation motion was found in the deformed region, which is multiple dislocation interactions, such as cross-slip and tangles. The massive dislocation motion pile up at the grain boundaries, and the resultant high stress concentrations in these regions facilitate the concentrated deformation along grain boundaries. This occurred because the deformation temperature at 800 °C was not high enough to facilitate dislocation movement and diffusion to relieve stress concentration. For a $Re_{0.5}MoNbW\ (TaC)_{0.5}$ RHEA composite deformed at 1200 °C, a high density of dislocations was observed in the BCC and FCC-MC phases upon severe compression compared to the as-cast microstructure [99]. The phase interface after deformation revealed screw dislocation motion in BCC close to the interface. Furthermore, severe dislocation entanglement and dipolar dislocation walls existed in the $Re_{0.5}MoNbW(TaC)_{0.5}$ high-entropy alloy. Dislocation dipoles created by dislocation cross-slip and distinguishable pinning effects were evidently observed in the compressed BCC phase. In general, the substructures of dipolar dislocation walls originate from the BCC phase.

In the hot deformation study of MoNbTaTiV RHEA produced by powder metallurgy, increase in temperatures and decrease in strain rates promote the involvement of the grain boundary gliding mechanism [95]. This resulted in a decrease in intragranular dislocation generation. Grain deformation is dominant at low deformation temperature and high strain rate, which results in an increase in the dislocation density and many dislocation entanglements. Feng et al. [100] investigated the dislocation features of CrMoNbV RHEA at 700, 800 and 900 °C. It was found that non-screw dislocation that are less mobile due to pinning are the dominant dislocation motion during high-temperature deformation in the CrMoNbV RHEA. This effect contributed to the observed superior high-temperature strength in the deformed CrMoNbV RHEA. Prior to the mechanical deformation, no clear pre-existing dislocations were observed. However, at 900 °C and plastic compression of 3.3%, considerable pinned and curved dislocation motion are seen. This means that the strong pinning effect applied on the dislocation motion specifies strong connections between dislocation motion and severe distorted local lattice/local compositional fluctuations. The solute atoms along the pathways of a gliding dislocation are independent point obstacles that pin the dislocation, which bows out in the regions between the solutes.

6 Unsafe deformation behavior in hot deformed RHEA

During the deformation process, stress concentration occurs, which causes a sharp increase in local energy. When the stress concentration reaches a value, crack propagation begins to appear, releasing energy. According to Prasad et al. [101], the unsafe deformation behavior include: flow localisation, void formation, inter-crystalline cracking, wedge cracking, kink bands and adiabatic shear bands. Unsafe deformation behavior have been reported in metallic alloys: IN738LC (deformation bands and grain boundary cracking) [102]; Ni3Al (flow localization, adiabatic shear bands and cracks) [74]; $Ti_{15}Mo_3Al_3Nb_{0.2}Si$ (cracks) [60] and TB8 titanium alloy (flow localization and shear bands) [61]. The unsafe deformation behavior have also been reported in RHEAs.

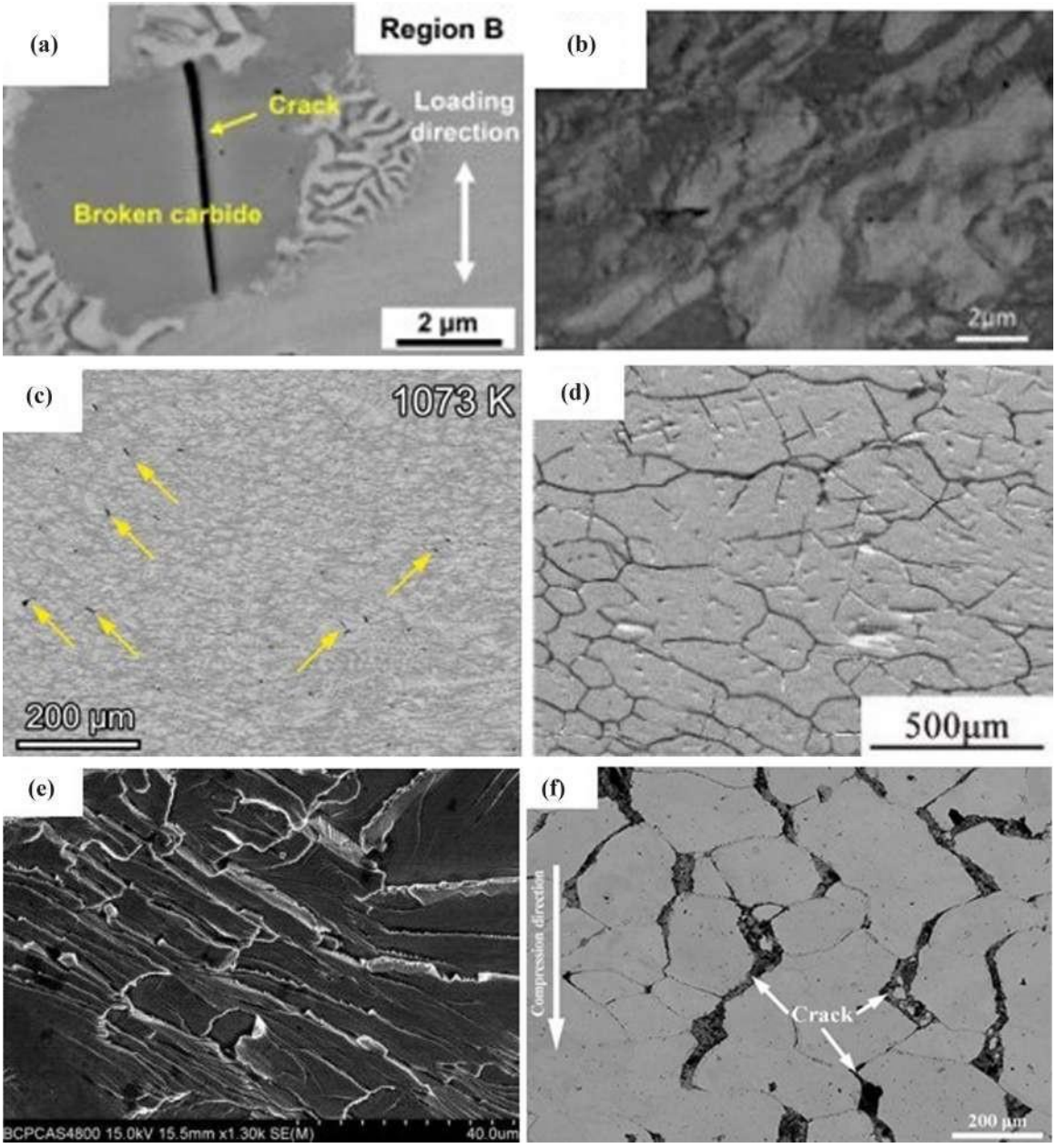

Fig. 10. Crack propagation in hot compressed refractory high entropy alloys at 800 °C (a–e) and 1600°C (f): (a) Broken carbide and crack in TiNbTaZrHf RHEA based composite [104]. (b) Microcracks observed inside the silicides containing $HfNbTiVSi_{0.5}$ RHEA [55]. (c) Microcracks observed inside the deformed $Nb_{40}Ti_{25}Al_{15}V_{10}Ta_5Hf_3W_2$ RHEA [41]. (d) Severe cracks at grain boundaries of $W_{0.4}MoNb_xTaTi$ RHEA [76]. (e) Fracture feature of river-like appearance for $ZrTiHfNbMo_2$ RHEA [105]. (f) Propagation of cracks in WReTaMo RHEA [82].

The $V_{20}Nb_{20}Mo_{20}Ta_{20}W_{20}$ RHEA exhibited much lower plastic strain, and its fracture started via crack propagation along a direction inclined at 10° relative to the loading axis, with significant involvement of grain boundaries during crack growth [49]. In the deformed microstructures of $(VNbTiTa)_{100-x}Si_x$ (x = 2.5, 5) RHEAs at 1000 °C, silicide was discovered in eutectics which became broken after compression and the broken fragments are circulated within the original inter-dendrite areas [103]. At 1200 °C, silicide elongated and broke in $Si_{2.5}$ and Si_5 alloys. Similarly, some of the carbides are cracked along the loading direction at the side regions of the TiNbTaZrHf-based composites by Li et al. [104] compressed at 800 °C (Fig. 10a). The appearance of microcracks at the sides of carbides confirms their load-bearing effect during the high temperature deformation process. Furthermore, at 1000 and 1200 °C, a small amount of carbides crack along the loading direction but drops significantly, indicating that carbides continue to play a role in sharing and transferring applied stress from the

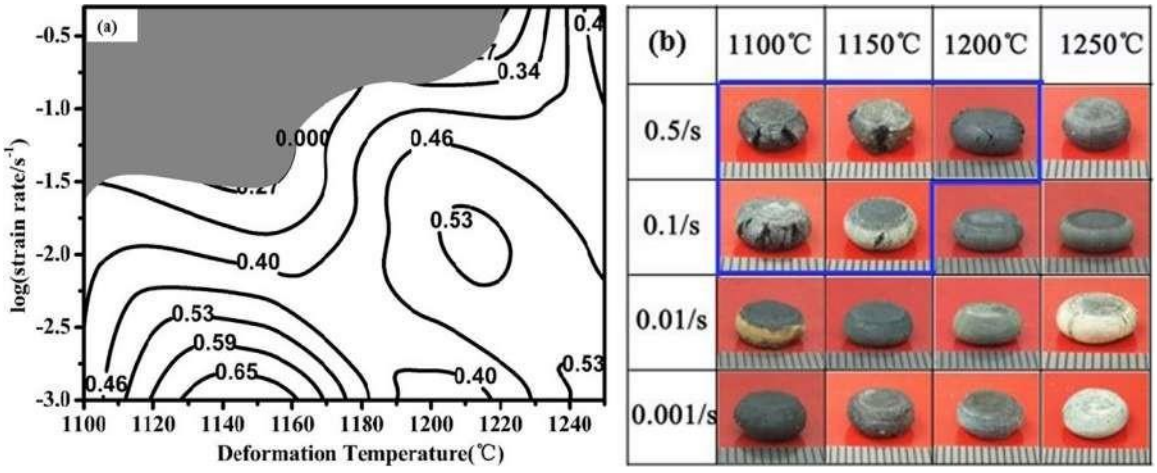

Fig. 11. The processing maps for the MoNbHfZrTi RHEA (grey part is the instability zone) (a); Distribution of cracks of the deformed specimens at a series of processing parameters (blue region is the instability zone) (b) [40].

matrix during the deformation process. In Figure 10b, the silicide containing $HfNbTiVSi_{0.5}$ RHEA deformed at 800 and 1000 °C showed severe deformation due to plastic flow, and a few microcracks were observed inside the silicides [55]. A few microcracks observed in the silicide containing $HfNbTiVSi_{0.5}$ RHEA correspond to high interfacial adhesion between the matrix and silicides.

In the deformation of $Nb_{40}Ti_{25}Al_{15}V_{10}Ta_5Hf_3W_2$ RHEA, Pang et al. [41] observed some microcracks at 800 and 900 °C. The microcracks in Figure 10c is intergranular, and the widespread microcracks originated from triple grain boundaries at 800 °C after compression. Microcracks were also observed at 900 °C but decreased with increasing temperatures until no microcracks could be seen at 1000 °C. According to Pang et al. [41], the pile up of massive dislocations at grain boundaries and its resultant stress concentration speeds up the formation and extension of microcracks (Fig. 10c), which are detrimental to deformation stability. Crack propagation occurred in hot deformed $W_{0.4}MoNb_xTaTi$ RHEA at temperatures of 800, 1000, and 1100 °C [76]. At 800 °C, the $Nb_{1.3}$ alloy in Figure 10d showed severe cracks at grain boundaries. The cracks originated at the grain boundaries and later circulated along the grain boundaries. Meanwhile, few cracks extended into the grains. However, at an increased temperature of 1000–1100 °C with an increased niobium concentration ($Nb_{1.5}$), the propagation of cracks was suppressed. As the deformation temperature increases, the atomic activity and dislocation migration rate increase significantly. Therefore, the local stress concentration could be efficiently improved, which would prevent crack initiation and propagation. When the molybdenum content of the $ZrTiHfNbMo_{2.0}$ alloy was increased, poor plasticity and a river-like appearance for the fracture feature (Fig. 10e) were observed at 800 °C [105]. Rhenium containing WReTaMo RHEA deformed at 1600 °C by Wan et al. [82] experienced grain boundary sliding that contributes to the deformation as only intergranular cracks are observed. As shown in Figure 10f, the cracks originate at the grain boundaries initially and then spread along the grain boundaries.

In summary, microcracks and fracture which is an unsafe deformation behavior, were observed in some hot deformed RHEAs but decreased with increasing temperatures. The microcracks in the RHEAs are mostly intergranular. The next section briefly describes the constitutive modelling and processing maps in hot deformed RHEAs.

7 Optimising deformation conditions in hot deformed RHEAs

Hot working processes can be optimised using a combination of experimental stress–strain curves, constitutive equations, and processing maps. However, the selection of an appropriate constitutive model to accurately describe the stress–strain behaviour and the dominant mechanisms requires a detailed understanding of the various constitutive models. The activation energy for hot working is an important parameter which gives an indication of the material's resistance to deformation and is also used for the prediction of flow stress [65,106,107]. In addition, it could also provide insights into the microstructural mechanisms influencing the deformation process [65,108]. Constitutive models are largely classified into phenomenological models, physical models, and artificial neural network models [109,110]. The most common phenomenological model is the Johnson-Cook model [111] while the Arrhenius model [112] is the simplest form of phenomenological model. Understanding hot deformation behaviour is critical for controlling the microstructures and properties of RHEAs. Hot workability of RHEAs has rarely been reported. Especially in establishing a constitutive connection between the flow stress (s), deformation temperature (T), strain rate ($\dot{\varepsilon}$) and strain (ε). As in other conventional alloys, constitutive modelling has been used on hot worked RHEA to predict flow stress. Processing maps have also been used in RHEA to determine optimum deformation parameters. According to [101], processing maps not only identify the ideal combination of processing parameters for

shaping and microstructural control, but they can also distinguish the "safe" and "unsafe" combinations of processing parameters.

Dong et al. [40] performed high temperature compression tests on the MoNbHfZrTi RHEA at temperatures of 1100–1250 °C and strain rates: 10^{-3}–0.5 s^{-1} to determine the hot workability and processing maps. In their study, the apparent activation energy (Q) was determined to be 326.1 kJ/mol. Constitutive equation predicted the flow stress of the hot deformed TaNbHfZrTi RHEA. The hot-processing map of the MoNbHfZrTi RHEA shown in Figure 11 indicates a contour area with a power dissipation factor (h) and the shaded portion, which is the instability zone. Dong et al. [40] reported the instability region to be at 1100–1220 °C and $10^{-1.5}$–0.5 s^{-1}, with values fluctuating from 0.15 to 0.27 in the instability area (Fig. 11a). This coincides with the occurrence of cracks (Fig. 11b) in the deformed alloy at a strain rate of 0.5 s^{-1} at temperatures (1100–1200 °C) and a strain rate of 10^{-1} s^{-1} at temperatures (1100–1150 °C). In the stable region, the h occur at 1110–1170 °Cand 10^{-3}–$10^{-2.5}$ s^{-1}. In Wang etal. [113] studyon the effects of V concentration on the mechanical properties of V_xNbMoTa RHEAs at temperatures 900–1100 °C, it was shown that at a strain range of 0.1–0.5, the activation energy decreases continuously when increasing the vanadium concentration. This indicates that the alloys of higher V content are easier to deform at high temperatures and, therefore, have lower strain hardening rates. Using an improved Johnson-Cook (J-C) constitutive model, Hu et al. [97] describe the deformation behaviour of TaNbHfZrTi RHEA at a strain rate of 400 s^{-1} to 2600 s^{-1}. It was found that fitting values of the J-C constitutive model corresponded well with the experimental findings, indicating that the modified J-C model can be used to accurately predict the hot deformation behaviours of the TaNbHfZrTi RHEA.

At e = 0.1, Bai et al. [72] discovered that the Q value for $TiAlVNb_2$ RHEA is approximately 401 kJ mol^{-1}. Furthermore, the Q value at strain of 0.3, 0.5, and 0.69 were calculated to be 387, 379, and 375 kJ mol^{-1}, respectively. The Q value vary in a slight range between 401 and 375 kJ mol^{-1} and are nearly constant at strain of 0.5 (379–375 kJ mol^{-1}), though with increasing strain they show a slight decreasing trend. According to Bai et al. [72], the results showed the thermal deformation process in $TiAlVNb_2$ RHEA is quite stable. Similarly, Yul et al. [71] investigated the flow stress analysis and hot processing region of $AlNbTi_3VZr_{1.5}$ RHEA using Arrhenius constitutive equation and processing maps. The Q value was calculated to be 228.1 kJ/mol. The Q value was lower than $TiAlVNb_2$ RHEA [72] when Zr was added to the composition. Arrhenius constitutive equation was found suitable to predict the flow stress of $AlNbTi_3VZr_{1.5}$ RHEA. Using the processing map, the appropriate processing region is determined at 1200–1250 °C and $10^{-0.75}$–1 s^{-1}.

Eleti et al. [34] studied the deformation behaviour in high temperature compression of HfNbTaTiZr RHEA. It was discovered that the Q value was approximately 258 kJ mol^{-1} at strain of 0.1. The value was lesser than the Q for self-diffusion of the elements comprised in the alloy, such as Nb and Ta, but greater than the activation energies for self-diffusion in Ti, Hf and Zr. Also, the Q value gradually decreased when strain was increased, but all values were in a slight range of 258–232 kJ mol^{-1}. The attained slopes gave the Q value of ~258 kJ mol^{-1} at the definite strain of 0.1. In particular, the Q value after e = 0.3 was nearly constant at 232–229 kJ mol^{-1}. Eleti and co-workers attribute the large activation energy (258 kJ mol^{-1}) at strain of 0.1 to being likely affected by the drop in stress noticed in the stress-strain curves. A higher value of strain-rate sensitivity (m = 0.33) was reported for HfNbTaTiZr RHEA, which signifies the occurrence of grain boundary sliding. Similarly, an earlier study on the deformation behaviour of HfNbTaTiZr RHEA by Senkov et al. [50] reported activation enrgy of ~226 kJ mol^{-1} which is in the range (258–232 kJ mol^{-1}) obtained from the Eleti et al. [34] study. Li et al. [69] found a low Q value of 144–119 kJ/mol^{-1} over a range of strains (0.1–0.6) for $Ti_2ZrHfV_{0.5}Ta_{0.2}$ RHEA. Since a high Q value correlates with high resistance to softening at elevated temperature, $Ti_2ZrHfV_{0.5}Ta_{0.2}$ RHEA became less competitive at higher temperatures. The low Q value was attributed to excessive concentration of Ti, Zr, and Hf elements, which tend to have low self-diffusion activation energies. The relationship among flow stress, temperature, and strain rate of $Ti_2ZrHfV_{0.5}Ta_{0.2}$ RHEA was predicted by the Arrhenius-type constitutive equations.

This section has shown that the apparent activation energy values in RHEAs decrease with an increasing strain. RHEAs with a high Q value are more competitive at higher temperatures than RHEAs with a low Q value. Based on the available literatures, constitutive model predicted the flow stress of hot worked RHEAs. Also, the hot-processing map can be used to determine the safe and unsafe region of hot deformed RHEAs. Section 8 reports the yield strength and resistance to high temperature softening of hot deformed RHEAs.

8 Yield strength of RHEA during hot deformation

A fast decrease in the strength of RHEA is known to mostly occur due to the intensification of diffusion-related processes above 0.5–0.6T_m [50,114]. The high solid solution hardening effect and strong atomic bonding contribute to the good mechanical properties of RHEAs at high temperatures [115]. According to Senkov et al. [116], the RHEAs have very high strength at temperatures of 800–1000 °C, single-phase RHEAs are usually stronger at $T \geq$ 1000–1200 °C than multi-phase RHEAs. The rapid loss of strength of multi-phase RHEAs at 800–1000 °C was discovered to be caused by secondary phase dissolution at solvus temperatures.

Senkov and Woodward [52] deformed $Nb_{20}Cr_{20}Mo_{10}Ta_{10}Ti_{20}Zr_{20}$ RHEA at 800, 1000, and 1200 °C and a strain rate of 10^{-3} s^{-1} in 2011. At 800 °C, the yield stress and peak strength of the alloy decreased to 983 and 1100 MPa. When the temperature increased to 1000 °C, at strain rate of 0.001 s^{-1}, the yield stress and peak strength of the alloy decreased to 546 and 1100 MPa. Finally, at a temperature of

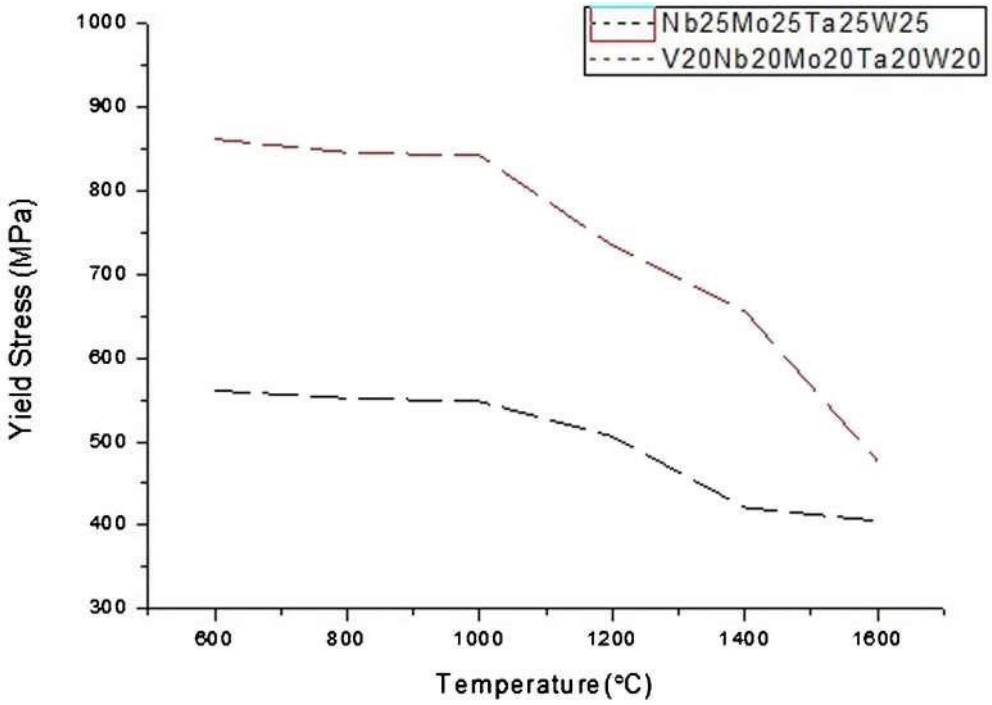

Fig. 12. The effect of temperature on the yield stress of $Nb_{25}Mo_{25}Ta_{25}W_{25}$ and $V_{20}Nb_{20}Mo_{20}Ta_{20}W_{20}$ RHEAs.

1200 °C, the yield stress was 170 MPa while the peak stress of 190 MPa was attained shortly after yielding and followed by weak softening. Senkov et al. [49] studied the high temperature properties of $Nb_{25}Mo_{25}Ta_{25}W_{25}$ and $V_{20}Nb_{20}Mo_{20}Ta_{20}W_{20}$ RHEAs at 600–1600 °C and a fixed strain rate of 0.001 s^{-1}. Figure 12 shows the temperature effect on the yield stress of $Nb_{25}Mo_{25}Ta_{25}W_{25}$ and $V_{20}Nb_{20}Mo_{20}Ta_{20}W_{20}$ RHEAs. The yield stress of $Nb_{25}Mo_{25}Ta_{25}W_{25}$ and $V_{20}Nb_{20}Mo_{20}Ta_{20}W_{20}$ RHEAs decreased steadily as temperature increased (Fig. 12). The resistance to high temperature softening of the $Nb_{25}Mo_{25}Ta_{25}W_{25}$ and $V_{20}Nb_{20}Mo_{20}Ta_{20}W_{20}$ RHEAs is likely due to slow diffusion of elements, which directly relates to the T_m of RHEAs [49].

At 800 and 900 °C, Chen et al. [105] studied the high temperature strength of $ZrTiHfNbMo_x$ RHEA (x = 0.5, 1.0, 1.5). At 800 and 900 °C, the yield stress of the $ZrTiHfNbMo_{0.5}$ RHEA is 585 MPa and 288 MPa with plasticity of 50% respectively. When the molybdenum content of $ZrTiHfNbMo_x$ RHEA increases to x = 1.0 at 800 °C and 900 °C, the yield stress increases significantly to 1099 MPa and 804 MPa, with plasticity greater than 40% and 50%. If the molybdenum content is increased to x = 1.5 at 800 °C and 900 °C, the yield stress rises to 1155 MPa with plasticity <15% and 897 MPa with plasticity > 25%. Chen et al. [105] attributed the high temperature strength to controlling the molybdenum content addition in the $ZrTiHfNbMo_x$ RHEAs. For the high temperature compressive study of Cr containing CrMoNbV RHEA by Feng et al. [100] at 300-1000 °C. The yield strength of CrMoNbV is 1062 MPa at 1000 °C. The rhenium containing WReTaMo RHEA by Wan et al. [82] deformed at 1600 °C and at a strain rate of 0.001 s^{-1} showed a yield strength of 172 MPa, peak compressive strength of 244 MPa, and plasticity >25%, which is attributed to the high melting temperature.

Similarly, by substituting Re with Nb and Ti, Wan et al. [117] studied the high temperature compression properties of WTaMoNbTi RHEA at 1600 °C at a strain rate of 0.001 s^{-1}. The WTaMoNbTi RHEA showed a yield strength of 173 MPa and a peak strength of 218 MPa with plasticity above 25%. Wan et al. [117] demonstrated that adding Ti to WTaMoNb RHEA improved its high temperature strength and plasticity. Furthermore, the addition of Ti increased the lattice constant, thereby intensify the effect of solid solution hardening. The effect of Ti content on the high temperature mechanical properties of Ti_xZrVNb RHEAs with varying elemental compositions by Huang et al. [85] revealed high strength. At 600 °C, the TiZrVNb, $Ti_{1.5}ZrVNb$ and Ti_2ZrVNb RHEAs exhibited high strength of 923, 886, and 922 MPa with plasticity >25%. However, the yield strengths decreased at 800 °C to 233, 236, and 211 MPa for the TiZrVNb, $Ti_{1.5}ZrVNb$ and Ti_2ZrVNb RHEAs due to high temperature softening. Table 5 summarizes the yield strength of other hot deformed RHEAs at different strain rates, strains, and temperatures.

In summary, the addition of Cr, Al, W, V, Nb, Mo, Ta, Zr, Ti, and Hf contributed to the high temperature strength and plasticity of RHEAs. The addition of Mo has shown a good ability to softening resistance of RHEAs at higher temperatures than RHEAs without Mo. However, the excessive addition of Mo tends to decrease the high temperature yield strength. W and Mo have strongstrengthening effects, which induce phase boundaries that act as dislocation movements

Table 5. Summary of yield strength of hot deformed RHEAs at 800–1400 °C.

Alloy composition	Strain	Strain rate (s^{-1})	Temperature (°C)	Yield strength (MPa)	Plasticity (%)	References
HfMoNbTaTiZr	–	10^{-3}	800	1007	>20	[87]
			1000	814	30	
			1200	556	30	
$AlNb_2TiV$	0.3	10^{-3}	800	694	>30	[118]
			1000	612	>30	
NbTiVZr	0.69	10^{-3}	800	500	>40	[119]
			1000	200	50	
$Zr_{2.0}TiHfVNb_{2.0}$	0.69	10^{-3}	800	647	50	[81]
			900	476	50	
			1200	165	50	
HfNbTaTiZrW	–	10^{-3}	800	535	>35	[120]
			1000	295	>35	
			1200	92	>35	
HfNbTaTiZrMoW	–	10^{-3}	800	577	>35	[120]
			1000	409	>35	
			1200	345	>35	
$TiAl_{20}VNbMo$	–	10^{-3}	800	624	>50	[57]
			1000	180	>50	
NbMoCrTiAl	–	10^{-3}	800	860	0.135	[121]
			1000	594	>0.15	
			1200	105	>0.24	
$NbTaW_{0.5}(Mo_2C)_{20}$	–	10^{-3}	1200	1026	22.3	[122]
			1400	697	>30	
$C_{0.25}Hf_{0.25}NbTaW_{0.5}$	–	10^{-3}	1000	868	50	[123]
			1200	792	50	
			1400	749	50	
Reo.5MoNbW(TaC)o.5	0.48	10^{-3}	1000	937	15.9	[124]
			1200	901	35	
$Ti_2VNbMoZr_2$	–	10^{-3}	800	977	>50	[125]
$Zr_1NbMoTaW$	–	10^{-3}	1000	555	25	[98]
$(VNbTiTa)_{90}Si_{10}$	–	10^{-3}	1000	646	>50	[103]
			1200	133	>50	
TiNbTaZrHf	–	10^{-3}	800	1351	38.5	[126]
			1000	508	44	
			1200	105	>50	
$ZrTiHfNb_{0.5}Ta_{0.5}O_{0.2}$	–	10^{-3}	800	966	>50	[127]
				537	>50	
$HfNbTiVSi_{0.5}$	0.69	10^{-3}	800	875	50	[55]
			1000	240	50	
$ZrTiHfNb_{0.5}Ta_{0.5}$	0.69	10^{-3}	800	170	50	[78]
			900	112	50	
$ZrTiHfNb_{0.5}Mo_{0.5}$	0.69	10^{-3}	800	539	50	[78]
			900	274	50	
$W_{0.4}MoNb_{1.3}TaTi$	0.69	10^{-3}	800	1125	44.7	[76]
			1000	905	37.2	
			1100	425	48.3	
TiVNbMoTaW	–	10^{-3}	800	791	>10	[128]
			1000	753	>25	
			1200	659	10	
$V_1NbMoTa$	–	10^{-3}	800	933	>51	[113]
			1000	811	>51	

and therefore strengthen RHEA at high temperatures. The addition of Ti and Zr into RHEA simultaneously helps with high temperature strength, plasticity and density reduction. Excessive additions of Ti, Zr, and Hf weaken the high temperature yield strength due to their melting points and self-diffusion activation energies. Cr also enhances the high temperature strength of RHEA through the formation of second-phase particles and solid solution strengthening. Research progress has been made in creating a balance in the toughening and high temperature strength of RHEA by introducing carbides, silicides, and oxides (Tab. 5). As seen from reported literature, carbides and oxides containing RHEAs tend to have better strength and plasticity at higher temperatures. Good softening resistance and plasticity at higher temperatures can be achieved for RHEAs through optimization of elemental compositions or the addition of composite particulates.

9 Summary

The deformation behavior of RHEAs at high temperatures have been reviewed in this work. Based on the outcome of this review, the conclusions can be summarised as follows:

- All the probable mechanisms influencing deformation in metallic alloys, such as WH, DRX, and DRV, have also been observed in refractory high entropy alloys. The DDRX and CDRX occurred concurrently in some of the hot deformed RHEAs.
- Sharp drops in flow stress occur in RHEA, which may be attributed to the unlocking of dislocations pinned by the Cottrell atmosphere or short-range order.
- The resistance to high temperature softening of RHEAs can be attributed to slow diffusion of elements, high thermal stability, and second phase strengthening mechanism. A balance between toughness and strength at higher temperatures for RHEAs can be achieved through optimization of elemental contents or the addition of composite particulates to induce a dual-phase structure.
- The microcracks in RHEA based composites are mostly intergranular. The appearance of microcracks at the sides of carbide reinforced RHEAs confirms their load-bearing effect during the high temperature deformation process.
- Constitutive modelling can be used to accurately predict flow stress of hot worked RHEAs. Hot deformation processing maps can be employed to avoid microstructural defects and improve the mechanical and functional properties of RHEAs during hot deformation processing.

10 Future research perspective

- Constitutive modelling provides insights into the microstructural mechanisms influencing the deformation process. Among the constitutive models, the Arrhenius model is commonly used in the modelling of flow curves in RHEAs. The use of improved Johnson-Cook, Zerilli-Armstrong, and other promising models can be investigated since they are rarely reported.
- The use of hot-processing maps to obtain the safe processing window for the hot forming of RHEAs is rarely reported. Apart from the flow curve shape in determining the softening behaviour in RHEAs, cracks and other defects might occur during the hot forming process. Therefore, more studies required on hot-processing maps of RHEAs.
- Studies on the optimization of hot deformation properties and deformation behaviour of composite reinforced RHEAs is expected to constitute a major part of future work because it has been reported to have high yield strength and plasticity at elevated temperatures. Also, the effects of different temperatures and high strain rates on the deformation behaviour of carbide reinforced refractory high entropy alloy.
- The low angle grain boundary formed to bridge bulged grain boundaries, which led to the formation of fine grains. Investigation into the effect of different strain rates on the evolution of low angle grain boundary misorientation can be explored.
- More extensive research is needed on the dislocation motion mechanisms of hot deformed powder metallurgy RHEAs since only one article was found reporting on the dislocation motion mechanisms.

Declaration of competing interests

The authors declare that they have no known competing financial interests or personal relationships that could have appeared to influence the work reported in this paper.

Funding

This research did not receive any specific grant from unding agencies in the public, commercial, or not-for-profit sectors.

References

1. J.W. Yeh, S.K. Chen, S.J. Lin, J.Y. Gan, T.S. Chin, T.T. Shun, C.H. Tsau, S.Y. Chang, Nanostructured high-entropy alloys with multiple principal elements: novel alloy design concepts and outcomes, Adv. Eng. Mater. 6 (2004) 299–303
2. A. Takeuchi, T. Wada, H. Kato, Solid solutions with bcc, hcp, and fcc Structures formed in a composition line in multicomponent Ir Rh Ru W Mo system, Mater. Trans. 60 (2019) 2267–2276
3. J. Tang, J.L. Xu, Z.G. Ye, X.B. Li, J.M. Luo, Microwave sintered porous CoCrFeNiMo high entropy alloy as an efficient electrocatalyst for alkaline oxygen evolution reaction, J. Mater. Sci. Technol. 79 (2021) 171–177
4. B. Cantor, I.T.H. Chang, P. Knight, A.J.B. Vincent, Microstructural development in equiatomic multicomponent alloys, Mater. Sci. Eng. A 375–377 (2004) 213–218
5. O.N. Senkov, G.B. Wilks, D.B. Miracle, C.P. Chuang, P.K. Liaw, Refractory high-entropy alloys, Intermetallics 18 (2010) 1758–1765
6. M.C. Gao, Progress in high-entropy alloys, JOM 66 (2014) 1964–1965

7. M.H. Tsai, J.W. Yeh, High-entropy alloys: a critical review, Mater. Res. Lett. 2 (2014) 107–123
8. S. Praveen, J.W. Bae, P. Asghari-Rad, J.M. Park, H.S. Kim, Ultra-high tensile strength nanocrystalline CoCrNi equi-atomic medium entropy alloy processed by high-pressure torsion, Mater. Sci. Eng. A 735 (2018) 394–397
9. C.L. Chen, Sutrisna, Study of NiFeCoCr medium entropy alloy as a binder phase on W-Mo heavy tungsten alloy by secondary ball milling, Intermetallics 138 (2021) 107320
10. Y.S. Lee, R.J. Cava, Superconductivity in high and medium entropy alloys based on MoReRu, PhysicaC 566 (2019) 1353520
11. S. Uporov, E. Sterkhov, I. Balyakin, Magnetocaloric effect in ScGdHo medium-entropy alloy, J. Supercond. Nov. Magn. (2022) 1539–1545
12. M.O. Bodunrin, B.A. Obadele, L.H. Chown, P.A. Olubambi, Corrosion behaviour of Al-Fe-Ti-V medium entropy alloy, IOP Conf. Ser. Mater. Sci. Eng. 272 (2017)
13. D.B. Miracle, O.N. Senkov, A critical review of high entropy alloys and related concepts, Acta Mater. 122 (2017) 448–511
14. Q. Li, X. Bao, S. Zhao, Y. Zhu, Y. Lan, X. Feng, Q. Zhang, The influence of AlFeNiCrCoTi high-entropy alloy on microstructure, mechanical properties and tribological behaviors of aluminum matrix composites, Int. J. Metalcast. 15 (2021) 281–291
15. M. Tsai, J. Yeh, High-entropy alloys: a critical review, Mater. Res. Lett. 2 (2014) 107–123
16. O.N. Senkov, D.B. Miracle, K.J. Chaput, J.P. Couzinie, Development and exploration of refractory high entropy alloys a review, J. Mater. Res. 33 (2018) 3092–3128
17. S. Praveen, H.S. Kim, High-entropy alloys: potential candidates for high-temperature applications an overview, Adv. Eng. Mater. 1700645 (2018) 1–22
18. L. Raman, A. Anupam, G. Karthick, C.C. Berndt, A.S.M. Ang, S.V.S. Narayana Murty, D. Fabijanic, B.S. Murty, R.S. Kottada, Strengthening mechanisms in CrMoNbTiW refractory high entropy alloy, Mater. Sci. Eng. A 819 (2021) 1–10
19. S.A. Alvi, Synthesis and Characterisation of High Entropy Alloy and Coating (Lulea University of Technology, Sweden, 2019)
20. V. Bhardwaj, Q. Zhou, F. Zhang, W. Han, Y. Du, K. Hua, H. Wang, Effect of Al addition on the microstructure, mechanical and wear properties of TiZrNbHf refractory high entropy alloys, Tribol. Int. 160 (2021) 1–11
21. M. Sahlberg, D. Karlsson, C. Zlotea, U. Jansson, Superior hydrogen storage in high entropy alloys, Sci. Rep. 6 (2016) 1–6
22. C. Zhang, A. Song, Y. Yuan, Y. Wu, P. Zhang, Z. Lu, X. Song, Study on the hydrogen storage properties of a TiZrNbTa high entropy alloy, Int. J. Hydrogen Energy 45 (2020) 5367–5374
23. R. Floriano, G. Zepon, K. Edalati, G.L.B.G. Fontana, A. Mohammadi, Z. Ma, H.W. Li, R.J. Contieri, Hydrogen storage in TiZrNbFeNi high entropy alloys, designed by thermodynamic calculations, Int. J. Hydrogen Energy 45 (2020) 33759–33770
24. J. Montero, G. Ek, L. Laversenne, V. Nassif, G. Zepon, M. Sahlberg, C. Zlotea, Hydrogen storage properties of the refractory Ti-V-Zr-Nb-Ta multi-principal element alloy, J. Alloys Compd. 835 (2020) 155376
25. H. Li, L. Zhao, Y. Yang, H. Zong, X. Ding, Improving radiation-tolerance of bcc multi-principal element alloys by tailoring compositional heterogeneities, J. Nucl. Materi. 555 (2021) 1–10
26. T. Li, L. Yiping, C. Zhiqiang, W. Tongmin, L. Tingju, Opportunity and challenge of refractory high-entropy alloys in the field of reactor structural materials, Acta Metall. Sin. 57 (2021) 42
27. I.A. Ivanov, A. Ryskulov, A. Kurakhmedov, A. Kozlovskiy, D. Shlimas, M.V. Zdorovets, V.V. Uglov, S.V. Zlotski, J. Ke, Radiation swelling and hardness of high-entropy alloys based on the TiTaNbV system irradiated with krypton ions, J. Mater. Sci.: Mater. Electr. 32 (2021) 27260–27267
28. X. Shang, S. Bo, Y. Guo, Q. Liu, ZrC reinforced refractory-high-entropy-alloy coatings: compositional design, synthesis, interstitials, and microstructure evolution effects on wear, corrosion and oxidation behaviors, Appl. Surf. Sci. 564 (2021) 1–11
29. S.B. Hung, C.J. Wang, Y.Y. Chen, J.W. Lee, C.L. Li, Thermal and corrosion properties of V-Nb-Mo-Ta-W and V-Nb-Mo-Ta-W-Cr-B high entropy alloy coatings, Surf. Coat Technol. 375 (2019) 802–809
30. S.K. Bachani, C.J. Wang, B.S. Lou, L.C. Chang, J.W. Lee, Fabrication of TiZrNbTaFeN high-entropy alloys coatings by HiPIMS: effect of nitrogen flow rate on the microstructural development, mechanical and tribological performance, electrical properties and corrosion characteristics, J. Alloys Compd. 873 (2021) 1–15
31. A. Ostovari, J. Pasandideh, A. Abdollahzadeh, N.A. Shaburova, E. Trofimov, On the application of NbTaTiVW refractory high entropy alloy particles in the manufacturing process of WC based matrix body drill bits, Int. J. Refract. Metals Hard Mater. 99 (2021) 1–7
32. R.R. Eleti, T. Bhattacharjee, A. Shibata, N. Tsuji, Unique deformation behavior and microstructure evolution in high temperature processing of HfNbTaTiZr refractory high entropy alloy, Acta Mater. 171 (2019) 132–145
33. F.J. Humphreys, M. Hatherly, Hot deformation and dynamic restoration, in: Recrystallization and Related Annealing Phenomena, edited by M. Hatherly and F.J. Humphreys, 2nd edn. (Elsevier, Oxford, 2004), pp. 415–451
34. R.R. Eleti, Deformation Mechanisms and Microstructure Evolution in HfNbTaTiZr High Entropy Alloy during Thermo-mechanical Processing at Elevated Temperatures (Kyoto University, Japan, 2019)
35. C.M. Sellars, W.J.M. Tegart, Hot workability, Int. Metall. Rev. 17 (1972) 1–24
36. T. Sakai, J.J. Jonas, Plastic deformation: role of recovery and recrystallization, Mater. Sci. Technol. (2001) 7079–7084
37. X.M. Chen, Y.C. Lin, D.X. Wen, J.L. Zhang, M. He, Dynamic recrystallization behavior of a typical nickel-based superalloy during hot deformation, Mater. Des. 57 (2014) 568–577
38. R.D. Doherty, D.A. Hughes, F.J. Humphreys, J.J. Jonas, D. Juul Jensen, M.E. Kassner, W.E. King, T.R. McNelley, H.J. McQueen, A.D. Rollett, Current issues in recrystallization: a review, Mate. Sci. Eng. A (1997) 219–274
39. M. lei Hu, W. dong Song, D. bo Duan, Y. Wu, Dynamic behavior and microstructure characterization of TaNbHfZrTi high-entropy alloy at a wide range of strain rates and temperatures, Int. J. Mech. Sci. 182 (2020) 105738
40. F. Dong, Y. Yuan, W. Li, Y. Zhang, P.K. Liaw, X. Yuan, H. Huang, hot deformation behavior and processing maps of an equiatomic MoNbHfZrTi refractory high entropy alloy, Intermetallics (Barking) 126 (2020) 1–10

41. J. Pang, H.H. Zhang, L. Zhang, Z. Zhu, H. Fu, H. Li, A. Wang, Z. Li, H.H. Zhang, A ductile Nb40Ti25Al15V10-Ta5Hf3W2 refractory high entropy alloy with high specific strength for high-temperature applications, Mater. Sci. Eng. A 831 (2022) 1–9
42. Z. Savaedi, R. Motallebi, H. Mirzadeh, A review of hot deformation behavior and constitutive models to predict flow stress of high-entropy alloys, J. Alloys Compd. 903 (2022) 1–21
43. H.Y. Diao, R. Feng, K.A. Dahmen, P.K. Liaw, Fundamental deformation behavior in high-entropy alloys: an overview, Curr. Opin. Solid State Mater. Sci. 21 (2017) 252–266
44. J. Brechtl, S. Chen, C. Lee, Y. Shi, R. Feng, X. Xie, D. Hamblin, A.M. Coleman, B. Straka, H. Shortt, R.J. Spurling, P.K. Liaw, A review of the serrated-flow phenomenon and its role in the deformation behavior of high-entropy alloys, Metals (Basel) 10 (2020) 1–72
45. A.H. Chokshi, High temperature deformation in fine grained high entropy alloys, Mater. Chem. Phys. 210 (2018) 152–161
46. E.P. George, W.A. Curtin, C.C. Tasan, High entropy alloys: a focused review of mechanical properties and deformation mechanisms, Acta Mater. 188 (2020) 435–474
47. E.P. George, W.A. Curtin, C.C. Tasan, High entropy alloys: a focused review of mechanical properties and deformation mechanisms, Acta Mater. 188 (2020) 435–474
48. E.S. Vieira, J.A.N.F. Gomes, A comparison of scopus and web of science for a typical university, Scientometrics 81 (2009) 587-600
49. O.N. Senkov, G.B. Wilks, J.M. Scott, D.B. Miracle, Mechanical properties of Nb25Mo25Ta25W25 and V20Nb20Mo20Ta20W refractory high entropy alloys, Intermetallics 19 (2011) 698–706
50. O.N. Senkov, J.M. Scott, S.V Senkova, F. Meisenkothen, D.B. Miracle, C.F. Woodward, Microstructure and elevated temperature properties of a refractory TaNbHfZrTi alloy, J. Mater. Sci. 47 (2012) 4062–4074
51. C.C. Juan, M.H. Tsai, C.W. Tsai, C.M. Lin, W.R. Wang, C.C. Yang, S.K. Chen, S.J. Lin, J.W. Yeh, Enhanced mechanical properties of HfMoTaTiZr and HfMoNbTaTiZr refractory high-entropy alloys, Intermetallics (Barking) 62 (2015) 76–83
52. O.N. Senkov, C.F. Woodward, Microstructure and properties of a refractory NbCrMo0. 5Ta0.5TiZr alloy, Mater. Sci. Eng. A 529 (2011) 311–320
53. O.N. Senkov, C. Woodward, D.B. Miracle, Microstructure and properties of aluminum-containing refractory high-entropy alloys, JOM 66 (2014) 2030–2042
54. N.N. Guo, L. Wang, L.S. Luo, X.Z. Li, R.R. Chen, Y.Q. Su, J.J. Guo, H.Z. Fu, Hot deformation characteristics and dynamic recrystallization of the MoNbHfZrTi refractory high-entropy alloy, Mater. Sci. Eng. A 651 (2016) 698–707
55. Y. Zhang, Y. Liu, Y. Li, X. Chen, H. Zhang, Microstructure and mechanical properties of a refractory HfNbTiVSi0.5 high-entropy alloy composite, Mater. Lett. 174 (2016) 82–85
56. W. Guo, B. Liu, Y. Liu, T. Li, A. Fu, Q. Fang, Y. Nie, Microstructures and mechanical properties of ductile NbTaTiV refractory high entropy alloy prepared by powder metallurgy, J. Alloys Compd. 776 (2019) 428–436
57. Z.Q. Xu, Z.L. Ma, M. Wang, Y.W. Chen, Y.D. Tan, X.W. Cheng, Design of novel low-density refractory high entropy alloys for high-temperature applications, Mater. Sci. Eng. A 755 (2019) 318–322
58. T. Yan, E. Yu, Y. Zhao, Constitutive modeling for flow stress of 55SiMnMo bainite steel at hot working conditions, Mater. Des. 50 (2013) 574–580
59. X.M. Chen, Y.C. Lin, M.S. Chen, H.B. Li, D.-X. Wen, J.L. Zhang, M. He, Microstructural evolution of a nickel-based superalloy during hot deformation, Mater. Des. (2015) 41–49
60. C.W. Park, M.S. Choi, H. Lee, J. Yoon, H.R. Javadinejad, J.H. Kim, High-temperature deformation behavior and microstructural evolution of as-cast and hot rolled-21S alloy during hot deformation, J. Mater. Res. Technol. 9 (2020) 13555–13569
61. Q. Yang, M. Ma, Y. Tan, S. Xiang, F. Zhao, Y. Liang, Initial b grain size effect on high-temperature flow behavior of tb8 titanium alloys in single b phase field, Metals (Basel). 9 (2019) 1–19
62. Y. Wan, J. Mo, X. Wang, Z. Zhang, B. Shen, X. Liang, Mechanical properties and phase stability of WTaMoNbTi refractory high-entropy alloy at elevated temperatures, Acta Metall. Sin. (English Letters). 34 (2021) 1585–1590
63. Q. Liu, G. Wang, Y. Liu, X. Sui, Y. Chen, S. Luo, Hot deformation behaviors of an ultrafine-grained MoNbTaTiV refractory high-entropy alloy fabricated by powder metallurgy, Mater. Sci. Eng. A 809 (2021) 1–10
64. M. Azarbarmas, M. Aghaie-Khafri, J.M. Cabrera, J. Calvo, Dynamic recrystallization mechanisms and twining evolution during hot deformation of Inconel 718, Mater. Sci. Eng. A 678 (2016) 137–152
65. Y.C. Lin, M.S. Chen, J. Zhong, Constitutive modeling for elevated temperature flow behavior of 42CrMo steel, Comput. Mater. Sci. 42 (2008) 470–477
66. H. Wu, S.P. Wen, H. Huang, K.Y. Gao, X.L. Wu, W. Wang, Z.R. Nie, Hot deformation behavior and processing map of a new type Al-Zn-Mg-Er-Zr alloy, J. Alloys Compd. 685 (2016) 869–880
67. S. Miura, Y. Murasato, Y. Sekito, Y. Tsutsumi, K. Ohkubo, Y. Kimura, Y. Mishima, T. Mohri, Effect of microstructure on the high-temperature deformation behavior of Nb-Si alloys, Mater. Sci. Eng. A 510–511 (2009) 317–321
68. E.P. George, D. Raabe, R.O. Ritchie, High-entropy alloys, Nat. Rev. Mater. 4 (2019) 515–534
69. T. Li, Y. Lu, Z. Li, T. Wang, T. Li, Hot deformation behavior and microstructure evolution of non-equimolar Ti2ZrHf V0. 5Ta0.2 refractory high-entropy alloy, Intermetallics (Barking) 146 (2022) 1–11
70. O.N. Senkov, J.P. Couzinie, S.I. Rao, V. Soni, R. Banerjee, Temperature dependent deformation behavior and strengthening mechanisms in a low density refractory high entropy alloy Al10Nb15Ta5Ti30Zr40, Materialia (Oxf) 9 (2020) 1–16
71. Z. Yu, B. Xie, Z. Zhu, B. Xu, M. Sun, High-temperature deformation behavior and processing maps of a novel AlNbTi3VZr1.5 refractory high entropy alloy, J. Alloys Compd. 912 (2022) 1–11
72. Z.C. Bai, X.F. Ding, Q. Hu, M. Yang, Z.T. Fan, X.W. Liu, Unique deformation behavior and microstructure evolution in high-temperature processing of a low-density TiAlVNb2 refractory high-entropy alloy, J. Alloys Compd. 885 (2021)
73. H. Liang, H. Guo, Y. Nan, C. Qin, X. Peng, J. Zhang, The construction of constitutive model and identification of dynamic softening mechanism of high-temperature deformation of Ti-5Al-5Mo-5V-1Cr-1Fe alloy, Mater. Sci. Eng. A. 615 (2014) 42–50

74. Y. Wu, Y. Liu, C. Li, X. Xia, Y. Huang, H. Li, H. Wang, Deformation behavior and processing maps of Ni3Al-based superalloy during isothermal hot compression, J. Alloys Compd. 712 (2017) 687–695
75. T. Sakai, A. Belyakov, R. Kaibyshev, H. Miura, J.J. Jonas, Dynamic and post-dynamic recrystallization under hot, cold and severe plastic deformation conditions, Prog. Mater. Sci. 60 (2014) 130–207
76. W. Wei, T. Wang, C. Wang, M. Wu, Y. Nie, J. Peng, Ductile Wo. 4MoNbxTaTi refractory high-entropy alloys with excellent elevated temperature strength, Mater Lett. 295 (2021) 1–4
77. Q. Liu, G. Wang, Y. Liu, X. Sui, Y. Chen, S. Luo, Hot deformation behaviors of an ultrafine-grained MoNbTaTiV refractory high-entropy alloy fabricated by powder metallurgy, Mater. Sci. Eng. A 809 (2021) 140922
78. R. Feng, B. Feng, M.C. Gao, C. Zhang, J.C. Neuefeind, J.D. Poplawsky, Y. Ren, K. An, M. Widom, P.K. Liaw, Superior high-temperature strength in a supersaturated refractory high-entropy alloy, Adv. Mater. 33 (2021) 1–9
79. Y. Zhang, J.P. Liu, S.Y. Chen, X. Xie, P.K. Liaw, K.A. Dahmen, J.W. Qiao, Y.L. Wang, Serration and noise behaviors in materials, Prog. Mater. Sci. 90 (2017) 358–460
80. X.W. Liu, Z.C. Bai, X.F. Ding, J.Q. Yao, L. Wang, Y.Q. Su, Z.T. Fan, J.J. Guo, A novel light-weight refractory high-entropy alloy with high specific strength and intrinsic deformability, Mater. Lett. 287 (2021) 1–4
81. Y. Chen, Y. Li, X. Cheng, C. Wu, B. Cheng, Z. Xu, The microstructure and mechanical properties of refractory high-entropy alloys with high plasticity, Materials 11 (2018) 1–11
82. Y. Wan, Q. Wang, J. Mo, Z. Zhang, X. Wang, X. Liang, B. Shen, WReTaMo refractory high-entropy alloy with high strength at 1600 °C, Adv. Eng. Mater. 24 (2022) 1–31
83. N. Yurchenko, E. Panina, D. Shaysultanov, S. Zherebtsov, N. Stepanov, Refractory high entropy alloy with ductile intermetallic B2 matrix/hard bcc particles and exceptional strain hardening capacity, Materialia (Oxf) 20 (2021) 1–7
84. S. Wu, D. Qiao, H. Zhang, J. Miao, H. Zhao, J. Wang, Y. Lu, T. Wang, T. Li, Microstructure and mechanical properties of CxHf0.25NbTa W0. 5 refractory high-entropy alloys at room and high temperatures, J. Mater. Sci. Technol. 97 (2022) 229–238
85. T. Huang, S. Wu, H. Jiang, Y. Lu, T. Wang, T. Li, Effect of Ti content on microstructure and properties of TixZrVNb refractory high-entropy alloys, Int. J. Minerals Metall. Mater. 27 (2020) 1318–1325
86. C. Yang, H. Bian, K. Aoyagi, Y. Hayasaka, K. Yamanaka, A. Chiba, Synergetic strengthening in HfMoNbTaTi refractory high-entropy alloy via disordered nanoscale phase and semicoherent refractory particle, Mater. Des. 212 (2021) 110248
87. K.K. Tseng, C.C. Juan, S. Tso, H.C. Chen, C.W. Tsai, J.W. Yeh, Effects of Mo, Nb, Ta, Ti, and Zr on mechanical properties of equiatomic Hf-Mo-Nb-Ta-Ti-Zr alloys, Entropy 21 (2019) 1–14
88. A. Chaudhuri, A. Sarkar, R. Kapoor, J.K. Chakravartty, R.K. Ray, S. Suwas, Understanding the mechanism of dynamic recrystallization during high-temperature deformation in Nb-1Zr-0. 1C alloy, J. Mater. Eng. Perform. 28 (2019) 448–462
89. O.N. Senkov, J. Gild, T.M. Butler, Microstructure, mechanical properties and oxidation behavior of NbTaTi and NbTaZr refractory alloys, J. Alloys Compd. 862 (2021) 1–14
90. Y. Jia, L. Zhang, P. Li, X. Ma, L. Xu, S. Wu, Y. Jia, G. Wang, Microstructure and mechanical properties of Nb-Ti-V-Zr refractory medium-entropy alloys, Front. Mater. 7 (2020) 1–11
91. Y. Guo, J. He, W. Lu, L. Jia, Z. Li, The evolution of compositional and microstructural heterogeneities in a TaMo0. 5ZrTi1.5Al0.1Si0.2 high entropy alloy, Mater. Charact. 172 (2021) 1–11
92. R.R. Eleti, A.H. Chokshi, A. Shibata, N. Tsuji, Unique high-temperature deformation dominated by grain boundary sliding in heterogeneous necklace structure formed by dynamic recrystallization in HfNbTaTiZr BCC refractory high entropy alloy, Acta Mater. 183 (2020) 64–77
93. B.S. Murty, J.W. Yeh, S. Ranganathan, High-Entropy Alloys, 1st ed. (Butterworth-Heinemann, UK, 2014)
94. Y. Zhang, Y. Liu, Y. Li, X. Chen, H. Zhang, Microstructure and mechanical properties of a refractory HfNbTiVSi0.5 high-entropy alloy composite, Mater. Lett. 174 (2016) 82–85
95. Q. Liu, G. Wang, Y. Liu, X. Sui, Y. Chen, S. Luo, Hot deformation behaviors of an ultrafine-grained MoNbTaTiV refractory high-entropy alloy fabricated by powder metallurgy, Mater. Sci. Eng. A 809 (2021) 1–10
96. H.Y. Yasuda, Y. Yamada, K. Cho, T. Nagase, Deformation behavior of HfNbTaTiZr high entropy alloy singe crystals and polycrystals, Mater. Sci. Eng. A 809 (2021) 1–10
97. M. Lei Hu, W. Dong Song, D. Bo Duan, Y. Wu, Dynamic behavior and microstructure characterization of TaNbHfZrTi high-entropy alloy at a wide range of strain rates and temperatures, Int. J. Mech. Sci. 182 (2020) 1–12
98. T.T. Li, W. Jiao, J. Miao, Y. Lu, E. Guo, T. Wang, T.T. Li, P.K. Liaw, A novel ZrNbMoTaW refractory high-entropy alloy with in-situ forming heterogeneous structure, Mater. Sci. Eng. A 827 (2021) 1–9
99. Q. Wei, G. Luo, R. Tu, J. Zhang, Q. Shen, Y. Cui, Y. Gui, A. Chiba, High-temperature ultra-strength of dual-phase Re0. 5MoNbW(TaC)0.5 high-entropy alloy matrix composite, J. Mater. Sci. Technol. 84 (2021) 1–9
100. R. Feng, B. Feng, M.C. Gao, C. Zhang, J.C. Neuefeind, J.D. Poplawsky, Y. Ren, K. An, M. Widom, P.K. Liaw, Superior high-temperature strength in a supersaturated refractory high-entropy alloy, Adv. Mater. 33 (2021) 1–9
101. Y.V.R.K. Prasad, K.P. Rao, S. Sasidhara, Hot Working Guide, 2nd edn. (ASM International, Ohio, 2015)
102. S.A. Sajjadi, A. Chaichi, H.R. Ezatpour, A. Maghsoudlou, M.A. Kalaie, Hot deformation processing map and microstructural evaluation of the Ni-based superalloy IN-738LC, J. Mater. Eng. Perform. 25 (2016) 1269–1275
103. Z.Q. Xu, Z.L. Ma, Y. Tan, M. Wang, Y. Zhao, X.W. Cheng, Effects of Si additions on microstructures and mechanical properties of VNbTiTaSix refractory high-entropy alloys, J. Alloys Compd. 900 (2022) 1–9
104. X. Li, A. Fu, Y. Cao, S. Xu, S. Gao, High-temperature mechanical properties and deformation behavior of carbides reinforced TiNbTaZrHf composite, J. Alloys Compd. 894 (2022) 1–10

105. Y.W. Chen, Y.K. Li, X.W. Cheng, C. Wu, B. Cheng, High-temperature mechanical properties and microstructure of $ZrTiHfNbMo_x$ (x = 0.5, 1.0, 1.5) refractory high entropy alloys, IOP Conf. Ser. Mater. Sci. Eng. 359 (2018) 1–5
106. A.N. Behera, R. Kapoor, A. Sarkar, J.K. Chakravartty, Hot deformation behaviour of niobium in temperature range 700–1500°C, Mater. Sci. Technol. 30 (2014) 637–644
107. K. Wu, G.Q. Liu, B.F. Hu, C.Y. Wang, Y.W. Zhang, Y. Tao, J.T. Liu, Effect of processing parameters on hot compressive deformation behavior of a new Ni-Cr-Co based P/M superalloy, Mater. Sci. Eng. A 528 (2011) 4620–4629
108. A. Momeni, The physical interpretation of the activation energy for hot deformation of Ni and Ni-30Cu alloys, J. Mater. Res. 31 (2016) 1077–1084
109. C. Shi, X.G. Chen, Evolution of activation energies for hot deformation of 7150 aluminum alloys with various Zr and V additions, Mater. Sci. Eng. A 650 (2016) 197–209
110. Y.C. Lin, X.M. Chen, A critical review of experimental results and constitutive descriptions for metals and alloys in hot working, Mater. Des. 32 (2011) 1733–1759
111. G.R. Johnson, W.H. Cook, A computational constitutive model and data for metals subjected to large strain, high strain rates and high pressures, in The Seventh International Symposium on Ballistics, Den Haag, Netherlands (1983) pp. 541–547
112. J.J. Jonas, C.M. Sellars, W.J.M.G. Tegart, Strength and structure under hot-working conditions, Metall. Rev. 14 (1969) 1–24
113. M. Wang, Z.L. Ma, Z.Q. Xu, X.W. Cheng, Designing VxNbMoTa refractory high-entropy alloys with improved properties for high-temperature applications, Scr. Mater. 191 (2021) 131–136
114. T. Sakai, M. Ohashi, K. Chiba, J.J. Jonas, Recovery and recrystallization of polycrystalline nickel after hot working, Acta Metall. 36 (1988) 1781–1790
115. Z.D. Han, N. Chen, S.F. Zhao, L.W. Fan, G.N. Yang, Y. Shao, K.F. Yao, Intermetallics effect of Ti additions on mechanical properties of NbMoTaW and VNbMoTaW refractory high entropy alloys, Intermetallics 84 (2017) 153–157
116. O.N. Senkov, S. Gorsse, D.B. Miracle, High temperature strength of refractory complex concentrated alloys, Acta Mater. 175 (2019) 394–405
117. Y. Wan, J. Mo, X. Wang, Z. Zhang, B. Shen, X. Liang, Mechanical properties and phase stability of WTaMoNbTi refractory high - entropy alloy at elevated temperatures, Acta Metall. Sin. 34 (2021) 1585–1590
118. X.W. Liu, Z.C. Bai, X.F. Ding, J.Q. Yao, L. Wang, Y.Q. Su, Z.T. Fan, J.J. Guo, A novel light-weight refractory high-entropy alloy with high specific strength and intrinsic deformability, Mater. Lett. 287 (2021) 1–4
119. Y. Jia, L. Zhang, P. Li, X. Ma, L. Xu, S. Wu, Y. Jia, Microstructure and mechanical properties of Nb-Ti-V- Zr refractory medium-entropy alloys, Front Mater. 7 (2020) 1–11
120. M. Wang, Z. Ma, Z. Xu, X. Cheng, Microstructures and mechanical properties of HfNbTaTiZrW and HfNbTaTiZr-MoW refractory high-entropy alloys, J. Alloys Compd. 803 (2019) 778–785
121. H. Chen, A. Kauffmann, B. Gorr, D. Schliephake, C. Seemüller, J.N. Wagner, H.J. Christ, M. Heilmaier, Microstructure and mechanical properties at elevated temperatures of a new Al-containing refractory high-entropy alloy Nb-Mo-Cr-Ti-Al, J. Alloys Compd. 661 (2016) 206–215
122. S. Wu, D. Qiao, H. Zhao, J. Wang, Y. Lu, A novel NbTa W0. 5 (Mo2C)x refractory high-entropy alloy with excellent mechanical properties, J. Alloys Compd. 889 (2022) 1–12
123. S. Wu, D. Qiao, H. Zhang, J. Miao, H. Zhao, J. Wang, Y. Lu, T. Wang, T. Li, Microstructure and mechanical properties of CxHf0. 25NbTa W0. 5 refractory high-entropy alloys at room and high temperatures, J. Mater. Sci. Technol. 97 (2022) 229–238
124. Q. Wei, G. Luo, R. Tu, J. Zhang, Q. Shen, Y. Cui, Y. Gui, A. Chiba, High-temperature ultra-strength of dual-phase Re0. 5MoNbW(TaC)0.5 high-entropy alloy matrix composite, J. Mater. Sci. Technol. 84 (2021) 1–9
125. T. Li, J. Miao, Y. Lu, T. Wang, T. Li, Effect of Zr on the as-cast microstructure and mechanical properties of lightweight Ti2VNbMoZrx refractory high-entropy alloys, Int. J. Refract. Metals Hard Mater. 103 (2022) 1–8
126. X. Li, A. Fu, Y. Cao, S. Xu, S. Gao, High-temperature mechanical properties and deformation behavior of carbides reinforced TiNbTaZrHf composite, J. Alloys Compd. 894 (2022) 1–10
127. Y. Chen, Y. Li, X. Cheng, Z. Xu, C. Wu, B. Cheng, M. Wang, Interstitial strengthening of refractory ZrTiHfNb0. 5Ta0.5O_x (X = 0.05, 0.1, 0.2) high-entropy alloys, Mater. Lett. 228 (2018) 145–147
128. Z.D. Han, N. Chen, S.F. Zhao, L.W. Fan, G.N. Yang, Y. Shao, K.F. Yao, Effect of Ti additions on mechanical properties of NbMoTaW and VNbMoTaW refractory high entropy alloys, Intermetallics 84 (2017) 153–157

Cite this article as: Olufemi Sylvester Bamisaye, Nthabiseng Maledi, Josias Van der Merwe, Desmond Edem Primus Klenam, Michael Oluwatosin Bodunrin, Akeem Damilola Akinwekomi, A comprehensive review on the deformation behavior of refractory high entropy alloys at elevated temperatures, Manufacturing Rev. 10, 12 (2023)

Journal of Alloys and Compounds 983 (2024) 173803

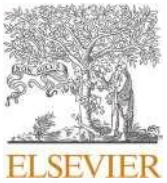

Contents lists available at ScienceDirect

Journal of Alloys and Compounds

journal homepage: www.elsevier.com/locate/jalcom



Microstructure, hardness, oXidation, and corrosion behavior of TiNbTaVW refractory high entropy alloy in 3.5 wt% NaCl and 1 M H_2SO_4

Olufemi Sylvester Bamisaye [a,c,*], Nthabiseng Maledi [a,b], Josias Van der Merwe [a,b], Michael Oluwatosin Bodunrin [a,b]

[a] School of Chemical and Metallurgical Engineering, Faculty of Engineering and the Built Environment, University of the Witwatersrand, Johannesburg, South Africa
[b] DSI-NRF Centre of Excellence in Strong Materials, University of the Witwatersrand, Johannesburg, South Africa
[c] Mechanical Engineering Department, Faculty of Air Engineering, Air Force Institute of Technology, Kaduna, Nigeria

A R T I C L E I N F O

Keywords:
Solid solution strengthening
Single-phase RHEA
Internal stress
Corrosion
Oxidation

A B S T R A C T

Refractory high entropy alloys (RHEAs), which comprise high-melting-point refractory elements, have been regarded as potential candidates that can substitute nickel-based superalloys used in high-temperature applications. This study investigated the microstructure, hardness, corrosion, and oxidation behavior of the TiNbTaVW RHEA compared with commercial-grade IN718 alloy. The equiatomic TiNbTaVW RHEA was produced using an arc melting furnace. The microstructure of the as-cast RHEA consisted of a body-centered cubic solid-solution phase with a dendritic structure corresponding to the empirical phase prediction. The RHEA exhibited a higher hardness of 522 ± 10 HV than the IN718 alloy with 301 ± 14 HV. The higher hardness is due to solid-solution strengthening and grain refinement. The RHEA had a lower corrosion rate in 3.5 wt% NaCl (0.0003 mm/yr) and 1 M H_2SO_4 (0.0009 mm/yr) than the commercial IN718 alloy (0.054 mm/yr and 1.12 mm/yr, respectively). At 850 °C after 15 h and 1050 °C after 15 h, the IN718 alloy exhibited a mass gain of 4.41 mg/cm^2 and 10.84 mg/cm^2, respectively, while the TiNbTaVW RHEA exhibited a mass loss of — 23.58 mg/cm^2 and — 45.92 mg/cm^2, respectively, indicating that the IN718 alloy exhibited the best oxidation resistance. Thermal and growth stresses contributed to the pores, voids, cracks, and oxide layer spallation observed in the TiNbTaVW RHEA.

1. Introduction

Since the inception of superalloys in the 1940 s, new alloy design concepts and upgrades of existing conventional alloys have been proposed for developing components with superior performance for various engineering applications. Since the existing conventional superalloys, such as IN718 used for aero and land-based turbine engines, are limited to operating temperatures below 1150 °C [1,2], new alloy design concepts have led to the development of refractory high entropy alloys (RHEAs) as potential substitutes. RHEAs emerged in 2010 as a high-temperature structural material because of their excellent soft- ening resistance, high-temperature strength, outstanding corrosion resistance, and surface protection ability [3–8]. In understanding the different solid-solution phases formed in most high entropy alloys (HEAs), the Hume-Rothery rules developed in the 1950 s and 1960 s have been extended by several researchers to apply to HEAs. These rules are currently being utilized in the process of predicting phase stability and body-centered cubic (BCC) and face-centered cubic (FCC) simple solid-solution phases in HEAs. These parameters include entropy of mixing, enthalpy of mixing, valence electron concentration, lattice distortion, electronegativity difference, and thermodynamic parameters [9–13]. In RHEAs, the solid-solution formation is normally a BCC structure. Recently, alloying enhancement using elements like Hf, Ti, Zr, Nb, Cr, V, and Re has been reported to influence the mechanical properties of RHEA [9–11]. Senkov et al. [12] investigated the hardness and compressive strength of the BCC phase of the $Nb_{25}Mo_{25}Ta_{25}W_{25}$ RHEA and found a high hardness of 533 HV and a compressive strength of 1211 MPa. The high hardness and compressive strength are attributed to solid solution strengthening. Huang et al. [13] investigated the microstructure, hardness, and compressive properties of the TiZrVNb alloy, reporting a single BCC phase with a hardness value of 435 HV and compressive strength of 2287 MPa. This alloy's high hardness and

* Corresponding author at: School of Chemical and Metallurgical Engineering, Faculty of Engineering and the Built Environment, University of the Witwatersrand, Johannesburg, South Africa.
E-mail addresses: bamisayesylvester1988@gmail.com, 2503285@students.wits.ac.za (O.S. Bamisaye).

https://doi.org/10.1016/j.jallcom.2024.173803
Received 27 November 2023; Received in revised form 1 February 2024; Accepted 5 February 2024
Available online 10 February 2024
0925-8388/© 2024 The Author(s). Published by Elsevier B.V. This is an open access article under the CC BY-NC-ND license (http://creativecommons.org/licenses/by-nc-nd/4.0/).

compressive strength are due to a solid solution-like strengthening mechanism. Han et al. [9] investigated the microstructure and mechanical properties of TiNbMoTaW and TiVNbTaMoW RHEAs. A single BCC phase was found in the alloys, with hardness and compressive strength values of 511 HV and 1343 MPa, respectively, for TiNbMoTaW, while 533 HV and 1515 MPa were found for the TiVNbTaMoW RHEA. The segregation of Ti and Nb at the inter-dendrite regions promotes the accumulation of strain that enhances the RHEA's hardness and compressive strength.

Despite the increase in hardness and compressive properties, limited work has focused on the corrosion resistance of RHEAs in chloride and acidic environments. Corrosion is regarded as one of the most prevalent failure causes for metals, accounting for 3% of the global gross domestic product [14]. The cost of metal corrosion in the oil and gas production industry is estimated to be US$1372 billion [15]. Corrosion can lead to the degradation of materials' performance and result in service risks and waste [16]. High corrosion-resistant RHEAs with large amounts of passivity-promoting elements like Ti and Cr can facilitate the formation of stable barrier films and excellent corrosion resistance [17,18]. A stable and compact protective passive film can be formed on the surfaces of HEAs to prevent pitting corrosion [19]. Furthermore, the HEA's single solid solution phase can prevent pitting corrosion, which would preferably occur at the phase boundaries where the composition exhibits significant changes [20]. Studies on the corrosion behavior of single-phase RHEA in acidic and chloride solutions have been investi- gated [21–30]. Gao et al. [22] investigated the corrosion behavior of a single-phase $Mo_{15}Nb_{20}Ta_{10}Ti_{35}V_{20}$ RHEA in 3.5 wt% NaCl solution and found that the accumulation of corrosion products (TiO_2 and Ti_2O_3) blocked chloride ion channels and inhibited corrosion development. Peng et al. [26] investigated the corrosion behavior of the $AlCrTiV_{0.5}$ RHEA in 0.6 wt% NaCl solution. A low corrosion current density (0.131 $\mu A/cm^2$) and high negative potential (−0.411 V) were observed. No obvious corrosion was found in the surface morphology of the $AlCrTiV_{0.5}$ RHEA. The corrosion resistance of the alloy was attributed to the single BCC phase structure and lack of composition segregation. Yan et al. [28] studied the corrosion performance of the single-phase ReTaWNbMo RHEA in 3.5 wt% NaCl solution and found the surface morphology filled with pits. The single-phase structure could not inhibit localized corrosion in the ReTaWNbMo RHEA. Li et al. [25] evaluated the corrosion resistance of a single-phase $TiCrVNb_{0.5}Al_{0.5}$ RHEA in 1 M HCl solution and found the surface covered with wide and open pits. The passive film layer containing Cr_2O_3 and Al_2O_3 was not enough to prevent pitting corrosion because the oxide on the surface was converted into chloride-rich ions when the potential was increased. This means that single-phase RHEAs can also suffer from localized pitting corrosion in chloride and acidic solutions.

Apart from single-phase microstructure, elemental segregation, interface defects, and composition differences in the passive film promote galvanic cell formation, accelerating the electrochemical process and deteriorating the corrosion resistance [31–33]. Since only a few studies are available on the corrosion properties of RHEAs, the effects of elemental segregation and compositional differences on the localized corrosion of RHEAs in chloride and acidic environments are not mentioned. This study investigates the corrosion behavior of a TiNbTaVW RHEA compared to the IN718 alloy.

Oxidation resistance is a vital property for alloys working for a long time at high temperatures since it can severely deteriorate the materials' mechanical properties. In many applications, components experience cyclic oxidation that involves periodic start-up and shutdown at high temperatures. The oxide scale may fail due to several external loads that contribute to cracking and spalling the oxide scale and eventually to exposure of the bare-metal surface [34]. The adhesion of the oxide layer to the steel substrate is determined by the scale's thickness, its growth rate, the stress state, the interfacial energy, and the oxide's elastic properties [35]. Cracks are generally due to the volumetric expansion mismatch among the different oxides formed [36]. The cyclic-oxidation behavior is more complicated than isothermal oxidation because of the spalling process during cooling [34]. According to Hashim et al. [37], cyclic oxidation is important for the material characterization and performance ranking of high-temperature materials. The oxidation behavior of single-phase RHEAs at high temperatures has been investigated [38–45]. Yan et al. [44] reported a specific mass gain of 31.83 mg/cm^2 after 48 h of oxidation at 1000 °C for the WTaNbTiAl RHEA. The outer oxide layer consisting of $AlNbO_4$ serves as an effective protection layer for oxygen's inward diffusion in the oxidized WTaNbTiAl RHEA. Romero et al. [41] studied the oxidation behavior of CrMoNbTaW for 24 h at 600 to 1400 °C. A parabolic mass gain was reported from 600 to 1100 °C, while mass loss started from 1200 until 1400 °C. The identified surface oxides ($CrNbO_4$, Ta_2WO_8, and NbWO) did not protect the CrMoNbTaW RHEA at high temperatures. Moghaddam et al. [46] reported a low mass gain for oxidized WTaTiCr (9.3 mg/cm^2), WMoTaTiCr (14.49 mg/cm^2), WTaAlCr (17.55 mg/cm^2), and WMoTaAlCr (7.2 mg/cm^2) at 1000 °C after ten hours. The good oxidation resistance was due to the formation of WO_3 that prohibited the evolution of the protective oxide layer of $AlTaO_4$, $CrTaO_4$, and Al_2O_3.

Most RHEA oxidation studies have been conducted in isothermal rather than cyclic conditions, making it difficult to study the spallation behavior and oxide scale compactness of RHEAs when exposed to high temperatures. Furthermore, the effect of growth and thermal stresses on the formation of holes and cracks in oxidized RHEAs has not been reported. Understanding the spallation behavior, growth and thermal stresses, and overall oxidation resistance is crucial for designing and developing RHEAs for potential use in high-temperature environments. In this study, the empirical parameters of entropy of mixing, enthalpy of mixing, valence electron concentration, lattice distortion, electronegativity difference, and thermodynamic parameter were used to design, predict the phases and stability of an equiatomic TiNbTaVW RHEA. The addition of V has been reported to enhance the mechanical properties of RHEAs due to grain refinement [47]. V has been reported to protect RHEAs from localized corrosion, such as pitting, in NaCl and H_2SO_4 solutions [48]. The addition of Nb, W, and Ta has been reported to reduce the rate of dissolution of materials [30,49]. Kumar et al. [50] reported that RHEAs without W are more susceptible to pitting corrosion in a 3.5 wt% NaCl solution. The alloys containing W, Ti, and Nb have strong passivation potentials, which enable oxide films to form in HEAs with compact packing structures, and chloride ions cannot simply penetrate [51]. The elemental addition of Ti and Ta was also considered due to their ability to form stable oxides of TiO_2 and $TiTaO_4$ that can prevent the influx of oxygen to the outer interface and reduce the oxidation kinetics [52].

Therefore, in this study, the TiNbTaVW RHEA was synthesized via vacuum arc melting. The microstructure, hardness, and corrosion properties of the RHEA were investigated and compared with those of the commercial IN718 nickel-based superalloy. This study provides relevant information on the microstructure and hardness properties. Furthermore, the study established whether the passive film is stable and resistant to pitting. The oxidation mechanism, spallation behavior, and internal stress of the oxidized TiNbTaVW RHEA are further elucidated.

2. Materials and methods

2.1. Material preparation

The TiNbTaVW RHEA was synthesized by means of vacuum arc melting under ultra-high-purity argon gas on a water-cooled copper hearth to obtain an arc-melted alloy. Commercial high-purity raw elemental powders comprising Nb (99.9 wt% purity), V (99.9 wt% purity), Ta (99.95 wt% purity), Ti (99.7 wt% purity), and W (99.9 wt% purity) supplied by Weartech (Pty) Limited, South Africa, were used to produce the RHEA. The RHEA samples were flipped and remelted at least three times to ensure chemical homogeneity. A commercial IN718

superalloy was also obtained. The TiNbTaVW RHEA and IN718 alloy samples were cut to precision using a Gold San CNC wire-cutting EDM machine operating at 20 V. The cut samples were hot mounted in phenolic resin (Struers Polyfast) using a Bainmount twin H auto hot mounting press at 160 °C and 150 bar. The mounted samples were automatically ground on the Struers Tegramin-20 grinding machine using Struers MD-Piano 2000 and Struers MD-Piano 4000 resin-bonded diamond grinding discs. After grinding, the samples were polished using an Akasel polishing cloth with a 3.0 μm two-in-one polycrystalline diamond suspension.

2.2. Composition and microstructure analysis

The TiNbTaVW RHEA and IN718 alloy samples were microstructurally analyzed using a high-resolution Zeiss Sigma Field Emission Scanning Electron Microscope (FEG-SEM) on secondary electron (SE) and backscattered electron (BSE) detectors at 20 kV. SEM was also used in combination with energy-dispersive X-ray (EDX) for elemental composition analysis. Image **J** software (open-source software for image analysis, National Institutes of Health) was used to calculate the sizes of grain, pores, voids, and cracks. The phase identification of the as-cast samples was examined using a Bruker D2 phase diffractometer with a Co Kα radiation source [λ = 1.78899 Å] at 30 kV and 25 mA within the 2θ range of 20 to 120° at 25 °C.

2.3. Hardness testing

The Vickers hardness test was conducted on the polished cross-sectional area of the TiNbTaVW RHEA and IN718 alloy samples using a FutureTech Vickers hardness tester (FM-800) equipped with a diamond indenter. The measurements were taken under a load of 300 gf and a dwell time of 15 s according to the ASTM standard E92–17 [53]. Ten readings were taken at different positions on each sample to obtain a Vickers hardness average.

2.4. Oxidation testing

For the oxidation tests, the TiNbTaVW and IN718 samples were sectioned using a Gold San CNC wire-cutting EDM machine to nominal dimensions of 6.0 × 6.0 × 7.0 mm^3. The surfaces of the samples were ground using P1200 SiC paper, cleaned in ultrasonic acetone, and dried in air. The oxidation test was carried out in an open-ended tube muffle furnace under laboratory air at 850 °C and 1050 °C for 15 h. The mass changes of the alloy samples before and after oxidation were measured using a Boeco digital weighing balance (accuracy ± 0.0001 g) to characterize the oxidation kinetics. The surface microstructure and cross sectional morphology of oxidized samples were examined using FEG-SEM were examined using FEG-SEM on SE and BSE detectors at 20 kV. The identification of the oxides was determined using a Bruker D2 phase diffractometer with a Co Kα radiation source [λ = 1.78899 Å] at 30 kV and 25 mA within a 2θ range of 20 to 120° at 25°C.

2.5. Corrosion testing

The machined TiNbTaVW RHEA and IN718 alloy samples were hot-mounted in clear resin at 180 °C and 150 bar, ground, and polished until a mirror-like finish was obtained. After polishing, the samples were rinsed in water and air-dried. The samples with a surface area of 0.283 cm^2 were subjected to corrosive solutions. The corrosion test was performed using a three-electrode electrochemical cell connected to a Gamry® potentiostat. The TiNbTaVW RHEA and IN718 alloy samples were used as the working electrode, while a platinum wire and Ag/AgCl saturated with 3 M KCl were used as the counter and reference electrodes, respectively. The electrochemical tests were performed in a 3.5 wt% NaCl and 1 M H_2SO_4 solution at room temperature. An open circuit potential (OCP) test in the 3.5 wt% NaCl and 1 M H_2SO_4 solutions was conducted for 3600 s after immersion in the solutions to reach a stable value. Afterward, potentiodynamic polarization tests were performed at a scan rate of 0.167 mV/s in the potential range of − 0.5 to 2.5 V. The corrosion products were characterized by XRD using a Bruker D2 Phaser with Co Kα radiation (λ = 1.78899 Å) operated at 30 kV within a 2θ range of 20 to 120° at 25 °C. The microstructure of the samples after the corrosion test was studied using FEG-SEM on SE and BSE detectors at 20 kV. The corrosion current density (I_{corr}), corrosion potential (E_{corr}), and corrosion rate were determined using the polarization resistance method described in ASTM G102–89 [54].

3. Results

3.1. Microstructure and phase analysis of the TiNbTaVW RHEA

The phases and microstructures of the TiNbTaVW RHEA and IN718 alloy are presented in Fig. 1. In Fig. 1(a), the XRD analysis result of the TiNbTaVW RHEA shows the peaks are indexed as the BCC solid solution phase, which was observed at a wide range of 2θ values between 46° and 103°. The indexed BCC solid solution phase was of the space group Im-3 m (229) and lattice parameter (a = b = c = 3.2350 Å). The SEM image of TiNbTaVW RHEA exhibited a dendritic microstructure with an average grain size of 64.32 ± 2.7 μm, which segregated into grey dendritic regions and dark inter-dendritic regions (Fig. 1b). As seen in the EDS analysis result in Table 1a, the composition of the TiNbTaVW RHEA was near-equiatomic ratio. During the casting process, elements with a higher melting point tend to segregate in the dendritic regions, while elements with a lower melting point tend to segregate in the interdendrite regions [3,55,56]. This is evidenced in the EDS analysis result in Table 1a, where Ta and W were more prominent in the dendritic region, while the lower melting point elements comprising V and Ti segregated more in the interdendrite region. However, Nb was distributed evenly in both the dendritic and interdendrite regions. This highlights the influence of melting points on segregation typical in cast alloys. The chemical composition of the IN718 alloy is presented in Table 1b. The IN718 alloy in this study had a higher composition of Fe than Ni. Fig. 1(c) depicts the XRD spectra, showing that two major peaks ($\gamma + \gamma''$) are present. The peak values of the γ phase at 2θ were 51.7°, 60.3°, and 90.1°, while the peak values of the γ'' phase at 2θ were 51.7°, 60.3°, 90.1°, and 111.7°. The γ phase (FeMnNi) was of the space group Fm-3 m (225) and lattice parameter (a = b = c = 3.2350 Å). The γ'' phase (Ni_3Nb) was of the space group Fm-3 m (225) and lattice parameter (a = b = c = 3.6150 Å). The microstructure analysis of the IN718 alloy shows a fine distributed γ grains and γ'' precipitated grains structure (Fig. 1d). According to Ganji and Rajyalakshmi [57], the γ phase is soft in nature, while the γ'' phase is the main strengthening phase in most precipitation hardenable Ni-base superalloys.

3.2. Hardness of the TiNbTaVW RHEA

The average hardness value of the TiNbTaVW RHEA (522 ± 10 HV) was higher than that of the IN718 alloy (301 ± 14 HV). The TiNbTaVW RHEA hardness was higher than some reported as-cast RHEAs such as $Ti_2ZrHf_{0.5}Nb_{0.5}Al_1$ (460 HV) [58], AlMoNbTi (508 HV) [59], and $Hf_{0.25}NbTaW_{0.5}$ (514 HV) [60]. The grain size and solid solution strengthening effect are two possible influences that resulted in the higher hardness of TiNbTaVW RHEA. Fine grain strengthening lies in the effect of the grain boundary on dislocation slip, which serves as a pinning point impending further dislocation propagation [61]. The distribution of Ti and Ta with a high atomic radius of 1.46 Å and V with a smaller atomic radius of 1.32 Å likely introduces lattice strains in both the dendrite and interdendrite regions. These lattice strains could favor hardness. This agrees with TiNbMoTaW and TiVNbMoTaW RHEAs [9], where the addition of Ti resulted in the segregation of Ti and Nb at the interdendrite regions that favored accommodation of the increased

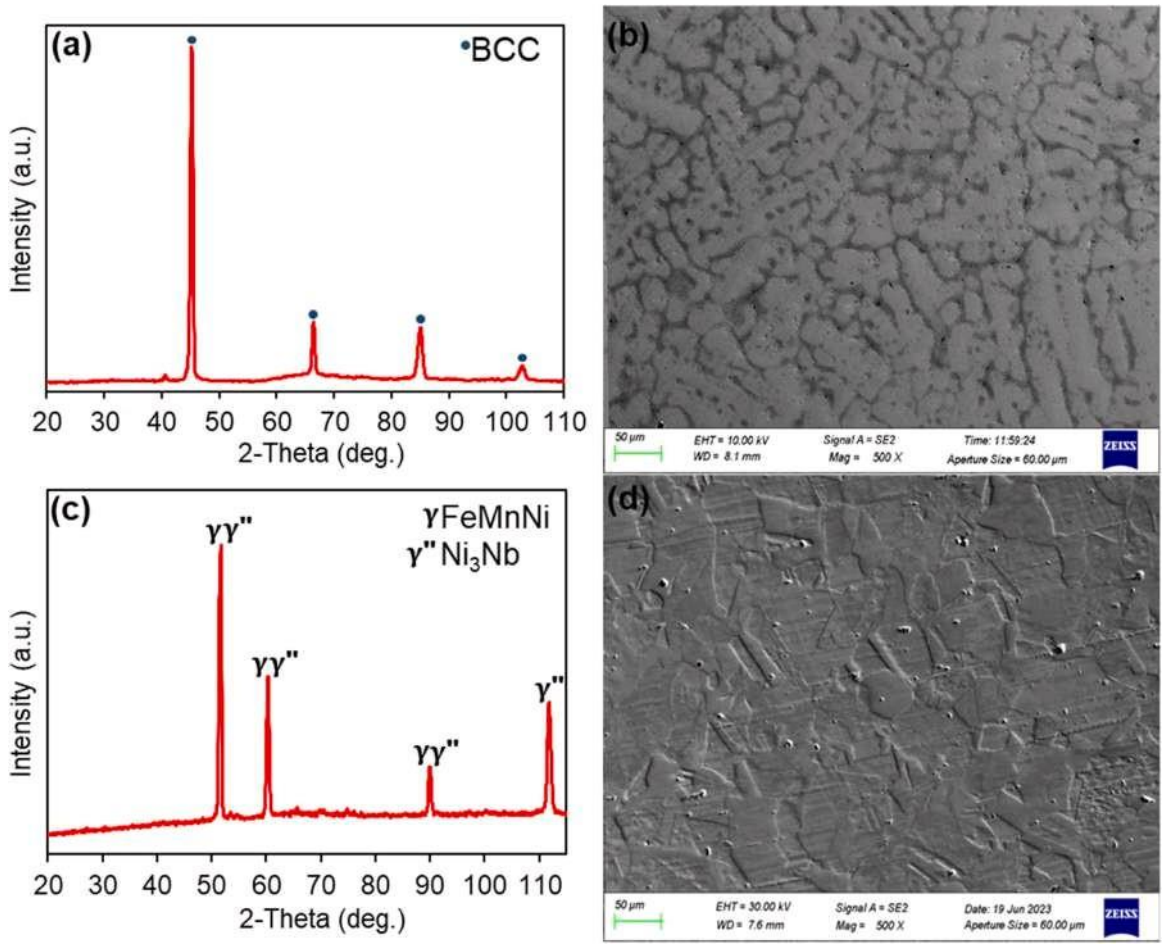

Fig. 1. Phase and microstructural analysis: (a) XRD pattern of the phase present in the TiNbTaVW RHEA; (b) SEM-BSE image of the as-cast TiNbTaVW RHEA; (c) XRD pattern of the phase present in the IN718 alloy; (d) SEM-BSE image of the IN718 alloy.

Table 1a
Composition distribution of the TiNbTaVW RHEA (at%).

TiNbTaVW RHEA	Element	Ti	Nb	Ta	V	W
	Actual	19	20	21	20	20
		± 0.4	± 0.2	± 0.2	± 0.3	± 0.2
	Dendrite (grey)	14	19	24	15	28
		± 0.8	± 0.5	± 0.5	± 1.1	± 1.9
	Interdendrite	32	19	12	29	8.0
	(dark)	± 1.5	± 0.3	± 0.8	± 0.6	± 1.0

strain, improving the hardness. The solid solution strengthening caused by large lattice misfit is an important component of solid solution/hardening mechanism in HEAs [62,63]. Cui et al. [64] showed that large lattice misfit among phases contributed mainly to the excellent strengthening effect and mechanical properties of $Ti_{41}V_{27}Hf_{15}Nb_{15}O_2$ RHEA.

3.3. Electrochemical corrosion behavior

3.3.1. Open circuit potential and potentiodynamic polarization measurement of the TiNbTaVW RHEA and IN718 alloy in a chloride solution

The OCP and potentiodynamic polarization curves of the TiNbTaVW RHEA and IN718 alloy in 3.5 wt% NaCl are presented in Fig. 2. The stability of the oxide film formed on the surface of the TiNbTaVW RHEA and IN718 alloy was evaluated by OCP for 3600 s, as seen in Fig. 2(a). The TiNbTaVW RHEA exhibited an initial potential of 0.20 V before a rapid decrease in the first 600 s and a slight increase at 650 s. Afterward, the OCP continued to decrease until it became stable at— 0.217 V with increasing exposure time. The OCP for the IN718 alloy showed an initial potential of — 0.186 V in the first 22 s before a rapid decrease until 3600 s were reached at — 0.24 V. Steady potential was achieved for both the TiNbTaVW RHEA and IN718 alloy after the oxide film was formed on the alloy surface. A stable OCP has been attributed to the building of dense and protective oxide films on the surface of the alloy [65,66]. However, the TiNbTaVW oxide film of TINbTaVW RHEA was more stable than the IN718 alloy in a 3.5 wt% NaCl solution. More fluctuations were observed in the OCP curve of the IN718 alloy, indicating dissolution and re-passivation of the oxide film on the alloy's surface

Table 1b
Composition distribution of the IN718 alloy (at%).

IN718 alloy	Ti	Nb	Fe	Ni	Mn	S	C	Co	Al	Si	P	Cu
	0.12	0.22	57.95	36.56	0.5	0.06	3.63	0.14	0.12	0.37	0.1	0.23
	± 0.02	± 0.02	± 0.1	± 0.4	± 0.1	± 0.1	± 0.1	± 0.04	± 0.02	± 0.02	± 0.01	± 0.01

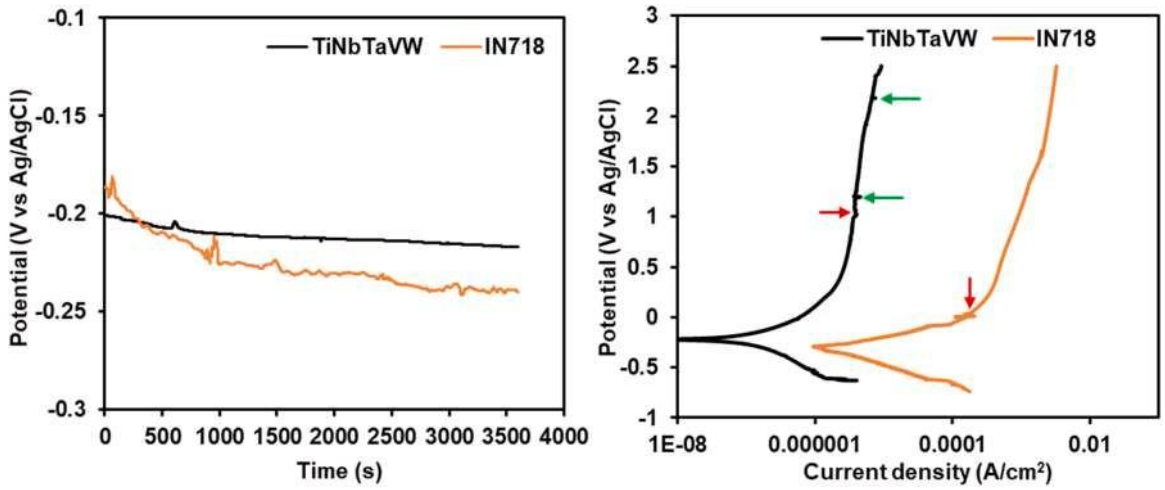

Fig. 2. (a) OCP curves for the TiNbTaVW RHEA and IN718 alloy in a 3.5 wt% NaCl solution; (b) potentiodynamic polarization curves for the TiNbTaVW RHEA and IN718 alloy in a 3.5 wt% NaCl solution.

[67]. The fluctuations could also be attributed to the instability caused by the chloride ions in the solution.

Fig. 2(b) shows the potentiodynamic polarization curves of both the TiNbTaVW RHEA and IN718 alloy in 3.5 wt% NaCl. The potentiodynamic polarization curve of TiNbTaVW RHEA exhibited passivation, while the curve for IN718 alloy exhibited pseudo-passive behavior up to 1.63 V and later passivated until the final potential. The passive zone is usually correlated to the stability of the passive film; a wide passive zone means a fairly stable passive film on the surface of HEAs [25]. The areas with the red arrow in the TiNbTaVW and IN718 anodic curves indicate that active corrosion took place when exposed to a chloride environment. The chloride ions attack and breaks the protective layers, but the oxide layer starts rebuilding, as evidenced by the pseudo-passive and passive behaviors. Also, transient currents were observed in two locations (green arrows) on the passive region of TiNbTaVW RHEA, indicating instability of the passive film in response to chloride ion attack. The electrochemical corrosion parameters such as E_{corr}, I_{corr}, and corrosion rates obtained from the potentiodynamic polarization curves in the chloride solution are presented in Table 2. Both TiNbTaVW and IN718 had high negative E_{corr} values of — 0.189 V and — 0.295 V, indicating high susceptibility to corrosion. The TiNbTaVW RHEA had a lower I_{corr} value of 0.055 μA/cm^2 than the IN718 alloy with 5.299 μA/cm^2. Based on the electrochemical parameters in Table 2, it is evident that the corrosion rate was lower in the TiNbTaVW RHEA than in the IN718 alloy.

3.3.2. *Microstructural observation of the TiNbTaVW RHEA and IN718 alloy in a chloride solution*

The corrosion resistance of metals and alloys is correlated with their passive film properties [68]. The SEM images and XRD of the TiNbTaVW RHEA and IN718 alloy after potentiodynamic polarization in 3.5 wt% NaCl are presented in Fig. 3. No obvious corrosion regions were found on the surface of TiNbTaVW RHEA (Fig. 3a); localized corrosion (pits) of average size 5.65±2.1 μm was initiated mainly on the dendritic region (Fig. 3b). The corrosion products formed on the surface of the TiNbTaVW RHEA were identified as TiO_2 and VO (Fig. 3c). Ti has strong passivation potentials, which enable oxide films to form in HEAs with compact packing structures [51]. The EDX compositions (Table 3 and Supporting Information S1) of the TiNbTaVW RHEA after potentiodynamic polarization in a chloride solution show the presence of oxygen, suggesting oxide formation on the surface. The deposition of Cl was also detected in the TiNbTaVW RHEA, signifying that chloride might have broken through the alloy's film, evidenced in the few pits found on the surface of TiNbTaVW RHEA. Compared to compositions of Ti and V, W, Ta, and Nb have low compositions in both the dendrite and interdendrite regions. The observed elemental segregation and composition differences can induce the pits observed on the TiNbTaVW RHEA. The elemental segregation, interface defects, and composition differences in the passive film accelerate the electrochemical process and deteriorate the corrosion resistance [31–33].

The surface of the IN718 alloy was highly corroded, and pits of an average size of 14.86±2.2μ m were also visible (Fig. 3d). The EDX compositions of the IN718 alloy after potentiodynamic polarization in the chloride solution showed the presence of Cl, signifying that the chloride ions broke through the film of the alloy (Table 3 and Supporting Information S2). This was further evidenced by the pits and corroded surface (Fig. 3d). The XRD pattern of the IN718 alloy after potentiodynamic polarization showed a reduction of peaks between 60° and 110° (Fig. 3e). No new peaks were formed, which shows that limited corrosion products were deposited on the surface of IN718. The few deposited corrosion products did not provide effective protection in chloride solution.

Table 2
Electrochemical parameters for TiNbTaVW and IN718 in 3.5 wt% NaCl.

Alloy	E_{corr} (V vs. Ag/AgCl)	I_{corr} (μA/cm^2)	Corrosion rate (mm/yr)
TiNbTaVW	-0.189 ± 0.021	0.055 ± 0.003	0.0003 ± 0.0002
IN718	-0.295 ± 0.01	5.299 ± 2.06	0.054 ± 0.02

3.3.3. *Open circuit potential and potentiodynamic polarization measurement of the TiNbTaVW RHEA and IN718 alloy in an acidic solution*

The OCP and potentiodynamic polarization curves of the TiNbTaVW RHEA and IN718 alloy in 1 M H_2SO_4 at room temperature are presented in Fig. 4. The OCP curve of TiNbTaVW RHEA in Fig. 4(a) showed an initial noble value (—0.11 V) in the first 5 second due to the formation and growth of the passive film on the surface, but the OCP later dropped drastically till 3600 s. The IN718 alloy OCP curve is noticeably unstable, indicating the breaking and rebuilding of the oxide film on the alloy's surface. The TiNbTaVW RHEA had a higher potential for noble values than the IN718 alloy, indicating that a well-protective passive film was formed. Fig. 4(b) shows the potentiodynamic polarization curves of both the TiNbTaVW RHEA and IN718 alloy in 1 M H_2SO_4. The potentiodynamic polarization curve of TiNbTaVW RHEA exhibited passive behavior up to the final potential of 2.5 V. A breakage in the anodic curve was observed from 1.06 V to 1.13 V (red circle), which signifies that active corrosion took place when exposed to an acidic environment. The IN718 alloy potentiodynamic polarization curve exhibited active

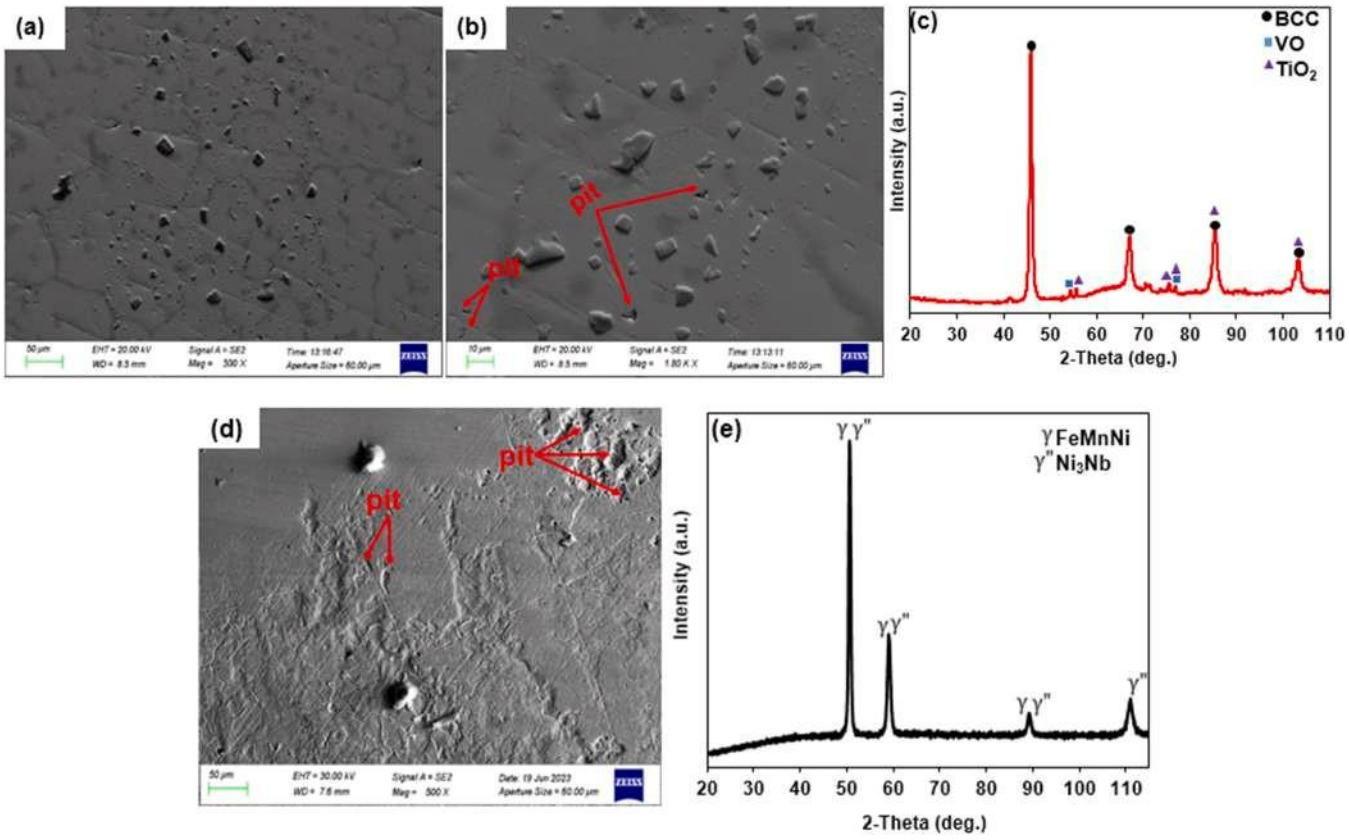

Fig. 3. Microstructure and XRD of the TiNbTaVW RHEA and IN718 alloy after exposure in 3.5 wt% NaCl at room temperature: (a) SEM image of the surface of the TiNbTaVW RHEA after potentiodynamic polarization; (b) Higher magnification SEM image of the surface of the IN718 alloy after potentiodynamic polarization; (c) XRD of corrosion products formed on the TiNbTaVW RHEA's surface; (d) SEM image of the surface of the IN718 alloy after potentiodynamic polarization; (e) XRD of the IN718 alloy after potentiodynamic polarization.

Table 3
EDX compositions (at%) of the TiNbTaVW RHEA and IN718 alloy after exposure in 3.5 wt% NaCl.

IN718										
Al	Si		P	Ti	Mn	Fe	Ni	O	Na	Cl
0.15 ± 0.01	0.42 ± 0.2		0.07 ± 0.01	0.06 ± 0.02	0.23 ± 0.01	41.23 ± 15.6	23 ± 5.7	28 ± 8.5	5.5 ± 2.7	1.34 ± 0.7
TiNbTaVW										
	Ti	Nb	Ta		V	W	O	Na	Cl	
Dendrite	15 ± 1.5	1 ± 2.0	9 ± 2.5		16 ± 1.0	10 ± 1.0	32 ± 3.5	5.0 ± 2.0	3.0 ± 1.0	
Interdendrite	16 ± 2.1	1 ± 2.0	11 ± 1.5		17 ± 3.2	8.0 ± 1.2	34 ± 6.5	-	2.0 ± 3.0	

corrosion/dissolution, passivation, and transpassivation. The sulfate ions attack the protective layer of the IN718 alloy, and the layer breaks, but the oxide layer starts rebuilding, as evidenced by the passivation region. Based on the electrochemical parameters in Table 4, it is evidenced that the corrosion rate of the TiNbTaVW RHEA was lower than the IN718 alloy in an acidic environment. The low corrosion rate of TiNbTaVW in 1 M H_2SO_4 shows that an oxide protective layer was formed on the surface.

3.3.4. *Microstructural observation of the TiNbTaVW RHEA and IN718 alloy in an acidic solution*

The SEM images and XRD of the TiNbTaVW RHEA and IN718 alloy after potentiodynamic polarization in 1 M H_2SO_4 are presented in Fig. 5. Corrosion products and pits of an average size of 4.1 ± 0.9 μm were found mostly in the interdendrite (dark region) of the TiNbTaVW RHEA (Fig. 5a).

The observed pits imply that the sulfate ions broke through the passive layer of the TiNbTaVW RHEA. Elemental segregation and composition differences of Ti in the dendrite region with segregation and composition differences of Ta and W in the interdendrite region could enable pits (Table 5 and Supporting Information S3). The XRD pattern of the TiNbTaVW RHEA after potentiodynamic polarization in the acidic solution is shown in Fig. 5(b). The TiNbTaVW RHEA only contains WO_3 and BCC solid solution phases (Fig. 5b). Although good corrosion resistance was observed for the RHEA, the passive layer containing WO_3 could not prevent pits. The surface of the IN718 alloy was corroded with circular pits of an average size of 6.27 ± 0.68 μm (Fig. 5c). The EDX compositions of IN718 (Table 5 and Supporting Information S4) after the test showed the elemental compositions that were still intact after exposure to the acidic solution. Similar to the chloride solution, no new peaks were observed for the IN718 alloy in the acidic solution, but peaks were reduced between 90° and 110° (Fig. 5d). These show that low or minimal corrosion products were deposited on the surface of the IN718 alloy after potentiodynamic polarization. The lack of a protective film explains the corroded surface and pits observed in the IN718 alloy when exposed to the acidic solution.

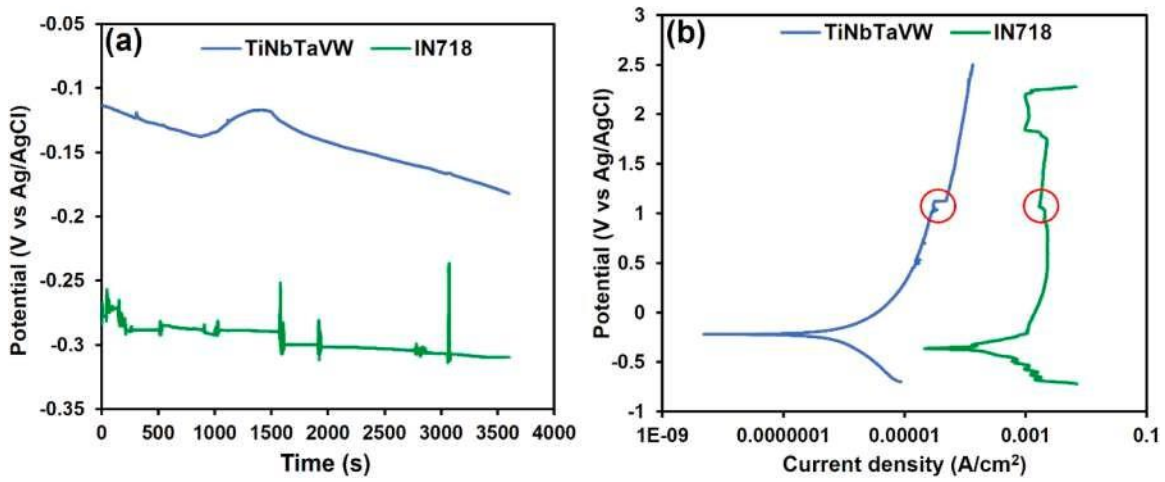

Fig. 4. (a) OCP curves and (b) potentiodynamic polarization curves for the TiNbTaVW RHEA and IN718 alloy in 1 M H_2SO_4.

Table 4

Electrochemical parameters for the TiNbTaVW RHEA and IN718 alloy in 1 M H_2SO_4.

Alloy	Ecorr (V)	I_{corr} (μA/cm^2)	Corrosion rate (mm/yr)
TiNbTaVW	— 0.172 ± 0.02	0.175 ± 0.09	0.0009 ± 0.0005
IN718	— 0.377 ± 0.01	104.59 ± 4.01	1.12 ± 0.001

3.4. Oxidation analysis of the TiNbTaVW RHEA and IN718 alloy

3.4.1. Cyclic oxidation behavior of TiNbTaVW and IN718

The oxidation mass curves of TiNbTaVW and IN718 at 850 °C and 1050 °C are shown in Fig. 6. At 850 °C, the TiNbTaVW RHEA exhibited mass gain at the initial stages of oxidation before mass loss and then became stationary with increasing oxidation time (Fig. 6a). The rapid mass gain observed for the TiNbTaVW RHEA in the initial 7 hours is related to the fast growth of the oxide scale due to the reaction with oxygen [69]. The oxidation rate of the TiNbTaVW RHEA slowed down at some point with increasing time, indicating that the oxygen diffusion processes became slower as the oxide scale got thicker. At 1050 °C, mass gain was observed for the TiNbTaVW RHEA after three hours, followed by continuous mass loss with increasing oxidation time (Fig. 6b). The IN718 alloy exhibited an almost stationary trend throughout the oxidation test (Figs. 6a and 6b). Therefore, the IN718 alloy had a lower mass gain of 4.41 mg/cm^2 and 10.84 mg/cm^2 at 850 °C and 1050 °C, respectively, whereas the TiNbTaVW RHEA exhibited mass losses of — 23.58 mg/cm^2 and 45.92 mg/cm^2 at these temperatures. The IN718 alloy had a better oxidation resistance than the TiNbTaVW RHEA over the entire 15 h of oxidation.

3.4.2. Phase analysis and surface morphologies of the oxidized TiNbTaVW and IN718

The XRD patterns of the oxidized TiNbTaVW and IN718 samples at 850 °C and 1050 °C are shown in Fig. 7. The identified oxides of the TiNbTaVW RHEA at 850 °C were VO_2, V_2O_3, Ta_2O_5, TiO_2, WO_3, Ta_2O_5, $TiVO_4$, $TiTaO_4$, and $Nb_2O_5WO_3$ (Fig. 7a). The oxides of the TiNbTaVW RHEA at 1050 °C were Ti_2O_3, TiO_2, VO_2, V_2O_5, WO_3, $TiNbO_4$, and $Ta_8W_8O_{44}$ (Fig. 7b). The identified oxides of the IN718 alloy at 850 °C were MnO, MnO_2, Al_2O_3, Fe_3O_4, SiO_2, TiO_2, Fe_2O_3, and Ni_2Ti_4O (Fig. 7c). While at 1050 °C, the identified oxides were MnO, MnO_2, Fe_3O_4, Mn_2O_3, $NiMn_2O_4$, and Fe_2MnO_4 (Fig. 7d).

The SEM images of the surface oxides of the TiNbTaVW RHEA at 850 °C and 1050 °C after 15 h are shown in Fig. 8. A compact surface oxide layer containing spalled W-rich oxide particles, cracks (14.7 ± 0.97 μm), and pores (4.9 ± 0.39 μm) was observed for the TiNbTaVW RHEA at 850 °C (Fig. 8a and Supporting Information S5). Viewing the surface scale layer under higher magnification revealed granular-shaped and rod-shaped oxides with sizes of 0.98 ± 0.07 μm and 1.61 ± 0.19 μm dispersed all over the surface (Fig. 8b). Some of the rod-shaped and granular-shaped oxides were attached to one another like a chain of networks. Rod-shaped and granular-shaped oxides have been observed in some RHEAs like NbTiZrV [70] and CrMoNbTaV [71]. The granular-shaped oxides are Ti-rich, while rod-shaped oxides are mostly NbTaWV-rich (Supplementary Information S5). The SEM images of the surface oxides at 1050 °C after 15 h are shown in Fig. 8(c). The surface scale layer of the TiNbTaVW was compact with a crack of 6.1 ± 0.34 μm thickness and spalled Ti-rich oxides (Fig. 8c and Supplementary Information S6). Viewing the surface scale layer at higher magnification revealed granular-shaped and rod-shaped oxides with sizes of 1.47 ± 0.13 μm and 1.83 ± 0.23 μm dispersed all over the surface (Fig. 8d). The granular-shaped and rod-shaped oxides were somewhat larger at 1050 °C than those observed at 850 °C. Therefore, high temperatures have a major effect on the growth and nucleation of oxides. The granular-shaped oxides were Ti-rich, while rod-shaped oxides were mostly NbTaWTi-rich (Supplementary Information S6).

The SEM images of the surface oxides of the IN718 alloy at 850 °C and 1050 °C after 15 h are shown in Fig. 9. The IN718 alloy surface oxide layer at 850 °C consisted of a compact structure with hillocks but no cracks, pores, or voids (Fig. 9a). According to Jayaraj et al. [17], the formation of a crack-free stable surface oxide layer, which protects the alloy from direct contact with oxygen and diffusion through the oxide layer, becomes the rate-controlling process for the oxidation reaction. Viewing the top surface oxides of the IN718 alloy at higher magnification revealed block-shaped (0.45 ± 0.04 μm), rod-shaped (0.39 ± 0.03 μm), round-shaped (0.53 ± 0.05 μm), and cloudy-shaped oxides (0.50 ± 0.04 μm) (Fig. 9b). The block-shaped oxides were Fe-rich, rod-shaped oxides were FeMnNi-rich, round-shaped oxides (white) were TiFeSi-rich, and cloudy-shaped oxides (dark) were AlSi-rich (Supplementary Information S7). The surface oxide layer of IN718 alloy surface was comprised by a more refined structure free of cracks, pores, or voids at 1050 °C (Fig. 9c). The surface oxides exhibited globular (0.35 ± 0.02 μm) and block-shaped oxide (1.11 ± 0.12 μm) structures mostly enriched in Fe (Supplementary Information S7).

3.4.3. Cross-section analysis of the oxidized TiNbTaVW and IN718

The cross-sections of the oxidized TiNbTaVW and IN718 after 15 h at 850 °C and 1050 °C are shown in Fig. 10. A 368 ± 1.1 μm thick oxidized layer with a dark contrast and internal oxidation region was

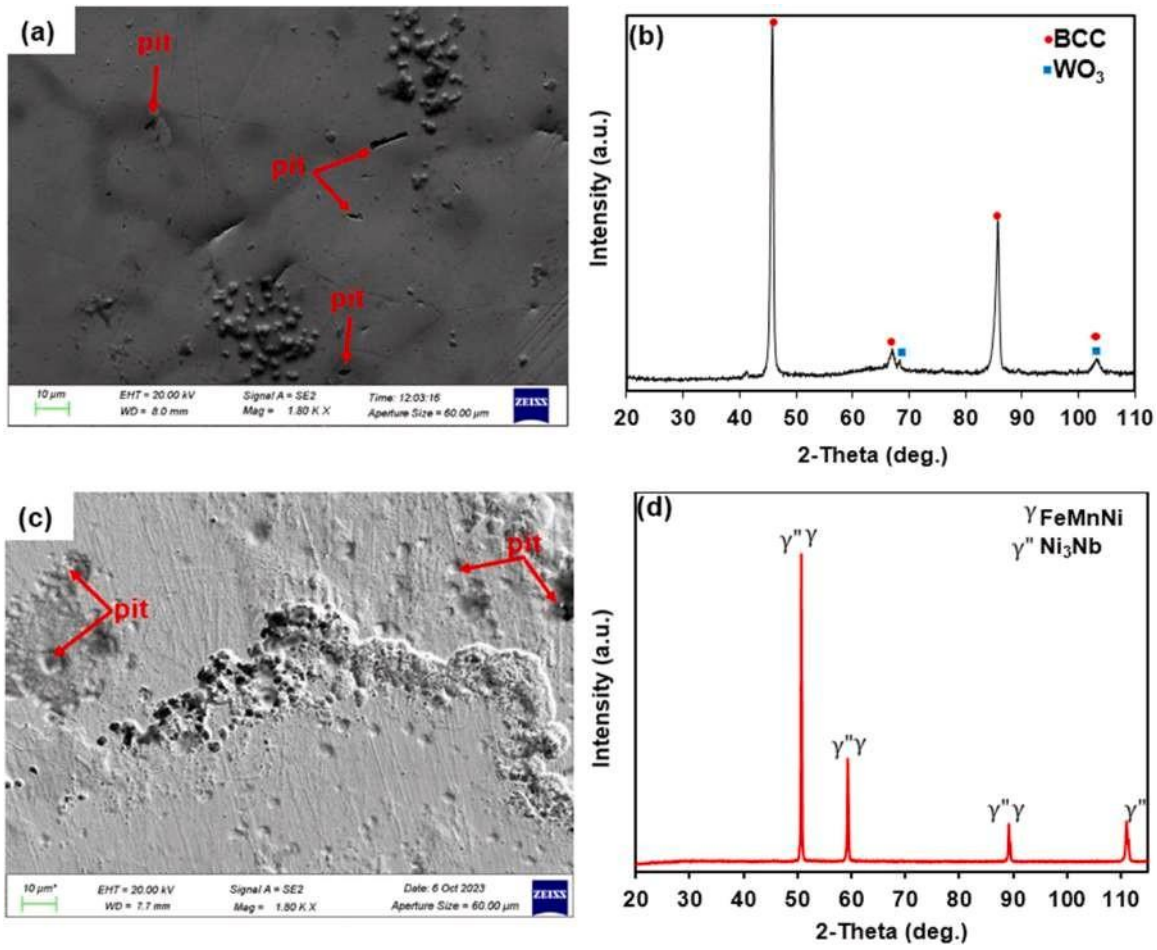

Fig. 5. (a) SEM image of pits and corrosion products in the TiNbTaVW RHEA after exposure in a 1 M H_2SO_4 solution; (b) XRD of the TiNbTaVW RHEA after exposure in a 1 M H_2SO_4 solution; (c) SEM images of the IN718 alloy's corroded surface and pits after exposure in a 1 M H_2SO_4 solution; (d) XRD of the IN718 alloy after exposure in 1 M H_2SO_4 solution.

Table 5

EDX composition (at%) of the TiNbTaVW RHEA and IN718 alloy after potentiodynamic polarization in 1 M H_2SO_4.

TiNbTaVW						
Regions	Ti	Nb	Ta	V	W	O
Dendrite	12 ± 0.9	15 ± 0.6	15 ± 0.6	14 ± 0.5	16 ± 0.9	28 ± 2.8
Interdendrite	20 ± 1.2	16 ± 0.9	12 ± 0.9	19 ± 1.1	9 ± 1.2	24 ± 4.2
IN718						
Si	P	S	Mn	Fe	Ni	O
0.42 ± 0.09	0.15 ± 0.08	3.06 ± 0.01	0.26 ± 0.10	46.16 ± 8.4	25.04 ± 3.1	24.91 ± 9.9

observed for the TiNbTaVW RHEA at 850 °C (Fig. 10a). The thick oxide layer contained cracks with a thickness of 22 ± 1.1 μm spread throughout the oxide layer. The EDS compositions at 850 °C showed mostly NbTaWV-rich oxides for the thick oxide layer and VTiNb-rich oxides for the internal oxidation zone (Supplementary Information S9). A 375 ± 3.7 μm thick oxidized layer with dark contrast and an internal oxidation region was also observed for the TiNbTaVW RHEA at 1050 °C (Fig. 10b). Cracks of 15.7 ± 1.1 μm were also observed in the thick oxide layer (Fig. 10b). The EDS compositions of the thick oxide layer at 1050 °C were mainly VNbWTa-rich oxides and TiVNbW-rich oxides for the internal oxidation zone (Supplementary Information S10). The thickness of the oxide layer increased from 368 μm to 375 μm as the oxidation temperature increased from 850 °C to 1050 °C. The cracks that formed at 850 °C and 1050 °C limited the formation of a reliable diffusion barrier because cracks allow the ingress of oxygen to the metallic substrate, therefore increasing the oxidation rate of the metallic substrate.

The IN718 alloy displayed two layers at 850 °C and 1050 °C, which were defined as the outer and internal oxide layer (Fig. 10c). At 850 °C after 15 h, a 38.6 ± 1.1 μm thick outer oxide layer and 46.1 ± 1.4 μm thick internal oxide layer was observed. The EDS composition of the outer oxide layer at 850 °C after 15 h was mostly the FeNi-rich oxide phase, while the internal oxide layer consisted of mostly FeNi-rich oxides (Supplementary Information S11). At 1050 °C, the outer oxide layer was 15.34 ± 0.6 μm thick, while the internal oxide layer was 66.8 ± 3.3 μm thick (Fig. 10d). The EDS compositions of the outer and internal oxide layers at 1050 °C after 15 h comprised mostly FeNi-rich oxide (Supplementary Information S12). The internal oxide layer had more thickness than the outer oxide layer at 850 °C and 1050 °C. The oxidation rate of IN718 was lower at both temperatures because the outer and internal oxide layers served as diffusion barriers.

4. Discussion

4.1. TiNbTaVW phase prediction

The physical properties of elements in the RHEAs and the enthalpy of mixing for the selected alloy's binary subsystem are shown in Table 6. In

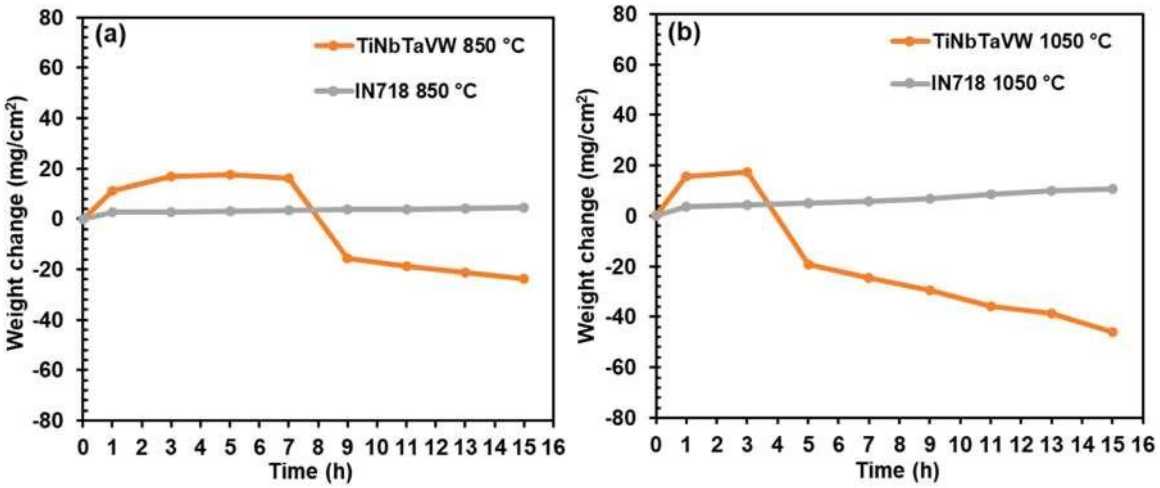

Fig. 6. (a) Cyclic oxidation curve of TiNbTaVW RHEA and IN718 alloy at (a) 850 °C; (b) 1050 °C.

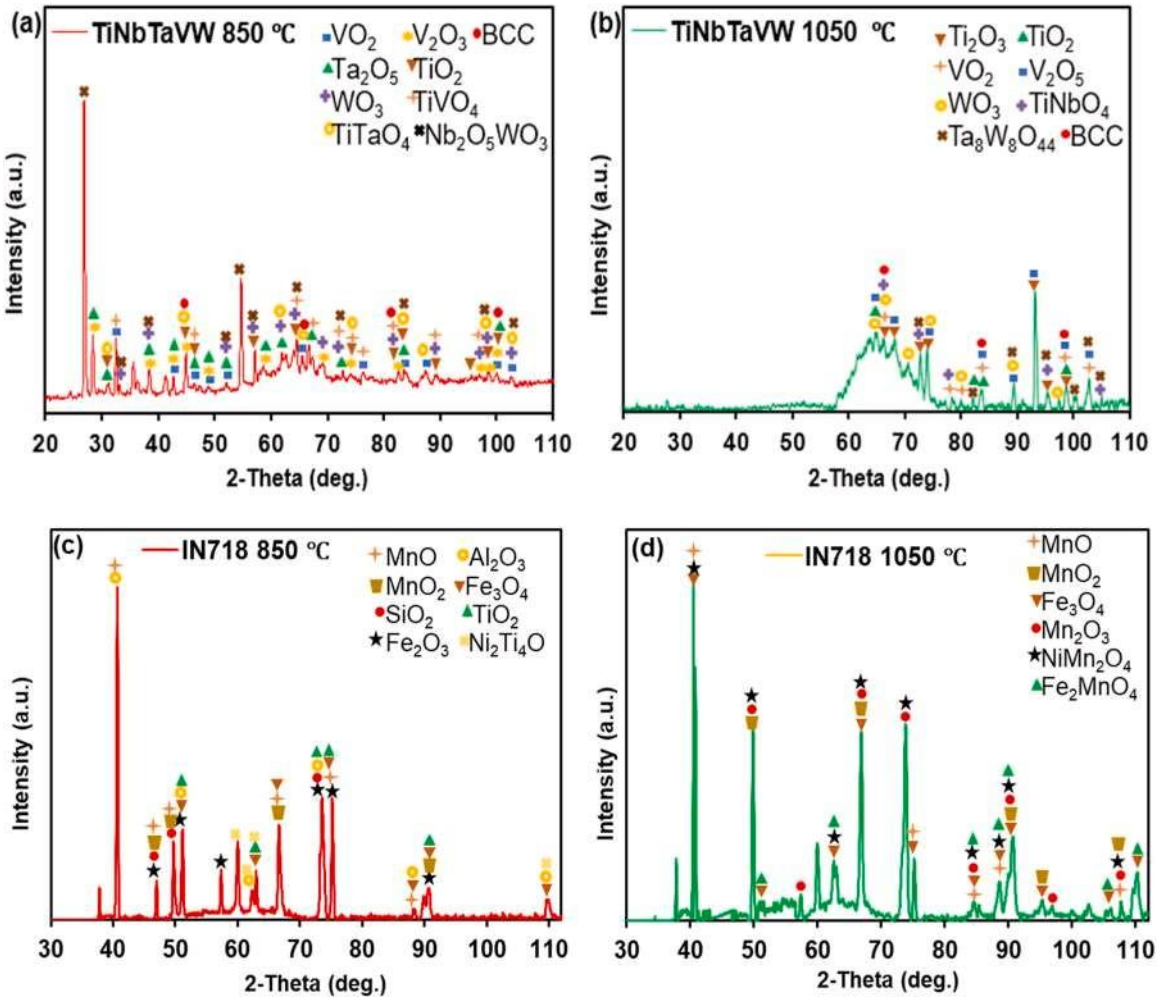

Fig. 7. . (a-b) XRD patterns of identified oxides in the TiNbTaVW RHEA at 850 °C and 1050 °C; (c-d) XRD patterns of identified oxides in the IN718 alloy at 850 °C and 1050 °C.

Table 6, Ta and Ti have the largest atomic radius and least electronegativity, while V has the smallest atomic radius. There could have been atomic distortion during the elements' mixing due to the large atomic size difference between the mixing elements, leading to an increase in lattice strain. The large atomic size difference between so many components would considerably impact the formation of solid solutions in multi-component alloys [72,73]. To predict the phases and stability of the TiNbTaVW RHEA, the empirical parameters of entropy of mixing (ΔS_{mix}), enthalpy of mixing ($\Delta H_{ij\ mix}$), valence electron concentration (VEC), lattice distortion (δ), electronegativity difference (ΔX), and

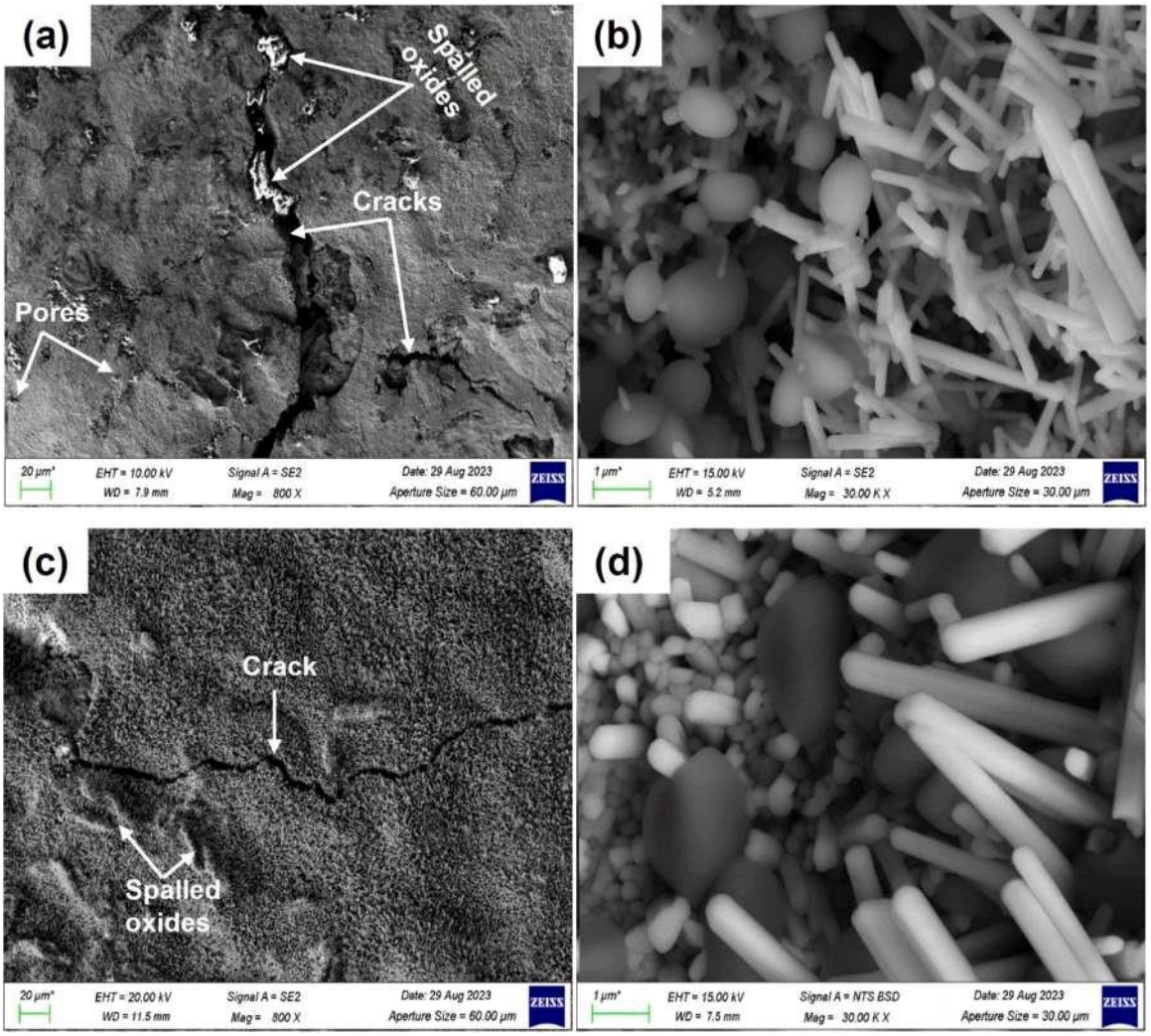

Fig. 8. (a) SEM-BSE of the TiNbTaVW RHEA's surface morphology showing cracks, pores, and spalled oxides at 850 °C after 15 h; (b) higher magnification of the TiNbTaVW RHEA's surface morphology showing granular and rod-shaped oxides at 850 °C after 15 h; (c) SEM-BSE of the TiNbTaVW RHEA's surface morphology showing crack and spalled oxides at 1050 °C after 15 h; (d) higher magnification of the TiNbTaVW RHEA's surface morphology showing granular and rod-shaped oxides at 1050 °C after 15 h.

thermodynamic parameter (Ω) are shown in Table 7.

The enthalpy of mixing for TiNbTaVW shows that the TiTa (1), NbTa (0), NbV (—1), TaV (—1), and VW (—1) binary systems have good mutual solubility (Table 6). When the value of ΔH_{mix} is close to zero, the different elements can randomly distribute in the alloy, and the solid solution phases can stably occur in the solid phase [73]. Therefore, the formation of a solid solution phase is promoted in the TiNbTaVW RHEA. Whereas NbW (_8), TaW (_7), and TiW (_6) have a significant negative enthalpy of mixing, indicating the tendency of intermetallic compounds. The more negative ΔH_{mix}, the larger the binding force between elements [73]. However, an intermetallic phase was not observed was not observed in the TiNbTaVW RHEA SEM micrograph. The calculated empirical parameters for the TiNbTaVW RHEA in Table 7 was compared with three proposed criteria [72,73,79] and was used to further predict the phases and crystal structure. Firstly, a disordered solid solution phase forms when $\Omega > 1.1$ and $\delta < 6.6\%$ [73]. The TiNbTaVW RHEA had $\Omega = 9.1$, which is greater than 1.1, while δ (3.73%) was less than 6.6%. The intermetallic phase was suppressed by the combination of Ω and δ. Hence, only the disordered solid solution BCC phase forms. Although Ω was greater than 1.1, it cannot differentiate between single and multi-phase solid solutions. To fill the void, the Λ parameter [80] was proposed where $\Lambda = \Delta S_{mix}/\delta^2$ to predict the formation of single and multi-phase solid solutions in multi-component alloys. If $\Lambda > 0.96$, a single-phase disordered solid solution forms, whereas $0.24 < \Lambda < 0.96$ gives two-phase mixtures.

The TiNbTaVW RHEA has a greater geometrical parameter of 0.96, which indicates a single-phase solid solution structure. Secondly, according to Guo et al. [72], FCC and BCC crystal structures would be stable if VEC$\geq$ 8.0 and VEC $\leq$ 6.87, respectively. In such a way, VEC $<$ 6.87 = BCC, VEC $\geq$ 8.0 = FCC, and 6.87 $\leq$ VEC $<$ 8.0 = BCC + FCC. The TiNbTaVW RHEA had a VEC of 5.0, which is less than 6.87. A stable BCC crystal structure formed. Thirdly, Laves phase forms when $\Delta\chi > 7$ and $\delta > 5\%$ in HEAs [79]. In the TiNbTaVW RHEA, $\Delta\chi = 0.32$, which is lower than 7. Also, δ for TiNbTaVW is 3.73%, which is lower than 5%. This shows that the Laves phase is not expected to occur in the TiNbTaVW RHEA. The three criteria successfully predicted a single BCC solid solution phase without Laves phase formation. The XRD results also confirmed a single BCC solid solution phase (Fig. 1). The EDS and SEM backscattered images also confirmed a BCC phase without a hexagonal close-packed phase. Hence, the empirical calculations, XRD, and SEM accurately predicted the single BCC solid solution phase in the TiNbTaVW RHEA. A single BCC solid solution phase can be beneficial to the mechanical properties and surface protection ability of RHEAs [22,29,46,81,82].

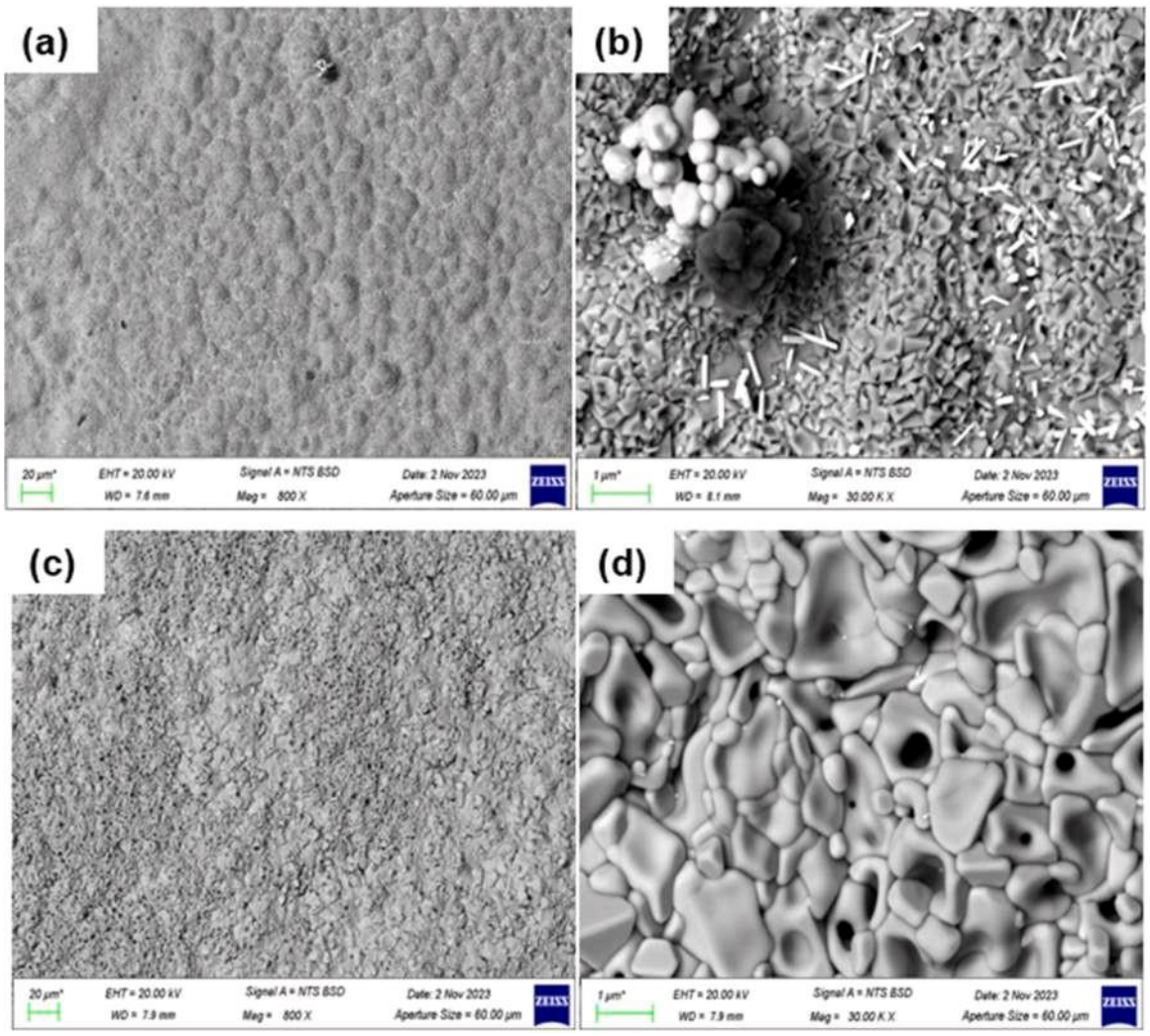

Fig. 9. (a) SEM-BSD of the IN718 alloy's surface morphology showing its compact structure with hillocks at 850 °C after 15 h; (b) higher magnification of the IN718 alloy's surface morphology showing block-shaped, rod-shaped, round-shaped, and cloudy-shaped oxides at 850 °C after 15 h; (c) SEM-BSD of the IN718 alloy's surface morphology showing its compact and refined structure at 1050 °C after 15 h; (d) higher magnification of the IN718 alloy's surface morphology showing globular and block-shaped oxides at 1050 °C after 15 h.

4.2. Corrosion resistance of the TiNbTaVW RHEA in 3.5 wt% NaCl and 1 M H_2SO_4 solution

The TiNbTaVW RHEA had nobler values in the 3.5 wt% NaCl and 1 M H_2SO_4 solutions than the IN718 alloy, as shown in Tables 2 and 4. An increase in OCP toward a nobler value has been attributed to building the oxide layer on alloys [83]. Fluctuations in OCP were observed for the IN718 alloy in the 3.5 wt% NaCl and 1 M H_2SO_4 solutions but less for the TiNbTaVW RHEA. Fluctuations have been attributed to the dissolution and re-passivation of passive films formed on the alloys [14,48]. Dissolution of the oxide film occurs in both solutions for the IN718 alloy, indicating that the observed fluctuations in OCP result from rebuilding the oxide layer on the surface of the alloy. Based on the OCP results, it can be concluded that the surface film of the TiNbTaVW RHEA is more stable than the IN718 alloy in the 3.5 wt% NaCl and 1 M H_2SO_4 solutions. The good corrosion resistance of titanium-containing alloys in many chloride and sulfide solutions has been attributed to the stable and adherent passive film that forms spontaneously on the metal surface [83–85]. These oxides have two layers comprising the inner layer (TiO) and outer layer (TiO_2) passive films of the exposed samples [84–87]. TiO_2 and VO were found on the surface of the TiNbTaVW RHEA after potentiodynamic polarization in a chloride-containing solution. Ti exhibits a low passivation potential and is easily passivated, forming TiO_2 that further improves corrosion resistance [88,89]. In the acidic solution, WO_3 only formed on the alloy's surface. WO_3 is a selective cation oxide that could act as an effective pitting inhibitor that restricts the binding of anions such as chloride and bromide [50,90].

In the passive region during potentiodynamic polarization tests of RHEAs, the passive film could include a combination of TiO_2, Nb_2O_5, and Ta_2O_5 that have been reported to aid the formation of continuous, stable, and protective passive films [49]. Passivation is a characteristic of HEAs, arising due to the addition of passivity-promoting elements such as Ti, Cr, Al, Zr, Ta, Nb, and Hf [49]. The passivating promoting element may influence the alloy's structure and passive film composition, giving rise to different electrochemical responses depending on the alloying type and content [91]. The preferential corrosion sites in HEAs are phase boundaries, defects, elemental segregation, and multi-phase microstructure [25,29]. Hence, the microstructure uniformity and chemical composition can prevent localized corrosion in the alloy [25]. Alloying enhancement using Ti has been reported to improve the corrosion resistance of RHEAs [22,30,82]. Kumar et al. [50] also reported that RHEAs without W are more prone to pitting corrosion in a 3.5 wt% NaCl solution than alloys containing W. In RHEAs with less or no W particles, chloride ions gather at the pitted regions, and the adsorption of chloride ions weakens the neighboring passive film of the pits, worsening pit formation [92]. Despite the presence of TiO_2, VO,

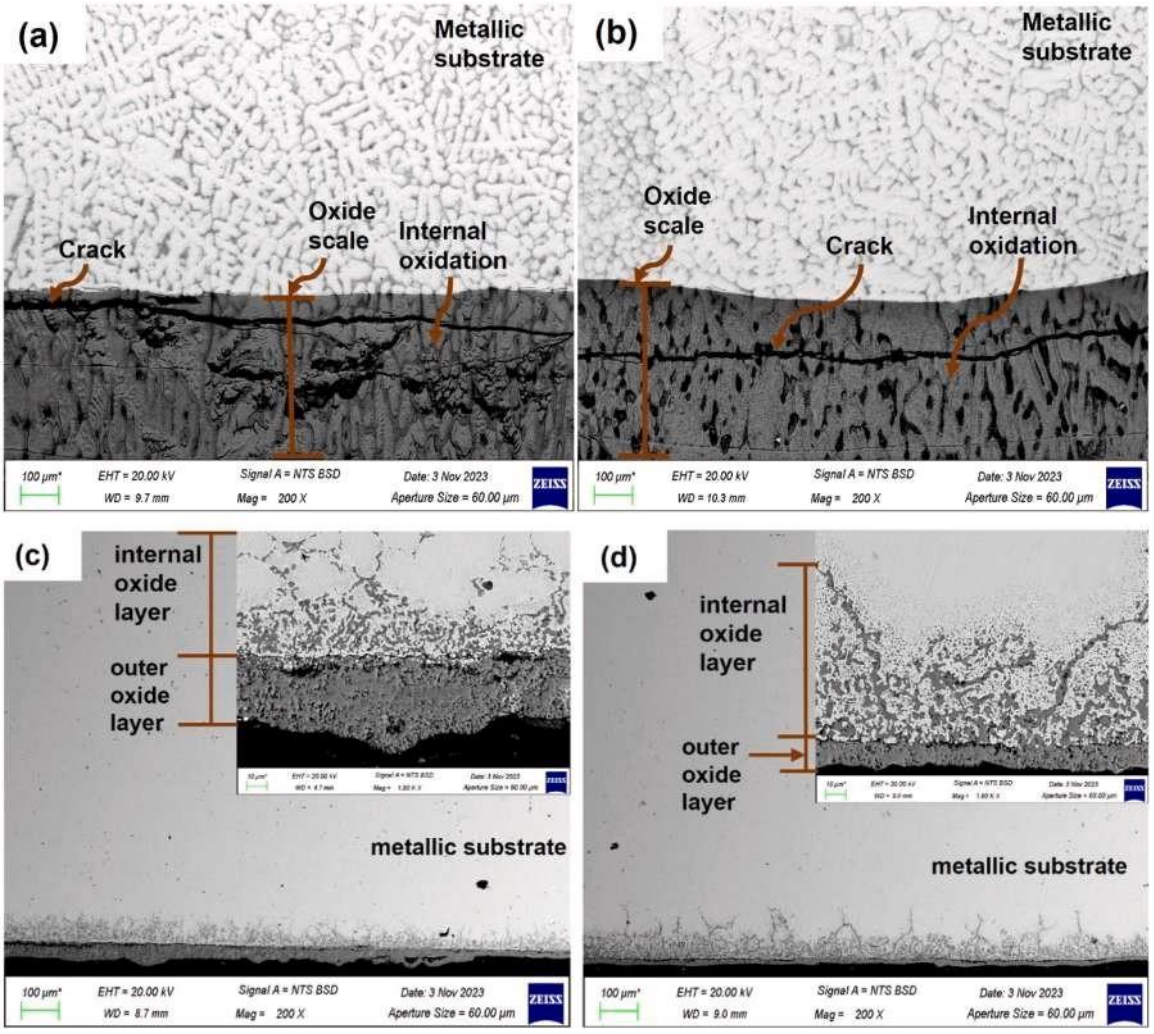

Fig. 10. SEM-BSD of the (a-b) TiNbTaVW RHEA's cross-sectional morphology at 850 °C and 1050 °C after 15 h and (c-d) IN718 alloy's cross-sectional morphology at 850 °C and 1050 °C after 15 h.

Table 6
Physical properties of elements in the TiNbTaVW RHEA and their binary enthalpy of mixing [74].

Elements	Ti			Nb		Ta	V		W	
Atomic radius (Å)	1.46			1.43		1.46	1.32		1.39	
Density (Kg/m^3)	4.50			8.57		16.4	6.0		19.3	
Melting temperature (°C)	1670			2477		3017	1910		3414	
Valence electron	4			5		5	5		6	
Electronegativity(χ)	1.54			1.60		1.50	1.63		2.36	
Hardness (HV)	99			134		89	64		349	
Binary enthalpy of mixing[1]										
i - j	TiNb	TiTa	TiV	TiW	NbTa	NbV	NbW	TaV	TaW	VW
ΔH_{ijmix}	2	1	−2	−6	0	−1	−8	−1	−7	−1

1 rsc.org

and WO_3 on the TiNbTaVW RHEA's surface, few pits were found after potentiodynamic polarization in the chloride and acidic solutions. The next paragraph provides insight into why the pit eventually formed.

The main corrosion mechanism of the TiNbTaVW RHEA in chloride and acidic solutions is localized corrosion due to the segregation of the elemental compositions in both the dendrite and interdendrite regions (Fig. 11). The pits mainly appear at the dendrite region when exposed to the chloride solution, which is related to the break-down of the passive film on the alloy's surface (Fig. 11a). Since pitting is related to the metal surface passive film, pits observed in single-phase alloys exposed to the chloride solution can be attributed to the destruction of the alloy's surface passive film by chloride ions [93]. Uniform microstructures and non-segregation of elemental compositions can inhibit the inhomogeneity of electrochemical performance among phases and grain boundaries [94]. In a chloride solution, segregation of elemental compositions was observed, in which there is a higher Ti and V content in both the dendrite and interdendrite regions than the NbTaW content in both regions (Fig. 11a). The elemental composition segregation might have resulted in different electrochemical responses in the dendrite and interdendrite regions to cause a protective layer breakdown (Fig. 11a). The breakdown of the layer allowed the ingress of chloride ions, which replace the O element especially at the passive film's weak spots, and

Table 7
Calculated empirical phase parameters.

Solid solution parameters	References	Range of parameters	Calculated values for the TiNbTaVW RHEA
$VEC = \sum_{i=1}^{n} C_i\ (VEC)i$	[72,75]	VEC < 6.87 = BCC VEC ≥ 8 = FCC 6.87 ≤ VEC < 8 = BCC + FCC	5.0
$\Delta H_{mix} = \sum_{i=1, i\neq j}^{n} 4\Delta H_{ij}^{mix} C_i\ C_j$	[72,73]	— 15 kJ/mol ≤ ΔH_{mix} ≤ 5 kJ/mol	— 3.68 kJ/mol
$\Delta S_{mix} = -R \sum_{i=1}^{n} C_i \ln C_i$	[72,73]	High value of entropy of mix is important in stabilizing the solid solution phases	13.38 J/K mol
$\delta = \sqrt{\sum_{i=1}^{n} C_i \times \left(1 - \frac{r_i}{\sum_{i=1}^{n} C_i \times r_i}\right)^2}$	[72,76,77]	δ ≤ 60.6% = BCC δ ≥ 6.6% = FCC and Laves	3.73%
$\Omega = \frac{T_m \Delta S_{mix}}{\lvert \Delta H_{mix} \rvert}, T_m = \sum_{i=1}^{n} C_i T_m$	[73]	Ω ≥ 1.1	9.1
$\Delta\chi = \sqrt{\sum_{i=1}^{n} C_i \left(1 - \frac{\chi_i}{\sum_{i=1}^{n} C_i \chi_i}\right)^2}$	[78]	ΔX must be small to form a solid solution	0.32

pits were formed. In the acidic solution, TiV-rich compositions were found in the interdendrite region and near evenly distributed TiNbTaVW compositions in the dendrite region. At this rate, the TiV-rich interdendrite region became the anode, while the near evenly distributed TiNbTaVW dendrite region became the cathode. The coupling effect of the elemental segregations resulted in the protective layer's breakdown, and the ingress of sulfate ions was allowed at the weak spots of the passive film. These eventually led to pits forming in the interdendrite region (Fig. 11b). This phenomenon has been reported in other HEAs, such as MoTaNbVW [95], and TiVCrNb [29]. The fact that there are just a few pits on the surface of the TiNbTaVW RHEA in both the chloride and acidic solutions is evidence of limited localized corrosion.

4.3. Oxidation mechanism of the TiNbTaVW RHEA

At 850 °C (3 to 7 hours) and 1050 °C (1 to 3 hours), the elements in the TiNbTaVW RHEA oxidized to form an initial oxide scale containing simple oxides, and the oxidation rate was stationary because it was controlled by diffusion (Fig. 7). According to Zhang et al. [69], the initial oxide scale can protect the alloy from directly contacting oxygen. The mutual diffusion rates of oxygen and the constituent elements through the oxide layer become critical, and the oxidation process is transformed into a diffusion-controlling mechanism [69]. After 7 hours at 850 °C and 3 hours at 1050 °C, oxide scale spallation occurred with increasing time. This might be attributed to the formation of non-protective simple and complex oxides that offer a limited continuous passive oxide layer. Continuous spallation happens when the surface oxide cannot form a continuous passive layer [96]. The oxidation behavior of the IN718 alloy at 850 °C and 1050 °C after 15 h was better than that of the TiNbTaVW RHEA because the surface oxides formed a continuous passive layer, and, therefore, a controlled diffusion mechanism was observed. This happens when the volume of the oxides is equal to or greater than the volume of the alloy involved in the reaction, and the oxide is well attached to the matrix [96].

Oxygen was dissolved in the initial stages of the TiNbTaVW RHEA's oxidation at both temperatures, which led to the formation of simple oxides: TiO_2, VO_2, V_2O_3, Ta_2O_5, WO_3, Ti_2O_3, and V_2O_5. The standard Gibbs free energy (ΔG) of simple oxides observed in the TiNbTaVW RHEA have been reported [42,44,97–99] and are summarized in Supplementary Information Table 1. At 850 °C, the stability and formation of favorable oxides followed the following order: $TiO_2 > V_2O_3 > Ta_2O_5 > VO^2 > WO^3$. At 1050 °C, the order was $Ti^2O^3 > TiO^2 > VO^2 > V^2O^5 > WO_3$. At 850 °C and 1050 °C, WO_3 had the largest negative ΔG, making it the least stable simple oxide formed on the surface of the TiNbTaVW RHEA after 15 h. As oxidation proceeded, the simple oxides continuously reacted and combined into complex oxides with increasing temperature and oxidation time. The possible reactions involved in the formation of the complex oxides at 850 °C and 1050 °C are represented in Eqs. (2) to (6).

$$8WO_3(s) + 4Ta_2O_5(s) \rightarrow Ta_8W_8O_{44}(s) \quad (2)$$

$$TiO_2(s) + VO_2(s) \rightarrow TiVO_4(s) \quad (3)$$

$$TiO_2(s) + NbO_2(s) \rightarrow TiNbO_4(s) \quad (4)$$

$$TiO_2(s) + TaO_2(s) \rightarrow TiTaO_4(s) \quad (5)$$

$$2TaO_2(s) + VO_2(s) \rightarrow Ta_2VO_6(s) \quad (6)$$

The oxidized TiNbTaVW RHEA at 850 °C and 1050 °C after 15 h exhibited pores, cracks, and voids. The observed voids and pores developed into cracks, making the scale porous, which led to a direct diffusion of oxygen into the substrate. Oxygen enrichment and oxide growth can lead to accumulated stress that is released by cracking. Therefore, the pores and voids affected the oxidation rate by contributing to the mass loss observed in the TiNbTaVW RHEA. According to Sheikh et al. [100], the destructive oxidation process originates from areas not having adherent and protective scales combined with inward diffusion of oxygen that is aided via cracked oxide scales, base

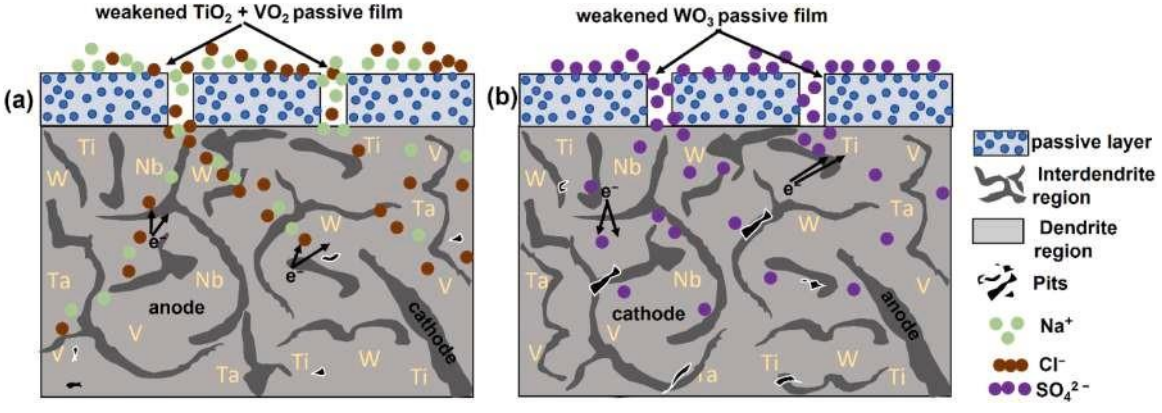

Fig. 11. Schematic diagrams of the TiNbTaVW RHEA's corrosion process during the potentiodynamic polarization tests in (a) 3.5 wt% NaCl and (b) 1 M H_2SO_4.

alloy/oxide interface, and grain/sub-grain boundaries.

The formation of $TiTaO_4$ can prevent the influx of Ti to the outer interface and reduce the oxidation kinetics [52]. $TiTaO_4$ formed in the TiNbTaVW RHEA at 850 °C, possibly serving as a barrier for outward Ti diffusion. Oxide scales of Nb and Ta have a strong bond to the base metals that get weakened at higher temperatures and could form oxides (Nb_2O_5 and Ta_2O_5) that are non-protective [101]. Ta_2O_5 was observed at the surface of the TiNbTaVW RHEA at 850 °C. This might suggest that Ta_2O_5 contributed to the observed cracks, pores, and voids that led to rapid oxygen ingress and an increased oxidation rate. Oxides such as VO_2 and V_2O_5 are volatile at high temperatures and initiate pores and spallation [102]. VO_2 and V_2O_5 oxides were found in the $AlNbTiVZr_{0.25}$ RHEA, causing pores, cracks, and spallation that serve as preferential sites for the rapid ingress of oxygen toward the exposed metal and the primary cause of severe oxidation [71,103]. VO_2 and V_2O_5 were also observed at 850 °C and 1050 °C after 15 h, which could hinder the formation of protective oxides and facilitate the nucleation of pores and cracks in the TiNbTaVW RHEA. WO_3 is easy to sublimate due to its lower sublimation temperature and can react with Ta_2O_5 and Nb_2O_5 to form complex oxides ($Ta_8W_9O_{47}$ and $Nb_8W_9O_{47}$) [44]. The formed $Ta_8W_9O_{47}$ oxide during the oxidation of WTaNbTiAl was ineffective in protecting the alloy substrate [44]. However, $Ta_8W_8O_{44}$, not $Ta_8W_9O_{47}$, was found in the TiNbTaVW RHEA. The protectivity of the $Ta_8W_8O_{44}$ oxide cannot yet be ascertained.

The oxides of the IN718 alloy after 15 h at 850 °C and 1050 °C consisted of both simple and complex oxides. The simple oxides are MnO, FeO, Al_2O_3, SiO_2, Fe_3O_4, MnO_2, NbO, TiO_2, and Mn_2O_3. According to Sheikh et al. [100], the formation of SiO_2 results in a local volume change and internal pressures that lead to decohesion and microcrack formation. The observed SiO_2 might contribute to the observed small decohesion of the IN718 alloy's oxide scale at 850 °C and 1050 °C. The simple oxides such as Al_2O_3 protected the formation and volatilization of Mn_2O_3 in the IN718 alloy at 850 °C, and the oxidation rate was further reduced. The Al_2O_3 layer acted as a diffusion barrier against oxygen ingress into the alloy, thereby improving the performance against of the alloy high-temperature oxidation [104]. The oxide layer containing FeO is often loose, porous, and easily shed, which significantly reduces oxidation resistance [105]. FeO also formed in the IN718 alloy at 1050 °C, which might have also contributed to the small decohesion of the IN718 alloy's oxide scale. However, Fe_3O_4 was observed at 850 °C and 1050 °C, which further formed a protective continuous layer and lowered the oxidation rate. Mixed or complex oxides of $(Fe, Mn)_2TiO_4$, Fe_2SiO_4, Fe_2MnO_4, and $NiMn_2O_4$ were also observed in the IN718 alloy after 15 h at 850 °C and 1050 °C. Some complex oxides have detrimental effects on scale protectiveness and weaken the adhesion of the oxide/substrate interface [106]. The oxide scale of MnO at 850 °C could accelerate the outward diffusion of Mn and Ti ions to form a new oxide (Mn_2TiO_4) on the alloy's surface, further increasing the oxidation rate [107]. Some complex oxides can also offer scale protection and strengthen the adhesion of the oxide/substrate interface. As Si is more easily oxidized thermodynamically, it can react with Fe to form Fe_2SiO_4, which could protect the alloy from oxidation [108]. According to Liu et al. [109], Fe_2SiO_4 can provide a certain level of high oxidation resistance for alloys because it can inhibit the migration of iron cations in the scale. Once Fe migration is hindered, the amount of iron cations in the scale would reduce, slowing the alloy's oxidation rate [109]. The formation of Fe_2TiO_4 during isothermal oxidation improves oxidation resistance by lowering weight gain compared to the bare samples in isothermal oxidation [110].

The adhesion of the oxide layer to the metallic substrate is determined by the thickness of the scale and its growth rate, the stress state, the interfacial energy, and the elastic characteristics of the oxide [111]. In a typical cyclic oxidation process, the oxide scale thickens through diffusional growth, and as the sample cools, the oxide spalls, reducing the oxide thickness to bare metal [112]. As the sample is returned to the furnace for further oxidation, the oxide scale growth continues as before, but the growth rate corresponds to the reduced scale thickness. According to Jeong et al. [113], the metal substrate contracts faster than the oxide layer when the oxidized sample cools down, causing compressive stresses and the formation of shear cracks within the oxide layer. The oxygen enrichment of the surface of the alloy is strongly related to oxide cracking because oxygen dissolution increases lattice constants and, hence, the oxides' volumetric expansion [100]. The volumetric expansion mismatch causes stresses in the oxides, which increase as the oxides grow and are later released by cracking and then spallation of the oxides from the base alloy. There are two internal stresses in the oxide scale that cause spalling. The first is the growth stress, which develops during the oxidation process, and the second is thermal stress, which develops due to the temperature change [114]. At 850 °C after 15 h and 1050 °C after 15 h, cracks, pores, and oxide layer spallation appeared in the TiNbTaVW RHEA, which can be attributed to both the oxidized samples' growth stress during oxidation and the thermal stress during cooling to room temperature. The growth stress is formed mainly by the volume difference between the oxide and the metal forming the oxide and can be expressed by the Pilling-Bedworth ratio (PBR) in Eq. (7) [115].

$$\mathrm{PBR} = \frac{\text{volume per metal ion in oxide}}{\text{volume per metal atom in metal}} \tag{7}$$

The oxide scale is discontinuous and porous if PBR < 1 [116]. For PBR > 2, the internal stress between oxides and matrix is high, which easily leads to the formation of pores and cracks around the oxides [116]. The formed pores and cracks will merge and cause separation between the oxide scale and the metallic substrate. Using Eq. (7), the PBR for TiO_2, VO_2, V_2O_3, Ta_2O_5, WO_3, Ti_2O_3, and V_2O_5 was 1.77, 2.17, 1.84, 2.48, 3.39, 1.50, and 3.24. The internal stress between VO_2, Ta_2O_5, WO_3, V_2O_5, and the TiNbTaVW substrate was high, leading to the formation of pores, cracks, and spallation of the oxide layer.

The growth strain (ε) induces a change in volume that is expressed in Eq. (8) [117].

$$\varepsilon = \sqrt[3]{\mathrm{PBR}} - 1 \tag{8}$$

The ε value was calculated by substituting the PBR values for VO_2, Ta_2O_5, WO_3, and V_2O_5 in Eq. (8). If PBR > 1, a compressive stress develops in the oxides scale, while a tensile stress develops in the scale when PBR < 1. Since PBR > 1 for the observed oxides, it is assumed that a compressive stress was produced on the oxide scale. The calculated ε values for VO_2, Ta_2O_5, WO_3, and V_2O_5 were 0.296, 0.353, 0.503, and 0.481. The growth stress (σ_G) can be calculated based on growth strain in Eq. (9) [114].

$$\sigma_G = \varepsilon E_{oxides} \tag{9}$$

Where E_{oxides} is the Young's Modulus of the VO_2 (140 GPa) [118], Ta_2O_5 (217 GPa) [119], WO_3 (300 GPa) [120], and V_2O_5 (286 GPa) [121] oxides. By substituting E_{oxides} and ε values into Eq. (9), the σ_G was calculated to be 41.4 GPa, 76.6 GPa, 150.8 GPa, and 105.7 GPa for VO_2, Ta_2O_5, WO_3, and V_2O_5, respectively. The σ_G in VO_2 was less than that of Ta_2O_5, WO_3, and V_2O_5. Since the σ_G of VO_2 was lower, only decohesion was initiated on the oxide scale, but cracks, pores, and spalling were initiated by Ta_2O_5, WO_3, and V_2O_5. As mentioned earlier, thermal stress (σ_T) occurs during cooling to room temperature and is formed due to different thermal expansions between the oxide scales and the TiNbTaVW RHEA. The σ_T is expressed in Eq. (10) [114].

$$\sigma_T = E_{oxides}(\alpha_{alloy} - \alpha_{oxides})\Delta T \tag{10}$$

Where α_{alloy} and α_{oxides} are the thermal expansion coefficients of the TiNbTaVW RHEA and the oxides, respectively. ΔT is the difference between the oxidation temperature and room temperature during cooling. The $\alpha_{TiNbTaVW}$ was calculated to be $10.781 \times 10^{-6}\ K^{-1}$ using the rule of mixture. While the α_{oxides} for VO_2, Ta_2O_5, WO_3, and V_2O_5 were $2.1 \times 10^{-6}\ K^{-1}$ [118], $3.0 \times 10^{-6}\ K^{-1}$ [119], $8.9 \times 10^{-6}\ K^{-1}$ [122], and $7.0 \times$

10^{-6} K^{-1}, respectively [121]. The σ_T is assumed to be generated mainly by VO_2, Ta_2O_5, WO_3, and V_2O_5 at 850 °C and by VO_2, WO_3, and V_2O_5 at 1050 °C. The σ_T generated by VO_2, Ta_2O_5, WO_3, and V_2O_5 at 850 °C was estimated to be 1.003 GPa, 1.393 GPa, 0.466 GPa, and 0.686 GPa, respectively. At 1050 °C, the σ_T generated by VO_2, WO_3, and V_2O_5 was 1.246 GPa, 0.578 GPa, and 0.853 GPa. From the results, σ_T is lower than σ_G, and the thermal expansion coefficient of the alloy was larger than that of the oxides. Hence, the σ_T in the scale should be compressive, which is the same as growth stress [114].

The summary of the oxidation mechanism of the TiNbTaVW RHEA at 850 °C and 1050 °C after 15 h is given in Fig. 12.

During the initial stage of oxidation at 850 °C and 1050 °C, oxygen diffused inside the dendrite and the interdendrite regions of the TiNbTaVW RHEA. The oxygen reacted with the RHEA's elements, forming simple and complex oxides on the surface and cross-sectional morphologies. Some of the formed oxide scales might not be protective due to the mismatch in volume expansion between the oxides and TiNbTaVW substrates. This mismatch will eventually generate two internal stresses (growth stress and thermal stress). During cooling, spallation, pores, and cracks emerged due to thermal stress caused by the different thermal expansion coefficients of the oxides and metallic substrates (Figs. 12a and 12b). Growth stress due to the micro-inhomogeneity of the oxide species formed, which was eventually released via pores and cracks (Figs. 12a and 12b). The observed pores and cracks served as fast migration channels for oxygen into the TiNbTaVW substrates and eventually increased the oxidation rate. Therefore, the major factors influencing the pores and cracks observed in the TiNbTaVW RHEA at 850 °C and 1050 °C after 15 h were growth stress and thermal stress. Despite the observed cracks and pores, the TiNbTaVW RHEA remained intact after 15 h of oxidation at high temperatures (Figs. 12c and 12d).

5. Conclusions

The microstructure, hardness, oxidation, and corrosion behavior of the TiNbTaVW RHEA were investigated. The results were compared to a commercial-grade nickel-based superalloy, the IN718 alloy. The following conclusions are drawn from the study:

- The as-cast TiNbTaVW RHEA exhibited a BCC solid solution phase with a dendritic microstructure with an average grain size of 64.32 ± 2.7 μm, which segregated into dendrite and interdendrite regions. The empirical calculations, XRD, and SEM accurately predicted the single BCC solid solution phase in the TiNbTaVW RHEA.
- The hardness value of the TiNbTaVW RHEA was 522 ± 10 HV, which is higher than the IN718 alloy (301 ± 14 HV). The higher hardness of

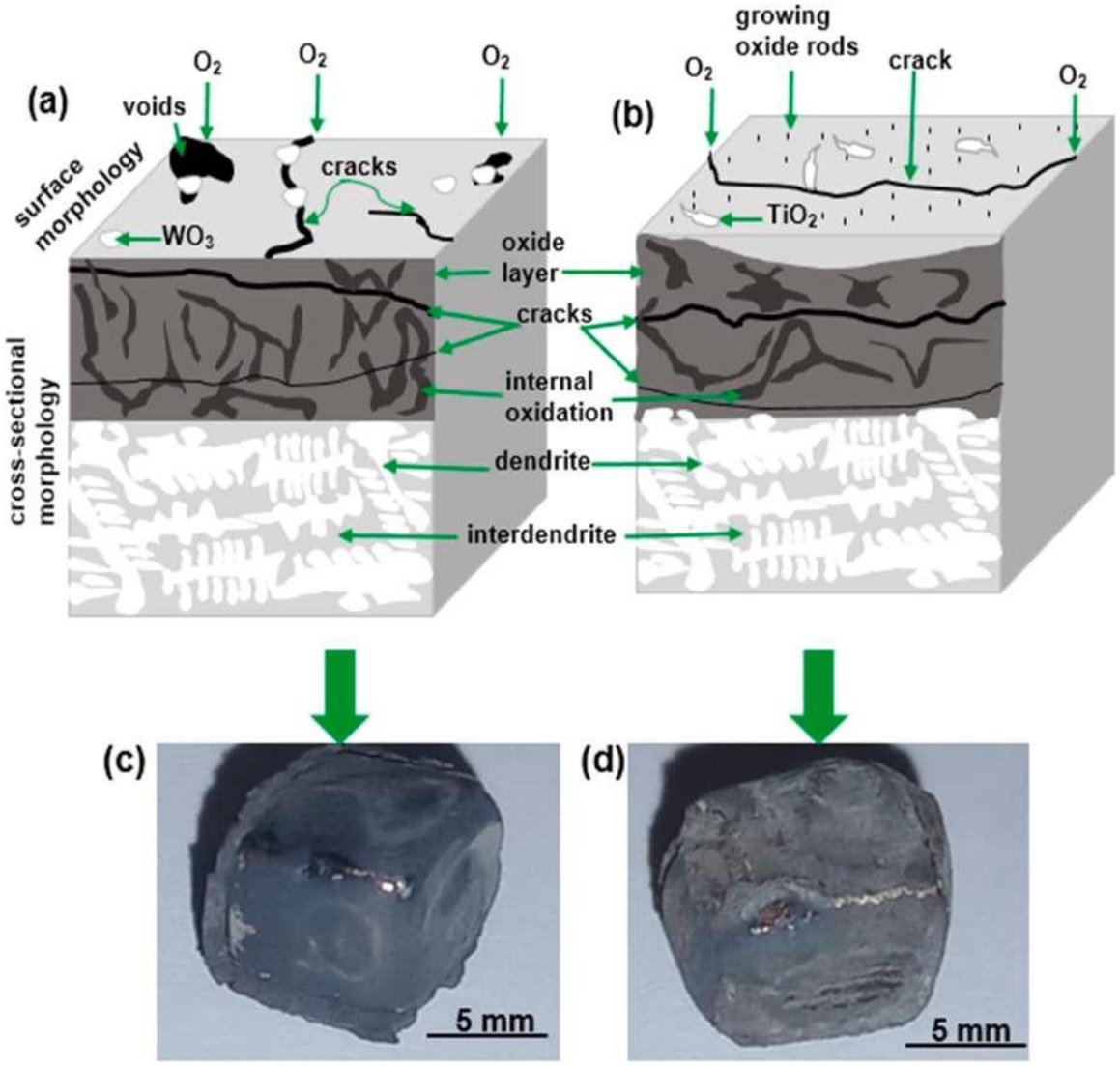

Fig. 12. The TiNbTaVW RHEA showing the oxidation mechanism schematically and visually at (a, c) 850 °C after 15 h and (b, d) 1050 °C after 15 h.

the TiNbTaVW RHEA is attributed to solid solution hardening caused by lattice distortion and grain refinement.

- OCP fluctuations were observed for the TiNbTaVW RHEA and IN718 alloy in both 3.5 wt% NaCl and 1 M H_2SO_4 solutions but more severe in the IN718 alloy.
- Few pits were observed on the RHEA's surface after potentiodynamic polarization in 3.5 wt% NaCl and 1 M H_2SO_4. The formed pits were due to the segregation of elemental compositions that resulted in different electrochemical potentials, eventually breaking down the protective layer and allowing the ingress of chloride and sulfate ions.
- The TiNbTaVW RHEA had a lower corrosion rate of 0.0003 mm/yr in 3.5 wt% NaCl than the IN718 alloy (0.0539 mm/yr) and a lower corrosion rate of 0.0009 mm/yr in 1 M H_2SO_4 than the IN718 alloy (1.115 mm/yr). Therefore, we concluded that the TiNbTaVW RHEA synthesized in this study has better corrosion resistance in both 3.5 wt% NaCl and 1 M H_2SO_4 solutions.
- The IN718 alloy had a lower mass gain of 4.41 mg/cm^2 and 10.84 mg/cm^2 at 850 °C after 15 h and 1050 °C after 15 h. The TiNbTaVW RHEA exhibited a mass loss of — 23.58 mg/cm^2 and — 45.92 mg/cm^2 at 850 °C after 15 h and 1050 °C after 15 h, respectively. In general, the IN718 alloy has a better oxidation resistance than the TiNbTaVW RHEA.
- Thermal stress and growth stress contributed to pores, cracks, and oxide layer spallation observed in the TiNbTaVW RHEA at 850 °C and 1050 °C.

CRediT authorship contribution statement

Bodunrin Michael Oluwatosin: Writing – review & editing, Supervision, Resources, Methodology, Conceptualization. **Bamisaye Olufemi Sylvester:** Writing – original draft, Methodology, Investigation, Formal analysis, Conceptualization. **Van der Merwe Josias:** Supervision, Resources, Methodology, Conceptualization. **Maledi Nthabiseng:** Writing – review & editing, Supervision, Resources, Methodology, Conceptualization.

Declaration of Competing Interest

The authors declare that they have no known competing financial interests or personal relationships that could have appeared to influence the work reported in this paper.

Data availability

Data will be made available on request.

Appendix A. Supporting information

Supplementary data associated with this article can be found in the online version at doi:10.1016/j.jallcom.2024.173803.

References

[1] G. Ouyang, High temperature structure materials beyond nickel base superalloy, Mater. Sci. Nanomater 1 (2017) 8–9.

[2] D.B. Miracle, O.N. Senkov, A critical review of high entropy alloys and related concepts, Acta Mater. 122 (2017) 448–511, https://doi.org/10.1016/j.actamat.2016.08.081.

[3] O.N. Senkov, G.B. Wilks, D.B. Miracle, C.P. Chuang, P.K. Liaw, Refractory high-entropy alloys, Intermetallics 18 (2010) 1758–1765, https://doi.org/10.1016/j.intermet.2010.05.014.

[4] B. Gorr, F. Müller, M. Azim, H.J. Christ, T. Müller, H. Chen, A. Kauffmann, M. Heilmaier, High-temperature oxidation behavior of refractory high-entropy alloys: effect of alloy composition, Oxid. Met. 88 (2017) 339–349, https://doi.org/10.1007/s11085-016-9696-y.

[5] R. Feng, B. Feng, M.C. Gao, C. Zhang, J.C. Neuefeind, J.D. Poplawsky, Y. Ren, K. An, et al., Superior high-temperature strength in a supersaturated refractory high-entropy alloy, Adv. Mater. 33 (2021) 1–9, https://doi.org/10.1002/adma.202102401.

[6] N. Razumov, T. Makhmutov, A. Kim, B. Shemyakinsky, A. Shakhmatov, V. Popovich, et al., Refractory CrMoNbWV high-entropy alloy manufactured by mechanical alloying and spark plasma sintering: Evolution of microstructure and properties, Materials 14 (2021) 1–14, https://doi.org/10.3390/ma14030621.

[7] S. Sheikh, S. Shafeie, Q. Hu, J. Ahlström, C. Persson, J. Veselý, J. Zýka, U. Klement, S. Guo, Alloy design for intrinsically ductile refractory high-entropy alloys, J. Appl. Phys. 120 (2016) 1–5, https://doi.org/10.1063/1.4966659.

[8] C. Lee, F. Maresca, R. Feng, Y. Chou, T. Ungar, M. Widom, J.D. Poplawsky, Y. Chou, et al., refractory high-entropy alloys, Nat. Commun. 12 (2021) 6–13, https://doi.org/10.1038/s41467-021-25807-w.

[9] Z.D. Han, N. Chen, S.F. Zhao, L.W. Fan, G.N. Yang, Y. Shao, K.F. Yao, Effect of Ti additions on mechanical properties of NbMoTaW and VNbMoTaW refractory high entropy alloys, Intermetallics 84 (2017) 153–157, https://doi.org/10.1016/j.intermet.2017.01.007.

[10] Y. Tong, L. Bai, X. Liang, Y. Chen, Z. Zhang, J. Liu, Y. Li, Y. Hu, Influence of alloying elements on mechanical and electronic properties of $NbMoTaW_X$ (X = Cr, Zr, V, Hf and Re) refractory high entropy alloys, Intermetallics 126 (2020) 1–9.

[11] J. Yi, S. Tang, C. Zhang, M. Xu, L.I.N. Yang, L.U. Wang, L. Zeng, Microstructure and mechanical properties of a new refractory equiatomic CrHfNbTaTi high-entropy alloy, JOM 73 (2021) 934–940, https://doi.org/10.1007/s11837-020-04557-y.

[12] O.N. Senkov, G.B. Wilks, J.M. Scott, D.B. Miracle, Mechanical properties of $Nb_{25}Mo_{25}$ $Ta_{25}W_{25}$ and $V_{20}Nb_{20}Mo_{20}Ta_{20}W_{20}$ refractory high entropy alloys, Intermetallics 19 (2011) 698–706, https://doi.org/10.1016/j.intermet.2011.01.004.

[13] T. Huang, S. Wu, H. Jiang, Y. Lu, T. Wang, T. Li, Effect of Ti content on microstructure and properties of Ti_xZrVNb refractory high-entropy alloys, Int. J. Miner. Metall. Mater. 27 (2020) 1318–1331.

[14] Q. Zhou, S. Sheikh, P. Ou, D. Chen, Q. Hu, S. Guo, Corrosion behavior of $Hf_{0.5}Nb_{0.5}Ta_{0.5}Ti_{1.5}Zr$ refractory high-entropy in aqueous chloride solutions, Electrochem. Commun. 98 (2019) 63–68, https://doi.org/10.1016/j.elecom.2018.11.009.

[15] T.E. Perez, Corrosion in the oil and gas industry: an Increasing challenge for materials, JOM 65 (2013) 1033–1042, https://doi.org/10.1007/s11837-013-0675-3.

[16] G.H. Koch, M.P.H. Brongers, N.G. Thompson, Y.P. Virmani, J.H. Payer, Corrosion costs and preventive strategies in the United States, NACE Int., Houst. (2002).

[17] J. Jayaraj, P. Thirathipviwat, J. Han, A. Gebert, Microstructure, mechanical and thermal oxidation behavior of AlNbTiZr high entropy alloy, Intermetallics 100 (2018) 9–19, https://doi.org/10.1016/j.intermet.2018.05.015.

[18] Y. Qiu, S. Thomas, M.A. Gibson, H.L. Fraser, N. Birbilis, Corrosion of high entropy alloys, Npj Mater. Degrad. 1 (2017) 17, https://doi.org/10.1038/s41529-017-0009-y.

[19] J. Shi, S. Ling, Y. Kuang, Y. Tong, Y. Hu, D. Deng, Influence of microstructure of CoCrNi medium entropy alloy on its corrosion behavior, Anti-Corros. Method Mat. 70 (2023) 438–448, https://doi.org/10.1108/acmm-06-2023-2840.

[20] Y. Shi, B. Yang, P.K. Liaw, Corrosion-resistant high-entropy alloys: a review, Metals 7 (2017) 1–18, https://doi.org/10.3390/met7020043.

[21] Z. Cai, Z. Wang, W. Yang, P. Zhang, Y. Lu, J. Pu, Microstructure and corrosion behavior of AlCrTiV-X (X = Cu, Mo, Cu, Mo) high-entropy alloy films in 3.5 wt% NaCl solution, Surf. Interfaces 27 (2021) 101558, https://doi.org/10.1016/j.surfin.2021.101558.

[22] Y. Gao, K. Chong, L. Qiao, Y. Li, C. Liu, F. Guo, D. Wu, Y. Zou, Synthesis and corrosion behavior of $Mo_{15}Nb_{20}Ta_{10}Ti_{35}V_{20}$ refractory high entropy alloy, Mater. Des. 228 (2023) 1–15, https://doi.org/10.1016/j.matdes.2023.111820.

[23] Y. Gao, K. Chong, C. Liu, Y. Cao, D. Wu, Y. Zou, Electrochemical corrosion and high temperature hot corrosion behavior of NbTaTiV and CrNbTaTiV high entropy alloy, J. Mater. Res. Technol. 28 (2024) 216–234, https://doi.org/10.1016/j.jmrt.2023.11.247.

[24] Z.H. Gu, Z.S. Nong, H.Y. Wang, J.J. Wang, Microstructures, mechanical and electrochemical properties of MoNbTa-based refractory multi-component alloys, JOM 74 (2022) 4344–4351, https://doi.org/10.1007/s11837-022-05499-3.

[25] M. Li, Q. Chen, X. Cui, X. Peng, G. Huang, Evaluation of corrosion resistance of the single-phase light refractory high entropy alloy $TiCrVNb_{0.5}Al_{0.5}$ in chloride environment, J. Alloy. Compd. 857 (2021) 1–10, https://doi.org/10.1016/j.jallcom.2020.158278.

[26] Z. Peng, B. Li, Z. Luo, X. Chen, Y. Tang, G. Yang, P. Gong, A lightweight $AlCrTiV_{0.5}Cu_x$ high-entropy alloy with excellent corrosion resistance, Materials 16 (2023) 2922, https://doi.org/10.3390/ma16072922.

[27] H. Wang, W. Chen, Z. Fu, C. Chu, Z. Tian, Z. Jiang, H. Wen, Lightweight Ti-Zr-Nb-Al-V refractory high-entropy alloys with superior strength-ductility synergy and corrosion resistance, Int. J. Refract. Met. Hard Mater. 116 (2023) 106331, https://doi.org/10.1016/j.ijrmhm.2023.106331.

[28] D. Yan, K. Song, Microstructures, mechanical properties, and corrosion behaviors of refractory high-entropy ReTaWNbMo alloys, J. Mater. Eng. Perform. 29 (2020) 399–409, https://doi.org/10.1007/s11665-019-04540-y.

[29] J.Y. Yao, L.B. Serrano, S.F. Santos, K.R. Cardoso, Microstructure and corrosion behavior of the Ti-V-Cr-Nb high-entropy alloys in 3.5 wt% NaCl solution, Corros. Sci. 218 (2023) 111149, https://doi.org/10.1016/j.corsci.2023.111149.

[30] Z. Wang, Y. Yan, Y. Wu, X. Huang, Y. Zhang, Y. Su, L. Qiao, Corrosion and tribocorrosion behavior of equiatomic refractory medium entropy TiZr(Hf, Ta, Nb) alloys in chloride solutions, Corros. Sci. 199 (2022) 110166, https://doi.org/10.1016/j.corsci.2022.110166.

[31] G.S. Frankel, T. Li, J.R. Scully, Perspective—localized corrosion: passive film breakdown vs pit growth stability, J. Electrochem. Soc. 164 (2017) C180–C181, https://doi.org/10.1149/2.1381704jes.

[32] D.E. Williams, Y. Yang, E.G. Webb, R.C. Alkire, Explanation for initiation of pitting corrosion of stainless steels at sulfide inclusions, J. Electrochem. Soc. 147 (2000) 1763–1766, https://doi.org/10.1149/1.1393431.

[33] T. Li, O.J. Swanson, G.S. Frankel, A.Y. Gerard, P. Lu, J.E. Saal, J.R. Scully, Localized corrosion behavior of a single-phase non-equimolar high entropy alloy, Electrochim. Acta 306 (2019) 71–84, https://doi.org/10.1016/j.electacta.2019.03.104.

[34] C.O. Moon, S.B. Lee, Analysis on failures of protective-oxide layers and cyclic oxidation, Oxid. Met. 39 (1993) 1–13.

[35] S.N. Lekakh, O. Neroslavsky, M. Li, L. Godlewski, W. Zhu, Effect of spallation on oxidation kinetics of heat-resistant Cr–Ni austenitic steels on air and combustion atmosphere, High. Temp. Corr. Mater. 99 (2023) 79–99, https://doi.org/10.1007/s11085-022-10139-x.

[36] S. Sheikh, L. Gan, A. Ikeda, H. Murakami, S. Guo, Alloying effect on the oxidation behavior of a ductile $Al_{0.5}Cr_{0.25}Nb_{0.5}Ta_{0.5}Ti_{1.5}$ refractory high-entropy alloy, Mater. Today Adv. 7 (2020) 1–12, https://doi.org/10.1016/j.mtadv.2020.100104.

[37] A.A. Hashim, A.S. Hammood, N.J. Hammadi, Evaluation of high-temperature oxidation behavior of Inconel 600 and hastelloy C-22, Arab. J. Sci. Eng. 40 (2015) 2739–2746, https://doi.org/10.1007/s13369-015-1766-y.

[38] Y. Du, D. Ding, L. Lai, S. Xiao, N. Guo, B. Song, S. Guo, Effect of Y on the high-temperature oxidation behavior of CrMoTaTi refractory high entropy alloy, Int. J. Refract. Met. Hard Mater. 103 (2022) 105755, https://doi.org/10.1016/j.ijrmhm.2021.105755.

[39] S. Lu, X. Li, X. Liang, W. Yang, J. Chen, Effect of V and Ti on the oxidation resistance of WMoTaNb refractory high-entropy alloy at high temperatures, Metals 12 (2022), https://doi.org/10.3390/met12010041.

[40] D. Ouyang, Z.J. Chen, H.B. Yu, K.C. Chan, L. Liu, Oxidation behavior of the $Ti_{38}V_{15}Nb_{23}Hf_{24}$ refractory high-entropy alloy at elevated temperatures, Corros. Sci. 198 (2022) 1–11, https://doi.org/10.1016/j.corsci.2022.110153.

[41] R. Romero, I.J. Beyerlein, C.V. Ramana, Microstructure and oxidation behavior of a CrMoNbTaW refractory high entropy alloy, ACS Appl. Eng. Mater. 1 (2023) 132–139, https://doi.org/10.1021/acsaenm.2c00025.

[42] R. Su, H. Zhang, G. Ouyang, L. Liu, D.D. Johnson, J.H. Perepezko, Oxidation mechanism in a refractory multiple-principal-element alloy at high temperature, Acta Mater. 246 (2023) 118719, https://doi.org/10.1016/j.actamat.2023.118719.

[43] Y.Z. Wang, N. Gao, X.W. Liu, W.M. Chen, H.T. Zheng, The oxidation behavior of a ductile $Hf_{0.5}Nb_{0.5}Ta_{0.5}Ti_{1.5}Zr$ refractory high-entropy alloy in pure oxygen condition at 500–900 °C, J. Mater. Res. Technol. 25 (2023) 5457–5468, https://doi.org/10.1016/j.jmrt.2023.07.003.

[44] Y. Yan, K.A. McGarrity, D.J. Delia, C. Fekety, K. Wang, The oxidation-resistance mechanism of WTaNbTiAl refractory high entropy alloy, Corros. Sci. 204 (2022) 110377, https://doi.org/10.1016/j.corsci.2022.110377.

[45] R. Zhang, J. Meng, J. Han, K. Tulugan, Oxidation resistance properties of refractory high-entropy alloys with varied $Al_xCrTiMo$ content, J. Mater. Sci. 56 (2021) 3551–3561, https://doi.org/10.1007/s10853-020-05480-y.

[46] A.O. Moghaddam, M. Sudarikov, N. Shaburova, D. Zherebtsov, V. Zhivulin, I. A. Solizoda, et al., High temperature oxidation resistance of W-containing high entropy alloys, J. Alloy. Compd. 897 (2022) 1–10, https://doi.org/10.1016/j.jallcom.2021.162733.

[47] M. Wang, Z.L. Ma, Z.Q. Xu, X.W. Cheng, Effects of vanadium concentration on mechanical properties of $V_xNbMoTa$ refractory high-entropy alloys, Mater. Sci. Eng. 808 (2021) 1–8, https://doi.org/10.1016/j.msea.2021.140848.

[48] J. Li, X. Yang, R. Zhu, Y. Zhang, Corrosion and serration behaviors of $TiZr_{0.5}NbCr_{0.5}V_xMo_y$ high entropy alloys in aqueous environments, Metals 4 (2014) 597–608, https://doi.org/10.3390/met4040597.

[49] C. Nyby, X. Guo, J.E. Saal, S.C. Chien, A.Y. Gerard, H. Ke, T. Li, et al., Electrochemical metrics for corrosion resistant alloys, Sci. Data 8 (2021) 58, https://doi.org/10.1038/s41597-021-00840-y.

[50] D. Kumar, O. Maulik, V.K. Sharma, Y.V.S.S. Prasad, V. Kumar, Understanding the effect of tungsten on corrosion behavior of $AlCuCrFeMnW_x$ high-entropy alloys in 3.5 wt% NaCl solution, J. Mater. Eng. Perform. 27 (2018) 4481–4488, https://doi.org/10.1007/s11665-018-3536-y.

[51] K. Patel, M. Sadeghilaridjani, M. Pole, S. Mukherjee, Understanding the effect of tungsten on corrosion behavior of $AlCuCrFeMnW_x$ high-entropy alloys in 3.5 wt% NaCl solution, J. Mater. Eng. Perform. 27 (2018) 4481–4488, https://doi.org/10.1007/s11665-018-3536-y.

[52] S. Schellert, M. Weber, H.J. Christ, C. Wiktor, B. Butz, M.C. Galetz, S. Laube, et al., Formation of rutile $(Cr,Ta,Ti)O_2$ oxides during oxidation of refractory high entropy alloys in Ta-Mo-Cr-Ti-Al system, Corros. Sci. 211 (2023) 110885, https://doi.org/10.1016/j.corsci.2022.110885.

[53] ASTM E92–17, E92–17 Standard test methods for Vickers hardness and Knoop hardness of metallic materials, ASTM International, 2009.

[54] ASTM Standard G102–89, Standard practice for calculation of corrosion rates and related information from electrochemical measurements, PA, 1999.

[55] S.H. Chen, J.S. Zhang, S. Guan, T. Li, J.Q. Liu, F.F. Wu, Y.C. Wu, Microstructure and mechanical properties of $WNbMoTaZr_x$ (x=0.1, 0.3, 0.5, 1.0) refractory high entropy alloys, Mater. Sci. Eng. A 835 (2022) 1–10.

[56] K.K. Tseng, C.C. Juan, S. Tso, H.C. Chen, C.W. Tsai, J.W. Yeh, Effects of Mo, Nb, Ta, Ti, and Zr on mechanical properties of equiatomic Hf-Mo-Nb-Ta-Ti-Zr alloys, Entropy 21 (1) (2019) 14, https://doi.org/10.3390/e21010015.

[57] D.K. Ganji, G. Rajyalakshmi, Influence of alloying compositions on the properties of nickel-based superalloys: A review, in: H. Kumar, P.K. Jain (Eds.), Recent Advances in Mechanical Engineering, Springer Science and Business Media, Deutschland GmbH, 2020, pp. 537–555, https://doi.org/10.1007/978-981-15-1071-7_44.

[58] D. Qiao, H. Liang, S. Wu, J. He, Z. Cao, Y. Lu, T. Li, The mechanical and oxidation properties of novel B2-ordered $Ti_2ZrHf_{0.5}VNb_{0.5}Al_x$ refractory high-entropy alloys, Mater. Charact. 178 (2021) 111287, https://doi.org/10.1016/j.matchar.2021.111287.

[59] F.G. Coury, T. Butler, K. Chaput, A. Saville, J. Copley, J. Foltz, P. Mason, K. Clarke, M. Kaufman, A. Clarke, Phase equilibria, mechanical properties and design of quaternary refractory high entropy alloys, Mater. Des. 155 (2018) 244–256, https://doi.org/10.1016/j.matdes.2018.06.003.

[60] S. Wu, D. Qiao, H. Zhang, J. Miao, H. Zhao, J. Wang, Y. Lu, T. Wang, T. Li, Microstructure and mechanical properties of $C_xHf_{0.25}NbTaW_{0.5}$ refractory high-entropy alloys at room and high temperatures, J. Mater. Sci. Technol. 97 (2022) 229–238, https://doi.org/10.1016/j.jmst.2021.05.015.

[61] H. Zhang, P. Liu, J. Hou, J. Qiao, Y. Wu, Prediction of strength and ductility in partially recrystallized $CoCrFeNiTi_{0.2}$ high-entropy alloy, Entropy 21 (2019) 1–11, https://doi.org/10.3390/e21040389.

[62] A. Roy, P. Sreeramagiri, T. Babuska, B. Krick, P.K. Ray, G. Balasubramanian, Lattice distortion as an estimator of solid solution strengthening in high-entropy alloys, Mater. Charact. 172 (2021) 1–10, https://doi.org/10.1016/j.matchar.2021.110877.

[63] W. Zheng, S. Lü, S. Wu, X. Chen, W. Guo, Development of $MoNbVTa_x$ refractory high entropy alloy with high strength at elevated temperature, Mater. Sci. Eng. A. 850 (2022) 143554, https://doi.org/10.1016/j.msea.2022.143554.

[64] D. Cui, Y. Zhang, L. Liu, Y. Li, L. Wang, Z. Wang, J. Li, J. Wang, F. He, Oxygen-assisted spinodal structure achieves 1.5 GPa yield strength in a ductile refractory high-entropy alloy, J. Mater. Sci. Technol. 157 (2023) 11–20, https://doi.org/10.1016/j.jmst.2023.01.038.

[65] P. Murmey, U. Nichul, M. Chikode, V. Hiwarkar, Effect of post-processing on corrosion behavior of LPBF built Inconel 718 alloy, JOM 75 (2023) 32–44, https://doi.org/10.1007/s11837-022-05565-w.

[66] Z.J. Zheng, Y. Gao, Y. Gui, M. Zhu, Corrosion behaviour of nanocrystalline 304 stainless steel prepared by equal channel angular pressing, Corros. Sci. 54 (2012) 60–67, https://doi.org/10.1016/j.corsci.2011.08.049.

[67] V.P. Parkhutik, Oscillations of open-circuit potential during immersion plating of silicon in $CuSO_4$/HF solutions, Russ. J. Electrochem. 42 (2006) 512–522, https://doi.org/10.1134/S1023193506050090.

[68] Y. Tang, X. Shen, Y. Qiao, L. Yang, J. Chen, D. Lu, Z. Zhang, Corrosion behavior of a selective laser melted Inconel 718 Alloy in a 3.5 wt% NaCl solution, J. Mater. Eng. Perform. 30 (2021) 5506–5514, https://doi.org/10.1007/s11665-021-05909-8.

[69] Y. Zhang, D. Zou, Y. Li, Y. Wang, W. Zhang, X. Zhang, Effect of Al content on the high-temperature oxidation behavior of 18Cr–Al–Si ferritic heat-resistant stainless steel, J. Mater. Res. Technol. 11 (2021) 1730–1740, https://doi.org/10.1016/j.jmrt.2021.02.024.

[70] T.M. Butler, K.J. Chaput, J.R. Dietrich, O.N. Senkov, High temperature oxidation behaviors of equimolar NbTiZrV and NbTiZrCr refractory complex concentrated alloys (RCCAs), J. Alloy. Compd. 729 (2017) 1004–1019, https://doi.org/10.1016/j.jallcom.2017.09.164.

[71] Y. Xiao, W. Kuang, Y. Xu, L. Wu, W. Gong, J. Qian, Q. Zhang, Y. He, Microstructure and oxidation behavior of the CrMoNbTaV high-entropy alloy, J. Mater. Res. 34 (2019) 301–308, https://doi.org/10.1557/jmr.2018.340.

[72] S. Guo, C. Ng, J. Lu, C.T. Liu, Effect of valence electron concentration on stability of FCC or BCC phase in high entropy alloys, J. Appl. Phys. 103505 (2011) 1–6, https://doi.org/10.1063/1.3587228.

[73] X. Yang, Y. Zhang, Prediction of high-entropy stabilized solid-solution in multi-component alloys, Mater. Chem. Phys. 132 (2012) 233–238, https://doi.org/10.1016/j.matchemphys.2011.11.021.

[74] Y. Xiang, Li Guo, Wenmin Liu, Bin Fu, Ao Li, Jianbo Fang, Qihong Liu, Microstructure and mechanical properties of $TaNbVTiAl_x$ refractory high-entropy alloys, Entropy 1 (2020) 1–13.

[75] L. Brewer, Prediction of transition metal phase diagrams, J. Nucl. Mater. 51 (1974) 2–11, https://doi.org/10.1016/0022-3115(74)90107-X.

[76] B.Y. Zhang, Y.J. Zhou, J.P. Lin, G.L. Chen, P.K. Liaw, Solid-solution phase formation rules for multi-component alloys, Adv. Eng. Mater. 10 (2008) 534–538, https://doi.org/10.1002/adem.200700240.

[77] M. Zhang, X. Zhou, J. Li, Microstructure and mechanical properties of a refractory CoCrMoNbTi high-entropy alloy, J. Mater. Eng. Perform. 26 (2017) 3657–3665, https://doi.org/10.1007/s11665-017-2799-z.

[78] J.C. Phillips, Heats of formation of interstitial compounds and their alloys, J. Phys. Chem. Solids 34 (1973) 1051–1058, https://doi.org/10.1016/S0022-3697(73)80012-5.

[79] N. Yurchenko, N. Stepanov, G. Salishchev, Laves-phase formation criterion for high-entropy alloys, Mater. Sci. Technol. (U. Kingd.). 33 (2017) 17–22, https://doi.org/10.1080/02670836.2016.1153277.

[80] A.K. Singh, A. Subramaniam, On the formation of disordered solid solutions in multi-component alloys, J. Alloy. Compd. 587 (2014) 113–119, https://doi.org/10.1016/j.jallcom.2013.10.133.

[81] T.M. Butler, K.J. Chaput, Native oxidation resistance of $Al_{20}Nb_{30}Ta_{10}Ti_{30}Zr_{10}$ refractory complex concentrated alloy (RCCA), J. Alloy. Compd. 787 (2019) 606–617, https://doi.org/10.1016/j.jallcom.2019.02.128.

[82] A. Poulia, C. Mathiou, A. Karantzalis, Electrochemical study of MoTaNbVTi high entropy alloy in aqueous environments, Ann. De. Chim.: Sci. Des. Mater. 43 (2019) 199–205, https://doi.org/10.18280/acsm.430401.

[83] M. Atapour, A. Pilchak, G.S. Frankel, J.C. Williams, M.H. Fathi, M. Shamanian, Corrosion Behavior of Ti-6Al-4V with different thermomechanical treatments and

microstructures, Corros. 66, 065004–065004–065009. https://doi.org/10.5006/1.3452400.
[84] M.Q. Neto, W.M. Rainforth, Effect of potential and microstructure on the tribocorrosion behaviour of beta and near beta Ti alloys I, Biotribology. 24, 100141. https://doi.org/10.1016/j.biotri.2020.100141.
[85] A. Pandey, A. Awasthi, K.K. Saxena, Metallic implants with properties and latest production techniques: a review, Adv. Mater. Process. 6 (2020) 405–440, https://doi.org/10.1080/2374068X.2020.1731236.
[86] C. Ciszak, I. Popa, J.M. Brossard, D. Monceau, S. Chevalier, NaCl induced corrosion of Ti-6Al-4V alloy at high temperature, Corros. Sci. 110 (2016) 91–104, https://doi.org/10.1016/j.corsci.2016.04.016.
[87] J. Pouilleau, D. Devilliers, F. Garrido, S. Durand-Vidal, E. Mahé, Structure and composition of passive titanium oxide films, Mater. Sci. Eng. B. 47 (1997) 235–243, https://doi.org/10.1016/S0921-5107(97)00043-3.
[88] Y. Fu, J. Li, H. Luo, C. Du, X. Li, Recent advances on environmental corrosion behavior and mechanism of high-entropy alloys, J. Mater. Sci. Technol. 80 (2021) 217–233, https://doi.org/10.1016/j.jmst.2020.11.044.
[89] Z. Zhou, H. Li, Y. Liu, T. Niu, H. Li, Effect of Ti on the corrosion behavior of $(FeCrCoNi)_{100-x}Ti_x$ alloy, Corros. Sci. 209, 110807. https://doi.org/10.1016/j.corsci.2022.110807.
[90] M. PourbaiX, Applications of electrochemistry in corrosion science and in practice, Corros. Sci. 14 (1974) 25–82, https://doi.org/10.1016/S0010-938X(74)80006-5.
[91] C.B. Nascimento, U. Donatus, C.T. Ríos, M.C.L. De Oliveira, R.A. Antunes, A review on corrosion of high entropy alloys: exploring the interplay between corrosion properties, alloy composition, passive film stability and materials selection, Mater. Res. 25 (2022) 1–16, https://doi.org/10.1590/1980-5373-MR-2021-0442.
[92] Z. Zhou, L. Wang, X. Zhao, J. Wu, F. Zhang, J. Pi, Effects of W addition on the corrosion behaviors of FeCoNiCrMn high entropy alloy composites in the 3.5 wt% NaCl solution, Surf. Interfaces 23 (2021) 1–8, https://doi.org/10.1016/j.surfin.2021.100956.
[93] C. Liu, Y. Gao, K. Chong, F. Guo, D. Wu, Y. Zou, Effect of Nb content on the microstructure and corrosion resistance of $FeCoCrNiNb_x$ high-entropy alloys in chloride ion environment, J. Alloy. Compd. 935 (2023) 168013, https://doi.org/10.1016/j.jallcom.2022.168013.
[94] X.W. Xing, J.K. Hu, Y. Liu, W. Li, Effect of Mo on microstructure, mechanical and corrosion properties of $FeCrNiMnMo_x$ high-entropy alloys, China Foundry 19 (2022) 464–472, https://doi.org/10.1007/s41230-022-1161-8.
[95] E. Ananiadis, K.T. Argyris, T.E. Matikas, A.K. Sfikas, A.E. Karantzalis, Microstructure and corrosion performance of aluminium matriX composites reinforced with refractory high-entropy alloy particulates, Appl. Sci. 11 (2021) 1–12, https://doi.org/10.3390/app11031300.
[96] O.N. Senkov, S.V. Senkova, D.M. Dimiduk, C. Woodward, D.B. Miracle, Oxidation behavior of a refractory $NbCrMo_{0.5}Ta_{0.5}TiZr$ alloy, J. Mater. Sci. 47 (2012) 6522–6534, https://doi.org/10.1007/s10853-012-6582-0.
[97] X. Zhang, X. Cui, G. Jin, Y. Dong, Z. Wang, Y. Qi, Microstructure evolution and performance enhancement of NbTaTiV-(Cr, Zr, W) single-phase refractory high-entropy alloy coatings: Role of additional elements, J. Alloy. Compd. 951 (2023) 169918, https://doi.org/10.1016/j.jallcom.2023.169918.
[98] B.M. Hunter, A. Oxidation behavior of refractory complex concentrated alloys: Computational and experimental studies, Thesis. University of Alabama, 2019.
[99] L. Zheng, M.C. Zhang, R. Chellali, H. Bouchikhaoui, J.X. Dong, Oxidation property of powder metallurgy EP741NP Ni based superalloy at elevated temperatures, Mater. Technol. 28 (2013) 122–128, https://doi.org/10.1179/1753555712Y.0000000030.
[100] S. Sheikh, M.K. Bijaksana, A. Motallebzadeh, S. Shafeie, A. Lozinko, L. Gan, et al., Accelerated oxidation in ductile refractory high-entropy alloys, Intermetallics 97 (2018) 58–66, https://doi.org/10.1016/j.intermet.2018.04.001.
[101] F. Müller, B. Gorr, H.J. Christ, J. Müller, B. Butz, H. Chen, A. Kauffmann, M. Heilmaier, On the oxidation mechanism of refractory high entropy alloys, Corros. Sci. 159 (2019) 1–11, https://doi.org/10.1016/j.corsci.2019.108161.
[102] K.C. Lo, A.C. Yeh, H. Murakami, Microstructural investigation of oxidized complex refractory high entropy alloys, Mater. Trans. 59 (2018) 556–562, https://doi.org/10.2320/matertrans.MJ201611.
[103] N. Yurchenko, E. Panina, S. Zherebtsov, G. Salishchev, N. Stepanov, Oxidation behavior of refractory $AlNbTiVZr_{0.25}$ high-entropy alloy, Materials 11 (2018) 1–15, https://doi.org/10.3390/ma11122526.
[104] S. Abbaszadeh, A. Pakseresht, H. Omidvar, A. Shafiei, Investigation of the high-temperature oxidation behavior of the $Al_{0.5}CoCrFeNi$ high entropy alloy, Surf. Interfaces 21 (2020) 100724, https://doi.org/10.1016/j.surfin.2020.100724.
[105] X. Yang, Z. Zeng, X. Wang, X. Li, C. Guo, X. Xiao, B. Yang, High-temperature oxidation behaviors of 321 Steel with Y or Nb micro-alloying, Crystals 13 (2023) 781, https://doi.org/10.3390/cryst13050781.
[106] M. Garg, H.S. Grewal, R.K. Sharma, B. Gwalani, H.S. Arora, High oxidation resistance of AlCoCrFeNi high entropy alloy through severe shear deformation processing, J. Alloy. Compd. 917 (2022) 165385, https://doi.org/10.1016/j.jallcom.2022.165385.
[107] W. Zhang, B. Hua, J. Yang, B. Chi, J. Pu, L. Jian, Performance evaluation of a new Fe-Cr-Mn alloy in the reducing atmosphere of solid oxide fuel cells, J. Alloy. Compd. 769 (2018) 866–872, https://doi.org/10.1016/j.jallcom.2018.08.002.
[108] L. Xing, C. Gu, Z. Lv, Y. Bao, High-temperature internal oxidation behavior of surface cracks in low alloy steel bloom, Corros. Sci. 197 (2022) 110076, https://doi.org/10.1016/j.corsci.2021.110076.
[109] J. Liu, Y. Chen, J. Zhang, Oxidation behavior of Ni–Mo–Si alloy coatings fabricated on carbon steel by laser cladding, Surf. Coat. Technol. 375 (2019) 903–910, https://doi.org/10.1016/j.surfcoat.2019.08.001.
[110] S. Keshavarz, M. Zandrahimi, H. Ebrahimifar, Isothermal and cyclic oxidation behavior of AISI 430 ferritic stainless steel coated with titanium, J. Adv. Mater. Process 6 (2018) 12–23.
[111] H. Jahangiri, S. Mohagheghi, A. Asghari Alamdari, K. Gürcan Bayrak, E. Ayas, U. Ünal, A. Motallebzadeh, High temperature oxidation behavior of the AlCrFeMnTi light-weight high-entropy alloy, ACS Appl. Eng. Mater. (2023) 1766–1774, https://doi.org/10.1021/acsaenm.3c00161.
[112] C.A. Barrett, Effect of 0.1 at% zirconium on the cyclic oxidation resistance of beta-NiAI, Oxid. Met. 30 (1988) 5–6, https://doi.org/10.1007/BF00659006.
[113] H. Jeong, S.H. Kim, W.S. Choi, P.P. Choi, Spallation resistance of oxide scales on Alloy 617 enhanced by boron addition, Corros. Sci. 140 (2018) 196–204, https://doi.org/10.1016/j.corsci.2018.06.002.
[114] L. Zheng, M. Zhang, R. Chellali, J. Dong, Investigations on the growing, cracking and spalling of oxides scales of powder metallurgy Rene95 nickel-based superalloy, Appl. Surf. Sci. 257 (2011) 9762–9767, https://doi.org/10.1016/j.apsusc.2011.06.005.
[115] R. Mevrel, Cyclic oxidation of high-temperature alloys, Mater. Sci. Technol. 3 (1986) 531–535, https://doi.org/10.1080/02670836.1987.11782264.
[116] Y.K. Cao, Y. Liu, B. Liu, W.D. Zhang, J.W. Wang, M. Du, Effects of Al and Mo on high temperature oxidation behavior of refractory high entropy alloys, T. Nonferr. Met. Soc. (Engl. Ed. 29 (2019) 1476–1483, https://doi.org/10.1016/S1003-6326(19)65054-5.
[117] B. Panicaud, J.L. Grosseau-Poussard, J.F. Dinhut, On the growth strain origin and stress evolution prediction during oxidation of metals, Appl. Surf. Sci. 252 (2006) 5700–5713, https://doi.org/10.1016/j.apsusc.2005.07.075.
[118] F. Song, B.E. White, Growth of ultrathin vanadium dioxide thin films using magnetron sputtering, Condens. Matter. (2016). http://arxiv.org/abs/1608.03911 .
[119] C.M. Weyant, K.T. Faber, J.D. Almer, J.V. Guiheen, Residual stress and microstructural evolution in tantalum oxide coatings on silicon nitride, J. Am. Ceram. Soc. 88 (2005) 2169–2176, https://doi.org/10.1111/j.1551-2916.2005.00396.x.
[120] Y. Zhu, Y. Zhang, F.C. Cheong, C.H. Sow, C.T. Lim, Annealing effects on the elastic modulus of tungsten oxide nanowires, J. Mater. Res. 23 (2008) 2149–2156, https://doi.org/10.1557/jmr.2008.0277.
[121] F. Jachmann, C. Hucho, High elastic modulus in b-axis-oriented single crystal V_2O_5, Solid State Commun. 135 (2005) 440–443, https://doi.org/10.1016/j.ssc.2005.05.027.
[122] E. Besozzi, D. Dellasega, V. Russo, C. Conti, M. Passoni, M.G. Beghi, Thermomechanical properties of amorphous metallic tungsten-oxygen and tungsten-oxide coatings, Mater. Des. 165 (2019) 107565, https://doi.org/10.1016/j.matdes.2018.107565.

International Journal of Refractory Metals and Hard Materials 121 (2024) 106661

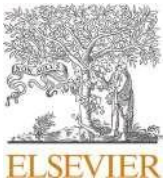

Contents lists available at ScienceDirect

International Journal of Refractory Metals and Hard Materials

journal homepage: www.elsevier.com/locate/IJRMHM

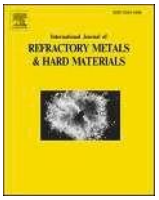

Microstructure, hardness, oxidation and corrosion behavior of $Cr(VNb)_2$ Laves containing CrNbTaVW RHEA in 3.5 wt% NaCl and 1 M H_2SO_4

Olufemi Sylvester Bamisaye [a,c,*], Nthabiseng Maledi [a,b], Josias Van der Merwe [a,b], Michael Oluwatosin Bodunrin [a,b]

[a] School of Chemical and Metallurgical Engineering, Faculty of Engineering and the Built Environment, University of the Witwatersrand, Johannesburg, South Africa
[b] DSI-NRF Centre of Excellence in Strong Materials, University of the Witwatersrand, Johannesburg, South Africa
[c] Mechanical Engineering Department, Faculty of Air Engineering, Air Force Institute of Technology, Kaduna, Nigeria

ARTICLE INFO

Keywords:
Laves phase strengthening
Multi-phase RHEA
Corrosion resistance
Thermal stress
Growth stress
Oxidation properties

ABSTRACT

In this study, CrNbTaVW RHEA was produced via vacuum arc melting. The microstructure, hardness, corrosion and oxidation properties were explored in comparison with the commercial IN718 alloy. The results indicated that CrNbTaVW RHEA exhibited a dendritic microstructure that was segregated into BCC1, BCC2, and $Cr(VNb)_2$ Laves. The CrNbTaVW RHEA has a higher hardness of 688 HV than the IN718 alloy with 301 HV. The higher hardness is due to Laves phase solid solution strengthening and grain refinement. From the corrosion results, CrNbTaVW RHEA had a lower corrosion rate in 3.5 wt% NaCl (0.000097 mm/yr) and 1 M H_2SO_4 (0.00013 mm/yr) than the commercial IN718 alloy (0.054 mm/yr and 1.12 mm/yr). The cyclic oxidation analysis at 850 °C and 1050 °C after 15 hours confirmed a mass gain of 4.41 mg/cm^2 and 10.84 mg/cm^2 for IN718 alloy, while CrNbTaVW RHEA exhibited a mass loss of —25.17 mg/cm^2 and — 35.91 mg/cm^2, respectively, indicating that the IN718 alloy exhibited the best oxidation resistance. Thermal and growth stresses contributed to the pores, voids, cracks, and spallation observed in the CrNbTaVW RHEA.

1. Introduction

The development of new functional materials, metals, and alloys has been the primary driving force behind the progression of human civilization. In 2004, Cantor et al. [1] and Yeh et al. [2] first reported high entropy alloy (HEA) as a type of novel structure material that demonstrated superior properties to those of conventional alloys. The HEAs have exceptional mechanical properties, such as strength, hardness, high temperature phase stability, improved wear, corrosion, and oxidation resistance [1,3,4]. Refractory high entropy alloy (RHEA) which comprise mostly groups IV, V, and VI elements have also been developed and considered as potential high temperature structural materials for applications such as nuclear reactors, heat exchanger tubing, and rocket engine nozzles [5,6]. The RHEAs provide a unique opportunity in the area of alloy design by raising the temperature capability against conventional alloying strategies and improving corrosion and oxidation resistance. The elemental addition of elements such as Ta, W, Cr, V, Nb can significantly influence the mechanical properties of RHEAs [7–10]. Most especially, Cr forming Laves phase that have been reported to significantly enhance the mechanical properties of RHEAs [11–13]. Fang et al. [12] found an increase in hardness (567 HV) and compressive strength (1389 MPa) for $ZrNbTaHf_{0.2}Cr_x$ RHEA due to the volume fraction of the C15_Laves phase. Xiang et al. [14] reported the hardness and compressive strength of MoNbFeCrV to be 827 HV and 2688 MPa and MoNbFeCrTi RHEA to be 792 HV and 1811 MPa respectively, due to the formation of the C15_Laves phase.

Despite the increase in hardness and compressive properties, limited work has focused on the corrosion resistance of RHEAs in chloride and acidic environments. Corrosion is the degradation of materials that occurs as a result of electrochemical reactions between the material and the environment [15]. In materials design, elemental addition might affect the corrosion performance by altering the structure of the phase, multiphase and element segregation, reducing the passivity and nobility of the phases, and influencing the dissolution kinetics [16]. Studies on the corrosion behavior of single-phase RHEA in acidic and chloride solutions have been investigated [17–19]. Zhou et al. [20] investigated the

* Corresponding author at: School of Chemical and Metallurgical Engineering, Faculty of Engineering and the Built Environment, University of the Witwatersrand, Johannesburg, South Africa.
E-mail addresses: 2503285@students.wits.ac.za, bamisayesylvester1988@gmail.com (O.S. Bamisaye).

https://doi.org/10.1016/j.ijrmhm.2024.106661
Received 4 December 2023; Received in revised form 16 March 2024; Accepted 19 March 2024
Available online 21 March 2024
0263-4368/© 2024 The Authors. Published by Elsevier Ltd. This is an open access article under the CC BY-NC-ND license (http://creativecommons.org/licenses/by-nc-nd/4.0/).

corrosion resistance of $Hf_{0.5}Nb_{0.5}Ta_{0.5}Ti_{1.5}Zr$ RHEA in chloride solution and found the alloy to have better corrosion resistance than that of 316 L stainless steel, due to formation of a single phase and passivation promoting elements. Gao et al. [21] found single BCC phase $Mo_{0.5}Nb_{20}Ta_{10}Ti_{35}V_{20}$ RHEA to have better corrosion resistance than that of 316 L stainless steel in chloride solution. Open pits were found in single phase $TiCrVNb_{0.5}Al_{0.5}$ RHEA when exposed to acidic solution [22]. This means like all commonly used corrosion resistant alloys; single phase RHEAs can also undergo localized pitting corrosion. For the dual-phase RHEAs, Xiang et al. [14] studied the corrosion behavior of dual phase (BCC and V-rich sigma phase) MoNbFeCrV RHEA and found only the V-rich sigma phase to be preferentially dissolved when exposed to acidic solution. Bi et al. [23] studied the corrosion behavior of dual phase (BCC and Zr_5Al_3) AlNbTiZr RHEA and found preferential corrosion and pitting within the Zr_5Al_3 phase regions when exposed to chloride solution. However, corrosion studies on dual-phase and multi-phase RHEA containing C15_Laves phase in chloride and acidic solution have not been reported so far. Hence, it is important for the corrosion performance of dual-phase and multi-phase RHEA containing C15_Laves phases to be evaluated to determine their functionality in chloride and acidic environments.

Oxidation resistance is a vital property for alloys working for a long time at high temperatures since it can severely deteriorate the mechanical properties of the materials. The oxidation resistance of the alloys is affected by the compactness of the oxide scale, which can be described through the Pilling–Bedworth ratio (PBR) [24]. According to Lekakh et al. [25], the oxide layer adhesion to the steel substrate depends on various parameters: scale thickness, growth rate, stress rate, interfacial energy, and elastic properties of the oxide. In many applications, oxide scale may fail due to various external loads that may lead to cracking and spalling of the oxide scale and ultimately to exposure of the bare-metal surface [26]. The cyclic-oxidation behavior is more complicated than isothermal oxidation because of the spalling process during cooling [26]. Most oxidation studies of RHEAs are conducted in isothermal conditions rather than in cyclic conditions [27–31]. These have made it difficult to study the spallation behavior of RHEAs when exposed to high temperatures. Furthermore, the effect of growth stress and thermal stress on the formation of holes and cracks in oxidized RHEAs has not been fully reported.

In this study, the empirical parameters of entropy of mixing, enthalpy of mixing, valence electron concentration, lattice distortion, electronegativity difference, and thermodynamic parameter were used to design, predict the phases and stability of an equiatomic CrNbTaVW RHEA. Second phase hardening such as the addition of Cr have been reported to induce a Laves phase for increased hardness [11,32,33]. The addition of V has been reported to enhance the mechanical properties of RHEAs due to grain refinement [34]. V has been reported to protect RHEAs from localized corrosion, such as pitting, in NaCl and H_2SO_4 solutions [35]. The addition of Nb, W, and Ta has been reported to reduce the rate of dissolution of materials [36,37]. The alloys containing W, Cr, Nb have strong passivation potentials, which enable oxide films to form in HEAs with compact packing structures [14,38–40]. The high diffusion of Cr can enable the synthesis of $CrTaO_4$, Cr_2O_3, and $CrNbO_4$ that would form a barrier for both inward diffusion of oxygen and outward diffusion. These will provide protection against oxidation at high temperatures [41–44].

Hence, this study developed and investigated the microstructure, hardness, corrosion, and oxidation properties of multiphase CrNbTaVW RHEA and compared them with the commercial IN718 nickel-based superalloy. The corrosion mechanism of the multiphase RHEA was explained in 3.5 wt% NaCl and 1 M H_2SO_4. The oxidation mechanism of the multiphase RHEA was further elucidated after 15 hours exposure. This study is expected to provide more information on the microstructure, hardness, corrosion, and oxidation properties of multiphase RHEA.

2. Experimental procedures

2.1. Material preparation

Metallic powders (Cr, Nb, Ta, V, and W) with purity >99.7 wt% purchased from Weartech Pty Limited, South Africa, were melted and solidified by a vacuum arc melting furnace in a high purity argon atmosphere on a water-cooled Cu hearth to obtain CrNbTaVW RHEA samples. The samples were turned and remelted three times to ensure chemical homogeneity. A commercial IN718 super alloy was also obtained. The CrNbTaVW RHEA and commercial IN718 super alloy samples were cut to precision using Gold San CNC wire cutting EDM machine operating at 20 V. The sectioned samples were hot mounted in phenolic resin (Struers Polyfast) using a Bainmount twin H auto hot mounting press at a temperature of 160 °C and a pressure of 150 bar. The mounted samples were automatically grounded on the StruersTegramin-20 grinding machine using Struers MD-Piano 2000 and Struers MD-Piano 4000 resin bonded diamond grinding discs. After the grinding operation, the samples were polished using Akasel polishingcloth, with 3 μm two-in-one polycrystalline diamond suspension.

2.2. Hardness testing

Vickers hardness tests were conducted on polished cross-sectional area of the CrNbTaVW RHEA and IN718 alloy samples using a FutureTech Vickers hardness tester (FM-800) equipped with a diamond indenter. The measurements were taken under a load of 300 gf and a dwell time of 15 s for CrNbTaVW RHEA and IN718 alloy according to ASTM standard E92–17 [45]. Ten readings were taken at different positions on samples to obtain the average of the Vickers hardness.

2.3. Corrosion testing

The sectioned CrNbTaVW RHEA and IN718 alloy samples were hot mounted in clear resin at a temperature of 180 °C and a pressure of 150 bar, ground, and polished until a mirror-like finish was obtained. After polishing, the samples were rinsed in water and air-dried. The samples, with a surface area of 0.283 cm^2 were subjected to the corrosive solutions. The corrosion test was performed using a three-electrode electrochemical cell connected to a Gamry® potentiostat. CrNbTaVW RHEA and IN718 alloy samples was used as the working electrode, while a platinum wire and Ag/AgCl saturated with 3 M KCl solution were used as the counter and reference electrodes, respectively. Open circuit potential (OCP) test in 3.5 wt% NaCl and 1 M H_2SO_4 solutions was conducted for 3600 s after immersion in the solutions to reach a stable value. Afterwards, potentiodynamic polarization tests were performed at a scan rate of 0.167 mV/s in the potential range of —0.5 to 2.5 V at room temperature. The corrosion current density (I_{corr}), corrosion potential (E_{corr}), and corrosion rate were determined using the polarization technique according to ASTM standard G59–97 [46].

2.4. Oxidation testing

The CrNbTaVW RHEA and IN718 samples for the oxidation tests were sectioned using a Gold San CNC wire cutting EDM machine to nominal dimensions of 6 × 6 × 7 mm^3. The surfaces of the samples were ground using SiC papers grade to P1200, cleaned in an ultrasonic acetone and then dried in air. Afterwards, oxidation test was carried out in an open-ended tube muffle furnace under laboratory air at 850 °C and 1050 °C for 15 hours. The mass changes of the alloy samples before and after oxidation was measured using a Boeco digital weighing balance (accuracy = 0.0001 g) to characterize the oxidation kinetics.

2.5. Composition and microstructure analysis

The microstructural analysis of the samples was examined using a

high-resolution Zeiss Sigma Field Emission Scanning Electron Microscope (FEG-SEM) in secondary electron (SE) and backscattered electron (BSE) detectors at 20 kV. The microstructure of the samples after the corrosion test, surface and cross-sectional morphology of the oxidized samples were also examined using FEG-SEM. SEM was also used in combination with energy dispersive X-ray (EDX) for elemental compositions. Image **J** software (Open-source software for image analysis, National Institutes of Health) was used to calculate the grain size, pores, voids, and cracks. The phase identification of the samples, corrosion products, and oxides were examined using a Bruker D2 phase diffractometer, with a Co Kα radiation source [λ = 1.78899 Å] at 30 kV and a current of 25 mA within the range of 2θ = 20–120° at a temperature of 25 °C.

3. Results

3.1. Microstructure and phase analysis of CrNbTaVW and IN718

The phases and microstructure present in the as-cast CrNbTaVW RHEA and IN718 were identified by XRD analysis and SEM, as presented in Fig. 1. The XRD analysis result of the CrNbTaVW RHEA shows the peaks are indexed as two BCC solid solution phases and $Cr(VNb)_2$ C15-Laves phase (Fig. 1a). The BCC 1 structure is the primary phase (Im-3 m (229); a = b = c = 3.1980; reference: 96–900-6501), BCC 2 structure is the secondary phase (Im-3 m (229); a = b = c = 3.0240; reference: 96–901-2771), and the $Cr(VNb)_2$ C15-Laves phase (Fd-3 m (227); a = b = c = 7.0790; reference: 96–152-3579). SEM images of CrNbTaVW in Figs. 1(b) and (c) showed that the alloy exhibited a dendritic microstructure that segregated into a white phase (BCC1), grey phase (BCC2), and dark phase ($Cr(VNb)_2$). BCC and Laves phases have been reported in some Cr containing as-cast RHEAs, for example, CrNbTiZr RHEA [47] and CrHfNbTaTi [48]. According to Butler et al. [49], Laves particles precipitated inside grains during cooling in the solid state due to decreasing Cr solubility in the BCC phase. During the nucleation and growth of a new phase, the coordinated diffusion of several elements is important because it requires the redistribution of all elements to reach the desired composition [50]. The average grain size of the dendrites and the Laves phase is 47.3 ± 2.1 μm and 11 ± 0.7 μm respectively. The XRD results in Fig. 1(d) showed that two major phases are present in IN718 alloy, namely, the γ phase (FeMnNi) with space group Fm-3 m (225) and lattice parameter (a = b = c = 3.2350 Å) and the γ'' phase of Ni_3Nb (Fm-3 m (225); a = b = c = 3.6150). The microstructure of the IN718 alloy has uniformly distributed (γ + γ'') phases (Fig. 1e). According to Ganji and Rajyalakshmi [51], the γ phase is soft in nature, while the γ'' phase is the main strengthening phase in most precipitation hardenable nickel base super-alloys.

Table 1 shows the chemical composition of CrNbTaVW RHEA. It was found that the higher melting point elements of W and Ta segregated in the dendritic region (BCC1), while lower melting point elements of V and Cr segregated more in the inter-dendritic regions of (BCC2) and Cr $(VNb)_2$ Laves phase. Nb is distributed evenly in both the dendritic and inter-dendritic regions. This highlights the influence of melting points on segregation that is typical in as-cast alloys. The chemical composition of IN718 alloy is presented in Table 2. It can be seen that the IN718 alloy in this study has a higher composition of Fe than Ni.

Table 1
Composition distribution of the CrNbTaVW RHEA (at. %).

Element	Cr	Nb	Ta	V	W
Actual	16 ± 0.5	22 ± 0.2	21 ± 0.2	22 ± 0.2	19 ± 0.9
BCC1	8 ± 0.4	19 ± 0.4	26 ± 0.6	17 ± 1.1	30 ± 1.4
BCC2	32 ± 1.2	20 ± 0.4	13 ± 0.5	30 ± 0.8	5 ± 0.6
$Cr(VNb)_2$ Laves	34 ± 2.1	19 ± 0.9	11 ± 0.3	33 ± 1.5	3 ± 0.5

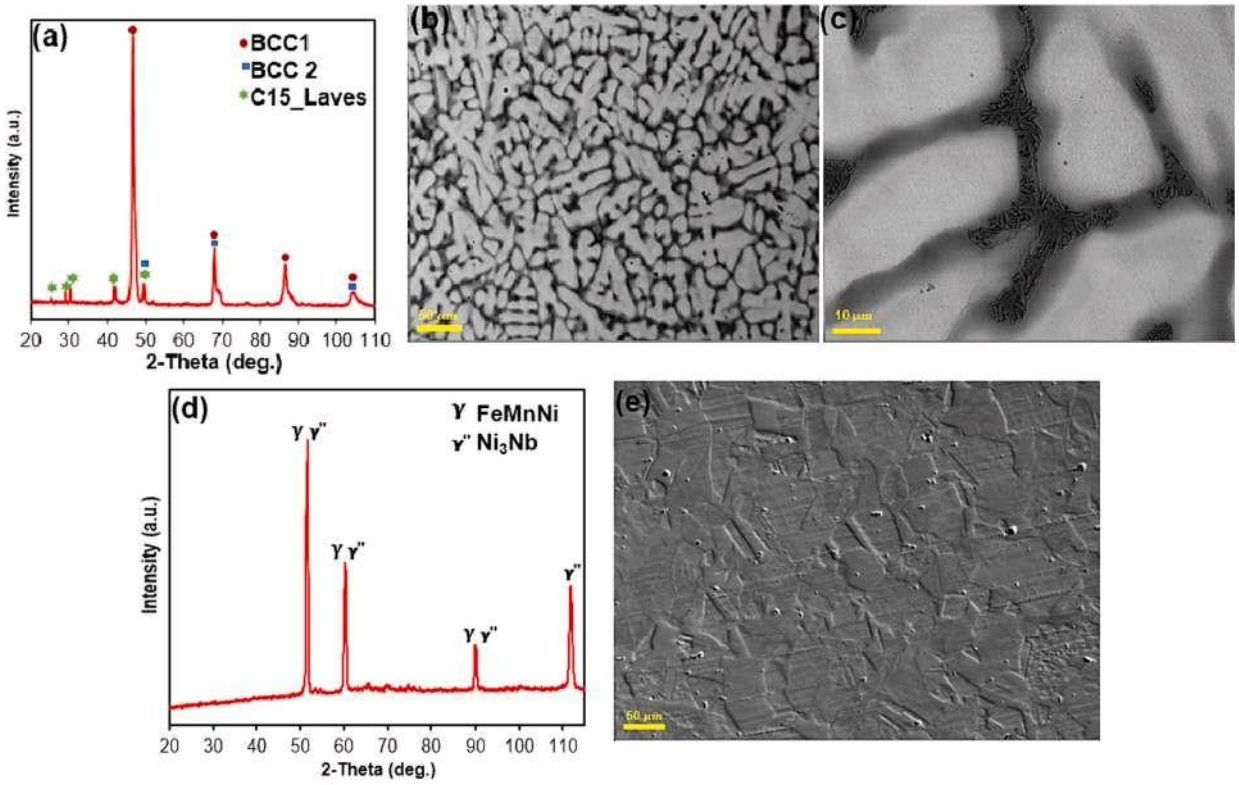

Fig. 1. Phase composition of the CrNbTaVW RHEA showing BCC1, BCC2, and $Cr(VNb)_2$ C15-Laves phase (a); Dendritic microstructure of the CrNbTaVW RHEA (b); Higher magnification image of the CrNbTaVW RHEA showing BCC1, BCC2, and $Cr(VNb)_2$ C15-Laves phase (c); Phase composition of the IN718 alloy showing γ + γ'' phases (d); Microstructure of the IN718 alloy showing γ + γ'' (e).

Table 2
Composition distribution of the IN718 alloy (at. %).

Ti	Nb	Fe	Ni	Mn	S	C	Co	Al	Si	P	Cu
0.12 ± 0.02	0.22 ± 0.02	57.95 ± 0.1	36.56 ± 0.4	0.5 ± 0.1	0.06 ± 0.1	3.63 ± 0.1	0.14 ± 0.04	0.12 ± 0.02	0.37 ± 0.02	0.1 ± 0.01	0.23 ± 0.01

3.2. Hardness properties of CrNbTaVW

The hardness test result of CrNbTaVW RHEA after ten indentations is 688 ± 21 HV, which is higher than IN718 (301 ± 14 HV). The CrNbTaVW RHEA has higher hardness than some reported as-cast RHEAs: CrMoTaTi (630 HV) [11], WNbMoTaZr (557 HV) [52], TiMoNbZr$_{0.5}$ (516 HV) [53], and Hf$_{0.25}$NbTaW$_{0.5}$ RHEA (514 HV) [33]. The higher hardness can be attributed to Laves phase solid solution strengthening and grain refinement. Grain refinement by the elemental addition of V can contribute to finer grain size that has a significant influence on hardness. For example, grain size refinement was achieved in WNbMoTaV RHEA and V$_1$NbMoTa RHEA due to the strong solute effect of V, which contributed to growth restrictions [5,54]. Furthermore, grain growth can be restricted by Cr(VNb)$_2$ Laves phase precipitation in the microstructure, which reduces grain size, and improve hardness. The increased Cr composition to form the Cr(VNb)$_2$ Laves phase in CrNbTaVW RHEA thus led to solid solution strengthening, which further enhanced the hardness. The presence of the Cr promoting Laves phase have been reported to increase the hardness properties of RHEAs [11,13].

3.3. Electrochemical corrosion behavior

3.3.1. Open circuit potential, potentiodynamic polarization measurement, and microstructural observation of CrNbTaVW and IN718 in chloride solution

The OCP and potentiodynamic polarization curves of CrNbTaVW RHEA and IN718 alloy in 3.5 wt% NaCl are presented in Fig. 2. The stability of the oxide film formed on the surface of the CrNbTaVW RHEA and IN718 alloy was evaluated by OCP for 3600 s, as seen in Fig. 2(a). The OCP curve of CrNbTaVW RHEA is stable throughout immersion, which indicates a stable passive film. The OCP curve of the IN718 alloy exhibited several oscillations until 3600 s, which can be attributed to the dissolution and re-passivation of the oxide films formed on the alloy surface [20,55]. These results suggest that CrNbTaVW RHEA oxide film is more stable than the IN718 alloy in a 3.5 wt% NaCl solution. Stable OCP has been attributed to the building of compact and protective oxide films on alloy surfaces [56,57]. The potentiodynamic polarization curves of the CrNbTaVW RHEA and IN718 alloy in 3.5 wt% NaCl after the OCP test are presented in Fig. 2(b). It was observed that the anodic curve of CrNbTaVW RHEA exhibited a wide passivation region up to the final potential of 2.5 V, which indicates that the passive film of CrNbTaVW RHEA is stable and good. The polarization curve of the IN718 alloy exhibited pseudo-passive behavior up to 1.63 V and later passivated until the final potential. Active corrosion took place when the IN718 alloy was exposed to a chloride solution, which is identified by the red arrow in the anodic curve. The Cl^- ions attacked the protective layer, breaking the passive layer. However, the oxide layer was rebuilt as evidenced by the pseudo-passive and passive behaviors. The electrochemical corrosion parameters such as E_{corr}, I_{corr}, and corrosion rates obtained from the polarization curve in a 3.5 wt% NaCl solution are presented in Table 3. The CrNbTaVW has a higher negative E_{corr} value of −0.139 V than the IN718 with −0.295 V, which indicates its susceptibility to corrosion. The CrNbTaVW RHEA has a lower I_{corr} value of 0.0026 μA/cm^2 than the IN718 alloy with 5.299 μA/cm^2. Based on the corrosion parameters, it is obvious that the CrNbTaVW RHEA show a very low corrosion rate in 3.5 wt% NaCl compared to the IN718 alloy.

The SEM images and XRD of the CrNbTaVW RHEA and IN718 alloys after potentiodynamic polarization in 3.5 wt% NaCl are presented in Fig. 3. Pits with an average size of 2.43 ± 0.4 μm and corrosion products were observed on the surface of CrNbTaVW RHEA (Fig. 3a and b). The IN718 alloy surface is highly corroded, and pits of an average size of 14.86 ± 2.2 μm were seen in different regions (Fig. 3c). Corrosion products were also seen in corroded and non-corroded areas of the IN718 alloy surface. The EDX compositions obtained from the regions of the IN718 alloy and CrNbTaVW RHEA after potentiodynamic polarization

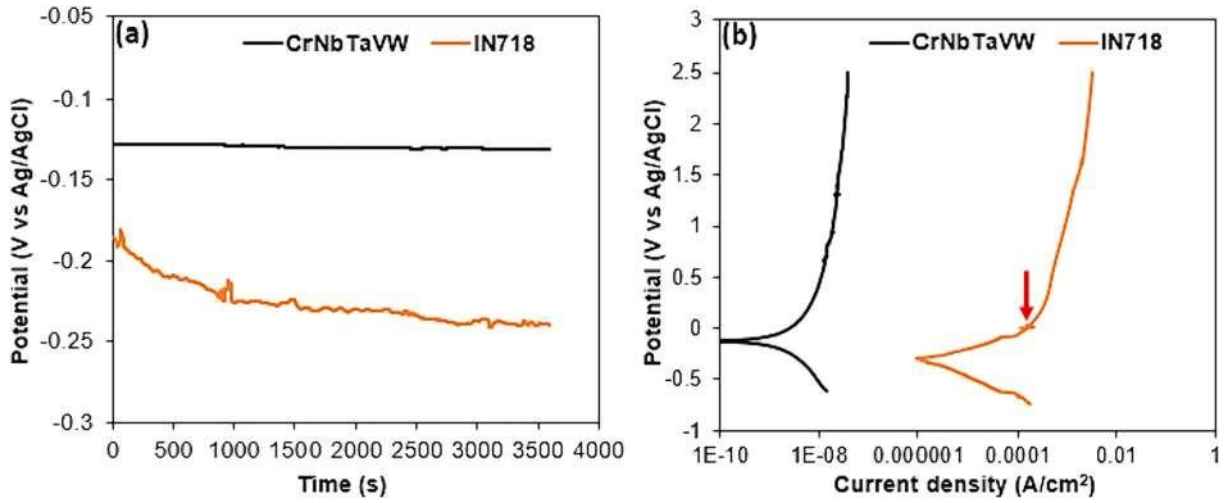

Fig. 2. OCP and polarization curves for CrNbTaVW RHEA and IN718 alloy in 3.5 wt% NaCl solution at room temperature: (a) OCP curves of CrNbTaVW RHEA and IN718 alloy for 3600 s. (b) Potentiodynamic polarization curves for CrNbTaVW RHEA and IN718 alloy.

Table 3
Electrochemical parameters for CrNbTaVW and IN718 in 3.5 wt% NaCl.

Alloy	E_{corr} (V)	I_{corr} (μA/cm^2)	Corrosion rate (mm/yr)
CrNbTaVW	—0.139 ± 0.011	0.0026 ± 0.001	0.000097 ± 0.0008
IN718	—0.295 ± 0.01	5.299 ± 2.06	0.054 ± 0.02

in 3.5 wt% NaCl are presented in Supplementary Table 1 and Supplementary Figs. 1 and 2. The presence of oXygen was observed in the alloys, which implies oXide formed on the surface of the CrNbTaVW RHEA and IN718 alloys. The deposition of Cl element in the compositions signified the presence of Cl^- which broke through the oXide layer of the IN718 alloy and led to the corroded surface and pits. Also, Cl^- broke through the passive layer of CrNbTaVW alloy and led to a few smaller pits.

The CrNbTaVW RHEA did not show dissolution of elemental composition in both the dendrite and interdendrite regions (Supplementary Table 1). The addition of V protects RHEAs from localized corrosion, such as pitting in NaCl and H_2SO_4 solutions [58]. Despite substantial amount of V and almost evenly distributed Nb compositions in all the three phases, few pits were still observed at the RHEA surface. It was found that low W and Ta compositions were observed at BCC1 and

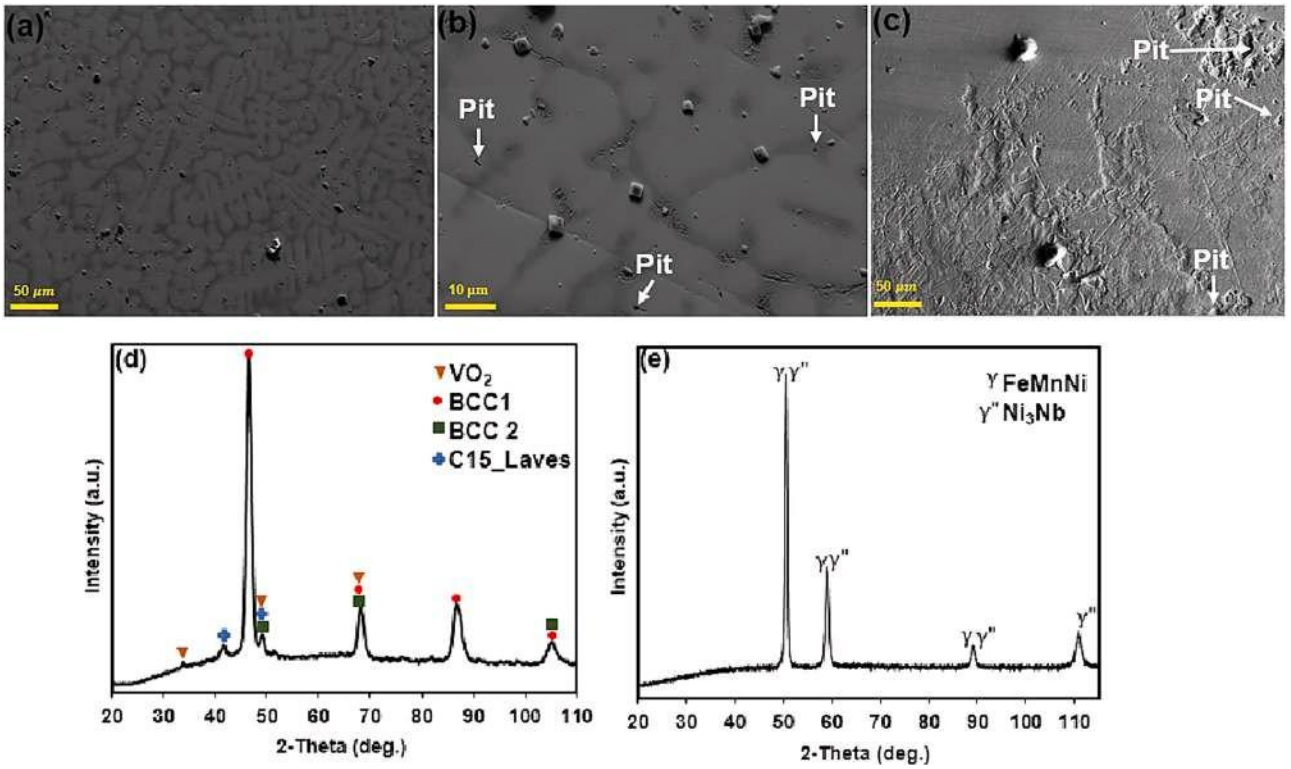

Fig. 3. Surface morphology of the CrNbTaVW RHEA after exposure in 3.5 wt% NaCl (a); Higher magnification image of the CrNbTaVW RHEA surface showing pits after exposure in 3.5 wt% NaCl (b); Surface morphology of corroded surface and pits formed on the IN718 after exposure in 3.5 wt% NaCl (c); Phase analysis of corrosion products present in the CrNbTaVW RHEA (d); Phase analysis of corrosion products present in the IN718 alloy (e).

$Cr(VNb)_2$ phases, which suggest that elemental segregation might have played a role in the formed pits. X-ray diffraction analysis in Fig. 3(d) identified the corrosion product formed on the CrNbTaVW RHEA to be VO_2. All the initial phases are still present, suggesting that no preferential phase dissolution occurred in the CrNbTaVW RHEA when exposed to a chloride solution. The XRD pattern of the IN718 alloy after potentiodynamic polarization showed a reduction of peaks between 60° and 110° (Fig. 3e) that differed from initial phase peaks. It was also observed that no new peaks were formed, which shows that limited oxides were deposited on the IN718 alloy surface. Therefore, no protection was offered and this led to a corroded surface and pits when exposed to 3.5 wt% NaCl solution.

3.3.2. Open circuit potential, potentiodynamic polarization measurement, and microstructural observation of CrNbTaVW and IN718 in acidic solution

The stability of the oxide film formed on the surface of the CrNbTaVW RHEA and IN718 alloys was evaluated by OCP for 3600 s in 1 M H_2SO_4 is presented in Fig. 4. The OCP curve of CrNbTaVW RHEA in Fig. 4(a) showed an initial increase in OCP but later dropped in potential to 2586 s. Afterwards, stability was achieved in the OCP for 3600 s at −0.17 V. In the IN718 alloy, the OCP curve is noticeably unstable. Fluctuations were seen in both alloys, suggesting the breaking and rebuilding of the oxide film on the alloy surface. The potentiodynamic polarization curve of the CrNbTaVW RHEA and IN718 alloy in 1 M H_2SO_4 after the OCP test is presented in Fig. 4(b). Active dissolution and pits (indicated by red circle) were observed in the anodic curve of CrNbTaVW RHEA at 0.18 V to 0.46 V and later passivated to a final potential of 2.5 V. The IN718 alloy polarization curve exhibited active corrosion, passivation, and transpassivation. Sulphate ions attack the protective layer of the CrNbTaVW RHEA and IN718 alloy, causing the oxide layer to break. However, the oxide layer begins to repair as seen in the passivation region (Fig. 4b). The electrochemical corrosion parameters such as E_{corr}, I_{corr}, and corrosion rates obtained from the polarization curve in 1 M H_2SO_4 solution are presented in Table 4. It is evidenced from the electrochemical parameters that the corrosion rate of CrNbTaVW RHEA is lower than the IN718 alloy in acidic environment.

The SEM images and XRD analysis of the CrNbTaVW RHEA and IN718 alloy after potentiodynamic polarization in 1 M H_2SO_4 are presented in Fig. 5. Deposits of corrosion products were seen on different regions of the CrNbTaVW RHEA surface (Fig. 5a and b). At higher resolution, pits of an average size of 2.46 ± 0.23 μm were found at BCC1 (white region) of the CrNbTaVW RHEA surface, suggesting that the sulphate ions broke the oxide films (Fig. 5b). The IN718 alloy surface also corroded with circular pits of average size of 6.27 ± 0.68 μm (Fig. 5c and d). The EDX compositions of the IN718 alloy and CrNbTaVW RHEA after polarization in 1 M H_2SO_4 are presented in Supplementary Table 2 and Supplementary Figs. 3 and 4. The presence of oxygen was observed in the compositions of both alloys suggesting oxide formation.

Table 4
Electrochemical parameters for CrNbTaVW RHEA and IN718 alloy in 1 M H_2SO_4.

Alloy	E_{corr} (V)	I_{corr} (μA/cm^2)	Corrosion rate (mm/yr)
CrNbTaVW	−0.147 ± 0.02	0.0039 ± 0.01	0.00013 ± 0.00012
IN718	−0.377 ± 0.01	104.59 ± 4.01	1.12 ± 0.001

In the CrNbTaVW RHEA, BCC1 which was segregated in the dendritic region still retained a substantial amount of Nb, Ta, V, W but lower Cr compositions. BCC2 in the interdendritic region still retained a substantial amount of Cr, Nb, and V but lower W and Ta compositions. The $Cr(VNb)_2$ C15-Laves phase dissolved after corrosion exposure in 1 M H_2SO_4 (Fig. 5b). This might be correlated with the OCP in Fig. 4(a), where there was a rapid increase in the potential and oscillations due to the dissolution and rebuilding of the oxide film on the alloy surface. Elemental segregation of Cr in the dendrite region and segregation of Ta and W in interdendrite region might play a role in the pits and phase dissolution that was observed. Selective dissolution of Cr_2Nb Laves phases was observed in CrMoNbWV HEA in the 0.5 M H_2SO_4 solution [59]. The formation and dissolution behavior of the film in an acidic solution was also observed for Cr containing $AlCoCrFeNi_{2.1}$ HEA [60]. Also, selective dissolution of the V-rich Sigma phase was also reported in a MoNbFeCrV RHEA after the potentiodynamic polarization test in 0.5 M H_2SO_4 solution [14].

XRD analysis in Fig. 5(e) identified the corrosion product formed on the CrNbTaVW RHEA to be VO_2. BCC1 and BCC2 phases are still present, while the peaks of $Cr(VNb)_2$ C15-Laves phase are no longer present. This further indicate that active dissolution of $Cr(VNb)_2$ C15-Laves phase actually occurred when exposed to acidic solution. The formed VO_2 is not sufficient to protect the CrNbTaVW RHEA from pits and the dissolution of $Cr(VNb)_2$ C15-Laves phase. The XRD pattern of IN718 alloy (Fig. 5f) after potentiodynamic polarization showed that no new peaks were formed, signifying that limited or no oxides were deposited on the IN718 alloy surface. Hence, the highly corroded surface and pits observed in the IN718 alloy when exposed to an acidic solution.

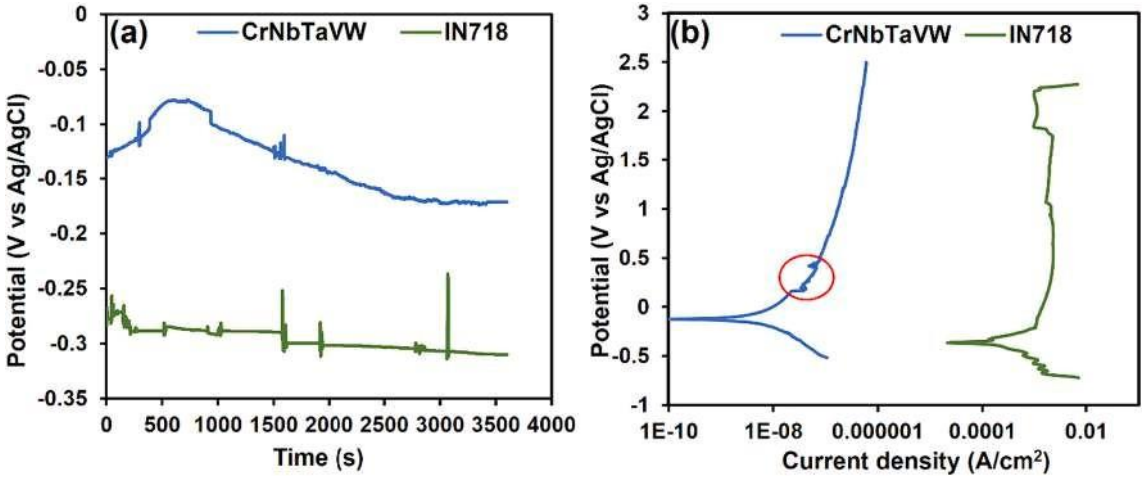

Fig. 4. OCP and potentiodynamic polarization curves for CrNbTaVW RHEA and IN718 alloy in 1 M H_2SO_4 solution: (a) OCP curves of CrNbTaVW RHEA and IN718 alloy in 1 M H_2SO_4. (b) Potentiodynamic polarization curves of CrNbTaVW RHEA and IN718 alloy in 1 M H_2SO_4.

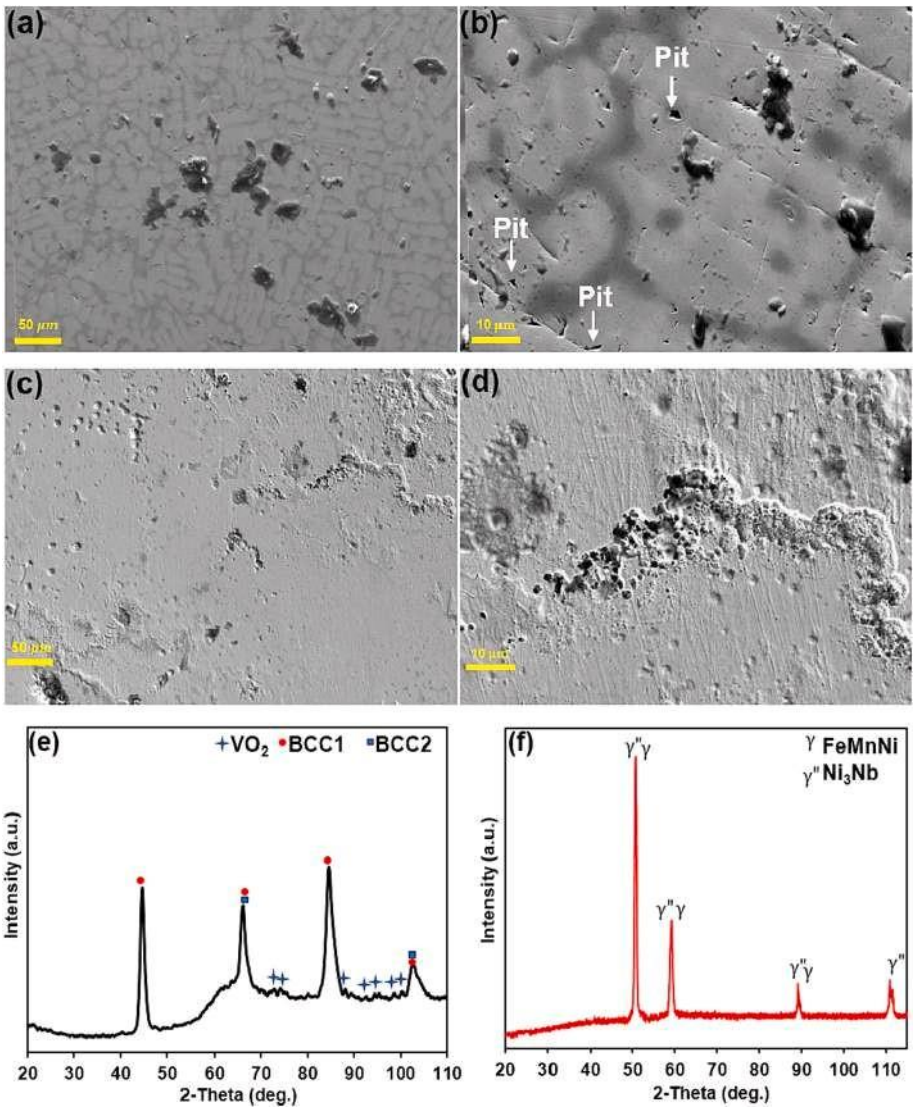

Fig. 5. Surface morphology of the CrNbTaVW RHEA showing the corrosion products and pits after exposure in 1 M H_2SO_4 (a-b); Surface morphology of the IN718 alloy corroded surface and pits after exposure in 1 M H_2SO_4 (c-d); Phase analysis of corrosion products present in the CrNbTaVW RHEA (e); Phase analysis of corrosion products present in the IN718 alloy (f).

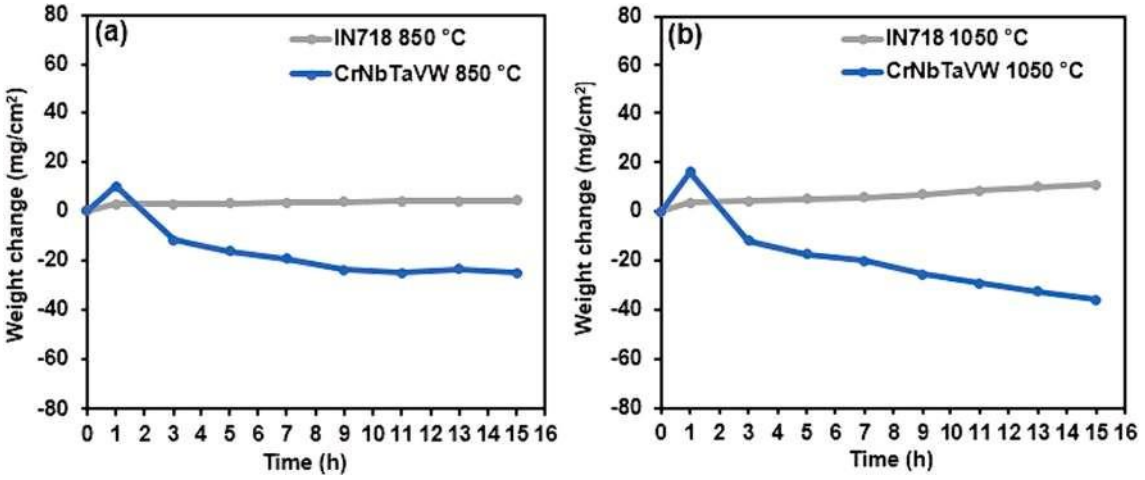

Fig. 6. Cyclic oxidation curve of CrNbTaVW RHEA and IN718 alloy at 850 ˚C (a); Cyclic oxidation oxidation curve of CrNbTaVW RHEA and IN718 alloy at 1050 ˚C (b).

4. Oxidation analysis of CrNbTaVW and IN718

4.1. Cyclic oxidation behavior of CrNbTaVW and IN718

The mass gain curves of the CrNbTaVW and IN718 at 850 ˚C and 1050 ˚C after 15 hours are shown in Fig. 6. At 850 ˚C and 1050 ˚C (Fig. 6a and b), the CrNbTaVW RHEA shows a mass gain at the initial stages due to the alloys reaction with oxygen that facilitated the fast growth of the oxide scale [61]. After 3 hours of oxidation at both temperatures, CrNbTaVW RHEA exhibited rapid mass loss which can be attributed to spallation. At 850 ˚C (9–15 hours), the mass curve is stationary because the oxide scale gets thicker, thereby protecting the surface of the CrNbTaVW RHEA from direct contact with oxygen. Hence, a decrease in mass loss. However, at 1050 ˚C (9–15 hours), a continuous mass loss was observed for CrNbTaVW RHEA. The IN718 alloy exhibited an almost stationary trend throughout the oxidation test (Fig. 6a and b). Therefore, the IN718 alloy has a lower mass gain of 4.41 mg/cm^2 and 10.84 mg/cm^2 over the entire 15 hours of oxidation at 850 ˚C and 1050 ˚C. Unlike the CrNbTaVW RHEA which exhibited a high mass loss of ⁻25.17 mg/cm^2 and ⁻35.91 mg/cm^2 at 850 ˚C and 1050 ˚C (Fig. 6a and b). The IN718 alloy has a better oxidation resistance than the CrNbTaVW RHEA over the entire 15 hours of oxidation.

4.2. Phase analysis and surface morphologies of oxidized CrNbTaVW and IN718

The XRD patterns of the oxidized CrNbTaVW and IN718 samples at 850 ˚C and 1050 ˚C are shown in Fig. 7. The identified oxides of CrNbTaVW RHEA at 850 ˚C are composed of VO_2, V_2O_3, WO_3, Cr_2O_3, $CrVO_3$, Cr_2WO_6, and $Nb_2O_5WO_3$ (Fig. 7a). At 1050 ˚C, identified oxides are VO_2, V_2O_3, WO_3, Cr_2O_3, Cr_2WO_6, $CrVO_3$, $Nb_2O_5WO_3$, and $CrTaO_4$ (Fig. 7b). The identified oxides of IN718 at 850 ˚C were composed of MnO, Ni_2Ti_4O, Al_2O_3, MnO_2, Fe_2O_3, Fe_3O_4, SiO_2, and TiO_2 (Fig. 7c). At 1050 ˚C, identified oxides are MnO, Fe_3O_4, Mn_2O_3, MnO_2, Fe_2MnO_4, and $NiMn_2O_4$ (Fig. 7d).

The SEM images of the surface oxides of CrNbTaVW RHEA at 850 ˚C and 1050 ˚C after 15 hours are shown in Fig. 8. At 850 ˚C, the surface scale layer is spalled with cracks (15.5 ± 2.14 μm), pores (6.1 ± 0.39 μm), and voids (12.7 ± 0.39 μm) (Fig. 8a). The Cr-rich spalled oxides are also found on the surface (Fig. 8a and Supplementary Fig. 5). Higher magnification of the surface morphology at 850 ˚C reveals granular-shaped (0.68 ± 0.04 μm) and rod-shaped (1.24 ± 0.11 μm) oxides that were dispersed all over the surface (Fig. 8b). The observed rod-shaped and granular-shaped oxides have been observed in some RHEAs such as CrMoNbTaV [43], NbTiZrV [44], and CrMoNbTaW [62]. The EDS compositions at 850 ˚C showed that the granular-shaped oxides are rich in Cr, while rod-shaped oxides are NbTaW-rich (Supplementary Fig. 5). Fig. 8(c) shows that the surface morphology of CrNbTaVW RHEA at 1050 ˚C is spalled with voids (18 ± 1.09 μm). Higher magnification of the surface oxides also contains granular-shaped (0.66 ± 0.03 μm) and rod-shaped (2.73 ± 0.21 μm) that were dispersed all over the alloy surface (Fig. 8d). However, the size of rod-shaped oxides is slightly larger than that observed at 850 ˚C. Therefore, high temperatures have a major impact on the growth and nucleation of oxides. The EDS compositions at 1050 ˚C showed that the granular-shaped oxides are rich in Cr, while rod-shaped oxides are rich in Nb/Ta/W (Supplementary Fig. 6).

The SEM images of the surface oxides of IN718 at 850 ˚C and 1050 ˚C after 15 hours are shown in Fig. 9. The surface oxide layer of the IN718 at 850 ˚C showed a compact structure but no cracks, pores, or voids (Fig. 9a). Higher magnification of the top surface oxides of IN718 revealed block-shaped (0.45 ± 0.04 μm), rod-shaped (0.39 ± 0.03 μm),

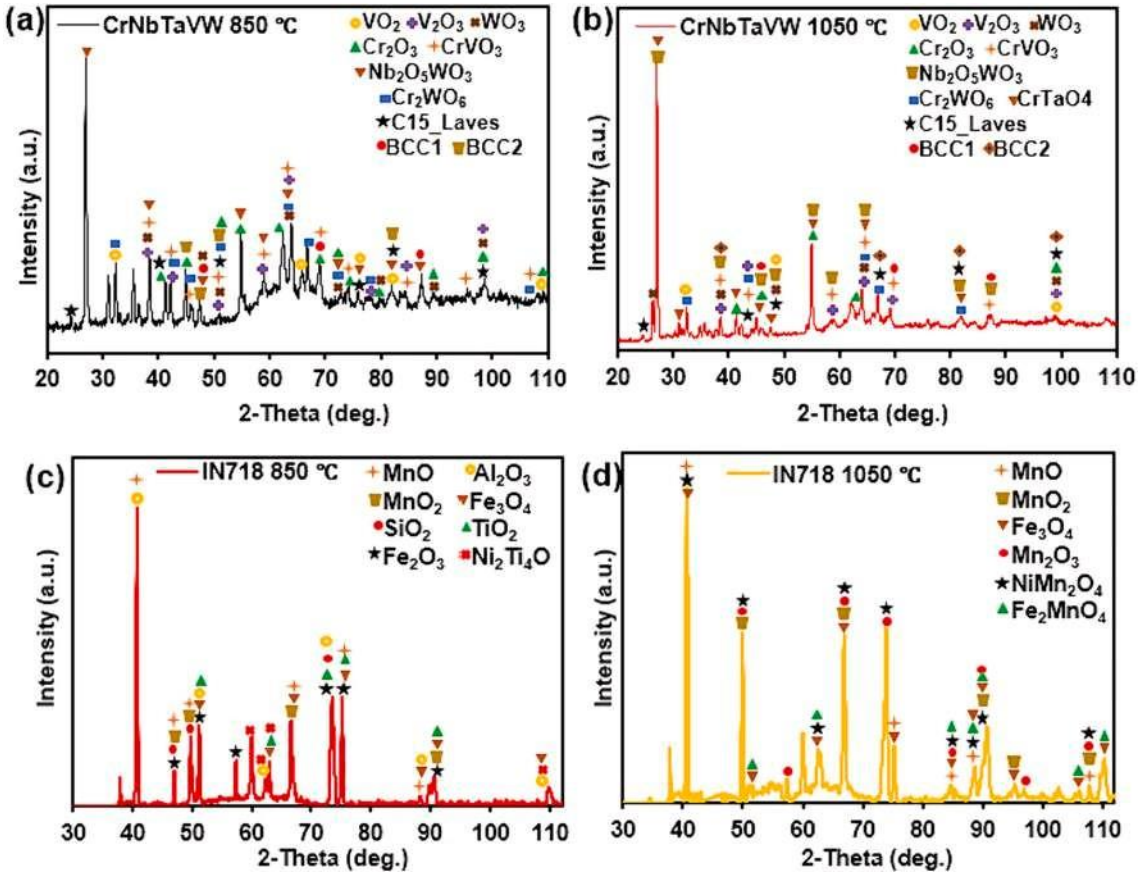

Fig. 7. Phase analysis of identified oxides in CrNbTaVW at 850 ˚C (a) and 1050 ˚C (b); Phase analysis of identified oxides in IN718 at 850 ˚C (c) and 1050 ˚C (d).

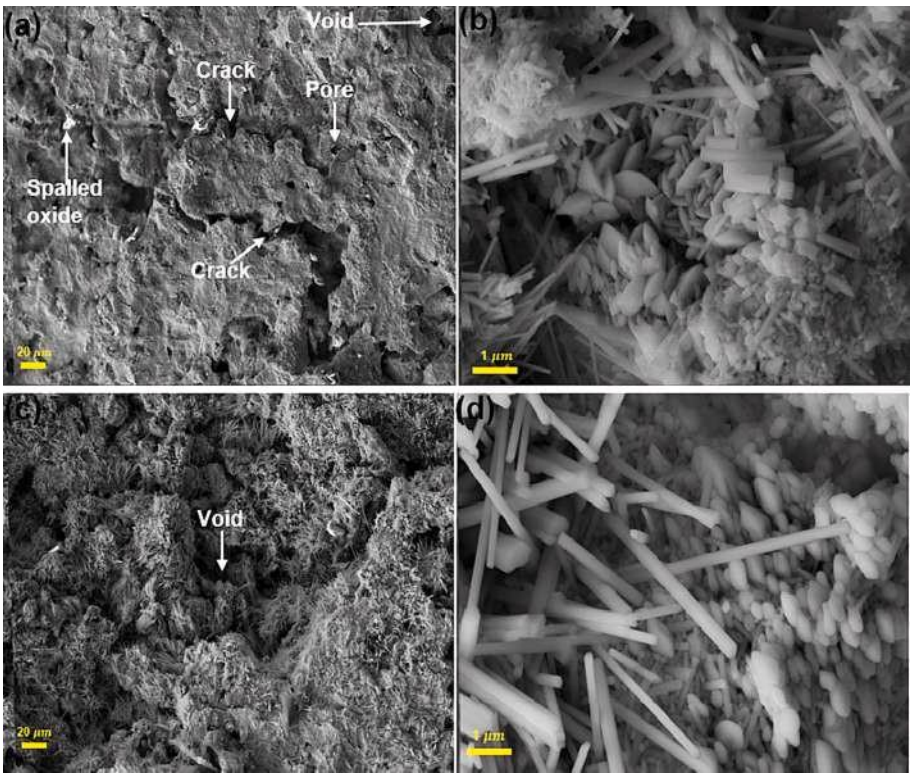

Fig. 8. Surface morphology of the CrNbTaVW RHEA showing voids, cracks, pores, and spalled oxides at 850 °C after 15 hours (a); Higher magnification of the CrNbTaVW RHEA surface morphology showing granular and rod-shaped oxides at 850 °C after 15 hours (b); Surface morphology of the CrNbTaVW RHEA showing voids and spalled oxides at 1050 °C after 15 hours (c); Higher magnification of the CrNbTaVW RHEA surface morphology showing granular and rod-shaped oxides at 1050 °C after 15 hours.

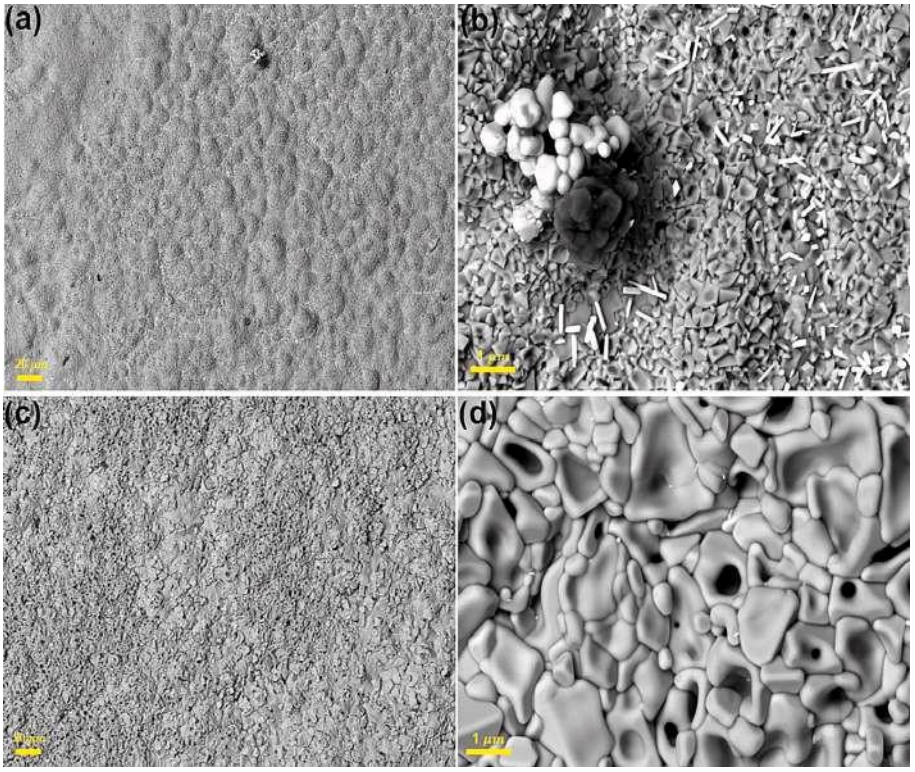

Fig. 9. Surface morphology of the IN718 alloy showing a compact structure at 850 °C after 15 hours (a); Higher magnification of IN718 alloy surface morphology showing block-like, rod-like, round, and cloudy shaped oxides at 850 °C after 15 hours (b); Surface morphology of the IN718 alloy showing a compact and refined structure at 1050 °C after 15 hours (c); Higher magnification of IN718 alloy surface morphology showing globular and block-like oxides at 1050 °C after 15 hours.

round-shaped (0.53 ± 0.05 μm) and cloudy-shaped oxides (0.50 ± 0.04 μm) (Fig. 9b). The EDS compositions at 850 °C showed that the block shaped oxides are Fe-rich, rod-shaped oxides are FeMnNi-rich, round shaped oxides (white) are TiFeSi-rich, and cloudy shaped oxides (dark) are AlSi-rich (Supplementary Fig. 7). At 1050 °C, IN718 surface oxide layer comprises a more refined structure that is free of cracks, pores, or voids (Fig. 9c). Higher magnification of the surface oxides revealed globular (0.35 ± 0.02 μm) and block-shaped oxide structures (1.11 ± 0.12 μm) (Fig. 9d). The EDS compositions at 1050 °C showed that the globular and block-like oxide structures are majorly enriched in Fe (Supplementary Fig. 8).

4.3. Cross sectional morphologies of oxidized CrNbTaVW and IN718

SEM-BSD images of the cross-section morphologies of CrNbTaVW RHEA and IN718 alloy after oxidation at 850 °C and 1050 °C for 15 hours are shown in Fig. 10. At 850 °C, a 260 ± 7.8 μm thick oxidized layer with grey contrast and a 29 ± 5.5 μm thick internal oxidation zone was observed for CrNbTaVW RHEA (Fig. 10a). The thick oxide layer contains tiny cracks that are connected to voids that are 31 ± 1.7 μm thick. It is believed that the cracks grow to form the observed voids. The EDS compositions at 850 °C/15 hours showed mostly WNbTa-rich oxides for both the thick oxide layer and internal oxidation zone (Supplementary Fig. 9). At 1050 °C, a 603 ± 9.1 μm thick oxidized layer with grey contrast was observed for CrNbTaVW RHEA (Fig. 10b). Cracks and voids of 8.5 ±0.81 μm and 35 ±2.71 μm was also observed in the thick oxide layer (Fig. 10b). The EDS compositions of the thick oxide layer at 1050 °C/15 hours showed mainly WNbTaCr-rich oxides (Supplementary Fig. 10). As the oxidation temperature increased from 850 °C to 1050 °C, the thickness of the oxide layer increased from 260 μm to 603 μm. Oxide layer tends to serve as a reliable diffusion barrier that effectively isolates the substrate from oxygen and therefore the oxidation rate of the metallic substrate is decreased [3]. The oxide layers are porous with voids and cracks at 850 °C and 1050 °C that limit the formation of a reliable diffusion barrier. The voids and cracks allow the ingress of oxygen into the metallic substrate and therefore the oxidation rate of the metallic substrate is increased.

At 850 °C and 1050 °C, the IN718 alloy displays two layers, which are defined as the outer oxide layer and the internal oxide layer. At 850 °C, a 38.6 ± 1.1 μm thick outer oxide layer and 46.1 ± 1.4 μm thick internal oxide layer was observed (Fig. 10c). The EDS compositions of the outer oxide layer at 850 °C/15 hours showed mostly Fe-rich oxide, while internal oxide layer comprise of mostly FeNi-rich oxides (Supplementary Fig. 11). At 1050 °C, the outer oxide layer has a thickness of 15.34 ± 0.6 μm, while the internal oxide layer has a thickness of 66.8 ±3.3 μm (Fig. 10d). EDS compositions of the outer oxide layer and internal oxide layer at 1050 °C/15 hours comprise mostly FeNi-rich oxides (Supplementary Fig. 11). It was observed that the internal oxide layer has higher thickness than the outer oxide layer at 850 °C and 1050 °C. The IN718 oxidation rate is lower at both temperatures because the outer and internal oxide layers serve as diffusion barriers.

5. Discussion

5.1. CrNbTaVW phase prediction

The physical properties of elements in the CrNbTaVW RHEA and enthalpy of mixing for the selected alloy binary subsystem are shown in Table 5. In Table 5, Ta possesses the largest atomic radius and smallest electronegativity, while Cr possesses the smallest atomic radius. There could have been atomic distortion during the mixing of elements due to the large atomic size difference between the elements, leading to an increase in lattice strain. The large atomic size difference between so many components would considerably impact the formation of solid solutions in multi-component alloys. The empirical phase parameters are calculated and shown in Table 6.

In Table 5, CrNb (−7), CrTa (−7), NbW (−8), TaW (−7), CrV (−2) have a significant negative enthalpy of mixing, indicating the formation

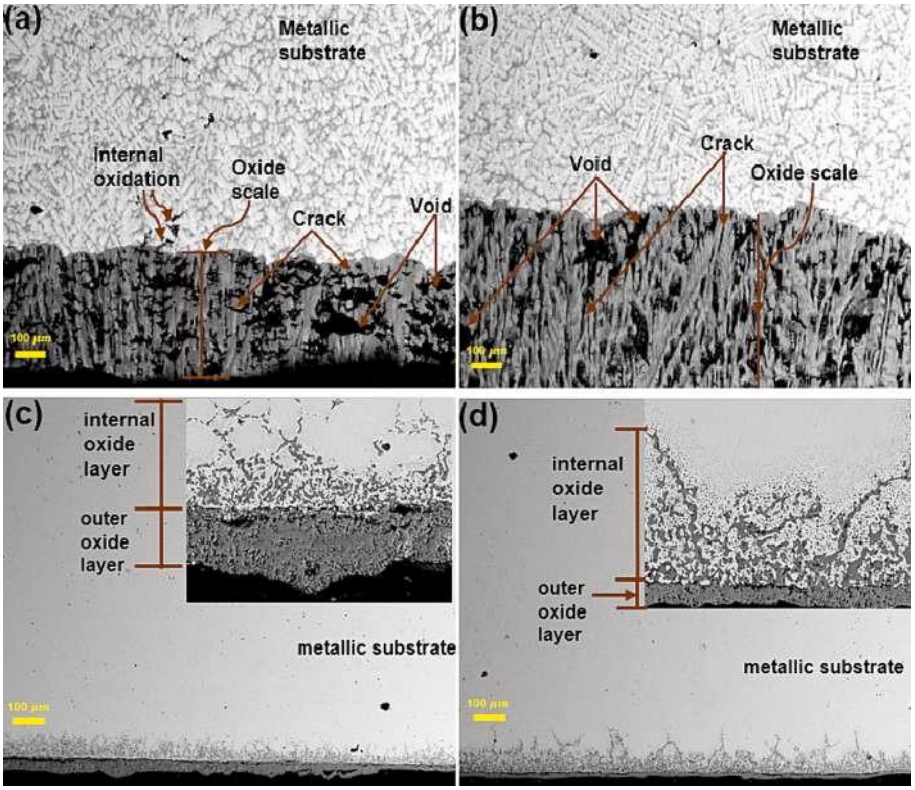

Fig. 10. Cross-sectional morphology of CrNbTaVW RHEA at 850 °C and 1050 °C after 15 hours (a-b); Cross-sectional morphology of IN718 at 850 °C and 1050 °C after 15 hours (c-d).

Table 5
Physical properties of elements in the CrNbTaVW RHEA and their binary enthalpy of mixing [5,63].

Elements	Cr	Nb	Ta	V	W
Atomic radius (Å)	1.27	1.43	1.46	1.32	1.39
Density (Kg/m^3)	7.19	8.57	16.4	6.0	19.3
Melting temperature (°C)	1907	2477	3017	1910	3414
Valence electron	6	5	5	5	6
Electronegativity(χ)	1.66	1.60	1.50	1.63	2.36
Hardness (HV)	108	134	89	64	349

Binary enthalpy of mixing[1]										
i - j	CrNb	CrTa	CrV	CrW	NbTa	NbV	NbW	TaV	TaW	VW
ΔH_{ijmix}	7	—7	—2	1	0	—1	—8	—1	—7	—1

[1] rsc.org

Table 6
Calculated empirical phase parameters.

Solid solution parameters	References	Range of parameters	Calculated values for the CrNbTaVW RHEA
$VEC = \sum_{i=1}^{n} C_i(VEC)_i$	[64,65]	VEC < 6.87 = BCC VEC ≥ 8 = FCC 6.87 ≤ VEC < 8 = BCC + FCC	5.4
$\Delta H_{mix} = \sum_{i=1, i<j}^{n} 4\Delta H_{ij}^{mix} C_i C_j$	[65,66]	—15 kJ/mol ≤ ΔH_{mix} ≤ 5 kJ/mol	—5.03 kJ/mol
$\sum_{i=1}^{n}$	[65,66]	$\Delta S = -R$ High value of entropy of mix is important in stabilizing the solid solution phases	13.38 J/K mol
$\delta = \sqrt{\sum_{i=1}^{n} C_i\left(1 - \frac{r_i}{\sum_{j=1}^{n} C_j r_j}\right)^2}$	[65,67,68]	δ ≤ 6.6% = BCC	5.09%
$T_m \Delta S_{mix}$	[66]	δ ≥ 6.6% = FCC and Laves	
$\Omega = \frac{\Delta H_{mix}}{T_m \Delta S_{mix}}, T_m = \sum_{i=1}^{n} C_i (T_m)_i$		Ω ≥ 1.1	6.77
$\Delta\chi = \sqrt{\sum_{i=1}^{n} C_i\left(1 - \frac{\chi_i}{\bar{\chi}}\right)^2}$	[69]	$\Delta\bar{X}$ must be small to form a solid solution	0.31
$\Lambda = \Delta S_{mix}/\delta^2$	[70]	Λ > 0.96 = single phase. 0.24 < Λ <0.96 = two-phase	0.52

of intermetallic compound. A good mutual solubility is revealed in the NbTa (0), NbV (−1), TaV (−1) and VW (−1) binary systems, indicating the formation of a solid-solution phase. The CrW is the only positive binary enthalpy of mixing among each pair of the constituent elements in the CrNbTaVW RHEA that specifies phase separation. According to [71], segregation phenomenon can be described based on positive binary enthalpy of mixing among each pair of the constituent elements. The more positive ΔH_{mix} means the less miscibility of the different elements in the liquid alloy, which leads to separation of phases or segregation of different elements in the alloy [66]. As seen in Fig. 1(a), a Laves phase was formed which is in agreement with the binary enthalpy (CrV (−2)), since it has a higher negative enthalpy among the binary enthalpies. The presence of Laves phases can significantly influence the physical and mechanical properties of HEAs [11,72-74] Senkov, Senkova, Woodward, et al., 2013; Xiang et al., 2020). The main factors affecting the Laves phase structure are the atomic size factor and the electron concentration factor [73]. The Laves phase formed due to the difference in atomic size and electronegativity between Cr and the other four elements making up the CrNbTaVW RHEA. The binary enthalpies alone cannot predict the phases and crystal structure. The calculated empirical parameters for the CrNbTaVW RHEA in Table 6 compared with three proposed criteria [65,66,75] were used to further predict the phases and crystal structure.

The first criterion states that the disordered solid solution phase forms when Ω >1.1 and δ < 6.6% [66]. The CrNbTaVW RHEA has Ω = 6.77 which is >1.1, while δ (5.09) was <6.6%. This means that the disordered solid solution BCC phase will occur. Although Ω was >1.1, it cannot differentiate between single and multi-phase solid solutions. To fill the void, Λ in Table 6 was proposed and the CrNbTaVW RHEA has a lesser geometrical parameter of 0.52, which indicates a multiphase solid solution structure. The second criterion states that FCC and BCC crystal structures would be stable, if VEC ≥ 8 and VEC ≤ 6.87 respectively [65]. The CrNbTaVW RHEA has a VEC of 5.4 which is <6.87. A stable BCC crystal structure formed. The third criterion states that Laves phase forms when Δχ > 7% and δ > 5% in HEAs [75]. In the CrNbTaVW RHEA, Δχ 0.31 and is lower than 7%. However, the atomic size mismatch parameter for CrNbTaVW is 5.09%, which is higher than 5%. Hence, the Laves phase is expected to occur in the CrNbTaVW RHEA. The first two criteria successfully predicted a multi-phase solid solutions phase, whereas in criterion three, only the lattice distortion parameter predicted the Laves phase. This provides a reasonable agreement with the experimental results as evidenced in Fig. 1. The phase separation agrees with Λ parameter by Singh and Subramaniam [70], which predicted the formation of multi-phase solid solutions in CrNbTaVW RHEA.

5.2. Corrosion resistance of CrNbTaVW RHEA in 3.5 wt% NaCl and 1 M H_2SO_4 solution

Passivation is a characteristic of HEAs, arising due to the addition of passivating promoting elements such as Cr and Ti. The passivating promoting element may influence the alloy structure and passive film composition, giving rise to different electrochemical responses depending on the alloying type and content [76]. The SEM images of the CrNbTaVW RHEA in chloride solution showed few pits, while in acidic solution, more pits and selective dissolution of $Cr(VNb)_2$ Laves took place. HEAs that contain Cr compositions greater than 13 wt% can be associated with enhanced corrosion resistant properties [77]. Despite the high chromium compositions in the RHEA, pits were still found when exposed to NaCl solution. In the H_2SO_4 solution, low Cr composition (10 wt%) was observed in the BCC1, which may have caused the few pits observed in the BCC1 region and none in the BCC2 (Fig. 7b). Regardless of the effects of the aggressive corrosive solutions, the resistance to passive film breakdown is determined by the properties of the passive film including its continuity, formation ability, and film stability [19]. Only VO_2 was formed on the surface of the CrNbTaVW RHEA in both chloride and acidic solutions. The VO_2 layer was able to

prevent phase dissolution and surface corrosion in chloride solution, but not enough protection against localized corrosion (pitting). The microstructure and composition are the two main factors in the corrosion performance of an alloy [77]. Alloy heterogeneities such as inclusions, impurities, and second phases have been reported to be detrimental to the continuity of the overlying passive film of alloys because the oxides formed at these sites or along their edge are often not protective. Thus, the oxide in these areas often acts as the weak spot for breakdown [78,79].

Fig. 11 illustrates the corrosion mechanism of the CrNbTaVW when exposed to 3.5 wt% NaCl and 1 M H_2SO_4 solutions. At the beginning of corrosion in NaCl environment (Fig. 11a), Cl^- is adsorbed on the passive film, which makes some metal cations in the passive film dissolve into the solution. The CrNbTaVW RHEA comprise multiphases of BCC1, BCC2, and $Cr(VNb)_2$ Laves, Cl^- will be preferentially adsorbed in these phases and detrimental to the passive film continuity. It was observed that pitting occurred mostly in BCC1 and regions between the BCC1 and BCC2 phases (Fig. 11b). The pits can be initiated by the elemental segregation of the elements that comprises the two phases. If there is a significant potential difference between the two phases, galvanic coupling can result in localized corrosion (pits) [80,81]. The passive film properties made BCC1 phase the anode and BCC2 phase the cathode, the passive film eventually weakened resulting in the pitting of BCC1 phase under the combined effect of galvanic coupling and Cl^- (Fig. 11b).

In an acidic solution, fluctuations were observed in passive film indicating dissolution of the protective film (Fig. 4a). The dissolution of the protective film on the alloy can be attributed to the SO_4^{2-} ions in the solution (Fig. 11c). As the CrNbTaVW RHEA is immersed in the 1 M H_2SO_4, the anode and cathode areas are electrically connected and constitute the corrosion cell, leading to the existence of electric potential. Pits initiate mainly on the BCC1 phase and the boundaries of the BCC1 and BCC2 phases (Fig. 11d). The observed pit in the BCC1 phase could be attributed to combined effect of SO_4^{2-} ions and galvanic coupling of the BCC1 phase (anode) and BCC2 phase (cathode) (Fig. 11d). The $Cr(VNb)_2$ Laves phase was formed on top of the BCC2 phase and boundaries between the two phases are often weak zones and preferential to initiate corrosion. The potential difference between dual phases brings about a strong driving force for phase dissolution [80,82]. As a result of coupling effects between the $Cr(VNb)_2$ Laves phase (anode) and BCC2 phase (cathode), the $Cr(VNb)_2$ Laves was eventually dissolved (Fig. 11d). Despite the pits observed in the BCC1 phase and the dissolution of $Cr(VNb)_2$ Laves, the CrNbTaVW RHEA still has a high corrosion resistance in both the chloride and acidic solutions.

5.3. Oxidation mechanism

At 850 °C and 1050 °C, simple oxides of VO_2, V_2O_3, WO_3, and Cr_2O_3 form on the oxidized CrNbTaVW at the initial stages. The stability and formation of the simple oxides at 850 °C using the Gibbs free energy ($\triangle G$) values follow the following order: V_2O_3 (—639) > Cr_2O_3 (—555) > VO_2 (—521) > WO_3 (—384) [31,83]. At 1050 °C, the stability and the formation of favorable oxides follows the order: V_2O_3 (—602) > Cr_2O_3 (—527) > VO_2 (—467) > WO_3 (—346) [31,83]. The WO_3 has the largest $\triangle G$ values which makes it the least stable simple oxide formed on the surface of the CrNbTaVW RHEA at 850 °C and 1050 °C. At increasing oxidation time, the simple oxides will continuously react and combine into complex oxides, as seen in Eqs. (1)–(6).

$$CrO\ (s) + VO_2\ (s) = CrVO3\ (s) \quad (1)$$

$$Cr_2O_3\ (s) + WO_3(s) = Cr_2WO_6\ (s) \quad (2)$$

$$8WO_3(s) + 4Ta_2O_5(s) = Ta_8W_8O_{44}\ (s) \quad (3)$$

$$Nb_2O_5\ (s) + WO_3(s) = Nb_2O_5.WO_3\ (s) \quad (4)$$

$$1/2Cr_2O_3\ (s) + 1/2Ta_2O_5\ (s) = CrTaO_4\ (s) \quad (5)$$

$$1/2Cr_2O_3\ (s) + 1/2Nb_2O_5\ (s) = CrNbO_4\ (s) \quad (6)$$

The high diffusion coefficient of Cr enables the synthesis of VO_2, Ta_2O_5, and Nb_2O_5 into $CrVO_3$, $CrTaO_4$, and Nb_2O_5. Also, Cr_2O_3 react with poor stability WO_3 to synthesize Cr_2WO_6 through the solid–state reaction. Similarly, Ta_2O_5 and Nb_2O_5 reacts with WO_3 to form $Ta_8W_8O_{44}$ and $Nb_2O_5.WO_3$. Complex oxide such as $Ta_8W_9O_{47}$ has been reported to possess low $\triangle G$ (—5400 kJ/mol), leading to a stable oxide layer [84]. In regards to $CrVO_3$ and $Nb_2O_5.WO_3$, it is still unclear whether the oxides would offer oxidation resistance. The addition of V in alloys forms VO_x that volatilizes at high temperatures and prevents the formation of a protective oxide layer [56,68,69]. An oxide layer containing $CrTaO_4$ has been reported to effectively retard oxygen diffusion and provide protection against oxidation at high temperatures [41,43,85]. Similarly, $CrTaO_4$ oxide layer was observed in W containing MoTaTiCr RHEAs that retarded oxygen diffusion and provided great protection against

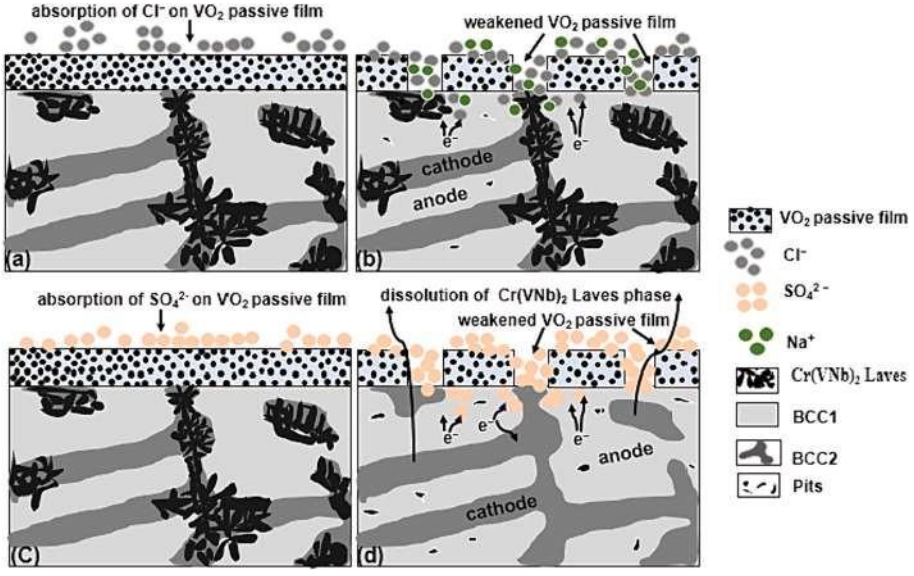

Fig. 11. Schematic diagram of the pits of BCC1 phase in CrNbTaVW RHEA in 3.5 wt% NaCl solution (a-b); Schematic diagram of the pits of BCC1 phase and dissolution of $Cr(VNb)_2$ Laves phase in CrNbTaVW RHEA in 1 Mol H_2SO_4 solution (c-d).

oxidation at 1000 °C [86]. In WCr alloys by Hou et al. [87], oxide scale of Cr_2WO_6 is poor and does not offer protection for further oxidation. However, the Cr_2O_3 scale was sufficient to offer a better protective scale for the WCr alloys. At a particular stage in CrNbTaVW RHEA oxidation at 1050 °C/15 hours, oxides of $CrTaO_4$, $CrNbO_4$, and Cr_2O_3 would have formed a barrier for both inward diffusion of oxygen and outward diffusion. These would have prevented more pores, cracks, and total degradation of the CrNbTaVW RHEA. The oxygen ions diffusion is hindered to some extent by Cr_2O_3 which slowed down the oxidation rate of oxidized CrNbTaVW RHEA.

Small decohesion of the oxide layer was observed for IN718 alloy oxide scale at 850 °C and 1050 °C which might be attributed to the volume change and internal pressures of SiO_2. According to Sheikh et al. [88], formation of MoO_3 and SiO_2 results in a local volume change and internal pressures that lead to decohesion and microcrack formation. Since there are no micro cracks and pores, the observed SiO_2 might not be detrimental to the oxidation resistance of IN718 alloy. The simple oxides such as Al_2O_3 protected the formation and volatilization of Mn_2O_3 in the IN718 at 850 °C and the oxidation rate was further reduced. The Al_2O_3 layer acts as a diffusion barrier against oxygen ingress into the alloy, thereby improving the alloy performance against high-temperature oxidation [89]. The oxide layer containing FeO on the surface is usually loose, porous, and easy to shed, which greatly reduces oxidation resistance [90]. FeO also formed in the IN718 at 1050 °C which might have also contributed to the small decohesion of IN718 alloy oxide scale. Fe_3O_4 observed at 850 °C and 1050 °C further formed a protective continuous layer and lowered the oxidation rate.

The volumetric expansion mismatch generates stresses in the oxides, which accumulate when the oxides grow and later released by cracking, and spallation of oxides from the base alloy [91]. In oxide scales, mechanical stress has two origins: the first is the growth stress, which develops during the oxidation process, and second is the thermal stress which develops due to the change in temperature [91]. The oxide layer of oxidized RHEAs can exfoliate from the metallic substrate during the cooling process from oxidation temperature to room temperature, which is attributed to different coefficients of thermal expansion and specific volume of the oxide and the alloy [92,93]. The growth stress can be quantified by the volume difference between the oxide and the metal forming the oxide and can be expressed by the Pilling-Bedworth ratio (PBR) in Eq. (7) [94].

$$\text{PBR} = \frac{\text{volume per metal ion in oxide}}{\text{volume per metal atom in metal}} \tag{7}$$

The oxide scale is discontinuous and porous if PBR < 1 [24]. For PBR > 2, the internal stress between oxides and matrix is high, and easily leads to the formation of pores, cracks, and spallation [24]. Spallation possibly occurs during the sample cooling due to the large differences between the thermal expansion coefficients of the oxide and the metal [88]. During the cooling stage, the metal substrate contracts more rapidly than the oxide layer, causing compressive in-plane stresses and the creation of shear cracks in the oxide layer [95]. At 850 °C and 1050 °C, cracks, pores, and voids were observed.

Using Eq. (7), the PBR for VO_2, V_2O_3, WO_3, and Cr_2O_3 is 2.17, 1.84, 3.39, and 2.02, respectively. The internal stress between VO_2, WO_3, and Cr_2O_3 and CrNbTaVW substrate is high, which led to the formation of pores and cracks at 850 °C and 1050 °C. In the WMoTaTiCr RHEA, WO_3 exhibited a large PBR that hinders the continuous protective layer [86]. According to Kuang et al. [96], volume expansion ratio of WO_3 would cause a large interface stress that would even tear the adhesive surface oxide scale, providing a channel for oxygen internal diffusion. The growth strain (ε) induces a change in volume that is expressed in Eq. (8) [97].

$$\varepsilon = \sqrt[3]{\text{PBR}} - 1 \tag{8}$$

The ε value was calculated by substituting the PBR values for VO_2, WO_3, and Cr_2O_3 in Eq. (8). The calculated ε value for VO_2, WO_3, and Cr_2O_3 is 0.296, 0.503, and 0.264, respectively. The growth stress (σ_G) can be calculated based on growth strain in Eq. (9) [91].

$$\sigma_G = \varepsilon E_{oxides} \tag{9}$$

Where E_{oxides} is the Young's modulus of VO_2 (140 GPa) [98], WO_3 (300 GPa) [99], and Cr_2O_3 (260 GPa) [91]. By substituting E_{oxides} and ε values into Eq. (9), the σ_G is calculated to be 41.4 GPa, 150.8 GPa, and 68.7 GPa for VO_2, WO_3, and Cr_2O_3, respectively. It can be observed that the σ_G in VO_2 and Cr_2O_3 is less than that of WO_3. It can be assumed that decohesion is only initiated on the oxide scale by VO_2 and Cr_2O_3, while cracks, pores, voids and spalling is initiated by WO_3.

Thermal stress (σ_T) occurred during cooling to room temperature and it was formed due to different thermal expansions between the oxide scales and the CrNbTaVW RHEA. The σ_T can be expressed in Eq. (10) [91].

$$\sigma_T = E_{oxides} \left(\alpha_{alloy} - \alpha_{oxides}\right) \Delta T \tag{10}$$

Where α_{alloy} and α_{oxides} are the thermal expansion coefficients of CrNbTaVW RHEA and the oxides respectively. ΔT is the difference between oxidation temperature and room temperature during cooling. The $\alpha_{CrNbTaVW}$ was calculated to be $10.698 \times 10^{-6}\ K^{-1}$ using the rule of mixture. While α_{oxides} for VO_2, WO_3, and Cr_2O_3 is $2.1 \times 10^{-6}\ K^{-1}$ [98], $8.9 \times 10^{-6}\ K^{-1}$ [100], and $9.6 \times 10^{-6}\ K^{-1}$ [91]. The σ_T is assumed to be generated mainly by VO_2, WO_3, and Cr_2O_3 at 850 °C and 1050 °C. The σ_T generated by VO_2, WO_3, and Cr_2O_3 at 850 °C is estimated to be 0.993 GPa, 0.445 GPa, and 0.199 GPa. At 1050 °C, σ_T generated by VO_2, WO_3, and Cr_2O_3 is 1.234 GPa, 0.553 GPa, and 0.248 GPa. From the results, it can be observed that σ_T is lower than σ_G and the thermal expansion coefficient of the alloy is larger than that of the oxides. Hence, the σ_T in the scale should be compressive, which is the same as growth stress [91]. The failure of protective oxide scales could be due to the mismatch in volume expansion between VO_2, WO_3, and Cr_2O_3 oxides, and CrNbTaVW substrates, which led to the build-up of thermal stress and growth stress.

The summary of the oxidation mechanism of CrNbTaVW RHEA at 850 °C and 1050 °C for 15 hours is shown in Fig. 12. During the initial stage, oxygen dissolves and diffuses internally through the BCC1, BCC2 and $Cr(VNb)_2$ Laves. At higher temperatures, the oxides react with elements that comprise the RHEA and form the simple and complex oxides. The formed oxides at 850 °C and 1050 °C might not be protective due to the mismatch in volume expansion between the oxides and CrNbTaVW substrates. In the oxide scales of CrNbTaVW RHEA, thermal and growth stress was observed. As oxides grows during oxidation, growth stress due to micro-inhomogeneity of oxide species was formed and eventually released via pores, cracks, and voids (Fig. 12a and b). During the cooling to room temperature of CrNbTaVW RHEA, spallation, pores, and voids appear due to thermal stress caused by the different thermal expansion coefficients of the oxides and metallic substrate. The observed pores, cracks, voids, and spallation stresses serves as fast migration channels for oxygen that increases the oxidation rate of the CrNbTaVW RHEA.

6. Conclusions

The microstructure, hardness, corrosion, and oxidation behavior of CrNbTaVW RHEA have been investigated. The results were compared to commercial grade IN718 nickel-based superalloy. The following conclusions are drawn from the study:

- The as-cast CrNbTaVW RHEA exhibited a dendritic microstructure that segregated into BCC1, BCC2, and $Cr(VNb)_2$ Laves. The empirical calculations, XRD, and SEM accurately predicted the phases in the CrNbTaVW RHEA.
- The hardness test result of CrNbTaVW RHEA after ten indentations found the hardness value to be 688 ± 21 HV, which is higher than

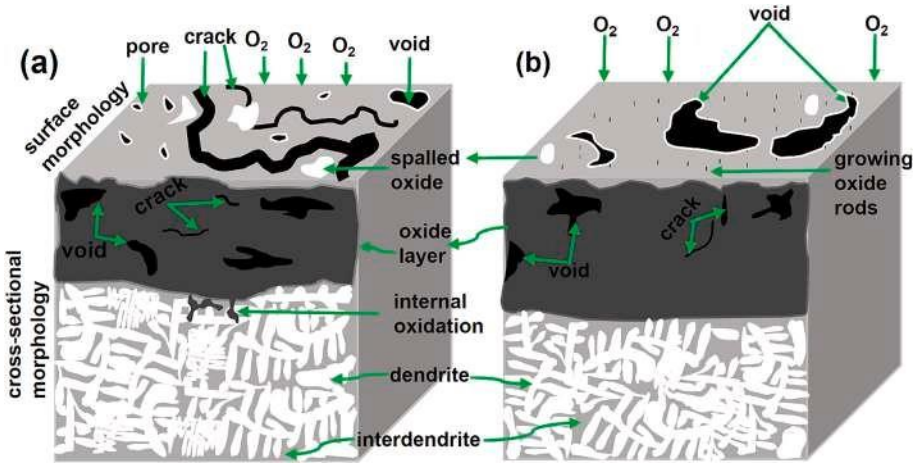

Fig. 12. Schematic diagram of the oxidation mechanism of CrNbTaVW at 850 °C and 1050 °C after 15 hours (a-b).

IN718 (301 ±14 HV). The high hardness of CrNbTaVW RHEA is attributed to Laves phase solid solution strengthening and grain refinement.

- Fluctuations in OCP were observed for CrNbTaVW RHEA in 1 M H_2SO_4 solutions and IN718 alloy in both 3.5 wt% NaCl and 1 M H_2SO_4 solutions.
- The CrNbTaVW RHEA has a lower corrosion rate of 0.000097 mm/yr in 3.5 wt% NaCl solution than the IN718 alloy (0.054 mm/yr). In acidic solution, CrNbTaVW RHEA has a low corrosion rate of 0.00013 mm/yr in 1 M H_2SO_4 solution than the IN718 alloy (1.12 mm/yr). Therefore, it can be concluded that CrNbTaVW RHEA has superior corrosion resistance in 3.5 wt% NaCl and 1 M H_2SO_4 solution in comparison with commercial grade IN718.
- In chloride solution, BCC1 is more susceptible to pitting corrosion. In acidic solution, BCC1 is more susceptible to pitting corrosion, while the $Cr(VNb)_2$ Laves phase is more susceptible to selective dissolution.
- The IN718 alloy has a lower mass gain of 4.41 mg/cm^2 and 10.84 mg/cm^2 at 850 °C/15 hours and 1050 °C/15 hours. The CrNbTaVW RHEA exhibited a mass loss of —25.17 mg/cm^2 and — 35.91 mg/cm^2 at 850 °C/15 hours and 1050 °C/15 hours. In general, the IN718 alloy has a superior oxidation resistance than the CrNbTaVW RHEA.
- Thermal stress and growth stress contributed to pores, voids, cracks, and spallation observed in the CrNbTaVW RHEA at 850 °C and 1050 °C after 15 hours. The pores, cracks, and voids allow ingress of oxygen to the metallic substrate and increased the oxidation rate.

CRediT authorship contribution statement

Olufemi Sylvester Bamisaye: Writing – original draft, Methodology, Investigation, Formal analysis, Conceptualization. **Nthabiseng Maledi:** Writing – review & editing, Validation, Supervision, Resources, Methodology, Conceptualization. **Josias Van der Merwe:** Supervision, Resources, Methodology, Conceptualization. **Michael Oluwatosin Bodunrin:** Writing – review & editing, Validation, Supervision, Resources, Methodology, Conceptualization.

Declaration of competing interest

The authors declare that there is no conflict of interest to this work.

Data availability

Data will be made available on request.

Appendix A. Supplementary data

Supplementary data to this article can be found online at https://doi.org/10.1016/j.ijrmhm.2024.106661.

References

[1] B. Cantor, I.T.H. Chang, P. Knight, A.J.B. Vincent, Microstructural development in equiatomic multicomponent alloys, Mater. Sci. Eng. A 375–377 (2004) 213–218, https://doi.org/10.1016/j.msea.2003.10.257.
[2] J. Yeh, S. Chen, S. Lin, J. Gan, T. Chin, T. Shun, C. Tsau, C. Shou-Yi, Nanostructured high-entropy alloys with multiple principal elements: novel alloy design concepts and outcomes, Adv. Eng. Mater. 6 (2004) 299–303, https://doi.org/10.1002/adem.200300567.
[3] B. Gorr, F. Müller, M. Azim, H.J. Christ, T. Müller, H. Chen, A. Kauffmann, M. Heilmaier, High-temperature oxidation behavior of refractory high-entropy alloys: effect of alloy composition, Oxid. Met. 88 (2017) 339–349, https://doi.org/10.1007/s11085-016-9696-y.
[4] J.W. Yeh, S.K. Chen, S.J. Lin, J.Y. Gan, T.S. Chin, T.T. Shun, C.H. Tsau, S. Y. Chang, Nanostructured high-entropy alloys with multiple principal elements: novel alloy design concepts and outcomes, Adv. Eng. Mater. 6 (2004) 299–303, https://doi.org/10.1002/adem.200300567.
[5] O.N. Senkov, G.B. Wilks, D.B. Miracle, C.P. Chuang, P.K. Liaw, Refractory high-entropy alloys, Intermetallics 18 (2010) 1758–1765, https://doi.org/10.1016/j.intermet.2010.05.014.
[6] D.B. Miracle, O.N. Senkov, A critical review of high entropy alloys and related concepts, Acta Mater. 122 (2017) 448–511, https://doi.org/10.1016/j.actamat.2016.08.081.
[7] S. Nam, Y. Song, M. Son, et al., High-temperature mechanical and thermochemical properties of NbMoTaW refractory high-entropy alloy coatings produced via Nano particle deposition system (NPDS), Int. J. Refract. Met. Hard Mater. 99 (2021) 105594, https://doi.org/10.1016/j.ijrmhm.2021.105594.
[8] J. Liu, R.J. Scales, B.S. Li, et al., Controlling microstructure and mechanical properties of Ti-V-Cr-Nb-ta refractory high entropy alloys through heat treatments, J. Alloys Compd. 932 (2023) 1–7, https://doi.org/10.1016/j.jallcom.2022.167651.
[9] C. Duan, M. Reiberg, P. Kutlesa, et al., Strain-hardening properties of the high-entropy alloy MoNbTaTiVZr processed by high-pressure torsion, Contin. Mech. Thermodyn. 34 (2022) 475–489, https://doi.org/10.1007/s00161-021-01065-5.
[10] A. Poulia, E. Georgatis, A. Lekatou, et al., Microstructure and wear behavior of a refractory high entropy alloy, Int. J. Refract. Met. Hard Mater. 57 (2016) 50–63, https://doi.org/10.1016/j.ijrmhm.2016.02.006.
[11] F.G. Coury, T. Butler, K. Chaput, et al., Phase equilibria, mechanical properties and design of quaternary refractory high entropy alloys, Mater. Des. 155 (2018) 244–256, https://doi.org/10.1016/j.matdes.2018.06.003.
[12] L. Fang, J. Wang, X. Li, et al., Effect of Cr content on microstructure characteristics and mechanical properties of $ZrNbTaHf0.2Cr_x$ refractory high entropy alloy, J. Alloys Compd. 924 (2022), https://doi.org/10.1016/j.jallcom.2022.166593.
[13] O.N. Senkov, S.V. Senkova, D.B. Miracle, et al., Mechanical properties of low-density, refractory multi-principal element alloys of the Cr-Nb-Ti-V-Zr system, Mater. Sci. Eng. A 565 (2013) 51–62, https://doi.org/10.1016/j.msea.2012.12.018.
[14] C. Xiang, Z. Ming, Z. Hua, et al., Microstructure, mechanical properties, and corrosion behavior of MoNbFeCrV, MoNbFeCrTi, and MoNbFeVTi high-entropy alloys, Acta Metall. Sin. 32 (2019) 1053–1064, https://doi.org/10.1007/s40195-019-00935-x.

[15] D.H. Xia, C.M. Deng, D. Macdonald, et al., Electrochemical measurements used for assessment of corrosion and protection of metallic materials in the field: a critical review, J. Mater. Sci. Technol. 112 (2022) 151–183, https://doi.org/10.1016/j.jmst.2021.11.004.

[16] Y. Shi, B. Yang, P.K. Liaw, Corrosion-resistant high-entropy alloys: a review, Metals 7 (2017) 1–18, https://doi.org/10.3390/met7020043.

[17] D. Yan, K. Song, Microstructures, mechanical properties, and corrosion behaviors of refractory high-entropy alloys, J. Mater. Eng. Perform. 29 (2020) 399–409, https://doi.org/10.1007/s11665-019-04540-y.

[18] Q. Zhou, S. Sheikh, P. Ou, et al., Corrosion behavior of $Hf_{0.5}Nb_{0.5}Ta_{0.5}Ti_{1.5}Zr$ refractory high-entropy in aqueous chloride solutions, Electrochem. Commun. 98 (2019) 63–68, https://doi.org/10.1016/j.elecom.2018.11.009.

[19] T. Li, O.J. Swanson, G.S. Frankel, et al., Localized corrosion behavior of a single-phase non-equimolar high entropy alloy, Electrochim. Acta 306 (2019) 71–84, https://doi.org/10.1016/j.electacta.2019.03.104.

[20] Q. Zhou, S. Sheikh, P. Ou, et al., Corrosion behavior of $Hf_{0.5}Nb_{0.5}Ta_{0.5}Ti_{1.5}Zr$ refractory high-entropy in aqueous chloride solutions, Electrochem. Commun. 98 (2019) 63–68, https://doi.org/10.1016/j.elecom.2018.11.009.

[21] Y. Gao, K. Chong, L. Qiao, et al., Synthesis and corrosion behavior of $Mo_{15}Nb_{20}Ta_{10}Ti_{35}V_{20}$ refractory high entropy alloy, Mater. Des. 228 (2023) 1–15, https://doi.org/10.1016/j.matdes.2023.111820.

[22] M. Li, Q. Chen, X. Cui, et al., Evaluation of corrosion resistance of the single-phase light refractory high entropy alloy TiCrVNb0.5Al0.5 in chloride environment, J. Alloys Compd. 857 (2021) 1–10, https://doi.org/10.1016/j.jallcom.2020.158278.

[23] D. Bi, Y. Chang, H. Luo, et al., Corrosion behavior and passive film characteristics of $AlNbTiZrSi_x$ high-entropy alloys in simulated seawater environment, Corros. Sci. 111530 (2023), https://doi.org/10.1016/j.corsci.2023.111530.

[24] Y.K. Cao, Y. Liu, B. Liu, et al., Effects of Al and Mo on high temperature oxidation behavior of refractory high entropy alloys, Trans. Nonferrous Metals Soc. China 29 (2019) 1476–1483, https://doi.org/10.1016/S1003-6326(19)65054-5.

[25] S.N. Lekakh, O. Neroslavsky, M. Li, et al., Effect of spallation on oxidation kinetics of heat-resistant Cr–Ni austenitic steels on air and combustion atmosphere, High Temperat. Corros. Mater. 99 (2023) 79–99, https://doi.org/10.1007/s11085-022-10139-x.

[26] C.O. Moon, S.B. Lee, Analysis on failures of protective-oxide layers and cyclic oxidation, Oxid. Met. 39 (1993) 1–13.

[27] T.M. Butler, K.J. Chaput, Native oxidation resistance of $Al_{20}Nb_{30}Ta_{10}Ti_{30}Zr_{10}$ refractory complex concentrated alloy (RCCA), J. Alloys Compd. 787 (2019) 606–617, https://doi.org/10.1016/j.jallcom.2019.02.128.

[28] C.M. Liu, H.M. Wang, S.Q. Zhang, et al., Microstructure and oxidation behavior of new refractory high entropy alloys, J. Alloys Compd. 583 (2014) 162–169, https://doi.org/10.1016/j.jallcom.2013.08.102.

[29] S. Lu, X. Li, X. Liang, et al., Effect of V and Ti on the oxidation resistance of WMoTaNb refractory high-entropy alloy at high temperatures, Metals 12 (2022), https://doi.org/10.3390/met12010041.

[30] O.N. Senkov, S.V. Senkova, D.M. Dimiduk, et al., Oxidation behavior of a refractory $NbCrMo_{0.5}Ta_{0.5}TiZr$ alloy, J. Mater. Sci. 47 (2012) 6522–6534, https://doi.org/10.1007/s10853-012-6582-0.

[31] R. Su, H. Zhang, G. Ouyang, et al., Oxidation mechanism in a refractory multiple-principal-element alloy at high temperature, Acta Mater. 246 (2023) 118719, https://doi.org/10.1016/j.actamat.2023.118719.

[32] F. Xu, X. Gao, H. Cui, et al., Lightweight and high hardness $(AlNbTiVCr)100\text{-}xNi_x$ high entropy alloys reinforced by laves phase, Vacuum 213 (2023), https://doi.org/10.1016/j.vacuum.2023.112115.

[33] S. Wu, D. Qiao, H. Zhang, et al., Microstructure and mechanical properties of $C_xHf_{0.25}NbTaW_{0.5}$ refractory high-entropy alloys at room and high temperatures, J. Mater. Sci. Technol. 97 (2021) 229–238, https://doi.org/10.1016/j.jmst.2021.05.015.

[34] M. Wang, Z.L. Ma, Z.Q. Xu, et al., Effects of vanadium concentration on mechanical properties of $V_xNbMoTa$ refractory high-entropy alloys, Mater. Sci. Eng. A 808 (2021) 1–8, https://doi.org/10.1016/j.msea.2021.140848.

[35] J. Li, X. Yang, R. Zhu, et al., Corrosion and serration behaviors of $TiZr_{0.5}NbCr_{0.5}V_xMo_y$ high entropy alloys in aqueous environments, Metals 4 (2014) 597–608, https://doi.org/10.3390/met4040597.

[36] C. Nyby, X. Guo, J.E. Saal, et al., Electrochemical metrics for corrosion resistant alloys, Sci. Data 8 (2021) 58, https://doi.org/10.1038/s41597-021-00840-y.

[37] Z. Wang, Y. Yan, Y. Wu, et al., Corrosion and tribocorrosion behavior of equiatomic refractory medium entropy TiZr(Hf, ta, Nb) alloys in chloride solutions, Corros. Sci. 199 (2022) 110166, https://doi.org/10.1016/j.corsci.2022.110166.

[38] K. Patel, M. Sadeghilaridjani, M. Pole, et al., Hot corrosion behavior of refractory high entropy alloys in molten chloride salt for concentrating solar power systems, Sol. Energy Mater. Sol. Cells 230 (2021) 111222, https://doi.org/10.1016/j.solmat.2021.111222.

[39] J. Jayaraj, C. Thinaharan, S. Ningshen, et al., Corrosion behavior and surface film characterization of TaNbHfZrTi high entropy alloy in aggressive nitric acid medium, Intermetallics 89 (2017) 123–132, https://doi.org/10.1016/j.intermet.2017.06.002.

[40] Y. Qiu, S. Thomas, M.A. Gibson, et al., Microstructure and corrosion properties of the low-density single-phase compositionally complex alloy AlTiVCr, Corros. Sci. 133 (2018) 386–396.

[41] K.C. Lo, Y.J. Chang, H. Murakami, et al., An oxidation resistant refractory high entropy alloy protected by CrTaO4 -based oxide, Sci. Rep. 9 (2019) 3–4, https://doi.org/10.1038/s41598-019-43819-x.

[42] Y. Du, D. Ding, L. Lai, et al., Effect of Y on the high-temperature oxidation behavior of CrMoTaTi refractory high entropy alloy, Int. J. Refract. Met. Hard Mater. 103 (2022) 1–11, https://doi.org/10.1016/j.ijrmhm.2021.105755.

[43] Y. Xiao, W. Kuang, Y. Xu, et al., Microstructure and oxidation behavior of the CrMoNbTaV high-entropy alloy, J. Mater. Res. 34 (2019) 301–308, https://doi.org/10.1557/jmr.2018.340.

[44] T.M. Butler, K.J. Chaput, J.R. Dietrich, et al., High temperature oxidation behaviors of equimolar NbTiZrV and NbTiZrCr refractory complex concentrated alloys (RCCAs), J. Alloys Compd. 729 (2017) 1004–1019, https://doi.org/10.1016/j.jallcom.2017.09.164.

[45] ASTM E92-17, E92–17 Standard Test Methods for Vickers Hardness and Knoop Hardness of Metallic Materials, ASTM International, 2009.

[46] ASTM G59-97 standard test method for conducting Potentiodynamic polarization resistance measurements, ASTM Int. 97 (2020).

[47] O.N. Senkov, S.V. Senkova, C. Woodward, et al., Low-density, refractory multi-principal element alloys of the Cr-Nb-Ti-V-Zr system: microstructure and phase analysis, Acta Mater. 61 (2013) 1545–1557, https://doi.org/10.1016/j.actamat.2012.11.032.

[48] J. Yi, S. Tang, C. Zhang, et al., Microstructure and mechanical properties of a new refractory equiatomic CrHfNbTaTi high-entropy alloy, JOM 73 (2021) 934–940, https://doi.org/10.1007/s11837-020-04557-y.

[49] T.M. Butler, O.N. Senkov, M.A. Velez, et al., Microstructures and mechanical properties of CrNb, CrNbTi, and CrNbTaTi concentrated refractory alloys, Intermetallics 138 (2021) 107323, https://doi.org/10.1016/j.intermet.2021.107323.

[50] M. Tsai, J. Yeh, High-entropy alloys: a critical review, Mater. Res. Lett. 2 (2014) 107–123, https://doi.org/10.1080/21663831.2014.912690.

[51] D.K. Ganji, G. Rajyalakshmi, Influence of alloying compositions on the properties of nickel-based superalloys: A review, in: Lecture Notes in Mechanical Engineering, Springer Science and Business Media Deutschland GmbH, 2020, pp. 537–555, https://doi.org/10.1007/978-981-15-1071-7_44.

[52] S.H. Chen, J.S. Zhang, S. Guan, et al., Microstructure and mechanical properties of $WNbMoTaZr_x$ (x=0.1, 0.3, 0.5, 1.0) refractory high entropy alloys, Mater. Sci. Eng. A 835 (2022) 1–10.

[53] Y. Chen, G. Xiao, Y. Ji, et al., Effects of Zr content on the microstructure and performance of $TiMoNbZr_x$ high-entropy alloys, Metals 11 (2021) 1–12, https://doi.org/10.3390/met11081315.

[54] M. Wang, Z.L. Ma, Z.Q. Xu, et al., Designing $V_xNbMoTa$ refractory high-entropy alloys with improved properties for high-temperature applications, Scr. Mater. 191 (2021) 131–136, https://doi.org/10.1016/j.scriptamat.2020.09.027.

[55] V.P. Parkhutik, Oscillations of open-circuit potential during immersion plating of silicon in CuSO4/HF solutions, Russ. J. Electrochem. 42 (2006), https://doi.org/10.1134/S1023193506050090.

[56] Z.J. Zheng, Y. Gao, Y. Gui, et al., Corrosion behaviour of nanocrystalline 304 stainless steel prepared by equal channel angular pressing, Corros. Sci. 54 (2012) 60–67, https://doi.org/10.1016/j.corsci.2011.08.049.

[57] P. Murmey, U. Nichul, M. Chikode, et al., Effect of post-processing on corrosion behavior of LPBF built inconel 718 alloy, JOM 75 (2023) 32–44, https://doi.org/10.1007/s11837-022-05565-w.

[58] D. Kumar, O. Maulik, V.K. Sharma, et al., Understanding the effect of tungsten on corrosion behavior of $AlCuCrFeMnW_x$ high-entropy alloys in 3.5 wt% NaCl solution, J. Mater. Eng. Perform. 27 (2018) 4481–4488, https://doi.org/10.1007/s11665-018-3536-y.

[59] N. Razumov, T. Makhmutov, A. Kim, et al., Refractory CrMoNbWV high-entropy alloy manufactured by mechanical alloying and spark plasma sintering: evolution of microstructure and properties, Materials 14 (2021) 1–14, https://doi.org/10.3390/ma14030621.

[60] L. Wei, W. Qin, Corrosion mechanism of eutectic high-entropy alloy induced by micro-galvanic corrosion in sulfuric acid solution, Corros. Sci. 206 (2022), https://doi.org/10.1016/j.corsci.2022.110525.

[61] R. Zhang, J. Meng, J. Han, et al., Oxidation resistance properties of refractory high-entropy alloys with varied $Al_xCrTiMo$ content, J. Mater. Sci. 56 (2021) 1–11, https://doi.org/10.1007/s10853-020-05480-y.

[62] R. Romero, I.J. Beyerlein, C.V. Ramana, Microstructure and oxidation behavior of a CrMoNbTaW refractory high entropy alloy, ACS Appl. Eng. Mater. 1 (2023) 132–139, https://doi.org/10.1021/acsaenm.2c00025.

[63] O.N. Senkov, C.F. Woodward, Microstructure and properties of a refractory $NbCrMo_{0.5}Ta_{0.5}TiZr$ alloy, Mater. Sci. Eng. A 529 (2011) 311–320, https://doi.org/10.1016/j.msea.2011.09.033.

[64] L. Brewer, Prediction of transition metal phase diagrams, J. Nucl. Mater. 51 (1974) 2–11.

[65] S. Guo, C. Ng, J. Lu, et al., Effect of valence electron concentration on stability of fcc or bcc phase in high entropy alloys, J. Appl. Phys. 103505 (2011) 1–6, https://doi.org/10.1063/1.3587228.

[66] X. Yang, Y. Zhang, Prediction of high-entropy stabilized solid-solution in multi-component alloys, Mater. Chem. Phys. 132 (2012) 233–238, https://doi.org/10.1016/j.matchemphys.2011.11.021.

[67] B.Y. Zhang, Y.J. Zhou, J.P. Lin, et al., Solid-solution phase formation rules for multi-component alloys, Adv. Eng. Mater. 10 (2008) 534–538, https://doi.org/10.1002/adem.200700240.

[68] M. Zhang, X. Zhou, J. Li, Microstructure and mechanical properties of a refractory CoCrMoNbTi high-entropy alloy, J. Mater. Eng. Perform. 26 (2017) 3657–3665, https://doi.org/10.1007/s11665-017-2799-z.

[69] J.C. Phillips, Heats of formation of interstitial compounds and their alloys, J. Phys. Chem. Solids 34 (1973), https://doi.org/10.1016/S0022-3697(73)80012-5.

[70] A.K. Singh, A. Subramaniam, On the formation of disordered solid solutions in multi-component alloys, J. Alloys Compd. 587 (2014) 113–119, https://doi.org/10.1016/j.jallcom.2013.10.133.
[71] H.A. Aly, K.A. Abdelghafar, G.A. Gaber, et al., Fabrication, characterization, and corrosion behavior of a new $Cu_{40}Mn_{25}Al_{20}Fe_5Co_5Ni_5$ high-entropy alloy in HNO_3 solution, J. Mater. Eng. Perform. 30 (2021) 1430–1443, https://doi.org/10.1007/s11665-020-05390-9.
[72] C. Xiang, H.M. Fu, Z.M. Zhang, et al., Effect of Cr content on microstructure and properties of $Mo_{0.5}VNbTiCr_x$ high-entropy alloys, J. Alloys Compd. 818 (2020), https://doi.org/10.1016/j.jallcom.2019.153352.
[73] L. Fang, J. Wang, X. Li, et al., Effect of Cr content on microstructure characteristics and mechanical properties of $ZrNbTaHf_{0.2}Cr_x$ refractory high entropy alloy, J. Alloys Compd. 924 (2022) 166593, https://doi.org/10.1016/j.jallcom.2022.166593.
[74] O.N. Senkov, S.V. Senkova, C. Woodward, et al., Low-density, refractory multi-principal element alloys of the Cr–Nb–Ti–V–Zr system: microstructure and phase analysis, Acta Mater. 61 (2013) 1545–1557, https://doi.org/10.1016/j.actamat.2012.11.032.
[75] N. Yurchenko, N. Stepanov, G. Salishchev, Laves-phase formation criterion for high-entropy alloys, Mater. Sci. Technol. 33 (2017) 1153277, https://doi.org/10.1080/02670836.2016.1153277.
[76] C.B. Nascimento, U. Donatus, C.T. Ríos, et al., A review on corrosion of high entropy alloys: exploring the interplay between corrosion properties, alloy composition, passive film stability and materials selection, Mater. Res. 25 (2022) 1–16, https://doi.org/10.1590/1980-5373-MR-2021-0442.
[77] O. Swanson, Corrosion of High-Entropy Alloys in Chloride Solutions, Graduate School of The Ohio State University, 2018.
[78] G.S. Frankel, T. Li, J.R. Scully, Perspective—localized corrosion: passive film breakdown vs pit growth stability, J. Electrochem. Soc. 164 (2017) C180–C181, https://doi.org/10.1149/2.1381704jes.
[79] D.E. Williams, Y. Yang, E.G. Webb, et al., Explanation for initiation of pitting corrosion of stainless steels at sulfide inclusions, J. Electrochem. Soc. 147 (2000) 1763–1766, https://doi.org/10.1149/1.1393431.
[80] P. Wang, Y. Wang, F. Cui, et al., Microstructural evolution, mechanical properties and corrosion resistance of $CoCrFeNiW_{0.5}$ high entropy alloys with various annealing heat treatment, J. Alloys Compd. 918 (2022), https://doi.org/10.1016/j.jallcom.2022.165602.
[81] C. Liu, Y. Gao, K. Chong, et al., Effect of Nb content on the microstructure and corrosion resistance of $FeCoCrNiNb_x$ high-entropy alloys in chloride ion environment, J. Alloys Compd. 935 (2023), https://doi.org/10.1016/j.jallcom.2022.168013.
[82] Z. Peng, B. Li, Z. Luo, et al., A lightweight $AlCrTiV_{0.5}Cu_x$ High-entropy alloy with excellent corrosion resistance, Materials 16 (2023) 2922, https://doi.org/10.3390/ma16072922.
[83] B.M. Hunter, Oxidation Behavior of Refractory Complex Concentrated Alloys: Computational and Experimental Studies, University of Alabama, Thesis, 2019.
[84] X. Zhang, X. Cui, G. Jin, et al., Microstructure evolution and performance enhancement of NbTaTiV-(Cr, Zr, W) single-phase refractory high-entropy alloy coatings: role of additional elements, J. Alloys Compd. 951 (2023) 169918, https://doi.org/10.1016/j.jallcom.2023.169918.
[85] Y. Du, D. Ding, L. Lai, et al., Effect of Y on the high-temperature oxidation behavior of CrMoTaTi refractory high entropy alloy, Int. J. Refract. Met. Hard Mater. 103 (2022), https://doi.org/10.1016/j.ijrmhm.2021.105755.
[86] A.O. Moghaddam, M. Sudarikov, N. Shaburova, et al., High temperature oxidation resistance of W-containing high entropy alloys, J. Alloys Compd. 897 (2022) 1–10, https://doi.org/10.1016/j.jallcom.2021.162733.
[87] Q.Q. Hou, K. Huang, L.M. Luo, et al., Microstructure and its high temperature oxidation behavior of W-Cr alloys prepared by spark plasma sintering, Materialia 6 (2019) 100332, https://doi.org/10.1016/j.mtla.2019.100332.
[88] S. Sheikh, M.K. Bijaksana, A. Motallebzadeh, et al., Accelerated oxidation in ductile refractory high-entropy alloys, Intermetallics 97 (2018) 58–66, https://doi.org/10.1016/j.intermet.2018.04.001.
[89] S. Abbaszadeh, A. Pakseresht, H. Omidvar, et al., Investigation of the high-temperature oxidation behavior of the $Al_{0.5}CoCrFeNi$ high entropy alloy, Surf. Interf. 21 (2020) 100724, https://doi.org/10.1016/j.surfin.2020.100724.
[90] X. Yang, Z. Zeng, X. Wang, et al., High-temperature oxidation behaviors of 321 steel with Y or Nb micro-alloying, Crystals 13 (2023) 781, https://doi.org/10.3390/cryst13050781.
[91] L. Zheng, M. Zhang, R. Chellali, et al., Investigations on the growing, cracking and spalling of oxides scales of powder metallurgy Rene95 nickel-based superalloy, Appl. Surf. Sci. 257 (2011) 9762–9767, https://doi.org/10.1016/j.apsusc.2011.06.005.
[92] Y. Yan, K.A. McGarrity, D.J. Delia, et al., The oxidation-resistance mechanism of WTaNbTiAl refractory high entropy alloy, Corros. Sci. 204 (2022) 110377, https://doi.org/10.1016/j.corsci.2022.110377.
[93] O.S. Bamisaye, N. Maledi, J. Van der Merwe, M.O. Bodunrin, Microstructure, hardness, oxidation, and corrosion behavior of TiNbTaVW refractory high entropy alloy in 3.5 wt% NaCl and 1 M H_2SO_4, J. Alloys Compd. 983 (2024) 173803, https://doi.org/10.1016/j.jallcom.2024.173803.
[94] R. Mevrel, Cyclic oxidation of high-temperature alloys, Mater. Sci. Technol. 3 (1986) 531–535, https://doi.org/10.1080/02670836.1987.11782264.
[95] H. Jeong, S.H. Kim, W.S. Choi, et al., Spallation resistance of oxide scales on alloy 617 enhanced by boron addition, Corros. Sci. 140 (2018) 196–204, https://doi.org/10.1016/j.corsci.2018.06.002.
[96] J. Kuang, P. Zhang, Q. Wang, Z. Hu, X. Liang, B. Shen, Formation and oxidation behavior of refractory high-entropy silicide (NbMoTaW)Si_2 coating, Corros. Sci. 198 (2022) 110134, https://doi.org/10.1016/j.corsci.2022.110134.
[97] B. Panicaud, J.L. Grosseau-Poussard, J.F. Dinhut, On the growth strain origin and stress evolution prediction during oxidation of metals, Appl. Surf. Sci. 252 (2006) 5700–5713, https://doi.org/10.1016/j.apsusc.2005.07.075.
[98] F. Song, B.E. White, Growth of Ultra-Thin Vanadium Dioxide Thin Films Using Magnetron Sputtering, 2016, p. 03911. http://arxiv.org/abs/1608.03911.
[99] Y. Zhu, Y. Zhang, F.C. Cheong, et al., Annealing effects on the elastic modulus of tungsten oxide nanowires, J. Mater. Res. 23 (2008) 2149–2156, https://doi.org/10.1557/jmr.2008.0277.
[100] E. Besozzi, D. Dellasega, V. Russo, et al., Thermomechanical properties of amorphous metallic tungsten-oxygen and tungsten-oxide coatings, Mater. Des. 165 (2019) 107565, https://doi.org/10.1016/j.matdes.2018.107565.

ADVANCED ENGINEERING MATERIALS
www.aem-journal.com

Flow Behavior and Microstructure of Hot-Worked TiNbTaVW Refractory High-Entropy Alloy

Olufemi Sylvester Bamisaye, Nthabiseng Maledi, Josias Van der Merwe, Desmond Klenam, and Michael Bodunrin*

The high-temperature deformation behavior of an equiatomic TiNbTaVW refractory high entropy alloy (RHEA) was studied at temperatures of 950, 1000, and 1050 °C and a strain rate of 10^{-3} s^{-1}. The flow stress, high-temperature strength, and softening mechanisms were analyzed and compared with the IN718 nickel-based superalloy. The results indicate that the flow stress of both TiNbTaVW and IN718 is sensitive to deformation temperature, with high temperatures resulting in reduced flow stress. Globular grains and elongated grains were observed at 950 and 1000 °C for TiNbTaVW, signifying both dynamic recovery and dynamic globularization as the softening mechanisms. Globular grains were only observed at 1050 °C for TiNbTaVW, signifying dynamic globularization as the softening mechanism. The TiNbTaVW RHEA has a higher temperature strength of 910, 870, and 658 MPa compared to the IN718 alloy with 72, 87, and 61 MPa at 950–1000 °C/10^{-3} s^{-1}. By demonstrating comparable or superior performance in specific aspects, RHEAs can be considered in the near future for potential applications traditionally dominated by nickel-based superalloys.

1. Introduction

For over a decade, there has been a persistent demand for new materials with excellent mechanical properties to meet the requirements of various high-temperature structural applications, particularly in the aerospace industry. Currently, advanced materials, such as nickel-based superalloys, are among the main commercially used alloys. However, these materials are approaching their design limits as operating temperatures get closer to their melting points.[1,2] Therefore, there is a need for promising materials with high-temperature mechanical properties at or above 1200 °C. A new alloy design concept known as high-entropy alloys[3] has been utilized to develop novel refractory metals containing several principal elements at near or equiatomic concentrations.[4] Refractory high-entropy alloys (RHEAs) have attracted specific interest as potential candidates for higher-temperature functional materials due to their high-temperature strength, hardness, and wear resistance.[5–11] Understanding the high-temperature behavior of RHEAs is important before they can be used for structural and functional applications. Thermomechanical processing of RHEAs at high temperatures is an effective method of shaping and modifying the microstructure and properties after casting.[12,13]

In other metallic alloys, desirable softening mechanisms like dynamic recovery (DRV) and dynamic recrystallization (DRX) can occur during hot deformation in RHEAs.[5,14–19] Eleti et al.[17] deformed the HfNbTaTiZr RHEA at 1000 °C/10^{-3} s^{-1} and observed significant bulging along grain boundaries, leading to the emergence of DRX grains. Wang et al.[20] studied the isothermal compression of the NbZrTiTa RHEA at 900–1200 °C/10^{-3} s^{-1} and identified new fine grains near deformed grain boundaries, suggesting DRX. Li et al.[21] found dynamically recrystallized grains when deforming the $Ti_2ZrHfV_{0.5}Ta_{0.2}$ RHEA at 900–1100 °C/10^{-1}–10^{-3} s^{-1}. Bai et al.[19] investigated the isothermal compression behavior of the $TiAlVNb_2$ RHEA at 1000–1200 °C/10^{-1}–10^{-3} s^{-1} and identified the softening mechanisms as DRV and DRX. Unsafe deformation behaviors such as fracture, flow localization, wedge cracking, and adiabatic shear banding have also been observed in RHEAs.[10,22–28] Brittle and fracture behaviors have been found in some hot deformed RHEAs, limiting their deformation to a strain ≤30% and a

O. S. Bamisaye, N. Maledi, J. V. Merwe, D. Klenam, M. Bodunrin
School of Chemical and Metallurgical Engineering
Faculty of Engineering and the Built Environment
University of the Witwatersrand
Johannesburg 2050, South Africa
E-mail: 2503285@students.wits.ac.za

O. S. Bamisaye
Mechanical Engineering Department
Faculty of Air Engineering
Air Force Institute of Technology
800283 Kaduna, Nigeria

N. Maledi, J. V. Merwe, M. Bodunrin
DSI-NRF Centre of Excellence in Strong Materials
University of the Witwatersrand
Johannesburg 2050, South Africa

D. Klenam
Academic Development Unit
Faculty of Engineering and the Built Environment
University of Witwatersrand
Johannesburg 2050, South Africa

The ORCID identification number(s) for the author(s) of this article can be found under https://doi.org/10.1002/adem.202400538.

© 2024 The Author(s). Advanced Engineering Materials published by Wiley-VCH GmbH. This is an open access article under the terms of the Creative Commons Attribution-NonCommercial-NoDerivs License, which permits use and distribution in any medium, provided the original work is properly cited, the use is non-commercial and no modifications or adaptations are made.

DOI: 10.1002/adem.202400538

low strain rate of 10^{-3} s^{-1}. Typical RHEAs that have been reported include WTaMoNbTi (25%),[29] NbMoCrTiAl (20%),[23] $W_{0.4}MoNb_xTaTi$ (30%),[10] AlCrNbTiVZr (30%),[28] and $MoNbVTa_x$ (25%).[30]

TiNbTaVW is a single-body-centered-cubic (BCC) phase RHEA known for its high hardness and excellent corrosion resistance in chloride and acidic environments compared to the IN718 alloy.[31] However, the flow behavior, microstructural evolution, and high-temperature strength of the TiNbTaVW RHEA compared to IN718 have not been explored. Therefore, the softening mechanisms for the TiNbTaVW RHEA under high-temperature deformation are unknown. This study aimed to determine the isothermal compression behavior of the TiNbTaVW RHEA at temperatures of 950-1050 °C and a strain rate of 10^{-3} s^{-1} using the Gleeble 3500 thermomechanical simulator. Emphasis was placed on the flow behavior and microstructural evolution to determine the softening mechanisms and high-temperature strength.

2. Results and Discussion

2.1. Initial Phase and Microstructure

The phases and microstructures of the TiNbTaVW RHEA and IN718 alloy are presented in Figure 1 and are reproduced from previous work.[31] In Figure 1a, the X-ray diffraction (XRD) analysis result of the TiNbTaVW RHEA shows peaks indexed as the BCC solid solution phase (Im-3 m (229); $a = b = c = 3.2350$ Å), observed within a wide range of 2θ values between 46° and 103°. Also, a small peak at ≈41° was not accounted for because it could not be identified. The scanning electron microscope in backscattered electron (SEM-BSE) image of the TiNbTaVW RHEA exhibits a dendritic microstructure (Figure 1b). The XRD spectra of IN718 in Figure 1c show that γ(Fm-3 m (225); $a = b = c = 3.5920$ Å) and γ^{00} (Fm-3 m (225); $a = b = c = 3.6150$ Å) are the two major peaks present at a wide range of 2θ values between 51.7° and 111.7°. The γ and γ^{00} have been reported in some literature on wrought Inconel 718.[32-35] Microstructural analysis of the IN718 alloy shows fine-distributed γ grains and γ^{00} precipitated grains (Figure 1d). The elemental compositions of TiNbTaVW and IN718 are presented in Table 1 and 2 and are reproduced from previous work.

2.2. Stress-Strain Behavior

The stress-strain curves of the TiNbTaVW and IN718 obtained at 950 to 1050 °C and a strain rate of 10^{-3} s^{-1} are shown in Figure 2. The flow stress of both TiNbTaVW and IN718 is sensitive to deformation temperature, with high temperatures reducing the flow stress. High temperatures accelerate the movement of grain boundaries and dislocations, leading to softening and decreased stress.[19] At 950 °C, a steady-state flow stress followed

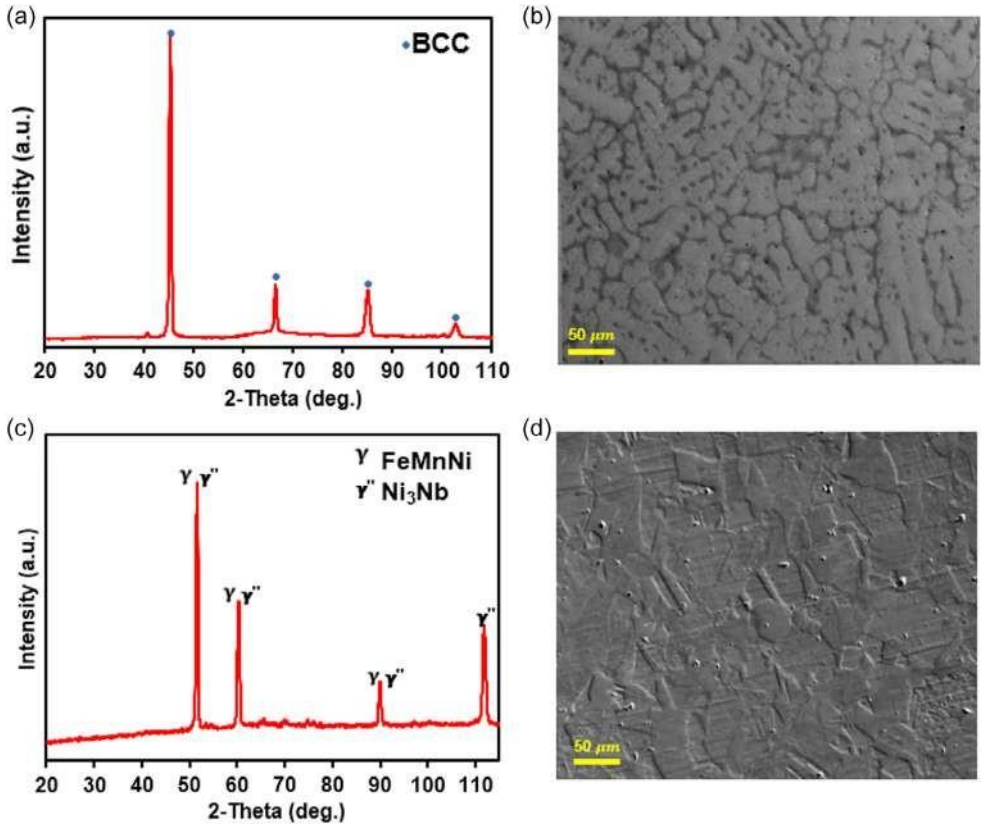

Figure 1. XRD pattern of the phase present in the TiNbTaVW RHEA: a) SEM-BSE image of the TiNbTaVW RHEA; b) XRD pattern of the phase present in the IN718 alloy; and c,d) SEM-BSE image of the IN718 alloy. Reproduced with permission.[31] Copyright 2024, Elsevier B.V.

© 2024 The Author(s). Advanced Engineering Materials published by Wiley-VCH GmbH

15272648, 0, Downloaded from https://onlinelibrary.wiley.com/doi/10.1002/adem.202400538 by Olufemi Sylvester Bamisaye - South African Medical Research, Wiley Online Library on [07/08/2024]. See the Terms and Conditions (https://onlinelibrary.wiley.com/terms-and-conditions) on Wiley Online Library for rules of use; OA articles are governed by the applicable Creative Commons License

Table 1. Composition distribution of the TiNbTaVW RHEA (at%). Reproduced with permission.[31] Copyright 2024, Elsevier B.V.

TiNbTaVW RHEA	Element	Ti	Nb	Ta	V	W
–	Actual	19 0.4	20 0.2	21 0.2	20 0.3	20 0.2
	Dendrite (grey)	14 0.8	19 0.5	24 0.5	15 1.1	28 1.9
	Interdendrite (dark)	32 1.5	19 0.3	12 0.8	29 0.6	8.0 1.0

Table 2. Composition distribution of the IN718 alloy (at%). Reproduced with permission.[31] Copyright 2024, Elsevier B.V.

IN718 alloy	Ti		Nb		Fe		Ni		Mn		S		C		Co		Al		Si		P		Cu	
–	0.12	0.02	0.22	0.02	57.95	0.1	36.56	0.4	0.5	0.1	0.06	0.1	3.63	0.1	0.14	0.04	0.12	0.02	0.37	0.02	0.1	0.01	0.23	0.01

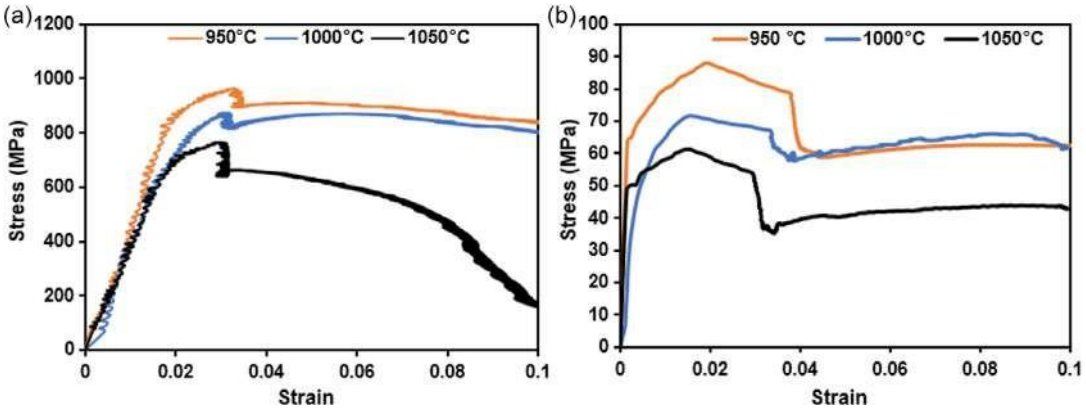

Figure 2. True stress-strain curves at 950–1050 °C and a strain rate of 10^{-3} s^{-1} for a) TiNbTaVW and b) IN718.

by a reduction in flow stress was observed in the TiNbTaVW (Figure 2a). At 1000 °C, a broad peak stress followed by a reduction in flow stress was observed. While at 1050 °C, continuous flow softening was observed in the TiNbTaVW. A broad peak stress has been attributed to DRX,[36,37] while continuous flow softening can suggest dynamic globularization, flow localization, or wedge cracking.[38,39] Continuous flow softening occurs when the rate of softening surpasses the work hardening rate.[40,41] Similarly, at 950 and 1050 °C, the flow curve of the IN718 alloy exhibits a steady-state flow stress (Figure 2b). While at 1000 °C, a steady-state stress followed by a reduction in flow stress was observed. A steady-state flow stress suggests either DRV or DRX.[42,43]

At 950–1050 °C, the flow curves of TiNbTaVW and IN718 at the elastic deformation stage exhibit a behavior characterized by a sudden increase in the flow stress followed by a drop. Similar phenomena have been reported in other alloys such as Ti-6Al-4 V,[44] HfNbTaTiZr,[12] $Ti_2ZrTa_{0.75}$,[45] $AlNbTi_3VZr_{1.5}$,[46] and $Ti_2ZrHfV_{0.5}Ta_{0.2}$.[21] This phenomenon may occur due to dislocation unlocking by solute atoms or the ending of short-range order.[21] Additionally, it could result from a change in strain rate at low strain during the hot deformation experiment.[44] Serrations were detected in the elastic region of the TiNbTaVW flow curve at 950–1050 °C. It was also detected at the plastic region of the TiNbTaVW and IN718 flow curves at 1050 and 1000 °C. Serrations occur due to the repeated pinning and depinning of solute atoms on dislocations.[47–50]

2.3. Microstructural Evolution

The optical and SEM-BSE images of TiNbTaVW and IN718 after deformation at 950, 1000, and 1050 °C at a strain rate of 10^{-3} s^{-1} are presented in Figure 3, 4, and 5. The deformed TiNbTaVW RHEA did not exhibit localized deformation features such as adiabatic shear bands but only voids (red arrows) at 950 °C (Figure 3a,b). The microstructure of TiNbTaVW at 950 °C comprises globular (black arrows) and elongated grains (blue arrows) (Figure 3a,b). Grain sizes of 44.45 5.0 μm were observed at 950 °C. At higher temperatures and lower strain rates, more time and energy can aid grain boundary migration and eventually promoting DRX. Elongated grains were also observed in some regions of the microstructure, suggesting DRV.

At 950 °C, no cracks or adiabatic shear bands appear in the microstructure of IN718 (Figure 3c,d). Equiaxed (black arrows) and elongated grains (blue arrows) are present in the microstructure at 950 °C, with grain sizes of 40.3 6.9 μm. Equiaxed grains (black arrows) are commonly seen in metals and alloys dynamically recrystallized during hot compression.[12]

At 1000 °C, the TiNbTaVW RHEA comprises globular (black arrows) and elongated grains (blue arrows) (Figure 4a,b). Some of the elongated grains are rotated in certain regions of the microstructure. The elongated grains suggest DRV. Finer grains (35.01 4.1 μm) were observed compared to grains at 950 °C (44.45 5.0 μm). Voids (red arrows) are still found in some

© 2024 The Author(s). Advanced Engineering Materials published by Wiley-VCH GmbH

15272648, 0, Downloaded from https://onlinelibrary.wiley.com/doi/10.1002/adem.202400538 by Olufemi Sylvester Bamisaye - South African Medical Research, Wiley Online Library on [07/08/2024]. See the Terms and Conditions (https://onlinelibrary.wiley.com/terms-and-conditions) on Wiley Online Library for rules of use; OA articles are governed by the applicable Creative Commons License

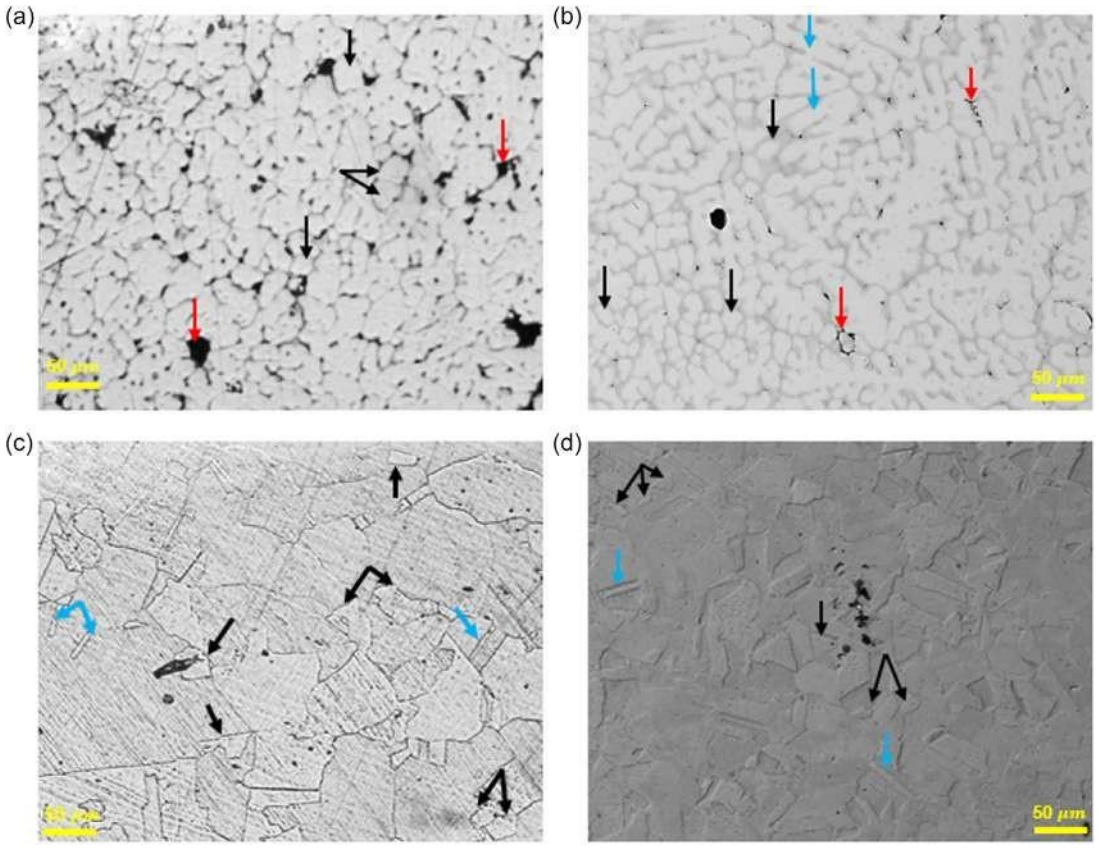

Figure 3. Microstructures of TiNbTaVW and IN718 after deformation at 950 °C/10^{-3} s^{-1}. a) Optical micrograph of TiNbTaVW showing globular grains (black arrows) and voids (red arrows); b) SEM-BSE image of TiNbTaVW showing globular grains (black arrows), elongated grains (blue arrows), and voids (red arrows); c) Optical micrograph of IN718 showing equiaxed grains (black arrows) and elongated grains (blue arrows); d) SEM-BSE image of IN718 indicating elongated (blue arrows) and equiaxed grains (black arrows).

regions of the microstructure. The globular grains also indicate that DRX occurred when the TiNbTaVW RHEA was deformed at 1000 °C. For the IN718 at 1000 °C, equiaxed (blue arrows) and globular (black arrows) grains were observed. A refined grain size of 38.31 7.5 μm was observed compared to 40.3 6.9 μm at 950 °C (Figure 4c,d). No visible cracks or voids are detected in the microstructure of IN718 at 1000 °C.

As the temperature was increased to 1050 °C, the TiNbTaVW RHEA exhibited mostly globular (black arrows) microstructures (Figure 5a,b). A few elongated grains (blue arrows) were observed at 1050 °C, indicating that most elongated grains at 1000 °C had fragmented into smaller globular grains. The presence of more globular grains indicates that the process of dynamic globularization was almost complete as the deformation temperature was increased to 1050 °C. This further signifies that the softening mechanism at 1050 °C is DRX. The grain size (31.43 3.9 μm) of the TiNbTaVW RHEA at 1050 °C is more refined compared to the grain sizes observed at 950 and 1000 °C. Voids were still observed at 1050 °C (Figure 5a,b). Few elongated (blue arrows) and several equiaxed (black arrows) grains were found in many regions of IN718 (Figure 5c,d). This signifies that the DRV and DRX softening mechanisms occur in IN718 at 1050 °C. The grain size of IN718 at 1050 °C is 34.84 3.9 μm, which is more refined than the grains observed at 950 °C and 1000 °C. Micro and huge voids (red arrows) appear in many regions of IN718 at 1050 °C. Some of the voids were found within elongated recrystallized and equiaxed grains.

2.4. Macrostructure of Deformed Samples

Stereo images of the hot deformed TiNbTaVW and IN718 at 950 °C to 1050 °C/10^{-3} s^{-1} are presented in Figure 6. Cracks appeared on the TiNbTaVW RHEA's surface at 950-1050 °C (Figure 6a-c). During the hot compression process, stress concentration occurs, leading to an increase in local energy. Once the stress concentration attains a certain threshold, energy is released in the form of cracks. According to Abubaker et al.[22] resultant stress concentration intensifies the creation and spread of microcracks unfavorable to deformation stability. At 950-1050 °C, surface spallation can be observed in the hot deformed IN718 alloy (Figure 6d-f).

2.5. High-Temperature Compression Strength

The high-temperature compression strength of the TiNbTaVW RHEA and the IN718 alloy, compared to other RHEAs and alloys used for high-temperature applications, is depicted in Figure 7.

© 2024 The Author(s). Advanced Engineering Materials published by Wiley-VCH GmbH

15272648, 0, Downloaded from https://onlinelibrary.wiley.com/doi/10.1002/adem.202400538 by Olufemi Sylvester Bamisaye - South African Medical Research, Wiley Online Library on [07/08/2024]. See the Terms and Conditions (https://onlinelibrary.wiley.com/terms-and-conditions) on Wiley Online Library for rules of use; OA articles are governed by the applicable Creative Commons License

15272648, 0, Downloaded from https://onlinelibrary.wiley.com/doi/10.1002/adem.202400538 by Olufemi Sylvester Bamisaye - South African Medical Research , Wiley Online Library on [07/08/2024]. See the Terms and Conditions (https://onlinelibrary.wiley.com/terms-and-conditions) on Wiley Online Library for rules of use; OA articles are governed by the applicable Creative Commons License

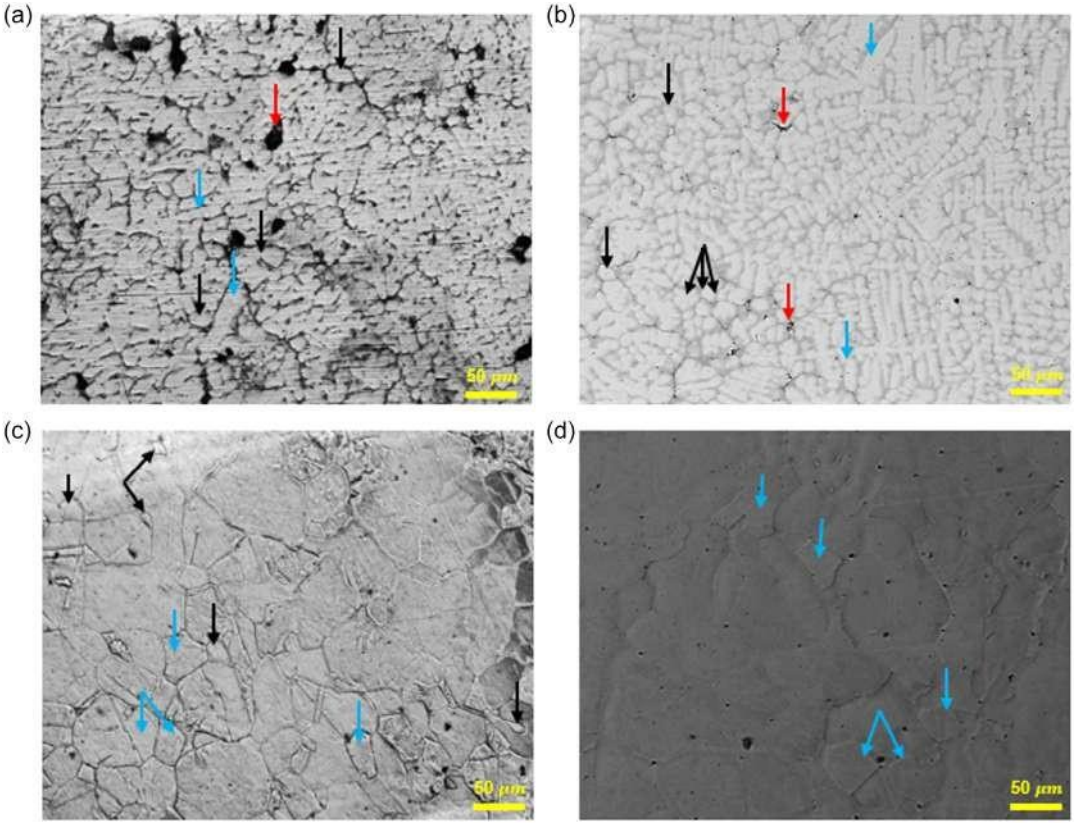

Figure 4. Microstructures of the TiNbTaVW and IN718 after deformation at 1000 °C/10^{-3} s^{-1}. a) Optical micrograph of TiNbTaVW showing globular grains (black arrows), elongated grains (blue arrows), and voids (red arrows); b) SEM-BSE image of TiNbTaVW showing globular grains (black arrows), elongated grains (blue arrows), and voids (red arrows); c) Optical micrograph of IN718 showing equiaxed grains (blue arrows) and globular grains (black arrows); d) SEM-BSE image of IN718 indicating equiaxed grains (blue arrows).

The TiNbTaVW RHEA exhibits higher temperature strengths of 910, 870, and 658 MPa compared to the IN718 alloy, which has 72, 87, and 61 MPa at 950, 1000, and 1050 °C/10^{-3} s^{-1}, respectively. The high-temperature strength of TiNbTaVW RHEA at 950–1050 °C surpasses that of the compared RHEAs and superalloys (Figure 7). However, at 1000 and 1050 °C, the high-temperature strength of TiNbTaVW decreases significantly. According to Yurchenko et al.[51] the loss of strength in RHEAs can be induced by the activation of diffusion-controlled processes.

According to Senkov et al.[52] the decreasing strength of RHEAs at higher temperatures can be attributed to diffusion-controlled processes that start to dominate as the solid solution diminishes. Compared with conventional alloys, RHEAs exhibit a higher softening temperature (0.6–0.8 T_m).[27,53] The high-temperature strength of the TiNbTaVW can be attributed to the addition of high-melting-point elements such as Nb, Ta, and W. The addition of Ta, Nb, and Mo can greatly balance the mechanical properties of RHEAs at higher temperatures.[30,54] Solid solution strengthening effectively functions in RHEAs at temperatures below 1186 °C.[52] Furthermore, the higher-temperature strength of the TiNbTaVW RHEA can also be linked to the considerably larger atomic radii of Ti (1.46Å), Ta (1.46Å), and Nb (1.43Å) compared to the atomic radii of V (1.32Å) and W (1.39 Å). This difference in atomic radii causes lattice distortion, which enhances strengthening via solid solution.[31] High-entropy alloys have excellent high-temperature strength due to the solid solution strengthening effect induced by severe lattice distortion and the thermodynamically favorable high-entropy effect.[30]

The strengthening mechanisms of alloys mainly comprise grain boundary strengthening (Hall-Petch), solid solution strengthening, and second-phase particle strengthening.[7,11,55,56] In this study, the TiNbTaVW RHEA has a single-phase BCC structure, so second-phase particle strengthening (precipitation strengthening and interstitial strengthening) does not exist in the solid solution. Therefore, grain boundary strengthening and solid solution strengthening are expected to be the main strengthening mechanisms. The solid solution strength can be determined as[7,30]

$$\sigma_{cs} \approx \sigma_{mix} + \sigma_{ss} \quad (1)$$

where σ_{cs} is the compressive strength of the TiNbTaVW RHEA at 950–1050 °C (910, 870, and 658 MPa), σ_{mix} is the individual elemental compressive strength at 950–1050 °C estimated using the rules of mixture, and $\Delta\sigma_{ss}$ is the solid solution strength. The individual elemental high-temperature values at 950–1050 °C for Ti (55, 44, and 37 MPa),[57] Nb (107, 97, and 87 MPa),[58] and Ta (150, 124, and 92 MPa)[59] are considered. Furthermore, the

© 2024 The Author(s). Advanced Engineering Materials published by Wiley-VCH GmbH

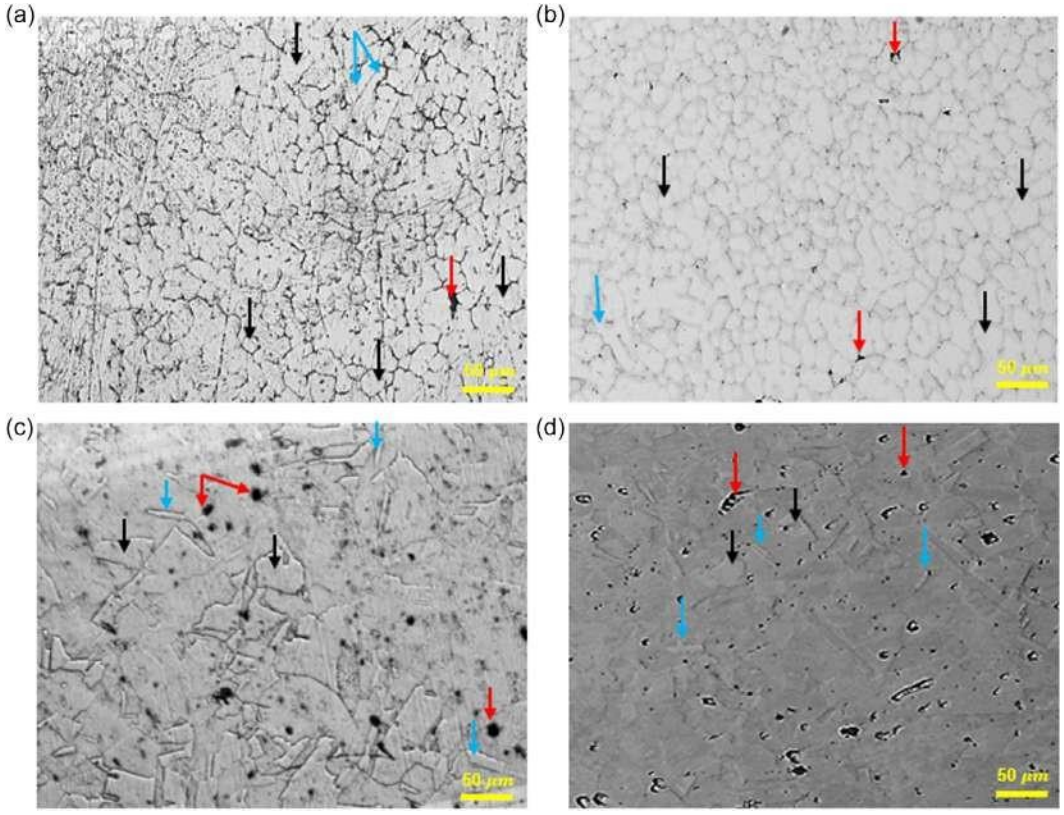

Figure 5. Microstructures of TiNbTaVW and IN718 after deformation at 1050 °C/10^{-3} s^{-1}. a) Optical micrograph of TiNbTaVW showing globular grains (black arrows), elongated grains (blue arrows), and voids (red arrows); b) SEM-BSE image of TiNbTaVW showing globular grains (black arrows), elongated grains (blue arrows), and voids (red arrows); c) Optical micrograph of IN718 showing equiaxed (black arrows), elongated recrystallized grains (blue arrows) and voids (red arrows); d) SEM-BSE image of IN718 indicating equiaxed (black arrows), elongated recrystallized grains (blue arrows) and voids (red arrows).

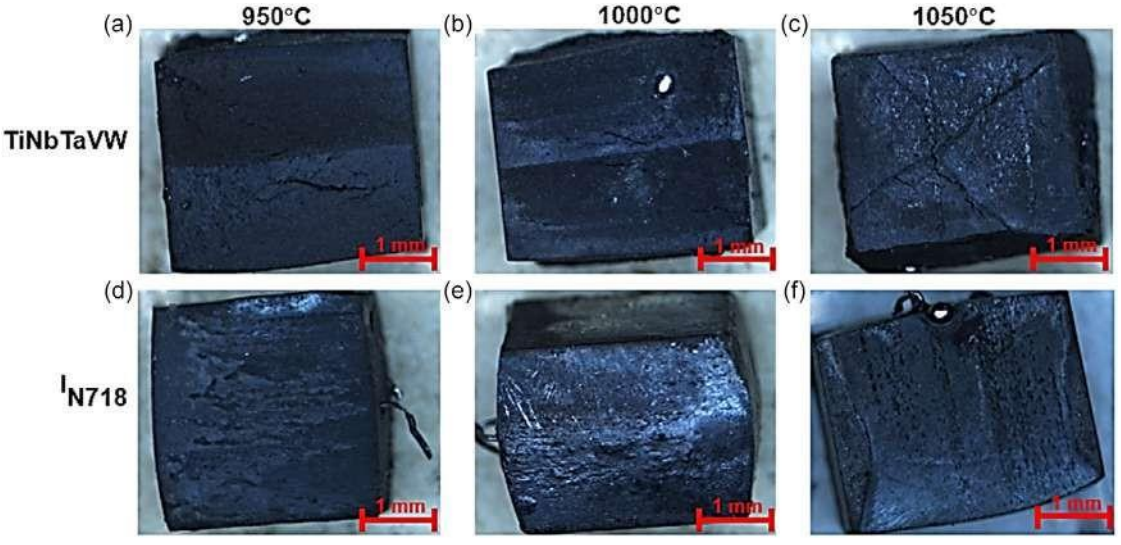

Figure 6. Stereo images of the TiNbTaVW and IN718 surface after deformation at 950–1050 °C/10^{-3} s^{-1}.

© 2024 The Author(s). Advanced Engineering Materials published by Wiley-VCH GmbH

15272648, 0, Downloaded from https://onlinelibrary.wiley.com/doi/10.1002/adem.202400538 by Olufemi Sylvester Bamisaye - South African Medical Research , Wiley Online Library on [07/08/2024]. See the Terms and Conditions (https://onlinelibrary.wiley.com/terms-and-conditions) on Wiley Online Library for rules of use; OA articles are governed by the applicable Creative Commons License

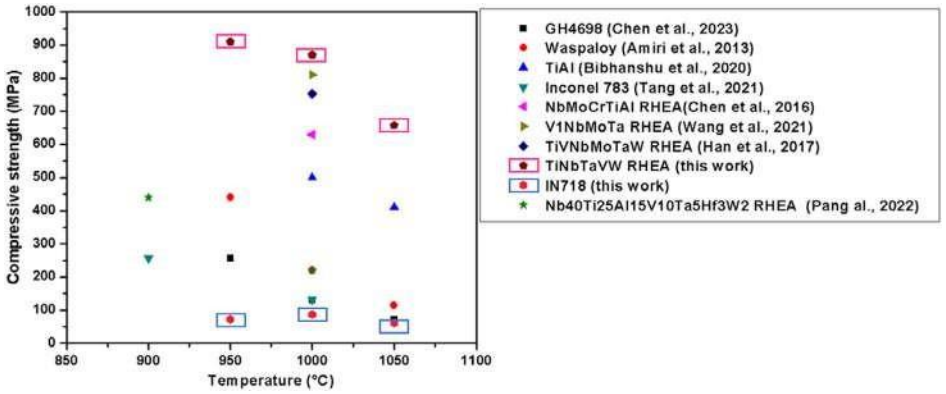

Figure 7. High-temperature strength of TiNbTaVW and IN718 compared to superalloys[77-80] and other RHEAs[23,26,81,82] at 950–1050 °C.

elemental high-temperature values are 155, 79, and 52 Mpa for V[58] and 407, 381, and 324 MPa for W.[60] Using Equation (1), the $\Delta\sigma_{ss}$ is 735, 726, and 538 MPa at 950, 1000, and 1050 °C, respectively.

In addition to solid solution strengthening, the effect of grain size was also considered. Grain boundary strengthening is recognized for its efficiency in grain refining, increasing the strength of polycrystalline metals and alloys.[61] The grain boundary contribution to the strength of the TiNbTaVW RHEA satisfies the temperature dependence of the Hall-Petch relationship as defined in Equation (2).[62]

$$\sigma_{cs}(T) = 120 + 659d^{-0.5} + 597\exp(-(T-120)/(-0.39Td^{-0.5})) \quad (2)$$

where d is the grain size of 44.45, 35.01, and 31.43 μm at temperatures of 950 °C (1223 K), 1000 °C (1273 K), and 1050 °C (1323 K). By substituting the d and T values into Equation (2), the grain boundary contribution to the compressive strength of TiNbTaVW RHEA is 147, 147, and 145 MPa, respectively. It is evident that both solid solution strengthening and grain boundary strengthening contribute to the high-temperature strength of the TiNbTaVW RHEA.

3. Discussion

3.1. Serrations and Sudden Stress Drop Phenomenon

Several softening mechanisms, such as DRV, DRX, dynamic globularization, superplasticity, and flow localization, can occur during hot deformation. Among these mechanisms, DRV, DRX, dynamic globularization, and superplasticity are considered safe, while flow localization, wedge cracking, and adiabatic shear banding are unsafe.[39,63] During the initial stages of deformation, flow stress increases as dislocations interact and multiply. As dislocation density rises, the driving force for recovery also increases.[64] Subsequently, due to the effect of DRX, dislocation density significantly decreases, leading to a gradual drop in flow stress. At 950 °C, the TiNbTaVW RHEA flow curve exhibits a steady-state flow stress followed by a drop in flow stress, indicating the occurrence of DRV and DRX (Figure 2a). At 1000 °C, a broad peak stress followed by a drop in flow stress indicates DRX. At 1050 °C, continuous flow softening was observed, indicating dynamic globularization as the main softening mechanism.[38,39] For the IN718 alloy, steady-state stress was more evident at 950 and 1050 °C, indicating the occurrence of DRV or DRX, while a drop in flow stress at 1000 °C indicates DRX (Figure 2b).

A series of initial peak rises and sudden stress drops were observed in TiNbTaVW and IN718 at 950-1050 °C, which differ from the stress drop phenomenon typically attributed to DRX.[37] Eleti et al.[12] conducted an interrupted hot deformation experiment to elucidate further the reason behind the initial peak rise and sudden stress drop. They found a distinctive drop in the flow stress of the HfNbTaTiZr RHEA around yielding at a strain of ≈0.1, followed by continuous flow softening at 1000-1200 °C/10^{-2}-10^{-4} s^{-1}. An interrupted test conducted at 1000 °C, held for 600 s, and then deformed at a strain rate of 0.001 s^{-1} revealed no clearly observed DRX grains corresponding to the large stress drop. The authors attributed this unusual stress drop to either dislocation unlocking by solute atoms or the ending of short-range ordered structures.

Li et al.[21] also found a stress drop at a strain of ≈0.05 when $Ti_2ZrHfV_{0.5}Ta_{0.2}$ was deformed at 900-1100 °C/10^{-1}-10^{-2} s^{-1}. An interrupted deformation test was carried out at 900 °C/10^{-1} s^{-1}, held for 0 and 600 s intervals, and then deformed at a strain rate of 0.1 s^{-1}. The drop in the flow stress of $Ti_2ZrHfV_{0.5}Ta_{0.2}$ was attributed to dislocation unlocking pinned by a Cottrell atmosphere or short-range order. However, in the TiNbTaVW, the pinning of dislocations by solute atoms or interstitial solute atoms (N and C) is unlikely to occur because it is an equiatomic alloy. The rapid increase in flow stress and subsequent stress drops in TiNbTaVW and IN718 in this study are not caused by dislocation pinning but rather by a change in strain rate at a strain of 0.03-0.035, as depicted in Figure 8. The high strain rates (0.06 s^{-1}) at the beginning of deformation, compared to 0.001 s^{-1}, contributed to a rapid increase in flow stress and stress drops observed on the flow curves of the TiNbTaVW RHEA. For IN718, the high strain rates (0.1 s^{-1}) at the beginning of deformation compared to 0.001 s^{-1} led to the rapid increase in flow stress and stress drops observed on the flow curves. Although the overall strain rate remained unaffected, the misleading initial peak rise and stress drops in the flow stress were not a consequence of the microstructural response to the imposed parameters but were due to variations in the hydraulic motion regulating the compression jaws of the Gleeble simulator.

© 2024 The Author(s). Advanced Engineering Materials published by Wiley-VCH GmbH

15272648, 0, Downloaded from https://onlinelibrary.wiley.com/doi/10.1002/adem.202400538 by Olufemi Sylvester Bamisaye - South African Medical Research, Wiley Online Library on [07/08/2024]. See the Terms and Conditions (https://onlinelibrary.wiley.com/terms-and-conditions) on Wiley Online Library for rules of use; OA articles are governed by the applicable Creative Commons License

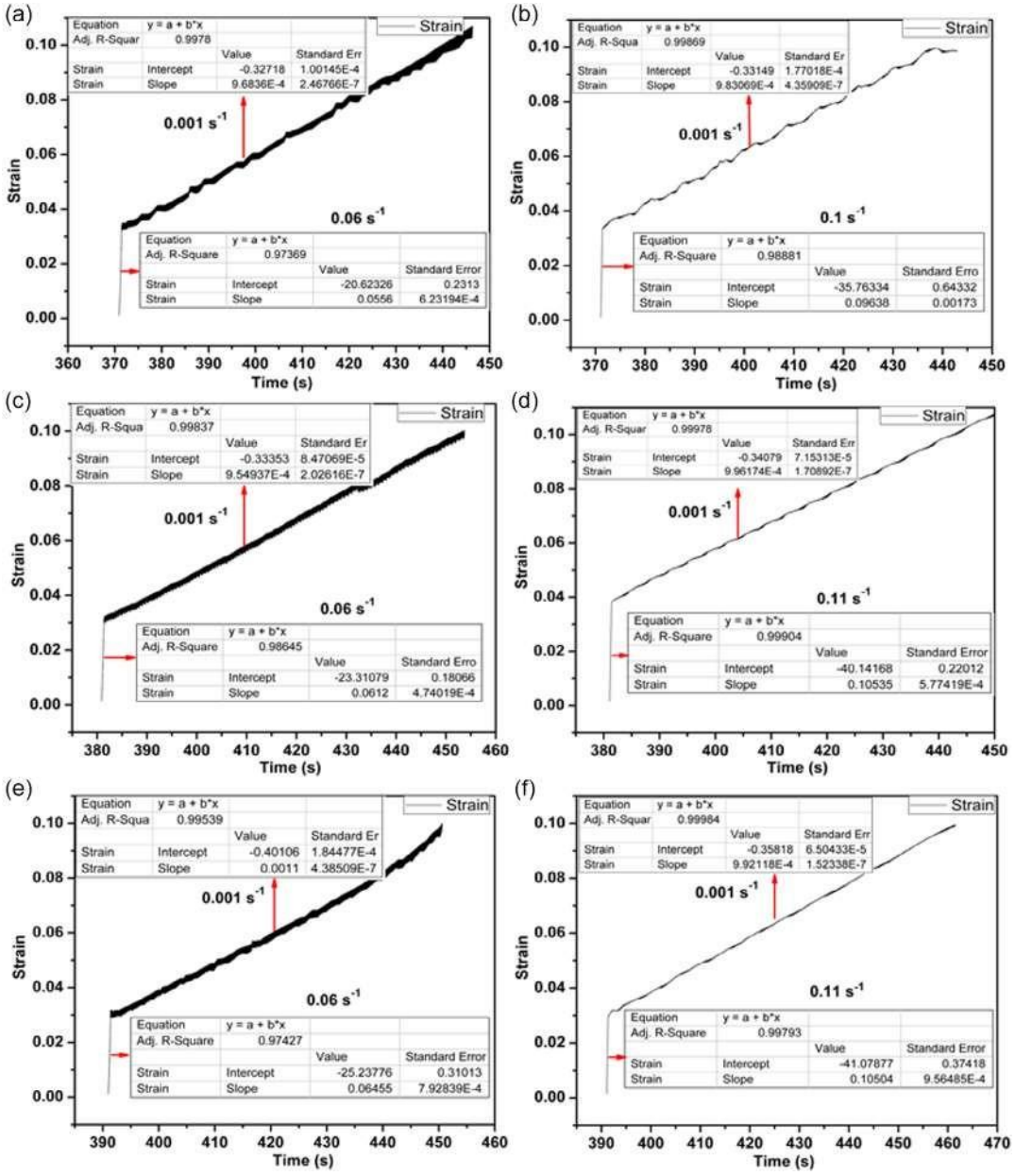

Figure 8. Strain versus time profile at 950 °C/10^{-3} s^{-1} for a) TiNbTaVW and b) IN718. Strain versus time profile at 1000 °C/10^{-3} s^{-1} for c) TiNbTaVW and d) IN718. Strain versus time profile at 1050 °C/10^{-3} s^{-1} for e) TiNbTaVW and f) IN718.

Serrations, characterized by jerky stress-strain curves in solid materials, arise from dislocation motion.[50] It has been observed in flow curves of hot deformed RHEAs such as $Ti_2ZrHfV_{0.5}Ta_{0.2}$,[21] $Al_xNb_{40}Ti_{40}V_{20}$-**x**,[51] and NbZrTiTa.[20] In the TiNbTaVW RHEA, serrations were seen in both the elastic and plastic regions. At the elastic deformation stage, serrations were observed in the initial peak flow curve of the TiNbTaVW RHEA at 950-1050 °C before the sudden stress drop. Serrated flow stress curves are classified into Type A, Type B, and Type C.[50] The observed serrations in the flow curve of the TiNbTaVW RHEA at the elastic region are similar to Type B.[45,50] Type-B serrations often emerge at the beginning of serrated flow stress, yielding higher temperatures and lower strain rates.[50] Type-B serrations emerge at multiple points along the flow curves, propagate briefly, and then disappear. The elastic region serrations in some RHEAs, like MoNbVTiHf,[65] MoNbTaW,[66] and HfNbTaTiZr,[67] also disappear before the stress drop and are often attributed to machine noise as dislocations at this stage are immobile. Since the serrations occurred at the elastic region in the TiNbTaVW RHEA and dislocation will be immobile at this stage, it can be said that the serrations are a result of machine noise. However, serrations observed in the plastic region of the flow curves of TiNbTaVW at 1050 °C and IN718 at 1000 °C can be attributed to dislocation motion.

© 2024 The Author(s). Advanced Engineering Materials published by Wiley-VCH GmbH

15272648, 0, Downloaded from https://onlinelibrary.wiley.com/doi/10.1002/adem.202400538 by Olufemi Sylvester Bamisaye - South African Medical Research, Wiley Online Library on [07/08/2024]. See the Terms and Conditions (https://onlinelibrary.wiley.com/terms-and-conditions) on Wiley Online Library for rules of use; OA articles are governed by the applicable Creative Commons License

15272648, 0, Downloaded from https://onlinelibrary.wiley.com/doi/10.1002/adem.202400538 by Olufemi Sylvester Bamisaye - South African Medical Research, Wiley Online Library on [07/08/2024]. See the Terms and Conditions (https://onlinelibrary.wiley.com/terms-and-conditions) on Wiley Online Library for rules of use; OA articles are governed by the applicable Creative Commons License

Dislocation motion is essential to describe plasticity in crystalline materials as their mobility controls the material's ability to accommodate strain and modify its microstructure.[68]

3.2. Occurrence of Dynamic Recovery and Recrystallization

Grain growth is primarily driven by atomic diffusion and lower strain rates coupled with higher temperatures.[14,20,45] This provides sufficient time and energy for atomic diffusion, facilitating grain boundary movement and eventual grain growth. Globular and elongated grains were observed in the TiNbTaVW alloy at 950 °C, signifying both DRV and dynamic globularization as the softening mechanisms. This corroborates with the flow curve at 950 °C having steady-state flow stress followed by a drop in flow stress. Similarly, at 1000 °C, globular and elongated grains were observed in the TiNbTaVW alloy. However, the flow curve only shows the characteristics of DRX and as confirmed by the globular grains. The occurrence of elongated grains also signifies DRV. Therefore, the softening mechanisms of TiNbTaVW at 1000 °C are still considered DRV and dynamic globularization. The occurrence of both globular and elongated grains has also been observed in the $TiAlVNb_2$ RHEA.[19] At 1050 °C, dynamic globularization is the softening mechanism, as corroborated by the continuous flow softening in the flow curve. Dynamic globularization has been previously reported as a form of DRX.[38,69–72] This mechanism occurs at low strain rates and high deformation temperatures.[44] Equiaxed and elongated grains were observed in IN718 at 950 °C and 1050 °C, as corroborated by steady-state stress, suggesting either DRV or DRX.[42,43] Due to the occurrence of equiaxed and elongated grains, the softening mechanisms for IN718 at 950 and 1050 °C are both DRX and DRV. However, at 1000 °C, mostly equiaxed grains were observed, as corroborated by oscillations and a reduction in the flow curve, signifying DRX. Therefore, DRX is the softening mechanism for IN718 at 1000 °C. The refinement of grains in TiNbTaVW and IN718 is attributed to the characteristics of repeated nucleation and limited growth during DRX. This DRX occurrence promotes grain refinement and reduces deformation resistance in alloys, enhancing their workability and mechanical properties.[14]

Voids were detected near recrystallized grains during the deformation of TiNbTaVW at 950–1050 °C (Figure 3–5). The presence of voids, cracks, and cavities at grain boundaries results from stress concentration, which is more prone to occur at grain boundaries and triple-junction points.[10,73] Under stress loading conditions, cracks propagate along high-angle grain boundaries, resulting in brittle fracture of the alloy in the intergranular region.[74] The higher presence of voids at 950 and 1000 °C compared to 1050 °C may be due to limited dislocation mobility and diffusion,[22,73] which fail to relieve stress concentrations. According to Zhao et al.[75] cracks, voids, and pores can be eliminated with increasing deformation temperature and decreasing strain rate. As the temperature was increased to 1050 °C in TiNbTaVW, the number of voids decreased. However, minipores and large voids were observed in IN718 at 1050 °C (Figure 5c,d), possibly due to stress concentration and inadequate diffusion rates at grain boundaries.[73] Refined grains can impede crack and pore propagation during deformation by increasing the energy barrier required to create new surfaces.[22,76] The TiNbTaVW RHEA at 1050 °C (Figure 5a,b) comprises refined globular grains, which could reduce void propagation.

4. Conclusion

This study investigated the deformation behavior, microstructural evolution, and high-temperature strength of the TiNbTaVW RHEA at 950, 1000, and 1050 °C, with a strain rate of 10^{-3} s^{-1}. This was compared with a commercial-grade nickel-based superalloy, IN718. The following conclusions are drawn from the study. 1) The TiNbTaVW RHEA exhibited a single-BCC phase with a dendritic structure. 2) The TiNbTaVW and IN718 flow curves decreased with an increasing deformation temperature at a constant strain rate. 3) The presence of both globular and elongated grains in the TiNbTaVW alloy at 950 and 1000 °C confirmed that dynamic globularization and DRV are the softening mechanisms. At 1050 °C, mainly globular grains were observed, indicating dynamic globularization as the softening mechanism. In IN718, equiaxed and elongated grains at 950 and 1050 °C suggested both DRX and DRV as the softening mechanisms. At 1000 °C, the dominance of equiaxed grains signified DRX as the only softening mechanism. 4) Voids were found in the microstructure of the TiNbTaVW RHEA at 950 to 1050 °C, whereas minipores and voids were only detected at 1050 °C for the IN718. 5) The TiNbTaVW RHEA has higher-temperature strengths of 910, 870, and 658 MPa, compared to the IN718 alloy, with 72, 87, and 61 MPa at 950, 1000, and 1050 °C/10^{-3} s^{-1}, respectively. The higher-temperature strength of the TiNbTaVW RHEA can be attributed to both solid solution strengthening and grain boundary strengthening.

This work resulted in an advance by providing a comprehensive analysis of the flow behavior and microstructure of the TiNbTaVW RHEA during hot deformation. By demonstrating comparable or superior performance in specific aspects, the RHEA could be considered in the near future for potential applications traditionally dominated by nickel-based superalloys. This opens new possibilities for RHEAs in high-temperature applications, traditionally dominated by nickel-based superalloys, thereby expanding the material options available for advanced engineering applications.

5. Experimental Section

The TiNbTaVW RHEA was produced through vacuum arc melting under ultrahigh-purity argon gas on a water-cooled copper hearth to obtain an arc-melted alloy. The RHEA was produced using commercial high-purity raw elemental powders comprising Ti (99.7 wt% purity), Nb (99.9 wt% purity), V (99.9 wt% purity), Ta (99.95 wt% purity), and W (99.9 wt% purity) supplied by Weartech (Pty) Limited, South Africa. The TiNbTaVW samples were flipped and remelted three times to ensure chemical homogeneity. Additionally, a nickel-based IN718 superalloy was acquired. Rectangular samples of 6 × 6 × 9 mm^3 for the hot compression tests were machined using a Gold San CNC wire cutting electrical discharge machining (EDM) machine. The alloys were subjected to hot deformation testing using a Gleeble 3500 thermomechanical simulator. A type R (platinum-rhodium) thermocouple was welded to the midspan of the rectangular test samples using a spot welder to ensure precise temperature control and measurement. Graphite foil and nickel paste were

© 2024 The Author(s). Advanced Engineering Materials published by Wiley-VCH GmbH

placed between the Iso-T tungsten carbide anvils and the specimens to reduce friction effects during deformation. Prior to the compression test, the deformation chamber was evacuated to 2.0 × 10^0 Pa and subsequently filled with inert Ar gas to prevent oxidation.

For each test, the samples were heated to a set deformation temperature of 950, 1000, and 1050 °C at a heating rate of 5 °C s^{-1} and held at this temperature for 180 s to ensure homogenization before compression. The deformation temperatures were chosen based on the hot working conditions of conventional superalloys.[77-79] The samples were deformed at a strain rate of 10^{-3} s^{-1} and a total strain of 0.1, followed by air cooling to retain the microstructure. The TiNbTaVW RHEA was only compressed to a strain of 0.10 due to its brittle nature at high temperatures. The RHEAs that were hot worked at a low strain rate of 10^{-3} s^{-1} included $WTaMoNbTi$,[29] $NbMoCrTiAl$,[23] $W_{0.4}MoNb_xTaTi$,[10] $AlCrNbTiVZr$,[28] and $MoNbVTa_x$.[30] Afterward, the stress–strain data obtained from the hot compression tests were plotted to analyze the shape of the stress–strain curves. For microstructural analysis, the deformed samples were sectioned into two halves, mounted, polished, and then etched in Kroll's reagent. The samples were examined under an Olympus SC50 optical microscope in bright-field mode and a high-resolution Zeiss Sigma field-emission SEM–BSE imaging mode at 15 kV.

Conflict of Interest

The authors declare no conflict of interest.

Author Contributions

Olufemi Sylvester Bamisaye: Conceptualization: (supporting); Data curation: (lead); Formal analysis: (lead); Investigation: (lead); Methodology: (equal); Validation: (equal); Visualization: (lead); Writing—original draft: (lead). Nthabiseng Maledi: Conceptualization: (lead); Funding acquisition: (lead); Methodology: (equal); Project administration: (lead); Resources: (lead); Supervision: (lead); Validation: (equal); Writing—review and editing: (lead). Josias Van der Merwe: Conceptualization: (lead); Funding acquisition: (lead); Methodology: (equal); Project administration: (lead); Resources: (lead); Supervision: (lead); Validation: (equal); Writing—review and editing: (lead). Michael Bodunrin: Conceptualization: (lead); Funding acquisition: (lead); Methodology: (equal); Project administration: (lead); Resources: (lead); Supervision: (lead); Validation: (equal); Writing—review and editing: (lead). Desmond Klenam: Contributions Validation: (equal); Writing—review and editing (lead).

Data Availability Statement

The data that support the findings of this study are available from the corresponding author upon reasonable request.

Keywords

dynamic globularization, dynamic recrystallization, elongated grain, hot working, softening mechanism

Received: February 29, 2024
Revised: July 6, 2024
Published online:

[1] R. C. Reed, in *The Superalloys Fundamentals and Applications*, Cambridge University Press, New York 2006.
[2] R. Jiang, Y. D. Song, P. A. Reed, *Int. J. Fatique* 2020, *141*, 105887.
[3] J. W. Yeh, S. K. Chen, S. J. Lin, J. Y. Gan, T. S. Chin, T. T. Shun, C. H. Tsau, S. Y. Chang, *Adv. Eng. Mater.* 2004, *6*, 299.
[4] O. N. Senkov, G. B. Wilks, D. B. Miracle, C. P. Chuang, P. K. Liaw, *Intermetallics* 2010, *18*, 1758.
[5] Q. Liu, G. Wang, Y. Liu, X. Sui, Y. Chen, S. Luo, *Mater. Sci. Eng. A* 2021, *809*, 140922.
[6] D. B. Miracle, O. N. Senkov, *Acta Mater.* 2017, *122*, 448.
[7] X. W. Nie, M. D. Cai, S. Cai, *Int. J. Refract. Metals Hard Mater.* 2021, *98*, 105568.
[8] M. Sadeghilaridjani, M. Pole, S. Jha, S. Muskeri, N. Ghodki, S. Mukherjee, *Wear* 2021, *478–479*, 203916.
[9] O. A. Waseem, H. J. Ryu, O. Ahmed, H. Jin, *J. Alloys Compd.* 2020, *845*, 155700.
[10] W. Wei, T. Wang, C. Wang, M. Wu, Y. Nie, J. Peng, *Mater. Lett.* 2021, *295*, 129753.
[11] L. Raman, A. Anupam, G. Karthick, C. C. Berndt, A. S. M. Ang, S. V. S. Narayana Murty, D. Fabijanic, B. S. Murty, R. S. Kottada, *Mater. Sci. Eng., A* 2021, *819*, 141503.
[12] R. R. Eleti, T. Bhattacharjee, A. Shibata, N. Tsuji, *Acta Mater.* 2019, *171*, 132.
[13] O. S. Bamisaye, N. Maledi, J. Van der Merwe, D. E. P. Klenam, M. O. Bodunrin, A. D. Akinwekomi, *Manuf. Rev.* 2023, *10*, 12.
[14] N. N. Guo, L. Wang, L. S. Luo, X. Z. Li, R. R. Chen, Y. Q. Su, J. J. Guo, H. Z. Fu, *Mater. Sci. Eng., A* 2016, *651*, 698.
[15] Y. Zhang, Y. Liu, Y. Li, X. Chen, H. Zhang, *Mater. Lett.* 2016, *174*, 82.
[16] F. Dong, Y. Yuan, W. Li, Y. Zhang, P. K. Liaw, X. Yuan, H. Huang, *Intermetallics* 2020, *126*, 106921.
[17] R. R. Eleti, A. H. Chokshi, A. Shibata, N. Tsuji, *Acta Mater.* 2020, *183*, 64.
[18] M-l. Hu, W-d. Song, D-b. Duan, Y. Wu, *Int. J. Mech. Sci.* 2020, *182*, 105738.
[19] Z. C. Bai, X. F. Ding, Q. Hu, M. Yang, Z. T. Fan, X. W. Liu, *J. Alloys Compd.* 2021, *885*, 160962.
[20] B. Wang, X. Shan, H. Zhao, S. Bai, B. Wang, Y. Tian, Y. Tang, *J. Alloys Compd.* 2023, *936*, 168059.
[21] T. Li, Y. Lu, Z. Li, T. Wang, T. Li, *Intermetallics* 2022, *146*, 107586.
[22] M. Abubaker, T. Wang, C. Feng, H. Sun, B. Wang, M. Hamza, M. A. Afifi, W. Liao, *Mater. Des.* 2022, *222*, 111034.
[23] H. Chen, A. Kauffmann, B. Gorr, D. Schliephake, C. Seemüller, J. N. Wagner, H. J. Christ, M. Heilmaier, *J. Alloys Compd.* 2016, *661*, 206.
[24] C. Duan, X. Li, E. Werner, *Int. J. Refract. Metals Hard Mater.* 2023, *115*, 106292.
[25] Y. Jia, L. Zhang, P. Li, X. Ma, L. Xu, S. Wu, Y. Jia, *Front Mater.* 2020, *7*, 00172.
[26] J. Pang, H. H. Zhang, L. Zhang, Z. Zhu, H. Fu, H. Li, A. Wang, Z. Li, H. H. Zhang, *Mater. Sci. Eng., A* 2022, *831*, 142290.
[27] O. N. Senkov, C. F. Woodward, *Mater. Sci. Eng., A* 2011, *529*, 311.
[28] N. Y. Yurchenko, E. S. Panina, G. A. Salishchev, N. D. Stepanov, *Phys. Mesomech.* 2021, *24*, 642.
[29] Y. Wan, Q. Wang, J. Mo, Z. Zhang, X. Wang, X. Liang, B. Shen, *Adv. Eng. Mater.* 2021, *2100765*, 00765.
[30] W. Zheng, S. Lü, S. Wu, X. Chen, W. Guo, *Mater. Sci. Eng., A* 2022, *850*, 143554.
[31] O. S. Bamisaye, N. Maledi, J. Van der Merwe, M. O. Bodunrin, *J. Alloys Compd.* 2024, *983*, 173803.
[32] W. Huang, J. Yang, H. Yang, G. Jing, Z. Wang, X. Zeng, *Sci. Eng., A* 2019, *750*, 98.
[33] N. El-Bagoury, M. M. Hessien, M. Alsawat, M. H. H. Mahmoud, A. K. Alanazi, N. A. Alshanbari, *Metallogr. Microstruct. Anal.* 2019, *8*, 642.
[34] S. Luo, W. Huang, H. Yang, J. Yang, Z. Wang, X. Zeng, *Addit. Manuf.* 2019, *30*, 100875.
[35] V. A. Popovich, E. V. Borisov, A. A. Popovich, V. S. Sufiiarov, D. V. Masaylo, L. Alzina, *Mater. Des.* 2017, *131*, 12.
[36] M. J. Luton, C. M. Sellars, *Acta Metall.* 1969, *17*, 1033.

© 2024 The Author(s). Advanced Engineering Materials published by Wiley-VCH GmbH

15272648, 0, Downloaded from https://onlinelibrary.wiley.com/doi/10.1002/adem.202400538 by Olufemi Sylvester Bamisaye - South African Medical Research, Wiley Online Library on [07/08/2024]. See the Terms and Conditions (https://onlinelibrary.wiley.com/terms-and-conditions) on Wiley Online Library for rules of use; OA articles are governed by the applicable Creative Commons License

[37] K. Huang, R. E. Logé, *Mater. Des.* 2016, *111*, 548.
[38] T. Seshacharyulu, S. C. Medeiros, W. G. Frazier, Y. V. R. K. Prasad, *Mater. Sci. Eng.* 2002, *A325*, 112.
[39] Y. V. R. K. Prasad, T. Seshacharyulu, *Int. Mater. Rev.* 1998, *43*, 243.
[40] G. Z. Quan, Y. Wang, Y. Y. Liu, J. Zhou, *Mater. Res.* 2013, *16*, 1092.
[41] T. Sakai, A. Belyakov, R. Kaibyshev, H. Miura, J. J. Jonas, *Prog. Mater. Sci.* 2014, *60*, 130.
[42] H. J. McQueen, C. A. C. Imbert, *J. Alloys Compd.* 2004, *378*, 35.
[43] H. J. McQueen, N. D. Ryan, *Mater. Sci. Eng., A* 2002, *322*, 43.
[44] M. O. Bodunrin, L. H. Chown, J. W. Van Der Merwe, K. K. Alaneme, *Mater. Sci. Eng., A* 2020, *791*, 139622.
[45] B. Wang, H. Zhao, X. Shan, Y. Tang, B. Wang, Y. Tian, *Mater. Character.* 2023, *203*, 113061.
[46] Z. Yu, B. Xie, Z. Zhu, B. Xu, M. Sun, *J. Alloys Compd.* 2022, *912*, 165220.
[47] J. Brechtl, S. Chen, C. Lee, Y. Shi, R. Feng, X. Xie, D. Hamblin, A. M. Coleman, B. Straka, H. Shortt, R. J. Spurling, P. K. Liaw, *Metals* 2020, *10*, 10081101.
[48] P. Rodriguez, *Bull. Mater. Sci.* 1984, *6*, 653.
[49] R. Sharghi-Moshtaghin, S. Asgari, *Mater. Sci. Eng., A* 2008, *486*, 376.
[50] Y. Zhang, J. P. Liu, S. Y. Chen, X. Xie, P. K. Liaw, K. A. Dahmen, J. W. Qiao, Y. L. Wang, *Prog. Mater. Sci.* 2017, *90*, 358.
[51] N. Yurchenko, E. Panina, A. Tojibaev, V. Novikov, G. Salishchev, S. Zherebtsov, N. Stepanov, *J. Alloys Compd.* 2023, *937*, 168465.
[52] O. N. Senkov, J. Gild, T. M. Butler, *J. Alloys Compd.* 2021, *862*, 100627.
[53] T. M. Butler, O. N. Senkov, M. A. Velez, T. I. Daboiku, *Intermetallics* 2021, *138*, 107323.
[54] M. Wang, Z. Ma, Z. Xu, X. Cheng, *J. Alloys Compd.* 2019, *803*, 778.
[55] O. S. Bamisaye, N. Maledi, J. Van der Merwe, M. O. Bodunrin, *Int. J. Refract. Metals Hard Mater.* 2024, *121*, 106661.
[56] D. G. Kalali, S. Antharam, M. Hasan, P. S. Karthik, P. S. Phani, K. Bhanu Sankara Rao, K. V. Rajulapati, *Mater. Sci. Eng., A* 2021, *812*, 141098.
[57] Y. Su, F. Kong, F. H. You, X. Wang, Y. Chen, *Vacuum* 2020, *173*, 109135.
[58] A. N. Behera, R. Kapoor, A. Sarkar, *Int. J. Refract. Metals Hard Mater.* 2024, *122*, 106711.
[59] F. Zarghani, G. R. Ebrahimi, J. Taheri, H. R. Ezatpour, *Mater. Today Commun.* 2023, *37*, 107235.
[60] D. Lin, J. S. Han, Y. S. Kwon, S. Ha, R. Bollina, S. J. Park, *Int. J. Refract. Metals Hard Mater.* 2015, *53*, 87.
[61] W. Huang, S. Yin, X. Wang, R. Guo, Y. Wu, J. Qiao, *J. Mater. Res.* 2023, *38*, 1719.
[62] S. J. Sun, Y. Z. Tian, H. R. Lin, X. G. Dong, Y. H. Wang, Z. J. Wang, Z. F. Zhang, *J. Alloys Compd.* 2019, *806*, 992.
[63] D. Mosoma, D. Klenam, T. Maunganidze, M. Bodunrin, *Int. J. Adv. Manuf. Tech.* 2023, *126*, 2025.
[64] F. J. Humphreys, M. Hatherly, in *Recrystallization and Related Annealing Phenomena*, Elsevier, Oxford 2004.
[65] G. Meng, R. Gao, F. Liu, J. Yu, *Mater. Today Commun.* 2022, *33*, 104320.
[66] J. Antonaglia, X. Xie, Z. Tang, C. W. Tsai, J. W. Qiao, Y. Zhang, M. O. Laktionova, E. D. Tabachnikova, J. W. Yeh, O. N. Senkov, M. C. Gao, J. T. Uhl, P. K. Liaw, K. A. Dahmen, *JOM.* 2014, *66*, 2002.
[67] W. C. Hsu, T. E. Shen, Y. C. Liang, J. W. Yeh, C. W. Tsai, *Acta Mater.* 2023, *253*, 118981.
[68] E. I. Galindo-Nava, A. Perlade, P. E. J. Rivera-Díaz-Del-Castillo, *Model Simul. Mater. Sci. Eng.* 2014, *22*, 015009.
[69] X. Li, S. Deng, S. Wang, H. Song, S. Zhang, K. Wang, D. Ouyang, *Mater. Character.* 2021, *171*, 110749.
[70] D. l. Ouyang, X. Cui, S. q. Lu, H. m. Du, *J. Mater. Res. Technol.* 2020, *9*, 15662.
[71] C. B. Wu, H. Yang, X. G. Fan, Z. C. Sun, *Trans. Nonferrous Met. Soc. China* 2011, *21*, 1963.
[72] M. O. Bodunrin, L. H. Chown, J. W. Van Der Merwe, K. K. Alaneme, *Int. J. Adv. Manuf. Tech.* 2019, *104*, 3017.
[73] S. A. Sajjadi, A. Chaichi, H. R. Ezatpour, A. Maghsoudlou, M. A. Kalaie, *J. Mater. Eng. Perform.* 2016, *25*, 1269.
[74] W. Huang, X. Wang, J. Qiao, X. Shi, P. K. Liaw, Y. Wu, *Mater. Sci. Eng. A* 2024, *902*, 146634.
[75] Q. Zhao, F. Yang, R. Torrens, L. Bolzoni, *Materials* 2019, *12*, 12030457.
[76] B. Xiao, W. Jia, H. Tang, J. Wang, L. Zhou, *J. Mater. Sci. Technol.* 2022, *108*, 54.
[77] A. Amiri, S. Bruschi, M. H. Sadeghi, P. Bariani, *Mater. Sci. Eng., A* 2013, *562*, 77.
[78] X. M. Chen, M. T. Ning, H. W. Hu, Y. C. Lin, X. J. Zhou, J. Zhang, X. Z. Lu, J. Chen, Y. X. Liu, *Mater. Character.* 2023, *201*, 112916.
[79] N. Bibhanshu, A. Bhattacharjee, S. Suwas, *J. Alloys Compd.* 2020, *832*, 154584.
[80] K. Tang, Z. Zhang, J. Tian, Y. Wu, F. Jiang, *J. Alloys Compd.* 2021, *860*, 158541.
[81] M. Wang, Z. L. Ma, Z. Q. Xu, X. W. Cheng, *Scr. Mater.* 2021, *191*, 131.
[82] Z. D. Han, N. Chen, S. F. Zhao, L. W. Fan, G. N. Yang, Y. Shao, K. F. Yao, *Intermetallics* 2017, *84*, 153.

© 2024 The Author(s). Advanced Engineering Materials published by Wiley-VCH GmbH

15272648, 0, Downloaded from https://onlinelibrary.wiley.com/doi/10.1002/adem.202400538 by Olufemi Sylvester Bamisaye - South African Medical Research , Wiley Online Library on [07/08/2024]. See the Terms and Conditions (https://onlinelibrary.wiley.com/terms-and-conditions) on Wiley Online Library for rules of use; OA articles are governed by the applicable Creative Commons License

ARUA Centre of Excellence
Materials, Energy and Nanotechnology
Mini Conference

Theme: "MATERIALS, ENERGY AND NANOTECHNOLOGY"

19th August 2022

BOOK OF ABSTRACTS

ARUA African Research Universities Alliance

UK Research and Innovation

ARUA CENTRE OF EXCELLENCE IN MATERIALS, ENERGY & NANOTECHNOLOGY

AFRICAN M·R·S

Dominant softening mechanisms in hot worked refractory high entropy alloys: an overview

*Olufemi Sylvester Bamisaye, Nthabiseng Maledi, Josias Van der Merwe, Desmond Edem Primus Klenam and Michael Oluwatosin Bodunrin

[a]School of Chemical and Metallurgical Engineering, Faculty of Engineering and the Built Environment, University of the Witwatersrand, Johannesburg, South Africa

DSI-NRF Centre of Excellence in Strong Materials, University of the Witwatersrand, Johannesburg, South Africa

Academic Development Unit, Faculty of Engineering and the Built Environment, University of the Witwatersrand, Johannesburg, South Africa

Corresponding author: 2503285@students.wits.ac.za

The world's technological growth and development drive a persistent demand for new materials having excellent mechanical properties to fulfil several high temperature structural applications. Refractory high entropy alloys (RHEA) which comprise high-melting-point refractory elements, were introduced in 2010 as potential candidates for higher temperature structural materials due to their high hardness, high oxidation resistance, wear resistance, and high temperature strength. Understanding the thermomechanical processing of refractory high entropy alloys (RHEA) at higher temperatures is very important since it is an effective method of modifying the alloy's microstructure, properties, and shaping into final components. In conventional alloys, safe and unsafe softening mechanisms which control their deformation behaviour have been established. However, little is known about the deformation behaviour of RHEA owing to a limited number of research. This systematic review covers the softening controlling deformation behaviour in RHEA based on the studies available between 2010 to date. Emphasis is placed on whether the dominant softening mechanisms in RHEA differ from mechanisms reported in hot deformed conventional alloys, particularly nickel-based super alloys which are currently used in the intended high temperature applications.

Keywords: Softening Mechanism, Refractory High Entropy Alloy, Thermomechanical Processing, Flow Stress, Microstructural Evolution